

**GEOCHEMISTRY OF LAVAS FROM SOUTHEASTERN NICARAGUA AND OF  
MANTLE XENOLITHS FROM CERRO MERCEDES, COSTA RICA**

by

**FARA N. LINDSAY**

A Dissertation submitted to the  
Graduate School-New Brunswick  
Rutgers, The State University of New Jersey  
in partial fulfillment of the requirements  
for the degree of  
Doctor of Philosophy  
Graduate Program in Geological Sciences  
written under the direction of  
Dr. Michael J. Carr  
and approved by

---

---

---

---

New Brunswick, New Jersey

October, 2009

**ABSTRACT OF THE DISSERTATION**

**GEOCHEMISTRY OF LAVAS FROM SOUTHEASTERN NICARAGUA AND OF**

**MANTLE XENOLITHS FROM CERRO MERCEDES, COSTA RICA**

**By FARA N. LINDSAY**

Dissertation Director:  
Dr. Michael J. Carr

Lavas from southeastern Nicaragua were geochemically analyzed, including several from a volcano never before sampled, in order to better understand the relationship between the chemistry of the lavas and the physical parameters of the Central American arc, which include depth to the slab, distance from the trench, slab dip and the age of the downgoing slab. The analyses were done by x-ray fluorescence, by high resolution inductively coupled plasma mass spectrometry, and by thermal ionization mass spectrometry. The results show that the abundance of high-field strength elements in the lavas is particularly influenced by the depth to the slab underlying a volcano and the distance of the volcano from the trench. Additionally, the results show that decompression melting is an important process in the generation of these lavas.

The chemistry of mantle xenoliths from Cerro Mercedes, Costa Rica, were studied to elucidate the compositional and physical state of the mantle wedge underlying Central American. The composition of the mantle wedge is clarified through analyses of the whole rock; information about the physical state of the mantle is obtained from analyses of the minerals that constitute the xenoliths. The analytical

methods used for the whole rock chemistry were x-ray fluorescence and high resolution inductively coupled plasma mass spectrometry. Electron probe microscopy and laser ablation inductively coupled plasma mass spectroscopy were used to analyze the minerals. Results show that the mantle wedge composition is predominantly peridotite (~65% modal olivine) that has experienced variable degrees of modification by melt- and fluid- rock reactions, with pockets of cumulate pyroxenite. Although the majority of the peridotites are multi-phase residues, one sample, CM52, may be a first-stage residue. The xenoliths are spinel facies rocks, which correspond to pressures between 1 – 2.5 GPa, and have equilibrium temperatures ranging from 860°C – 1030°C at 1 GPa, which place them between 30km and 85km within the mantle. The potential temperature of the system, based on whole rock major oxide modeling, is 1580°C. Estimated values for the oxidation state of the mantle range from  $\Delta f_{O_2}^{FMQ}$  +0.9 -  $\Delta f_{O_2}^{FMQ}$  +3.25 for the peridotites and up to  $\Delta f_{O_2}^{FMQ}$  +4.05 for the pyroxenites.

## **Acknowledgement and Dedication**

I would like to acknowledge everyone who supported me during my years of graduate school. This includes colleagues, teachers, friends and relatives. Particularly, I thank Michael J. Carr, my advisor, for his patience and understanding, and William J. Lindsay, my husband, without whom this would never have come to pass.

I dedicate this work to my father, Raymond C. Michalski, who believed in my academic ability long before I chose this path.

## Table of Contents

Abstract	ii
Acknowledgement and Dedication	iv
Table of Contents	v
List of tables	vi
List of figures	viii
Introduction	1
Chapter 1 – Geochemistry of lavas from southeast Nicaragua	4
Chapter 2 – Decompression melting behind a major offset of the volcanic front of Nicaragua: Concepción and Maderas volcanoes	86
Chapter 3 – Whole rock geochemistry of the host basalt and xenoliths from Cerro Mercedes, Costa Rica	122
Chapter 4 – Geochemistry of mineral separates from Cerro Mercedes xenoliths	194
Appendix A	268
References	278
Curriculum Vitae	288

## Lists of tables

Table 1.1	Newly collected sample data	69
Table 1.2	Previously acquired samples	70
Table 1.3	Major oxides of new samples	72
Table 1.4	Major oxides of previous samples and literature values	73
Table 1.5	Trace elements of all lavas	75
Table 1.6	Isotope values	83
Table 1.7	Samples used from CAgeochem database	84
Table 1.8	Trace element data from Bolge	85
Table 2.1	Major oxide data for Ometepe lavas	117
Table 2.2	Trace element data for Ometepe lavas	118
Table 2.3	Isotope values for Ometepe lavas	121
Table 3.1	Cerro Mercedes Sample Catalog	183
Table 3.2	Major oxides of mantle peridotite from literature	186
Table 3.3	List of analyzed samples	186
Table 3.4	Major oxides, trace elements and isotopes of host basalt	187
Table 3.5	Modal analysis of Cerro Mercedes xenoliths	188
Table 3.6	Major oxides, trace elements and isotopes of xenoliths	189
Table 3.7	Equilibrium temperatures	192
Table 3.8	Major oxide modeling results	193
Table 4.1	Olivine compositions in CM xenoliths	235
Table 4.2	Spinel compositions in CM xenoliths	243
Table 4.3	Orthopyroxene compositions in CM xenoliths	247
Table 4.4	Clinopyroxene compositions in CM xenoliths	251

Table 4.5	Calculated oxygen fugacity	258
Table 4.6	Mass balance calculations	259
Table 4.7	Mixing calculations	261
Table 4.8	Comparison of mass balance and mixing calculations	264
Table 4.9	Comparison of mineral modal weight percents	265
Table 4.10	Mixing calculations with Sarapiquí basalt	266

## List of figures

Figure I.1	Map of Central America	32
Figure I.2	Geologic map of Central America	33
Figure I.3	Map of Quaternary volcanoes of Central America	34
Figure I.4	Geochemical variations along Central America	35
Figure 1.1	Nd and Sr isotopes of Central America	36
Figure 1.2	Telica mixing trend	37
Figure 1.3	Map of study area, SE Nicaragua	38
Figure 1.4	MgO vs. SiO <sub>2</sub> ; Alkalies vs. SiO <sub>2</sub>	39
Figure 1.5	FeO* vs. MgO; AFM diagram	40
Figure 1.6	LS5 faux color thin section map	41
Figure 1.7	Mullen diagram; Ti discrimination diagrams	42
Figure 1.8	Rare earth element spidergrams	43
Figure 1.9	Extended trace element spidergrams	44
Figure 1.10	Sediment mixing trends	45
Figure 1.11	Variations in fluid contribution	46
Figure 1.12	Fractional crystallization in Las Sierras and Mombacho lavas	47
Figure 1.13	Amphibole melting	48
Figure 1.14	Ba/La vs. La/Yb; Ba/La vs. Na <sub>2</sub> O	49
Figure 1.15	PIRL diagrams	50
Figure 1.16	Sm <sub>N</sub> /Gd <sub>N</sub> vs. La <sub>N</sub> /Ce <sub>N</sub> ; Dy <sub>N</sub> /Yb <sub>N</sub> vs. La <sub>N</sub> /Ce <sub>N</sub>	51
Figure 1.17	Isotope systematics	52
Figure 1.18	DSDP sediment layer mixing and trace elements	53
Figure 1.19	Ca vs. Sr; mixing arrays	54

Figure 1.20	Mixing with altered lower MORB	55
Figure 1.21	Map of segments in Nicaragua and Costa Rica	56
Figure 1.22	Map of Nicaragua and Costa Rica	57
Figure 1.23	Extended trace element spidergram comparisons	58
Figure 1.24	Rare earth element spidergram comparisons	59
Figure 1.25	Regional geochemical variations	60
Figure 1.26	Mixing array comparisons	61
Figure 1.27	Fluid flux comparisons	62
Figure 1.28	Cs/Th vs. Yb <sub>N</sub> /La <sub>N</sub>	63
Figure 1.29	Flux melting vs. decompression melting	64
Figure 1.30	Th/Y vs. U/La	65
Figure 1.31	Ca vs. Sr; Ba/Th vs. Sr/Th	66
Figure 1.32	Mixing array comparisons	67
Figure 1.33	Cs/Yb vs. Th/Yb	68
Figure 2.1	Map of Ometepe	103
Figure 2.2	Regional variation along the Central American arc	104
Figure 2.3	Local variation of high field strength elements	104
Figure 2.4	Central American segments	104
Figure 2.5	Geometry of dip angle and depth to slab	105
Figure 2.6	K <sub>2</sub> O vs. SiO <sub>2</sub> ; AFM diagram; M10 hand sample photo	106
Figure 2.7	Fenner diagrams	107
Figure 2.8	Harker diagrams	108
Figure 2.9	Ce vs. Ce*	108
Figure 2.10	Extended trace element spidergram comparisons	109

Figure 2.11	Rare earth element spidergram comparisons	110
Figure 2.12	Isotope ratios	111
Figure 2.13	Mixing arrays	112
Figure 2.14	Physical parameters	113
Figure 2.15	$\text{Na}_{6.0}$ vs. distance; $\text{Na}_{6.0}$ vs. La/Yb	114
Figure 2.16	Ba/La vs. La/Yb	115
Figure 2.17	Zr vs. Nb	116
Figure 2.18	$\text{La}_N$ vs. distance; $\text{Yb}_N$ vs. distance	116
Figure 3.1	Mantle xenolith suites in the circum-Pacific	148
Figure 3.2	Geologic map of northeast Costa Rica	148
Figure 3.3	Cr# vs. Mg# of island arcs	149
Figure 3.4	Pt/Pd vs. $\text{Al}_2\text{O}_3$ of arc peridotites	149
Figure 3.5	Frey & Prinz GroupI and GroupII diagrams	150
Figure 3.6	Tectonic map of Central America	151
Figure 3.7	Topographic map of north Costa Rica	152
Figure 3.8	Geologic maps of the Miocene arc	153
Figure 3.9	LaBas diagram of host basanite	154
Figure 3.10	Fenner diagrams of host basanite	155
Figure 3.11	Harker diagrams of host basanite	156
Figure 3.12	Rare earth element spidergram, Ce vs. Ce*; Eu vs. Eu* of host basanite	157
Figure 3.13	Extended trace element spidergram, Cs/Pb vs. Ba/La of host basanite	158
Figure 3.14	Isotopes of host basanite	159
Figure 3.15	Embayment reaction area of CM50 photo	160

Figure 3.16	Veinlet in CM63 photo	161
Figure 3.17	Vermicular spinel in CM52 photo	162
Figure 3.18	Harker diagrams of xenoliths	163
Figure 3.19	Fenner diagrams of xenoliths	164
Figure 3.20	Extended trace elements spidergrams of xenoliths	165
Figure 3.21	Rare earth element spidergrams of xenoliths	166
Figure 3.22	$Gd_N/Lu_N$ vs. $La_N/Lu_N$ of peridotites	167
Figure 3.23	$Sr/Ti$ vs. $La_N/Gd_N$ of peridotites	167
Figure 3.24	Peridotite population discrimination	168
Figure 3.25	Sr isotope histograms	169
Figure 3.26	Sr and Nd Isotope comparisons	170
Figure 3.27	Lead isotope comparisons	171
Figure 3.28	Equilibrium temperatures	172
Figure 3.29	Host basanite trace element comparisons	173
Figure 3.30	$SiO_2$ vs. Mg# of xenoliths	174
Figure 3.31	$Tb/Yb$ vs. $Al_2O_3$ of peridotites	175
Figure 3.32	$FeO$ vs. $MgO$ modeling space	176
Figure 3.33	$FeO^*$ vs. $MgO$ modeling space	176
Figure 3.34	$Al_2O_3$ vs. $MgO$ modeling space	177
Figure 3.35	$SiO_2$ vs. $MgO$ modeling space	178
Figure 3.36	T-P-D diagram	179
Figure 3.37	P-T diagram for potential temperature	180
Figure 3.38	Lead isotopes compared to Galapagos domains	181
Figure 3.39	Summary of the mantle	182

Figure 4.1	Cr# vs. Mg# of arc peridotites	214
Figure 4.2	Oxygen fugacity buffers	214
Figure 4.3	Oxygen fugacity of spinel Iherzolite assemblages	215
Figure 4.4	Fo contents of xenolith olivine	216
Figure 4.5	Olivine grain line scans	217
Figure 4.6	NiO vs. Mg# of minerals	218
Figure 4.7	Compositional variation of spinel	218
Figure 4.8	Spinel series trigrams	219
Figure 4.9	Mg#(sp) vs. Cr#(sp)	219
Figure 4.10	$\text{Fe}^{3+}/(\text{Al}+\text{Cr}+\text{Fe}^{3+})$ (sp) vs. Mg# (sp)	220
Figure 4.11	Cr# (sp) vs. Fo (ol)	221
Figure 4.12	Cr# (sp) vs. Mg# (sp)	222
Figure 4.13	$\text{Fe}^{3+}/\sum \text{Fe}$ (sp) vs. Fo (ol); Mg# (sp) vs. Fo (ol)	223
Figure 4.14	Mg# (opx) vs. Fo (ol)	224
Figure 4.15	Orthopyroxene end member trigram	224
Figure 4.16	Orthopyroxene line scans	225
Figure 4.17	Clinopyroxene end member trigram	226
Figure 4.18	$\text{Cr}_2\text{O}_3$ (cpx) vs. $\text{Al}_2\text{O}_3$ (cpx)	226
Figure 4.19	$\text{TiO}_2$ vs. Mg#; $\text{Na}_2\text{O}$ vs. Mg#	227
Figure 4.20	$\text{Na}_2\text{O}$ (cpx) vs. Cr# (sp)	227
Figure 4.21	Clinopyroxene line scans	228
Figure 4.22	Clinopyroxene rare earth element spidergram	229
Figure 4.23	Clinopyroxene extended trace element spidergram	229
Figure 4.24	Orthopyroxene rare earth element spidergram	230

Figure 4.25	Orthopyroxene extended trace element spidergram	230
Figure 4.26	Estimated oxygen fugacity histogram	231
Figure 4.27	Oxygen fugacity vs. equilibrium temperature	232
Figure 4.28	Oxygen fugacity vs. Cr# (sp)	232
Figure 4.29	$\text{Fe}^{3+}/\sum \text{Fe}$ (sp) vs. Cr# (sp)	233
Figure 4.30	$\text{Al}_2\text{O}_3$ (pyx) vs. Cr# (sp)	233
Figure 4.31	Ti (cpx) vs. Zr (cpx)	234
Figure 4.32	Ti (cpx) vs. Dy (cpx)	234

## Introduction

### Background

Beginning in the late 19<sup>th</sup> century and into the early 20<sup>th</sup> century, geologic research in Central America received impetus from political interests such as Napoleon's American policy and the construction of the Panama Canal. In the mid 20<sup>th</sup> century, exploitation of ore deposits and fossil fuels extended geological research in Central America and by 1956, both El Salvador and Nicaragua established national geological services (Weyl, 1980; Bundschuh & Alvarado, 2007). The Central American volcanic arc a worthwhile location to study chemical recycling of oceanic lithosphere at convergent plate margins, due in part to the young, thin crust of the Caribbean Plate, which leaves the arc volcanics relatively uncontaminated as they rise through it. Indeed, Costa Rica and Nicaragua are focus areas for study in the Subduction Factory community, an initiative associated with the NSF MARGINS program whose mission is to understand the processes governing global continental margin evolution.

Along the western part of Central America, the active quaternary volcanic system stretches 1100km from northern most Guatemala through Costa Rica. The subduction of the Cocos plate under the Caribbean Plate causes the volcanic belt whereas the subduction of the Nazca Plate under the Caribbean Plate causes a less active volcanic belt in Panama (figI.1). Weyl (1980) listed 56 important volcanic vents of Central America; 18 of which are in Nicaragua (van Wyk de Vries, 1993). Traditionally, the chain was broken into two large sections based on the age of the basement rocks: the north, which comprises Guatemala through the northern part of the Nicaraguan Depression, and the south, which extends into Panama (figI.2).

Stoiber and Carr (1973) and Carr et al. (1984) defined eight segments of the arc

based upon transitional areas where the line of volcanoes deviates or changes strike (figI.3). Nicaragua is broken into two segments, the northwest and the southeast, by a transitional area (transverse break) cutting through Nejapa – Chiltepe (Stoiber & Carr, 1973; Weyl, 1980). Costa Rica has three transverse breaks, the middle of which abuts Arenal volcano. The geochemistry suggests this segmentation through variations in the ratios of Ba/La (Carr et al., 1990; Patino et al., 2000) and La/Yb (Carr, 1990) as well as decreases in alkalis (McBirney, 1969; Carr et al., 1984) (figI.4). In fact, as instrumentation becomes more accurate and more sensitive to even minute concentrations, geochemical data can be used to discern greater amounts of chemical variability on both a regional and local scale within the Central American active volcanic arc (Weyl, 1980).

### This Work

The subduction cycle input includes subducting oceanic lithosphere, continent derived sediment deposited into the trench and crust, marine sediments and both oceanic and meteoric waters, the composition of which can be directly measured. Some of the output compositions, such as volcanic rocks, tephra and gasses can also be directly measured. The composition of material transfers and petrochemical reactions occurring on the subducting lithosphere, within the mantle wedge and within magma chambers below a given volcano, on the other hand, cannot be measured directly and must be inferred using experimental constraints. Additionally, the composition of rocks within areas of such reactions, such as the mantle wedge, cannot be directly sampled unless material is brought to the surface as in the case of mantle xenoliths in lavas.

This work addresses output materials by examining lava samples from along strike of the Central American volcanic front (CAVF). Newly analyzed lavas by the

author are discussed and compared to lava analyses extant in a Central American database (Carr & Rose, 1987; Carr et al., 2003). In particular, lavas from southeast Nicaragua will be compared to adjacent segments along the CAVF including northwest Nicaragua and Costa Rica. Attention is given to both regional and local geochemical variations along the volcanic front as well as factors controlling the variations.

Analyses of mantle xenoliths from Cerro las Mercedes in northern Costa Rica, which include both peridotites and pyroxenites, are used to examine the composition of the mantle wedge underlying Central America. This composition can then be tested as the source of both lavas along the active front and the host basalt, which brought the xenoliths to the surface. Additionally, the mantled xenoliths may shed light upon pressure, temperature and oxygen fugacity within the mantle wedge, all of which have direct influence on mantle dynamics.

### **Format**

This dissertation is divided into 4 chapters: chapter one concentrates on lavas from the southeast Nicaragua segment and how they compare to lavas from adjacent segments; chapter two, designed to stand alone, focuses specifically on lavas from Concepción and Maderas volcanoes in southeast Nicaragua; chapter three examines whole rock composition of both the mantle xenoliths and the host basalt; chapter four considers the chemistry of separate mineral phases composing the mantle xenoliths. Each chapter will include its own background, results, discussion and conclusions. Appendices will detail analytical techniques used throughout this research as the techniques and methods overlap. Figures and tables for each chapter are directly after the text of that chapter; all references are at the end. Please note that symbols used in figures are different for each chapter due to the different scope of discussed areas.

## Chapter One – Geochemistry of lavas from Southeast Nicaragua

### Background

Subduction zones are a site of fundamental material transfer between the earth's mantle and crust. Such margins are the principal sites of both continental crust generation and oceanic crust recycling (White, 1998). Additionally, such margins are featured in models for the development of chemical heterogeneities in the upper mantle, for continental crust generation and for crust/mantle recycling (Hawkesworth et al., 1993; Hart & Staudigel, 1989).

The chemical composition of magma depends on the composition of the parent material, the degree of melting, fractionation and interactions between magma and country rock (Faure, 1986). Whereas island arc basalts (IAB) share similar major element composition with mid-ocean ridge basalts (MORB) and oceanic island basalts (OIB) (Plank & Langmuir, 1988), IABs are distinctive in certain minor and trace elements. Subduction related rocks have low abundances of high field strength elements (HFSE) relative to large ion lithophile elements (LILE) and rare earth elements (REE). These element relationships suggest fluid involvement in IAB genesis (Arculus, 1994), a relative depletion in the mantle wedge prior to melting (Thirlwall et al., 1994) and may describe the degree of dehydration on the subducting slab (Noll et al., 1996). Both high degrees of partial melting and fluid loss, during dehydration reactions within the subducting slab and its sediment, are reasons cited for the anomalously low HFSE abundances.

HFSE, those with high charge to ionic radius ratios (V, Ti, Zr, Nd, Ta, Hf), are compatible during melting (Woodhead et al., 1993) meaning that low abundances suggest

either melting of a more depleted source or a higher degree of melt. Rutile, which is stable in the mantle environment, retains HFSEs and may further suppress the flux of HFSEs relative to LILEs to the mantle wedge (Brenan et al., 1995). Experimentally, Stalder et al. (1998) found it impossible to produce a depleted HFSE signature in an IAB source with a metasomatizing fluid released from a rutile free source. They concluded that HFSE depletions could originate from a selective enrichment of the mantle wedge in low field strength elements (LFSE), such as Ba and Sr, and LREE by aqueous fluids derived from a rutile-bearing subducted slab. This indicates that either melts or fluids in equilibrium with rutile in the subducting slab are the cause of the described trace element characteristics (Foley et al., 2000).

Determining whether aqueous fluids or melts are generated during the subduction process becomes a question of the nature of the thermal regime under the volcanic front. Evidence of the decoupling of chalcophile and siderophile elements from lithophile elements favors a hydrous fluid flux from the slab rather than a slab melt (Noll et al., 1996). As oceanic crust generated at mid-ocean ridges travels toward subduction zones, hydrothermal alteration enriches the crust in siderophile/chalcophile elements such as Pb, As, Sb and Sn and LILEs such as Cs, Rb and Sr. During subduction, magmatic processes should not affect ratios of chalcophile/lithophile, such as Pb/Ce, whereas fluid influx would increase this ratio as liberated fluids from dehydration reactions within the subducting slab and its sediments preferentially transport relatively fluid-mobile elements (like Pb) to the mantle wedge (Noll et al., 1996). Peacock et al. (2005) calculate slab P-T paths such that, for an olivine-mantle rheology, subducted sediments and the upper most subducting oceanic crust undergo partial melting at depths of 65 – 100km, which corresponds to the depth of arc source magma. In fact, there are notable occurrences where slab melting is

indicated; for example, areas of young, hot subducting slab (Peacock et al., 1994) and areas of adakites (Aleutians; Yogodzinsky et al., 2000; Patagonia; Gorring et al., 2001) where the edge of the subducting plate is warmed by mantle flow.

A high REE/HFSE ratio is typical of IABs. REEs are a chemically coherent group in which the light rare earth elements (LREE) are systematically more incompatible than the heavy rare earth elements (HREE). That is, the LREEs are more prone to go into the melt phase than a crystalline phase. While REE profiles are variable between arcs and may display large ranges within any given arc (Thirlwall et al., 1994; White & Dupré, 1986), the enrichment of LREE relative to HREE in IABs is further evidence supporting the role of slab flux in arc magma genesis (McCulloch & Gamble, 1991). Thirlwall et al. (1994) argue that high LREE/HFSE ratios indicate a LREE-enriched slab component with variations in the LREEs themselves a function of partial melting processes. Hawkesworth et al. (1993) separate REE data into two categories: the first has a low Ce/Yb ratio with the two elements varying together; the second has higher and more variable Ce but similar Yb abundances. These categories, along with isotopic and tectonic data, show different trends in REE profiles of source rocks and/or in the bulk distribution coefficients and degree of melting.

As with trace and minor elements, radiogenic isotope signatures of IABs are distinctive with respect to the chemical domains of the mantle. Volcanic rocks in island arcs and along continental margins show a wide range of  $^{143}\text{Nd}/^{144}\text{Nd}$  and  $^{87}\text{Sr}/^{86}\text{Sr}$ . Whereas Sr-Nd systematics overlap the MORB and OIB fields to varying degrees (White, 1998), IABs show lower  $^{143}\text{Nd}/^{144}\text{Nd}$  and higher  $^{87}\text{Sr}/^{86}\text{Sr}$  ratios than does MORB (fig1.1A; Faure, 1986). The enrichment of oceanic crust by seawater causes the higher Sr/Nd ratio seen in IABs. Such enrichment affects Sr to a greater degree than Nd due to its

higher degree of both solubility and incompatibility in basaltic regimes unlike the behavior in mantle minerals, where Nd is more incompatible than Sr.

Island arc lavas have high  $^{207}\text{Pb}/^{204}\text{Pb}$  and  $^{206}\text{Pb}/^{204}\text{Pb}$  ratios relative to MORB (Hawkesworth et al., 1994) and low ratios relative to OIB (fig1.1B; Hofmann, 1997). This reflects the radiogenic isotopic composition of oceanic sediments that are recycled within subduction zone environments. In a similar manner, the budget of  $^{10}\text{Be}$  in arc lavas is largely determined by the subduction component. Formed by spallation of O and N in the atmosphere,  $^{10}\text{Be}$  is readily absorbed onto oceanic clay-rich sediment and, combined with its short half-life (1.5Myr), provides a tracer of sediment recycling along subduction zones (Morris et al., 1990).

### **Central American Volcanic Output Controls**

Some variables that control volcanic output along the Central American volcanic chain include changes in continental crustal thickness and composition, slab dip, the composition of the mantle wedge, fluids generated from the subducted slab by dehydration and/or melting, and the structure and composition of the subducted plate (Carr, 1984; Carr et al., 1990; Walker et al., 2001; You & Gieskes, 2001). Although there is widespread acceptance that these components play key roles in magma formation (Faure, 1986; McCulloch & Gamble, 1991; Hawkesworth et al., 1993; Arculus, 1994; Hawkesworth et al., 1994), the nature of each component, the amount each contributes and how they interact remain important questions.

There are, however, some constraints regarding these variables along the Central American arc. Crustal thickness is greatest in northern Central America (50km; Carr, 1984) which has Paleozoic crystalline basement and plutonites (Weyl, 1980) whereas the Cretaceous oceanic-type crust in southern Central America thins to less than 40km under

Nicaragua (Carr, 1984; Walker et al., 2001, Cameron et al., 2002) and regains thickness into central Costa Rica. In a similar manner, the dip of the subducting slab as defined by the top of the Waditi-Benioff zone is steepest under Nicaragua ( $84^\circ$ ; Protti, 1995) and shallows to both the northwest ( $45^\circ$ - $50^\circ$  beneath southeast Guatemala and western El Salvador; Carr, 1976) and the southeast ( $60^\circ$  beneath central Costa Rica; Protti, 1995). Although there is no consensus as to the exact mechanism of fluid release from the subducting slab, Rüpke et al. (2002) show that the intensity of fluid flux and the depth from which it originates may be dependent upon the incoming plate's composition and the degree of faulting on the plate. How trace elements move from the fluid to the mantle wedge above the slab is also unresolved, yet there is consensus that the mantle wedge is the site of melting that ultimately produces arc magmas. The composition of the mantle source also changes with northwestern Nicaragua having a mid-ocean ridge basalt (MORB) type source whereas central Costa Rica has a source similar to ocean-island basalt (OIB) (Carr et al. 1990; Leeman et al., 1994). Perhaps most well characterized is the composition of the sediments on the downgoing slab.

Analyses of DSDP drill core 495 (Carr et al., 1990; Patino et al., 2000), which is outboard of Guatemala, clarify the composition of the downgoing sediments and show a distinct three-part slab stratigraphy. The base of the section is mid-ocean ridge basalt (MORB) and altered oceanic crust (AOC). Carbonate ooze (CS) overlies the basalt and hemipelagic mud (HS) overlies the ooze. MORB and AOC sections, sampled in the eastern equatorial Pacific, contain an oxidized and alkali-enriched volcanic section, a fractured, hydrothermally altered and brecciated pillow basalt and hydrothermally altered upper and lower dike sequences (Alt et al., 1996). The two sediment packages have distinct geochemistries controlled by carbonate-rich biogenic sediments, detrital material and

organic matter (Patino et al., 2000). The compositional distinctions of the sediment layers allow the use of element ratios to discern both local and regional variations in the amount of each sediment component in the volcanic products along the Central American arc.

Chemical proxies measuring the flux intensity of the combined sediment sections are based upon those element ratios that are relatively constant across the two sediment layers. These include ratios of barium to lanthanum, (Ba/La), (Carr et al., 1990) and ratios of uranium to thorium, (U/Th), (Patino et al., 2000). Ratios of elements for which the two layers have contrasting abundances describe local variations due to varying the abundances of each sediment type. These include Ba/Th, which signifies the carbonate ooze, and U/La, which represents the hemipelagic mud (Patino et al., 2000). Boron, due to its high concentration in sea water and adsorptive behavior, is enriched in the AOC and upper-most sediments making it a good tracer of the subducted component (Morris et al., 1990). Combined with the cosmogenic isotope  $^{10}\text{Be}$ , which is highly concentrated in the upper most hemipelagic sediments, the relative influence of these two subduction components is measurable. Additionally, because it has a short half-life, volcanics with high  $^{10}\text{Be}$  require a recently incorporated subduction component (Morris et al., 1990; Edwards et al., 1993). In a similar manner, Leeman et al. (1994) use ratios of B/La to show a correlation between the magnitude of subducted sediment flux and regional geochemical variations along the Central American volcanic arc.

Use of Ba/Th and U/La tracers in prior work by Patino et al. (2000) at Telica volcano in northwestern Nicaragua revealed a local variation that defined a binary mixing array parallel to the mixing array between the carbonate and hemipelagic sediments (fig1.2). This suggests that the subducting plate's stratigraphy is geochemically recognizable in young volcanoes (Patino et al., 2000). Telica is a complex made of several

relatively small vents. Larger centers, like Masaya and San Cristóbal, have larger underlying magma chambers, which, in turn, allow longer residence time for magma and a greater opportunity for magma mixing (Walker et al., 1993). It may be that the mixing in the large complex of Masaya in southeastern Nicaragua obscures the systematics of separate sediment signatures. At the same time, Masaya volcano defines the global maximum of Be isotopic ratio (Morris et al., 1990) - a clear indication of the hemipelagic sediment signature. Of interest, then are the questions of whether lavas in southeastern Nicaragua reflect the subducting plate's stratigraphy and if so, whether there are local variations such as those in the northwest.

### **Setting**

The samples of southeastern Nicaragua included in this study are lavas from the following locations: Nejapa and Granada alignments, both of which are non-parasitic cinder cone fields that are localized in zones of extension, the former marking the boundary between the northwest and southeast segments (Walker, 1984); Masaya/Las Sierras, an extensive caldera formed by Plinian and ignimbrite deposits (van Wyk de Vries, 1993); Apoyo, a caldera that sits atop an older volcanic center (Sussman, 1985); Mombacho, a composite stratovolcano located southeast of the Granada alignment (Ui, 1972); Zapatera, a shield-like construct located within Lake Nicaragua (van Wyk de Vries, 1993); and Concepción and Maderas volcanoes, stratovolcanoes that make up Isla de Ometepe, also within Lake Nicaragua, which will be discussed in further detail in the next chapter (van Wyk de Vries, 1993; Borgia & van Wyk de Vries, 2003) (fig1.3). Fifteen new samples (table1.1) supplement previous samples (table1.2), some of which were re-analyzed for trace element data. Physical characteristics of the volcanoes in SE Nicaragua have been described by McBirney and Williams (1965), Ui (1972), Weyl (1980), Sussman

(1985), Hradecky (1987), van Wyk de Vries (1993), Walker et al. (1993), Rymer et al. (1998) and Borgia & van Wyk de Vries (2003), among others, and will not be considered in this thesis. Instead, the focus will be on the chemistry of lavas from the area (tables 1.3 - 1.6) and local variations within them and the geochemical regional variations by contrasting southwestern Nicaragua with the adjacent arc.

## Results

The major oxides display the normal relationships expected for arc volcanics. Bulk rock compositions have SiO<sub>2</sub> concentrations ranging from basaltic to dacitic (fig 1.4). The most evolved samples (low MgO, high alkalis) indicate fractional crystallization. The high weight percent of FeO\* (fig 1.5A) evident in Masaya volcano, shared by the closely related Las Sierras samples, some Nejapa and Apoyo samples, suggest a low-pressure fractionation trend. Most samples are tholeiitic on an AFM plot (fig 1.5B; Irvine and Baragar, 1971).

Note that one outlier, LS5 (open green circle), is anomalously high in MgO for Central American volcanics. A vesicular basalt with a felty groundmass of plagioclase crystals, it contains abundant olivine and clinopyroxene phenocrysts (27.5 and 24.0 modal wt%, respectively; fig 1.6A) and 2 grains of quartz. This highly magnesian basalt (15.58 MgO wt%) may have accumulated olivine by crystal settling. However, the presence of quartz as well as abundant olivine suggests that the olivine and perhaps the clinopyroxene phenocrysts may indeed be xenocrysts. Many of the olivine and clinopyroxene crystals are normally zoned (fig 1.6B), responding to changes in the magmatic environment that lead to disequilibrium during crystal growth, such as temperature variations. Some olivines exhibit reversed zoning, suggesting diffusion or a reheating event after assimilation. The significance of this particular sample is presently

unknown.

Also of note are two groups of lavas, Nejapa ND and Granada ND (unfilled symbols), that bear a chemical resemblance to MORB when plotted on a diagram categorizing tectonic regimes (fig1.7A). Walker (1984) called these MORB-like lavas NG lavas, based on their sampling location in the Nejapa and Granada alignments. They were originally defined as lavas with a weight%  $\text{TiO}_2 \geq 1$ . Subsequently, Reagan et al. (1994) defined them as having  $\text{Ti}/\text{K} \geq 2$  (fig1.7B). This distinction is made because, as shown in fig1.6A, these lavas, represented by unfilled symbols, do not necessarily have the highest amount of  $\text{TiO}_2$  in their composition. They do, however, have the lowest concentration of  $\text{K}_2\text{O}$  (figure 1.7C) indicating a high degree of partial melting (Tatsumi, 1997). The NG samples also exhibit higher Cr and  $\text{Yb}_{\text{N}}/\text{La}_{\text{N}}$  contents than their HFSE depleted counterparts (fig1.7D). Higher Cr reflects either a more primitive mantle source remaining relatively unmodified by mantle processes (Walker, 1984) or a lack of olivine fractionation (Best, 1982) whereas higher  $\text{Yb}_{\text{N}}/\text{La}_{\text{N}}$  indicates more extensive melting, which is consistent with lower  $\text{K}_2\text{O}$  concentration. Additionally, not all volcanic centers sampled have two populations of lavas in regard to Ti and K abundance. In southeast Nicaragua, they are found in the Nejapa and Granada alignments, Apoyo caldera and on Zapatera.

The most obvious feature of the trace element data for the majority of samples is enrichment in light rare earth elements (LREEs) (fig1.8a, b) and elevated large-ion lithophile element (LILE) concentrations (fig1.9a), both signatures of island-arc lavas. Small europium (Eu) anomalies occur in the Las Banderas samples (pink crosses in fig1.8a) and indicate higher degrees of plagioclase fractionation. Of note is the unusual pattern of relative enrichment in the heavy rare earth elements (HREEs) in lavas having

$\geq 52$  wt% SiO<sub>2</sub> (fig1.8a).

In contrast, the NG lava compositions show flat to depleted LREEs (fig1.8c). Additionally, the NG lavas do not show the same extent of enrichment in the LILEs (fig.1.9b) as do the other lavas. Significantly, the NG lavas show no relative depletion of high field strength elements (HFSEs); unusual for subduction zone lavas. Feigenson & Carr (1993) argue that the shape of the REE patterns and relatively high HFSEs of these lavas indicates their derivation from the remelting of enriched veins within a heterogeneous mantle. In fact, the lack of HFSE depletion is more consistent when speaking of these unusual lavas than their Ti or K content. Thus, they are better termed ND lavas (non-HFSE depleted) and will be referred to as such for the duration of this work (symbol legends will be notated as ND).

Plots of trace element ratios used as proxies for slab signature reveal local and regional variations along the arc. The local variation is clearest in Ba/Th vs. U/La space, which shows the estimated relative contribution of the two subducting sediment types (fig1.10A). Most lavas plot near a line connecting HS and mantle/oceanic crust (EM, DM, AOC), suggesting a mixing between HS and a mantle component. The ND lavas plot closer to the mantle and have a larger CS contribution, whereas the other lavas have a larger HS contribution.

Regionally, Ba/La vs. U/Th space represents the relative contribution of subducting slab sediments and mantle/ oceanic (fig1.10B). The southeastern lavas that have higher Ba/La ratios show a larger slab influence. The ND lavas contain a smaller overall sediment signal, lower values of both Ba/La and U/Th, and lie closer to mantle concentrations.

The ratio Cs/Th shows local hydrous fluid variation because Cs is an element

easily mobilized by fluids but only slightly more incompatible in melts than Th, with which it has similar partition coefficients for most mantle minerals (fig1.11A). Although all areas have some degree of variability, Nejapa and Apoyo have the largest variation as well as having lavas with the lowest Cs/Th. ND lava samples show consistently lower Cs/Th and U/La than HFSE depleted samples from the same volcanic centers. The difference in Cs/Th amongst the different volcanic complexes suggests a variation in the fluid flux along this segment of arc with Masaya having a larger influence from fluid mobile elements. Both the carbonate and hemipelagic sediments have similar Cs/Th (fig1.11A, B), suggesting that the variation of Cs/Th in the lavas is due to differential contributions from a hydrous fluid phase.

Variation is also seen in Cs/Th vs.  $\text{Yb}_N/\text{La}_N$  space (fig. 1.11B). Again, lavas having higher concentrations of hydrous fluid mobile elements (higher Cs/Th ratio) trend toward the sediments, which have similar Cs/Th. In contrast, the lavas with little hydrous fluid influence have higher  $\text{Yb}_N/\text{La}_N$  ratios, indicative of a higher concentration of compatible elements. This may suggest a higher degree of melt of the source mantle, or previous episodes of melting that depleted the source (Carr et al., 1990). Either way, whereas the majority of samples trend toward the sediment endmembers, the ND lavas trend toward a higher Yb/La with lower hydrous fluid input.

### ***Major Oxides***

It is clear from the major oxides (figs1.4, 1.5) that varying degrees of evolution occur in the lavas both along the southeastern Nicaraguan volcanic arc and within separate centers. Observations by McBirney & Williams (1965), Ui (1972) and Weyl (1980), among others, of the same volcanic center erupting basaltic through dacitic volcanics suggests that differentiation is normal for the Central American arc. The Las

Banderas - Las Sierras samples, which are a dark andesitic to dacitic ignimbrite deposit from either a proto-Masaya caldera (van Wyk de Vries, 1993; Rymer et al., 1998) or a postulated vent lying under Lake Managua (McBirney & Williams, 1965), show fractional crystallization whereas Masaya samples cluster together (fig1.12A). The fractionated samples may show temporal changes no longer apparent due to the shallow magma chamber under the active Santiago crater within the Masaya caldera (Walker et al., 1993; Rymer et al., 1998). Mombacho volcano also displays fractional crystallization (fig1.12B).

### ***Trace Elements***

Trace element patterns of lavas follow those for island arc basalts (IAB) with low abundances of high field strength elements (HFSE) relative to LILEs (filled symbols in fig.1.8). Enrichment in the LREEs (filled symbols in fig1.9), likewise characteristic for subduction zone lavas, is also demonstrated by these samples. However, Nicaraguan volcanic centers of Nejapa, Apoyo and Granada, which show two populations of lavas in regard to TiO<sub>2</sub> and K<sub>2</sub>O content (figs1.7B, C), also show contrasting behavior in the HFSEs and REEs (unfilled symbols in figs1.8, 1.9). The question arises as to whether the processes creating the HFSE anomaly in most IABs is absent during the development of the ND lavas, or, whether the source itself is different. If the source is different, is it at all related to the source of the HFSE depleted lavas? Additionally, is the magmatic source the only factor controlling the HFSE depletion?

First observed by Ui (1972), the ND basalts have high MgO and low K<sub>2</sub>O content, which suggested the possibility of their derivation from different primary magma. Ui (1972) also observed that, whereas major vents of the Central American arc lie en echelon and parallel to the Middle America trench (NW to SE trending), Nejapa and Granada cinder cones are positioned within the right-lateral displacements (e.g. Apoyo –

Mombacho; fig1.3) and trend N-S. Walker (1984) also recognized the Nejapa and Granada cinder cones to be in N-S alignment and suggested them as localized zones of extension. He concluded that peridotite in the mantle wedge is the magmatic source parental to the ND lavas.

Carr et al. (1990) observed that the ND lavas approached enriched mantle (EM) isotopically yet had low LILEs and La/Yb ratios that approached depleted mantle (DM). This led them to believe that the source of the Central American lavas is mainly DM modified by an incompatible-rich silicic fluid (IRS) flux of subduction components with small amounts of EM from decompression of the asthenosphere as it is drawn in and up toward the mantle wedge corner. However, the ND lavas had unusual geochemistry including depletion in LREEs, K and other elements with low distribution coefficients, indicating a previous episode of melting.

Feigenson and Carr (1993) refined the model of Carr et al. (1990) using variations in inverse modeling patterns of REE data. The modeled source magma is broadly homogenous with small local heterogeneities, most likely enriched garnet-bearing veins. Feigenson and Carr (1993) explain the heterogeneities as being due to variations in partial melting beneath arc segments, controlled by the amount of subduction-generated flux per unit mantle wedge. Feigenson and Carr (1993) argue that the ND lavas derive from the remelting of these enriched veins within a depleted mantle. The generated flux, selective sampling of the veins and degree of melt remain a function of slab dip.

Reagan et al. (1994) also advocate the remelting of mantle residues, which is initially MORB source mantle with possible ocean-island basalt (OIB) components, after the generation of HFSE depleted magmas as the source for ND lavas. They specify, however, that the generated HFSE depleted magmas are similar to lavas erupted

throughout Nicaragua and are different from those erupted in Costa Rica. Based upon U-series nuclides, Reagan et al. (1994) suggest three stages of subduction modification of the mantle wherein the ND and HFSE depleted magmas evolve in the same way until stage III, which represents the last metasomatism and melting event. Their scenario requires the retention of hornblende within the residual mantle, which leads to the enrichment of the middle rare earth elements (MREEs) and correlates to higher K/Rb ratios of the ND samples relative to the HFSE depleted samples (Reagan et al., 1994).

In the data presented within this work, REE patterns of the ND lavas are either flat or slightly bowed through the MREEs (open symbols - fig1.8). However, K/Rb ratios cover a wide range of values and do not necessarily reflect preferential melting of residual amphibole (fig1.13A). In fact, the trend of amphibole melting in K/Ba versus Ba/Sr space is oblique to the trend of the samples (Patino et al., 2000) giving further evidence that amphibole melting is not necessarily applicable in southeastern Nicaragua (fig1.13B).

Walker et al. (1990; 2001) agree with Reagan et al. (1994) that the mantle underlying Nicaragua is inherently more depleted than under Costa Rica. They offer a slab-based model in which variable addition of fluids from a rutile-saturated oceanic crust and melts from hemipelagic sediments lead to non-uniform HFSE depletions in Nicaraguan basalts. Walker et al. (2001) conclude that the HFSE depleted and non depleted basalts have fundamentally distinct source regions linked to variable contributions from the Cocos plate including the sediment cover. That is, the HFSE depleted basaltic magma with enriched LILE and LREE contents contain a clear slab signature whereas ND magmas have little slab and sediment influence. Based on the composition of sediments on the Cocos plate (Patino et al., 2000) and relative incompatibility of elements, Walker et al. (1990; 2001) argue that increases in more incompatible elements indicate an increase in the

concentration of fluid mobile elements coming from the slab.

This reasoning agrees with data from the southeast Nicaragua (fig1.10), which show the ND lavas having both less slab signal and less hemipelagic sediment influence than HFSE depleted samples. However, in Ba/Th vs. U/La space (fig1.10B) the data clearly shows that Ba/Th, a proxy for carbonate sediment, is a non-zero value everywhere and has a significant degree of variability, albeit not as great as the range shown by the hemipelagic contribution. Such differential carbonate addition is left unaddressed in the model of Walker et al. (2001). Moreover, whereas Walker et al. (2001) advocate a mantle source as a 1 to 3 mixture of OIB to MORB, respectively, they model a homogenous mantle wedge. This does not accurately reflect the potential heterogeneity of the mantle underlying the Nicaraguan volcanic front (Plank & Langmuir, 1998; Noll et al., 1996; Leeman et al., 1994; Feigenson & Carr, 1993; Carr et al., 1990; Morris et al., 1990).

Carr et al. (2003) suggest that tectonic factors could influence the association of ND and HFSE depleted lavas in Nicaragua by allowing a focused melt migration. With the steepest slab dip along the Central American arc, the seismic zone under Nicaragua is sub-vertical below about 120km (Protti et al., 1995). This creates conditions in which initial melting, if activated by the release of slab fluids, could occur at depths of ~130km within the convecting asthenosphere (Leeman et al., 1994) assuming a vertical fluid and melt migration (Elliot et al., 1997). In turn, the narrow width of fluid release may focus the fluid fluxes such that they interact with a smaller volume of mantle wedge material, yet melt to a higher degree (Carr et al., 1990).

That the ND lavas found in southeastern Nicaragua originate in areas of local extension (Ui, 1972; Walker, 1984; Sussman, 1985; Walker et al., 1990; Carr et al., 2003), suggests that decompression melting may play some role in the generation of

lavas of this area. Cameron et al. (2002) use Ba/La vs. La/Yb space to distinguish between fluid flux melting and decompression melting, respectively. Placing the southeastern Nicaraguan data within this space, the ND lavas clearly show the importance of decompression melting in their generation (fig1.14A). The importance of mantle decompression melting in the formation of magmas with low LILEs and LREEs relative to HFSEs is also seen in basalts from central Mexico (Cervantes & Wallace, 2003). They found that, whereas an H<sub>2</sub>O-rich component fluxing the mantle wedge explains their samples enriched in LILEs and LREEs relative to HFSEs, decompression melting better explains the formation of the samples closer in character to ND lavas.

The ND lavas also show a higher degree of melt (Na<sub>2</sub>O as proxy) and lower amount of slab input (Ba/La as proxy) as expected from steeper slab dip (fig1.14B). The evidence of the SE centers erupting both ND and HFSE depleted lavas suggests that both decompression melting and fluid flux melting are important mechanisms in southeastern Nicaragua. It may be that during extensional episodes, the behavior is that of a closed system with preferred decompression melting; the rate of extension would then control the degree of melting. During periods of relative quiescence, the system may be more open in which case fluid flux melting becomes equally or more important. That the HFSE depleted lavas from the centers with both ND and HFSE depleted lavas are more depleted in LILEs and LREEs than the centers with only HFSE depleted lavas (figs1.8, 1.9) further supports this idea. In summary, it seems apparent that melting mechanisms, tectonics, mantle wedge composition and variable slab input are all important parameters in HFSE concentrations.

### ***Mantle heterogeneity***

The new REE data reported in this thesis corroborates the findings of Carr et al.

(1990), Feigenson and Carr (1986; 1993) and Reagan et al. (1994) of two distinct mantle sources for the southeastern Nicaraguan lavas. Evidence of mantle heterogeneity comes from data regressions of  $\text{La}_N/\text{REE}_N$  vs.  $\text{La}_N$  (Feigenson & Carr, 1993) which indicate two distinct parental magmas for the ND and HFSE depleted lavas (fig1.15). The amount of scatter about the process identification regression lines (PIRL) indicates the degree of source homogeneity. As demonstrated by the lines in the Nd diagram, there are two clearly different slopes suggesting two sources as opposed to related magma genesis. The upward slope of the Las Banderas samples in the  $\text{La}_N/\text{Eu}_N$  diagram (circled) represents plagioclase fractionation. Additionally, the constant  $\text{La}_N/\text{Ce}_N$  ratio is inconsistent with fractional melting. That is, nothing can really fractionate these two elements from each other, so any difference in their ratio (i.e. between ND and HFSE depleted) suggests different sources. Figure 1.16 shows the shift in  $\text{La}_N/\text{Ce}_N$  between the ND and HFSE depleted lavas against both the MREEs and HREEs, suggestive of two distinct sources.

Isotope data from previous research (Feigenson & Carr, 1986, 1993; Carr et al., 1990), albeit for few samples, also reveals a separation between the ND and HFSE depleted samples of southeastern Nicaragua (fig1.17). Again, fractionation processes cannot explain this separation suggesting distinct mantle sources. The presence of a heterogeneous mantle would satisfy the data results. Feigenson & Carr (1993) proposed a depleted mantle with localized enriched veins beneath the CAVF that are selectively sampled as a function of slab dip. They further show that the ND lavas derive from the remelting of these enriched veins based on isotopic evidence. That a single volcano erupts both populations of lavas, therefore, indicates that the melt column underlying them is not necessarily originating in the same area of the mantle

wedge. In fact, it must be refocusing to allow the process of preferentially tapping a given source within a heterogeneous mantle.

### ***Slab Sediment Mixing Arrays***

Use of Ba/Th and U/La tracers by Patino et al. (2000) reveal a local variation at Telica volcano in NW Nicaragua that defines a binary mixing array (fig1.2) suggesting that the subducting plate's stratigraphy is geochemically recognizable (Patino et al., 2000). Overlapping NW Nicaragua data with that presented in this work, it becomes evident that the southeastern samples show no significant sub-parallel mixing array between the hemipelagic and carbonate components (fig1.10A). This is not to say that there is no variation; in fact, there is a significant difference between the ND and HFSE depleted samples. The ND samples have less influence from the hemipelagic sediment component than the HFSE depleted samples as shown by a lower U/La ratio.

Mixing of the carbonate and hemipelagic sediments with either DM or EM cannot account for the variation seen in the southeastern Nicaragua lavas (fig1.18A). A potential reason is that Ba/Th, due to the incompatibility of Ba, represents a hydrous fluid flux and does not necessarily reflect CS. Looking at the element concentrations of each sediment type (Patino, 1997; Patino et el., 2000), the hemipelagic sediment has greater concentrations of all incompatible elements relative to the carbonate sediment, although Ba is most similar (fig1.18B). Strontium (Sr), slightly more compatible than Ba in fluids, is the only element in greater abundance in the carbonate sediment; P is virtually the same in both. This suggests that Sr/Th may be a better proxy for CS.

The caveat here is that Sr can act both compatibly and incompletely as it readily replaces Ca. Additionally, assimilation-fractional crystallization processes (AFC) affect ratios involving Sr. Limiting SiO<sub>2</sub> to ≤ 55 wt% will effectively eliminate lavas affected by

AFC processes. With this limit in place, a plot of Ca vs. Sr showing a linear relationship indicates that Ca and Sr are both behaving compatibly; if they are not linearly related, Sr is acting incompatibly in the manner of Ba. Placing the southeastern Nicaragua lavas in this space shows that Sr is acting incompatibly in the southeastern Nicaragua samples (fig1.19A). This being so, a plot of Sr/Th vs. U/La will show the same separation of sediment components in terms of both ratio values and bulk concentrations (fig1.19B). The local variations seen in the southeastern Nicaragua samples, however, still does not fit within a mixing space of CS, HS and EM or DM (fig1.19B).

If, however, a flux from the lower altered MORB component (ALM) mixes with fluxes from the two sediments, the southeastern Nicaragua samples fall neatly into a triangle in both Sr/Th vs. U/La and Ba/Th vs. U/La space (fig1.20). This suggests that any mixing model should take at least these three slab components into account. In fact, Rüpke et al. (2002) show that the faults in the forearc of the slab subducting beneath Nicaragua are deep enough, due to the steep dip, to transport seawater into lithospheric mantle, which will serpentize the mantle. They also show that serpentized subducting lithospheric mantle holds stored water to a greater depth than the overlying sediments. This leaves large amounts of fluids available for release during deserpentinization of the subducting lithospheric mantle under Nicaragua. Because the parameter controlling water storage, depth of the faults in the subducting lithosphere, changes with the dip of the subducting slab, there are obvious ramifications of this idea for the entire Central American arc.

### **Contrasts between SE Nicaragua, NW Nicaragua and Costa Rica**

#### *Setting*

The areas of the Central American arc used to contrast the southeast (SE)

Nicaragua segment follow the segmentation of Stoiber and Carr (1974; fig1.21). Included are northwest (NW) Nicaragua (Cosigüina to Apoyeque), SE Nicaragua (Nejapa alignment to Concepción) and three segments in Costa Rica comprising volcanoes in the north (N CR) (Orosí to Tenorio/Cerro Chopo), the isolated Arenal volcano and volcanoes in central Costa Rica (C CR) (Platanar to Turrialba) (fig1.22). In a few plots, El Salvador (data from Carr & Rose, 1987 and Carr et al., 2004) is included for clarity and is represented by blue squares. Data used for contrasting southeast Nicaragua lavas are from (Carr & Rose, 1987 modified by Carr et al., 2003; table 1.7) and Bolge et al., (*in review*; table 1.8). Symbols for all graphs will follow the legend of fig. 1.22.

### ***Results***

Whereas the local variations within the southeast Nicaragua volcanic arc do not change the overall regional variations, there are facets of the southeast Nicaragua lavas that significantly contrast other areas of the Central American arc: namely, centers with 2 compositional populations of lava and the lack of simple mixing between CS and HS.

#### ***Contrast #1 – Trace Elements***

The first contrast is the occurrence of lavas that do not show a depletion in HFSEs relative to LILEs and LREEs in the SE Nicaragua samples whereas lavas of the adjacent arc segments display only HFSE depletion (fig1.23). Trace element spider diagrams, normalized to primitive mantle (McDonough & Sun, 1995) verify the difference in relative HFSE depletion between SE Nicaragua and adjacent arc segments. Further, they show that the ND samples of SE Nicaragua are the most depleted in highly fluid-mobile and incompatible elements (e.g., Cs, Ba). They are not, however, depleted in HFSEs (Nb, Zr, Ti). In fact, the pattern of the ND spider diagram has less of a slope going from incompatible to more compatible elements than the other areas included in

this study; that is, from left to right.

The shapes of REE spider diagrams also show a contrast between SE Nicaragua lavas and lavas from adjacent arc segments (fig1.24). Only the SE Nicaragua ND samples display a relative depletion in LREEs with a small convex shape in the MREEs. There are, however, some SE HFSE depleted and NW Nicaragua samples that are relatively flat. They are from the Nejapa alignment and Cerro Negro, a vent within the El Hoyo massif (van Wyk de Vries, 1993). This suggests that there may be local variations affecting the conditions responsible for HFSE depletion in the lavas. Additionally, HFSE depleted southeast Nicaragua lavas show the greatest range in LREE composition whereas C CR clearly has the greatest enrichment in LREEs.

#### *Contrast # 2 – Sediment mixing arrays*

The slab signature, shown by Ba/La, exhibits a robust regional variation in Central America with a maximum in central Nicaragua (fig1.25A) that decreases northwestward across El Salvador and southeastward, with a minimum in central Costa Rica. This regional variation is also evident in Ba/La vs. U/Th space (fig1.25B), which shows different amounts of sediment and mantle/MORB components for each segment of the arc. Again, NW Nicaragua is a relative maximum with a steady decrease into Costa Rica.

A local variation appears in Ba/Th vs. U/La space, which separates the two sedimentary units found on the Cocos plate (fig1.26). Most apparent in NW Nicaragua and Arenal, variability in the relative amount of sediments occurs to some extent in all segments of the Central American volcanic arc under consideration. Mixing arrays that are sub-parallel to a mixing line between the carbonate and hemipelagic sediment reflect simple variation in sediment proportions. In the cases of NW Nicaragua and

Arenal, this sub-parallel array is significant even though the amount of total slab influence on the two differs. North and central Costa Rica lavas display subtle variability in relative sediment proportions and show more carbonate sediment than hemipelagic sediment influence. Like Costa Rica, SE Nicaragua lavas have a greater CS influence. However, in contrast, volcanoes in SE Nicaragua define horizontal arrays that suggest another component must be involved in their genesis other than sediments derived from the subducting slab.

## **Discussion**

Since the occurrence of both ND and HFSE depleted lavas from a single volcanic center appears only in SE Nicaragua, any discussion here would only reiterate what's already been said previously. For this reason, this contrast will not be explicitly discussed in this section. That being said, the idea of a tectonically controlled, focused melt migration as influencing the association of ND and HFSE depleted lavas in Nicaragua may also be important in other contrasts found in the Central American volcanic front (CAVF).

The regional decrease in total slab signature, as shown by Ba/La (fig1.25), may be a matter of decreased fluid flux due to changes in the slab dip along the CAVF. Using Cs/Th as a proxy for fluid flux, there is a positive linear relationship between the fluid flux and slab signature, as shown by Ba/La (fig1.27A). This regional decrease is also shown by Cs/Th vs. distance along the arc (fig1.27B). The ratio systematics imply that the presence, or lack, of slab signal is intimately connected to the magnitude of fluid flux. In turn, the dip of the subducting slab, at a maximum under Nicaragua, also decreases under Costa Rica. This evidence corroborates the idea of Rüpke et al. (2002) who hypothesize that the steeper dip of the slab under Nicaragua leaves large amounts of

fluids available for release during deserpentinization of the mantle. This, of course, is assuming that the transport mechanism from the slab into the mantle is a fluid as opposed to a melt.

Melts are enriched in the more compatible elements such as Yb. Using Yb/La, normalized to chondritic values, then, is a good way to measure melt component. Placing that against a fluid proxy, such as Cs/Th, will show where samples fall relative to both a fluid and melt trend (fig1.28). The positive slope indicates that melting increases with an increase in fluids. This is not surprising since increased aqueous fluid will suppress phase solidi, allowing melt to begin at lower temperatures. Along with the regional variation seen along this slope, local variations in melt component are shown in SE Nicaragua and C Costa Rica; the other segments are roughly constant along the melt axis, yet variable along the fluid axis. As seen in the previous chapter, the melt component in SE Nicaragua can be explained in part by the process of decompression melting. However, this does not seem to be the case for C Costa Rica (fig1.29).

Separating a melt signal from the sediment flux signal may be achieved by using Th/Y vs. U/La space (fig1.30). This plot collapses the carbonate sediment onto the mantle creating a binary mixing array between CS/mantle and HS, where mantle is both EM and DM (open stars). Nicaragua samples fall between the binary mixing array whereas Arenal and, to a lesser extent, northern Costa Rica samples are trend toward an OIB (open star) endmember. The central Costa Rica samples, in contrast, separate into a vertical trend beyond OIB and so cannot be explained by mixing with any currently proposed endmember. Partial melting in the presence of garnet may be an explanation and may occur adjacent to a proposed slab tear beneath central Costa Rica (Abratis & Wörner, 2001; Johnston & Thorkelson, 1997). Whatever the explanation, this

vertical trend clearly shows a basic difference between central Costa Rica and the other segments of the Central American arc.

This is not surprising as differences between central Costa Rica and north Costa Rica and Nicaragua are already identified in the literature. There is general consensus that the mantle under Costa Rica is more enriched and OIB-like in character than that under Nicaragua (Carr et al., 1990; Feigenson & Carr, 1993; Reagan et al., 1994; Leeman et al., 1994; Feigenson et al., 2004; Hoernle et al., 2008; Gazel et al., 2009). Additionally, there is evidence suggesting that the mantle source under central Costa Rica has characteristics of the Galapagos hotspot. Herrstrom et al. (1995) argue that such an influx of asthenospheric mantle comes from behind the retreating Nazca plate. That is, a trench-parallel flow bringing an enriched component from South America. Johnston & Thorkelson (1997) and Abratis & Wörner (2001) propose a similar argument with asthenospheric influx occurring through a slab window, which underlies Panama.

Moreover, there is segmentation in the Wadati-Benioff zone, the Quesada Sharp Contortion (QSC), NE of Puerto Caldera (Protti et al., 1995) in Costa Rica. This leads to differences in the age of the subducting seafloor north and south of the QSC, with younger crust existing under central Costa Rica. Harry & Green (1999) postulate that age of the subducted plate influences the thermal structure of oceanic lithosphere, thereby affecting the process of devolatilization. Whether devolatilization occurs shallowly or at depth, in turn, will affect the geochemistry of the mantle wedge and so also erupting lava geochemistry.

Differences in total subducting sediment signal explain some geochemical contrasts between Central American arc lavas. HFSE depleted samples from southeast Nicaragua display a steep gradient in total subducted sediment signal in contrast to

northeast samples, which have a continuously high subducted sediment signal, and Costa Rica samples, which decrease regionally but are relatively constant locally (fig1.25A). Although SE Nicaragua samples have a wide range of mixing proportions with regard to hemipelagic and carbonate sediments, like NW Nicaragua, the total subducted sediment signal is lower, more like Costa Rica (fig1.26). It may be that the magmas have variable interaction with fluids that are transporting elements from different parts of the slab. It is unclear, however, if the shift in slab signal is sharp or gradational. The paucity of data from lava samples for the southernmost Nicaraguan volcanoes Concepción and Maderas, which may answer this question, will be addressed in a subsequent chapter of this work.

As pointed out to in the previous section, the use of Ba/Th as a carbonate proxy is questionable as it is both an incompatible and hydrous fluid-mobile element. To test if this ratio is showing only a hydrous fluid signature, other element ratios can be used to proxy a carbonate signature. Since Sr is in greater abundance in CS (Patino et al., 2000), its use is desirable if it is acting incompatibly. To check this, the relationship between Sr and Ca is examined (fig1.31A) for lavas that are filtered such that  $\text{SiO}_2 \leq 55\text{wt\%}$  in order to alleviate AFC effects. A linear relationship, (slope near one), means that Sr is acting compatibly. Here, it is evident that Sr is behaving as an incompatible element as there is no relationship between Ca and Sr. This being the case, and since there is a positive correlation between Sr/Th and Ba/Th (fig.1.31B), Ba/Th is a valid proxy for the carbonate sediment endmember.

With Ba/Th as a carbonate proxy and U/La as a hemipelagic proxy, Patino et al. (2000) attempted to fit Central American arc lavas into a simple mixing model with the sediments and mantle source as the triangular endmembers. When looking at mixing lines, however, it is evident that the lavas samples cannot be fully explained in this

manner (fig1.32A). However, if the altered lower MORB (ALM) is included, most of the lavas do fit into a simple mixing triangle (fig. 1.32B). This suggests that some southeastern Nicaragua and Costa Rica samples may have a larger contribution from fluids originating in the ALM. This would lead to either an enrichment/depletion reflecting the chemistry of ALM, or a dilution of sediment signatures. In fact, the lower altered oceanic crust has extremely low K<sub>2</sub>O (Alt et al., 1996), which may be part of the reason for ND samples found in SE Nicaragua. Furthermore, ALM is relatively depleted in fluid mobile elements such as Rb, Cs and U, which may explain why SE Nicaragua (especially the ND samples) and Costa Rica samples show lower relative amounts of Cs/Th (fig1.27).

Variations in the dip angle of the subducting slab along the Central American volcanic arc may influence both ratios of sediment to hydrous fluid release and serpentinized mantle to hydrous fluid release as well as the way in which transport of elements occurs (Rüpke et al., 2002; Carr et al., 1990, 2003). A more steeply dipping slab would allow deeper faulting, thereby creating a more hydrated mantle. Additionally, downgoing seawater will be able to sample deeper parts of the slab (i.e., ALM). During the subsequent dehydration reactions, a steeper slab will have a more focused distribution of flux thereby interacting with a smaller amount of mantle wedge prior to entering the volcanic plumbing system (Carr et al., 1990). However, as slab subduction continues, at some P-T condition, dehydration reactions will no longer occur at which time Si-rich fluids and/or slab melts may gain importance in element mobilization. If this is the case, lava chemistries would reflect this change and perhaps explain variations in the geochemistry of lavas in the CAVF.

Pearce & Peate (1995) showed that Cs is released more effectively via aqueous fluid whereas Th is released more effectively by siliceous fluid in subduction zone settings.

Plotting them against each other, both “normalized” to Yb, a compatible element with a high bulk distribution coefficient, preferences between hydrous vs. siliceous fluid element mobilization should be visible (fig1.33). Clearly, lavas of C Costa Rica, with higher Th/Yb ratios, show siliceous fluid flux signatures whereas the other segments along CAVF, with higher Cs/Yb ratios, show hydrous fluid flux signatures. This helps to explain the differences in the C Costa Rica lavas and suggests that they are not necessarily a good comparison to the rest of the CAVF.

### **Conclusions**

The SE segment of Nicaragua of the CAVF is unique insofar that its volcanoes erupt two distinctive populations of lavas: those depleted in HFSEs and those that are not depleted in HFSEs. The ND and HFSE depleted samples define two distinct paths of magmatic evolution as shown by REE process identification regression lines. The ND lavas experience a higher degree of melting and lower amount of slab input than their depleted counterparts, which supports the importance of decompression melting in the generation of the ND lavas.

The source of the ND lavas is veins of enriched material that occur within an otherwise depleted mantle wedge. Mantle heterogeneity is the best fit for the observed geochemistry and necessitates a dynamically refocusing melt column within the mantle wedge. Preferential tapping of enriched veins is further controlled by physical parameters, such as slab dip and the age of the slab, which change the focus of flux coming off the down-going slab and the composition of the slab, respectively.

Locally, in addition to the ND lavas, the SE Nicaragua segment of the CAVF contrasts adjoining segments of the CAVF in the amount of sediment contributions from the down-going slab. The NW Nicaragua segments show high contributions of both the

carbonate and hemipelagic sediment from the subducting slab. The SE Nicaragua segment, however, shows relatively low contributions of both sediment types.

Due to the low amounts of slab signal in SE Nicaragua, mixing arrays between the sediment layers of the subducting slab and enriched/depleted mantle, which have been used to examine lavas along the CAVF, do not work as well for the SE Nicaragua lavas. Using altered MORB as one component, however, better fits the data. This means that, not only does the mixing demand multiple components, but the nature of the mixing has slightly shifted thereby changing the importance of the sediment packages. Further modeling must take this into account.

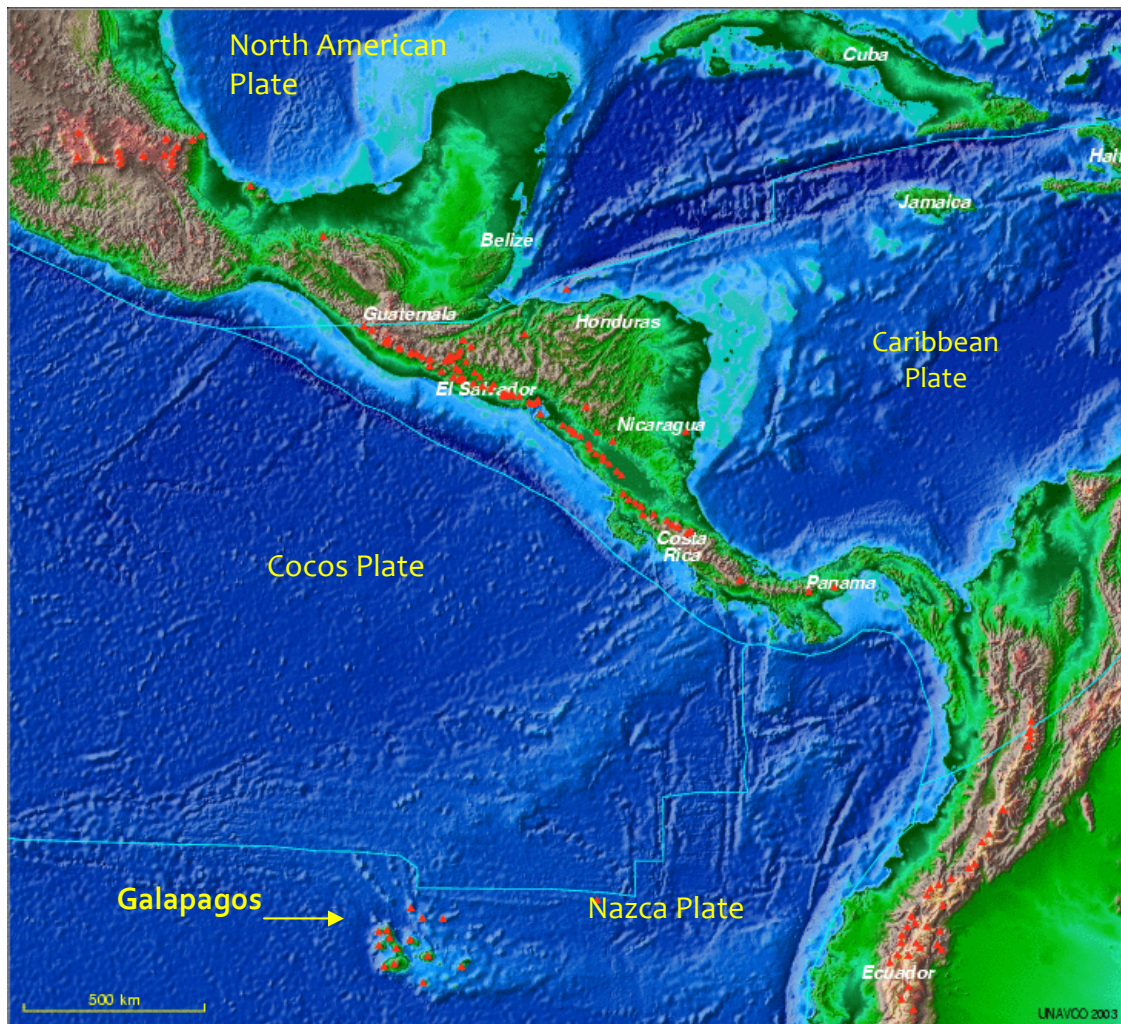


Figure I.1 Maps showing the location of the Central American volcanic front and Plate Tectonics of the region. Also shown is the Galapagos hot spot. Red triangles symbolize volcanoes. Adapted from UNAVCO 2003.

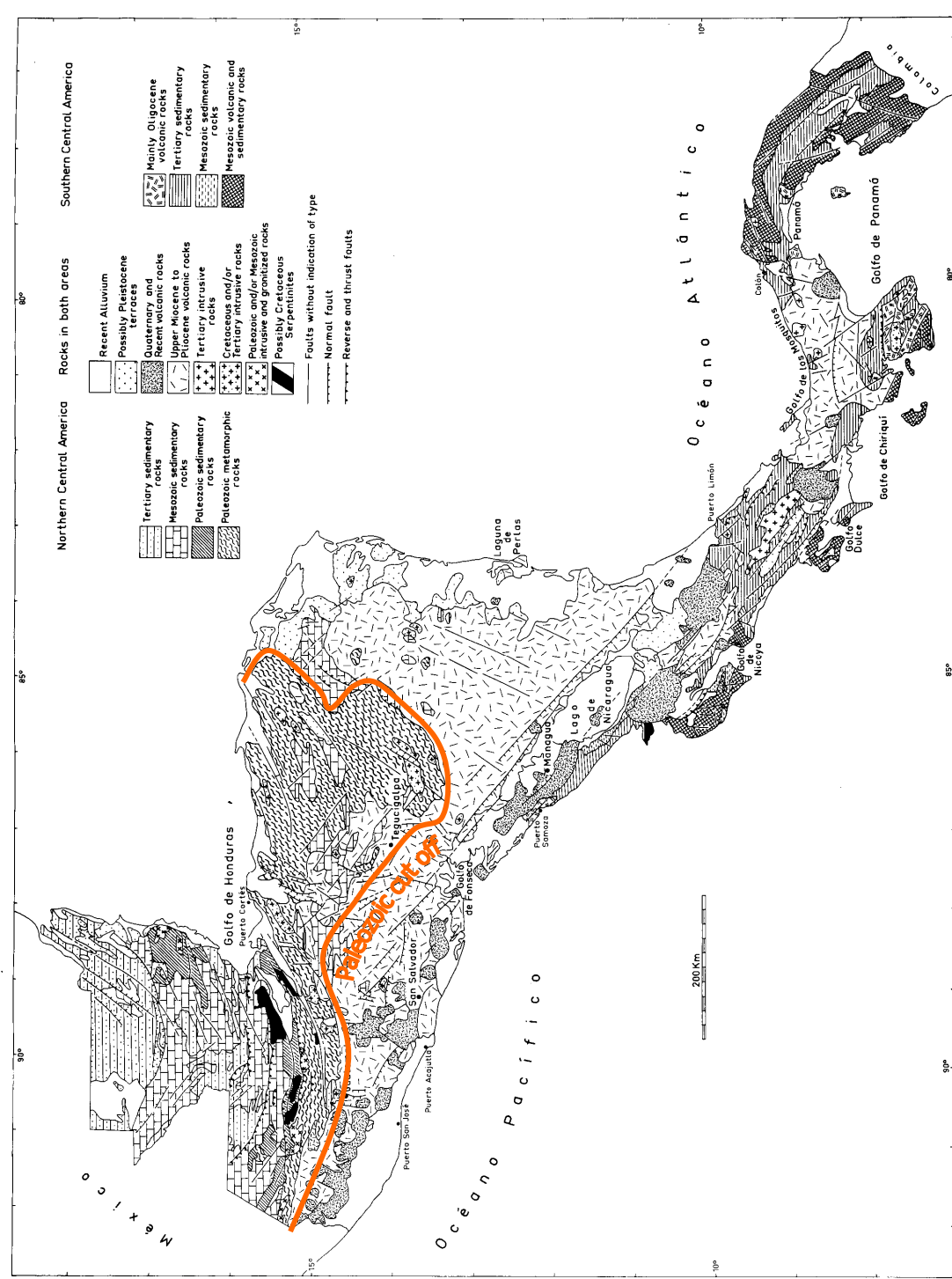
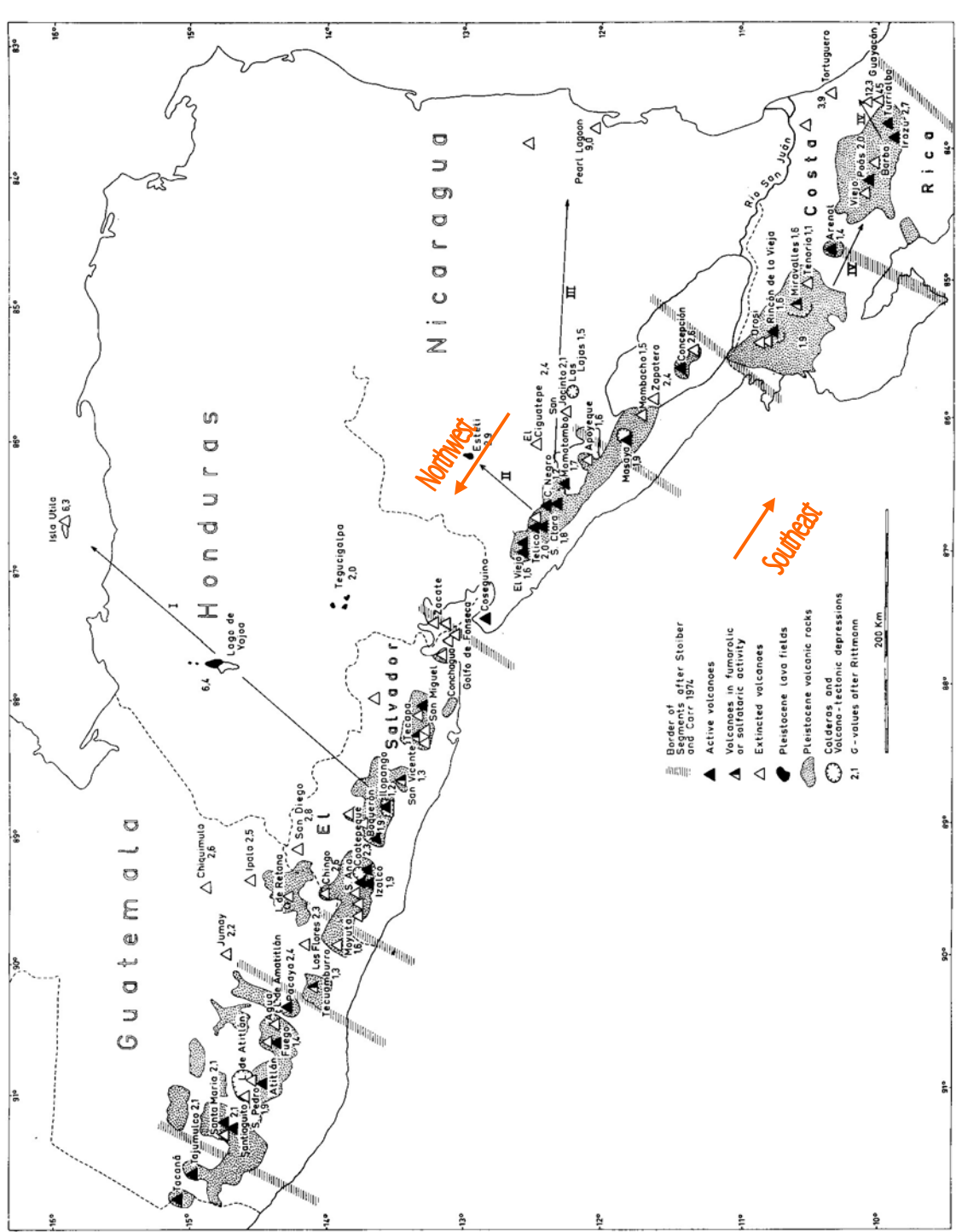


Figure I.2 – Geological map of Central America showing northern and southern sections based on the age of underlying basement adapted from Weyl (1980). The boundary is marked Paleozoic cutoff.



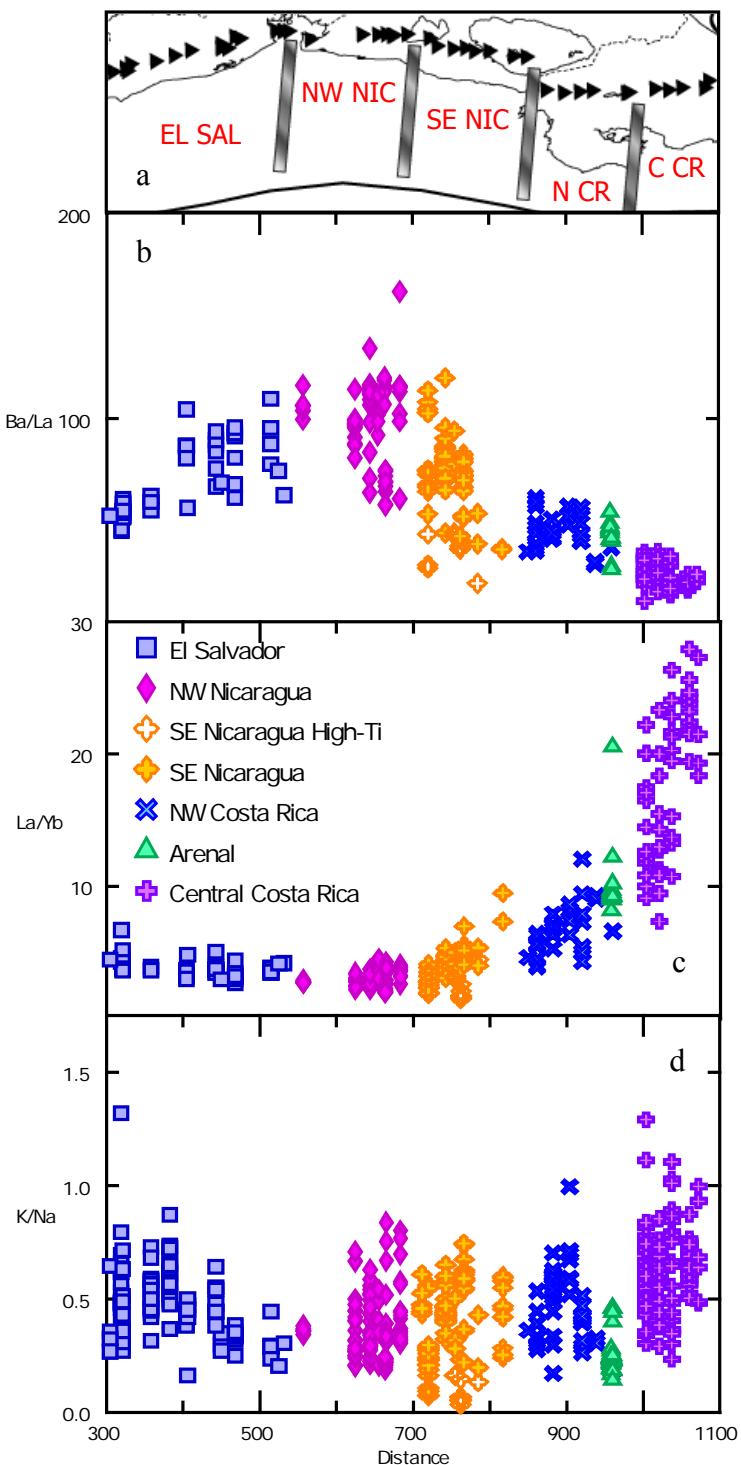


Figure I.4. Geochemical variations along the Central American margin (excluding Guatemala) correlated with the segments (a) of Stoiber & Carr (1973). b) Ba/La proxies slab input with a higher ratio meaning higher slab signature. c) La/Yb shows degree of melt with a higher ratio showing a higher degree of melt. d) The ratio K/Na reflects the variability of alkalis along the Central American arc. Data from this work and CAgeochem file with modifications by Carr et al. (2003).

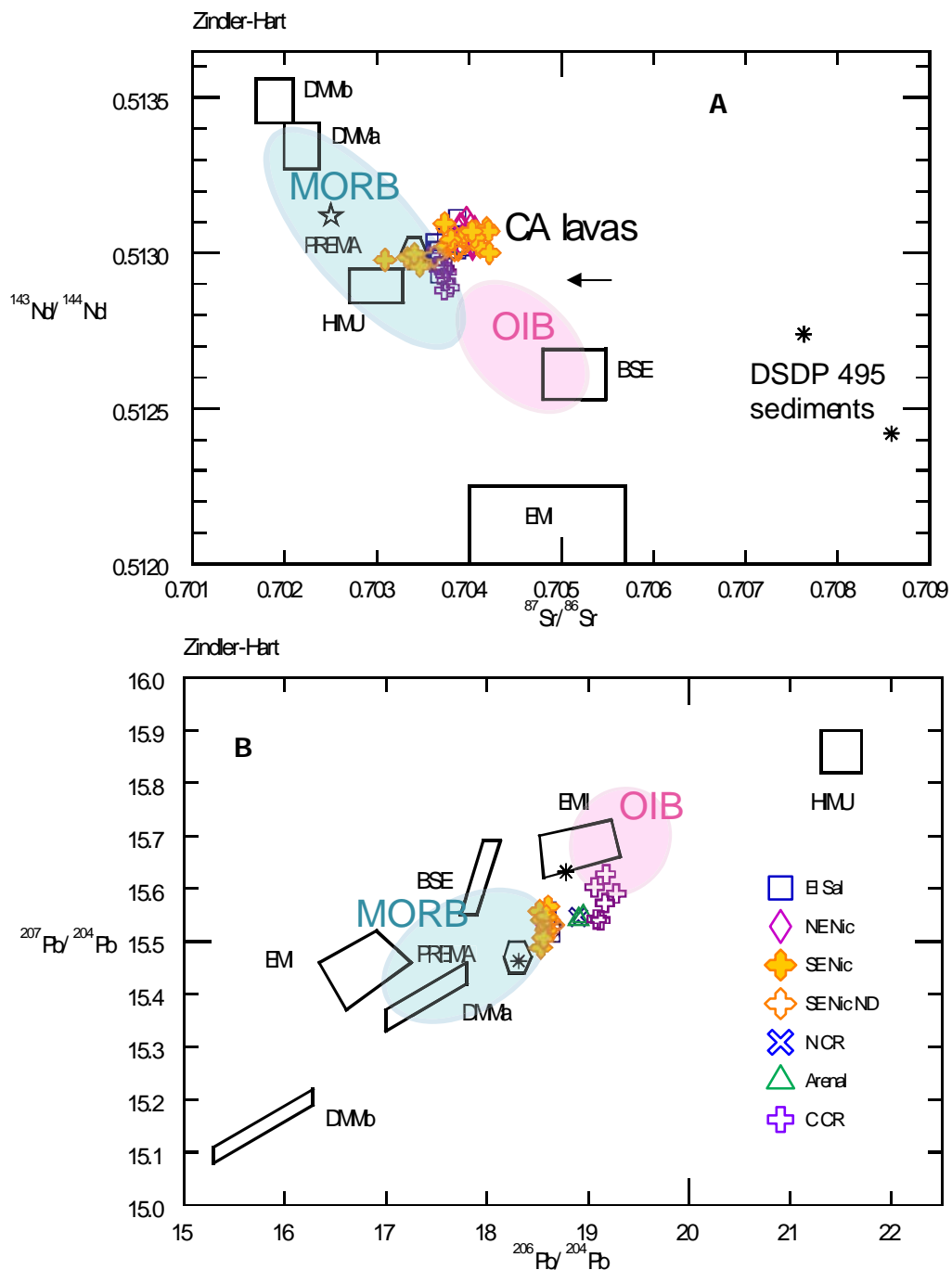


Figure 1.1 A) Nd and Sr isotopic compositions of Central American lavas (CA lavas), sediments from DSDP leg 495, MORB and OIB. CA data from Feigenson & Carr (1986); sediment data from Patino et al. (2000); MORB and OIB data is assembled from literature following Hofmann (1997). B) Pb isotope space contrasting the fields of OIB, MORB and subduction zone lavas.

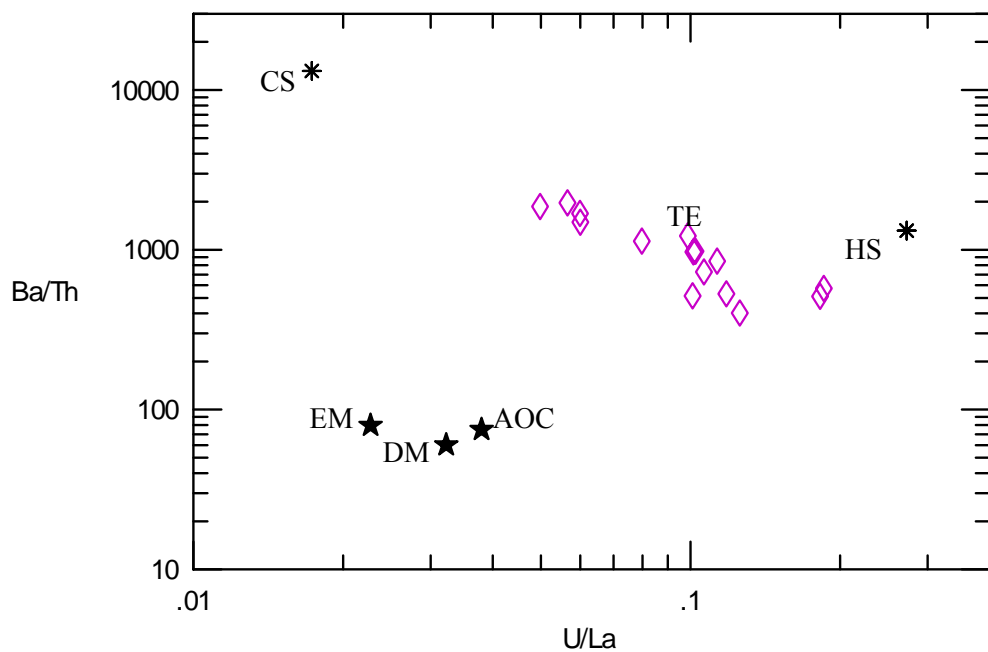


Figure 1.2 Purple diamonds are samples from Telica (TE) volcano. Their trend shows an apparent mixing between the carbonate (CS) and hemipelagic (HS) endmembers of the subducting Cocos plate. Compositions for enriched mantle (EM), depleted mantle (DM) and altered oceanic crust (AOC) are from literature (Hofmann, 1988; Sun and McDonough, 1989; McDonough and Sun, 1995).



Figure 1.3 Map of study area. Symbols are shown in the legend below. They will be used throughout this chapter. When these symbols are not filled, they represent high-titanium samples or, in the case of the one unfilled green circle, a peculiar high-magnesium sample.

## LEGEND

- |              |             |          |
|--------------|-------------|----------|
| Las Banderas | Las Sierras | Mombacho |
| Nejapa       | Apoyo       | Zapatera |
| Masaya       | Granada     |          |

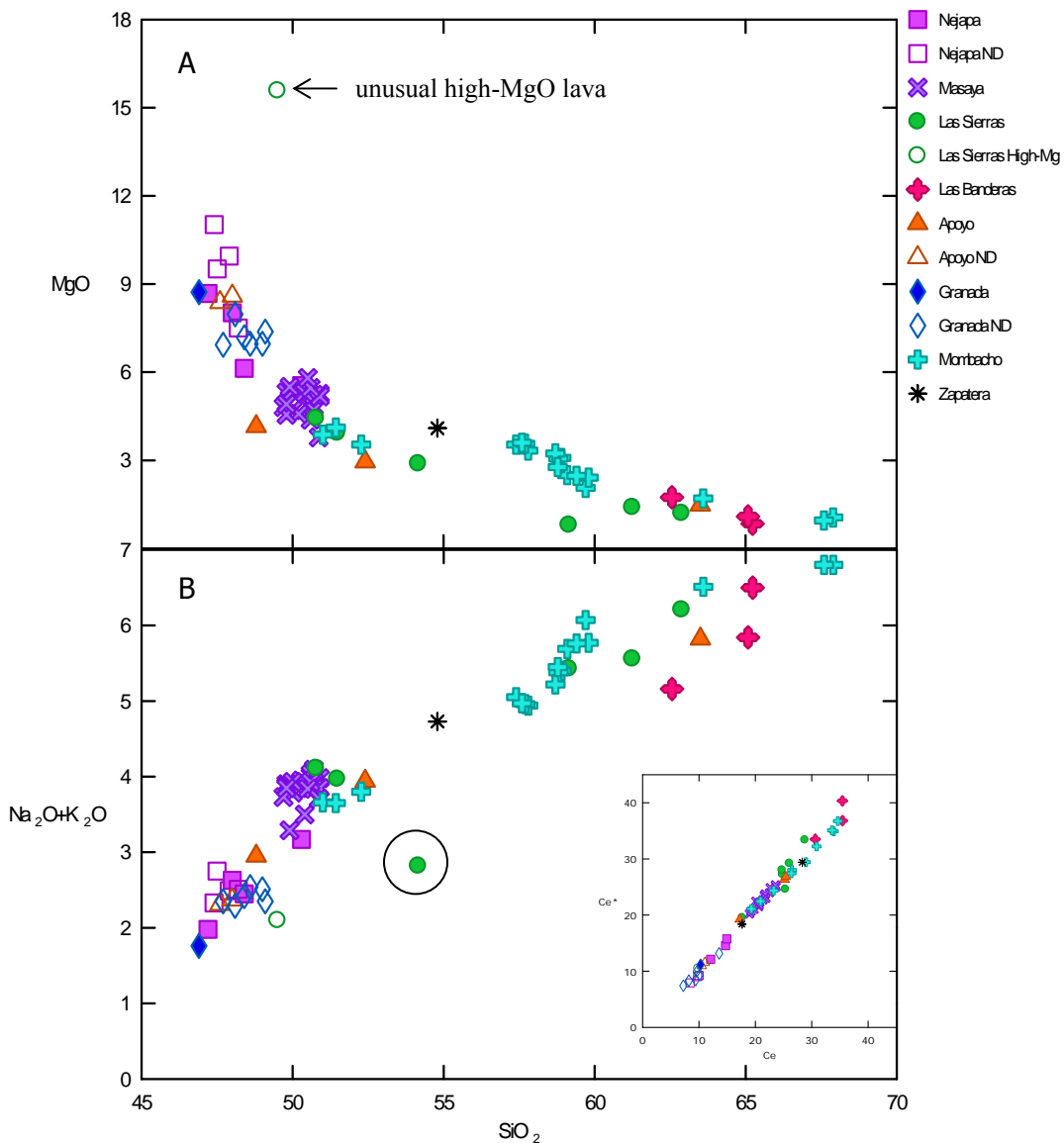
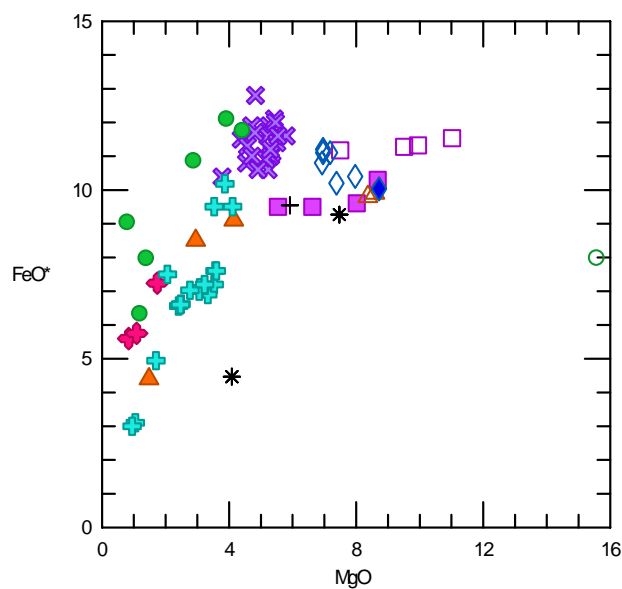


Figure 1.4 A) MgO vs.  $\text{SiO}_2$  B) Alkalies vs.  $\text{SiO}_2$ . The circled lava in B is potentially altered. However, the inset of  $\text{Ce}^*$  vs.  $\text{Ce}$  shows, by the strong linearity, that none of the sampled lavas have significant alteration. Symbols are the same for all figures. Open symbols: ND refers to lavas that are not depleted in HFSEs; high-Mg is the one unusual lava, LS5.

A.



■ Nájapa  
 □ NájapaND  
 × Masaya  
 ● Las Sierras  
 ♦ Las Banderas  
 ▲ Apoyo  
 △ ApoyoND  
 ◆ Granada  
 ◇ GranadaND  
 + Montebello  
 \* Zapatera  
 + ZapateraND

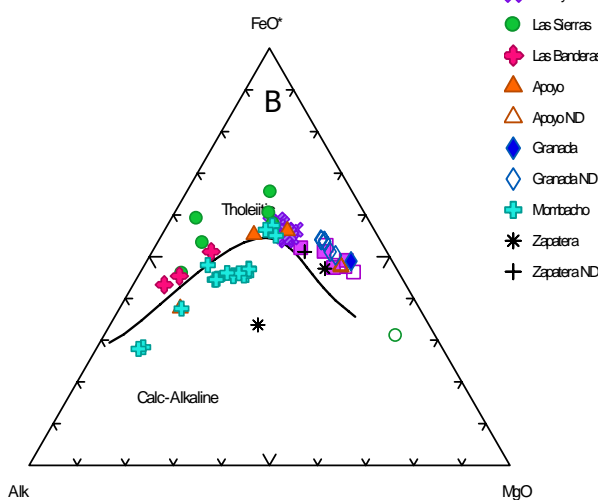


Figure 1.5A.  $\text{FeO}^*$  indicates total iron; that is, both +2 and +3 oxidation states. Note the open green circle – an unusually high Mg content for Central American lavas. B. AFM diagram (Irvine and Baragar, 1971) discriminating tholeiitic and calc-alkaline rock type.

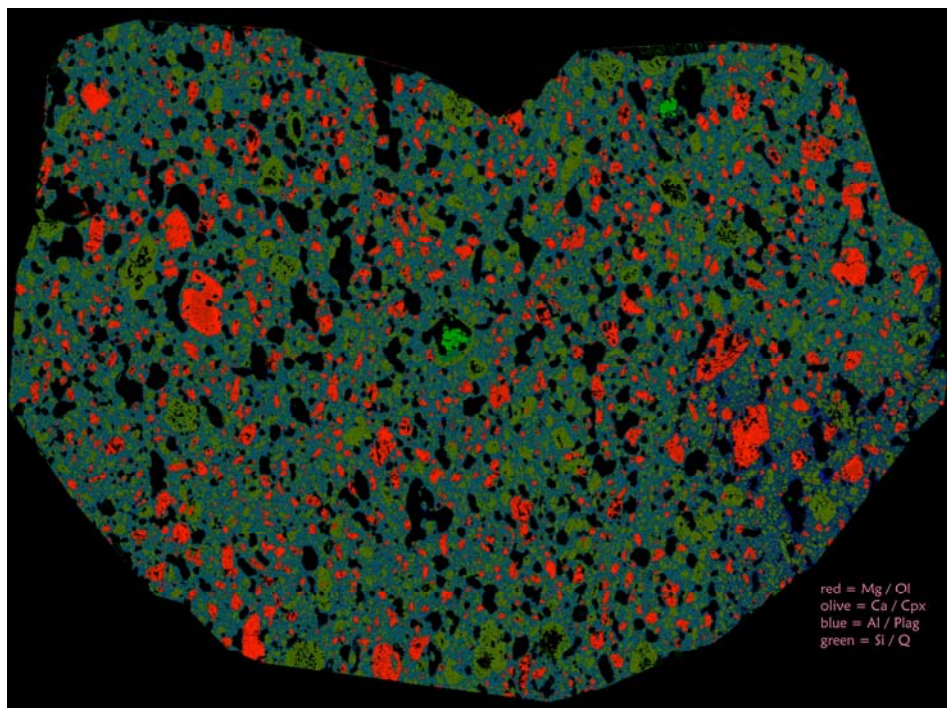
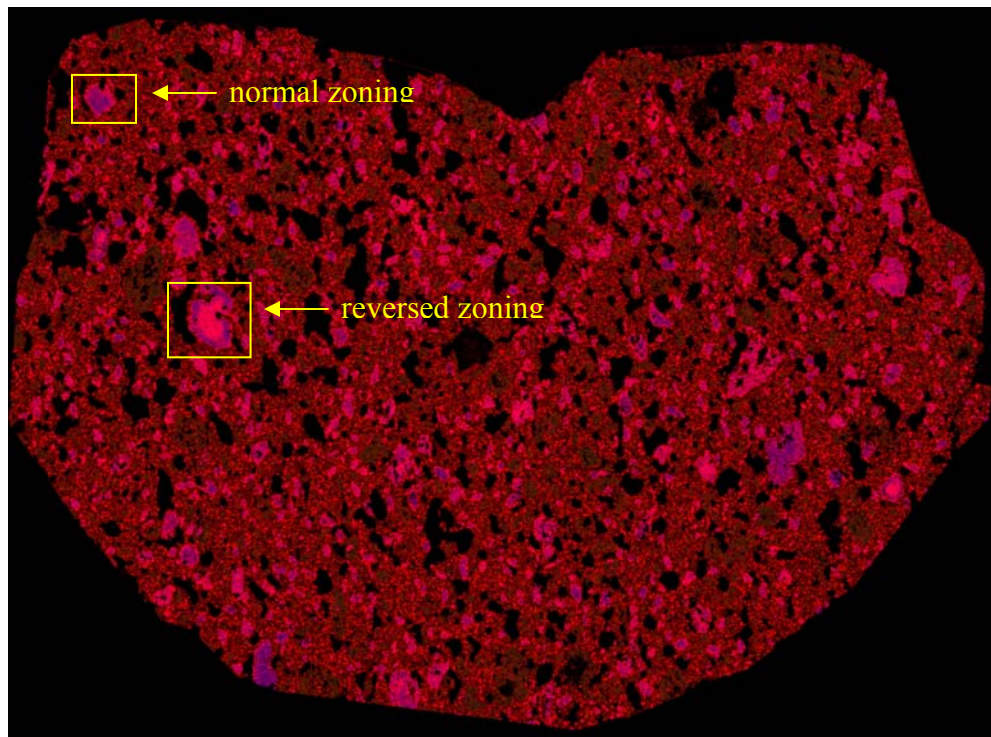


Figure 1.6. A. Faux color element map showing the main phases in LS5: red – olivine, olive green – clinopyroxene, blue – plagioclase groundmass, bright green – quartz. B. Coloring adjusted to enhance zoning of olivine: purple is Mg-rich, pink is Fe-rich.



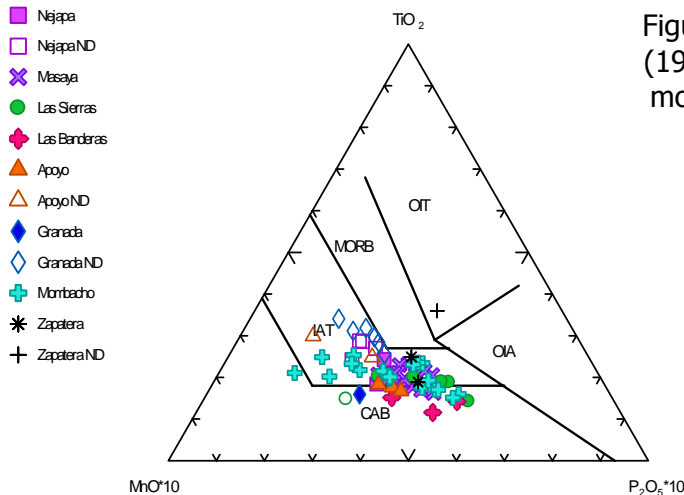


Figure 1.7A Diagram from Mullen (1983) showing the high- Ti samples moving towards the MORB field.

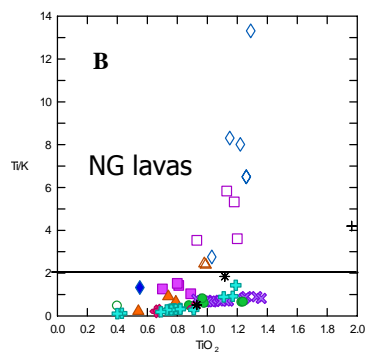


Figure 1.7B. graphic discrimination of NG lavas following Walker (1984) and Reagan et al. (1994): wt% of  $\text{TiO}_2 \geq 1\%$  and the ratio  $\text{Ti}/\text{K} \geq 2$ . NG lavas are represented as open symbols. Symbols as in previous figure.

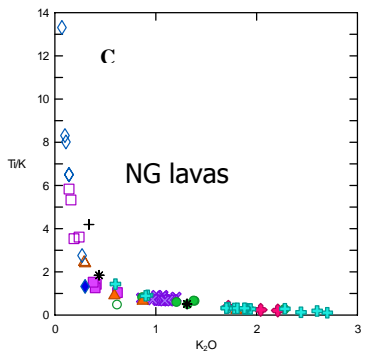


Figure 1.7C The high-Ti lavas have the lowest concentration of  $\text{K}_2\text{O}$  of the southeast Nicaragua lavas sampled. Low-K indicates a high degree of partial melting (Tatsumi, 1997).

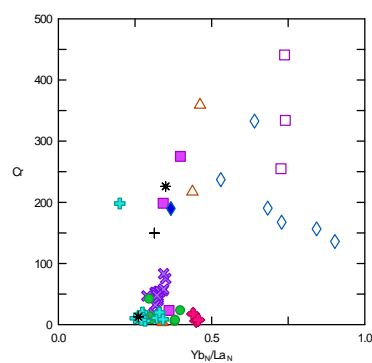


Figure 1.7D. The y-axis shows high-Ti samples to have a relative enrichment in Cr indicating either primary, or less modified, magma or a lack of olivine fractionation. The x-axis, normalized to chondritic values of McDonough and Sun (1995), indicates a relatively more extensive melt of the high-Ti samples.

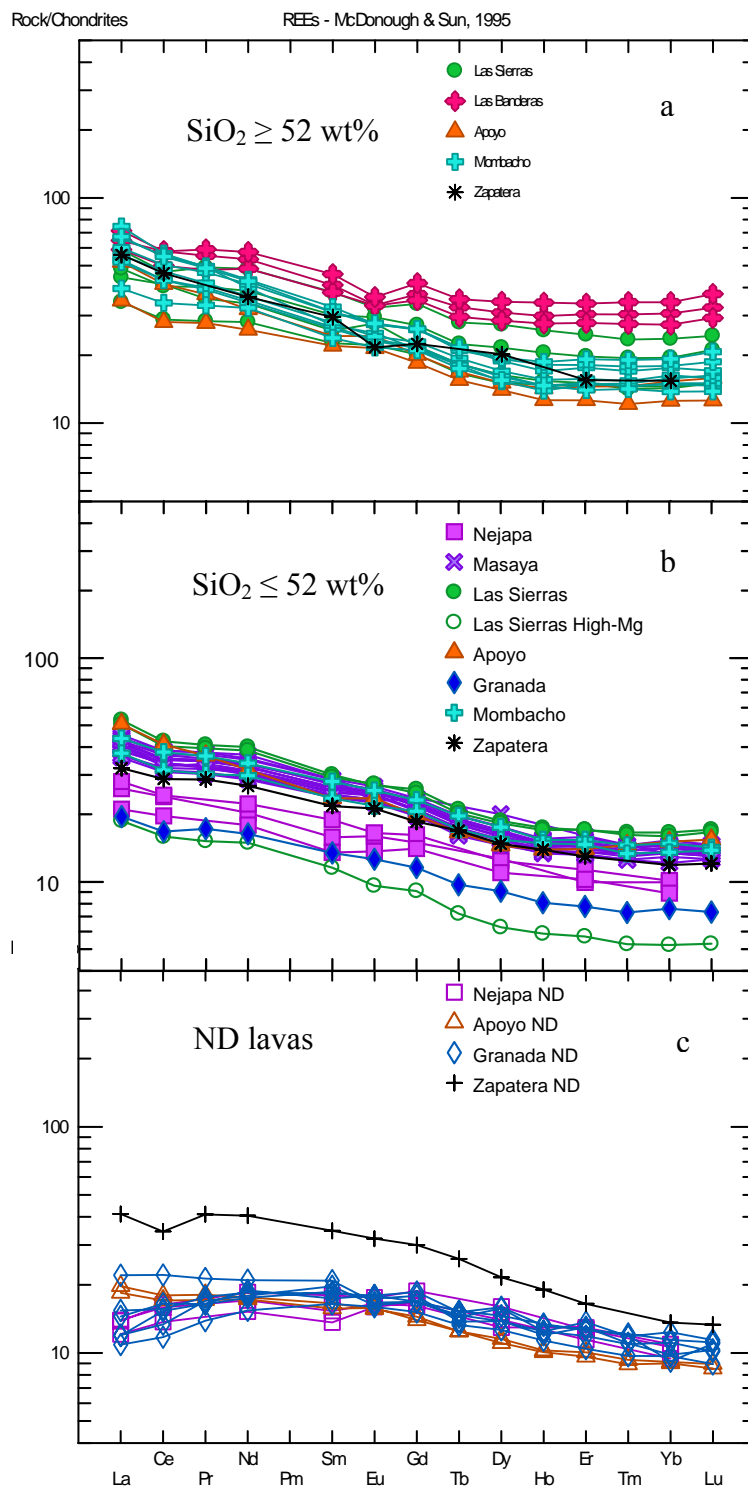


Figure 1.8 Spider diagrams normalized to chondritic values (McDonough & Sun, 1995), showing relative enrichment of the light rare earth elements (LREEs). Of note is the upswing in the HREEs of samples with  $\text{SiO}_2 \geq 52 \text{ wt\%}$ . The ND lavas show a relative depletion of the LREEs as compared to the other lavas, with the exception of Zapatera.

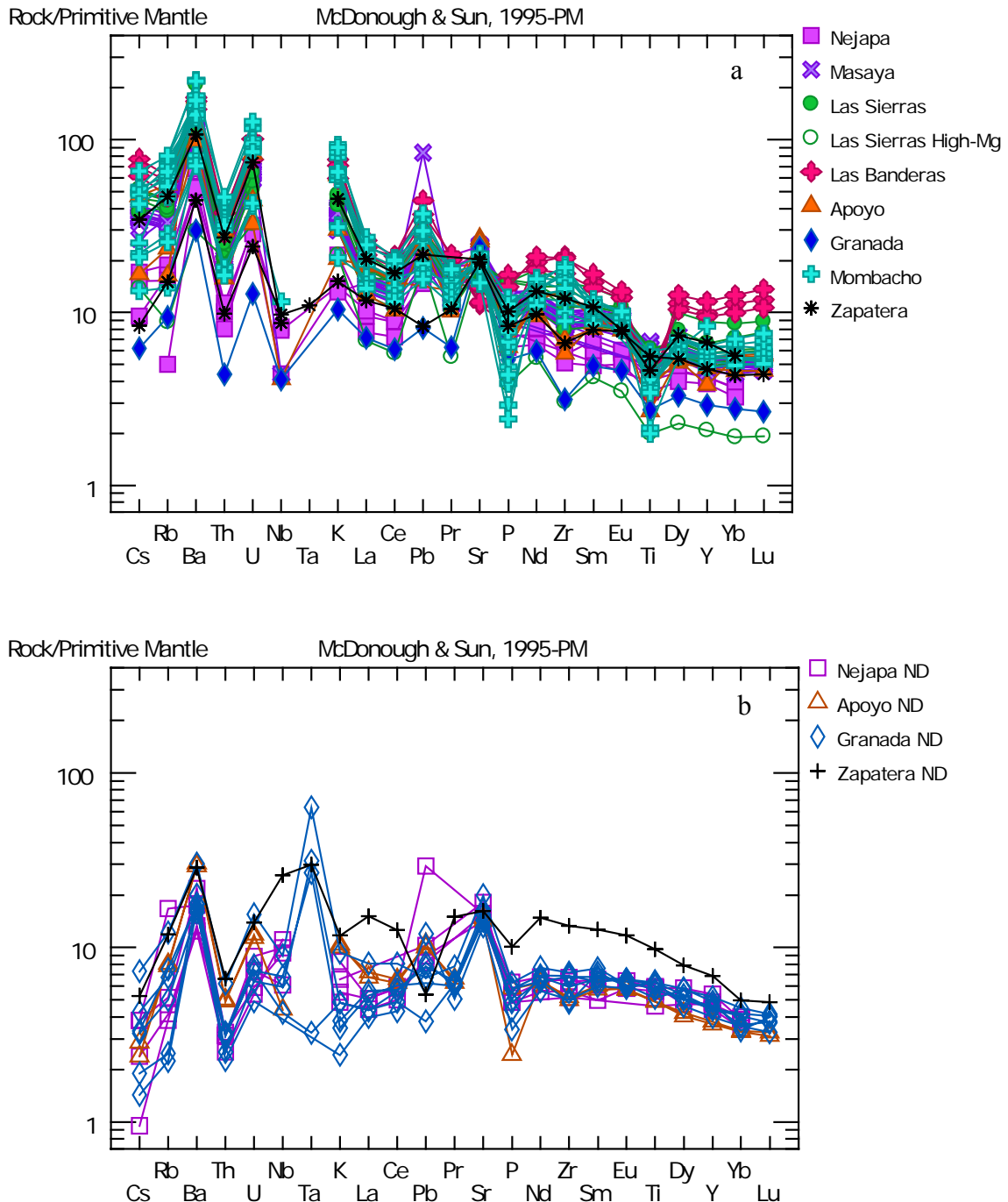


Figure 1.9 Spider diagrams normalized to Primitive Mantle values (Sun & McDonough, 1989) showing enrichment of incompatible elements relative to primitive mantle. Here, the elements become less incompatible from left to right. Notice that the ND lavas show distinctly lower concentrations overall of incompatible elements. Additionally, the ND lavas do not show depletion of high field strength elements (Nb, Ta, Zr, Ti).

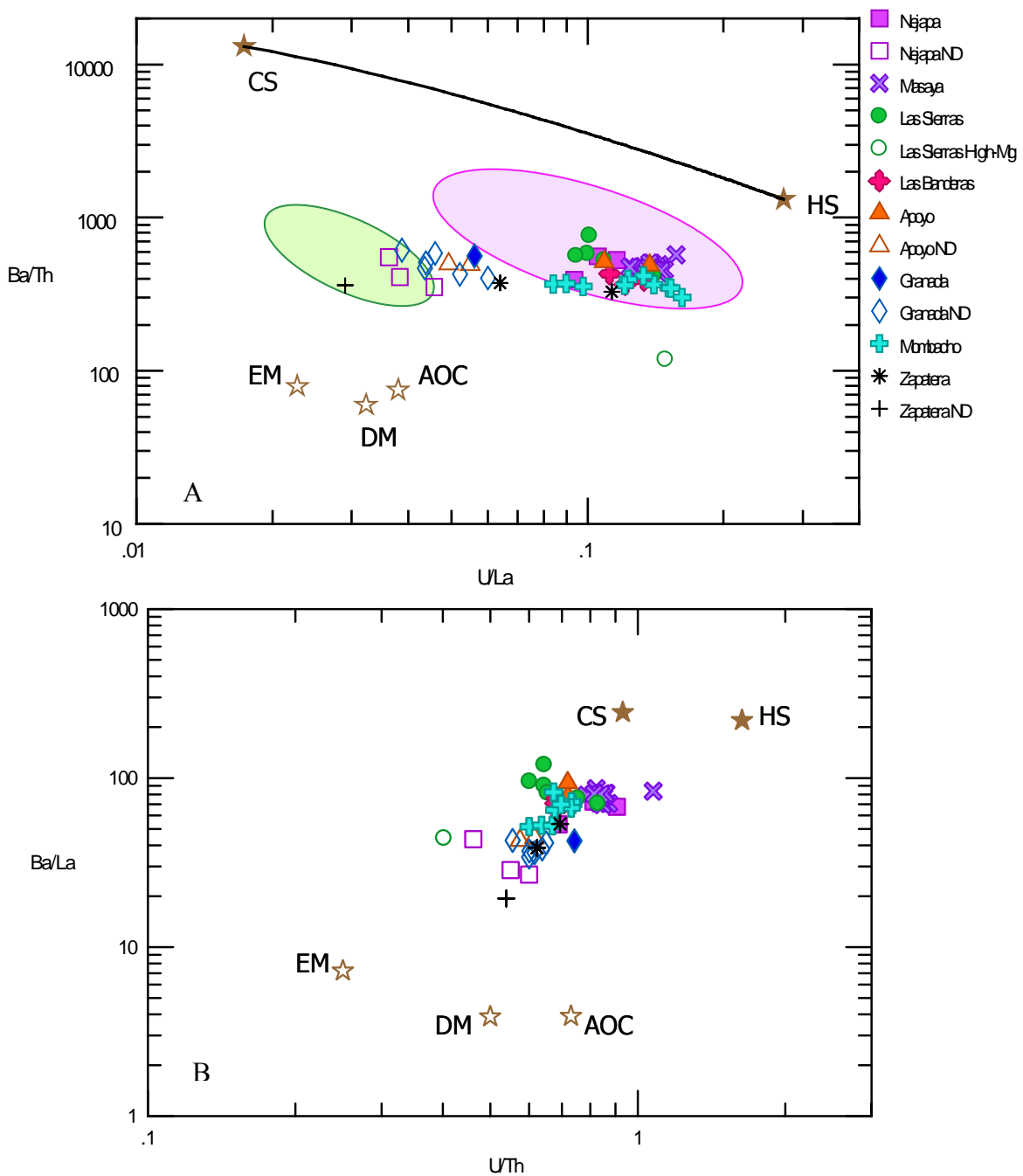


Figure 1.10 Abbreviations used are CS – carbonate sediment, HS- hemipelagic sediment and AOC – altered oceanic crust based on Patino et al. (2000); EM – enriched mantle and DM – depleted mantle based on Sun & McDonough (1989). A. shows local variations in the relative contribution of each sediment type. The shaded areas represent Telica volcano (pink) and Arenal (green), which show mixing sub-parallel to the mixing line (black line) connecting the HS and CS end-members. B. shows regional variations in slab signature.

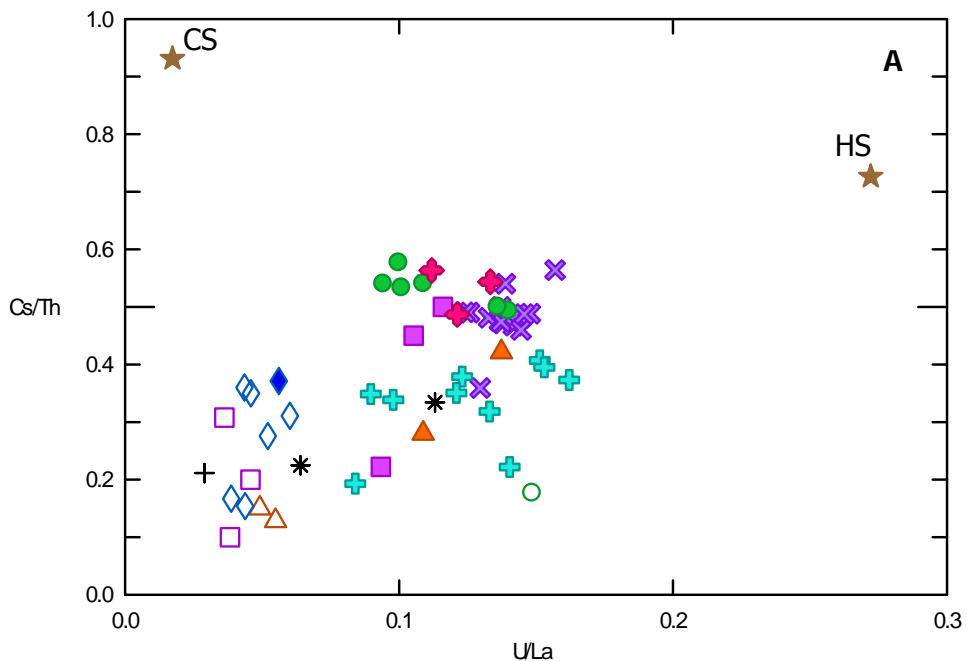
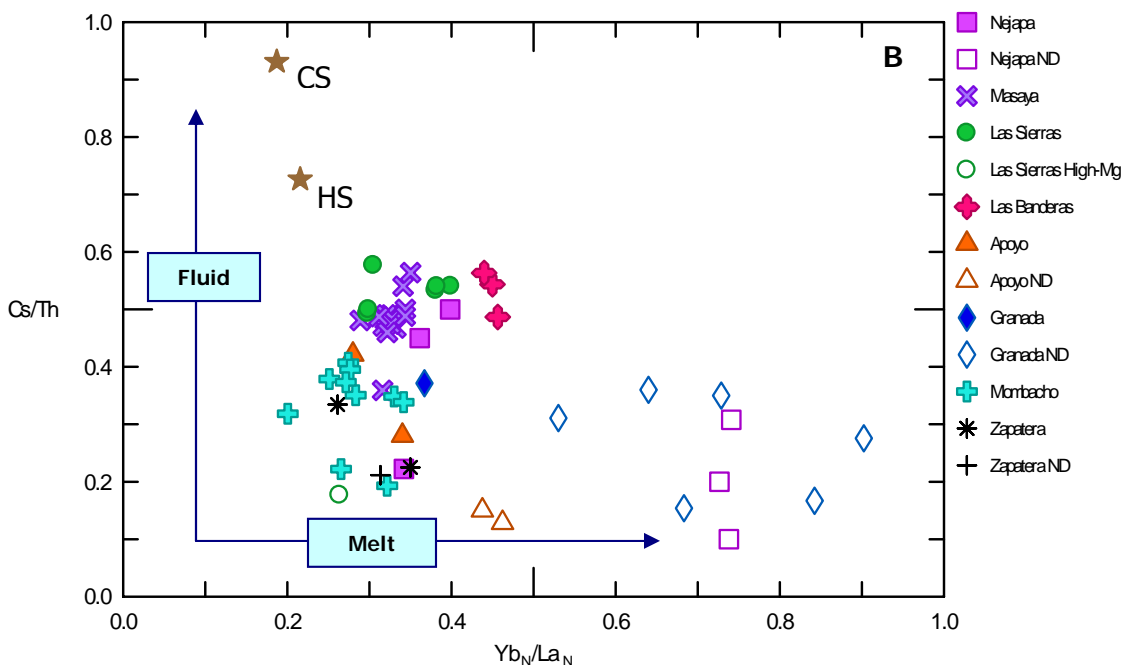


Figure 1.11 A. Variation in fluid contribution as shown by Cs/Th vs. U/La. Higher amounts of Cs/Th indicate a larger influence of fluid as Cs is a highly fluid mobile element. Higher amounts of U/La suggest stronger influence of hemipelagic sediment. Figure 1.11 B. Cs/Th vs.  $\text{Yb}_N/\text{La}_N$  space shows fluid vs. melt trend in terms of incompatible vs. compatible elements. REEs normalized to chondritic values (McDonough & Sun, 1995). Legend for both figures A & B as shown by B.



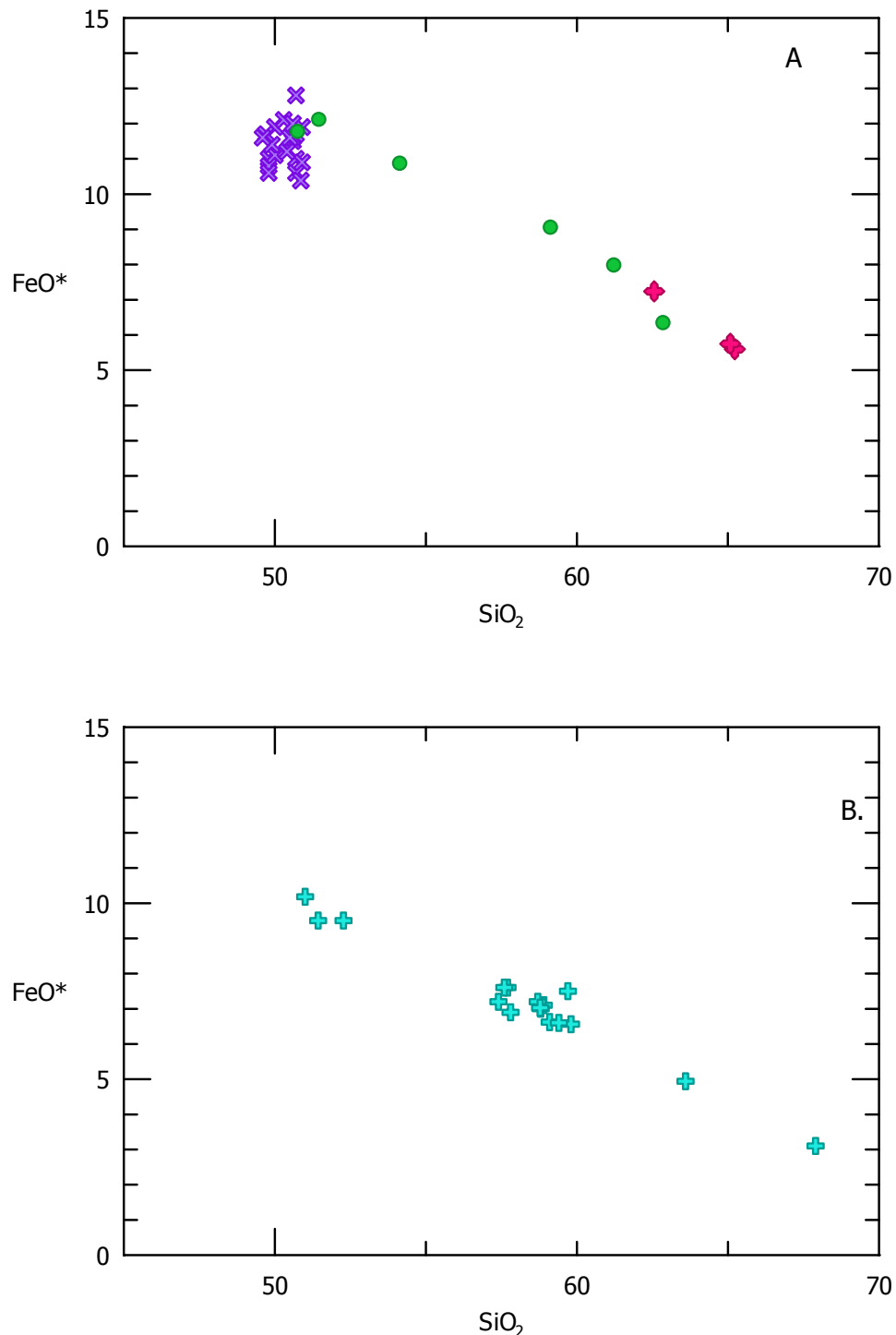


Figure 1.12 A. shows fractional crystallization from the Las Sierras ignimbrite including Masaya volcano. B. depicts Mombacho volcano, which shows a similar pattern.  $\text{FeO}^*$  represents total iron.

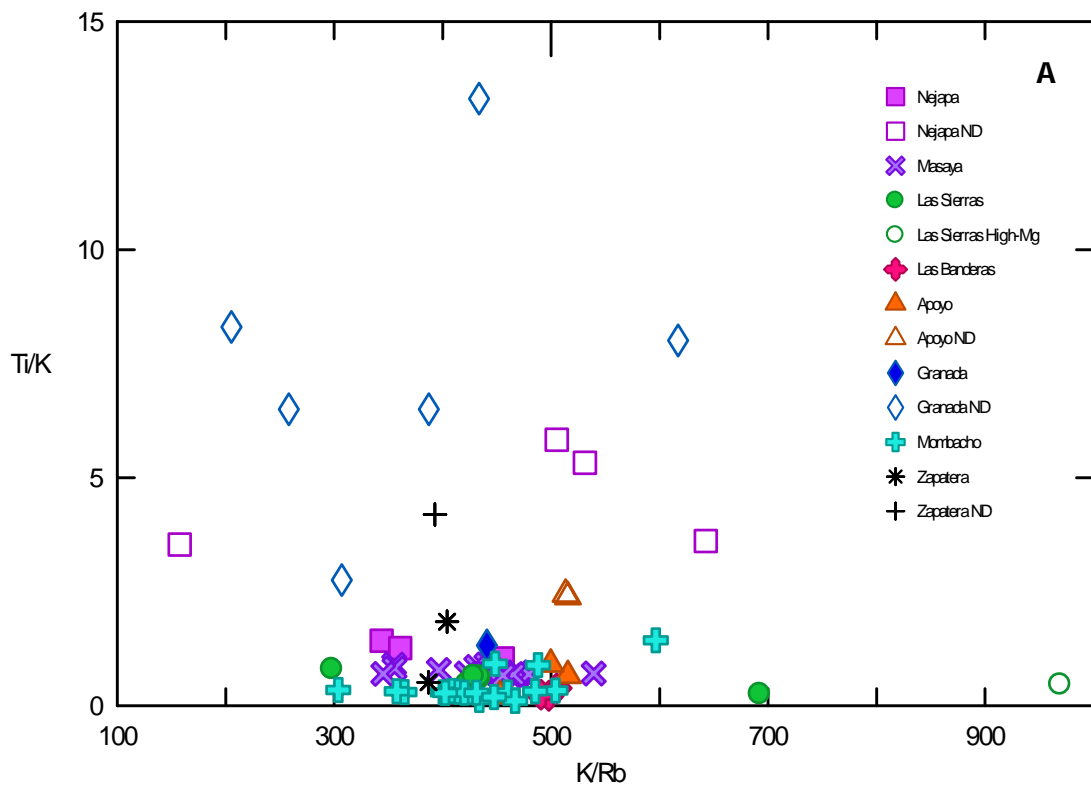
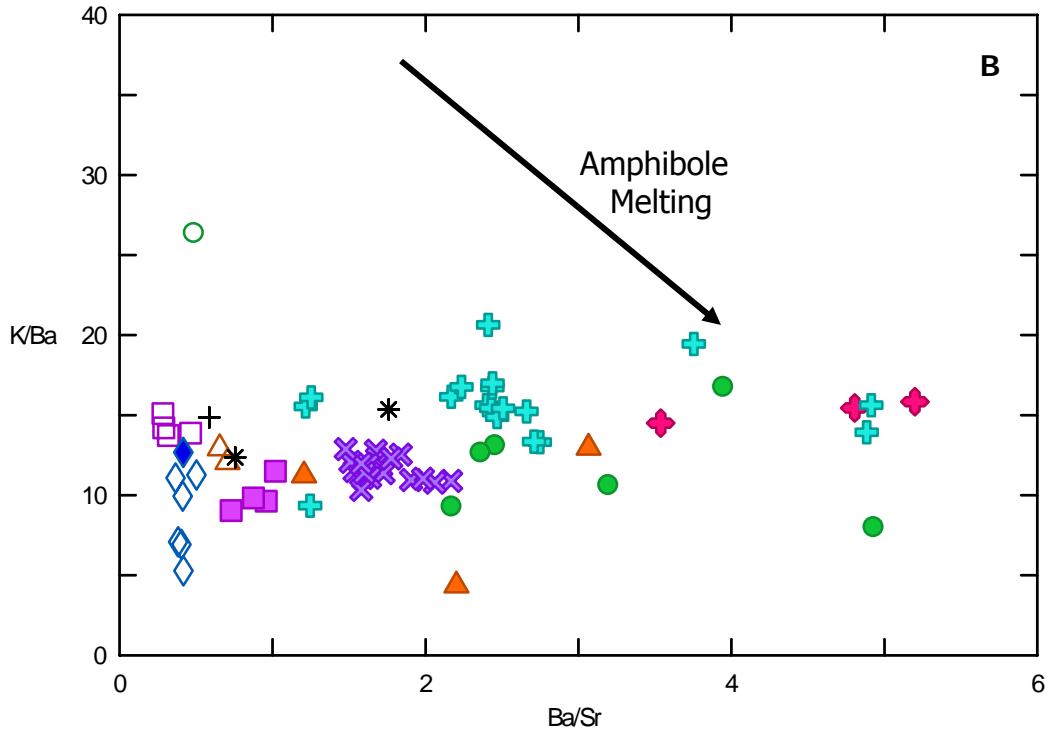


Figure 1.13 A. ND samples show a wide range of  $K/Rb$  suggesting that the preferential melting of amphibole as proposed by Reagan et al. (1994) may be incorrect. B. The melting trend of amphibole is oblique to southeastern Nicaragua samples indicating that the model may not be applicable to this region.



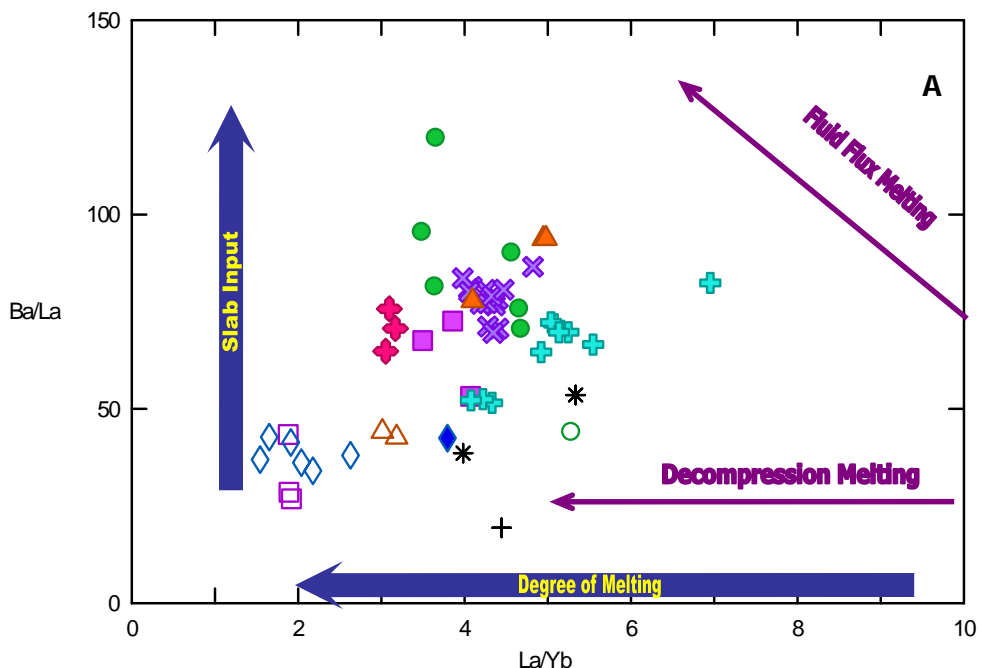
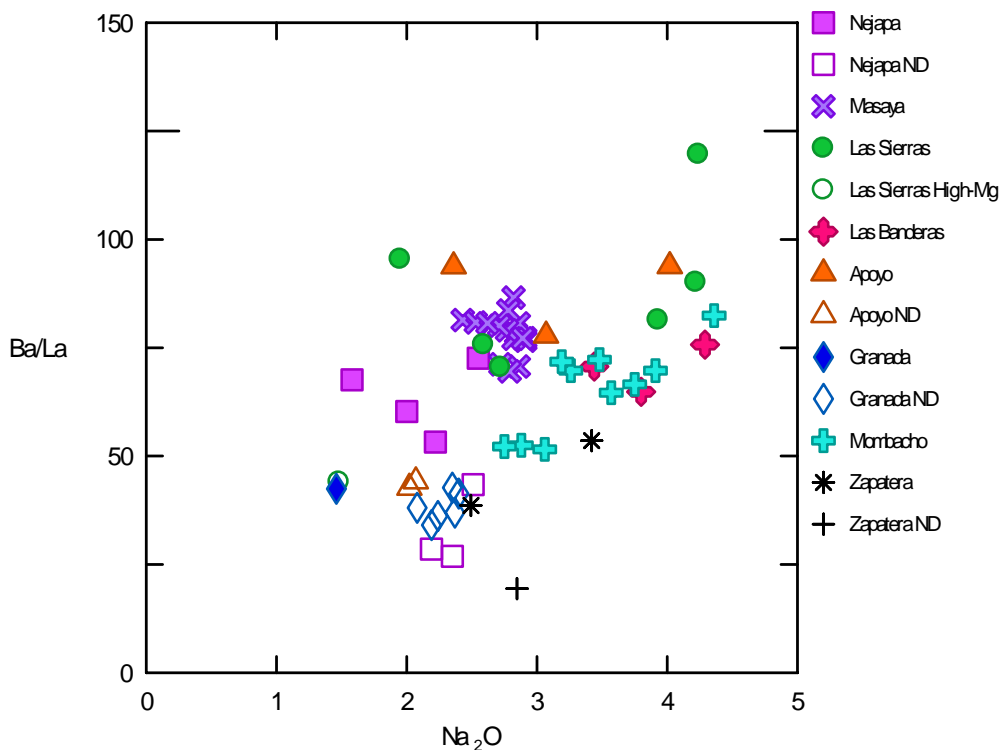


Figure 1.14. A. Ba/La vs. La/Yb shows the importance of decompression melting in the generation of the ND lavas. Compared to the depleted lavas, the ND lavas have a greater degree of melt and lower amount of slab input. B. A steeper slab dip in SE Nicaragua factors into both lower slab input signature (Ba/La) and greater degree of melting (lower Na<sub>2</sub>O). The latter is especially true of volcanic centers with bimodal distribution of ND and depleted lavas.



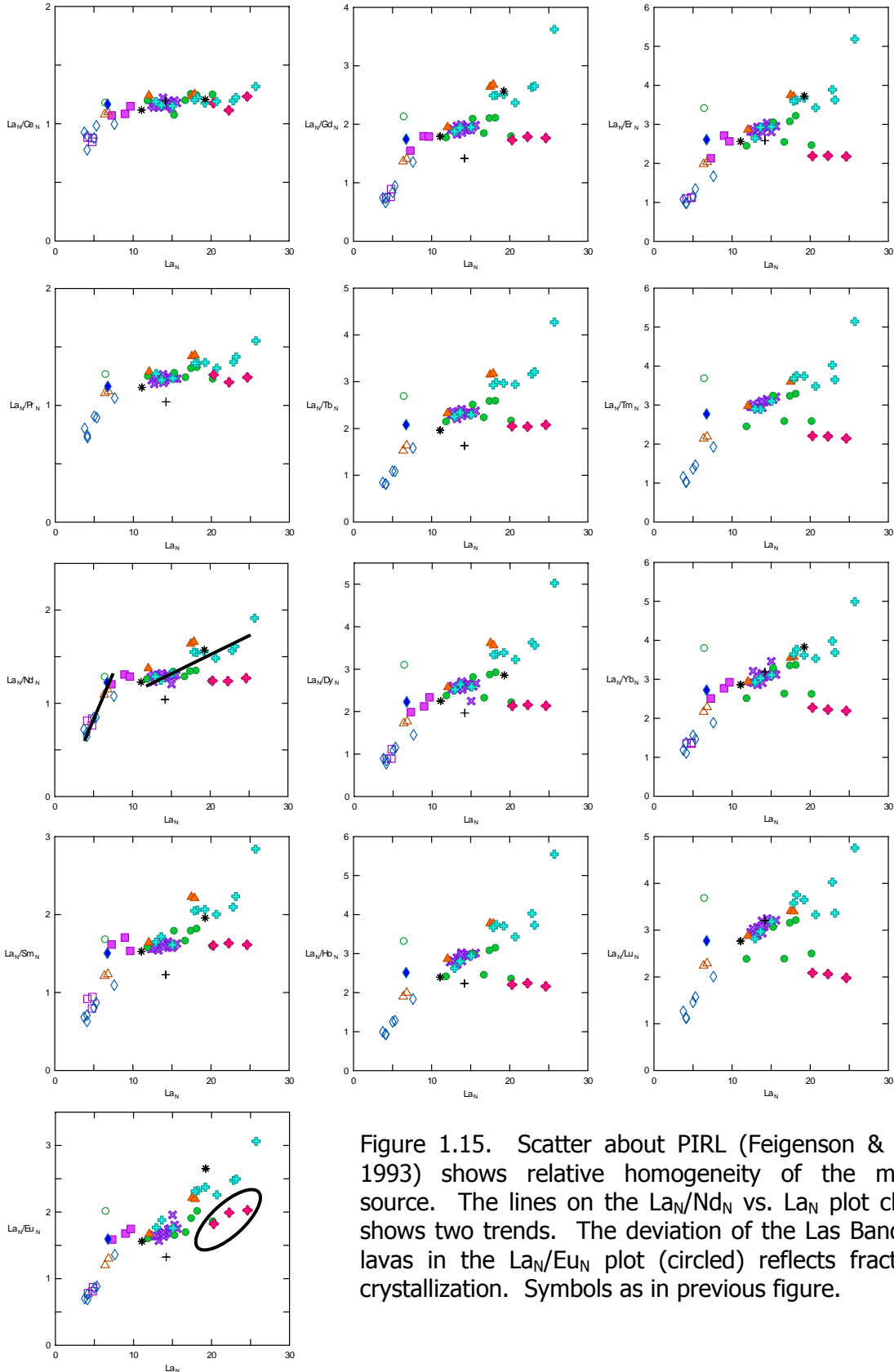


Figure 1.15. Scatter about PIRL (Feigenson & Carr, 1993) shows relative homogeneity of the mantle source. The lines on the  $\text{La}_N/\text{Nd}_N$  vs.  $\text{La}_N$  plot clearly shows two trends. The deviation of the Las Banderas lavas in the  $\text{La}_N/\text{Eu}_N$  plot (circled) reflects fractional crystallization. Symbols as in previous figure.

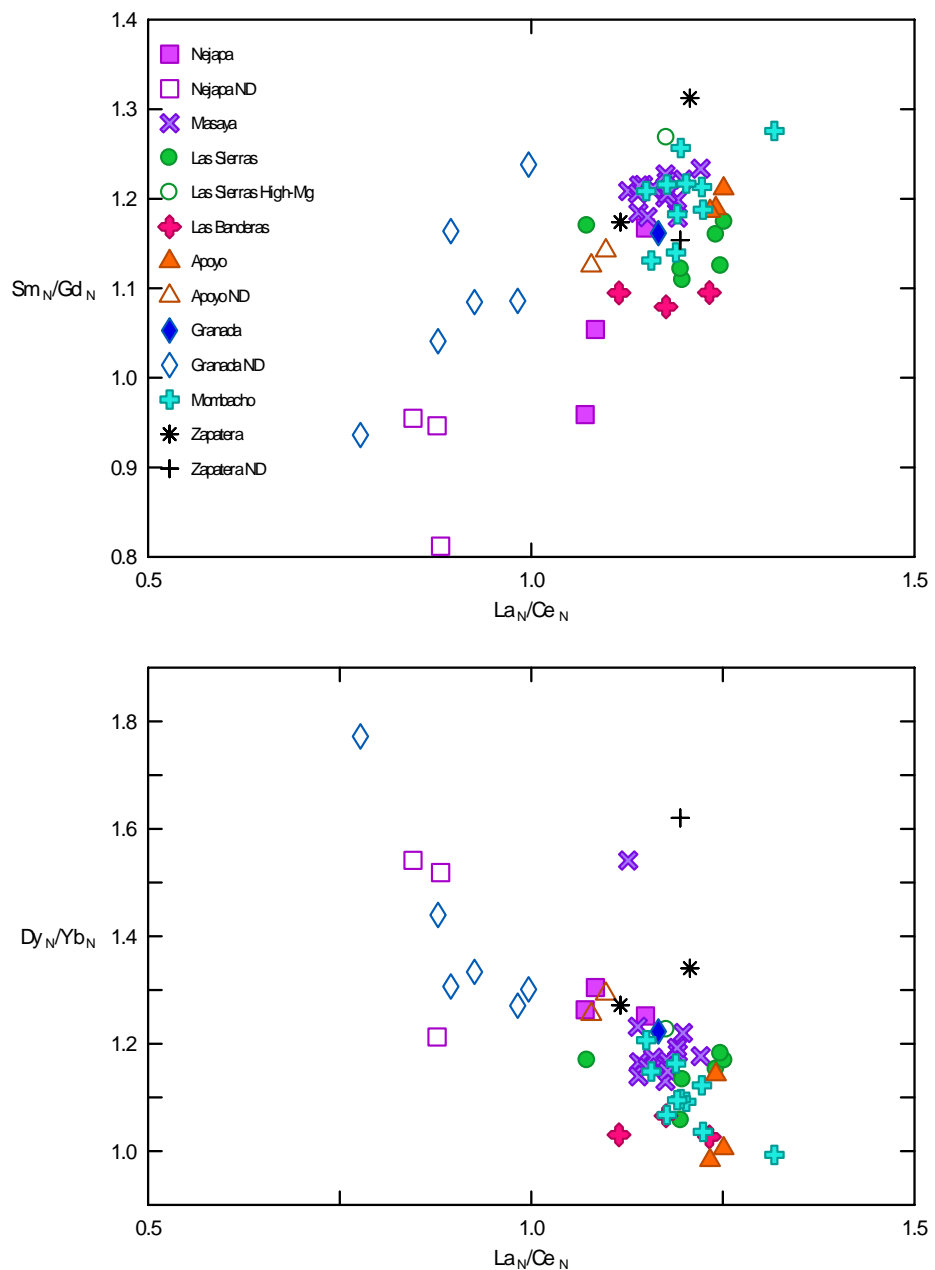


Figure 1.16. Differences in the ratio of La/Ce between the ND and depleted lavas are shown against both MREEs in A. and HREEs in B. This cannot be explained by fractionation. The subscript N signifies normalization to chondritic values (McDonough & Sun, 1995).

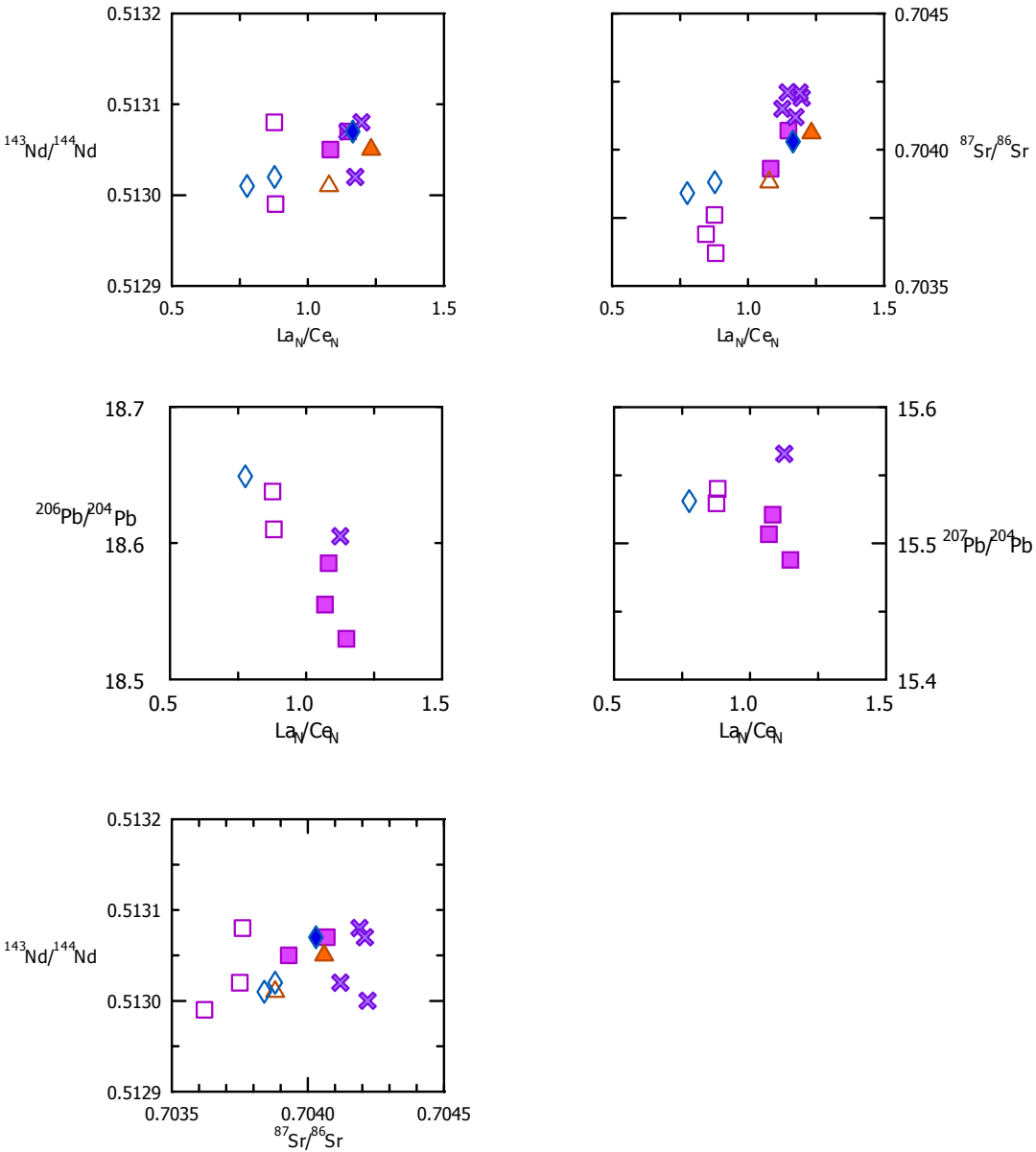


Figure 1.17. Isotope systematics against La/Ce (normalized to chondritic values) and Nd isotopes vs. Sr isotopes. The separation between the ND and depleted samples indicates two distinct sources as fractionation cannot explain the separate trends.

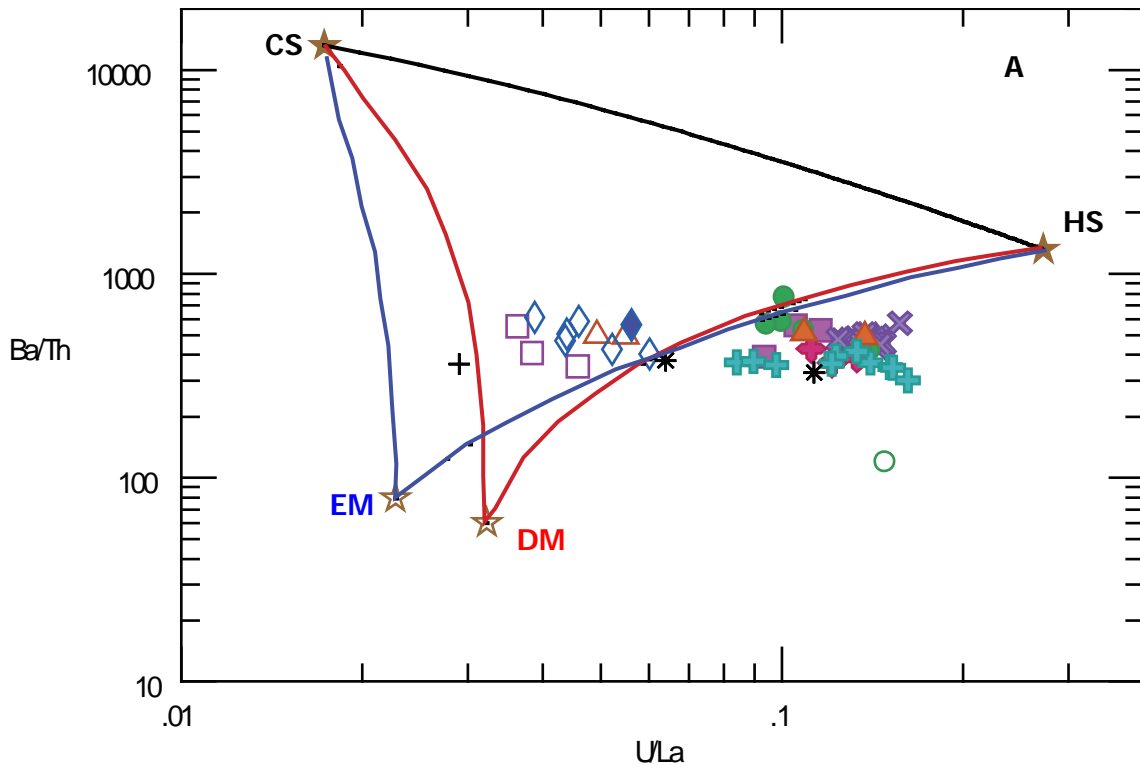
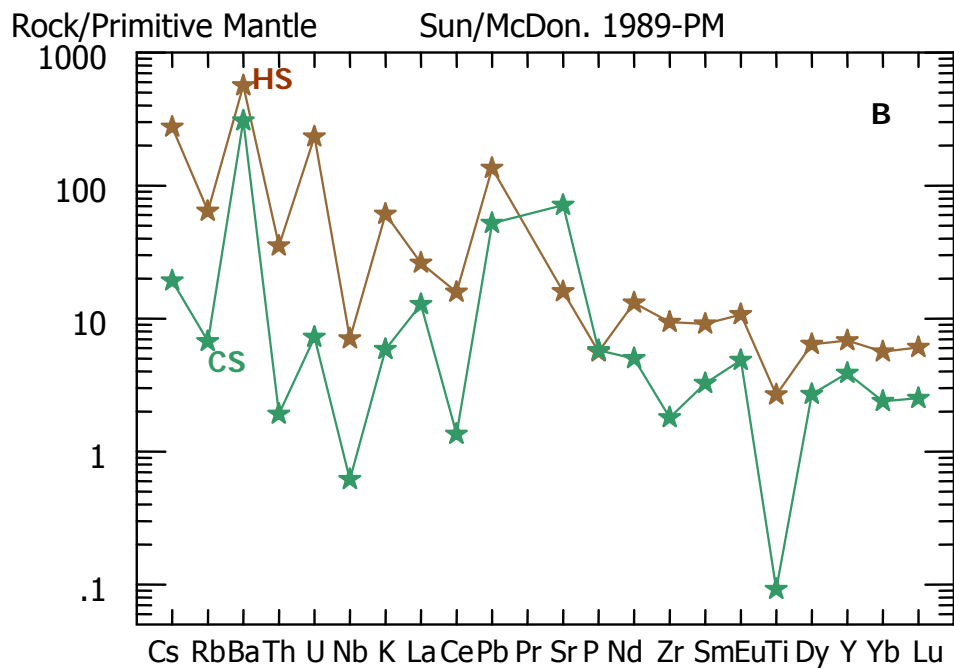


Figure 1.18. A. Using the two sediment layers (red lines show mixing with DM; blue lines shows mixing with EM) cannot account for all variations. B. Geochemistry of the sediment layers form DSDP 495 (Patino, 1997; Patino et al., 2000)



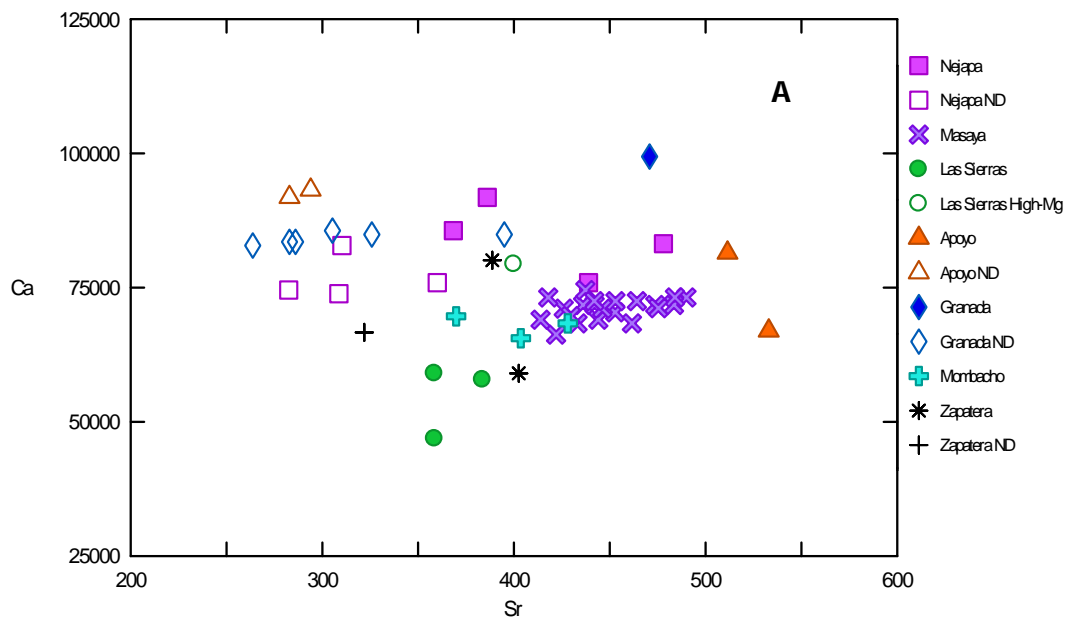
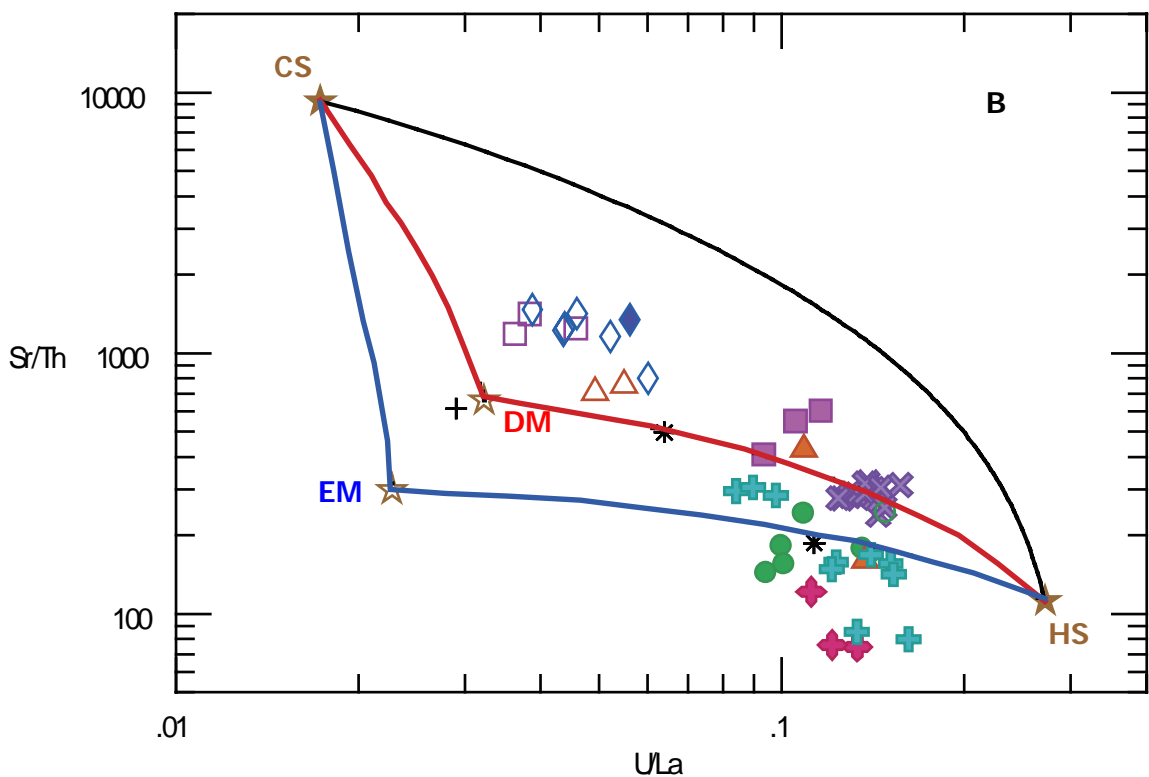


Figure 1.19A. Lack of a linear relationship between Ca and Sr shows the Sr to be behaving incomparably for lavas with  $\text{SiO}_2 \leq 55$  wt%. B. Binary mixing lines between CS, HS and DM or EM do not encompass all variations.



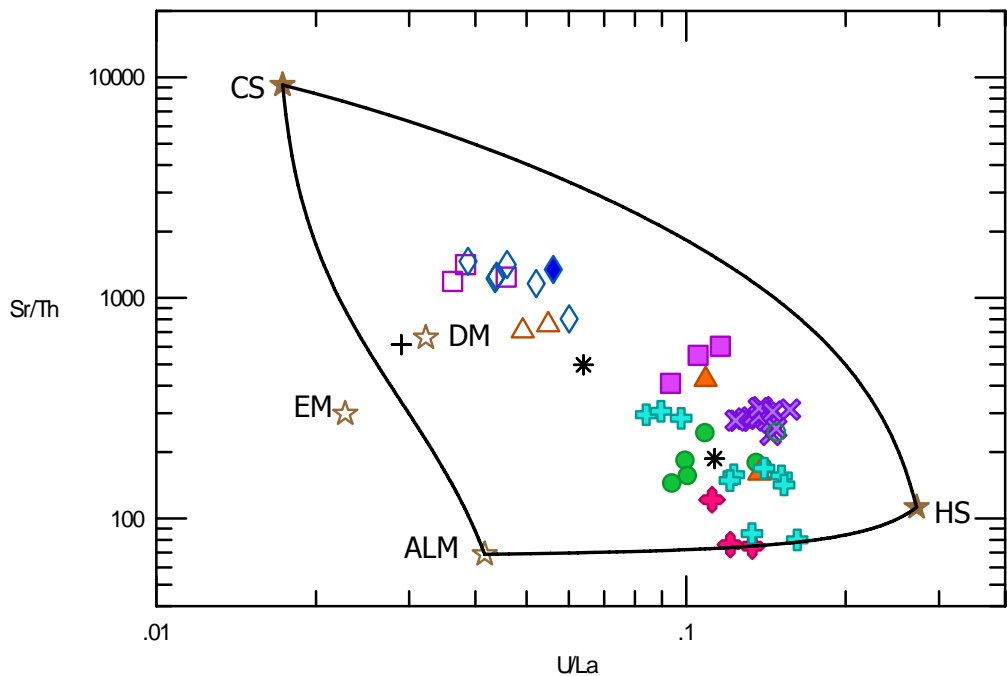
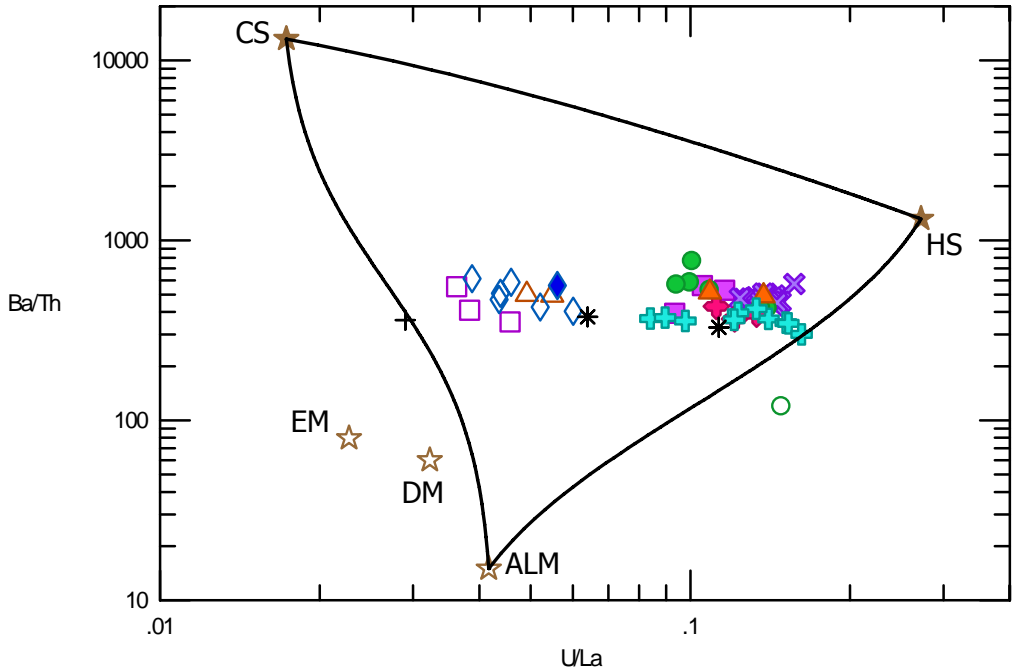


Figure 1.20 Symbols are as in last figure. A. Sr/Th vs. U/La space. Adding altered lower MORB (ALM) to a mixing model accounts for all variability seen in the samples. B. The same holds true in Ba/Th vs. U/La space, with the exception of the high-Mg LS lava, shown by the open green circle.



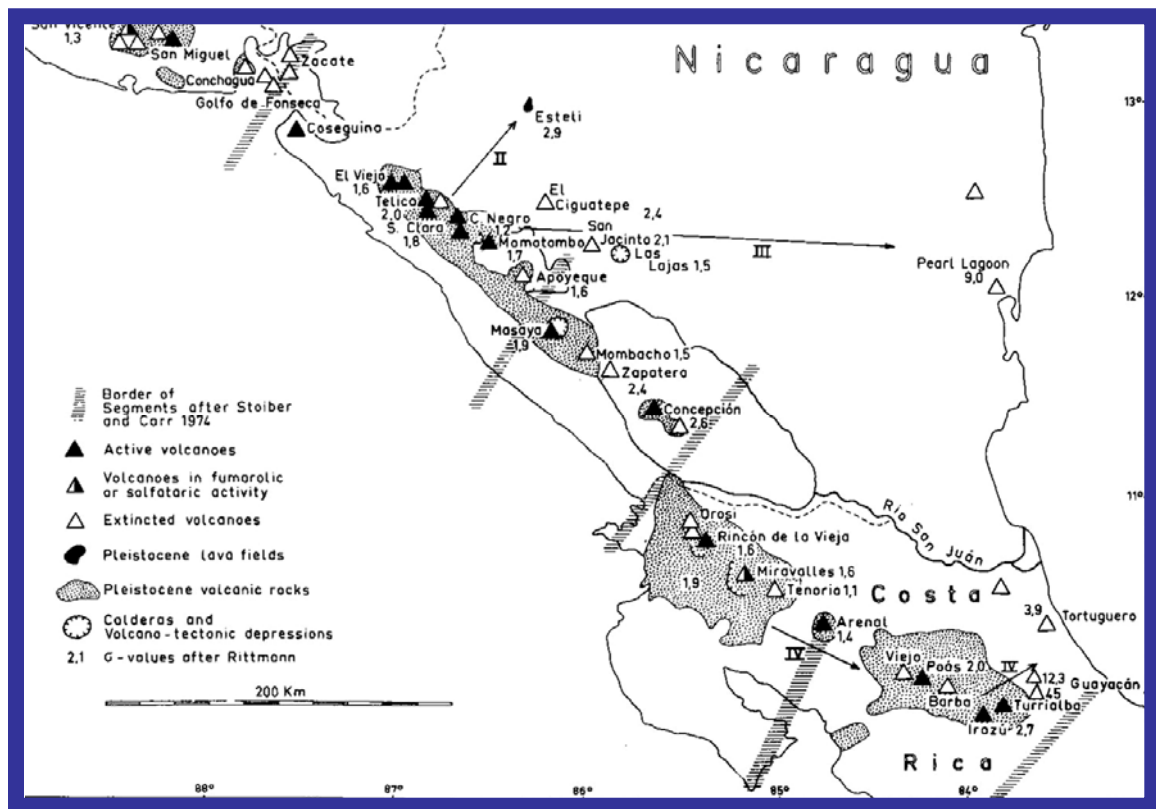
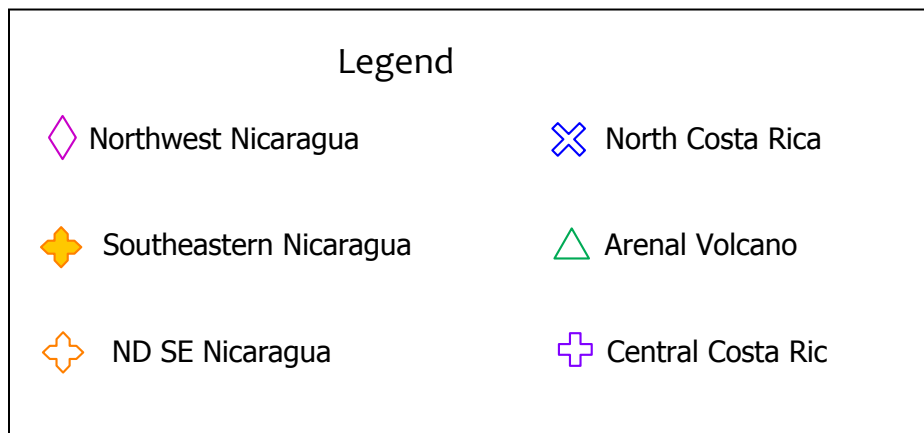


Figure 1.21 The segments of Nicaragua through Costa Rica as defined by Stoiber and Carr (1974). Notice that one segment delineation in Costa Rica goes through Arenal volcano. Figure adapted from Weyl (1980).



Figure 1.22 Map of Nicaragua and Costa Rica showing the symbols that correspond to each part of the arc used in chapter 3 of this thesis. Adapted from UNAVCO.



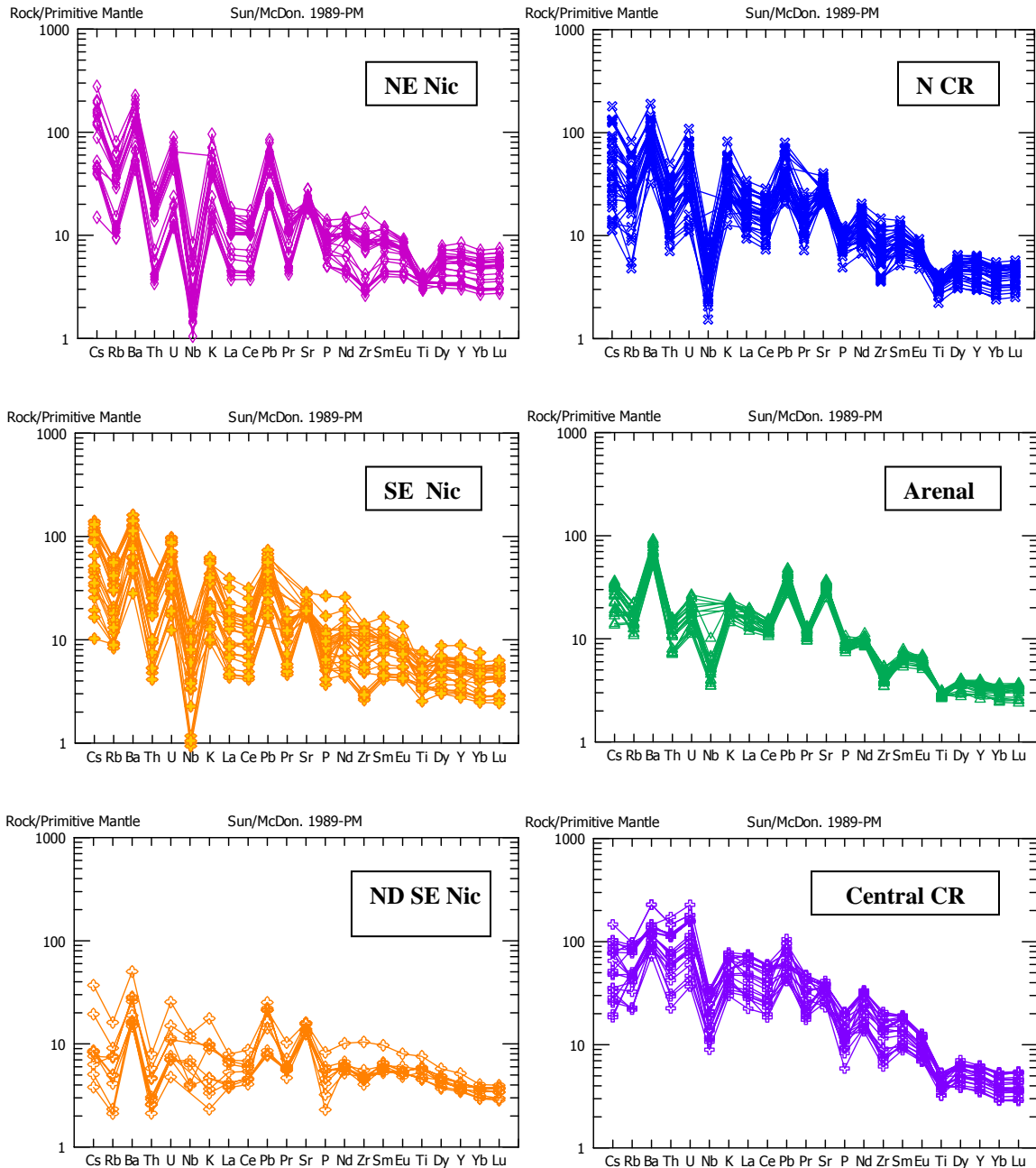


Figure 1.23 Spider diagrams, with increasingly compatible elements left to right, normalized to primitive mantle (Sun & McDonough, 1989). Notice that Nb in southeast Nicaragua ND lavas lacks the depletion seen in all other volcanic arc segments.

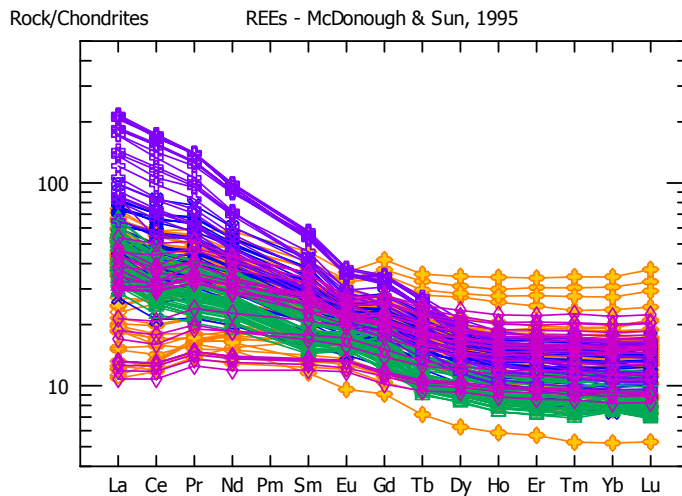
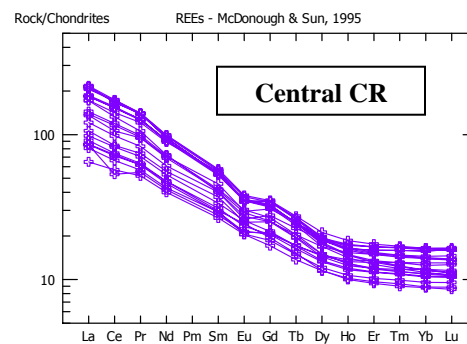
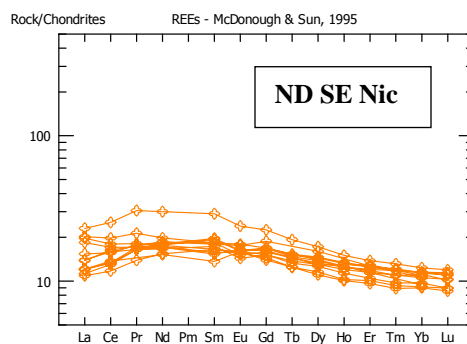
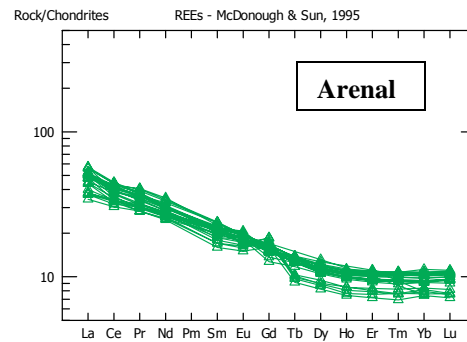
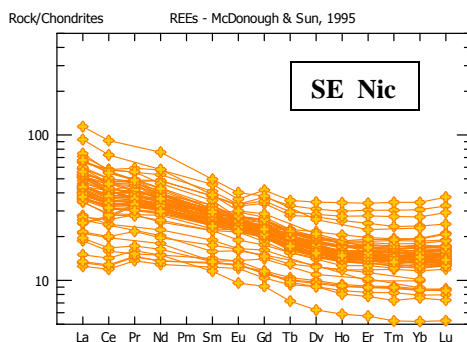
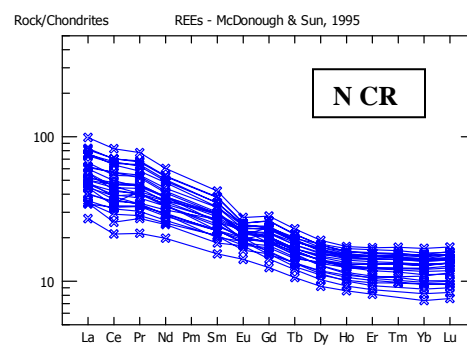
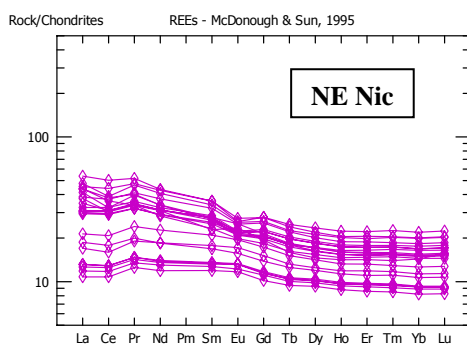


Figure 1.24 REE patterns of Nicaragua and Costa Rica together and separated by segment. Nicaragua lavas show a greater range in LREE composition whereas Costa Rica lavas show relative enrichment in LREEs, with the exception of Arenal lavas. Some N Costa Rica lavas give a hint of upturn in the HREEs akin to the more evolved samples in SE Nicaragua.



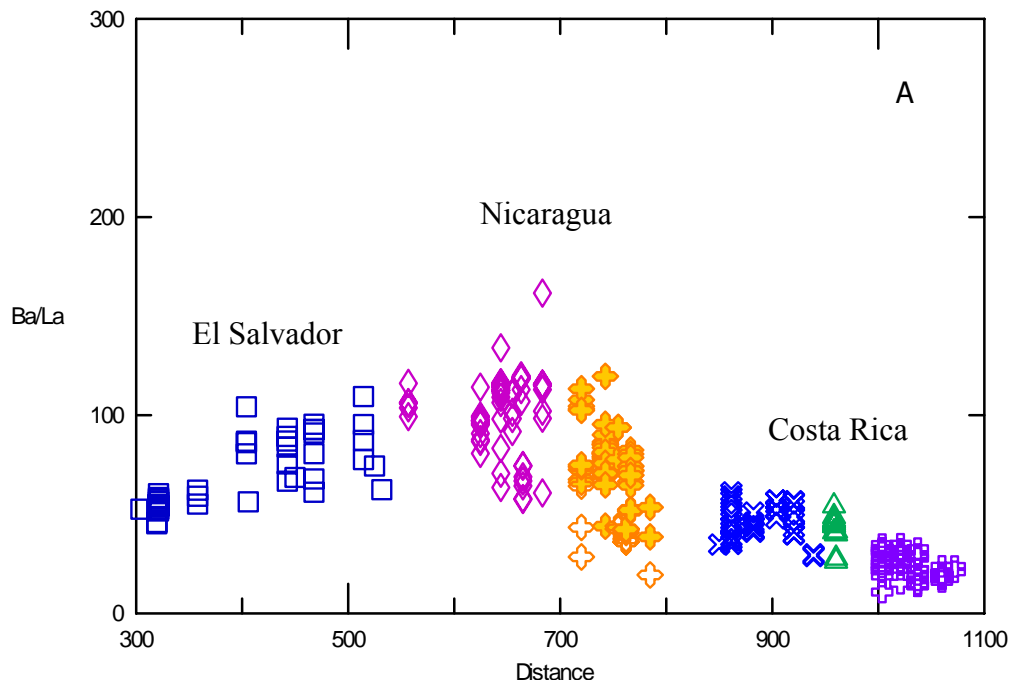
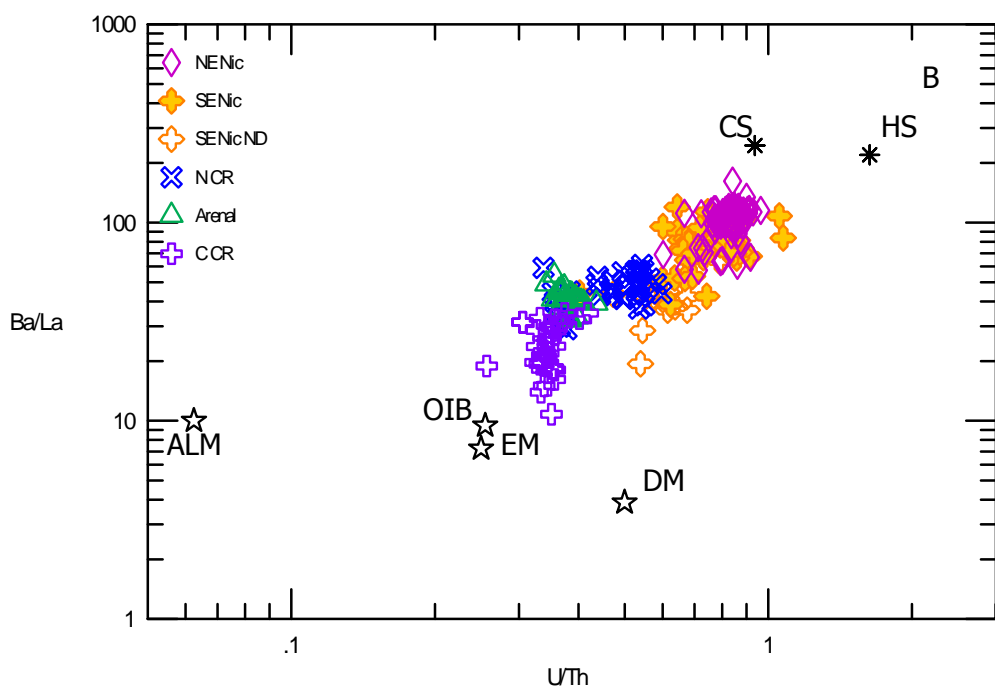
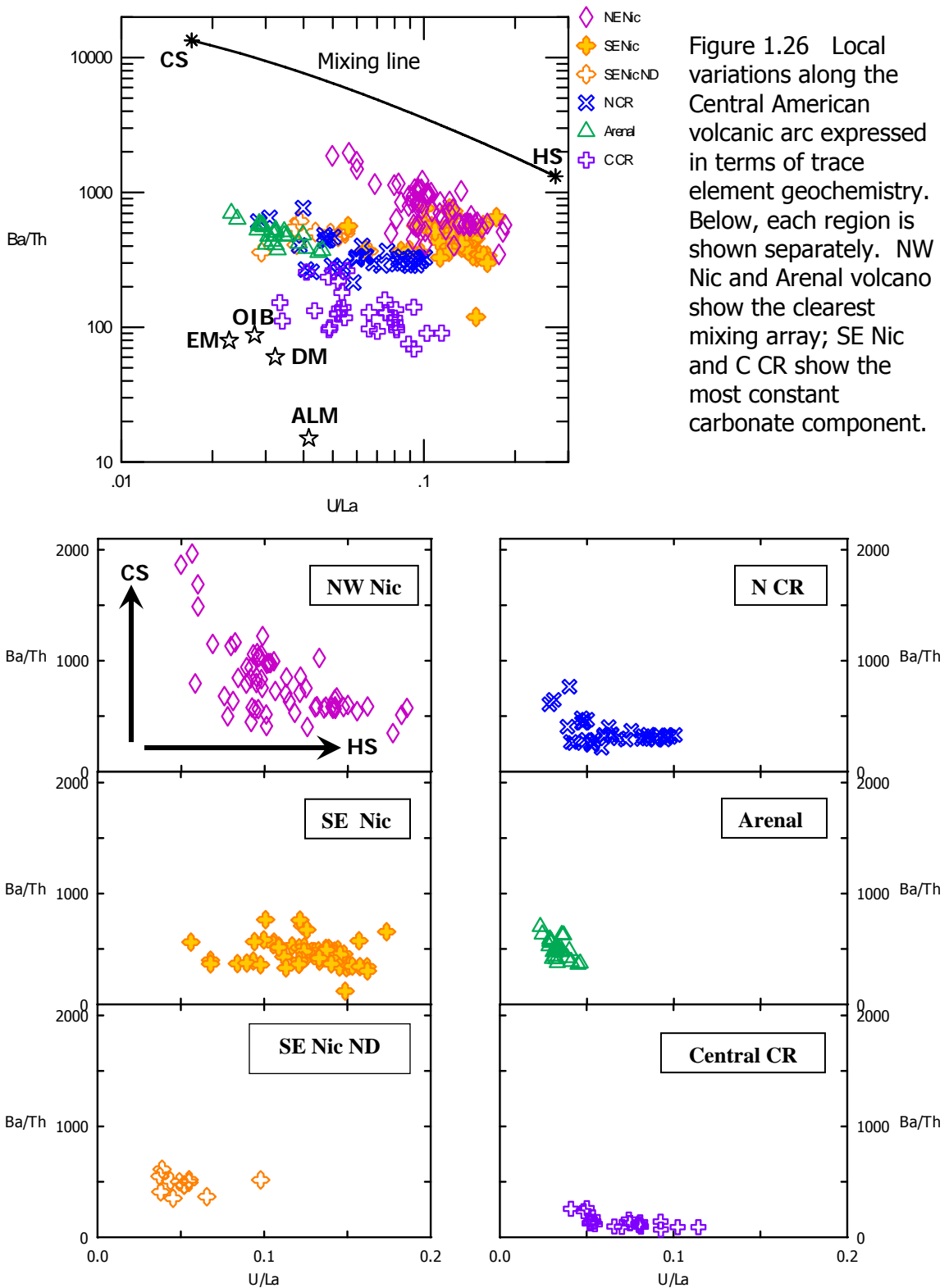


Figure 1.25 A. Regional variations in slab signature are evident along the Central American volcanic arc. Symbols as in figure below. B. Regional variations shown in terms of trace element ratios taken from Patino et al. (2000). CS – carbonate sediment; HS – hemipelagic sediment; ALM – altered lower MORB; OIB – oceanic island basalt; EM – enriched mantle; DM – depleted mantle.





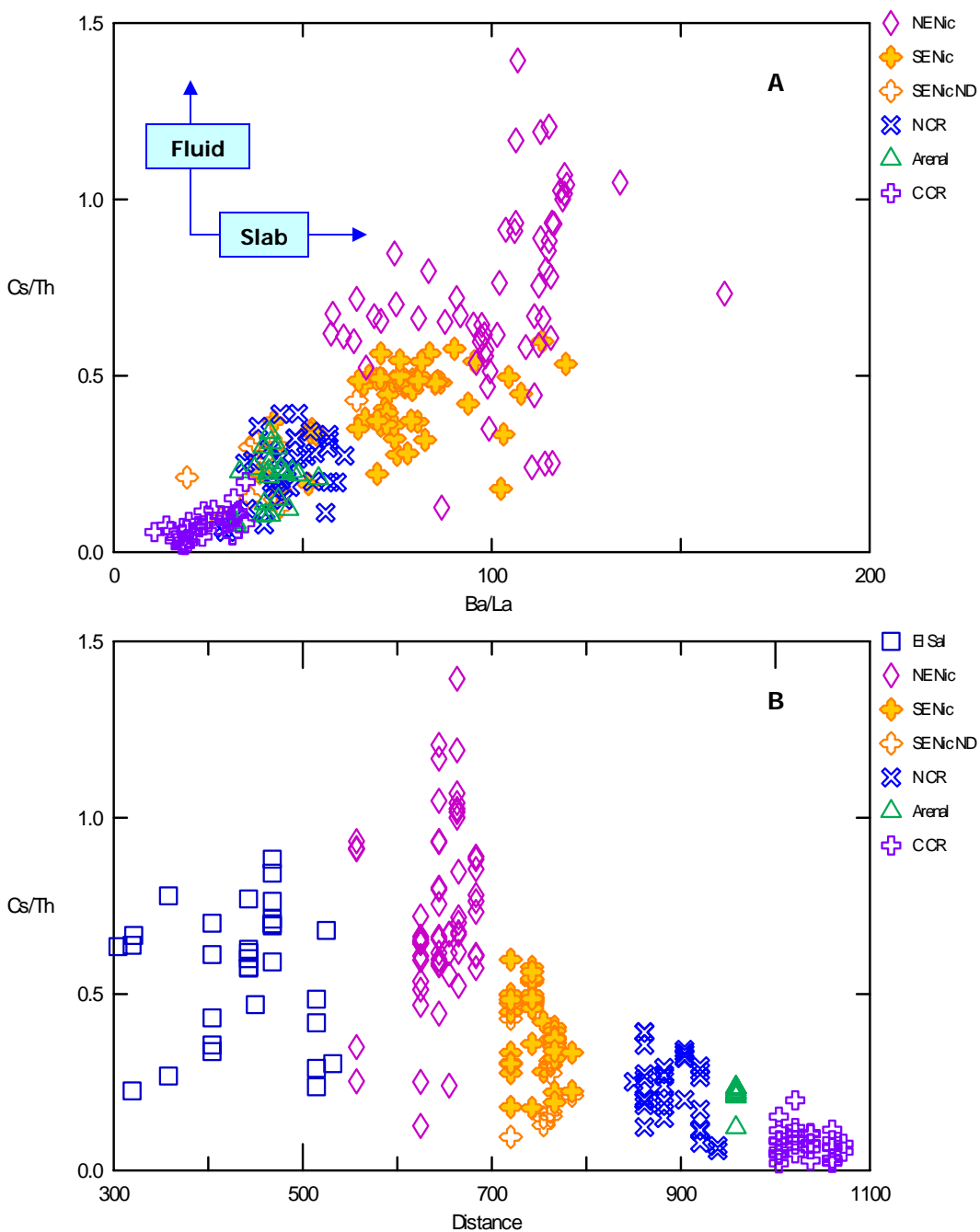


Figure 1.27 A. This plot shows a positive linear relationship between slab signature ( $\text{Ba/La}$ ) and fluid flux ( $\text{Cs/Th}$ ). B. Fluid flux decreases down the CA arc after a maximum in NW Nicaragua. Open blue square are Guatemala.

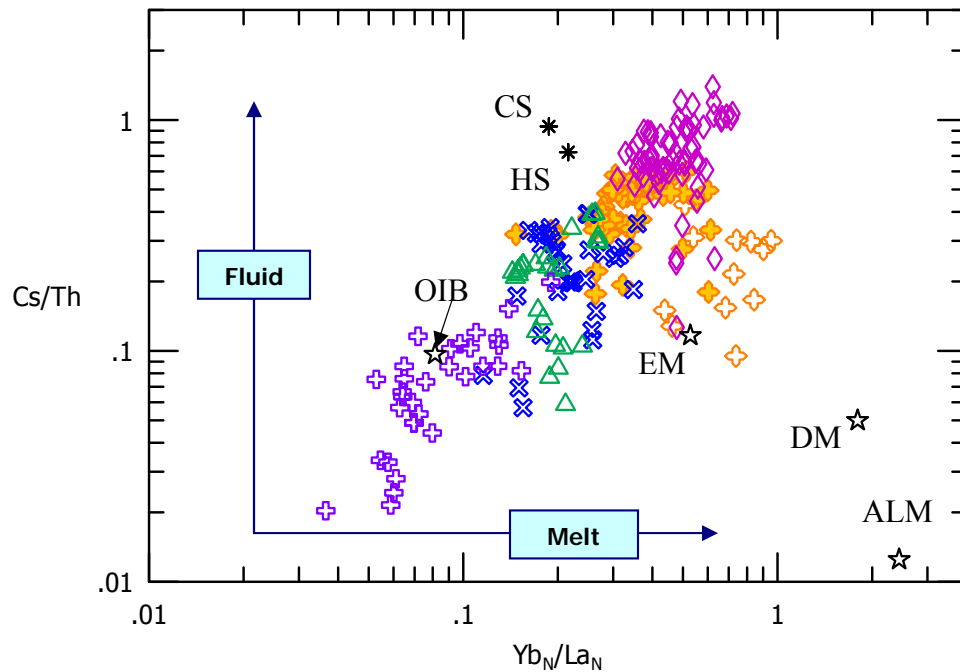
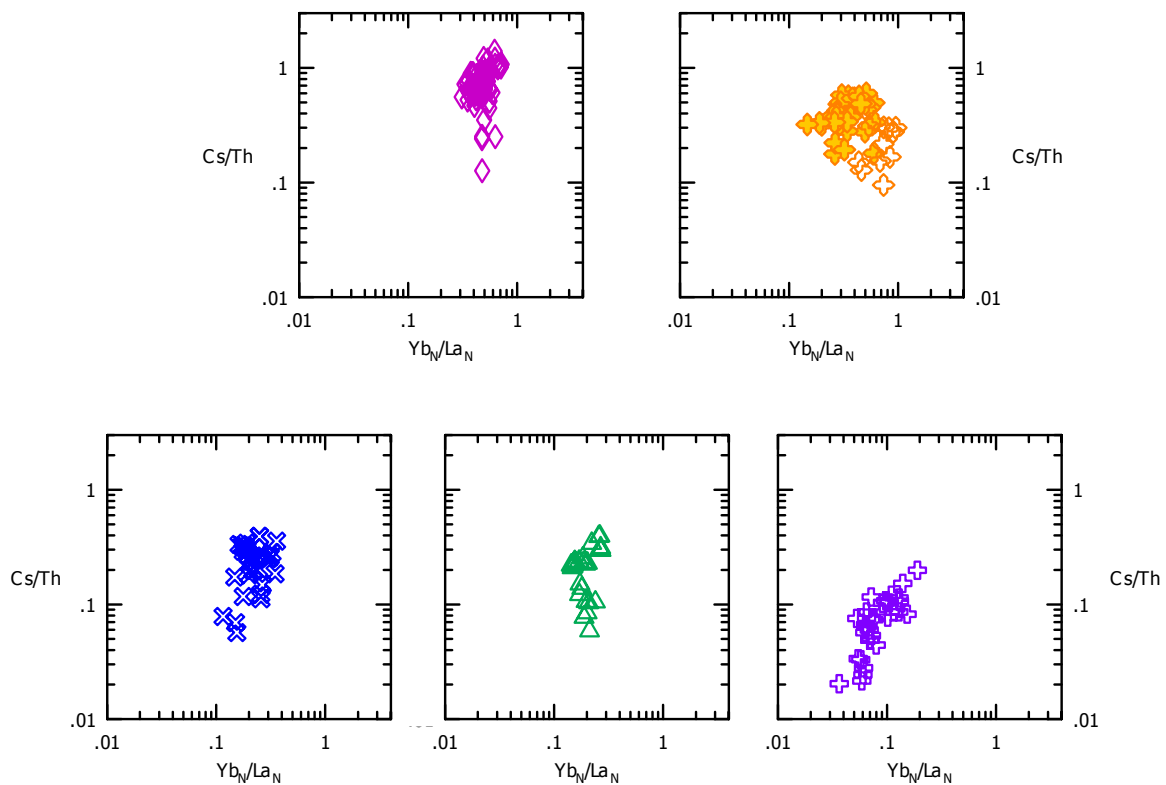


Figure 1.28  $\text{Yb/La}$ , normalized to chondritic values (McDonough & Sun, 1995), vs.  $\text{Cs/Th}$  shows where samples fall relative to fluid and melt trends. ALM - Altered Lower MORB. Below, each area of the arc is shown separately to show local variations.



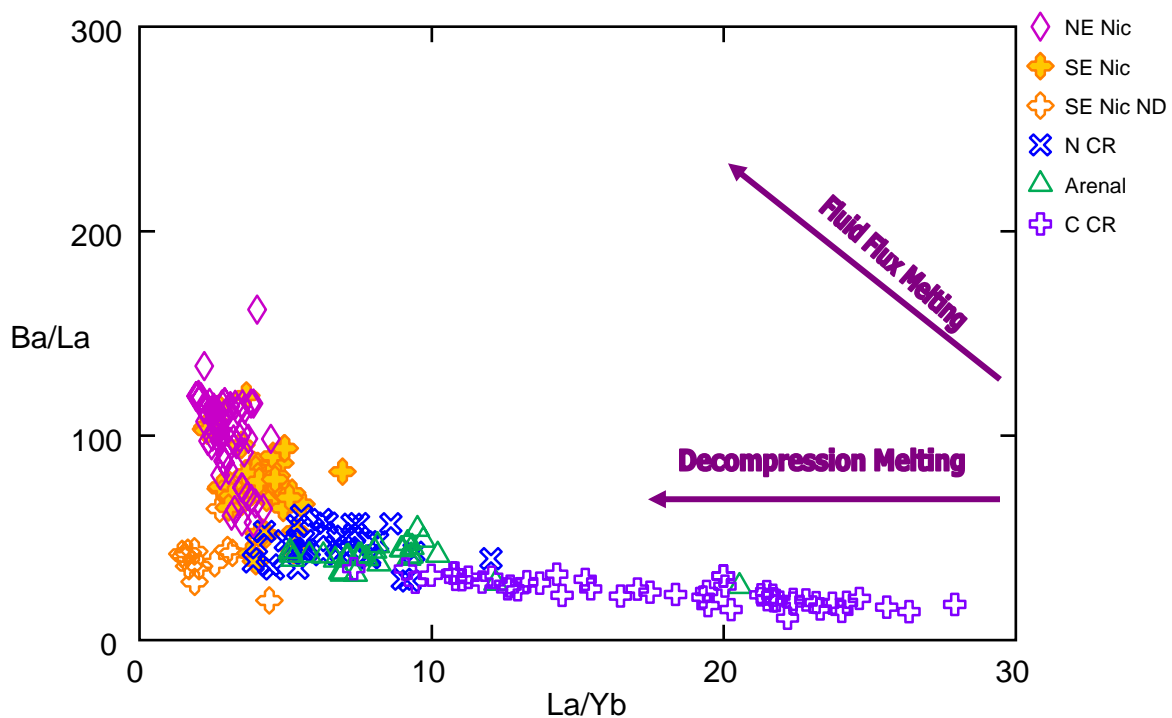


Figure 1.29 Shows the contribution of different melt styles and degrees of melt; adapted from Cameron et al. (2002). The ND lavas from Nicaragua show a low slab signal and the most decompression melting. C Costa Rica lavas also have a low slab signal, but do not show the amount of decompression melting as the ND lavas.

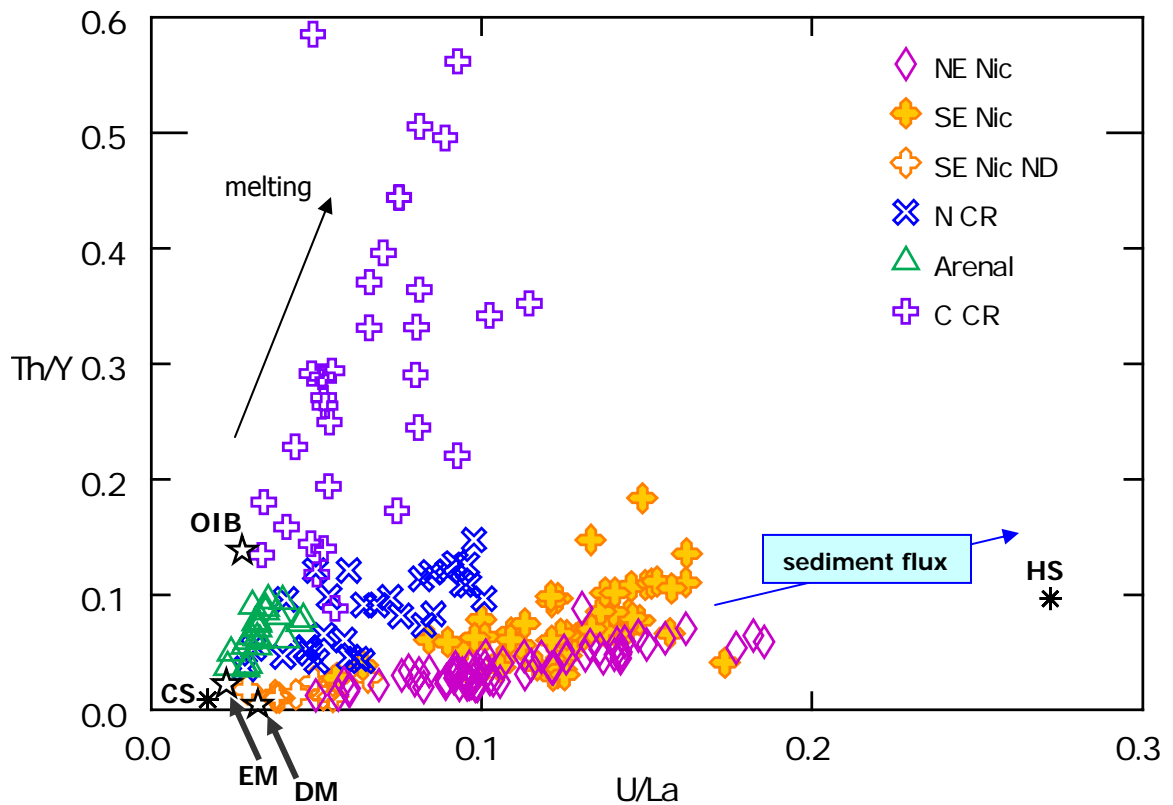


Figure 1.30. Th/Y vs. U/La space. Nicaragua samples clearly fall between mantle (EM, DM /carbonate and hemipelagic sediments whereas C Costa Rica and Arenal lavas trend toward an OIB end-member. Central Costa Rica samples go beyond OIB suggesting a residue or partial melting in the presence of garnet.

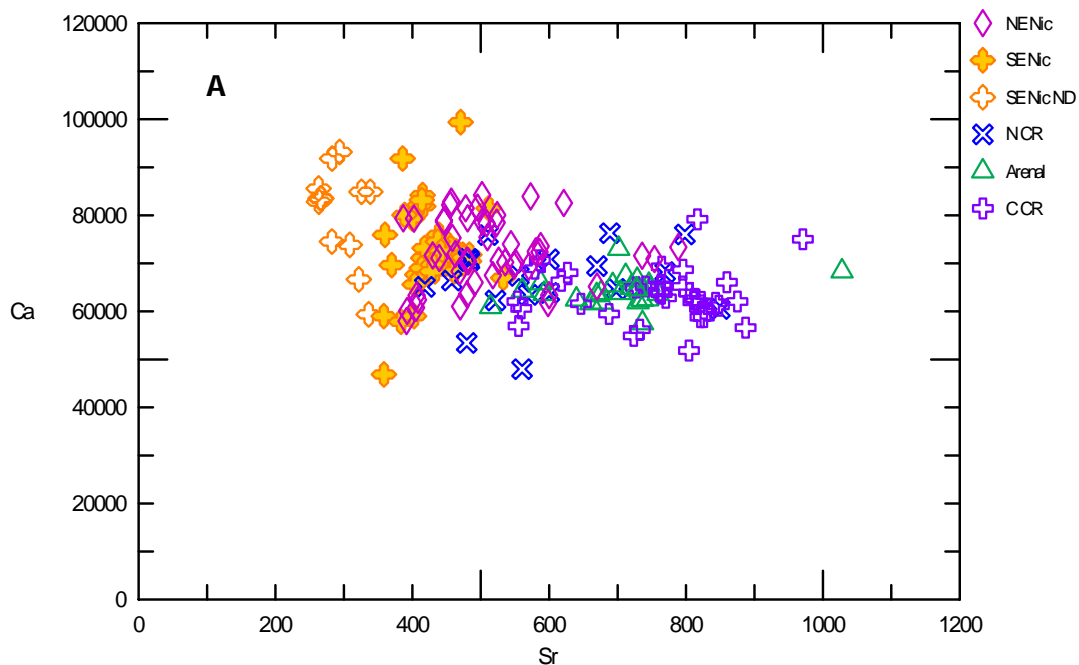
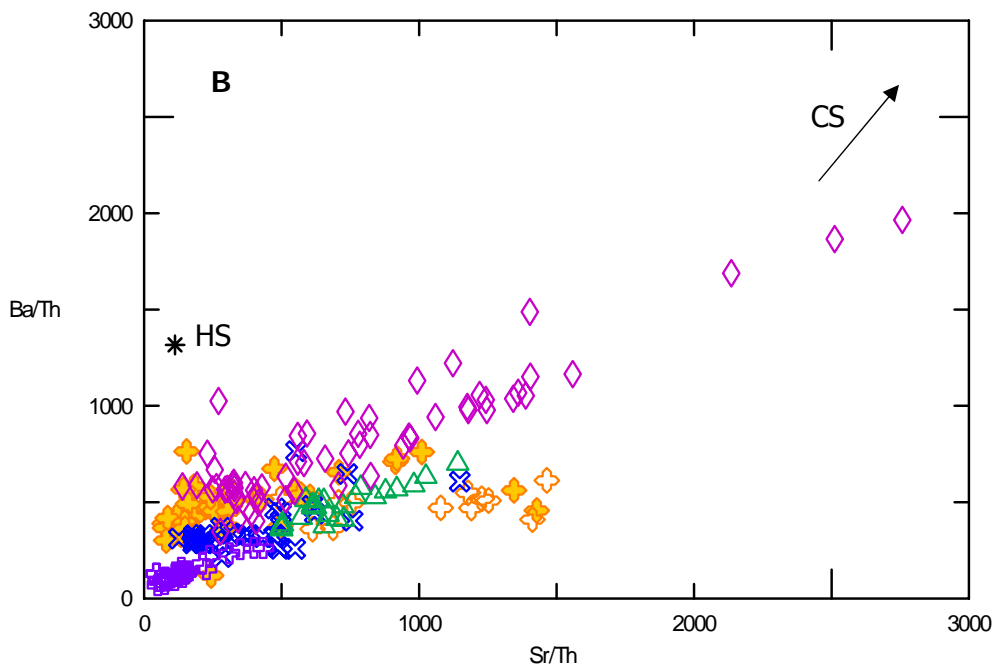


Figure 1.31. A. Ca vs. Sr checks on the behavior of Sr. Here, it is behaving incompatibly. Data filtered to  $\text{SiO}_2 \leq 55$  wt.% to eliminate fractionated samples. B. The linear relationship between  $\text{Sr/Th}$  and  $\text{Ba/Th}$  shows that  $\text{Ba/Th}$  is indeed a valid proxy for the carbonate sediment.



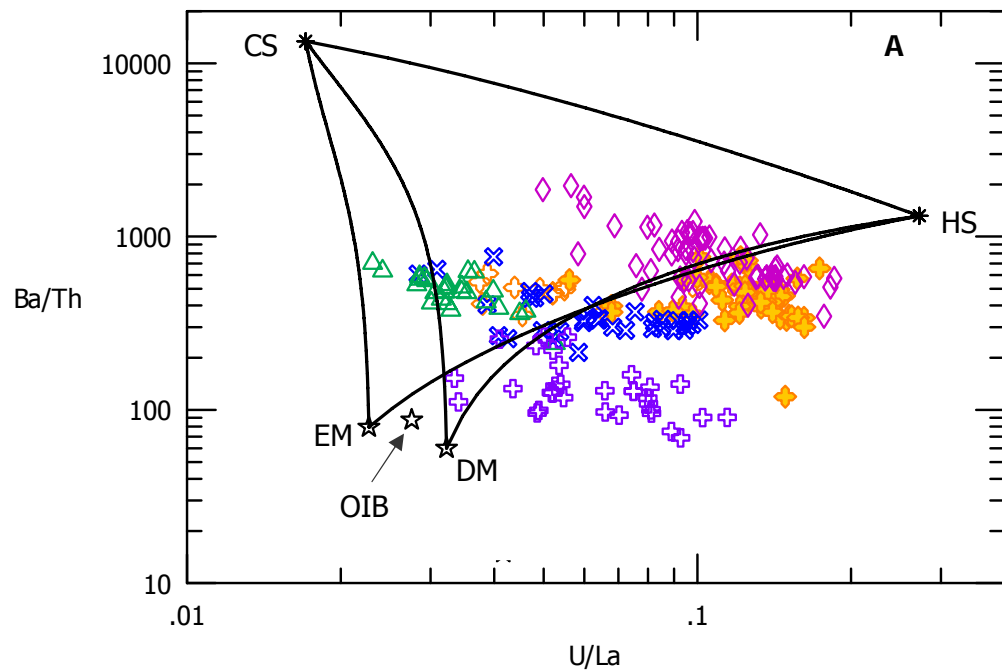
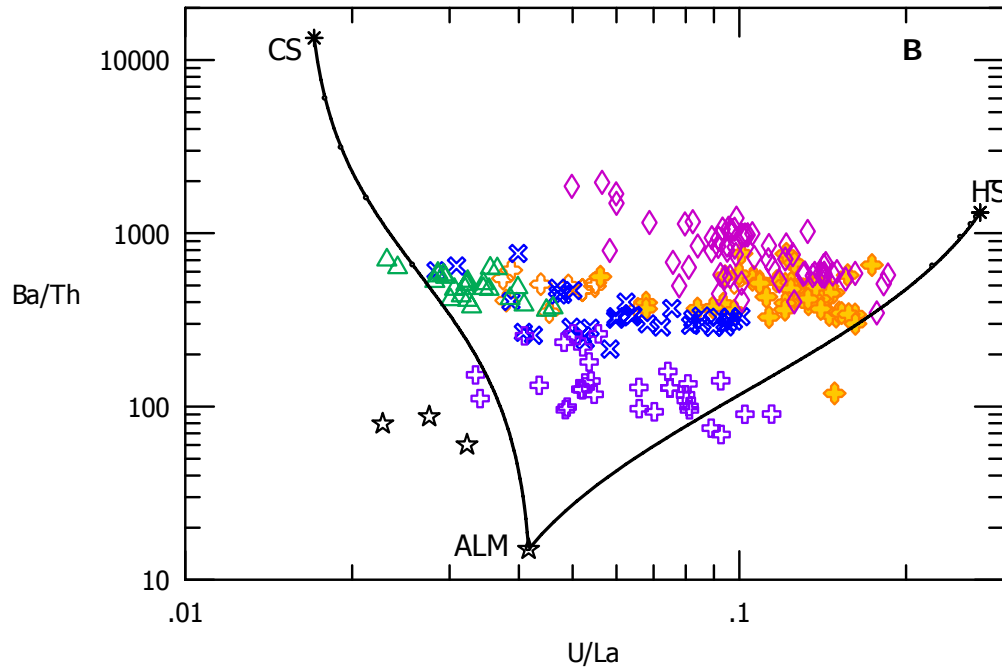


Figure 1.32 A. Simple mixing lines between the sediment end-members and either EM or DM cannot explain the variations seen in the Central American lavas. B. Adding altered lower MORB (ALM) as a component fits the data better.



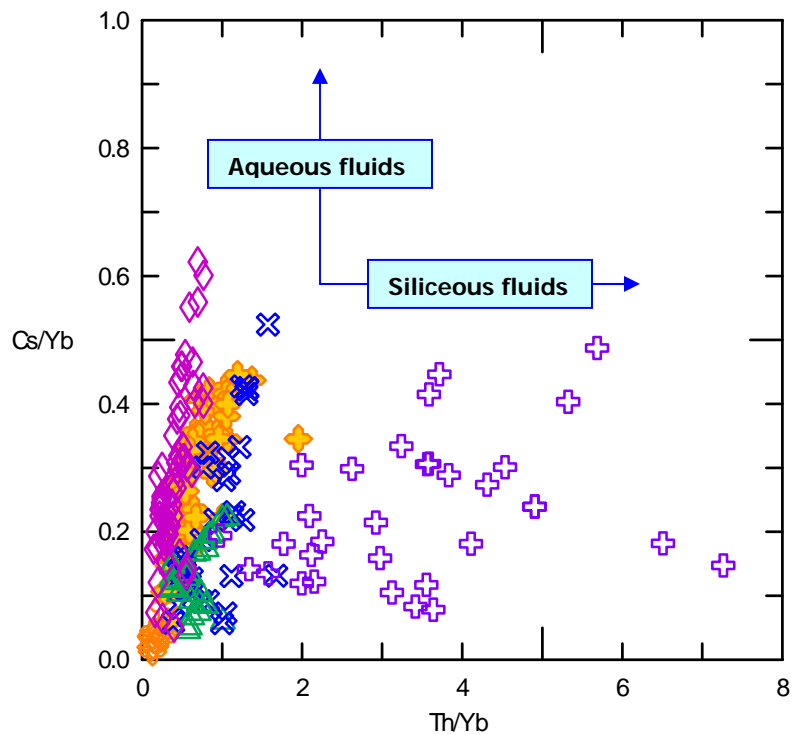


Figure 1.33. Cs/Yb vs. Th/Yb differentiates between aqueous and siliceous fluid mobilization since Th is mobilized by siliceous fluids whereas Cs is mobilized by aqueous fluids (Pearce & Peate, 1995).

**Table 1.1** Newly collected sample data.

Sample	Volcname	Descript.	Name	volclat	volclon	Easting	Northing
MS-2000-1	Masaya	scoraceous bomb	Masaya	11.98	86.15	590.6	1324.48
LS-2000-1L	Masaya	mafic scoria clast	Masaya	11.98	86.15	565.55	1315.69
LS-2000-1U	Masaya	mafic scoria clast	Masaya	11.98	86.15	565.55	1315.69
LS-2000-2	Masaya	mafic scoria clast	Masaya	11.98	86.15	571.08	1320.61
LS-2000-30b	Masaya	obsidian	Masaya	11.98	86.15	574.66	1323.59
LS-2000-3 Sc	Masaya	scoria	Masaya	11.98	86.15	574.66	1323.59
LS-2000-4	Masaya	mafic scoria clast	Masaya	11.98	86.15	561.19	1315.57
LS-2000-5	Masaya	lava	Masaya	11.98	86.15	571.1	1321.97
Ban 2000-1BM	Masaya?	mafic clast	Las Banderas	11.98	86.15	612.63	1362.1
Ban 2000-1T	Masaya?	mafic clast	Las Banderas	11.98	86.15	612.63	1362.1
Ban-2000-2	Masaya?	mafic clast	Las Banderas	11.98	86.15	613.68	1362.36
MOM-2000-1	Mombacho	lava	Mombacho	11.83	85.98	609.22	1310.79
MOM-2000-2	Mombacho	lava	Mombacho	11.83	85.98	610.25	1311.96
MOM-2000-3	Mombacho	lava	Mombacho	11.83	85.98	611.61	1311.61
MOM-2000-4	Mombacho	lava	Mombacho	11.83	85.98	608.92	1309

Table 1.2 Previously acquired samples.

Sample	Volcname	Collector - present locale	Name	volclat	volclon	Easting	Northing
MS1	Masaya	walker/ru	Masaya	11.98	86.15	595.28	1326.07
MS2	Masaya	walker/ru	Masaya	11.98	86.15	595.28	1326.07
MS3	Masaya	walker/ru	Masaya	11.98	86.15	595.28	1326.07
MS4	Masaya	walker/ru	Masaya	11.98	86.15	595.72	1326.12
MS5	Masaya	walker/ru	Masaya	11.98	86.15	595.51	1324.68
MS6	Masaya	walker/ru	Masaya	11.98	86.15	595.14	1323.35
MS7	Masaya	walker/ru	Masaya	11.98	86.15	594.66	1321.35
MS8	Masaya	walker/ru	Masaya	11.98	86.15	594.22	1320.75
MS9	Masaya	walker/ru	Masaya	11.98	86.15	594.18	1320.65
MS10	Masaya	walker/ru	Masaya	11.98	86.15	590.6	1324.48
MS11	Masaya	walker/ru	Masaya	11.98	86.15	590.67	1326.08
MS12	Masaya	walker/ru	Masaya	11.98	86.15	590.19	1327.31
MS13	Masaya	walker/ru	Masaya	11.98	86.15	589.64	1326.82
MS14	Masaya	walker/ru	Masaya	11.98	86.15	589.17	1325.77
MS15	Masaya	walker/ru	Masaya	11.98	86.15	590.97	1326.6
MS16	Masaya	walker/ru	Masaya	11.98	86.15	591.05	1333.89
MS17	Masaya	walker/ru	Masaya	11.98	86.15	591.05	1334
MS19	Masaya	walker/ru	Masaya	11.98	86.15	592.95	1337.13
MS20	Masaya	walker/ru	Masaya	11.98	86.15	592.23	1336.75
MS21	Masaya	walker/ru	Masaya	11.98	86.15	590.62	1329.27
AP2	Apoyo	walker/ru	Apoyo	11.93	86.05	603.24	1320.18
AP3	Apoyo	walker/ru	Apoyo	11.93	86.05	603.12	1320.05
AP4	Apoyo	walker/ru	Apoyo	11.93	86.05	603.02	1319.93
AP5	Apoyo	walker/ru	Apoyo	11.93	86.05	602.88	1318.51
AP6	Apoyo	walker/ru	Apoyo	11.93	86.05	604.02	1320.49
GR1	Granada	walker/ru	Granada	11.88	86	611.5	1314.6
GR2	Granada	walker/ru	Granada	11.88	86	610.3	1315.75
GR3	Granada	walker/ru	Granada	11.88	86	610.05	1316.05
GR4	Granada	walker/ru	Granada	11.88	86	610.6	1316
GR5	Granada	walker/ru	Granada	11.88	86	609.8	1314.95
GR6	Granada	walker/ru	Granada	11.88	86	609.8	1314.75
GR101	Granada	carr/ru	Granada	11.88	86	608.45	1311.85
MB1	Mombacho	walker/ru	Mombacho	11.83	85.98	613.55	1309.5
MB2	Mombacho	walker/ru	Mombacho	11.83	85.98	613.4	1309.7
MB3	Mombacho	walker/ru	Mombacho	11.83	85.98	613.35	1309.25
MB4	Mombacho	walker/ru	Mombacho	11.83	85.98	614.05	1310.95
MB5	Mombacho	walker/ru	Mombacho	11.83	85.98	614.35	1314.65
MB6	Mombacho	walker/ru	Mombacho	11.83	85.98	614.7	1316
MB7	Mombacho	walker/ru	Mombacho	11.83	85.98	614.7	1316
MB8	Mombacho	walker/ru	Mombacho	11.83	85.98	616.5	1315.45
MB9	Mombacho	walker/ru	Mombacho	11.83	85.98	616.5	1315.45
MB10	Mombacho	walker/ru	Mombacho	11.83	85.98	616.5	1315.45
MB101	Mombacho	carr/ru	Mombacho	11.83	85.98	610.4	1308.75
MB102	Mombacho	carr/ru	Mombacho	11.83	85.98	611.5	1302.5
MB103	Mombacho	carr/ru	Mombacho	11.83	85.98	611.5	1302.5

Sample	Volcname	Collector - present locale	Name	volclat	volclon	Easting	Northing
MB104	Mombacho	carr/ru	Mombacho	11.83	85.98	611.5	1302.5
AQ9	Nejapa	carr/ru	Nejapa	12.11	86.32	575.75	1352.95
NE201	Nejapa	carr/ru	Nejapa	12.11	86.32	573.3	1341.4
NE202	Nejapa	carr/ru	Nejapa	12.11	86.32	573.3	1341.4
NE203	Nejapa	carr/ru	Nejapa	12.11	86.32	573.3	1341.4
NE204	Nejapa	carr/ru	Nejapa	12.11	86.32	573.3	1341.4
NE1	Nejapa	walker/ru	Nejapa	12.11	86.32	575.2	1341.34
NE2	Nejapa	walker/ru	Nejapa	12.11	86.32	575.23	1341.24
NE3	Nejapa	walker/ru	Nejapa	12.11	86.32	573.96	1340.43
NE5	Nejapa	walker/ru	Nejapa	12.11	86.32	573.3	1349.4
NE6	Nejapa	walker/ru	Nejapa	12.11	86.32	574.14	1341.05
NE7	Nejapa	walker/ru	Nejapa	12.11	86.32	572.6	1347.3
NE8	Nejapa	walker/ru	Nejapa	12.11	86.32	572.6	1347.3
NE9	Nejapa	walker/ru	Nejapa	12.11	86.32	576.5	1352
NE10	Nejapa	walker/ru	Nejapa	12.11	86.32	573.2	1343.2
NE11	Nejapa	walker/ru	Nejapa	12.11	86.32	573.2	1343.2
NE12	Nejapa	walker/ru	Nejapa	12.11	86.32	573.58	1343.03
NE13	Nejapa	walker/ru	Nejapa	12.11	86.32	575.77	1340.8
NE14	Nejapa	walker/ru	Nejapa	12.11	86.32	572.45	1349.2
Zap-atr	Zapatera	Balzer/Plank/Carr	Zapatera	11.73	85.82		
Zap-smig	Zapatera	Balzer/Plank/Carr	Zapatera	11.73	85.82		
N101	Zapatera	McBirney/ru	Zapatera	11.73	85.82		

Sample	SiO <sub>2</sub>	TiO <sub>2</sub>	Al <sub>2</sub> O <sub>3</sub>	Fe <sub>2</sub> O <sub>3</sub>	FeO	MnO	MgO	CaO	Na <sub>2</sub> O	K <sub>2</sub> O	P <sub>2</sub> O <sub>5</sub>
MS-2000-1	50.86	1.00	18.26	11.54	0.00	0.19	3.78	10.31	2.62	1.09	0.25
LS-2000-1L	59.15	0.98	15.75	10.04	0.00	0.21	0.80	4.08	4.22	1.21	0.17
LS-2000-1U	61.25	0.88	14.86	8.85	0.00	0.17	1.40	4.63	4.24	1.32	0.18
LS-2000-2	54.16	0.97	15.95	12.06	0.00	0.22	2.89	6.79	1.95	0.87	0.16
LS-2000-30b	50.78	1.23	16.71	13.06	0.00	0.21	4.43	8.55	2.72	1.39	0.32
LS-2000-3 Sc	51.48	1.24	15.60	13.44	0.00	0.22	3.93	8.38	2.59	1.38	0.31
LS-2000-4	62.88	0.80	14.94	7.03	0.00	0.17	1.20	4.03	3.93	2.28	0.31
LS-2000-5	49.51	0.40	10.08	8.86	0.00	0.15	15.58	11.50	1.48	0.62	0.08
Ban 2000-1BM	65.23	0.66	13.88	6.22	0.00	0.20	0.84	3.00	4.29	2.21	0.17
Ban 2000-1T	62.56	0.91	14.37	8.04	0.00	0.21	1.74	4.44	3.44	1.72	0.34
Ban-2000-2	65.08	0.68	13.92	6.39	0.00	0.23	1.09	3.22	3.80	2.04	0.29
MOM-2000-1	52.27	1.17	17.98	10.56	0.00	0.18	3.53	9.50	2.88	0.92	0.20
MOM-2000-2	58.78	0.82	16.82	7.81	0.00	0.17	2.77	6.53	3.57	1.88	0.23
MOM-2000-3	63.60	0.69	15.69	5.49	0.00	0.13	1.70	4.52	3.91	2.60	0.16
MOM-2000-4	51.43	1.11	17.82	10.56	0.00	0.18	4.11	10.09	2.75	0.90	0.19

Table 1.3. Major Oxides of newly acquired lavas.

Sample	SiO <sub>2</sub>	TiO <sub>2</sub>	Al <sub>2</sub> O <sub>3</sub>	Fe <sub>2</sub> O <sub>3</sub>	FeO	MnO	MgO	CaO	Na <sub>2</sub> O	K <sub>2</sub> O	P <sub>2</sub> O <sub>5</sub>
MS1	50.60	1.24	16.00	0.00	11.50	0.21	4.38	10.40	2.86	1.14	0.27
MS2	50.00	1.33	15.50	0.00	11.90	0.22	4.71	10.30	2.72	1.07	0.22
MS3	50.70	1.36	14.70	0.00	12.80	0.25	4.83	9.60	2.89	1.20	0.27
MS4	50.90	1.14	14.80	0.00	11.90	0.23	5.26	9.90	2.82	1.16	0.27
MS5	50.70	1.03	15.40	0.00	11.70	0.23	5.21	10.20	2.91	1.13	0.22
MS6	50.60	1.05	15.50	0.00	11.60	0.23	5.22	9.90	2.91	1.12	0.20
MS7	49.80	1.00	16.20	0.00	11.00	0.22	5.31	10.60	2.86	1.04	0.19
MS8	49.70	1.26	16.40	0.00	11.70	0.21	4.81	10.60	2.72	1.01	0.25
MS9	50.20	1.25	16.40	0.00	11.30	0.22	4.58	10.40	2.79	1.06	0.20
MS10	49.80	1.04	17.30	0.00	10.80	0.21	4.55	10.40	2.84	1.03	0.26
MS11	50.70	1.02	16.40	0.00	11.00	0.21	4.72	10.50	2.86	1.07	0.22
MS12	50.70	0.97	16.20	0.00	10.60	0.22	5.23	10.50	2.82	1.02	0.23
MS13	50.30	1.14	15.00	0.00	12.10	0.24	5.43	10.00	2.78	1.17	0.23
MS14	50.00	0.99	16.10	0.00	11.10	0.22	5.35	10.30	2.89	1.04	0.16
MS15	50.90	0.99	16.40	0.00	10.90	0.22	5.17	10.60	2.79	1.06	0.18
MS16	49.90	0.93	16.20	0.00	11.40	0.21	5.50	10.80	2.43	0.86	0.27
MS17	50.40	0.96	16.20	0.00	11.20	0.22	5.30	10.50	2.53	0.97	0.25
MS19	50.60	1.12	15.60	0.00	12.00	0.23	5.46	10.00	2.78	1.15	0.29
MS20	49.80	1.02	16.90	0.00	10.60	0.20	4.91	10.40	2.77	1.08	0.18
MS21	50.50	1.09	15.70	0.00	11.60	0.22	5.80	10.10	2.71	1.13	0.19
AP2	47.60	0.98	15.50	0.00	9.80	0.18	8.37	13.30	2.02	0.29	0.05
AP3	48.00	0.99	15.60	0.00	9.90	0.18	8.59	13.50	2.07	0.30	0.12
AP4	52.40	0.79	20.10	0.00	8.50	0.20	2.95	9.70	3.07	0.87	0.17
AP5	48.80	0.74	20.40	0.00	9.10	0.19	4.15	11.80	2.36	0.59	0.14
AP6	63.50	0.54	16.20	0.00	4.40	0.14	1.48	4.60	4.02	1.80	0.13
GR1	48.40	1.29	16.30	0.00	11.10	0.18	7.18	12.00	2.35	0.07	0.07
GR2	47.70	1.22	16.40	0.00	10.80	0.18	6.93	12.30	2.24	0.11	0.09
GR3	48.60	1.26	16.40	0.00	11.20	0.18	6.96	12.10	2.40	0.14	0.12
GR4	49.00	1.26	16.40	0.00	11.10	0.17	6.96	12.10	2.37	0.14	0.10
GR5	48.10	1.15	16.10	0.00	10.40	0.17	7.97	12.40	2.19	0.10	0.12
GR6	49.10	1.03	16.40	0.00	10.20	0.17	7.38	12.30	2.08	0.27	0.13
GR101	46.90	0.55	15.90	0.00	10.03	0.18	8.72	14.40	1.46	0.30	0.11
MB1	59.70	0.91	15.50	0.00	7.50	0.20	2.06	5.40	3.79	2.28	0.23
MB2	57.40	0.82	16.70	0.00	7.20	0.17	3.53	7.70	3.33	1.72	0.13
MB3	57.80	0.78	16.40	0.00	6.90	0.15	3.33	7.50	3.24	1.70	0.08
MB4	57.70	0.76	16.70	0.00	7.60	0.17	3.56	7.70	3.26	1.70	0.06
MB5	57.60	0.75	16.40	0.00	7.60	0.17	3.60	7.90	3.19	1.78	0.10
MB6	67.90	0.43	15.30	0.00	3.10	0.12	1.05	3.40	4.36	2.44	0.05
MB7	67.60	0.40	15.00	0.00	3.00	0.12	0.95	3.30	4.10	2.70	0.03
MB8	58.90	0.76	16.50	0.00	7.10	0.17	3.08	7.00	3.48	1.92	0.14
MB9	58.80	0.78	16.70	0.00	7.00	0.17	3.06	7.20	3.49	1.89	0.14
MB10	58.70	0.79	16.60	0.00	7.20	0.17	3.23	7.30	3.41	1.81	0.09
MB101	51.00	1.19	18.60	0.00	10.18	0.18	3.87	9.90	3.06	0.60	0.21
MB102	59.80	0.76	17.10	0.00	6.56	0.15	2.41	6.50	3.89	1.88	0.25
MB103	59.10	0.76	17.00	0.00	6.62	0.16	2.49	6.40	3.75	1.94	0.21
MB104	59.40	0.73	17.20	0.00	6.60	0.16	2.47	6.50	3.87	1.89	0.25

Table 1.4. Major oxides of previously acquired lavas and literature values.

Sample	SiO <sub>2</sub>	TiO <sub>2</sub>	Al <sub>2</sub> O <sub>3</sub>	Fe <sub>2</sub> O <sub>3</sub>	FeO	MnO	MgO	CaO	Na <sub>2</sub> O	K <sub>2</sub> O	P <sub>2</sub> O <sub>5</sub>
NE201	47.90	0.93	15.30	0.00	11.32	0.19	9.95	11.00	2.30	0.19	0.10
NE202	47.50	1.20	15.40	0.00	11.28	0.19	9.51	10.70	2.51	0.24	0.11
NE203	47.40	1.13	14.90	0.00	11.53	0.18	11.02	10.80	2.19	0.14	0.10
NE3	50.30	0.89	18.10	0.00	9.50	0.19	5.54	11.00	2.55	0.62	0.15
NE5	48.00	0.81	16.30	0.00	9.60	0.19	8.02	12.40	2.22	0.41	0.17
NE6	47.20	0.70	14.80	0.00	10.30	0.18	8.68	13.30	1.58	0.40	0.13
NE12	55.90	1.66	15.30	0.00	9.10	0.16	4.86	8.20	3.16	0.64	0.20
CDP13	52.90	1.11	16.24	0.00	9.78	0.19	5.81	9.56	3.03	0.65	0.13
N101	54.80	0.93	18.03	0.00	4.47	0.19	4.09	8.55	3.42	1.31	0.21
ZAP-ATR-a		1.96	15.48	10.60	0.00	0.14	5.92	9.66	2.85	0.34	0.21
ZAP-SMIG-a		1.12	15.62	10.30	0.00	0.17	7.47	11.60	2.49	0.44	0.17
mean-hemi	55.80	0.58	11.82	6.25	0.00	0.14	2.20	2.70	2.08	1.84	0.12
meancarb	7.40	0.02	0.37	1.97	0.00	0.29	0.73	49.90	0.24	0.18	0.13
DM	0.00	0.20	0.00	0.00	0.00	0.00	0.00	0.00	0.00	0.01	0.02
EM	0.00	0.16	0.00	0.00	0.00	0.00	0.00	0.00	0.00	0.04	0.03
AOC	0.00	1.15	0.00	0.00	0.00	0.00	0.00	0.00	0.00	0.32	0.13
AltMorblo	49.00	1.00	14.00	0.00	0.00	0.00	0.00	11.00	2.50	0.02	0.14

Table 1.4 continued

Sample	Sc	V	Cr	Co	Ni	Cu	Zn	Rb
NE201	0.00	256.00	303.00	0.00	140.00	0.00	0.00	10.00
NE202	34.58	251.00	333.90	0.00	145.20	134.30	0.00	3.10
NE203	35.18	292.10	440.80	0.00	198.70	136.10	0.00	2.30
NE3	34.33	325.80	23.25	0.00	26.59	134.40	0.00	11.30
NE5	36.88	320.70	198.40	0.00	78.98	139.20	0.00	9.90
NE6	43.22	316.90	275.10	0.00	80.19	132.70	0.00	9.20
NE13	0.00	352.00	30.00	0.00	25.00	0.00	0.00	3.00
CDP12	0.00	37.99	323.20	255.00	0.00	99.71	106.40	0.00
MS1	32.06	412.54	52.58	40.46	19.26	226.81	113.30	21.26
MS2	0.00	384.00	47.00	0.00	38.00	0.00	0.00	25.00
MS3	0.00	391.00	23.00	0.00	29.00	0.00	0.00	28.00
MS4	38.42	439.90	46.94	0.00	31.18	258.60	0.00	22.10
MS5	35.59	386.64	33.47	36.44	18.02	221.38	106.53	19.64
MS6	34.39	388.86	39.80	37.20	17.78	233.59	107.18	19.80
MS7	0.00	327.00	46.00	0.00	22.00	0.00	0.00	25.00
MS8	33.16	428.79	46.64	34.50	26.80	185.05	124.67	19.04
MS9	31.51	382.10	52.01	33.21	26.51	230.71	108.85	20.42
MS10	29.71	347.91	32.27	33.43	18.19	162.53	101.06	18.22
MS11	32.56	380.51	54.29	33.58	17.78	231.10	105.88	20.02
MS12	32.35	353.16	53.73	35.61	26.67	227.10	176.59	18.66
MS13	0.00	384.00	50.00	0.00	35.00	0.00	0.00	23.00
MS14	33.01	358.09	43.59	35.60	18.41	208.54	98.02	18.01
MS15	0.00	341.00	49.00	0.00	31.00	0.00	0.00	20.00
MS16	34.14	348.99	55.39	94.38	22.40	156.25	97.90	18.00
MS17	34.84	368.68	58.05	39.79	22.35	181.40	101.81	18.29
MS19	27.20	408.90	75.34	37.58	33.72	207.09	120.47	17.70
MS20	31.46	352.29	47.78	31.94	23.82	209.62	97.23	19.27
MS21	31.92	380.81	83.19	35.40	42.67	215.05	108.76	21.13
MS-2000-1	28.36	362.77	18.69	28.42	13.51	228.55	100.69	19.85
LS-2000-1L	21.81	98.62	7.96	14.15	3.16	57.24	117.70	23.12
LS-2000-1U	21.72	113.39	5.30	12.94	2.12	47.05	112.75	25.91
LS-2000-2	27.57	212.92	22.86	26.44	8.71	203.37	101.27	24.22
LS-2000-30b	30.65	415.09	41.70	30.24	26.09	296.29	118.98	26.57
LS-2000-3 Sc	29.12	396.88	12.92	31.49	12.64	289.28	121.70	26.73
LS-2000-4	14.91	35.54	7.22	6.93	2.54	13.84	103.23	27.33
LS-2000-5	45.56	198.34	897.42	48.89	223.65	79.07	58.29	5.31
Ban 2000-1BM	14.99	13.86	6.02	3.11	1.00	16.07	119.10	36.85
Ban 2000-1T	19.38	68.08	17.56	9.89	1.21	86.51	143.25	28.26
Ban-2000-2	15.66	37.90	7.71	3.74	0.93	15.91	116.06	34.51
AP2	38.97	306.56	217.26	43.36	79.43	100.38	84.78	4.69
AP3	48.59	299.63	359.10	50.35	155.19	101.13	77.59	4.83
AP4	22.35	220.89	3.83	32.71	11.93	136.07	90.72	14.01
AP5	28.51	342.70	14.67	0.00	19.46	163.30	0.00	9.80
AP6	11.49	70.50	6.77	22.70	1.58	23.20	68.04	32.99

Table 1.5. Trace element data of all lavas and literature values used in chapter 1.

Sample	Sc	V	Cr	Co	Ni	Cu	Zn	Rb
GR1	34.60	264.25	156.56	39.39	62.23	123.96	96.12	1.34
GR2	37.09	291.29	190.29	41.65	54.43	135.52	94.99	1.48
GR3	38.48	307.30	167.40	0.00	74.03	168.60	0.00	4.50
GR4	0.00	254.00	136.00	0.00	74.00	0.00	0.00	3.00
GR5	40.66	289.80	332.60	0.00	94.82	137.50	0.00	4.04
GR6	38.89	302.80	237.00	0.00	79.57	131.70	0.00	7.30
GR101	51.81	309.53	189.84	48.19	42.83	136.94	70.20	5.65
MB1	19.36	127.10	11.60	19.65	0.15	68.30	100.45	41.14
MB2	0.00	206.00	24.00	0.00	18.00	0.00	0.00	47.00
MB3	0.00	172.00	16.00	0.00	41.00	0.00	0.00	28.00
MB4	24.67	214.87	13.56	24.51	7.31	77.80	72.73	34.56
MB5	24.95	206.60	19.74	23.68	6.07	73.24	72.88	35.62
MB6	7.76	38.81	197.86	15.17	118.24	11.79	51.67	46.68
MB7	0.00	48.00	6.00	0.00	12.00	0.00	0.00	48.00
MB8	21.91	187.36	11.21	22.56	3.40	53.18	72.91	37.95
MB9	0.00	197.00	18.00	0.00	30.00	0.00	0.00	43.00
MB10	0.00	194.00	18.00	0.00	19.00	0.00	0.00	42.00
MB101	27.29	308.17	10.83	30.03	9.84	125.34	99.29	8.35
MB102	0.00	146.00	16.00	0.00	10.00	0.00	0.00	39.00
MB103	17.85	139.12	10.43	26.67	3.44	44.65	77.10	37.35
MB104	0.00	143.00	14.00	0.00	10.00	0.00	0.00	39.00
MOM-2000-1	28.50	293.37	19.99	27.63	9.99	139.49	91.11	17.03
MOM-2000-2	20.18	156.72	6.03	18.15	6.50	30.29	80.29	32.16
MOM-2000-3	12.82	92.74	7.56	10.06	1.97	16.45	63.02	48.23
MOM-2000-4	29.02	275.41	8.56	26.95	10.82	133.14	85.66	15.31
N101	26.74	174.10	12.85	0.00	13.31	95.03	0.00	28.10
ZAP-ATR-a	28.35	229.61	149.60	36.04	74.01	90.57	18.00	7.14
ZAP-SMIG-a	36.11	270.06	225.99	37.58	64.48	102.43	16.74	9.00
mean-hemi	17.07	147.02	44.85	0.00	204.52	262.89	0.00	40.78
meancarb	2.63	49.47	15.52	0.00	27.27	76.11	0.00	4.28
DM	0.00	0.00	0.00	0.00	0.00	0.00	0.00	0.10
EM	14.88			104.00	2080.00	28.00		0.54
AOC	0.00	0.00	0.00	0.00	0.00	0.00	0.00	4.33
AltMorblo	0.00	0.00	0.00	0.00	100.00	50.00	0.00	0.20

Table 1.5 continued

Sample	Sr	Y	Zr	Nb	Ba	La	Ce	Pr
NE201	360.00	20.80	54.28	6.54	115.00	0.00	0.00	0.00
NE202	308.70	20.22	70.68	6.10	143.70	3.31	9.75	0.00
NE203	282.50	19.01	59.04	7.30	81.81	2.87	8.41	0.00
NE3	439.00	18.19	80.03	5.40	447.70	6.17	14.71	0.00
NE5	368.40	18.15	59.83	5.20	353.40	6.64	14.93	0.00
NE6	386.10	16.63	53.70	2.90	337.90	5.00	12.07	0.00
NE13	478.00	0.00	0.00	0.00	349.00	0.00	0.00	0.00
CDP12	2.50	310.30	23.19	67.06	4.00	88.00	3.28	10.02
MS1	442.11	24.32	103.73		741.11	10.49	22.62	3.43
MS2	426.00	0.00	0.00		812.00	0.00	0.00	0.00
MS3	422.00	0.00	0.00		915.00	0.00	0.00	0.00
MS4	433.20	25.86	105.10	2.90	893.20	10.32	23.67	0.00
MS5	452.87	22.48	93.75		762.39	9.95	21.58	3.20
MS6	461.65	22.56	96.17		779.87	10.10	22.53	3.30
MS7	490.00	0.00	0.00		780.00	0.00	0.00	0.00
MS8	417.94	23.35	100.15		713.21	10.02	21.75	3.26
MS9	436.08	23.74	106.92		746.19	10.73	23.56	3.51
MS10	483.53	20.97	87.30		743.18	9.50	20.10	3.12
MS11	452.96	22.13	92.77		781.85	9.70	21.87	3.21
MS12	464.23	20.76	87.32		701.03	9.10	20.61	3.00
MS13	444.00	0.00	0.00		881.00	0.00	0.00	0.00
MS14	446.14	21.17	86.54		725.16	9.40	20.67	3.05
MS15	484.00	0.00	0.00		793.00	0.00	0.00	0.00
MS16	437.34	19.68	81.14		691.50	8.50	18.95	2.81
MS17	441.96	20.34	83.25		707.16	8.75	19.24	2.86
MS19	413.94	19.98	94.65		761.43	9.11	20.65	3.04
MS20	473.76	20.85	87.82		749.17	9.48	20.79	3.01
MS21	429.60	21.63	107.67		763.21	9.53	21.38	3.21
MS-2000-1	475.42	19.52	80.40		702.99	8.72	19.78	2.96
LS-2000-1L	296.13	20.79	137.01		947.25	10.51	25.31	3.31
LS-2000-1U	278.60	28.50	148.65		1374.37	11.49	24.79	3.73
LS-2000-2	358.57	21.99	83.77		779.44	8.17	17.66	2.63
LS-2000-30b	358.52	24.87	122.05		881.14	12.50	26.02	3.79
LS-2000-3 Sc	383.64	25.26	113.81		906.92	11.98	24.72	3.66
LS-2000-4	286.34	37.94	156.84		1130.83	13.89	28.77	4.56
LS-2000-5	399.98	8.94	32.04		195.37	4.44	9.75	1.41
Ban 2000-1BM	222.79	42.48	221.79		1158.50	15.30	35.47	5.13
Ban 2000-1T	278.37	40.70	176.13		984.80	13.94	30.63	4.44
Ban-2000-2	228.08	49.75	216.30		1096.41	16.91	35.45	5.48
AP2	282.92	16.15	54.35		199.72	4.68	11.02	1.68
AP3	293.96	15.62	52.49	2.90	192.77	4.37	10.47	1.59
AP4	533.01	20.46	73.02		642.95	8.27	17.22	2.58
AP5	511.50	16.39	60.49	2.70	1126.92	12.02	25.18	3.40
AP6	376.13	23.14	143.61		1153.64	12.30	25.40	3.46

Table 1.5 continued

Sample	Sr	Y	Zr	Nb	Ba	La	Ce	Pr
GR1	263.71	17.17	52.77		110.23	2.58	7.20	1.29
GR2	325.86	19.02	62.22		132.00	3.65	9.60	1.64
GR3	282.90	21.06	72.28	3.90	117.00	2.83	9.41	0.00
GR4	286.00	0.00	0.00	2.79	105.00	0.00	0.00	0.00
GR5	305.30	19.91	71.23	4.50	117.20	3.44	10.12	0.00
GR6	395.00	22.41	75.28	5.90	199.00	5.23	13.56	0.00
GR101	470.87	12.56	32.90	2.70	196.49	4.63	10.26	1.60
MB1	380.51	35.90	172.69		917.00	0.00	0.00	0.00
MB2	381.00	0.00	0.00		914.00	0.00	0.00	0.00
MB3	376.00	0.00	0.00		914.00	0.00	0.00	0.00
MB4	402.85	23.55	138.87		873.92	12.54	26.50	3.70
MB5	394.29	23.08	142.56		881.89	12.29	26.41	3.63
MB6	297.86	23.68	197.35		1454.82	17.66	34.64	4.57
MB7	292.00	0.00	0.00		1435.00	0.00	0.00	0.00
MB8	391.21	24.78	181.79		953.59	13.20	28.98	3.88
MB9	387.00	0.00	0.00		1030.00	0.00	0.00	0.00
MB10	409.00	0.00	0.00		1010.00	0.00	0.00	0.00
MB101	428.12	23.75	120.20	7.60	533.29	10.35	23.25	3.38
MB102	427.00	0.00	0.00		1173.00	0.00	0.00	0.00
MB103	416.42	27.29	161.49		1043.98	15.69	33.92	4.60
MB104	434.00	0.00	0.00		1176.00	0.00	0.00	0.00
MOM-2000-1	403.63	22.41	105.29		491.62	9.37	20.93	3.09
MOM-2000-2	376.80	25.77	144.70		918.80	14.22	30.86	4.33
MOM-2000-3	295.64	27.30	191.48		1110.02	15.92	33.60	4.52
MOM-2000-4	369.88	20.73	93.69		463.76	8.89	19.32	2.81
N101	402.50	28.81	126.50	5.70	708.40	13.23	28.32	0.00
ZAP-ATR-a	321.93	29.53	139.43	17.05	188.96	9.75	21.10	3.81
ZAP-SMIG-a	388.78	20.25	69.98	6.39	294.28	7.62	17.64	2.66
mean-hemi	336.16	31.06	0.00	5.03	3941.49	17.96	28.05	0.00
meancarb	1504.12	17.69	0.00	0.44	2145.48	8.78	2.40	0.00
DM	13.20	4.10	11.40	0.31	1.20	0.31	0.95	0.00
EM	18.21	3.94	9.71	0.72	6.05	0.61	1.60	0.24
AOC	137.00	22.00	73.00	8.00	19.50	5.00	10.00	0.00
AltMorblo	55.00	22.00	73.00	0.90	12.00	1.20	3.50	

Table 1.5 continued

Sample	Nd	Sm	Eu	Gd	Tb	Dy	Ho	Er
NE201	0.00	0.00	0.00	0.00	0.00	0.00	0.00	0.00
NE202	7.81	2.27	0.93	3.22	0.00	3.19	0.00	2.07
NE203	6.96	2.02	0.90	3.34	0.00	3.45	0.00	1.83
NE3	9.29	2.34	0.90	2.98	0.00	3.12	0.00	1.59
NE5	10.18	2.80	0.93	3.22	0.00	3.05	0.00	1.81
NE6	8.19	2.00	0.77	2.80	0.00	2.70	0.00	1.64
NE13	0.00	0.00	0.00	0.00	0.00	0.00	0.00	0.00
CDP12	8.47	2.66	0.99	3.74	0.00	3.94	0.00	2.03
MS1	16.03	4.24	1.42	4.66	0.71	4.34	0.84	2.46
MS2	0.00	0.00	0.00	0.00	0.00	0.00	0.00	0.00
MS3	0.00	0.00	0.00	0.00	0.00	0.00	0.00	0.00
MS4	16.87	4.24	1.29	4.71	0.00	4.93	0.00	2.57
MS5	14.98	3.89	1.40	4.43	0.67	4.03	0.80	2.29
MS6	15.48	4.03	1.41	4.47	0.68	4.09	0.82	2.39
MS7	0.00	0.00	0.00	0.00	0.00	0.00	0.00	0.00
MS8	15.27	4.09	1.46	4.58	0.69	4.17	0.82	2.41
MS9	16.23	4.26	1.50	4.69	0.71	4.32	0.85	2.54
MS10	14.35	3.85	1.38	4.19	0.62	3.80	0.75	2.26
MS11	14.84	3.92	1.42	4.33	0.65	3.95	0.78	2.31
MS12	13.73	3.62	1.31	4.00	0.61	3.78	0.75	2.17
MS13	0.00	0.00	0.00	0.00	0.00	0.00	0.00	0.00
MS14	14.10	3.75	1.38	4.19	0.63	3.81	0.77	2.25
MS15	0.00	0.00	0.00	0.00	0.00	0.00	0.00	0.00
MS16	13.09	3.53	1.27	3.91	0.59	3.65	0.73	2.11
MS17	13.23	3.62	1.31	3.96	0.60	3.65	0.74	2.18
MS19	14.31	3.82	1.42	4.33	0.65	3.90	0.80	2.35
MS20	14.14	3.70	1.37	4.12	0.62	3.76	0.76	2.25
MS21	14.80	3.91	1.43	4.45	0.66	4.06	0.81	2.38
MS-2000-1	13.99	3.53	1.29	3.93	0.58	3.59	0.74	2.12
LS-2000-1L	15.50	3.80	1.56	4.36	0.66	4.02	0.84	2.41
LS-2000-1U	17.63	4.47	1.66	5.41	0.81	5.32	1.12	3.16
LS-2000-2	12.83	3.35	1.25	4.01	0.60	3.70	0.81	2.34
LS-2000-30b	18.28	4.45	1.52	5.15	0.76	4.60	0.95	2.72
LS-2000-3 Sc	17.61	4.33	1.54	4.95	0.73	4.49	0.93	2.73
LS-2000-4	22.15	5.64	1.83	6.73	1.01	6.73	1.41	3.95
LS-2000-5	6.83	1.71	0.54	1.81	0.26	1.54	0.32	0.91
Ban 2000-1BM	24.38	6.06	1.88	7.43	1.18	7.61	1.63	4.87
Ban 2000-1T	22.14	5.62	1.87	6.99	1.07	7.01	1.51	4.45
Ban-2000-2	26.27	6.78	2.04	8.31	1.28	8.50	1.87	5.43
AP2	8.05	2.45	0.88	2.88	0.45	2.84	0.56	1.61
AP3	7.89	2.33	0.89	2.78	0.45	2.72	0.55	1.54
AP4	11.86	3.26	1.21	3.68	0.56	3.45	0.69	2.02
AP5	14.46	3.49	1.33	3.95	0.60	3.57	0.76	2.24
AP6	14.61	3.60	1.37	3.99	0.61	3.71	0.78	2.32

Table 1.5 continued

Sample	Nd	Sm	Eu	Gd	Tb	Dy	Ho	Er
GR1	7.05	2.44	0.90	3.02	0.48	3.11	0.62	1.67
GR2	8.47	2.71	1.01	3.35	0.53	3.40	0.68	1.90
GR3	8.64	2.58	1.01	3.70	0.00	3.92	0.00	2.04
GR4	0.00	0.00	0.00	0.00	0.00	0.00	0.00	0.00
GR5	8.02	2.76	0.98	3.56	0.00	3.40	0.00	2.08
GR6	9.59	3.09	0.94	3.35	0.00	3.87	0.00	2.19
GR101	7.47	1.99	0.71	2.30	0.35	2.23	0.44	1.24
MB1	0.00	0.00	0.00	0.00	0.00	0.00	0.00	0.00
MB2	0.00	0.00	0.00	0.00	0.00	0.00	0.00	0.00
MB3	0.00	0.00	0.00	0.00	0.00	0.00	0.00	0.00
MB4	16.02	3.94	1.32	4.36	0.66	4.01	0.80	2.42
MB5	15.63	3.88	1.30	4.28	0.66	3.95	0.80	2.39
MB6	18.20	4.02	1.41	4.23	0.65	3.77	0.76	2.38
MB7	0.00	0.00	0.00	0.00	0.00	0.00	0.00	0.00
MB8	16.73	4.13	1.36	4.56	0.70	4.18	0.85	2.51
MB9	0.00	0.00	0.00	0.00	0.00	0.00	0.00	0.00
MB10	0.00	0.00	0.00	0.00	0.00	0.00	0.00	0.00
MB101	15.46	4.15	1.44	4.61	0.71	4.31	0.84	2.46
MB102	0.00	0.00	0.00	0.00	0.00	0.00	0.00	0.00
MB103	19.76	4.84	1.55	5.17	0.78	4.64	0.93	2.82
MB104	0.00	0.00	0.00	0.00	0.00	0.00	0.00	0.00
MOM-2000-1	14.82	3.53	1.22	4.19	0.63	3.81	0.80	2.24
MOM-2000-2	18.91	4.59	1.54	5.21	0.76	4.73	0.99	2.90
MOM-2000-3	19.50	4.61	1.56	5.21	0.78	4.80	1.02	3.07
MOM-2000-4	13.62	3.49	1.23	4.11	0.62	3.79	0.81	2.35
N101	16.60	4.37	1.22	4.47	0.00	4.97	0.00	2.48
ZAP-ATR-a	18.49	5.13	1.80	5.97	0.94	5.31	1.04	2.64
ZAP-SMIG-a	12.24	3.23	1.20	3.69	0.61	3.64	0.76	2.08
mean-hemi	17.77	4.05	1.80	4.13	0.00	4.72	0.00	3.19
meancarb	6.79	1.45	0.82	1.65	0.00	1.99	0.00	1.40
DM	0.86	0.32	0.10	0.37	0.00	0.45	0.00	0.30
EM	1.19	0.39	0.15	0.51	0.09	0.64	0.14	0.42
AOC	8.00	2.60	0.96	3.10	0.00	4.00	0.00	2.65
AltMorblo	7.00	2.60	0.91	2.97	0.00	3.55	0.00	2.31

Table 1.5 continued

Sample	Tm	Yb	Lu	Hf	Ta	Cs	Pb	Th	U
NE201	0.00	0.00	0.00	1.67	0.00	0.08	1.54	0.25	0.18
NE202	0.00	1.76	0.00	1.70	0.00	0.08	1.23	0.26	0.12
NE203	0.00	1.52	0.00	2.10	0.00	0.02	1.34	0.20	0.11
NE3	0.00	1.60	0.00	1.82	0.00	0.36	2.21	0.80	0.65
NE5	0.00	1.63	0.00	1.49	0.00	0.20	2.91	0.90	0.62
NE6	0.00	1.43	0.00	1.32	0.00	0.32	2.54	0.64	0.58
NE13	0.00	0.00	0.00	0.00	0.00	0.00	0.00	0.00	0.00
CDP12	0.00	1.71	0.00	1.38	0.00	0.05	4.38	0.25	0.15
MS1	0.36	2.38	0.36			0.56	3.44	1.56	1.36
MS2	0.00	0.00	0.00			0.00	0.00	0.00	0.00
MS3	0.00	0.00	0.00			0.00	0.00	0.00	0.00
MS4	0.00	2.14	0.00	2.70		0.87	4.82	1.81	1.49
MS5	0.34	2.28	0.33			0.76	3.66	1.58	1.32
MS6	0.35	2.36	0.35			0.77	3.79	1.62	1.38
MS7	0.00	0.00	0.00			0.00	0.00	0.00	0.00
MS8	0.35	2.34	0.34			0.74	3.38	1.51	1.26
MS9	0.36	2.47	0.36			0.77	12.60	1.57	1.33
MS10	0.33	2.16	0.32			0.73	3.50	1.55	1.31
MS11	0.34	2.28	0.34			0.79	3.80	1.63	1.38
MS12	0.33	2.17	0.32			0.72	3.70	1.54	1.29
MS13	0.00	0.00	0.00			0.00	0.00	0.00	0.00
MS14	0.33	2.20	0.33			0.73	3.63	1.54	1.29
MS15	0.00	0.00	0.00			0.00	0.00	0.00	0.00
MS16	0.31	2.08	0.31			0.74	2.88	1.37	1.18
MS17	0.32	2.16	0.32			0.70	3.39	1.40	1.20
MS19	0.34	2.29	0.34			0.75	4.80	1.33	1.43
MS20	0.33	2.19	0.33			0.80	3.88	1.74	1.37
MS21	0.35	2.35	0.35			0.82	3.76	1.68	1.41
MS-2000-1	0.31	1.95	0.31			0.76	3.34	1.56	1.27
LS-2000-1L	0.35	2.30	0.37			0.94	3.90	1.63	1.05
LS-2000-1U	0.48	3.14	0.52			0.96	4.15	1.80	1.16
LS-2000-2	0.36	2.34	0.37			0.80	3.75	1.48	0.89
LS-2000-30b	0.41	2.67	0.42			1.04	4.74	2.11	1.75
LS-2000-3 Sc	0.40	2.57	0.41			1.08	4.33	2.16	1.63
LS-2000-4	0.58	3.81	0.60			1.08	4.56	2.00	1.31
LS-2000-5	0.13	0.84	0.13			0.29	2.83	1.64	0.66
Ban 2000-1BM	0.75	4.94	0.80			1.62	6.65	2.98	2.04
Ban 2000-1T	0.68	4.40	0.72			1.29	5.10	2.29	1.56
Ban-2000-2	0.85	5.54	0.92			1.46	5.53	3.00	2.05
AP2	0.23	1.47	0.22			0.06	1.50	0.40	0.23
AP3	0.22	1.45	0.21			0.05	1.57	0.39	0.24
AP4	0.30	2.02	0.31			0.35	3.90	1.25	0.90
AP5	0.36	2.43	0.38	1.48		0.00	0.00	0.00	0.66
AP6	0.36	2.47	0.39			0.99	4.16	2.35	1.69

Table 1.5 continued

Sample	Tm	Yb	Lu	Hf	Ta	Cs	Pb	Th	U
GR1	0.24	1.56	0.22			0.03	1.79	0.18	0.10
GR2	0.27	1.79	0.25			0.04	1.16	0.26	0.16
GR3	0.00	1.48	0.00	1.84	1.16	0.07	1.23	0.20	0.13
GR4	0.00	0.00	0.00	1.63	0.12	0.00	0.00	0.00	0.00
GR5	0.00	1.58	0.00	1.48	0.99	0.09	0.94	0.25	0.15
GR6	0.00	1.99	0.00	1.70	2.34	0.00	0.00	0.00	0.00
GR101	0.18	1.22	0.18	1.18	0.00	0.13	1.22	0.35	0.26
MB1	0.00	0.00	0.00			1.04	5.14	2.57	1.84
MB2	0.00	0.00	0.00			0.00	0.00	0.00	0.00
MB3	0.00	0.00	0.00			0.00	0.00	0.00	0.00
MB4	0.36	2.39	0.36			0.53	2.66	2.39	1.76
MB5	0.36	2.42	0.37			1.03	3.90	2.53	1.86
MB6	0.37	2.54	0.40			1.11	5.12	3.49	2.35
MB7	0.00	0.00	0.00			0.00	0.00	0.00	0.00
MB8	0.38	2.62	0.39			1.09	4.35	2.76	2.02
MB9	0.00	0.00	0.00			0.00	0.00	0.00	0.00
MB10	0.00	0.00	0.00			0.00	0.00	0.00	0.00
MB101	0.36	2.39	0.35			0.28	2.86	1.45	0.87
MB102	0.00	0.00	0.00			0.00	0.00	0.00	0.00
MB103	0.42	2.83	0.42			1.00	4.31	2.64	1.93
MB104	0.00	0.00	0.00			0.00	0.00	0.00	0.00
MOM-2000-1	0.35	2.22	0.34			0.46	2.52	1.32	0.84
MOM-2000-2	0.44	2.89	0.46			0.89	4.44	2.54	1.72
MOM-2000-3	0.47	3.10	0.51			1.38	5.59	3.70	2.58
MOM-2000-4	0.33	2.18	0.34			0.44	2.33	1.30	0.87
N101	0.00	2.48	0.00			0.72	3.24	2.16	1.50
ZAP-ATR-a		2.19	0.33	3.72	1.10	0.11	0.81	0.53	0.28
ZAP-SMIG-a		1.91	0.30	2.05	0.41	0.18	1.25	0.78	0.49
mean-hemi	0.00	2.78	0.45			2.17	9.59	3.00	4.89
meancarb	0.00	1.18	0.19			0.15	3.70	0.16	0.15
DM	0.00	0.40	0.00	0.34		0.00	0.04	0.02	0.01
EM	0.06	0.41	0.06	0.26		0.03	0.18	0.08	0.02
AOC	0.00	2.70	0.00	2.04		0.07	0.69	0.26	0.19
AltMorblo		2.10	0.00	2.03	0.00	0.01	5.00	0.80	0.05

Table 1.5 continued

Sample	$^{87}\text{Sr}/^{86}\text{Sr}$	$^{143}\text{Nd}/^{144}\text{Nd}$	$^{206}\text{Pb}/^{204}\text{Pb}$	$^{207}\text{Pb}/^{204}\text{Pb}$	$^{208}\text{Pb}/^{204}\text{Pb}$
NE201	0.70375	0.51302			
NE202	0.70376	0.51308	18.6378	15.5293	38.1917
NE203	0.70362	0.51299	18.61	15.54	38.24
NE3	0.70393	0.51305	18.5852	15.521	38.2071
NE5	0.70407	0.51307	18.5298	15.4878	38.1708
NE6			18.5548	15.5067	38.1481
CDP12	0.70369				
MS1	0.70419	0.51308			
MS4	0.70415		18.605	15.5656	38.315
MS8	0.70421				
MS11	0.70421	0.51307			
MS14	0.70412	0.51302			
AP3	0.70388	0.51301			
AP5	0.70406	0.51305			
GR3	0.70384	0.51301	18.649	15.531	38.275
GR5	0.70388	0.51302			
GR101	0.70403	0.51307			
mean-hemi	0.70763	0.51274	18.783	15.631	38.673
meancarb	0.70858	0.512415	0	0	0
DM	0.7025	0.51312	0	0	0
EM	0.7025	0.51312	0	0	0

Table 1.6. Isotope values used in chapter 1.

NICARAGUA						
San Cristóbal	SC2 SC110	SC3 SC111	SC104	SC106	SC108	
Telica	TE1 TE114 TE123	TE3 TE115 TE124	TE6 TE116 TE125	TE111 TE117 TE127	TE112 TE119 TE128	
Rota	RO1	RO2	RO4	RO5	RO2000-1	
Las Pilas	LP1 LP107	LP2 LP108	LP101	LP102	LP103	
Asososca	AS1	AS2				
Momtombo	MT8	MT101	MT201			
Cerro Negro	CN10					
Nejapa	NE3	NE6	NE201	NE202	NE203	
COSTA RICA						
Orosí	G-92-1	672 Orosi-A	700 Orosi-A	Hacha 704-A	CACAO-a	
Rincón de la Vieja	RV1=R1	RV16=R16	RV-203			
Miravalles	665 Mirav-A					
Tenorio	TE1	632 Tenorio				
Cerro Chopo	600 Cerro Chopo-A	G-92-4				
Arenal	117080 132LA AR806 12/95 Arenal-A	117080 140A1 AR807 C2	100A4 143A2 AR391 127	101A3 AR82 ARENAL 8/89-a 52B	123LA AR805 ARENAL 5/92-a	
Platanar	PP1 PP11	PP3 PP12	PP4 PLA-7	PP5 PLA-47	PP8 PLA-105	
Poás	PO8310 PO2	PO8317 PO4	PO8387 PO10	PO8397		
Barba	B2 B8	B2B BHO-6A	B4B	B7		
Irazú	IZ-D2 IZ-V2	IZ-D7 IZ-63A	IZ84-1	I1	I2	

Table 1.7 Sample names for which data is from the cageochem file of Carr & Rose (1978) and Carr et al. (2004).

NICARAGUA						
Cosigüina	COS2	COS3	COS5	COSH	COS9A	
San Cristobal	sc001	SC1	SC101	SC102	SC209	
Cerro Negro	cn1	CN5	CN7	CN8	CN13	
Momotombo	mt001	mt002	mt003	mt004	mt005	mt006
Nejapa	NE1 NE10	NE2 NE11	NE4 NE12	NE8 NE13	NE9	
Masaya	MS2	MS3	MS7	MS13	MS15	
Mombacho	MB2	MB3	MB9	MB10	MB104	
COSTA RICA						
Orosí	OR03_1	OR03_2	OR03_3	OR03_4c	OR03_4f	OR03_5
Rincón de la Vieja	RV-201	RV-202	RV-204	RV-205	RV-206	
Miravalles	MV2	MV4	MV5	MV6	MV7	
Tenorio	TE2	TE4	TE9	TE10	TE11	
Arenal	102 133	105 134	117	124	131	
Platanar	PLA-13	PLA-14	PLA-25	PLA-43	PP10	
Poás	PO8349	PO8363	PO1	PO6	PO7	PO9
Barba	B1	B6	B9	B10	BH203D	
Irazú	IZ-V3	IZ-V5	D4	D5	D6	
Turrialba	TU1	TU2	TU6	TU8		

Table 1.8 Samples with trace element data from Bolge (*per. comm.*). Major Oxides are from the CAgeochem file of Carr & Rose (1987) and Carr et al. (2004).

## **Chapter 2 - Decompression melting behind a major offset of the volcanic front of Nicaragua: Concepción and Maderas volcanoes.**

### **Abstract**

The geochemistry of Concepción and Maderas, the two volcanoes that comprise Ometepe Island in Nicaragua reveal a minimum in slab signature due to a combination of physical parameters that lead to a predominance of decompression melting. This is contrary to much of the Central American volcanic front where lavas have large slab signatures and are dominated by flux melting mechanisms. We show that the decompression melting is allowed by a combination of physical parameters with a possible upwelling of mantle wedge material. The lavas from Maderas volcano, the first in present literature, and Concepción volcano, compliment work done previously by Borgia & van Wyk de Vries (2003) and van Wyk de Vries (1993).

### **Introduction**

Along the Pacific marginal zone of Central America (Dengo, 1968), the quaternary volcanic system, extending from northwestern Guatemala through central Costa Rica, arises because of the subduction of the Cocos plate under the Caribbean Plate (fig1 inset). Although Weyl (1980) listed 56 important volcanic vents of Central America, Carr et al. (2003) refined this into 39 volcanic centers; 11 of which are in Nicaragua. Stoiber and Carr (1973) and Carr et al. (1984) defined eight segments based upon transitions where the line of volcanoes breaks or changes strike. These breaks in the volcanic chain are right steps; the largest of which occurs between Nicaragua and Costa Rica, a right step of about 40km between the southernmost Nicaraguan volcano, Maderas, and the northernmost Costa Rican volcano, Orosí.

Isla Ometepe, built by Concepción and Maderas volcanoes, sits within Lago de Nicaragua in the southeastern part of Nicaragua (fig2.1). Concepción is presently active and records at least two periods of lava flows, one recent and one prehistoric (Borgia and van Wyk de Vries, 2003). Our geochemical study of lavas from the eastern side of the island complements the work of Borgia and van Wyk de Vries (2003) on tephra from the western side. Maderas is not historically active and has long been a private coffee plantation. Because public access began only recently, our analyses mark the first reported from this volcano within the geological community. Our results show that Ometepe lavas are significantly different from the adjacent volcanoes in Nicaragua and Costa Rica.

Geochemical variations along the Central American volcanic front (CAVF) occur both regionally and locally. We exclude Guatemala from this discussion because radiogenic isotopes show that the lavas from central and western Guatemala have been contaminated by Paleozoic crust. Further to the south, the crust is younger and radiogenic isotopes are not affected by crustal contamination. Regionally, the ratios Ba/La, La/Yb and many others describe generally smooth variations along the volcanic front (fig2.2; Carr, 1984; Plank and Langmuir, 1988; Carr et al., 1990; Leeman et al., 1994; and Patino et al., 2000; Carr et al., 2003). Overprinting this, HFSE ratios Zr/Nb and Hf/Ta describe a saw-tooth pattern (fig2.3; Lindsay et al., 2004; Bolge et al., *in review*), which defines segments, or lineaments of the volcanic front (fig2.4; Dollfus & Montserrat, 1868; Sapper, 1916; Stoiber & Carr, 1973).

Some variables that may control the geochemistry along the CAVF include changes in crustal thickness and composition (Carr et al., 1990; Cameron et al., 2002), slab dip (Carr, 1984; Protti, 1995), the composition of the mantle wedge (Feigenson et al., 2004;

Herrstrom et al., 1995; Leeman et al., 1994), fluids generated from the subducted slab by dehydration and/or melting (Walker, 1984; You & Gieskes, 2001; Rüpke et al., 2002) , and the composition of the subducted plate (Patino, 2000; Walker et al., 2001; Carr et al., 2003). Although there is widespread acceptance that these crustal and mantle components play key roles in arc geochemistry (Faure, 1986; McCulloch & Gamble, 1991; Hawkesworth et al., 1993; Arculus, 1994; Hawkesworth et al., 1994), the nature of each component, the amount each contributes and how they interact remain important questions. There are, however, some constraints regarding these variables along the CAVF.

Analyses of DSDP drill core 495 (Alt et al., 1996), outboard of Guatemala, show a distinct three-part slab stratigraphy: a base of mid-ocean ridge basalt (MORB) and two distinct sedimentary packages, one of carbonate ooze (CS), the other of hemipelagic mud (HS). The compositional distinctions between the sediment layers allow the use of element ratios to discern variations in both the proportion of each sediment component and overall flux intensities along the CAVF (Patino et al., 2000). This has led to the observation of both regional and local variation along the CAVF.

The mantle underlying Central America is known to shift from MORB-like under Nicaragua to OIB-like under Costa Rica (Carr et al., 1990; Leeman et al., 1994, Regan et al., 1994). Herrstrom et al. (1995) defined a transition zone in which this shift in mantle composition might occur. However, fluids and melts released from the subducting slab during dehydration cycle into the mantle wedge, where they not only initiate melting (Tatsumi et al., 1986) but also metasomatically modify the mantle wedge (Tatsumi, 1997). The mantle wedge is also modified by sediment recycling (Plank & Langmuir, 1998; Feigenson et al., 2004) and previous episodes of melting (Reagan et al., 1994).

These modifications may create enriched compositional domains within the mantle that is otherwise largely homogenous (Feigenson & Carr, 1993; Plank & Langmuir, 1998). Subsequent lavas may reflect mixing of both mantle compositions with additions of fluid/melt related enrichments (Chan et al., 2002).

Slab dip,  $\delta$ , changes along the CAVF; the greatest dip angle occurs underneath Nicaragua ( $84^\circ$ ) and shallows to both the northwest ( $45^\circ$ - $50^\circ$  beneath southeast Guatemala and western El Salvador) and southeast ( $60^\circ$  beneath central Costa Rica) (Syracuse & Abers, 2002; Protti et al., 1995; Carr, 1976). Carr et al. (1990) suggest that change in the dip angle of the slab may influence the way in which transport of elements through the mantle wedge occurs. That is, a more steeply dipping slab would have a more focused distribution of flux that interacts with a smaller volume of mantle wedge (fig2.5) leading to a higher degree of melting.

The composition of volcanic front lavas associated with subduction zones is generally controlled by flux melting mechanisms. With higher concentrations of flux, there is an increase in slab signature as shown by the proxy Ba/La. This is true along the Central American active front, which has a pronounced regional variation with the maximum slab signal located in Nicaragua (fig2.2a). Because of the strong role of flux melting in arc settings, decompression melting is sometimes overlooked. However, there is a growing body of evidence showing the importance of decompression melting above subduction zones. Pressure-release melting has been documented for high-MgO (10 – 11.8 wt%) and low H<sub>2</sub>O lavas at both the Cascades arc (Sisson et al., 1993) and Galunggung volcano (Sisson & Bronto, 1998). Likewise, Kohut et al. (2006) proposed that lavas, also high-MgO, from the Chaife seamount in the southern Mariana arc were derived from decompression melting of metasomatized mantle. Work by Cameron et al.

(2002), shows significant decompression melting in lavas with MgO <6wt% from the volcanic front in Guatemala, specifically from Pacaya and Agua. We propose that the observation of an anomalous signature in the Ometepe lavas is explained by decompression melting having primary control on their composition with little input from flux melting, in stark contrast to the rest of the arc.

### **Sample Location**

We focus on the lavas mapped on the eastern side of Concepción as mapped by Borgia and van Wyk de Vries (2003). On Concepción, two distinct flows were sampled; on Maderas, we collected samples from both the base of the volcano and from flows further up the edifice (fig2.1, yellow ticks). Samples were selected based on their apparent freshness and mineral content. Because we are interested in source processes more than shallow fractionation processes, we biased our sampling by choosing mafic samples.

### **Analytical Techniques**

Whole rock samples were powdered in an alumina ceramic mill and analyzed for major oxides by Thomas A. Vogel at the X-ray Spectrographic Laboratory, Michigan State University, with use of a SMAX Rigaku X-ray spectrophotograph (table2.1). Trace element data, measured at the Institute of Marine and Coastal Sciences of Rutgers University on a Finnigan MAT Element high resolution inductively coupled mass spectrometer (HR-ICP-MS), are obtained from powdered rock aliquots of 200mg. The powders are digested by standard HF-HNO<sub>3</sub> acid fluxing technique and introduced into the HR-ICP-MS at a 2000x dilution following Bolge (2000; table2.2). Digested aliquots of 500mg are run through cation/anion exchange columns, sequentially, to isolate Pb, Sr and Nd isotopes. Isotopic measurements are made in a Micromass multi-channel

thermal ionization mass spectrometer laboratory run by Dr. M. Feigenson at Rutgers University Department of Earth and Planetary Science (table 2.3).

## Results

The major element data define the lavas of Isla de Ometepe as basalts, basaltic andesites and andesites, typical of global island arc lavas. According to Peccerillo and Taylor (1976), this suite of lavas is calc-alkaline with two Maderas and several Concepción andesites falling within the high-K series (fig2.6a). There is one basalt from Maderas (M10) with anomalously low  $K_2O$ ,  $TiO_2$  and  $P_2O_5$  but high  $Al_2O_3$ ; this sample has accumulated plagioclase and is not a representative liquid (fig2.6c). In the AFM diagram, a Fe-rich Maderas sample (M12) edges into the tholeiitic field (fig2.6b).

In Fenner diagrams, lavas from both volcanoes fall into the field described by all Central American volcanic front (CAVF) samples (fig2.7). Most lavas from Maderas have higher wt% Mg and  $FeO^*$ , and lower  $SiO_2$  and alkali abundances than lavas from Concepción. The two exceptions are samples M1 and M2; thus, substantially less differentiation occurring in the lavas from Maderas. Likewise, a greater degree of fractionation is shown by Concepción lavas than Maderas lavas in Harker diagrams (fig2.8); again, exceptions are M1 and M2.

Given the climate of Nicaragua, weathering can potentially be a serious issue. Therefore, we sampled the interiors of flows and made petrographic assessments with thin sections. Neither of these safeguards, however, will reveal subtle weathering, which is identifiable through chemical analyses. Slight negative anomalies in both Ce and Eu in a few Maderas samples suggest weathering and plagioclase crystallization (inset, fig2.9). To better identify weathered samples, we plot Ce vs.  $Ce^*$  (fig2.9).  $Ce^*$  is the calculated concentration interpolated from La and Pr. With more weathering,

REEs in +3 oxidation states are enriched over Ce, due to its +4 oxidation state that makes it less mobile, thus creating a negative Ce anomaly (Patino et al., 2003). Using this discriminant, M2 is clearly weathered and will be excluded from the rest of this discussion. On the other hand, M1 is not weathered, yet is clearly more fractionated than the other Maderas samples.

Most subduction related volcanic rocks have low abundances of high field strength elements (HFSEs) relative to large ion lithophile elements (LILE) and rare earth elements (REE) and the Ometepe lavas are no exception. When normalized to primitive mantle (McDonough & Sun, 1995), the elemental pattern reveals overall enrichment decreasing toward the more compatible elements (fig2.10a). Overprinting this is the relative depletion of the high field strength elements (HFSEs) often found in lavas associated with subduction zones. The amount of HFSE depletion in the Ometepe lavas, however, is not as large as that seen in the lavas of Nicaragua and Costa Rica (shaded fields in figure 2.10a) and can be thought of as relatively small ratios of LILE and LREE to HFSEs. Breaking Nicaragua into NW/SE segments and Costa Rica into N/Central segments, the trace elements of Ometepe lavas are among those most enriched in Central America, more closely resembling lavas from central Costa Rica than from Nicaragua or northern Costa Rica (fig2.10b).

The HSFE ratio distribution forms a saw-tooth pattern (fig2.3; Lindsay et al., 2004; Bolge et al., *in review*) that corresponds to the right steps along the CAVF defined by Stoiber and Carr (1973) and Carr et al. (1984) (fig2.4). Each segment shows a decrease in HFSE ratios from NW to SE along the CAVF. Whereas the offset between Maderas and Orosí conforms to the HFSE pattern, it does not explain the discrepancy in the regional geochemistry. Thus, the Ometepe lavas represent a localized minimum

overprinted onto both the regional (slab signal) and segmented (HFSE) patterns.

There are volcanoes in Nicaragua where the products of a single vent form two populations with respect to HFSEs: those that are depleted in HFSEs and those that are not. Clearly that is not the case for either volcano of Ometepe (fig2.10). Again, M1 and M10 stand out from the other Maderas samples: M1 is the most enriched, particularly in Pb and Zr; M10 is the most depleted in P and Ti and has the only negative K anomaly. Clearly, M1 and M10 are outliers from an otherwise well behaved cluster of lavas.

The rare earth elements (REEs) are enriched in light to middle REEs (La – Dy); the heavy REEs (Ho – Lu) flatten at 10 – 25 log units above chondritic levels (fig2.11a). Values above chondritic levels are the result of crystal fractionation that creates andesites. Negative Eu anomalies in several samples point to removal of plagioclase. With the exception of andesitic M1, the Maderas lavas are less enriched than those from Concepción. On all the variation and spider diagrams, the Maderas samples appear consanguineous with the Concepción lavas; they define the same variation. Again, Ometepe REEs closely resemble central Costa Rican lavas. The steepness of slope in the LREEs of Ometepe lavas is consistent with a smaller degree of melting than other Nicaraguan lavas (also seen by La/Yb; fig 2b), but parallels that of Costa Rican lavas. However, the HREEs of the Ometepe lavas converge with those of NW Nicaragua (fig2.11b), not Costa Rica, suggesting that the source is the same as that associated with Nicaragua.

We infer that the lavas sampled from Maderas are older than lavas from Concepción because they appear to be the basaltic end of a basalt – andesite fractionation series. The work of Carr et al. (2007) supports the age differential. They measured a plateau  $^{40}\text{Ar}/^{39}\text{Ar}$  age for sample M10 of Maderas of  $76 \pm 6$  ka. For the

young lavas of Concepción, conclusive ages could not be measured, giving the lavas a virtual age of 0. That is to say, they are too young for  $^{40}\text{Ar}/^{39}\text{Ar}$  age dating, and so are younger than Maderas lavas. The Maderas sample dated, M10, is the least differentiated Maderas sample. Thus, being conservative, it may be a maximum age for the ongoing fractionation series observed at Ometepe.

$^{86}/^{87}\text{Sr}$  values range from 0.703879 – 0.704020;  $^{143}/^{144}\text{Nd}$  ratios range from 0.512942 to 0.513001 with the higher values from Maderas volcano (fig2.12a). The large error bars render the variation of Nd meaningless, whereas the small error bars associated with Sr indicate a true, but small, amount of variation. Lead ratios fall within the range of island arc volcanism (White, 1998) and have the following ranges:  $^{206}/^{204}\text{Pb}$ : 18.593 – 18.667;  $^{207}/^{204}\text{Pb}$ : 15.474 – 15.545;  $^{208}/^{204}\text{Pb}$ : 38.100 – 38.385 (fig2.12b). Lavas from both volcanic centers overlap, which indicates that they are sampling the same mantle reservoir. The lavas are slightly depleted in Nd isotopes and enriched in Sr isotopes when compared to N-MORB. In  $^{207}/^{204}\text{Pb}$  vs.  $^{206}/^{204}\text{Pb}$  space, both volcanic centers show a slight trend toward the EMII reservoir, with Concepción having the more enriched  $^{207}/^{204}\text{Pb}$  signal. These observations are consistent with sediment recycling mechanisms previously observed in Nicaraguan lavas (Feigenson et al., 2004).

Chemical proxies measuring the flux intensity of the combined sediment sections use element ratios that are relatively constant through the stratigraphy. Although Patino et al. (2000) use both Ba/La and U/Th, we consider Ba/La a superior proxy for slab signal (fig. 2a) because its variance is lower in the DSDP stratigraphy. Whereas the overall regional variation is like a chevron, there is a local minimum at 850km along the arc corresponding to Maderas and Concepción volcanoes. Maderas lavas have the minimum amount of slab signal along the entire Central American volcanic front, with

the exception of the central Costa Rican lavas (i.e., Barba, Irazú and Turrialba). Concepción lavas resemble lavas from Arenal volcano in Costa Rica in Ba/La. Together, the Ometepe lavas deviate from the otherwise smooth regional variation in Ba/La along the arc; a deviation that is not explained by varying abundances of subducting sediment type.

Mixing between the hemipelagic and carbonate layers of the subducting slab (Patino et al., 2000) is observed in some volcanic centers, such as Telica volcano in NW Nicaragua and Arenal in Costa Rica, which show a wide range of changing proportions between the hemipelagic (U/La) and carbonate (Ba/Th) sediments (fig2.13). Maderas shows a similar mixing trend, but the slope of the trend is not as steep as either Arenal or Telica, indicating a larger role of the mantle and a lesser role of subducted sediment. Concepción shows no discernable trend indicating that either the proportion of sediments is not significantly changing or magma mixing has homogenized the geochemical signal.

## **Discussion**

Local sediment mixing variations defined by Patino et al. (2000; fig2.13) may be explained by the relative size of a given volcano and its plumbing system. Telica, has abundant, relatively small vents compared to larger centers like Masaya and clearly shows a mixing trend between the hemipelagic and carbonate sediment packages. Arenal and Maderas show similar trends, but to lesser degrees and at much lower concentrations. Both volcanoes differ from Telica in that they have a single main vent. At the same time, they sit at an end of a segment and, following the logic of Bolge et al. (*in review*), should be relatively small due to less flux coming from the subducting slab. Concepción, although much smaller than the centrally located Masaya shield complex, is one of the

largest stratocones in Nicaragua, rising 1600m with a cone diameter of 14km (Borgia & van Wyk de Vries, 2003). Larger centers have larger underlying magma chambers, which, in turn, allow longer residence time for magma and a greater opportunity for magma mixing (Walker et al., 1993). Thus, larger complexes, such as Masaya and Concepción, overshadow the systematics of separate sediment signatures. Variations in physical parameters along the CAVF may explain the geochemical anomaly observed in the Ometepe lavas.

Syracuse & Abers (2006) compiled global variations in slab depth beneath arcs (H) and other physical parameters including slab dip ( $\delta$ ), the distance of volcanoes from the trench perpendicular to slab strike (T) and the average age of incoming seafloor at the trench (A). Important in constraining arc magmagenesis, they find correlation of these parameters with distance along the CAVF (fig2.14a-c). Corroborating this, Bolge et al. (*in review*) show that the HFSE ratio sawtooth pattern along the volcanic front (fig2.3) is due to both changes in the depth to slab, H (fig2.14a), and changes in the distance from the trench, T (fig2.14b). They propose that volcanic centers at the SE end of a given segment, as defined by Stoiber & Carr (1973), will have products least depleted in HFSE ratios as they sit further from the trench and so have greater depth to the slab. Consequently, there will be a longer melting column under these volcanoes, allowing more melt/mantle interaction time, thereby diluting/decreasing HFSE depletion. This means that within each segment, traveling northwest to southeast along the front, as HFSE depletion decreases, both the depth to the top of the slab and the distance from the trench increase. It would seem that their proposal fits the Ometepe data well. Maderas, the most SE volcano of its segment sits furthest from the slab and shows the least depletion of HFSE ratios (figs 2.3, 2.14a). According to Syracuse and Abers

(2006), however, it is no more distant from the trench than Apoyo caldera (both 180km), which has populations of both HFSE depleted and non-depleted lavas.

Age of the incoming seafloor at the trench (A) (Syracuse & Abers, 2006) versus distance along the CAVF forms a smooth curve and correlates with regional geochemical parameters of Ba/La, La/Yb and Zr/Nb (fig2.14d-f). Again, the Ometepe lavas form an irregularity in the otherwise smooth patterns. Additionally, as pointed out by Syracuse & Abers (2006), there is a natural correlation between  $\delta$  and H on a steepening slab, although the correlation is lost when averaging  $\delta$  in the direction of maximum dip as they do. Nonetheless, there must be a correlation due to geometry between the  $\delta$  and H (fig2.5) and so, by logic, between  $\delta$  and the segmental saw-tooth pattern, which correlates with H (fig2.14a).

As mentioned earlier, Carr et al. (1990) proposed that a more steeply dipping slab, having a more focused distribution of flux (fig2.5) would lead to a higher degree of melting. It would also call for a much larger role of the mantle and less of the subducting slab, explaining the small ratio of Ba/La in lavas extruded above such areas. The criteria of steep slab dip and relatively large distances to both slab and trench are satisfied by both Concepción and Maderas volcanoes and explain, in part, the geochemistry of their lavas. Age of the subducting slab and the relative size of the volcano's magma chamber also control facets of the geochemistry. However, the Ometepe lavas show a relatively small degree of melting, contrary to the model of Carr et al. (1990). Therefore, physical parameters alone are not enough to explain the geochemical deviation of the Ometepe lavas.

Syracuse and Abers (2006) correlate the physical and geochemical parameters H and Na<sub>6.0</sub> [composition at 6 wt% MgO used to adjust for variations in crustal thickness

along an arc; Plank & Langmuir (1988) such that H overprints  $\text{Na}_{6.0}$  along the CAVF (fig2.15a). They propose that, whereas Na is abundant in small melt fractions, an increase of H allows interactions with a larger vertical portion of mantle wedge, prompting a greater degree of melt thereby decrease/diluting Na. Plotting  $\text{Na}_{6.0}$  against La/Yb (fig2.15b), a proxy for degree of melting, not only emphasizes a large amount of scatter within each segment along the arc, particularly in Na concentration, but places north Costa Rica between Ometepe and the rest of the SE Nicaragua segment volcanoes. Furthermore, if H is the controlling factor for degree of melting, the decrease in degree of melting observed in the Ometepe lavas, relative to SE Nicaragua and N Costa Rica, suggests that the distance to the slab is undulatory in nature, contrary to seismic data (Protti et al., 1995). Thus, H alone cannot explain the deviation observed in the Ometepe lavas.

In fact, it is not the degree of melting, but the melting mechanism that distinguishes the Ometepe lavas from others along the CAVF. Cameron et al. (2002) use Ba/La vs. La/Yb space to distinguish between fluid flux melting and decompression melting, respectively. Flux melting, an open system process (Gribble et al., 1996), will correlate slab input with degree of melting (Hochstaedter et al., 1996); decompression melting, a closed system process, will be unaffected by slab input. Placing the Ometepe lavas within this space, the data clearly show the importance of decompression melting in their generation (fig2.16a). The importance of decompression melting of mantle in the formation of magmas in Central America is also seen in basalts from central Mexico (Cervantes & Wallace, 2003) and Guatemala (Cameron et al., 2002). Cervantes & Wallace (2003) found that, whereas an  $\text{H}_2\text{O}$ -rich component fluxing the mantle wedge explains some of their samples, samples with less depletion of the HFSEs relative to

LIFEs are formed by decompression melting. Likewise, Cameron et al. (2002) show that decompression melting is more important than flux melting to magma generation for volcanoes within an extensional regime.

This is not to say that flux melting plays no role in the generation of the Ometepe lavas. In comparison to back-arc basalts of the region, such as Yojoa in Honduras, Estelí in Nicaragua and Agua Zarcas in Costa Rica (fig2.16b), there is a significant addition of Ba/La in the Ometepe rocks, which increases with degree of melting. Behind the arc samples from Estelí in Nicaragua show a steeper gradient of Ba/La increase with a more constant degree of melting than the Ometepe lavas, indicating a different evolution from the Ometepe lavas, although it may simply be an artifact due to a paucity of Estelí sampling. In fact, the distribution of Zr and Nb (fig2.17), which are not affected by varied slab flux input due to their relative fluid-immobility (Keppler, 1996; Kogiso et al., 1997), reveals that Estelí lavas are near to N-type MORB. Back-arc samples from Yojoa are more enriched than OIB, while Agua Zarcas covers the full range between N-type MORB and OIB. The Ometepe lavas with an average Zr/Nb of 11, plot on the depleted side of E-type MORB. This indicates that extensional tectonics associated with back-arc and behind-the-arc environments do not fully control the genesis of the Ometepe rocks and shows the heterogeneity of their mantle source.

The idea of different mantle sources underlying NW Nicaragua and central Costa Rica (Carr et al., 1990; Leeman et al., 1994, Regan et al., 1994), along with Herrstrom et al., (1995) placing a mantle source transition zone between Concepción and Arenal volcanoes begs the question as to whether the mantle source of the Ometepe lavas can explain their observed deviations. Certainly the minimum slab signal (fig2.2a) observed

in Ometepe lavas, more similar to Costa Rica lavas than other Nicaragua lavas, could place the change of mantle composition under Lago de Nicaragua. Primary evidence against this idea comes from the volcanoes of north Costa Rica: they do not show the same lack of slab signature (fig2.2a); in fact they show an increase in Ba/La relative to the Ometepe lavas, although this might be explained by being nearer to the trench.

Further evidence comes from radiogenic isotope ratios. Isotopes of Nd vs. Sr show that the CAVF lavas have Nd values close to MORB (fig2.12a inset) with the exception of central Costa Rica, which trends toward HIMU. The Sr values increase as sediment derived fluids that incorporate into the mantle increase, consistent with the high slab signal seen in NW Nicaragua and some SE Nicaragua lavas. Pb isotope space shows that whereas Ometepe lavas trend toward a DM source reservoir, Arenal and central Costa Rican lavas trend toward EMII and/or HIMU reservoirs (fig2.12b). The separation of central Costa Rica lavas from the rest of CAVF, indicative of a different, more enriched source, makes it more likely that the change in mantle composition occurs near Arenal. Nonetheless, the trend shown by the Ometepe lavas in Pb space corroborates a temporal change in the amount of sediment contribution, with the older Maderas lavas having slightly less than Concepción lavas, as seen also in Ba/La space. Additionally, the overlap of the Ometepe lavas in isotope space strengthens the argument that the Ometepe lavas are a unified fractionation series generated by a batch of magma that fed both vents.

Abundances of REEs are consistent with a different mantle composition under northwestern Nicaragua and central Costa Rica as some have proposed (Leeman et al., 1994; Feigenson et al., 2004) with an increase in La/Yb observed in central Costa Rica indicating greater amounts of garnet in the residual mantle. Interestingly, it is an

increase in La abundance, not Yb, driving this ratio (fig2.18), indicating that different degrees of melting play a large role in REE patterns.

Although Ometepe, which sits in the morphologic low-land of the Nicaragua Depression (van Wyk de Vries, 1993), is not an extensional environment, the geochemistry clearly points to decompression melting. It has been suggested (Miller et al., 2004) that a discontinuity in the subducted lithosphere beneath an active volcano can cause the plate above it to rift. Based on this, we propose a model following that of Kohut et al. (2006) in which the mantle wedge experiences both enhanced upwelling and hydration from fluids associated with the downgoing slab. In this case, the relatively large distance to the trench and distance to the slab decreases the amount of fluid flux to the point that, although enough to impart the observed arc geochemical signature, it is insufficient to directly generate magma. Rather, a perturbation of the subducting slab beneath Ometepe stimulates upwelling within the mantle wedge leading to decompression melting. It is worth noting that such a discontinuity would explain the observed discrepancy in the relationship of H and degree of melting (Syracuse & Abers, 2006) between Ometepe and adjacent segments along the volcanic front noted previously.

### **Conclusions**

The calc-alkali lavas from Concepción and Maderas volcanoes are a unified basalt-andesite fractionation series generated by a single magma batch ~100Ka. The older Maderas lava, dated at 76Ka, represent the initiation of a presently ongoing fractionation series. The younger Concepción lavas show greater amounts of differentiation and fractionation, but show no variation in subducting sediment proportion, indicating a larger magma chamber that homogenizes the signal. Maderas

shows a small amount of sediment mixing, though less than either Telica or Arenal giving the mantle a more significant role than subducting sediments in the chemistry of the lavas. Compared to other Nicaragua lavas, both Maderas and Concepción are oddly low in Ba/La and high in La/Yb. They have no lavas that are non-depleted in HSFEs and show the lowest Hf/Ta, which coincides with the right step between Maderas and Orosí that is the largest in the CAVF.

Together, Ometepe lavas have a distinct geochemistry due to the visibility of both flux melting and decompression melting geochemical signatures. Flux melting, although present, is minimal as shown by low abundances of Ba/La. This is a result of the distance from the trench, the distance to the subducting slab, the slab dip and the relative age of the downgoing slab. The importance of decompression melting is evident in the relatively high LILE and LREE to HFSE ratios and in the lack of correlation between slab signature and degree of melting. We propose that the decompression is allowed by a perturbation in the downgoing slab that stimulates upwelling in a heterogeneous, but predominately enriched mantle wedge. This unique situation can be used to distinguish between chemistry due to subduction zone fluxes and chemistry due to decompression melting.

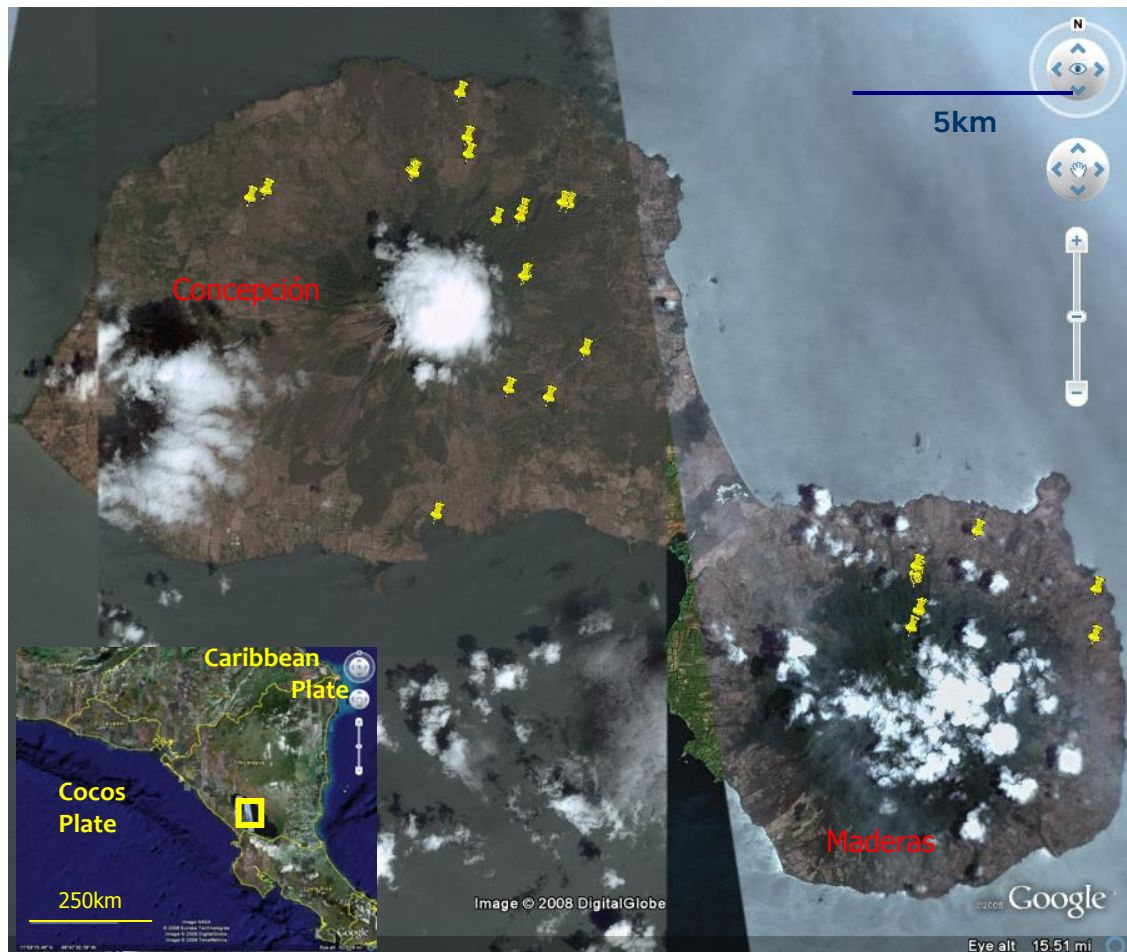


Figure 2.1. Map of Ometepe with yellow tacks showing locations of sampling on Concepción (left) and Maderas (right) volcanoes. Inset map showing the location of Ometepe (yellow square). Adapted from Google Earth 2008.

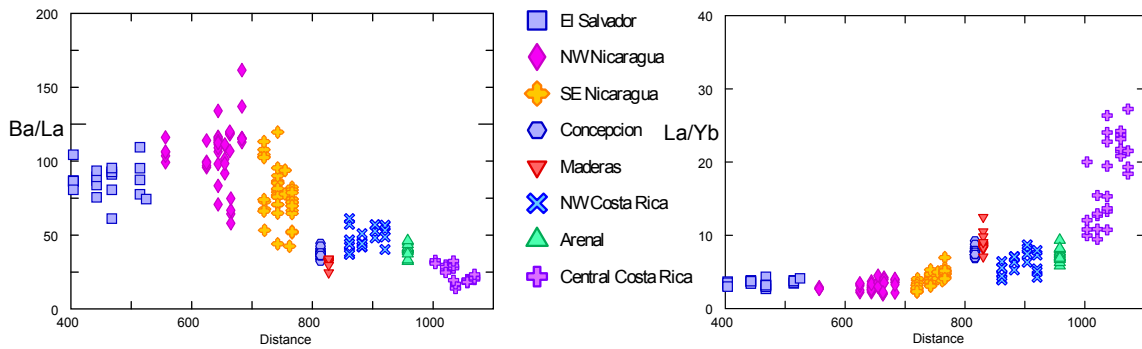


Figure 2.2. Regional variation of slab signal along the Central American active volcanic front. Ba/La proxies the signature from the subducting slab via flux melting; La/Yb reflects relative degree of melting.

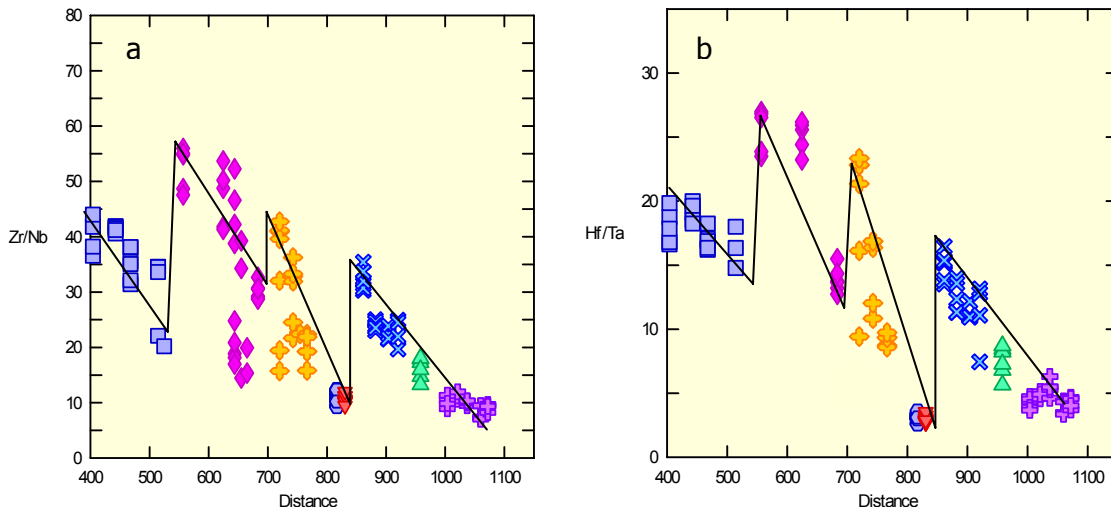


Figure 2.3. Local geochemical variations of HFSEs overprint the regional variations. The variations describe a saw-tooth pattern that roughly coincide with the segments along the arc. Symbols as in fig. 2.



Figure 2.4. Central American volcanic front showing right-stepping breaks (thin stippled rectangles) along the front as defined by Stoiber & Carr (1973). Figure courtesy of E. Gazel.

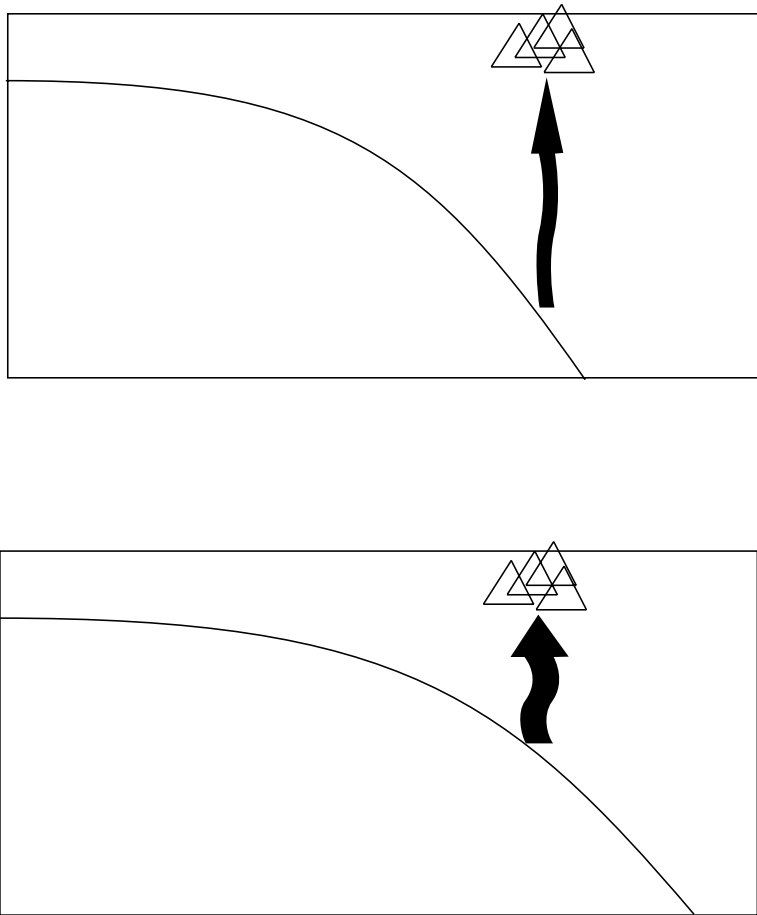


Figure 2.5. Cartoon – NOT TO SCALE – showing the difference in dip angle and corresponding difference in depth to slab. The top cartoon has a steeper slab dip resulting in a greater distance to slab than the cartoon below. Additionally, the melt/fluid flux is more focused, resulting in less horizontal interaction but more vertical interaction with the surrounding mantle wedge.

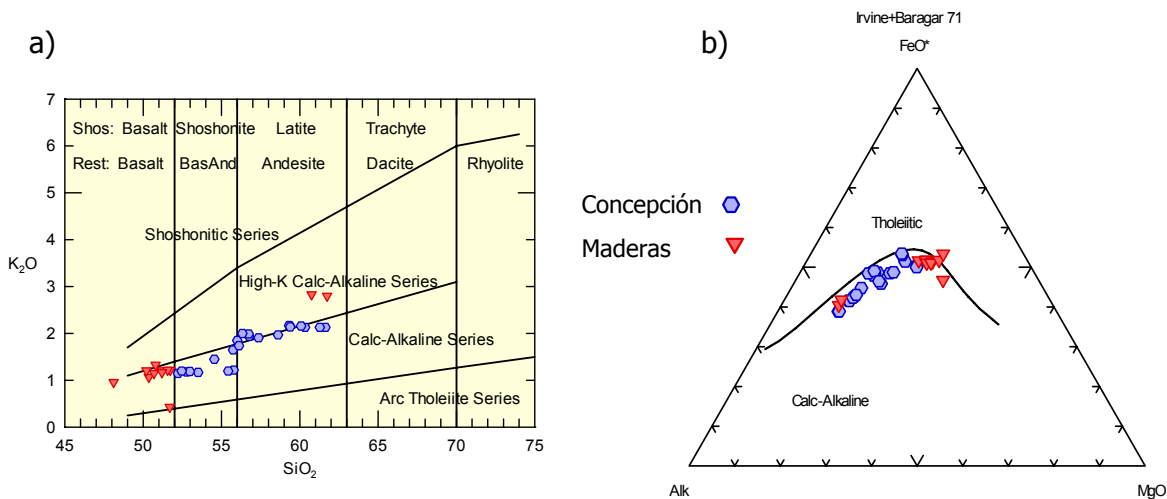
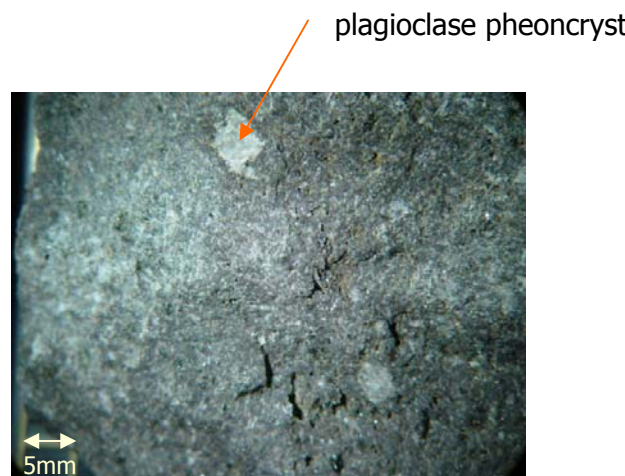


Figure 2.6. Major oxide results for Ometepe samples: a) Peccerillo & Taylor (1976) and b) AFM diagram; c) hand sample of M10 shows plagioclase phenocrysts within the matrix.



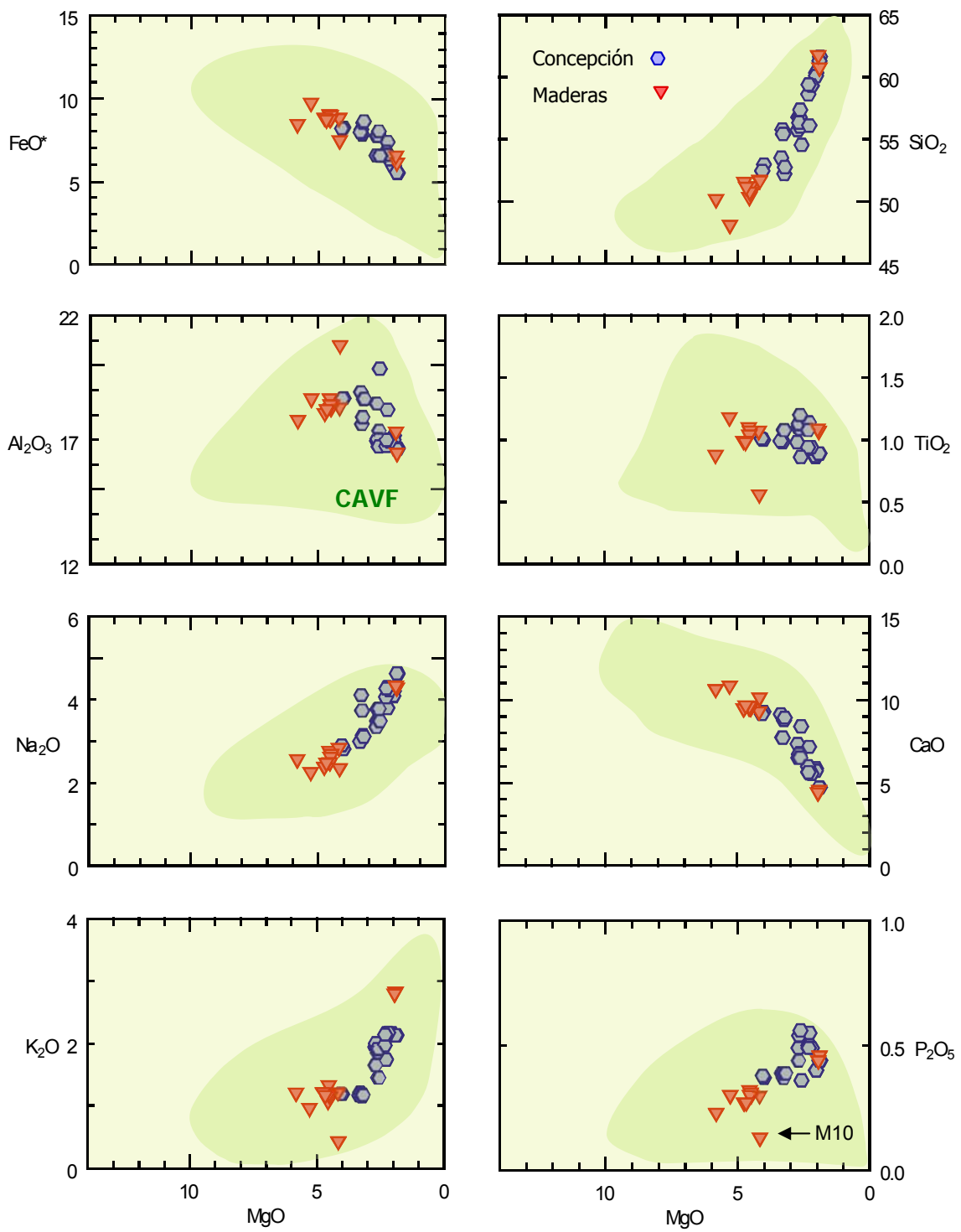


Figure 2.7. Green shaded area represents range of Central American volcanic front (CAVF) samples. Back-arc samples are not included. The outlier, M10, has plagioclase accumulation.

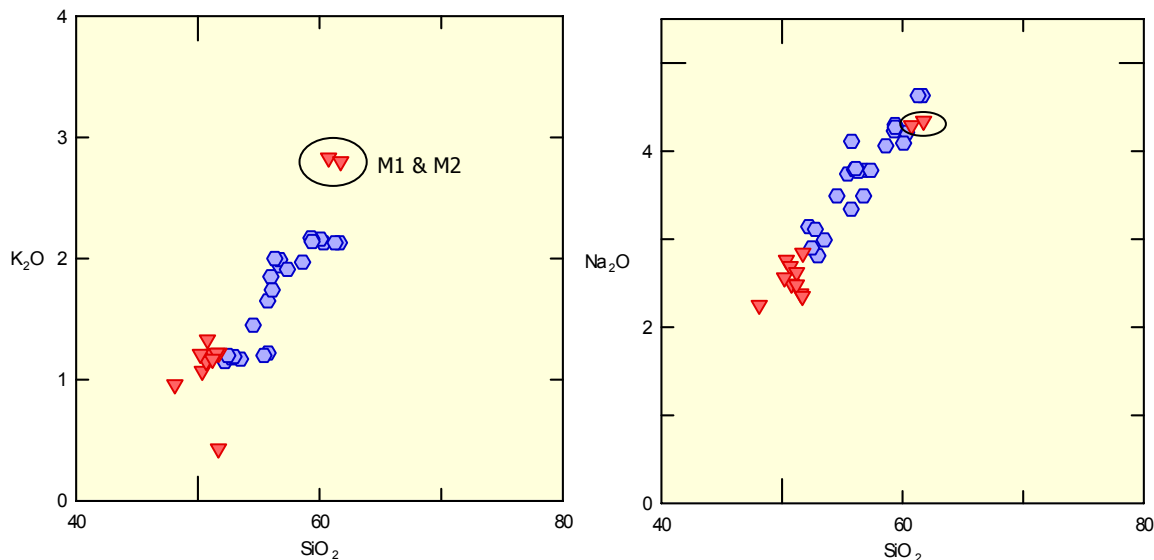


Figure 2.8. Harker diagrams show that Concepción lavas (blue hexagons) are more fractionated than those from Maderas (red inverted triangles). Exceptions are M1 and M2 (circled), both collected from the toe on the north side of Maderas.

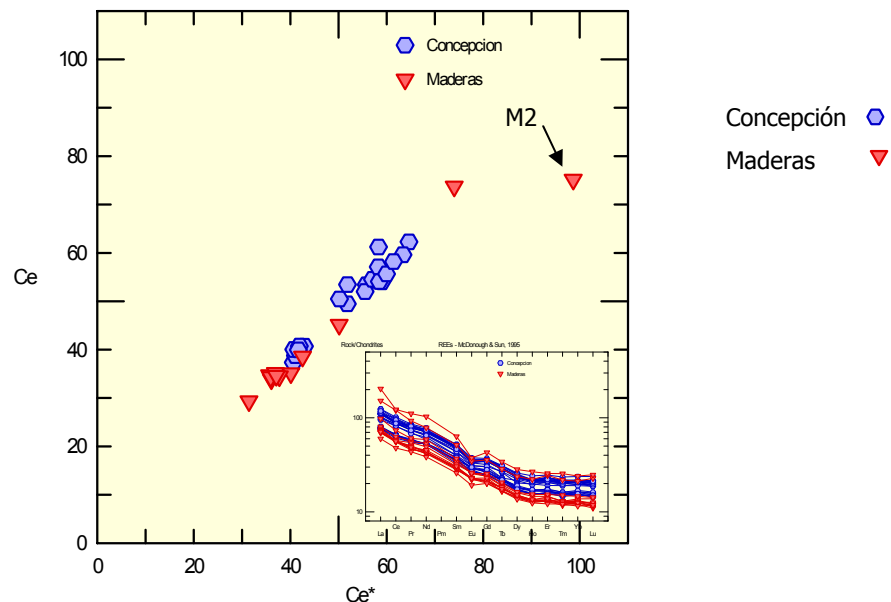


Figure 2.9. Ce vs.  $\text{Ce}^*$  is used to distinguish weathered samples. Increased weathering produces a loss of Ce, shown here by a deflection from a 1:1 trend. See text for further discussion.

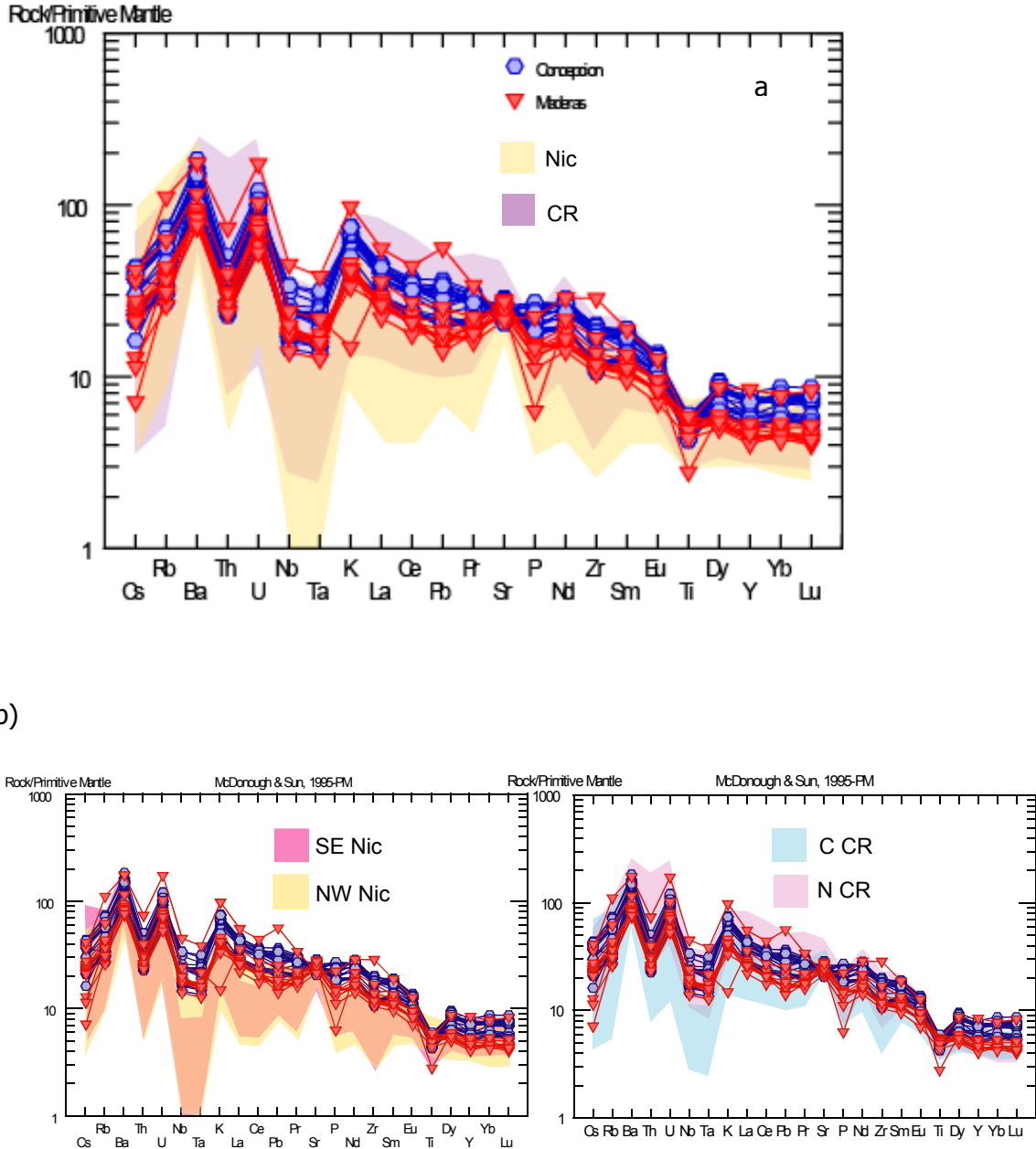
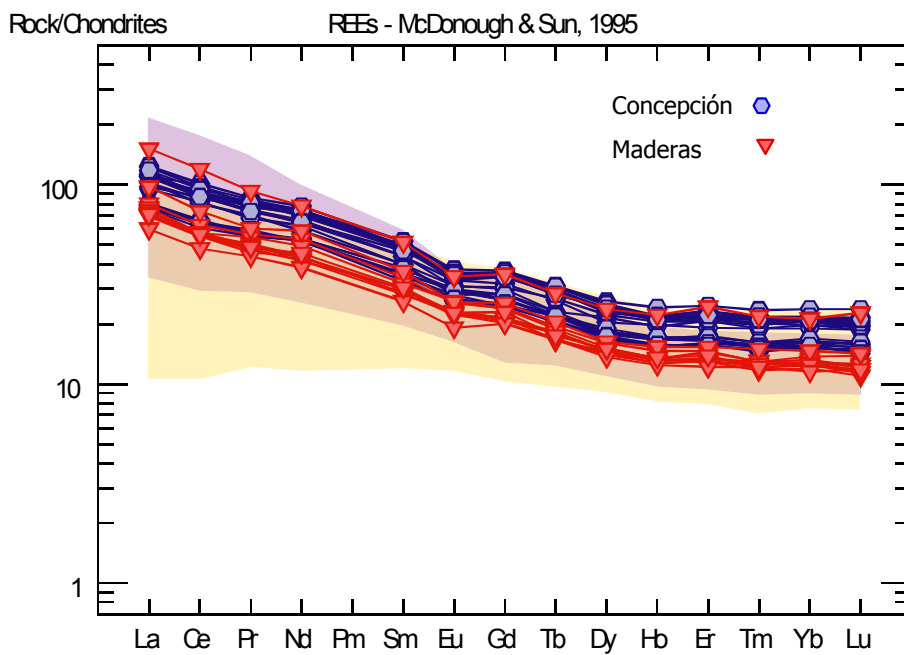


Figure 2.10. Ometepe lavas normalized to a) primitive mantle (McDonough & Sun, 1995). Shaded regions show range of lavas from Nicaragua and Costa Rica. b) Shaded regions broken down into segments of Nicaragua (NW, northwest; SE, southeast) and Costa Rica (N CR, northern Costa Rica; C CR, central Costa Rica). The Ometepe lavas have relatively low ratios of LILE and LREE to HFSE, similar to central Costa Rica.



b)

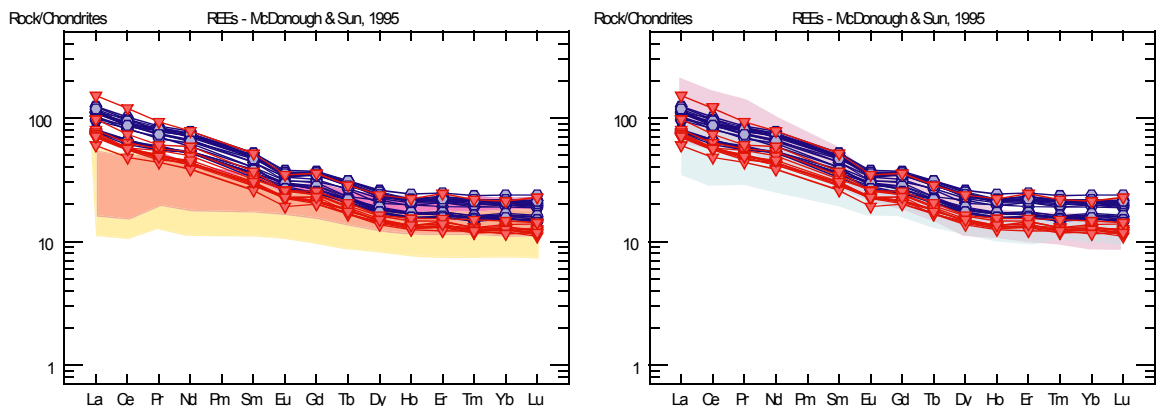


Figure 2.11. a) REE spidergram with the Ometepe lavas shown in relation to the ranges of lavas from Nicaragua and Costa Rica. b) Comparison of Ometepe lavas with lavas from separate segments of Nicaragua and Costa Rica. Shaded regions are as in fig2.10.

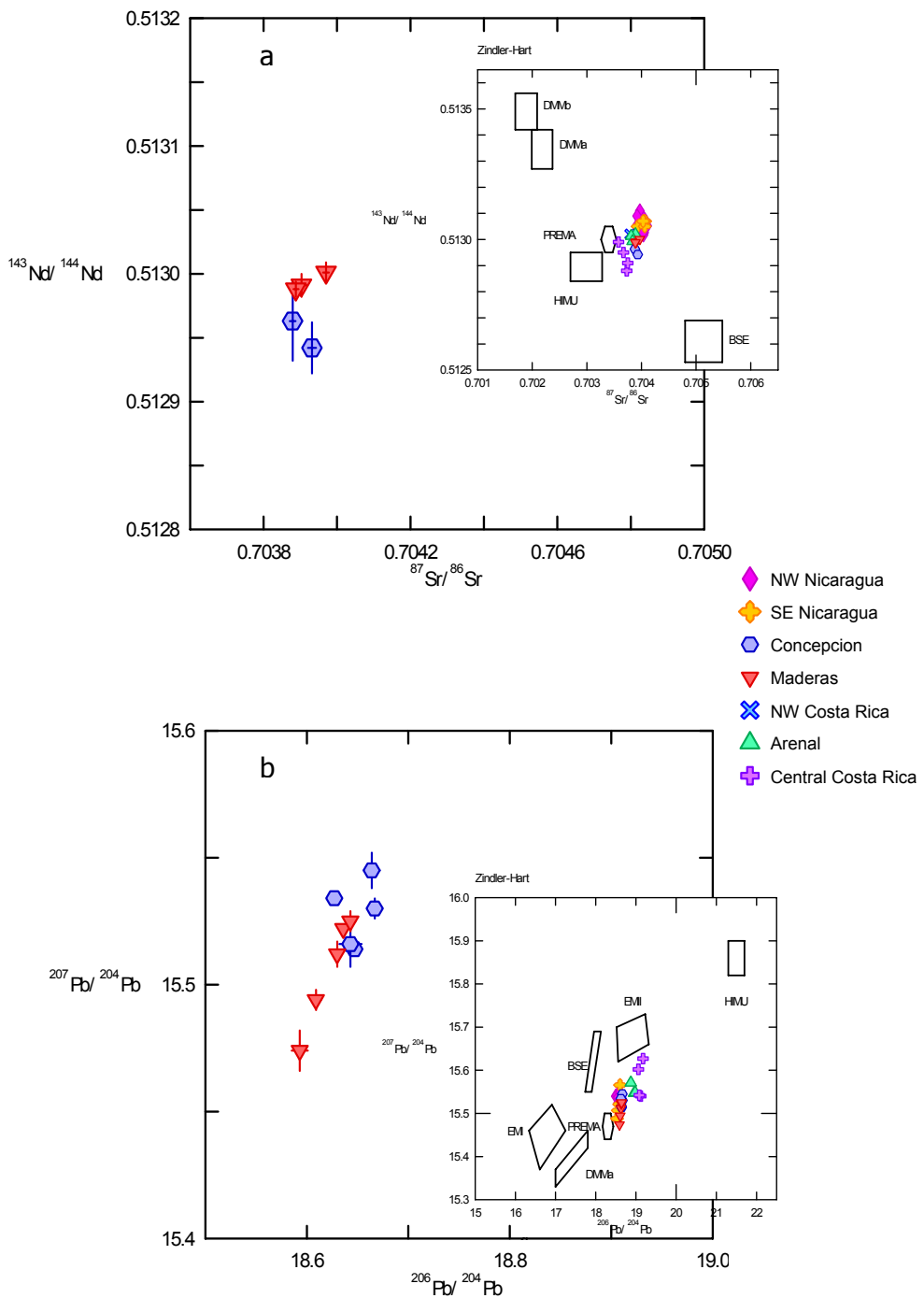


Figure 2.12. a. Nd vs. Sr isotope ratios and b. Pb isotope ratios with insets showing various mantle reservoirs and lavas of Nicaragua and Costa Rica. Error bars are  $1\sigma$ . Overlap of samples suggests the same source for the two volcanoes.

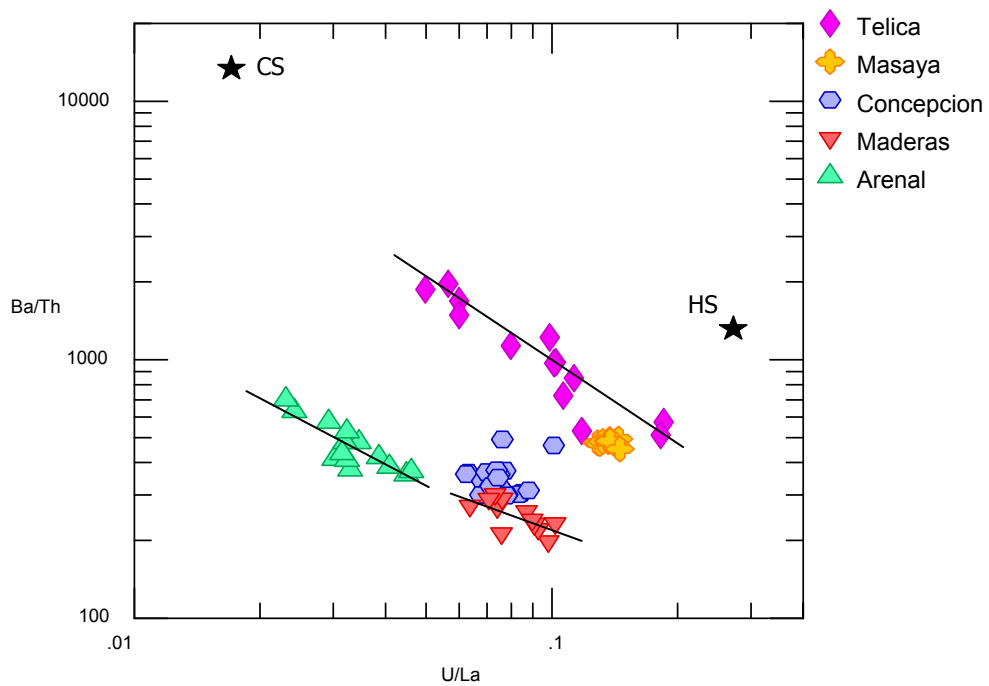


Figure 2.13. Mixing between the hemipelagic sediment layer of the downgoing slab (HS) and the carbonate sediments (CS) are evident in small volcanic centers, such as Telica volcano (Patino et al., 2000) in NW Nicaragua (pink diamonds). Whereas Maderas shows some evidence of this mixing, Concepción, like Masaya, does not.

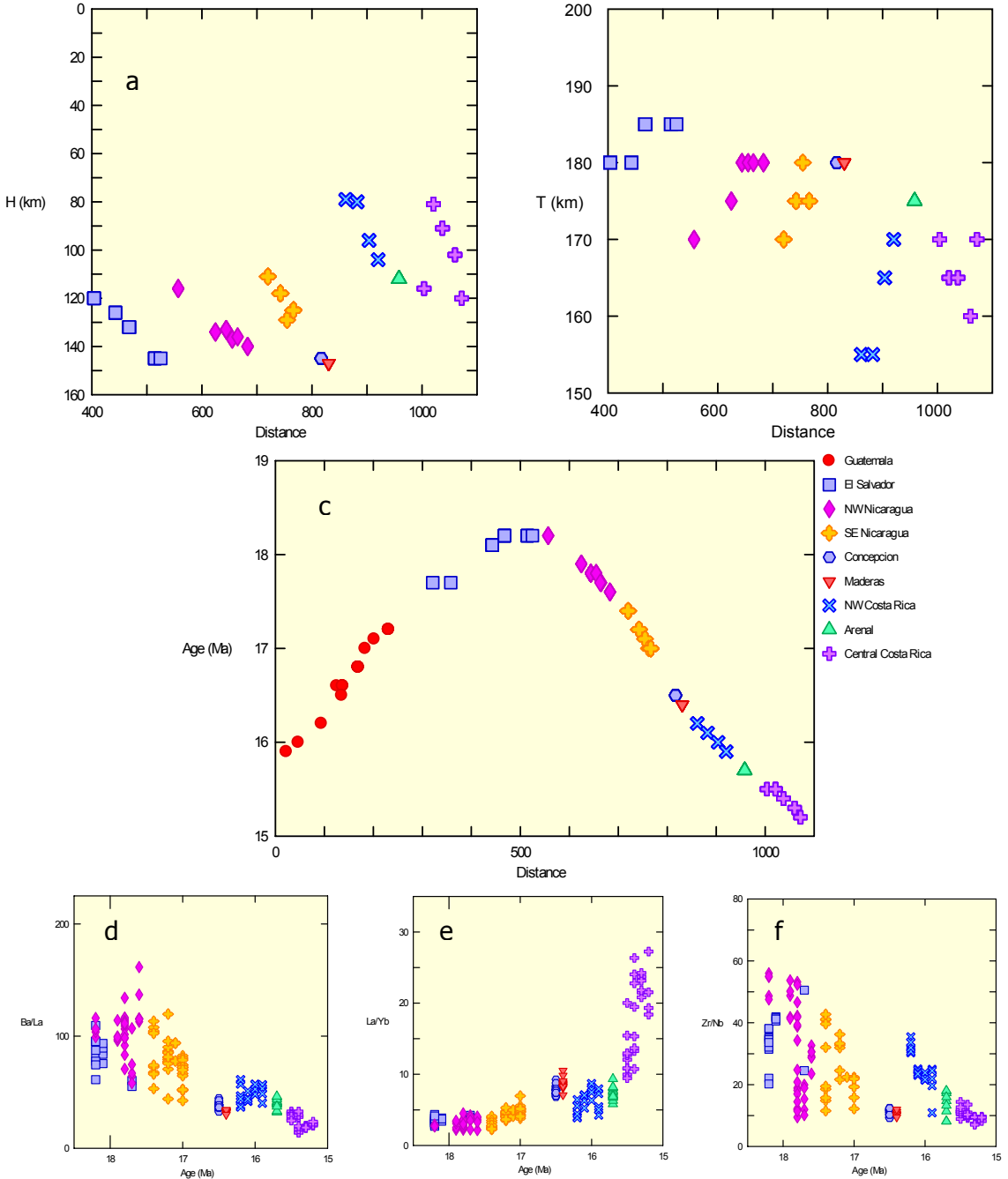


Figure 2.14. Using data from Syracuse & Abers (2006). The segmental saw-tooth pattern along the CAVF is seen clearly in the physical parameters of a) H (slab depth beneath the arc) and b) T (distance from the trench) and c) A (age of the incoming slab). The patterns of H and T correspond to that defined by HFSEs (compare to fig. 3). Note the Y-axis is inverted in a) to correspond with depth. The smooth pattern of A resembles the regional geochemical pattern of Ba/La, (d), La/Yb (e) and Zr/Nb (f). Note the x-axes are transposed to correspond to NW – SE directionality along the CAVF. In both parameters, Ometepe lavas show a deviation from an otherwise smooth pattern.

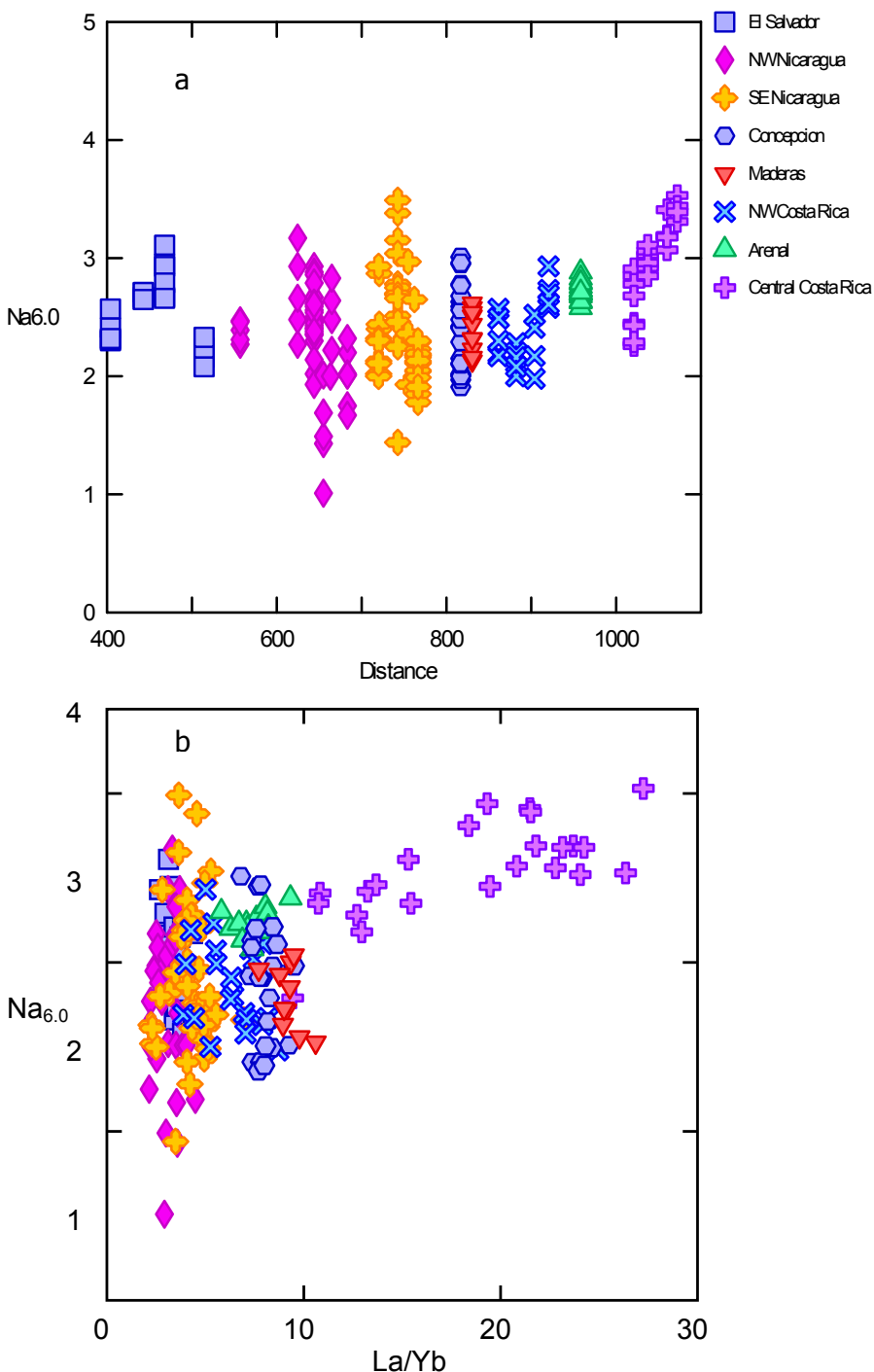


Figure 2.15. a.  $\text{Na}_{6.0}$  along the distance of CAVF.  $\text{Na}_{6.0}$  is the concentration of  $\text{Na}_2\text{O}$  at 6wt%  $\text{MgO}$  as determined from  $\text{Na}_2\text{O}-\text{MgO}$  linear regression for each volcano (Plank & Langmuir, 1988). b)  $\text{Na}_{6.0}$  vs.  $\text{La/Yb}$  shows scatter within each segments of the CAVF. It also splits SE Nic by placing north CR in between Mombacho and Concepción, further highlighting the anomalous behavior of the Ometepe lavas.

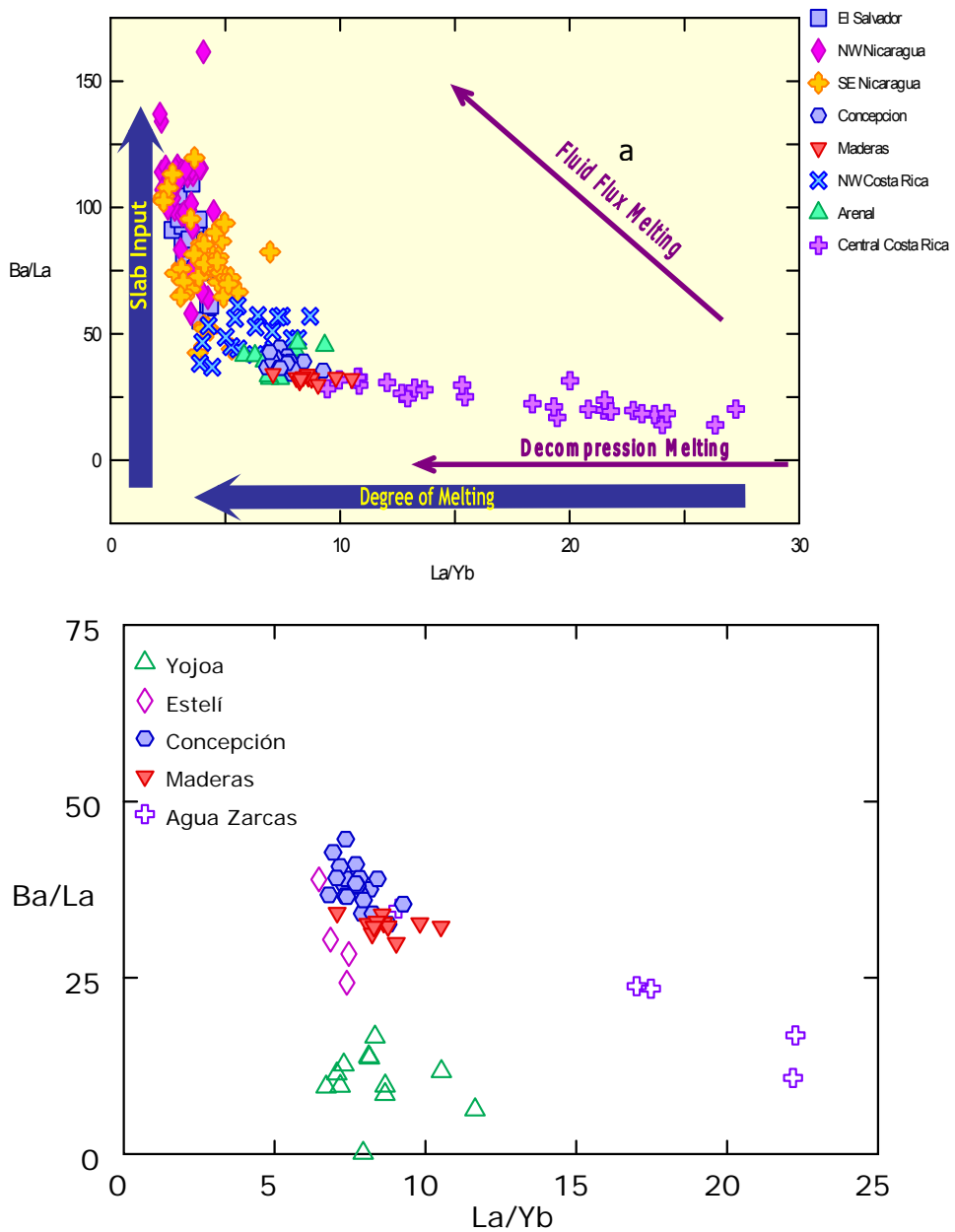


Figure 2.16. a)  $\text{Ba/La}$  vs.  $\text{La/Yb}$  (Cameron et al., 2002) shows the Ometepe lavas as experiencing decompression melting to a greater degree than most CAVF lavas, in contrast to the flux melting that occurs over much of the arc. b) Ometepe lavas show a small, but significant amount of flux melting influence when compared to suites that are formed by decompression and have constant  $\text{Ba/La}$  [Yojoa]. The small Estelí suite is consistent with flux melting having large changes in  $\text{Ba/La}$  for small changes in  $\text{La/Yb}$ . Ometepe lies between these two extreme endmembers.

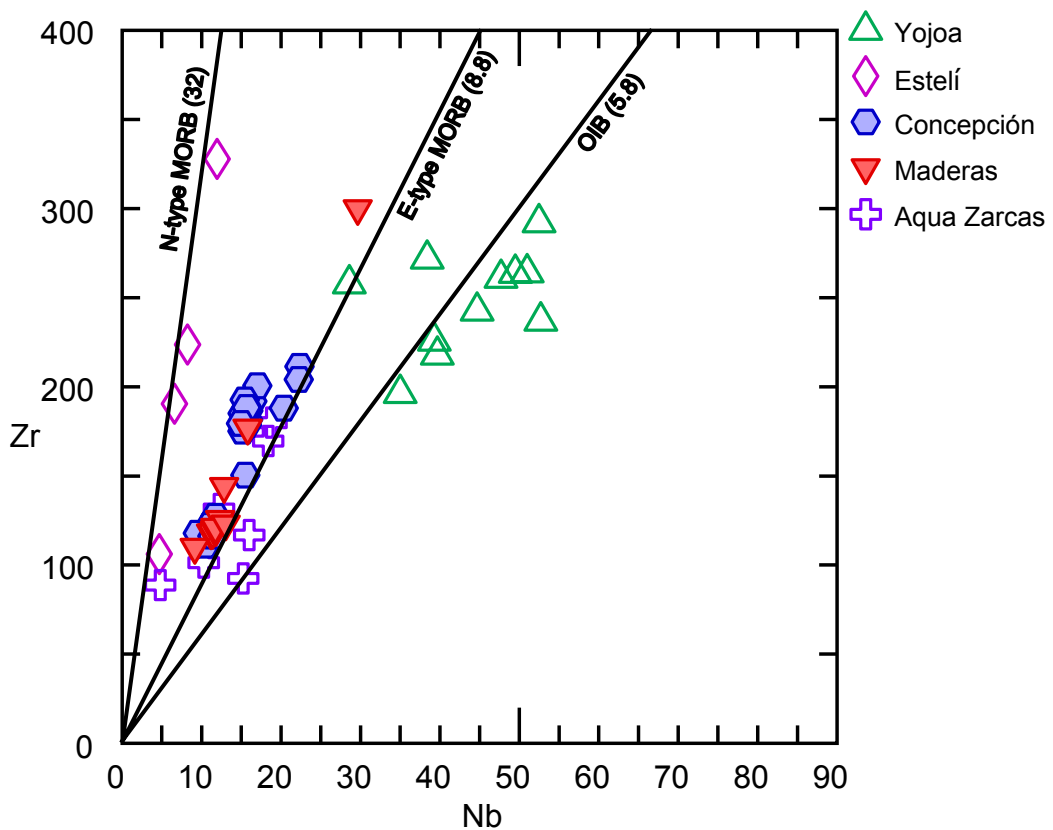


Figure 2.17. Ometepe lavas are more enriched in HFSEs than MORB, yet not as enriched as OIB. Estelí samples follow MORB trends, but behind the arc lavas of Costa Rica (Aqua Zarcas) are similar to Ometepe lavas. MORB and OIB values (in parentheses) from Sun & McDonough (1989).

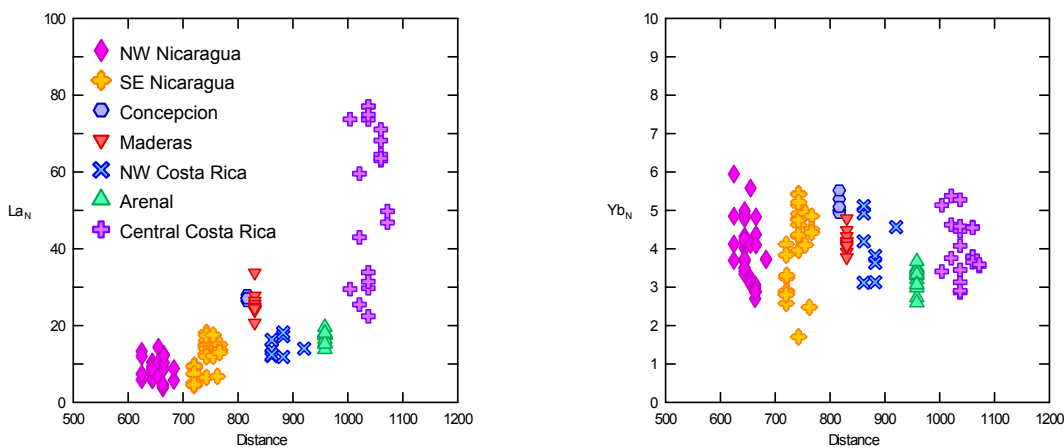


Figure 2.18. The abundance of La is the main control over the ratio La/Yb, indicating varying degree of melt, as La is relatively fluid mobile compared with Yb.

Table 2.1. Major oxide (wt%) for Ometepe lavas.

Sample	SiO <sub>2</sub>	TiO <sub>2</sub>	Al <sub>2</sub> O <sub>3</sub>	Fe <sub>2</sub> O <sub>3</sub>	MnO	MgO	CaO	Na <sub>2</sub> O	K <sub>2</sub> O	P <sub>2</sub> O <sub>5</sub>
C1	55.78	1	17.63	9.03	0.2	3.31	7.73	4.11	1.22	0.38
C2	55.43	0.98	17.92	8.68	0.2	3.28	7.71	3.74	1.2	0.37
C3	56.77	1.1	16.95	8.57	0.18	2.7	6.49	3.49	1.94	0.49
C4	55.74	0.98	18.45	7.27	0.17	2.73	7.34	3.34	1.65	0.44
C5	56.01	1.09	17.37	8.64	0.19	2.64	6.8	3.79	1.85	0.54
C6	56.74	1.14	16.9	8.73	0.19	2.65	6.62	3.78	1.99	0.54
C7	56.33	1.13	17.02	8.62	0.19	2.68	6.71	3.77	2	0.54
C8	56.12	1.14	18.2	8.18	0.18	2.29	7.16	3.8	1.74	0.55
C9	57.37	1.2	16.72	8.89	0.19	2.63	6.5	3.78	1.91	0.56
C10	60.34	0.86	17.16	6.62	0.17	2.03	5.86	4.21	2.13	0.4
C11	60.08	0.87	16.99	6.53	0.17	2.04	5.72	4.09	2.16	0.4
C12A	61.64	0.89	16.65	6.1	0.19	1.88	4.72	4.63	2.13	0.44
C12S0	61.64	0.89	16.65	6.1	0.19	1.88	4.72	4.63	2.13	0.44
C12	61.64	0.89	16.65	6.1	0.19	1.88	4.72	4.63	2.13	0.44
C13	61.28	0.89	16.6	6.13	0.19	1.91	4.71	4.63	2.13	0.44
C14	53.51	0.99	18.91	8.83	0.17	3.35	9.12	2.99	1.17	0.39
C15	58.61	1.08	16.74	7.53	0.18	2.33	5.98	4.06	1.97	0.5
C16	52.22	1.08	18.62	9.46	0.18	3.24	8.77	3.14	1.15	0.39
C17	52.77	1.08	18.64	9.56	0.18	3.21	8.92	3.11	1.18	0.39
C18	59.38	0.93	17.01	7.23	0.19	2.28	5.58	4.3	2.16	0.5
C19	59.31	0.94	16.93	7.01	0.18	2.20	5.54	4.23	2.17	0.49
C20	59.39	0.94	16.98	7.33	0.19	2.32	5.64	4.27	2.14	0.49
C21	52.98	1	18.67	9.15	0.17	4.01	9.28	2.81	1.19	0.37
C22	54.55	0.86	19.85	7.26	0.16	2.59	8.39	3.49	1.45	0.36
C23	52.46	1.01	18.65	9.07	0.17	4.07	9.13	2.9	1.2	0.38
M1	60.75	1.07	16.46	6.81	0.17	1.91	4.56	4.29	2.83	0.46
M2	61.74	1.09	17.32	7.26	0.17	1.95	4.40	4.34	2.80	0.44
M3	50.37	1.1	18.66	10.03	0.18	4.56	9.54	2.76	1.07	0.32
M4	51.73	1.07	18.29	9.79	0.17	4.18	9.3	2.84	1.22	0.3
M5	50.69	1.07	18.39	9.81	0.17	4.49	9.52	2.69	1.15	0.3
M6	51.22	1.07	18.26	9.97	0.17	4.51	9.53	2.62	1.21	0.31
M7	50.79	1.04	18.41	9.69	0.17	4.54	9.63	2.49	1.33	0.3
M8	51.56	0.99	18.06	9.82	0.17	4.76	9.48	2.38	1.22	0.27
M9	51.2	0.98	18.22	9.67	0.17	4.68	9.65	2.48	1.17	0.27
M10	51.70	0.56	20.80	8.28	0.15	4.16	10.13	2.35	0.43	0.13
M11	50.21	0.88	17.78	9.36	0.15	5.82	10.65	2.56	1.21	0.23
M12	48.12	1.18	18.65	10.8	0.17	5.29	10.85	2.25	0.96	0.3

Table 2.2. Trace element data for Ometepe Lavas (ppm)

Sample	Li	Sc	V	Cr	Co	Ni	Cu	Zn	Rb	Sr	Y	Zr
C1	10.49	19.88	165.13	2.54	17.45	2.49	51.08	81.04	23.19	547.48	25.46	122.19
C2	9.88	19.03	174.51	2.43	18.45	2.42	47.87	88.27	20.34	572.52	24.63	127.26
C3	9.57	19.77	183.96	2.92	17.26	1.91	96.85	87.43	34.99	450.12	29.67	184.94
C4	11.39	18.66	136.91	14.9	15.94	9.38	69.84	73.3	31.59	523.71	27.24	150.3
C5	10.6	17.86	134.45	2.3	14.26	1.76	49.72	77.46	33.97	466.48	30.36	181.47
C6	12.27	18.1	136.11	1.7	15.01	1.92	71.69	81.15	37.04	479.24	31.47	178.58
C7	11.57	17.37	139.67	1.84	15.73	1.91	85.49	80.37	34.66	470.19	32.82	174.98
C8	12.18	15.1	120.64	2.28	14.38	2	81.11	80.68	27.91	516.68	30.39	187.89
C9	10.63	12.6	142.88	2.97	17.13	2.57	83.25	90.56	16.2	486.72	29.1	211.37
C10	14.22	11.48	100.08	1.7	10.31	1.03	31.25	70.35	20.12	432.49	25.4	186.44
C11	14.7	14.87	94.15	1.7	10.42	1.12	33.97	73.39	44.3	451.45	30.7	191.88
C12	15.97	13.40	44.83	1.42	6.66	0.31	8.04	77.32	42.80	463.27	34.54	200.55
C13	14.88	12.64	44.04	1.23	6.51	0.32	7.62	73.68	35.69	422.26	31.03	187.43
C14	8.6	19.14	201.24	5.98	20.8	6.02	95.04	70.97	18.24	558.71	22.23	119.69
C15	13.43	14.95	111.8	2.02	13.78	2.01	61.85	76.74	34.88	431.53	30.3	204.1
C16	8.89	21.44	203.71	4.77	19.46	3.4	84.36	82.28	18.74	536.88	24.62	111.06
C17	9.86	20.45	192.59	3.62	19.33	3.54	80.38	71.74	22.07	540.05	24.89	122.18
C18	13.65	13.73	86.09	1.6	10.29	1.25	30.45	76.52	34.74	407.86	30.51	192.59
C19	13.89	14.69	90.87	1.48	10.63	1.23	33.83	79.65	38.39	413.25	29.57	188.35
C20	14.37	14.62	89.3	2.91	10.38	1.43	32.96	77.5	34.23	409.02	30.6	179.38
C21	9.13	25.24	192.62	14.26	20.77	7.89	72.28	66.5	20.8	518.82	22.69	118.09
C22	6.93	15.03	133.01	7.15	13.14	3.39	37.75	65.66	18.67	528.13	21.34	117.76
C23	7.99	21.6	187.03	13.33	21.1	7.58	67.69	64.88	18.05	515.15	22.71	116.16
M1	16.32	15.74	77.94	2.12	9.11	0.54	20.1	82.23	66.65	431.69	36.34	299.98
M2	14.13	17.13	85.36	1.6	10.22	0.3	22.36	84.37	57.68	416.37	43.71	314.27
M3	8.84	30.79	307.22	26.01	29.77	14.9	137.25	79.74	15.6	561.03	21.87	144.03
M4	8.64	28.46	292.56	26.17	27.16	11.9	95.3	77.02	23.88	530.19	21.22	125.57
M5	7.27	25.92	270	24.12	24.78	13	107.23	72.76	22.55	504.01	18.47	119.92
M6	8.25	26.38	274.65	23.63	26.78	12.52	128.9	75.28	22.57	497.51	19.03	117.99
M7	6.57	26.5	261.13	23.54	26.89	12.58	125.73	69.61	25.01	499.01	19.64	118.18
M8	5.59	25.21	233.95	19.43	23.54	13.13	96.91	67.3	22.02	448.53	18.21	119.72
M9	7.97	28.77	282.93	23.5	27.64	16.31	128.45	76.58	25.97	484.54	19.02	121.21
M10	9.35	24.32	210.24	12.23	21.66	10.74	98.76	71.44	37.25	484.98	22.81	176.78
M11	7.62	21.88	212.44	41.89	25.9	22.44	119.45	58.95	17.97	424.84	17.43	109.83
M12	5.38	29.24	322.24	10.99	34.61	19.68	149.06	80.33	18.64	543.3	19.98	123.06

Table 2.2 Continued

Sample	Nb	Mo	Cs	Ba	La	Ce	Pr	Nd	Sm	Eu	Gd	Tb
C1	11.11	1.02	0.34	657.21	17.89	37.34	5.13	24.05	5.32	1.66	5.23	0.79
C2	11.76	1.1	0.44	674.18	18.42	39.14	5.14	24.09	5.27	1.67	5.33	0.78
C3	15.18	1.67	0.82	973.89	25.95	53.41	6.92	29.48	6.44	1.87	6.34	0.95
C4	15.53	1.53	0.63	862.88	24.36	49.45	6.51	26.87	5.9	1.57	5.64	0.83
C5	15.89	1.57	0.8	937.62	24.4	52	7.41	32.88	7.02	1.96	6.8	1.05
C6	15.73	1.59	0.78	894.96	26.24	55.08	7.41	32.92	7.33	1.96	6.96	1.02
C7	15.17	1.54	0.78	959.96	25.89	54.51	7.59	31.69	7.06	2.02	7	1.06
C8	20.34	1.74	0.63	889.67	26.1	57.1	7.26	33.21	7.18	1.92	6.94	1.04
C9	22.32	1.81	0.51	996.51	26.26	61.21	7.2	32.89	7.28	1.96	7.17	1.08
C10	15.9	1.79	0.77	1005.67	22.53	50.45	6.31	28.53	5.9	1.75	5.98	0.83
C11	16.38	1.82	0.89	1082.85	27.76	54.02	6.93	30.52	6.5	1.74	6.07	0.97
C12	17.03	1.75	0.92	1208.98	29.44	62.27	7.98	35.65	7.73	2.12	7.38	1.12
C13	15.84	1.62	0.85	1039.91	26.6	54.08	7.23	32.35	7.05	1.87	6.88	1.04
C14	11.74	1.08	0.48	710.21	18.21	38.76	5.41	23.88	5.15	1.57	4.91	0.75
C15	22.25	2.06	0.77	951.7	29.2	59.59	7.8	34.14	7.29	1.9	7.09	1.06
C16	10.53	0.99	0.45	762.57	18.71	40.59	5.19	24.39	5.66	1.64	5.28	0.8
C17	11.06	1.04	0.51	751.53	19.2	40.69	5.32	24.58	5.59	1.68	5.58	0.8
C18	15.43	1.72	0.87	1021.81	26.86	55.63	7.68	34.23	7.35	1.98	7.07	1.11
C19	15.66	1.74	0.9	1007.72	27.99	58.2	7.55	33.83	7.7	2.04	7.16	1.12
C20	14.98	1.67	0.84	991.25	23.18	53.44	6.82	29.73	6.89	1.99	6.88	1.02
C21	11.51	1	0.49	661.02	18.06	40.04	5.51	23.75	5.27	1.48	5.07	0.73
C22	9.53	1.06	0.54	716.97	18.7	40.71	5.16	24.11	4.85	1.48	4.89	0.74
C23	11.37	1.04	0.48	677.43	18.57	39.92	5.24	24.04	5.19	1.51	4.96	0.79
M1	29.66	1.59	0.76	1160.03	35.97	73.71	8.64	35.86	7.63	1.95	7.09	1.03
M2	29.69	2.63	0.82	1199.96	48.3	75.13	10.28	47.1	9.4	2.11	8.54	1.23
M3	12.85	1.1	0.27	624.45	19.04	38.56	5.22	24.36	5.04	1.43	4.78	0.7
M4	12.36	1.02	0.24	585.55	18.14	35.13	5.06	22.52	4.72	1.47	4.74	0.68
M5	11.84	1.01	0.48	536.09	16.42	33.88	4.24	19.97	4.24	1.26	4.03	0.61
M6	11.21	1.05	0.45	562.38	16.54	34.7	4.44	19.05	4.43	1.24	4.27	0.6
M7	11.4	0.99	0.51	550.24	16.7	34.33	4.37	19.11	4.15	1.28	4.28	0.65
M8	11.7	1.1	0.54	548.48	17.55	34.5	4.68	20.01	4.23	1.28	4.12	0.65
M9	11.75	1.17	0.58	550.82	17.08	35.18	4.57	19.72	4.42	1.3	4.26	0.66
M10	15.81	1.59	0.87	759.11	23.17	45.15	5.61	26.89	5.45	1.45	5.07	0.74
M11	9.16	0.91	0.44	486.95	14.23	29.34	4.05	17.57	3.84	1.08	4	0.6
M12	13.06	0.92	0.15	503.13	16.81	34.58	4.51	20.72	4.51	1.28	4.57	0.63

Table 2.2 Continued

Sample	Dy	Ho	Er	Tm	Yb	Lu	Hf	Ta	W	Tl	Pb	Th	U
C1	4.51	0.92	2.64	0.39	2.63	0.39	1.8	0.55	0.23	2.95	3.14	1.8	1.13
C2	4.38	0.91	2.65	0.39	2.5	0.38	1.75	0.58	0.21	3.21	2.94	1.87	1.15
C3	5.01	1.08	3.06	0.47	3.18	0.46	2.5	0.77	0.36	6.02	4.61	3.08	1.87
C4	4.51	0.92	2.8	0.4	2.63	0.39	2.16	0.72	0.34	2.94	3.46	2.55	1.66
C5	5.62	1.17	3.44	0.5	3.36	0.49	2.44	0.84	0.34	4.07	3.75	2.82	1.76
C6	5.95	1.2	3.44	0.52	3.32	0.47	2.55	0.84	0.35	4.28	4.01	2.83	1.85
C7	5.85	1.14	3.48	0.52	3.31	0.5	2.69	0.84	0.35	6.41	4.10	2.93	1.88
C8	5.76	1.14	3.36	0.5	3.16	0.48	2.6	0.99	0.36	4.61	4.09	2.45	1.87
C9	5.88	1.19	3.75	0.51	3.39	0.51	2.99	1.1	0.38	3.53	4.04	2.03	2
C10	5.31	1.06	3.32	0.47	3.06	0.46	2.71	0.86	0.37	5.55	4.89	2.16	2.28
C11	5.47	1.12	3.28	0.49	3.3	0.48	2.64	0.84	0.36	5.71	4.90	3.55	2.35
C12	6.40	1.32	3.95	0.58	3.83	0.59	3.11	0.94	0.40	4.97	5.47	4.01	2.46
C13	5.7	1.2	3.7	0.54	3.4	0.53	2.89	0.85	0.36	4.86	4.90	3.46	2.08
C14	4.26	0.84	2.57	0.39	2.47	0.36	1.79	0.6	0.24	4.7	3.26	1.91	1.41
C15	5.63	1.18	3.38	0.52	3.33	0.5	2.98	1.17	0.37	4.72	4.29	3.18	1.97
C16	4.48	0.94	2.71	0.38	2.61	0.37	1.75	0.55	0.23	0.21	2.89	2.12	1.4
C17	4.68	0.94	2.75	0.4	2.72	0.4	1.83	0.55	0.25	0.6	3.00	2.05	1.34
C18	6.08	1.19	3.56	0.53	3.47	0.53	2.77	0.9	0.4	5.49	5.21	3.25	2.04
C19	6.21	1.2	3.65	0.54	3.52	0.53	2.82	0.81	0.38	5.49	5.04	3.38	2.18
C20	5.89	1.15	3.54	0.52	3.34	0.52	2.75	0.8	0.37	5.83	5.08	3.18	2.04
C21	4.22	0.85	2.52	0.36	2.46	0.36	1.81	0.61	0.25	4.17	3.10	2.04	1.29
C22	4.15	0.84	2.57	0.38	2.43	0.37	1.82	0.5	0.24	4.88	3.36	1.92	1.38
C23	4.28	0.86	2.49	0.37	2.51	0.35	1.83	0.59	0.23	3.65	3.15	1.94	1.38
M1	5.84	1.21	3.91	0.54	3.42	0.56	4.02	1.42	0.72	5.6	8.44	5.86	3.53
M2	6.95	1.46	4.11	0.63	3.87	0.61	4.21	1.54	0.89	5.53	5.60	5.64	3.66
M3	3.94	0.8	2.34	0.32	2.21	0.34	1.92	0.59	0.28	1.54	2.27	2.33	1.41
M4	3.74	0.73	2.31	0.32	2.07	0.3	1.75	0.6	0.29	1.98	2.47	2.02	1.38
M5	3.44	0.7	2.07	0.31	2.03	0.29	1.66	0.59	0.3	2.47	2.42	2.07	1.43
M6	3.55	0.73	2.07	0.29	1.93	0.27	1.63	0.59	0.27	2.54	2.53	1.86	1.21
M7	3.56	0.69	2.1	0.3	1.99	0.29	1.6	0.55	0.29	2.92	2.47	1.9	1.18
M8	3.62	0.71	2.14	0.32	2.13	0.3	1.83	0.6	0.32	3.45	2.82	2.48	1.63
M9	3.6	0.72	2.15	0.31	2.06	0.31	1.74	0.65	0.33	3.44	3.32	2.38	1.55
M10	4	0.84	2.45	0.37	2.36	0.35	2.27	0.8	0.41	5.08	3.78	3.16	2.08
M11	3.36	0.68	1.95	0.3	2.01	0.28	1.66	0.47	0.26	2.05	2.74	2.09	1.45
M12	3.69	0.74	2.22	0.3	1.86	0.29	1.7	0.59	0.23	0.98	2.10	1.85	1.07

Table 2.3. Isotope of Ometepe lavas

Sample	$^{87}\text{Sr}/^{86}\text{Sr}$	Error	$^{143}\text{Nd}/^{144}\text{Nd}$	Error	$^{206}\text{Pb}/^{204}\text{Pb}$	Error	$^{207}\text{Pb}/^{204}\text{Pb}$	Error	$^{208}\text{Pb}/^{204}\text{Pb}$	Error
C3	0.70395	0.000008			18.647	0.002	15.514	0.002	38.316	0.004
C4	0.70392	0.000009			18.664	0.008	15.545	0.007	38.385	0.016
C14	0.70388	0.000008	0.51296	0.000031	18.667	0.004	15.53	0.004	38.357	0.008
C16	0.70393	0.000011	0.51294	0.00002	18.643	0.011	15.516	0.009	38.298	0.022
C22	0.70402	0.000006			18.627	0.003	15.534	0.002	38.358	0.005
M4	0.70393	0.000008			18.63	0.004	15.512	0.005	38.308	0.007
M7	0.7039	0.000015	0.51299	0.000009	18.609	0.005	15.494	0.004	38.255	0.012
M9	0.70397	0.000008	0.513	0.000008	18.593	0.008	15.474	0.008	38.1	0.008
M11	0.70389	0.000007	0.51299	0.000006	18.636	0.001	15.522	0.001	38.32	0.003
M12	0.70395	0.000007			18.643	0.005	15.525	0.004	38.329	0.01

## Chapter 3 – Whole Rock Geochemistry of the Host Basalt and Xenoliths from Cerro Mercedes, Costa Rica

### Background

The Central American volcanic arc is an ideal place to study the chemical recycling of lithosphere at convergent margins, due in part to the young, thin crust in El Salvador, Nicaragua and north Costa Rica that leaves isotope systematics relatively uncontaminated by small amounts of crustal contamination. As a destructive plate margin, Central America is a site of both continental crust generation and oceanic crust recycling. Models for the development of chemical heterogeneities in the upper mantle (Carr, 1984; Walker, 1984; Plank and Langmuir, 1988; Carr et al., 1990; Leeman et al., 1994; Leeman et al., 1994; Herrstrom et al., 1995; Patino et al., 2000; You & Gieskes, 2001; Rüpke et al., 2002; Carr et al., 2003; Feigenson et al., 2004; Gazel et al., 2009; Bolge et al., in press), feature such margins because subduction zone magmatism is an essential avenue of interaction between the earth's continental crust and mantle.

The composition of the upper mantle, specifically the mantle wedge, is central to studies of arc volcanism. However, the mantle cannot be measured directly; it is only the occurrence of xenoliths (rock fragments within a compositionally distinct host rock) that allows direct analyses of mantle rock composition. In turn, the xenolith compositions can then be used to create and test geodynamic models of the upper mantle wedge, giving insight into the interactions between subducting oceanic plates, mantle wedge material and overlying crust.

Mantle xenoliths are brought to the Earth's surface in kimberlites and alkali basalts. Alkali basaltic magmas are thought to be generated by small degrees (<5%) of

partial melting at pressures greater than 10 kbar (Dasgupta et al., 2007). Accordingly, alkali basalts sample a shallower and thinner shell of the upper mantle than do many kimberlites, which originate within the diamond stability field >30 kbar (Ryan et al., 1996; Batumike et al., 2008). Thus, whereas kimberlites include ultramafic rocks with garnet as the aluminous phase, alkali basalts are more likely to include ultramafics with spinel as the aluminous phase.

Subduction zone xenoliths may clarify basalt petrogenesis in arc environments. Current consensus holds that flux melting of the mantle wedge gives rise to arc-type basalt (Elliot et al., 1997; Tatsumi, 1997; Bebout et al., 1999; Eiler et al., 2000; Carr et al., 2003; Portnyagin et al., 2005). If the melt is unmodified from its source region, it is considered primary. In this case, there will be an inherent relationship between arc-basalt and mantle wedge peridotite that underlies a given arc. When the composition of both the peridotite and basalt are known, petrologic modeling can be used to extract information about melt fraction and partition coefficients. However, there is a very small (to non-existent) chance that mantle peridotites will be directly related to their host alkali basalt as it would be difficult for a melt to entrap its own source. Additionally, since the host magma brings entrained xenoliths from a range of depths during ascent, the xenoliths clearly need not be samples of the alkali basalt source.

Mantle xenoliths from compressional environments are somewhat rare compared to tectonic environments such as continental lithosphere and peridotite massifs (Mysen et al., 1998; Parkinson and Arculus, 1999). The best known examples of subduction zone xenoliths are from the circum-Pacific (fig3.1) and include Vanuatu/Solomon Islands (Barsdell & Smith, 1989), Papua New Guinea (Franz et al., 2002), Izu Bonin/Marianas Trench (Parkinson & Pearce, 1998), Takashima/Noyamadake, Japan (Aoki, 1987),

Ichinomegata, Japan (Wood & Virgo, 1989), Kamtchatka (Yogodzinski, et al., 1993), Simcoe, Cascades (Brandon & Draper, 1996), Chihuahua, Mexico (Alva-Valdivia et al., 2003), Grenada, Lesser Antilles (Parkinson et al., 2003), Estancia Lote17 region of south Patagonia, Argentina (Gorring & Kay, 2000) and Gobernador Gregores Case, Patagonia (Laurora et al., 2001).

Mantle peridotite occurs as xenoliths in lavas and bombs at Cerro Mercedes (fig3.2), a Plio-Quaternary potassic alkaline basalt volcano approximately 70km behind the volcanic front of northern Costa Rica (Tournon and Alvarado, 1997). Mineral exploration led to the first discovery of abundant mantle xenoliths in Central America (Vargas and Alfaro, 1992). In January 2003, over 80 xenoliths were recovered from Cerro Mercedes including twenty having diameters of at least 3cm (table 3.1). The nodules are abundant in basalt outcrops and rare bombs. In spite of substantial soil development in a rain forest environment, both xenoliths and host lava remain well preserved.

### ***Characteristics***

Compared to xenoliths from other tectonic environments, those from subduction zones have characteristics that are apparently unique to their setting. These features include higher oxygen fugacity ( $f_{O_2}$ ) (Parkinson & Arculus, 1999), higher Cr# in spinel phases, higher Mg# with lower  $Al_2O_3$  (Bonatti & Michael, 1989) and non-chondritic Pt/Pd ratios (Kepezhinskas & Defant, 2001). Because  $f_{O_2}$  and spinel Cr# are calculated from mineral compositions, they will be considered in the next chapter that focuses on the mineral chemistry of the Cerro Mercedes xenoliths.

Higher Mg#, which can be thought of as an index of depletion as it increases with episodes of melt extraction, is demonstrated in fig3.3. That is, MgO increases with

increasing depletion as a rock becomes more olivine rich. The increased depletion of subduction zone peridotites was demonstrated by Bonatti & Michael (1989) when they compared peridotites from pre-oceanic rifts, passive margins, mature oceans and subduction zones. In the literature, reports of mantle peridotite compositions from arc environments are commonly  $\text{Fo}_{92}$  -  $\text{Fo}_{88}$  ( Frey & Prinz, 1987; Brandon & Draper, 1996; Parkinson & Pearce, 1998; Ertan & Leeman, 1999; Arai & Kida, 2000; Takazawa et al., 2000; Laurora et al., 2001; Franz et al., 2002; Peslier et al., 2002; Abe et al., 2003; Parkinson et al., 2003). Additionally, values of  $\text{Al}_2\text{O}_3$  are lower in arc settings than in other tectonic environments (fig3.4). This is also explained by progressive depletion of the mantle source from pre-oceanic rifts through to subduction zones, possibly through multiple episodes of melt extraction.

### ***Modal Mineralogy***

The mineralogy of island arc xenoliths includes olivine, pyroxene, spinel, plagioclase, amphibole, glass. Frey & Prinz (1978) classify mantle xenoliths as belonging to two groups: Group I, the chrome-diopside group, rich in Cr and Mg, and Group II, the aluminum-clinopyroxene group, rich in Fe and Ti (fig3.5). Garnet is absent from island arc xenoliths whereas it is common in xenolith suites in kimberlite (Mysen et al., 1998). Group I rocks are typically more common than Group II and are dominantly olivine rich harzburgite, lherzolite and dunite. Group II rocks, interpreted as high – pressure cumulates (Haggerty, 1995), contain variable compositions and include rocks such as spinel wehrlite, websterite and kaersutite peridotite (Frey & Prinz, 1978).

### ***Upper Mantle Composition***

The study of ultramafic rocks exposed at the Earth's surface allows direct study of the Earth's upper mantle. Broadly speaking, the upper mantle is solid lherzolite

composed of olivine, orthopyroxene and clinopyroxene with aluminous phases changing from plagioclase to spinel to garnet with increased pressure. With respect to major oxides, average weight% mantle composition reported in the literature, based on sampled peridotite xenoliths, is:  $\text{SiO}_2$ , 44.77;  $\text{TiO}_2$ , 0.09;  $\text{Al}_2\text{O}_3$ , 2.75;  $\text{Cr}_2\text{O}_3$ , 0.49;  $\text{FeO}_T$ , 7.95;  $\text{MnO}$ , 0.13;  $\text{MgO}$ , 40.98;  $\text{CaO}$ , 2.52;  $\text{NiO}$ , 0.27;  $\text{Na}_2\text{O}$ , 0.20;  $\text{K}_2\text{O}$ , 0.05 (Hutchison, 1974; Herzberg, 1993; Hirchmann et al., 1998; table3.2). Table 3.2 also gives experimental values based upon pyrolite and primitive mantle modeling for comparison. Pyrolite is a theoretical composition of the upper mantle (Ringwood, 1969) used in phase equilibria experiments as a starting material. Some researchers use pyrolite synonymously with silicate Earth (McDonough & Sun, 1995). Primitive mantle is a hypothetical reservoir of undifferentiated mantle with a composition derived from chondrites (Hoffman, 1988; Hart & Zindler, 1986).

Trace elements in mantle Iherzolite show a wide range in composition with respect to chondritic values. Rare earth elements (REEs) range from depleted to enriched and light rare earth elements (LREEs) are usually more depleted than heavy rare earth elements (HREEs). LREEs can be 0.004 log units below chondritic values and rarely exceed 10 log units above chondrites (Vaselli et al., 1995; Parkinson & Pearce, 1998; Takazawa et al, 2000; Conceição et al, 2005) suggesting that the upper mantle is heterogeneous. However, trace element heterogeneities may not be reflected in the mantle mineralogy, which retains a bulk modal uniformity. The observed depletions and enrichments are explained by partial melting events and metasomatic introduction of incompatible elements (Johnson et al., 1990; Kelemen et al., 1993). This is particularly true in the mantle wedge underlying a subduction zone where partial melts of mantle Iherzolite are modified by reactions with aqueous and/or siliceous fluxes derived from

the subducting slab. Thus, when recovered, subduction zone xenoliths illuminate mantle wedge processes such as melt generation and metasomatism because their composition is sensitive to these very processes.

### ***Mantle Melting***

Melting in the upper mantle begins when the source rock intersects its solidus. This is achieved by either a thermal perturbation, adiabatic decompression, or lowering the solidus by addition of volatiles and/or fluids (Wilson, 1989). In the initial stage of melting, the melt forms an interconnected network between crystals within the matrix. As melting continues, the melt may develop a density contrast with respect to the matrix and begin to segregate. Until that time, the composition of the liquid and solid are in equilibrium and the equations of batch melting (wherein the melt remains in contact with the matrix) apply.

If the permeability threshold of the mantle rock is exceeded, the melt will separate from the matrix. Without further contact between melt and residue, the system cannot maintain equilibrium; this defines fractional melting wherein melt is continuously removed from the system, changing the composition of the resulting residue. The composition of resultant residues hinges on the amount of melt extraction and the composition of that melt (Herzberg, 2004). As melting proceeds, incompatible elements preferentially go into the liquid, leaving the mantle residue depleted. This leads to the characteristic increase of MgO and decrease of Al<sub>2</sub>O<sub>3</sub> observed in subduction related ultramafic xenoliths. Nonetheless, mantle rocks remaining after an episode of partial melting, without further melt/rock interaction, are residues and can be used to obtain information about the mantle source.

Not all rocks from the mantle are residues, however; many are cumulates, which

do not reflect the complete chemistry of the source and so cannot be used to infer the source's composition. Debari et al. (1986) use the presence of orthopyroxene (opx) at high Mg# in a mantle xenolith as evidence of residual mantle origins and absence of opx at high Mg# indicating a cumulate origin. Additionally, Kelemen et al. (1998) point out that experimental data (Kinzler, 1997; Kinzler & Grove, 1992) show modal opx >30% cannot be attained in residues of partially melted primitive mantle at any pressure or degree of melting, regardless of Mg#.

### ***Mantle heterogeneity***

Metasomatic introduction of incompatible elements is likely common in subduction environments (Tatsumi & Kogiso, 1997; Ayers, 1998; McInnes et al., 2001; Chan et al., 2002). Mantle previously depleted by a magma extraction event can become refertilized by addition of incompatible element enriched fluids or partial melts. It is possible that multiple episodes of melt extraction and metasomatic enrichment can change the bulk chemistry of the residual mantle with or without changing its modal mineralogy, leading to the idea of multi-stage residues. It follows that melts generated within the same mantle space, but at different times, may have different compositions even without a subsequent metasomatic event. Thus, it is expected that mantle xenoliths brought to the surface will have compositional variability, reflecting different and complex histories.

Over time, convection should homogenize the upper mantle. However, the stirring models of Gurnis (1986) and Gurnis & Davies (1986) lack complete homogenization even after a few billion years. Thus, if partial melting and magma extraction operate throughout geologic time, the mantle must be heterogeneous, with both fertile and depleted peridotite. Additionally, there may be pockets of preserved

partial melt that failed to segregate and form magmas (Wilson, 1989). It becomes important, then, to consider how well a xenoliths suite represents the volume of mantle traversed by the ascending magma. Indeed, comparison of xenoliths from closely spaced kimberlites show systematic variation suggesting restricted sampling and localized mantle heterogeneities (Richardson et al., 1985).

### **Setting**

Central America sits atop the Caribbean Plate with subduction of the Cocos and Nazca Plates to the southwest and highly variable geology in the northeast. The crust changes from continental to oceanic delineated, to first approximation, by the division of the Chortis and Chortega blocks, respectively. Figure 3.6 shows the tectonic environment and a pink star represents Cerro las Mercedes, which rises about 140m from sea level and is located at  $10^{\circ} 58' 35.15N / 84^{\circ} 21' 15.59W$  in northern Costa Rica. It lies 70km NNW of Arenal, the closest volcano along the present day active front (fig3.7) and within the Hito Sar basalts of the Miocene Sarapiquí volcanic arc (fig3.8; Gazel et al., 2005).

Since the Miocene, the active volcanic front has migrated westward during which time back arc extension occurred during the Pleistocene to Holocene (Abratis & Wörner, 2001). In turn, the extensional environment allowed the eruption of the alkali basalts in Cerro Mercedes, which brought the mantle xenoliths to surface.

### **Analytical Methods**

Four samples of the host basalt were analyzed to estimate the variability of the host lava. Care was taken to use lava chips with few to no peridotite inclusions. Of the 83 xenoliths recovered (table 3.3), a subset of 30, chosen for freshness and amount of available material, were extracted from the host basalt using a Dremel Driver™

equipped with a 545 diamond wheel. Care was taken to leave a rim of xenolith material attached to the basalt in order to prevent contamination from the host rock. The xenoliths were then crushed in an agate mortar to be further powdered with an alumina ball and mill.

Both xenolith whole rock and host basalt major oxides were analyzed by XRF at the X-ray Spectrographic Laboratory, Michigan State University, with use of a SMAX Rigaku X-ray spectrograph. In one instance, CM39, only enough sample for XRF was obtained and so there are no trace element analyses.

Both xenolith whole rock and host basalt trace elements were analyzed on a Finnigan MAT Element high resolution inductively coupled mass spectrometer (HR-ICP-MS) at the Institute of Marine and Coastal Sciences at Rutgers University.

Sample digestion of the host basalt and xenoliths were different due to the oxide phases within the xenoliths. Whereas standard acid fluxing was used to digest the basalt, high pressure bombs with stronger acid cocktails were necessary to bring the xenoliths to full digestion. See Appendix A for details. Dilution, drift detection, rock standard solution, sample preparation, internal and external standardization, tuning parameters and data analysis of both host basalt and xenoliths follow Bolge (2000).

Digested aliquots of rock powder were run through cation/anion exchange columns, sequentially, to isolate Pb, Sr and Nd. Isotopic measurements for both whole rocks and host basalts were made in an Isoprobe T multi-collector thermal ionization mass spectrometer laboratory at Rutgers University Department of Earth and Planetary Sciences.

Modal mineral percentages of a subset of 19 xenoliths were constructed by taking backscattered electron images (BEI) and elemental maps of standard thin

sections on a JEOL 8200 Superprobe at Rutgers University. The images were further manipulated in both ImageJ and Adobe Photoshop<sup>®</sup> to retrieve modal information. Average end-member densities were used to calculate the weight of each phase and subsequently calculate the modal weight percent. Finally, the modal weight percent was used to name the rock after Harte (1983).

## Results

### *Host Basalt*

The host rock is nepheline normative potassic alkaline basanite (fig3.9; table 3.4) dated at 1.2Myr (Gans, pers. comm.). In Fenner diagrams, the Cerro Mercedes basanite (CMB) show slight variations with MgO (fig3.10). Although the concentrations of FeO\* and CaO are constant, forming clusters, small variations in other major oxide concentrations are evident in Harker diagrams (fig3.11).

The host rock, normalized to chondrites (McDonough & Sun, 1995) is strongly enriched in light rare earth elements (LREEs) (fig3.12a). With no Ce anomaly evident, weathering of the lava seems unlikely. A further test of this is to plot Ce against Ce\* (fig3.12b), which indicates a calculated concentration interpolated between La and Pr. The linearity of the lavas and their proximity to a 1:1 ratio confirms that they are not weathered. The slight negative Eu anomaly, indicating the removal of plagioclase, can be tested in a similar way. A plot of Eu against Eu\* (fig3.12c) shows linearity of the lavas offset from the 1:1 ratio. This suggests that there have been similar amounts of plagioclase removal from the basanite samples. However, it is likely difficult to remove plagioclase from a melt that is transporting xenoliths, suggesting that the Eu anomaly may be inherited from the basanite source.

Trace elements (fig3.13a), normalized to primitive mantle (McDonough & Sun

1995), show depletion in the high-field strength elements (HFSEs), which suggests possible influence by subduction zone processes. Although Nb and Ta are not as depleted as other Costa Rica lavas, depletions in Zr and Ti are greater, which indicates clinopyroxene (cpx) fractionation. Low amounts of Cs and the negative anomaly in Pb, which is not present in other Costa Rica lavas, suggest a diminished role of hydrous fluids as both elements are efficiently mobilized by water. In fact, comparing CM basanite to lavas from the Central American volcanic front (CAVF) in Cs/Pb vs. Ba/La space, shows that the CM basanite have little influence from the subducting slab as well as hydrous fluid fluxes (fig3.13b).

Nd and Sr isotopes (fig3.14a) show the CMB trending toward a HIMU reservoir overlapping with MORB (fig3.14a inset). They are more depleted in Sr isotopes than other CAVF lavas and are most similar in Nd isotopes to the most depleted of the Costa Rica lavas. In Pb space (fig3.14b), the CMB show more affinity to OIB lavas and overlap with the more radiogenic of the Costa Rica lavas. There is a slight trend toward the EMII reservoir, which correlates to a terrigenous sediment influence (Faure, 1984). This may correspond with the depletion seen in the HFSEs and makes a strong case for subducting slab involvement in the genesis of these lavas.

From these results, it becomes clear that: 1) the samples analyzed are similar enough to propose that the host basanite erupted during a single event; 2) it is likely that the CMB was influenced by subduction zone processes; 3) the CMB are distinctive in their trace elements compared to front arc lavas in Costa Rica; 4) CMB isotopes are comparable to the more radiogenic lavas of central Costa Rica.

### **Mantle Xenoliths**

#### *Petrography*

Images to accompany the results are available on disc from the author. Modal analyses of 19 xenoliths (table 3.5) reveal the Cerro Mercedes suite to include both peridotites and pyroxenites. The peridotites are spinel facies dunite, lherzolite and harzburgite; the pyroxenites are olivine clinopyroxenite, olivine websterite and websterite. All rocks are phanerocrystalline with fine to coarse grains that range from euhedral to anhedral in shape. Whereas many of the xenoliths seem unweathered internally, some show alteration either at the contact with the host basanite (CM17, CM40b, CM47, CM55, CM64) or on the rock's surface (CM1, CM8, CM19, CM20b, CM24, CM25, CM30, CM32, CM42b, CM63, CM67, CM68b, CM68c, CM69).

In thin section, embayments are often observed in grains that contact the host basanite (CM27, CM41) with thin reaction rims (<0.3mm) on the grain boundaries. Some embayments have larger areas of reaction (CM19, CM27, CM50) in which the Ca is leaching into the host basalt (fig. 3.15). Veinlets of host magma are present along grain boundaries in some xenoliths and, in a few instances (CM63, fig. 3.16; CM58), stretch across the entire xenolith. In the case of the few, more extensive reaction with the host magma is found internally by grains adjacent to the veinlet. Of note is an often observed band of feldspar grains within the basalt that rim the xenolith (CM11, CM14, CM21, CM29, CM32, CM44, CM52, CM53, CM64, CM69). They are larger than the felty groundmass suggesting extended cooling histories, possibly due to more extensive contact with the cooler mantle, or a temperature/diffusion front.

Spinel are associated with both peridotites and pyroxenites. Near the contact edge between xenolith and basanite, vermicular dissolution textures, with blebs of Cr-rich to Cr-poor, are observed (fig. 3.17). Zoned spinels are infrequent, but when found have cores richer in Cr and rims richer in Al and Fe (58T, CM69). Size and shape of the

spinel are variable and in some instances have a preferred linearity (CM21, CM47, CM48). Pyroxenes are mostly homogenous; some are normally zoned showing Fe enriched rims (CM47, CM50). Reaction rims are found generally when in contact with the host magma or vein material (CM63, CM20b). Rare pyroxene dissolution lamellae are limited to pyroxenites (CM63, CM70). Olivines in both peridotites and pyroxenites are generally homogenous. Zoning occurs across coarse grains that display undulatory extinction in cross-polarized light such that the grains appear banded, possibly due to stress from mantle flow (CM14, CM36, CM37, CM47, CM48).

### ***Chemistry***

In Harker diagrams, the xenoliths separate into populations of peridotites and pyroxenites (table 3.6) in major oxide space (fig 3.18), corroborating the modal mineralogy. There is one pyroxenite (CM67) that overlaps the peridotites in FeO\* space. Al<sub>2</sub>O<sub>3</sub> further separates the pyroxenites into two populations, with one enriched in Al (>6 wt%). Some fractionation is shown by the pyroxenites.

Fenner diagrams reveal MgO ranging from 40 – 51 wt% in the peridotites and 18 – 29 wt% in the pyroxenites (fig 3.19). Although unclear in FeO\* vs. MgO, the peridotites show linear to sub-linear trends in Al<sub>2</sub>O<sub>3</sub>, CaO and TiO<sub>2</sub>. The pyroxenites break into two trends: one is linear as are the peridotites; the other shows constant MgO with variation in the ordinate axis. The latter is particularly visible in Al<sub>2</sub>O<sub>3</sub> and TiO<sub>2</sub> space. Peridotites with similar MgO concentration and pyroxenites of similar MgO concentration have variable K<sub>2</sub>O content, which may be due to variable interaction with the host basanite.

Normalized to primitive mantle (McDonough & Sun, 1995), trace elements of both peridotites and pyroxenites show negative Nb and Ta anomalies (fig 3.20),

suggesting influence of subduction zone dynamics. Exceptions to this include CM27 and CM59, both of which show the Nb, but not the Ta anomaly. CM61, a peridotite, is the only xenolith to show a negative Sr anomaly. Several peridotites, CM8, CM41, CM47, CM57 and one pyroxenite, CM63, show a negative K anomaly; these same xenoliths also have the lowest Y abundance. Two peridotites, CM48 and CM59, having such low K that it was not detected by XRF analyses and also having low Y abundance, may be considered as having negative K anomalies. The xenoliths show a positive Pb anomaly, with few exceptions. The exceptions include pyroxenites CM13 and CM24, which show a slight negative Pb anomaly, and peridotite CM32, which shows no Pb anomaly at all. The negative Pb anomaly is also seen in the host basanite (fig3.13) suggesting that pyroxenites CM13 and CM24 may have been contaminated by the basanite during extraction procedures.

The pyroxenite REE patterns, all enriched relative to chondrites (McDonough & Sun, 1995), form two basic shapes (fig3.21a): a negatively sloped line and a convex upward curve. Abundances sloping downward from LREEs to HREEs suggest influence from a subduction environment. Again, the high LREEs of CM13 show possible contamination by the host rock. The curves, with enrichment in MREEs, suggest primary clinopyroxene mineralogy. In fact, one sample showing this curve, CM63, has modal mineralogy of an olivine-clinopyroxenite with 84.5 wt% clinopyroxene.

The peridotites REEs present a more complicated scenario. In these rocks, there are 3 basic REE abundance patterns (fig3.21b): a negatively sloping line that flattens in HREEs, a relatively flat line and a negatively sloping line that flattens in MREEs and/or slopes positively in HREEs. During modification, HREEs are generally less incompatible and less mobile than LREEs (Ishimaru et al., 2007). Thus, peridotites with the highest

La/Lu and Gd/Lu ratios are the most modified (fig3.22). Furthermore, Bizimis et al. (2000) showed that slab derived fluids, which are potential metasomatic agents of arc xenoliths, are likely to be rich in LREE/MREE ratios and Sr, and poor in HREE and Ti. Therefore, CM peridotites with the lowest LREE/MREE and Sr/HREE ratios are potentially the least modified (fig3.23), assuming a slab derived agent of modification. Using this basis, three populations of peridotites are distinguishable (fig3.24) in terms of relative degree of modification from least modified to most modified. The degree of modification will become better defined as this work continues. Of note is one sample, CM61, which seems to belong to the least modified group, based on fig3.23, but its relatively high LREE/HREE ratio and shallow "U" shaped REE pattern exclude it from this group. Thus, it is considered moderately modified.

### *Isotopes*

A histogram of Sr isotopes shows significant scatter in Sr isotopes, particularly in the most modified peridotites and pyroxenites, that corresponds to variable metasomatic signatures within both groups (fig3.25); higher  $^{87}\text{Sr}/^{86}\text{Sr}$  indicates larger amounts of sediment influence. Plotting  $^{143}\text{Nd}/^{144}\text{Nd}$  vs.  $^{87}\text{Sr}/^{86}\text{Sr}$  show the peridotites close to PREMA (prevalent mantle) (fig3.26 inset), although few Nd measurements are available. Compared to the Central America volcanic front (CAVF; fig 3.26), the CM xenoliths and basanite are most like central Costa Rica lavas with lower Sr and Nd isotope ratios than most CAVF lavas, signifying a lesser amount of sediment influence in the CM rocks. In  $^{87}\text{Sr}/^{86}\text{Sr}$  vs.  $^{206}\text{Pb}/^{204}\text{Pb}$  space (fig3.27), the CM rocks are similar to central Costa Rica and Arenal lavas and lay close to MORB values (fig3.27 inset); two rocks deviate toward higher Sr ratios. In  $^{207}\text{Pb}/^{204}\text{Pb}$  vs.  $^{206}\text{Pb}/^{204}\text{Pb}$  space (fig3.27a), the more modified peridotites and several pyroxenites trend toward enriched mantle reservoirs, indicating

the influence of subduction zone processes. The xenoliths show a wide range of  $^{207}\text{Pb}/^{204}\text{Pb}$  when compared to lavas from CAVF. Additionally, they lack a strong linear trend in  $^{208}\text{Pb}/^{204}\text{Pb}$  vs.  $^{207}\text{Pb}/^{204}\text{Pb}$  (fig3.27b), such as that delineated by the CAVF. Taken together, this suggests that the source for the CM mantle xenoliths is not a simple mixing of two reservoirs (e.g., chapter 2), but a multi-component mixing.

### ***Equilibration Temperature***

The temperature at which apparent observable diffusion within a rock stops provides information about the rock's cooling history. Calculations for equilibration temperatures of peridotitic and pyroxenitic systems use geothermometers that are based on the partitioning of major elements between constituent minerals phases. These include: 1) Fe-Mg exchange between garnet (gt) and pyroxene (Brey & Köhler, 1990), gt and olivine (ol) (O'Neill & Wood, 1979) or ol and spinel (sp) (Ballhaus et al., 1991); 2) Cr-Al partitioning between orthopyroxene (opx) and sp coexisting with ol (Witt-Eickschen & Seck, 1991); 3) the amount of Ca in opx coexisting with clinopyroxene (cpx) (Brey & Köhler, 1990); and 4) Fe-Mg exchange between two coexisting pyroxenes (Brey & Köhler, 1990). Whereas the lack of garnet in the CM xenoliths exclude those geothermometers that use the garnet phase, the others are viable. However, because the oxide phases in these rocks are variable (ranging from spinel to chromite), the choice to use the coexisting pyroxene method of Brey & Köhler (1990) seems most suitable, although calculations by the Witt-Eickschen & Seck (1991) method, which are systematically higher, are also presented in table 3.6.

Using the method of Brey and Köhler (1990), the range of equilibration temperature for the peridotites is 883°C to 1032°C and 863°C to 871°C for the pyroxenites at 1GPa. At 2.5GPa, the upper pressure limit for spinel facies rocks, the

ranges change slightly to 908°C to 1062°C for the peridotites and 895°C to 897°C for the pyroxenites (fig.3.28; table3.7). It should be noted here that this calculation uses both Fe<sup>2+</sup> and Fe<sup>3+</sup> of the pyroxenes, which was calculated by the method of Barnes and Roeder (2001) assuming an Fe<sup>3+</sup> /ΣFe of 0.11.

### **Discussion of Host Basalt**

#### ***Subduction Signature***

The extended trace elements show a clear subduction signature as shown by the relative depletion of HFSEs and relative enrichment of fluid mobile elements, such as Rb, Ba and Sr (fig.3.13). They are not as depleted in HFSEs as lavas from north and central Costa Rica (fig.3.29a,b) and show a strong negative Pb anomaly that is not evident in the Costa Rican lavas, suggesting that the slab signature seen in CMB is related to an earlier arc whose slab flux was compositionally different than that of present day, that the source material was different, or that the melting regime (flux versus decompression) was different.

Although older lavas of the Sarapiquí arc (fig.3.10; Gazel et al., 2005), which outcrop near Cerro Mercedes and are dated at approximately 12 Ma based upon Sr isotopes (Obando, 1995), show a subduction signature with depleted HFSEs (fig. 3.29c), they are quite different in their trace element abundances and do not have a negative Pb anomaly. Lavas from Fernandino Volcano in the Galapagos Islands (Geist et al., 2006) show a similar negative Pb anomaly (fig3.29d), but do not show the HFSE depletion common in arc lavas. The Galapagos Pb isotopes overlap both CMB and most lavas from Costa Rica and Nicaragua (fig3.29e and fig3.14), suggesting a similar source, although the wide range seen in Galapagos ratios make this evidence open to discussion. The tectonic evolution of the area shows that the current volcanism of the

Costa Rican active front began after a westward arc migration during the late Miocene (Hoernle et al., 2008). Volcanic front lavas that erupted at the same time as CMB (~1.2Ma ; Gans, *per. comm.*) were located further west in the Monteverde arc (Carr et al., 2007). It seems likely that the migration allowed local extension, which would support decompression melting mechanics such that the CMB could rise quickly enough to bring mantle xenoliths to the surface.

Clearly the area has been influenced by subduction processes for some time. Taking the geochemistry and tectonics together, I conclude that after the Sarapiquí arc was active, the area in which Cerro Mercedes erupted was subject to extension, allowing the CMB to erupt in a single, quick event, bringing with it mantle material from depth.

### ***Single Eruptive Event***

The lack of significant variation in major oxides and virtually constant SiO<sub>2</sub> in the CMB rules out large degrees of fractional crystallization, suggesting that the host lava is from a single eruptive event that brought the mantle rocks from depth relatively quickly. There is, however, a slight increase of Al<sub>2</sub>O<sub>3</sub>, Na<sub>2</sub>O and K<sub>2</sub>O with decreasing MgO (fig.3.10) pointing to some fractionation of feldspars, which are readily seen in hand sample and thin section. Additionally, linear trends of MgO with Ni and Cr (fig.3.10) suggest fractionation of both olivine and a spinel phase. Since feldspar is not stable to great depth, it is likely that the host magma evolved in two stages, with the olivine fractionating in the earlier stage.

Trace elements also support the contention of a single eruptive event by the tight cluster of the basanites in both REE and extended trace element spidergrams (fig.3.12 and 3.13). If there were significant fractionation within the magma body, these patterns would have more spread within the samples. Likewise, the basanites

cluster in isotope space (fig.3.14), within error, confirming that their source is the same.

## **Discussion of Xenoliths**

### ***Subduction Signature***

Xenoliths erupted near subduction zone commonly are enriched in SiO<sub>2</sub> relative to simple mantle residues (Parkinson and Pearce, 1998; Kelemen, 1998; Herzberg, 2004) due to the addition of silica during melt/rock reactions between the mantle and fluids derived from subducting sediments and basalt (Kelemen, 1998). Additionally when compared to fertile and depleted peridotite (Walter, 1998) whose Mg#s are 89.2 and 91.0, respectively, subduction influenced peridotites have higher Mg#s, due to increased depletion during episodes of melt (Bonatti & Michael, 1989). Some of the xenoliths from Cerro Mercedes are enriched in SiO<sub>2</sub> relative to an average mantle peridotite of 44.3wt% (Herzberg, 2004) and most of the peridotites have higher Mg#s compared to fertile peridotite, showing variable depletion (fig3.30). These peridotites are enriched enough in SiO<sub>2</sub> and high enough in Mg# to suggest melt/rock reaction. Oddly, most of the most modified peridotites do not show SiO<sub>2</sub> enrichment, although they have a wide range of Mg#.

This can be explained by differentiating between mantle material that is modified by melt/rock reactions and material that is modified by fluid/rock reaction. The ratio Tb/Yb can be used to not only distinguish between melting in the spinel vs. garnet field (Bodinier et al., 1988; McDonough & Frey, 1990), but also between melt and metasomatic trends (Peslier et al., 2002). Placing the CM peridotites in this space vs. a measure of depletion, such as Al<sub>2</sub>O<sub>3</sub>, it becomes clear that the least modified and the moderately modified peridotites follow the spinel field melting trend whereas the most modified peridotites follow a metasomatic trend (fig3.31).

The metasomatic trend of the most modified peridotites corroborates the scatter in Sr isotope space (fig3.25) and negative K anomaly (fig3.24b) as signs modification by slab derived fluid interaction. K acts as a non-conservative element within subduction zone settings (Pearce & Peate, 1995), thereby reflecting slab contribution. As such, the most modified peridotites are unlikely to aid in investigating the composition of the mantle wedge; those with the least modification, as shown by flat REE patterns (fig3.24) and positive K anomalies (fig3.25c ), are most likely to say something about the mantle wedge underlying Central America, even though they have had some melt/rock reaction.

### ***Residues vs. Cumulates***

Mantle residues, whose chemistry is comparable to the primary source can be used to infer the initial source composition; cumulates, being fractionates of the primary source, have chemistry that no longer fully reflect the initial composition. Discrete cumulate pyroxenites are thought to be high pressure crystal fractionates of mantle magmas (Müntener et al., 2001; Parlak et al., 2002) and may result from metasomatism of mantle peridotite by slab derived fluids (Berly et al., 2006), particularly when formed as networks of veins within mantle peridotite. However, veins of pyroxenite were not in evidence in the peridotites from Cerro Mercedes; all pyroxenites were discrete rocks. Nevertheless, it is clear that they are a cumulate phase, yielding little information about the mantle source. Since the CM xenolith suite has numerous peridotite samples, the duration of this discussion will focus on them to the exclusion of the pyroxenites.

Although many mantle peridotites in subduction zones that are produced by melt/rock reaction are not readily considered residues (Herzberg, 2004), there are a few reported suites. These include island arc peridotites from Grenada (Parkinson et al.,

2003) and back-arc basin peridotites from Patagonia, Japan and the Cascades, all of which show similarity to hot peridotite residues (Herzberg, 2004; Laurora et al., 2001; Brandon & Drapper, 1996; Aoki & Shiba, 1973). Since the CM peridotites surfaced within a back-arc environment, it is with the residues from Patagonia, Japan and the Cascades that the xenoliths from CM will be compared to deduce whether or not they are residues or cumulates.

Given that residues are the products of a mantle melt event, their major element composition is controlled by the mantle source composition and the degree of the melting, or, melt fraction, both relative to fertile peridotite, and the pressure of initial and final melting (Herzberg, 2004). Using fractional melting models proposed by Herzberg & O'Hara (2002) and Herzberg (2004), it is possible to both distinguish residues from cumulates and compare the CM peridotites with other arc peridotites. In their models, Herzberg & O'Hara (2002) and Herzberg (2004) use the liquid compositions of melting experiments on KR-4003, a fertile mantle peridotite (Walter, 1998), to calculate residue compositions within various geodynamic settings in a range of initial and final melting pressures.

Samples that plot inside the melting grids and show internal consistency in melting pressures and melt fractions in combined FeO, Al<sub>2</sub>O<sub>3</sub> and SiO<sub>2</sub> vs. MgO space can be considered potential residues. As an example, cratonic mantle and abyssal peridotites have distinct locations in FeO vs. MgO space (fig3.32) with cratonic mantle having higher initial and final melting pressures. This indicates a hotter mantle than abyssal peridotites and is expressed by less FeO and greater MgO. However, this modeling is designed for ferrous iron, which works well in environments with low oxidation potential.

To use this modeling for arc peridotites, which is likely variably oxidized due to high abundance of pyroxenes and Fe<sup>3+</sup>-rich spinel phases (Brandon & Drapper, 1996; Parkinson & Pearce, 1998; Parkinson & Arculus, 1999), FeO\* (\* refers to total Fe) is used to account for additional Fe<sub>2</sub>O<sub>3</sub>, which may be added from slab derived fluids and melts (Parkinson & Arculus, 1999). In this case, the melting grid is not applicable, as it is calculated for ferrous iron. Since potential residues are those lacking extensive reactions with migrating melts and/or fluids introduced into the mantle wedge, peridotites with the lowest FeO\* are possible mantle residues. Placing the CM peridotites into FeO\* vs. MgO space, with peridotites from Patagonia, Japan and the Cascades for comparison (fig3.33), there is some overlapping between the CM peridotites and those from other back-arc areas. The peridotites with enriched FeO\* and MgO are those already designated as most modified through metasomatism. Additionally, two of the most modified peridotites with over 11wt% FeO\* are not visible on the diagram.

In modeling Al<sub>2</sub>O<sub>3</sub> and SiO<sub>2</sub> vs. MgO, the melting grid can be used, giving not only information as to the consistency of the rocks, but also information about melt fraction and pressures of initial and final melting (fig3.34 and 3.35). Again, the most modified peridotites fall out of the melting grid and show no internal consistency. In contrast, five of the least and moderately modified peridotites are consistently within the melting grid in both Al<sub>2</sub>O<sub>3</sub> and SiO<sub>2</sub> vs. MgO, showing internal consistency. Upon closer examination (table3.8), two peridotites, Iherzolites CM52 and CM61, yield the same final pressure, initial pressure and melt fraction in both melting model spaces of Herzberg & O'Hara (2002) and Herzberg (2004). Thus, they are the best candidates for possible mantle residues. CM61, however, was categorized as a moderately modified peridotite

based on its “U” shaped REE pattern. Further, it shows a higher melt fraction (0.275) than CM52 (0.1) in the melting models. Taken together, confidence in CM61 as a first-stage residue falters. Notably, there are only trace amounts of modal spinel in CM52 and only 0.5 modal wt% spinel in CM61, whereas other peridotites have  $\geq 1$ wt% modal spinel.

Generally, the  $\text{Al}_2\text{O}_3$  space yields greater initial and final melting pressures than  $\text{SiO}_2$  space. It may be that the spinel phases, although only a small fraction of the bulk composition, displace these rocks to higher apparent  $\text{Al}_2\text{O}_3$  concentrations. That many most modified peridotites are too depleted in  $\text{SiO}_2$  to be simple residues corroborates that the modifying agent is a fluid introduced into the mantle via subduction processes. If it were a melt, the expected outcome would be enrichment in  $\text{SiO}_2$  (Kelemen, 1998; Herzberg, 2004). Regardless of melt/rock and fluid/rock reactions, there is at least 1 peridotite that can clearly be considered a residue: CM52.

### ***Mantle Temperature***

Calculated equilibrium temperatures for the peridotites place the xenoliths between 35km and 80km depth within the mantle (fig3.36). The depth range is controlled by the stability field of spinel phases as neither garnet nor plagioclase occurs in the peridotites. Equilibration temperatures, however, are the highest T recorded by a rock; not necessarily the highest T experienced by the rock. Consequently, equilibration temperature does not provide information about the mantle’s thermal state when the rocks formed. For such information, it is better to find the potential temperature, the temperature of the mantle that would exist if that particular piece of mantle was at atmospheric pressure, which is related to the composition of the rock.

The Iherzolites with internal consistency within the modeling of Herzberg &

O'Hara (2002) and Herzberg (2004) can provide information about the relationship between composition, mantle temperatures and pressures of fractional melting. Both CM52 and CM61 have a pressure of initial melting of 4.7GPa with a final melting pressure of 4GPa. Placing that on a T- P diagram from Herzberg & O'Hara (2002), the potential temperature of the system is 1580°C (fig3.37). This potential temperature is similar to a few rocks from Japan, Cascades and Patagonia with initial melting pressures of 3 to 5 GPa (figs3.34, 3.35), and, being hotter than abyssal peridotites, is considered "hot" mantle (Herzberg, 2004).

Although there is evidence for melt/rock reactions in the trace elements of the CM peridotites (fig3.24), major element trends do not show large amounts of added orthopyroxene, which would be seen by enrichment of SiO<sub>2</sub> and depletion in Al<sub>2</sub>O<sub>3</sub> compared to fertile mantle (figs3.33, 3.34). In this case, it seems appropriate to view the CM least and moderately modified peridotites as first-stage residues of a hot, fertile mantle. Furthermore, the high potential temperature indicates that the CM peridotites formed in a plume-like environment rather than a ridge-like environment. It has been proposed by Feigenson et al. (2004) and Carr et al. (2007) that the Galapagos plume has influenced the mantle underlying Costa Rica. That the CM xenoliths and host basanite overlap the Galapagos domains (Werner et al., 2003) in Pb isotopes space (fig3.38) supports their proposal and gives credence to the formation of the peridotites in a plume-like environment. The possibility that the CM peridotites formed in an oceanic plateau (Herzberg, 2004) that subsequently aided in subduction initiation (Niu et al., 2003) is an important consideration and needs further investigation.

### ***Summary***

I now summarize the picture of the mantle wedge under Costa Rica that has

emerged from this work with a cartoon based upon equilibration temperatures, amount of modification and compositional similarity to residues of fertile mantle (fig. 3.39). Residues left by the melting of a fertile mantle subsequently experienced melt/rock reactions during Miocene subduction; these first - stage residues are the least and moderately modified peridotites of Cerro Mercedes such as CM52 and CM69. At shallower depth, reactions with fluids from the subducting slab also occurred; these multi-stage residues are the most modified CM peridotites like CM27. High-pressure crystal fractionation of mantle material formed pyroxenites such as CM67. Finally, decompression of the system after the migration of the active arc allowed a quickly flowing magma, CMB, to bring the mantle xenoliths to the surface. It is fortuitous that the CM xenolith suite represents the heterogeneity of the mantle.

### **Conclusions**

The host rock is a Si-undersaturated, alkali basanite that shows evidence of subduction processes. Generated by decompression melting, they originate at a depth of spinel facies stability.

There are two main populations of mantle xenoliths: pyroxenites and peridotites. They each break down further: the pyroxenites into Al-enriched and Al-depleted; the peridotites into varied degrees of modification that have been termed least, moderately and most modified.

Equilibration temperatures for the peridotites range from 883°C to 1062°C at 1GPa and 908°C to 1062°C at 2.5GPa. The pyroxenites have lower equilibration temperatures ranging from 862°C to 871°C at 1GPa and 895°C to 897°C at 2.5GPa. The potential temperature of the system is 1580°C.

The peridotites were at one time in equilibrium with a fertile mantle. After

experiencing a melting event, some pods of mantle material were left untouched while others experienced further melting and/or reacted with fluids introduced by subduction processes.

Subduction processes influence the trace element chemistry of all the peridotites. The least and moderately modified peridotites experienced melt/rock reactions; the most modified peridotites became additionally metasomatized via fluid flux.

There are 2 peridotites, CM52 and CM61, which fulfill modeling criteria of first – stage residues. All others are considered multi-stage residues.

Figure 3.1. Cartoon of the circum-Pacific ring of fire with stars in approximate locations of mantle xenolith suites reported in the literature.

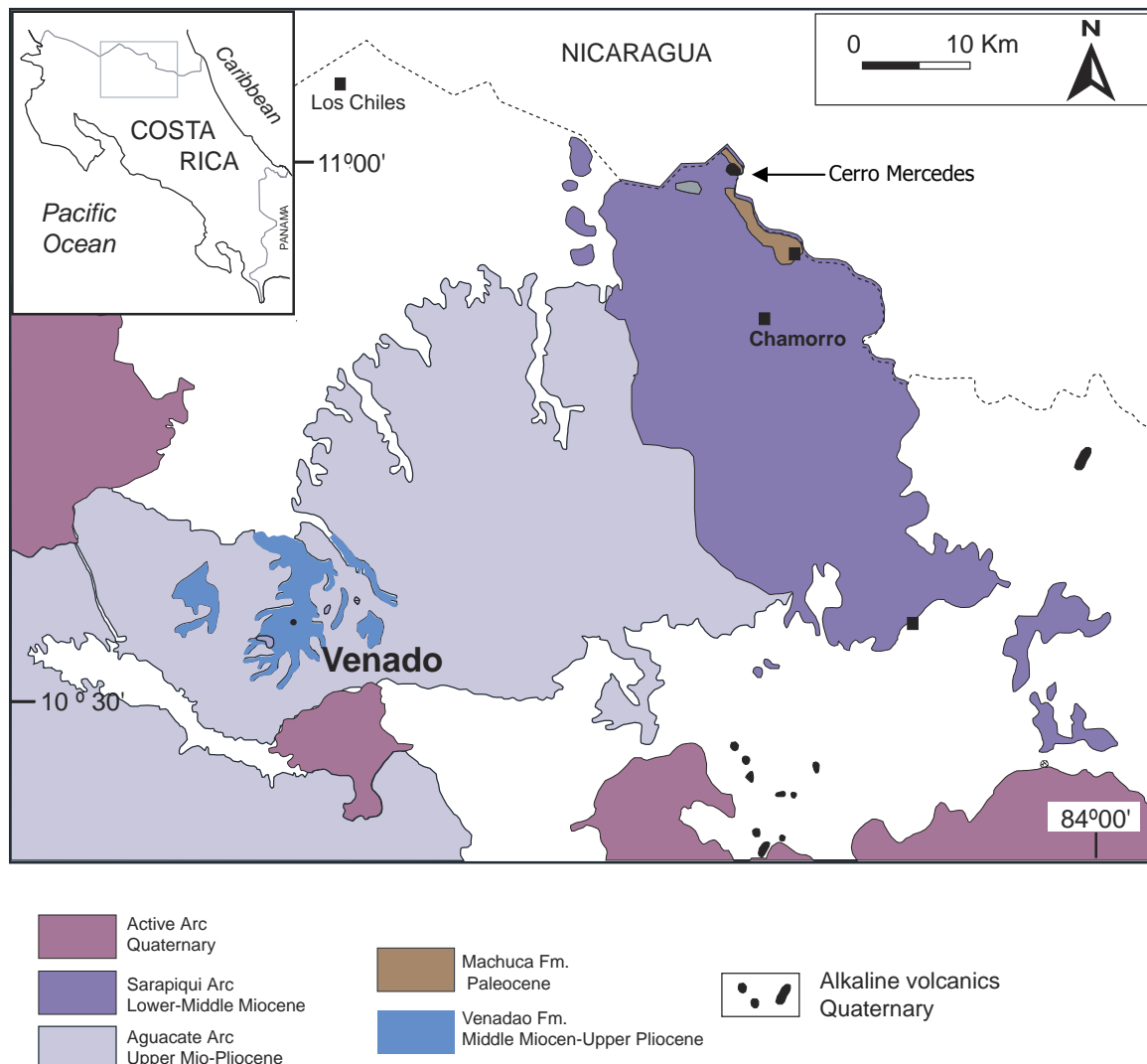
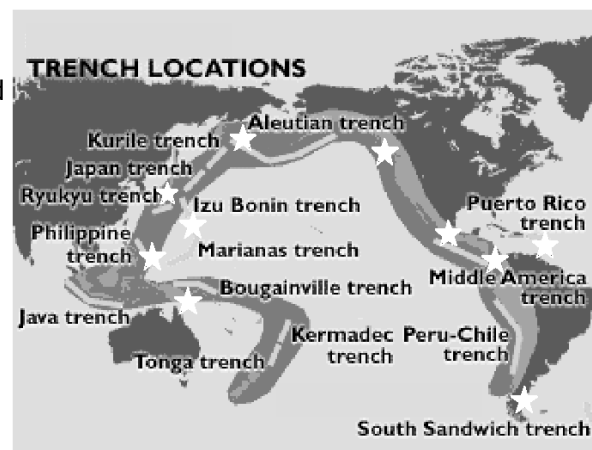


Figure 3.2. Geologic map of northeast Costa Rica including Miocene to Quaternary rocks. Inset shows area shown by map. Adapted from Tournon et al. (1995).

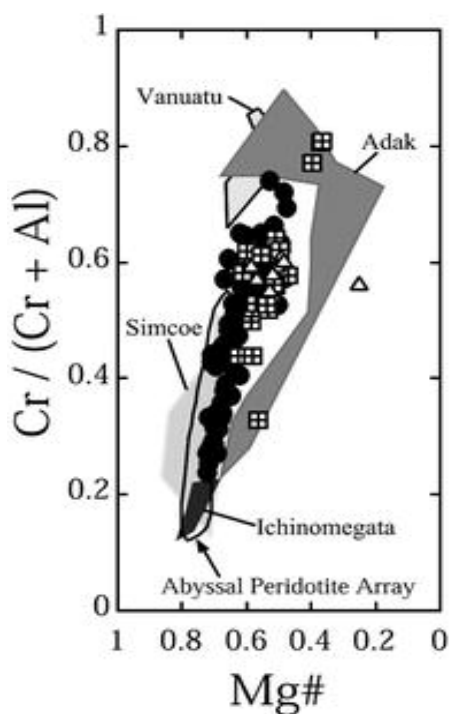


Figure 3.3. Peridotites from various arcs are plotted in Cr# vs. Mg# (from Parkinson et al., 2003).

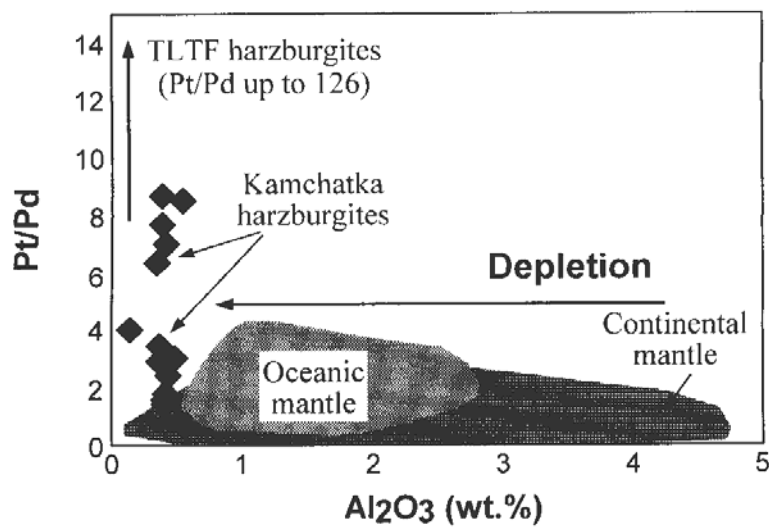


Figure 3.4. Pt/Pd vs. Al<sub>2</sub>O<sub>3</sub> space shows the relative depletion of arc peridotites as seen by Kamchatka harzburgites. The y-axis shows fractionation in platinum group elements platinum and palladium, which tend to be enriched in arcs and their related ore deposits. (From Kepezhinskas & Defant, 2001). TLTF - Tabar – Lihir – Tanga – Feni arc values from McInnes et al. (1999).

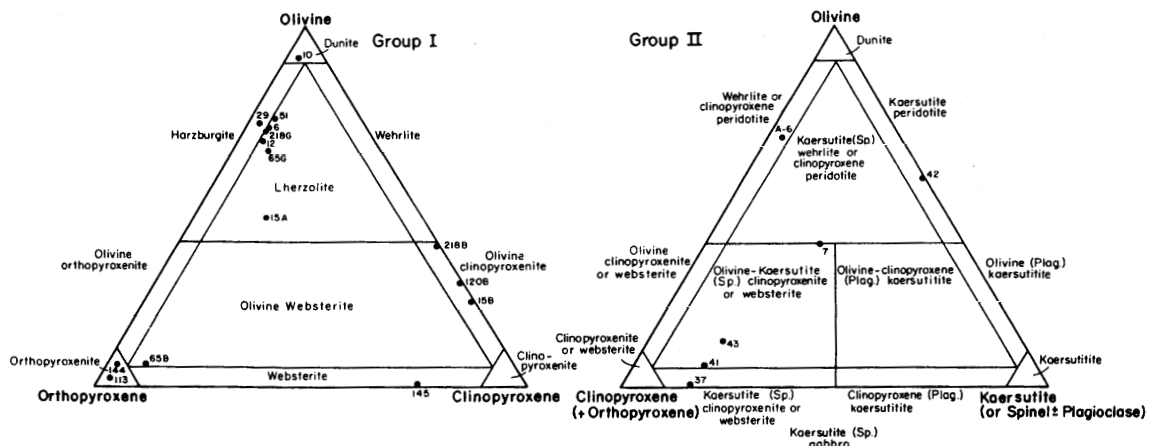


Figure 3.5. Modal proportions of phases in Group I and Group II as defined by Frey & Prinz (1987). The nomenclature is based on IUGS with some revision in Group II in which kaersutite replaces hornblende and spinel and/or plagioclase is added to the amphibole component.

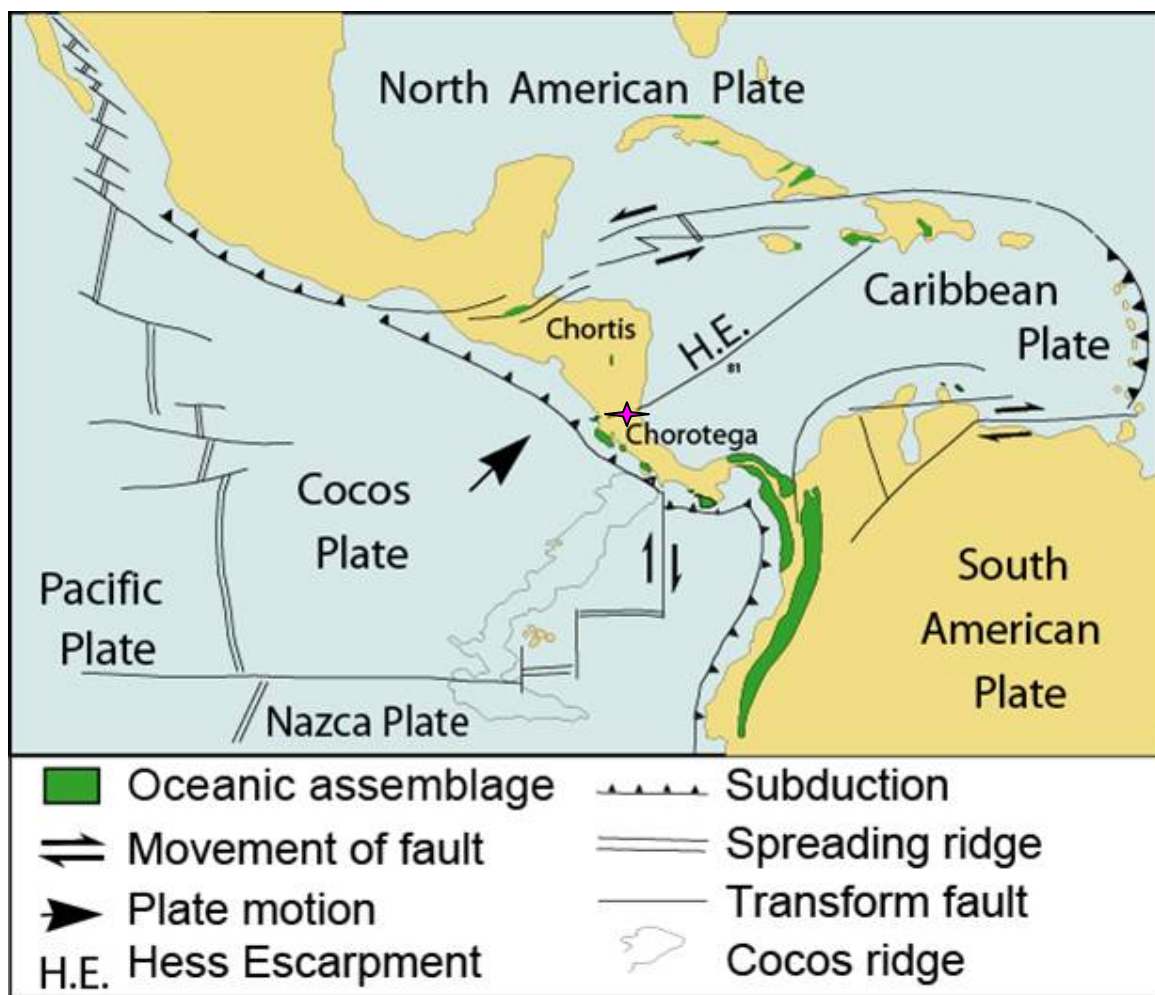


Figure 3.6. Tectonic setting of Central America. A  $\star$  shows an approximate location of Cerro Mercedes.

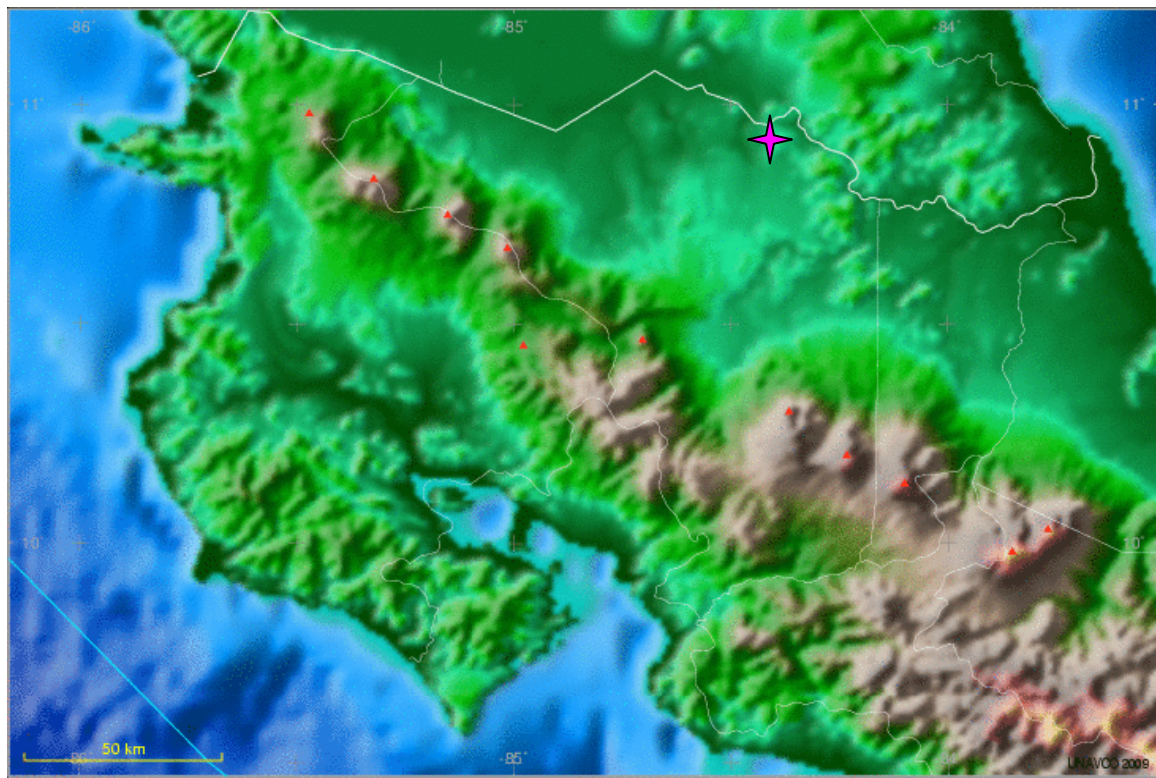


Figure 3.7. Topographic map of north Costa Rica. Red triangle are volcanoes along the active front. Pink star is Cerro Mercedes. Generated by the UNAVCO Facility with support from the National Science Foundation and NASA under NSF Cooperative Agreement No. EAR-0735156.

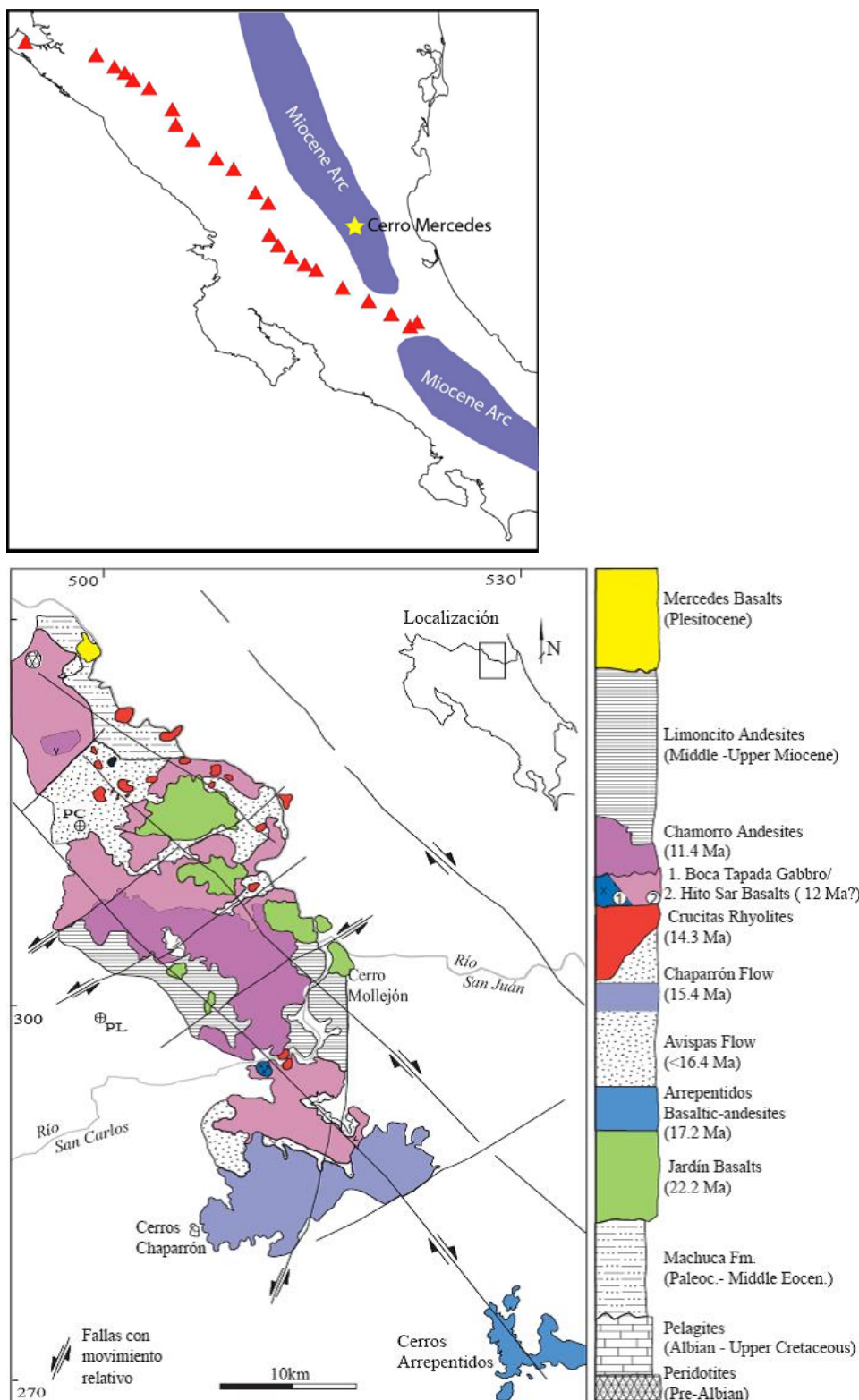


Figure 3.8. Geologic maps of the Miocene arc showing its relationship to the present active volcanic front and Cerro Mercedes. From Gazel et al. (2005).

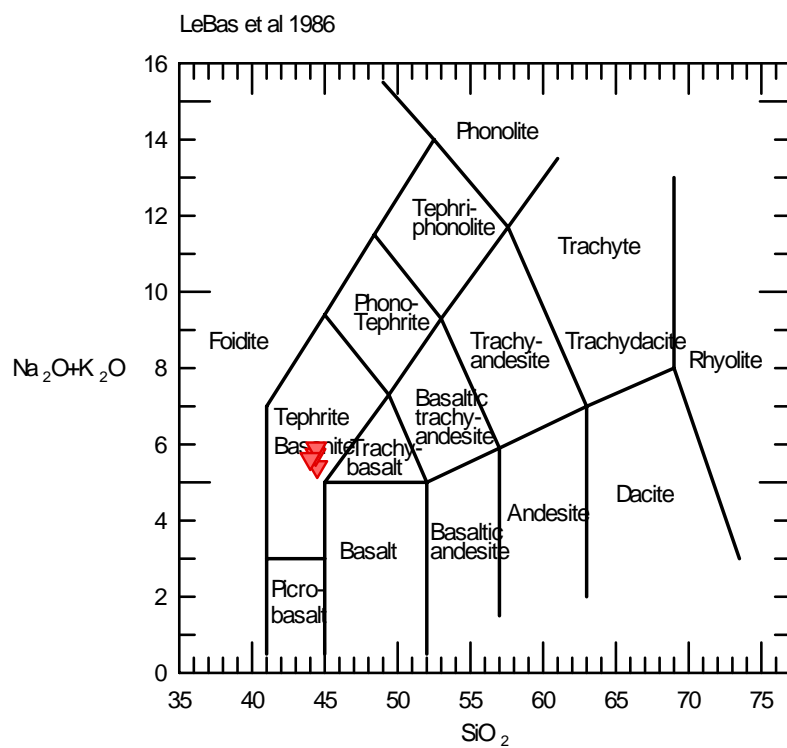


Figure 3.9. Total alkaline vs.  $\text{SiO}_2$  characterize host rocks as basanites.

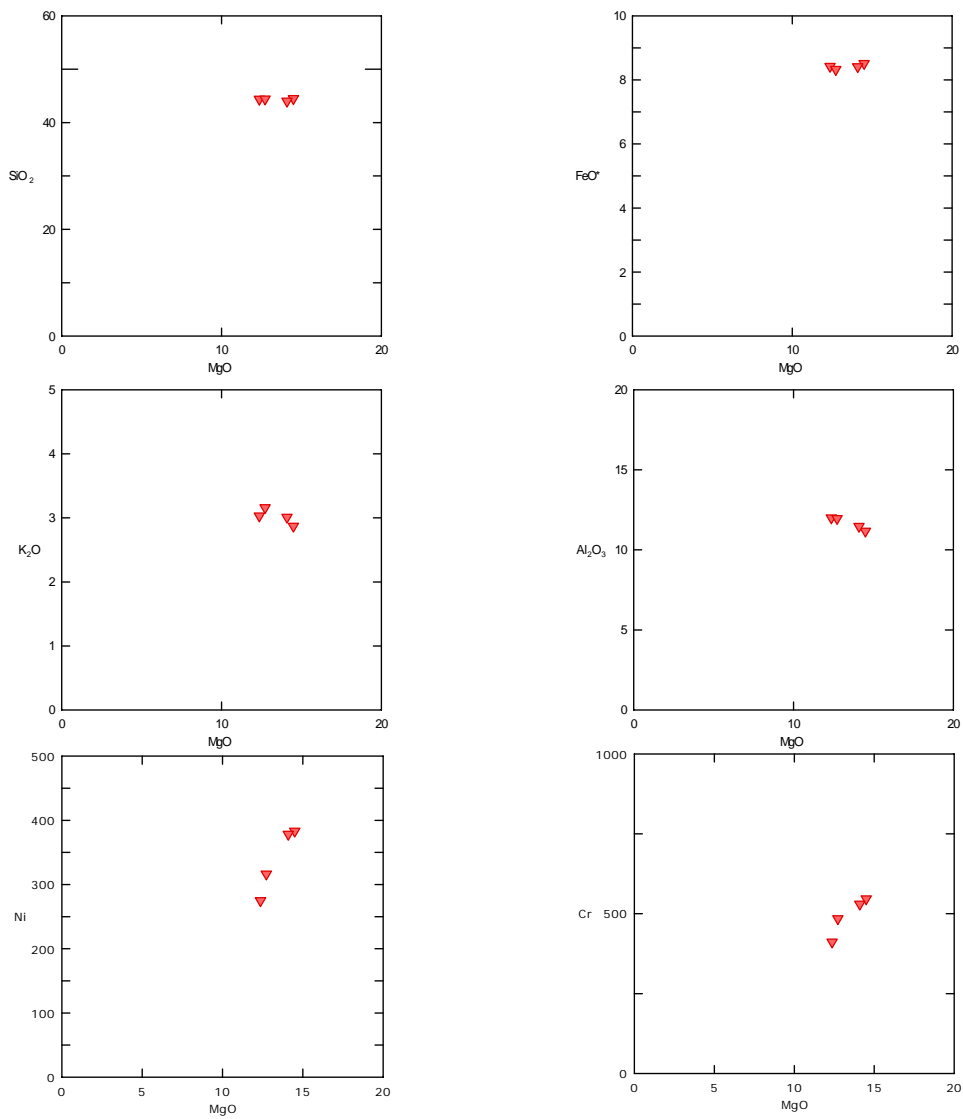


Figure 3.10. Slight variations are seen in Fenner diagrams within the CM host lava. Ni shows olivine fractionation; Cr shows magnetite/spinel.

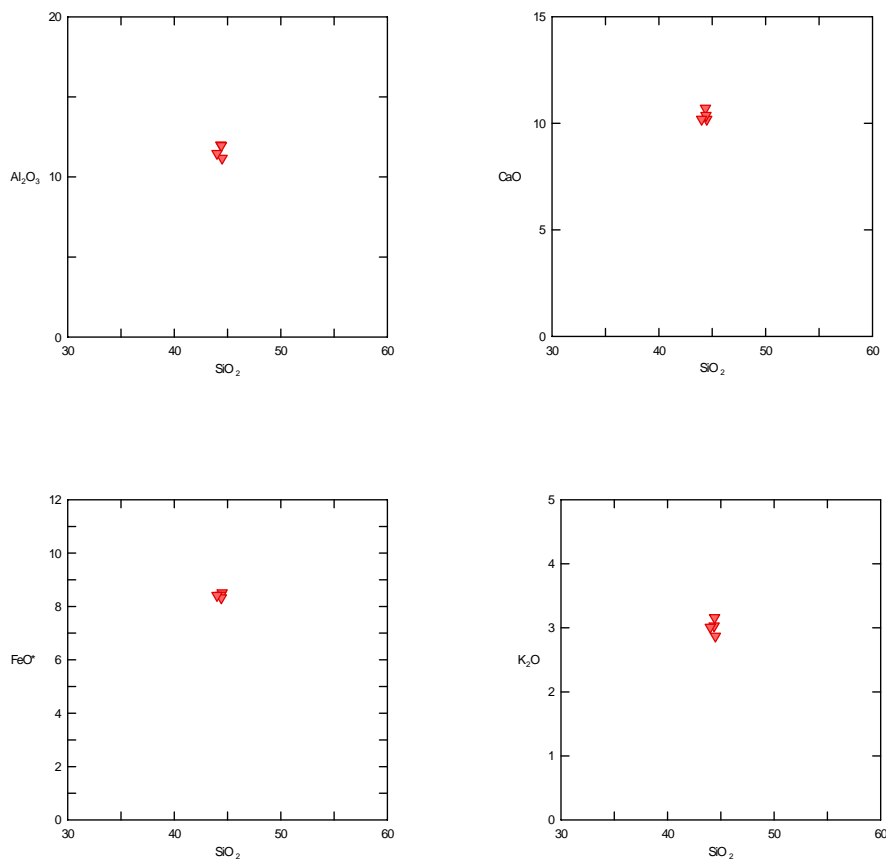


Figure 3.11. Little to no fractionation within the CM host lavas is evident in Harker diagrams.

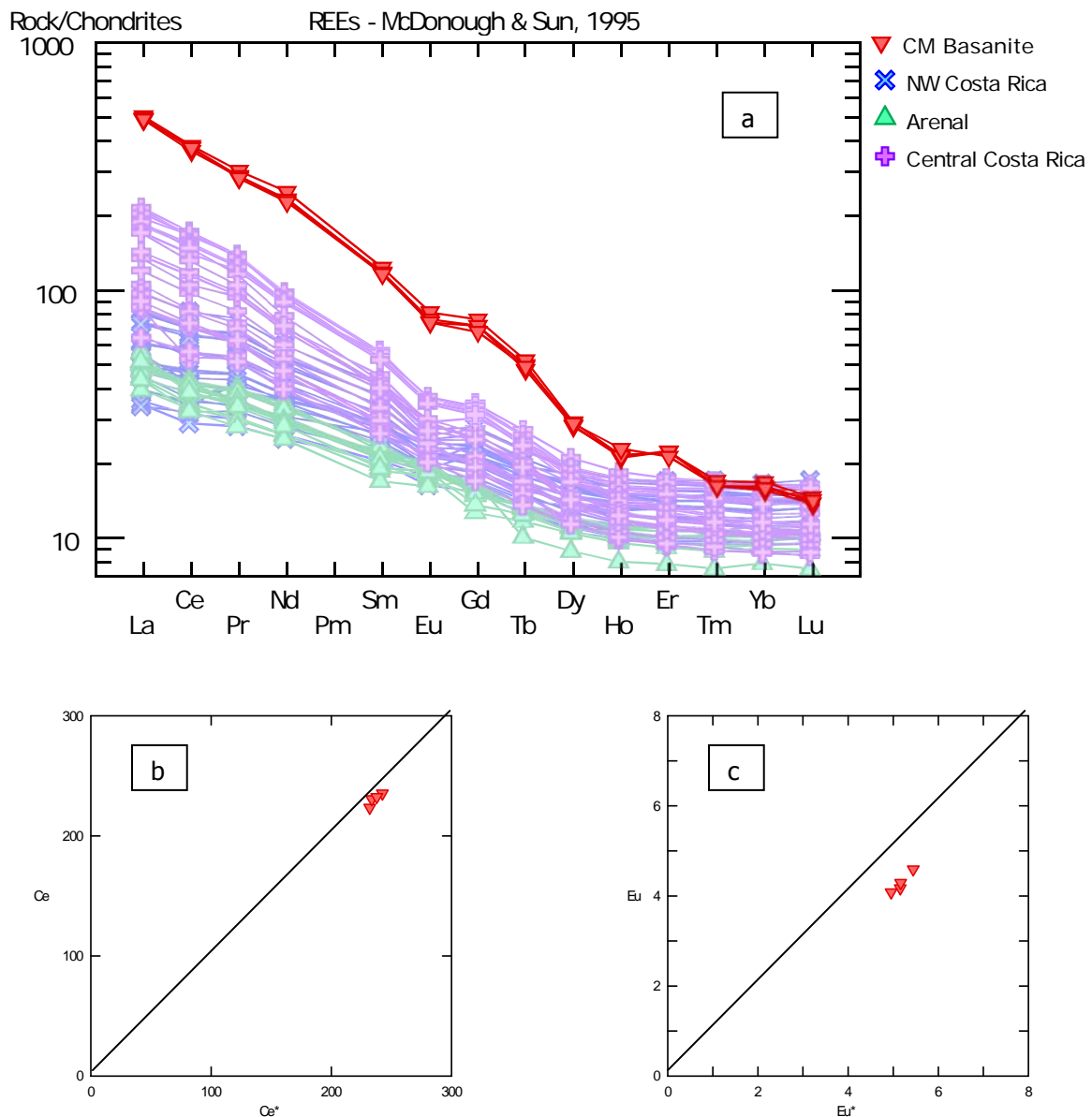


Figure 3.12. a) REE spidergram with Costa Rica front arc lavas as comparison. b) Ce vs Ce\*; the linearity shows that the samples are not weathered. c) Eu vs. Eu\*; here all samples are off the 1:1 ratio line, showing that plagioclase has been removed.

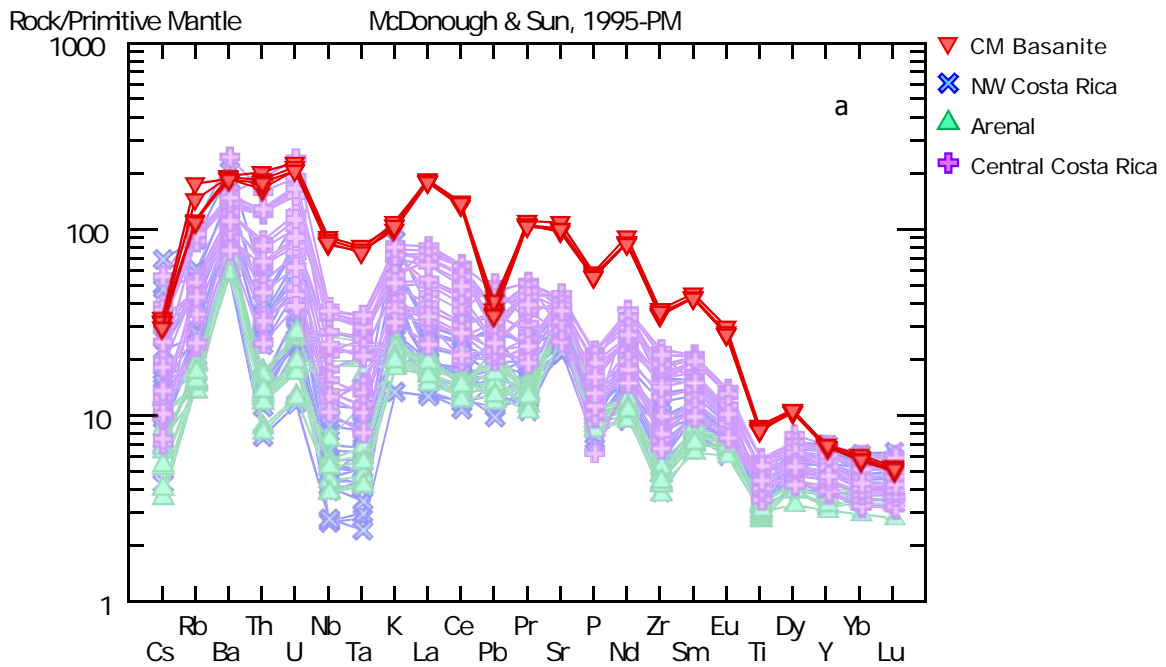
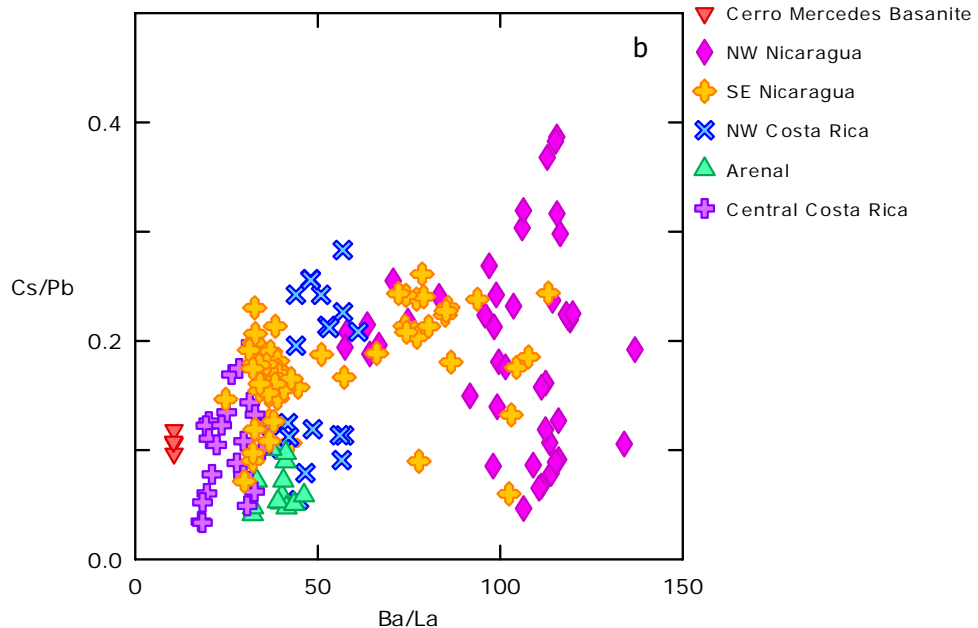


Figure 3.13. a) Trace element spidergram of CMB normalized to Primitive Mantle (McDonough & Sun, 1995) with Costa Rica front arc lavas as comparison. b) Cs/Pb vs. Ba/La shows the CM basanite to have little hydrous fluid influence compared to lavas from the Central American Volcanic Front (CAVF).



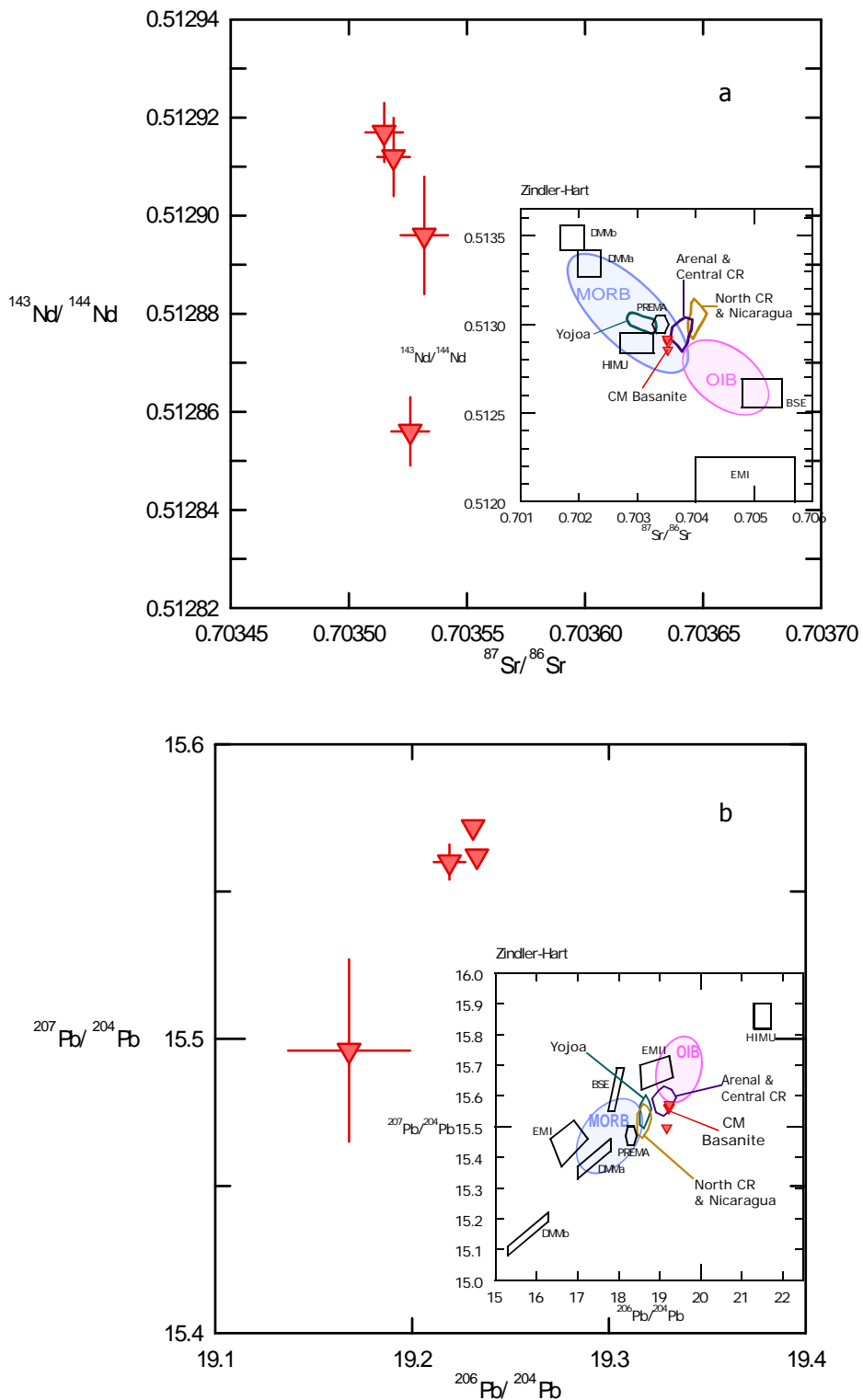


Figure 3.14. Isotope space. a) Nd vs. Sr isotopes; b) Pb isotopes. Insets compare the CM basanite to lavas from the Costa Rica and Nicaragua active front arc, back-arc lavas from Yojoa (Carr et al., 2003), MORB and OIB (Hofmann, 1997).

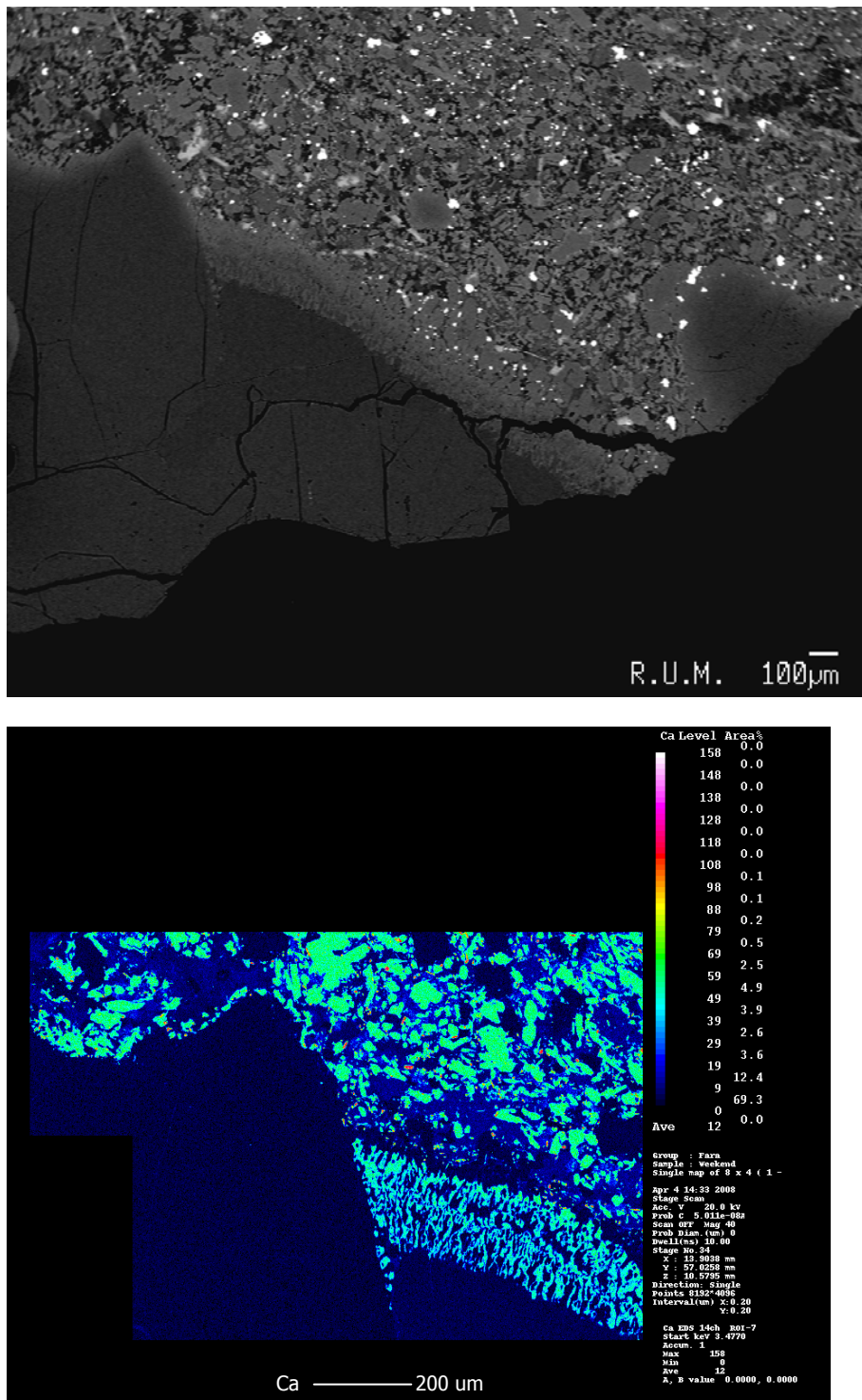


Figure 3.15. Reaction area in embayment of CM50. Top image backscattered electron; bottom image is a map of Ca. Note the different scale bars in each image. Both rendered on JEOL 8200 superprobe.

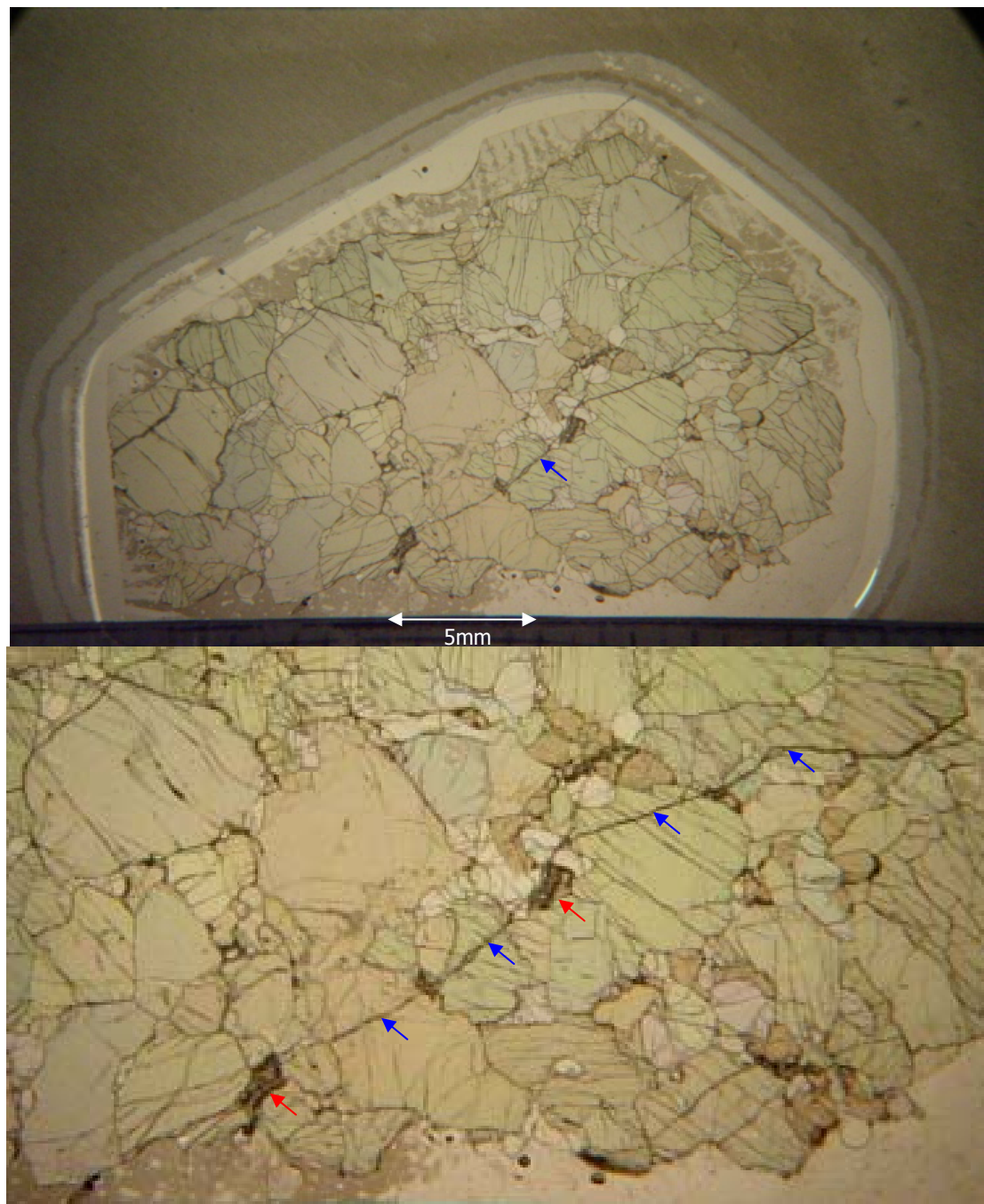


Figure 3.16. Veinlet of CM63. Top image is of full thin section with one polarized lens, scale as shown. Bottom photo is a close up of the veinlet (blue arrows) and areas of ponded material (red arrows). Qualitative probe analyses shows that the material is feldspar rich.

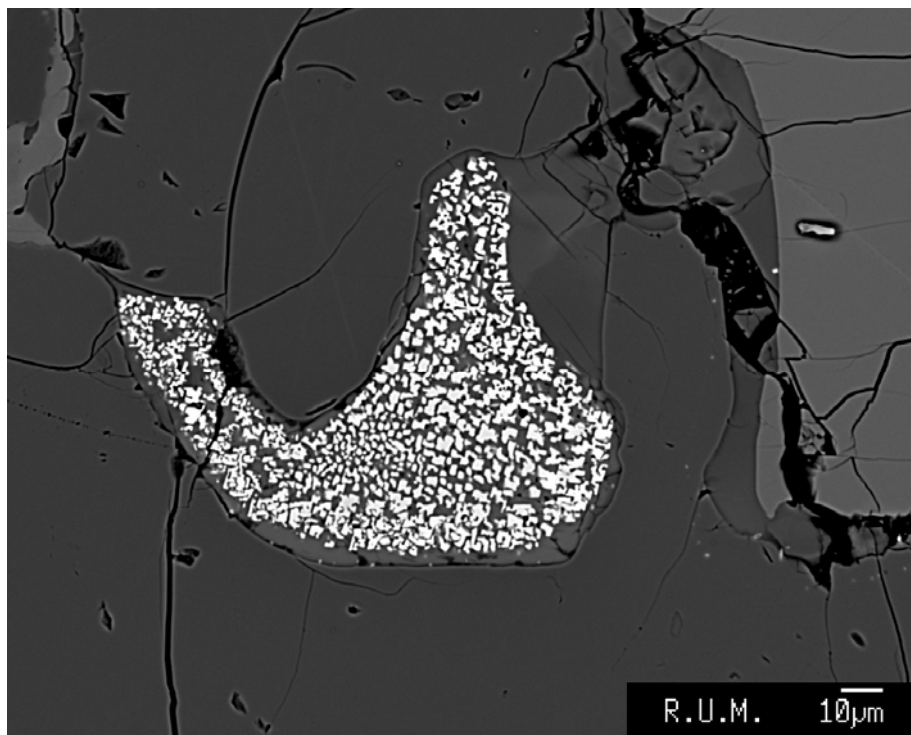


Figure 3.17. Vermicular spinel near to the contact with host basanite in CM52. Note the crack to the right of the grain.

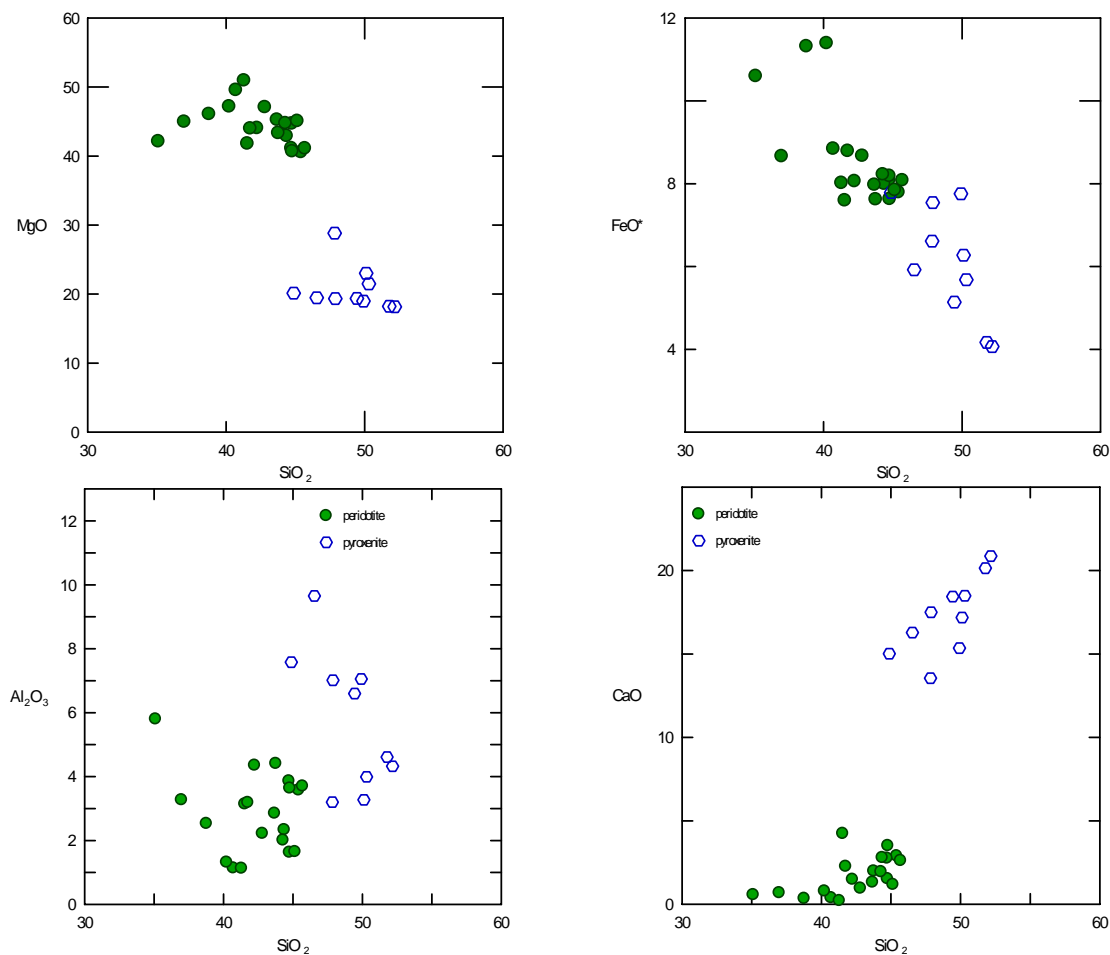


Figure 3.18. Harker diagrams showing two populations: peridotite and pyroxenites. The pyroxenites further split into  $\text{Al}_2\text{O}_3 > 6\text{wt\%}$  and  $< 6\text{wt\%}$ .

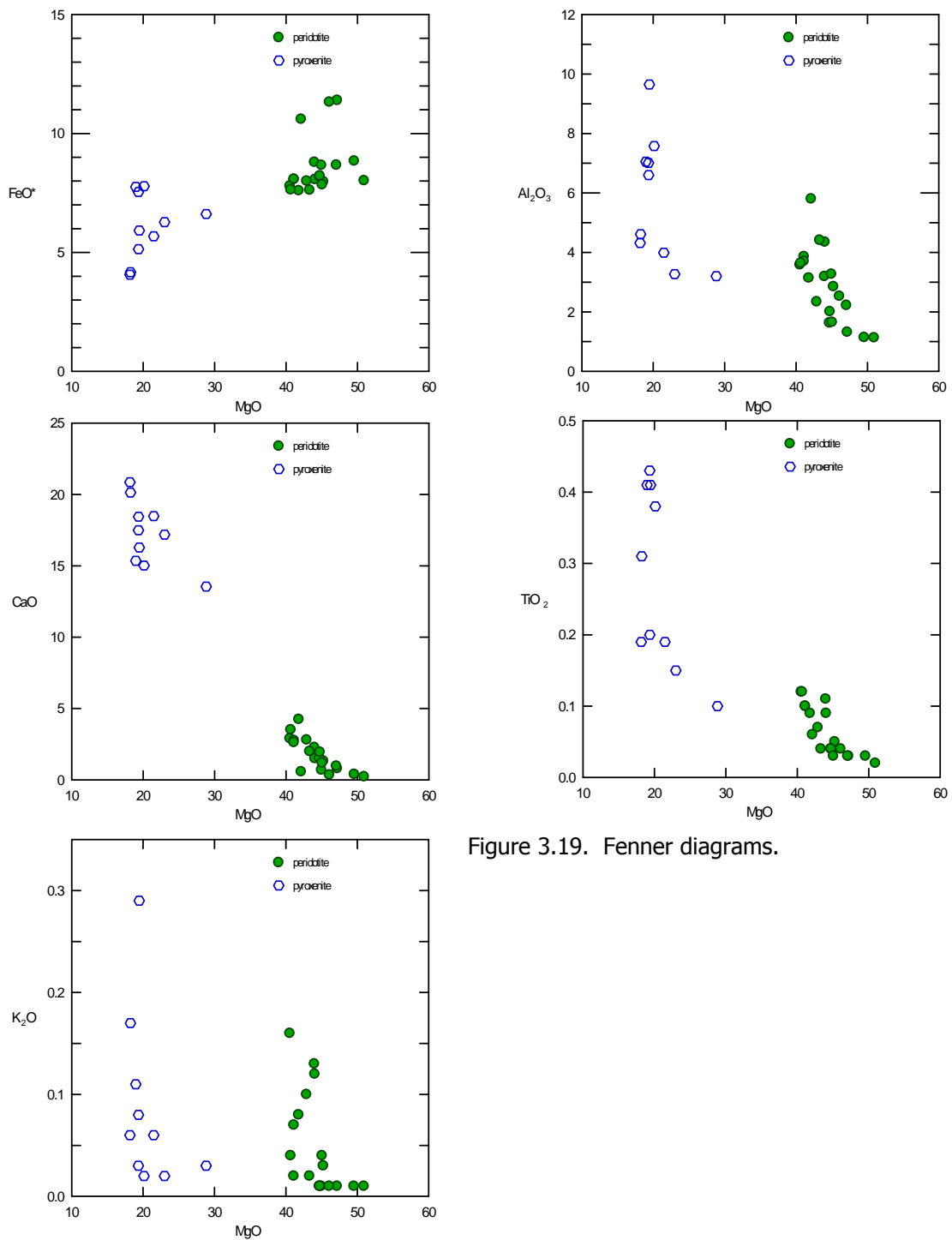


Figure 3.19. Fenner diagrams.

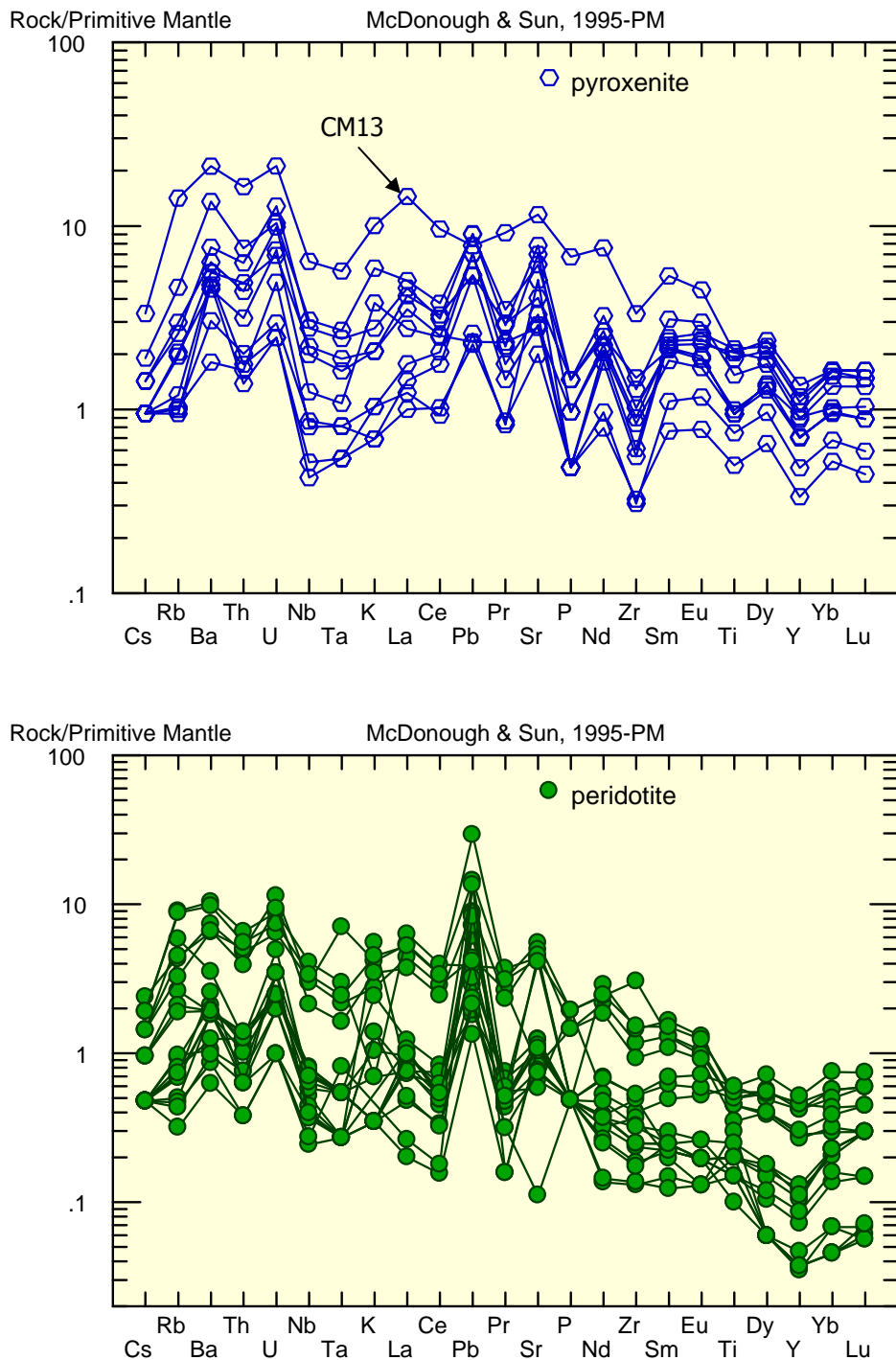


Figure 3.20. Trace element spidergram normalized to primitive mantle (McDonough & Sun, 1995). CM13, which resembles the host basanite, has been contaminated during the extraction process.

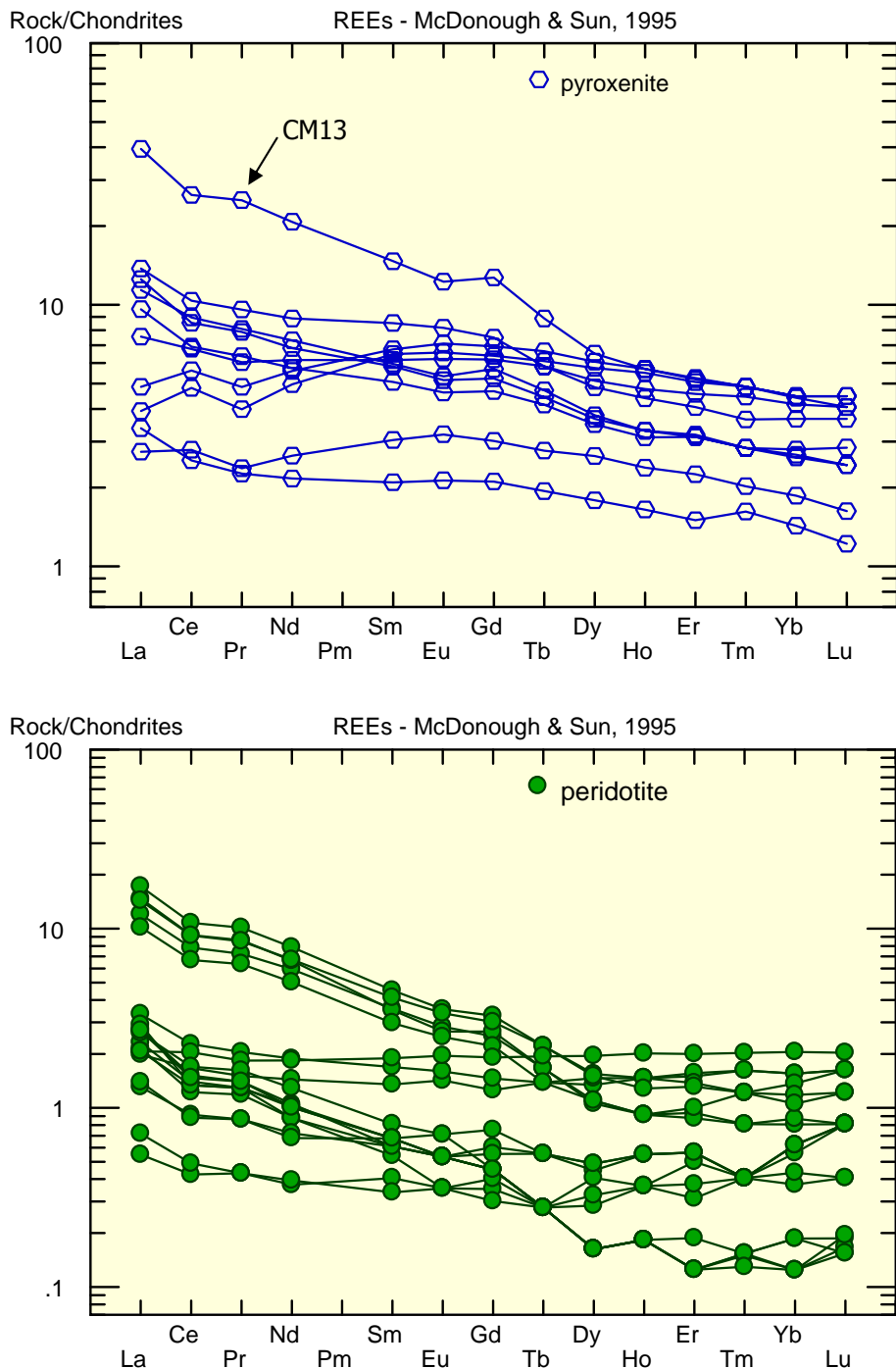


Figure 3.21. REE spidergrams of a) pyroxenites and b) peridotites normalized to chondrites (McDonough & Sun, 1995).

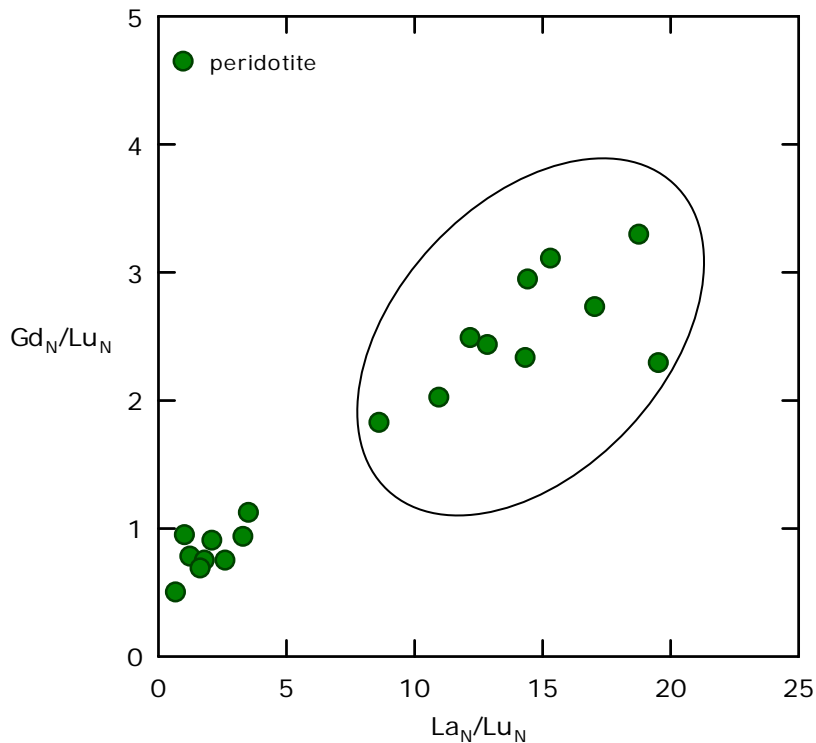


Figure 3.22. The peridotites with the higher La/Lu ratio (normalized to chondrites, McDonough and Sun, 1995) are the most modified (circled).

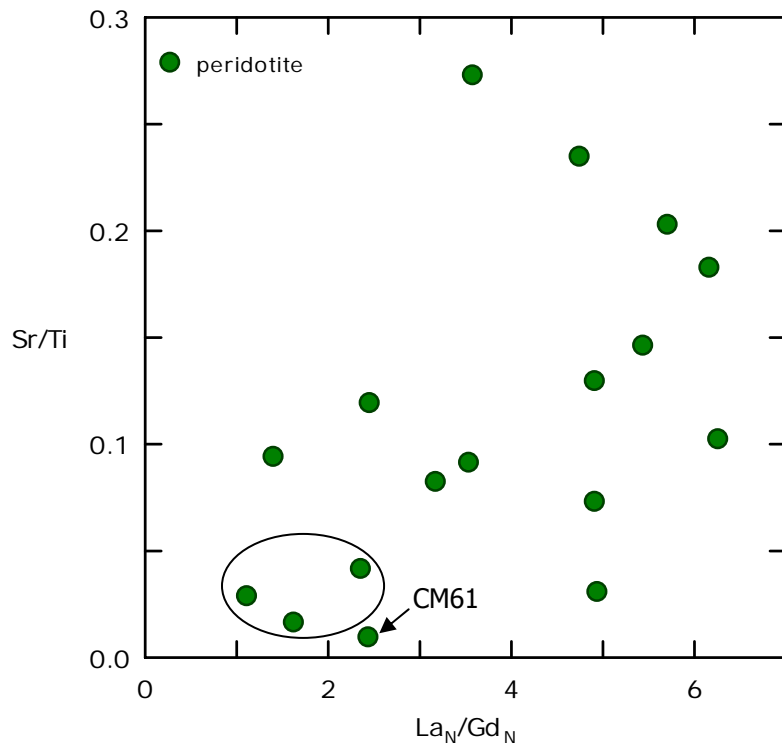


Figure 3.23. Sr/Ti vs. La<sub>N</sub>/Gd<sub>N</sub>. Peridotite with the lowest ratios in both parameters are potentially the least modified (circled). CM61 is moderately modified; see text for details.

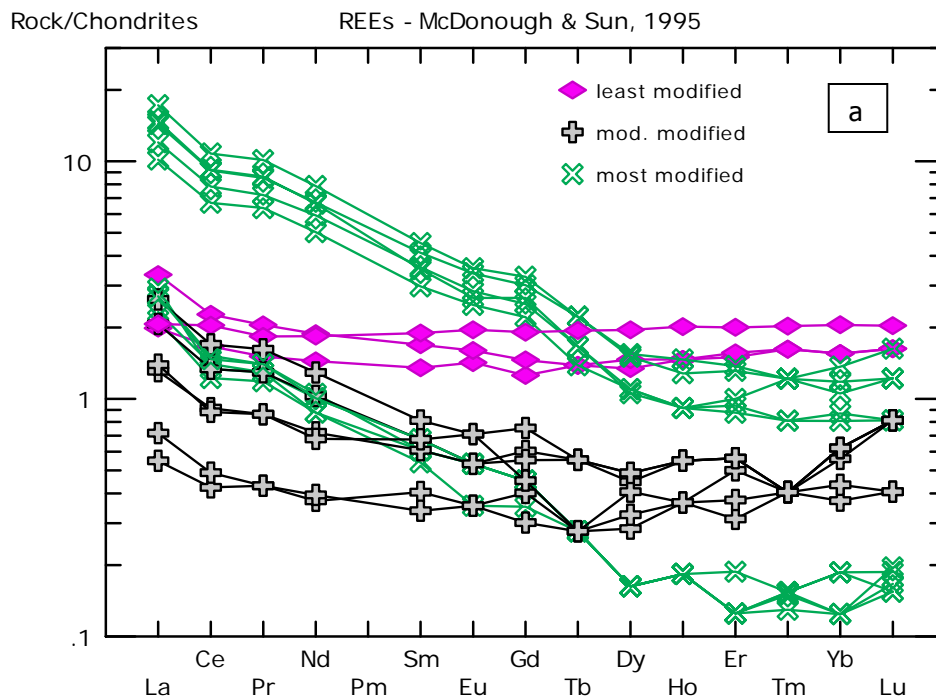
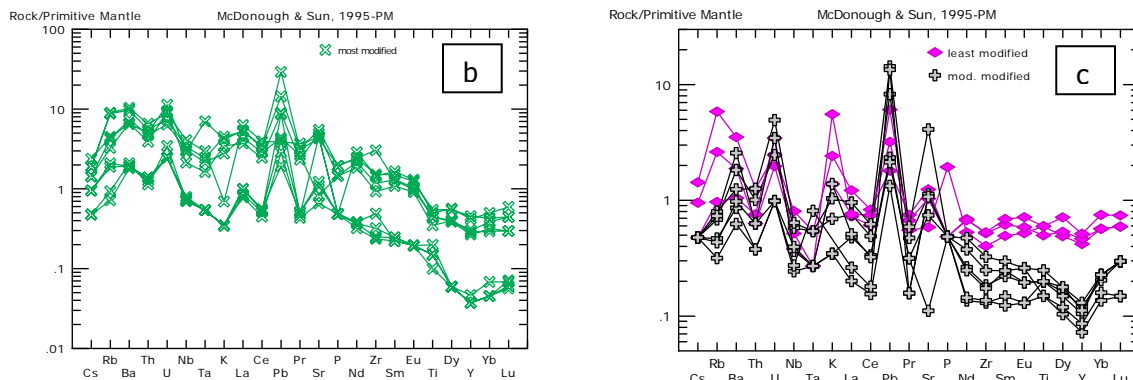


Figure 3.24. a) Peridotite populations based on REE patterns. Variable amounts of modification via metasomatism separate these populations. b) Several of the most modified peridotites show a negative K anomaly; c) many of the least and moderately modified peridotites show positive K anomalies.



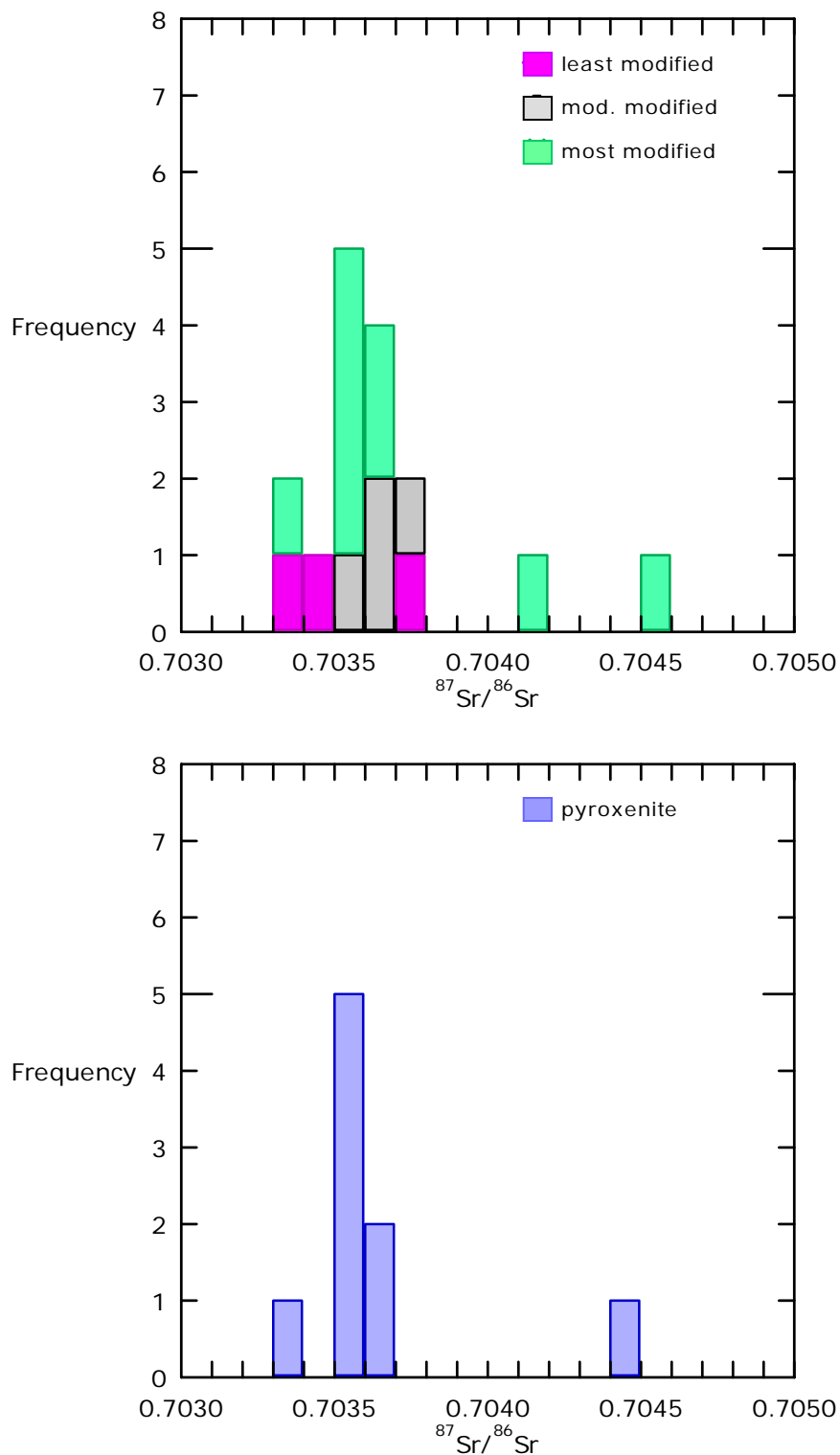


Figure 3.25. Histograms of Sr isotopes. The scatter shown by the most modified peridotites confirms influence by subduction processes.

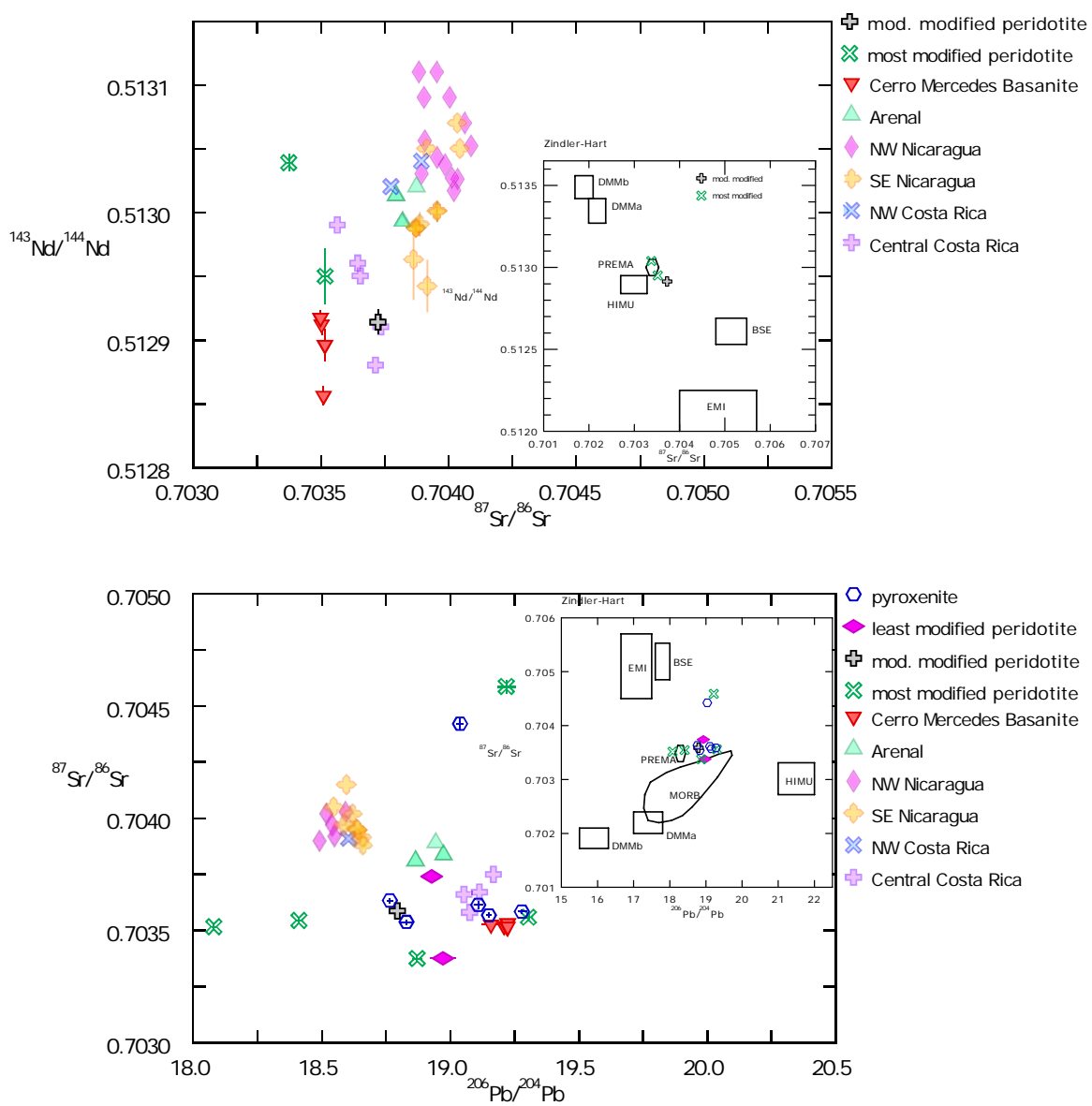


Figure 3.26. Isotope space with Central American front arc and CM basanite for comparison. Very few Nd isotope values are available for the peridotites at this time. Sr vs. Pb space shows values close to MORB. Insets show mantle reservoirs of Zindler & Hart (1986).

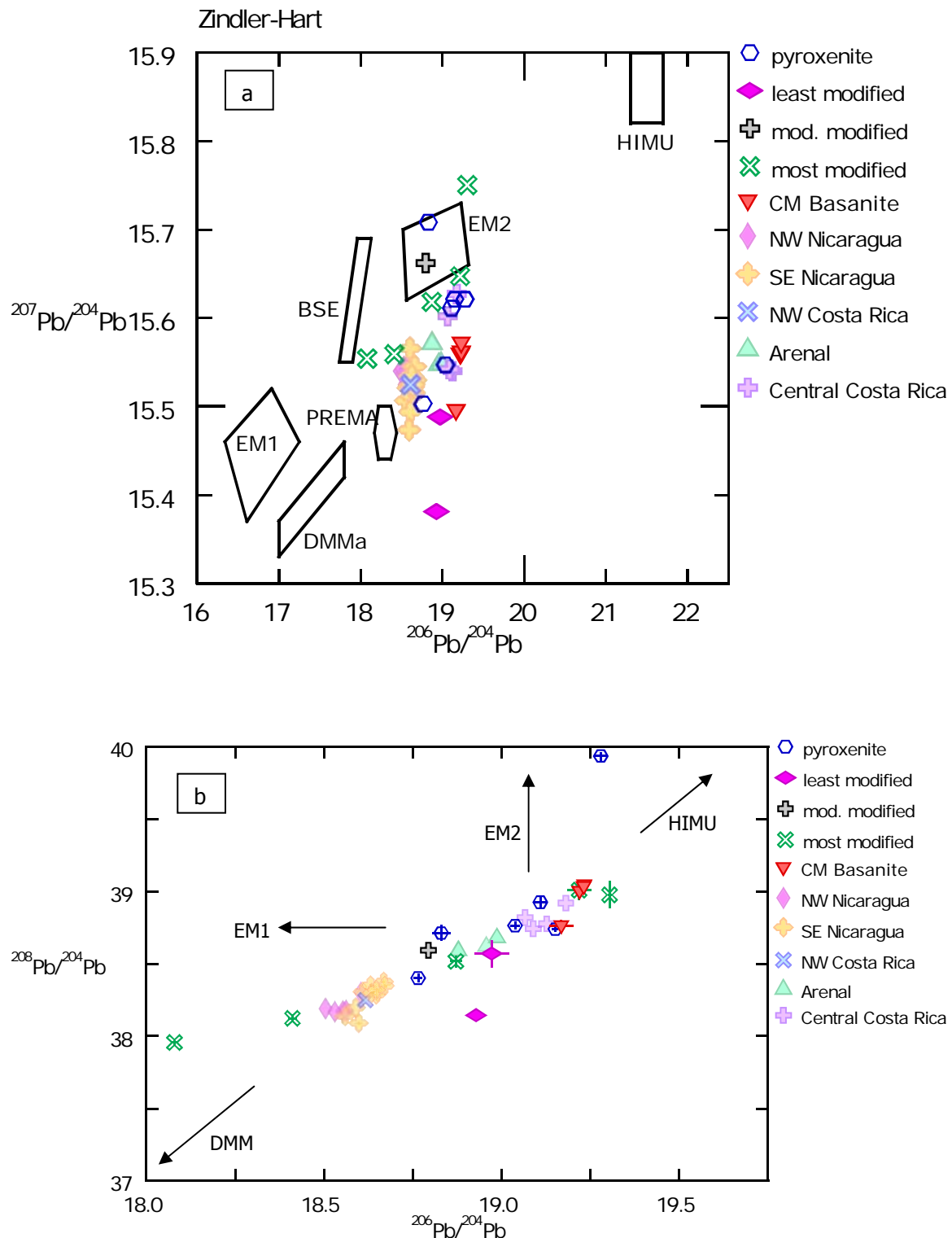


Figure 3.27. Lead isotope space. Mantle reservoirs of Zindler & Hart (1986) as shown in inset and with arrows.

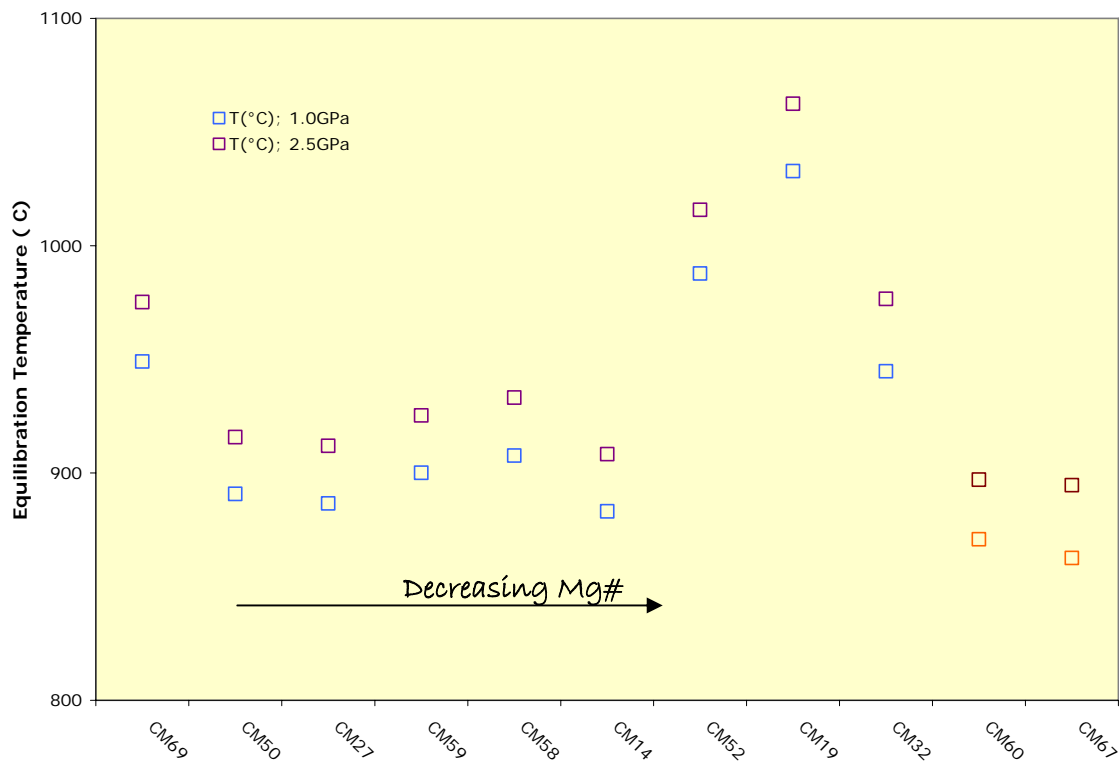


Figure 3.28. Equilibrium temperature results from calculations (Brey & Köhler, 1990). CM60 and CM67 are pyroxenites; all other included xenoliths are peridotites.

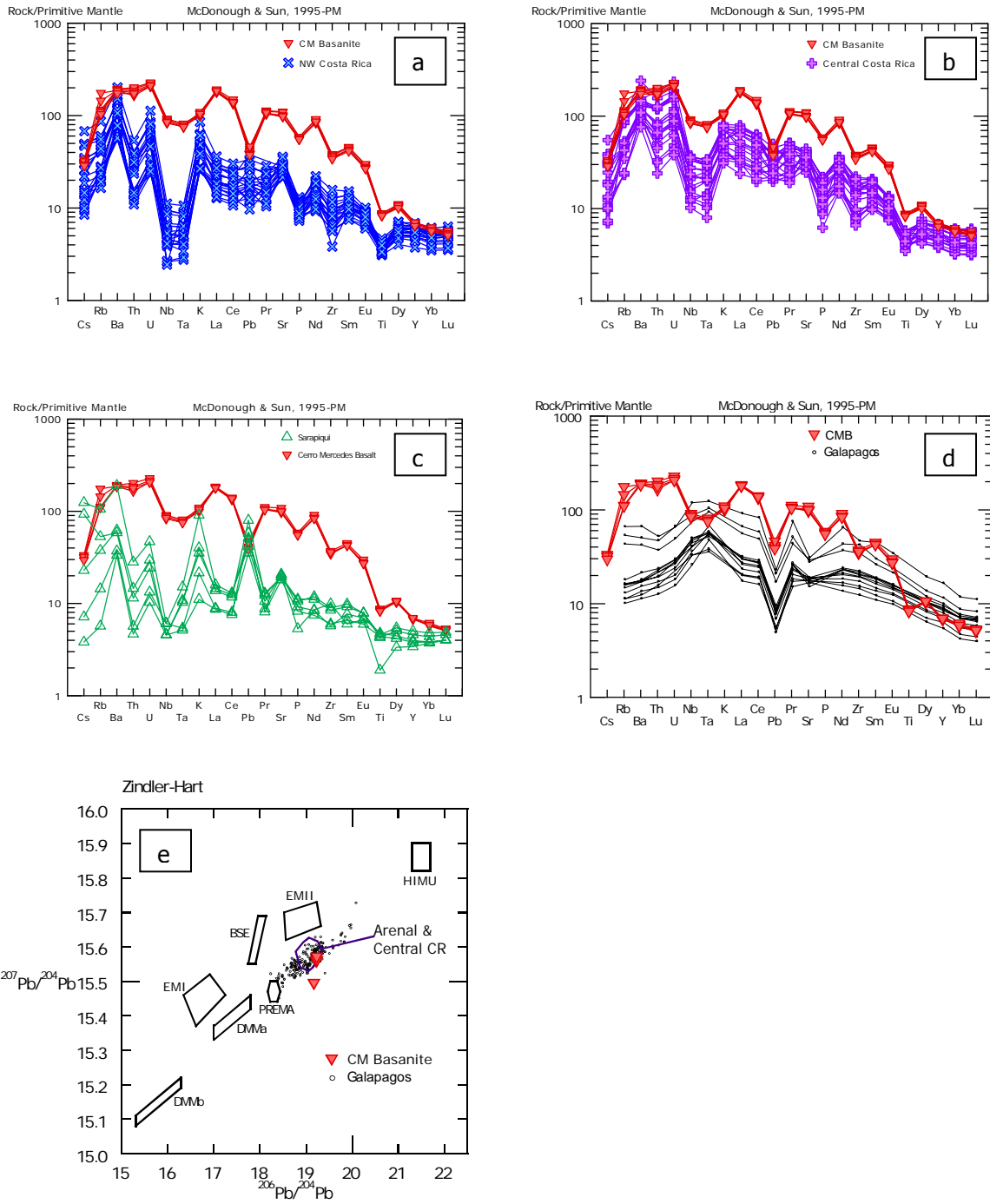


Figure 3.29. Comparison of CMB trace elements with a) North Costa Rica, b) Central Costa Rica, c) Miocene Sarapiquí arc and d) Galapagos lavas. Galapagos Pb isotope space (e) shows an overlap with both CMB and Costa Rica lavas, suggesting a similar source. Data for e) from the GEOROC database (Sarbas, 2008).

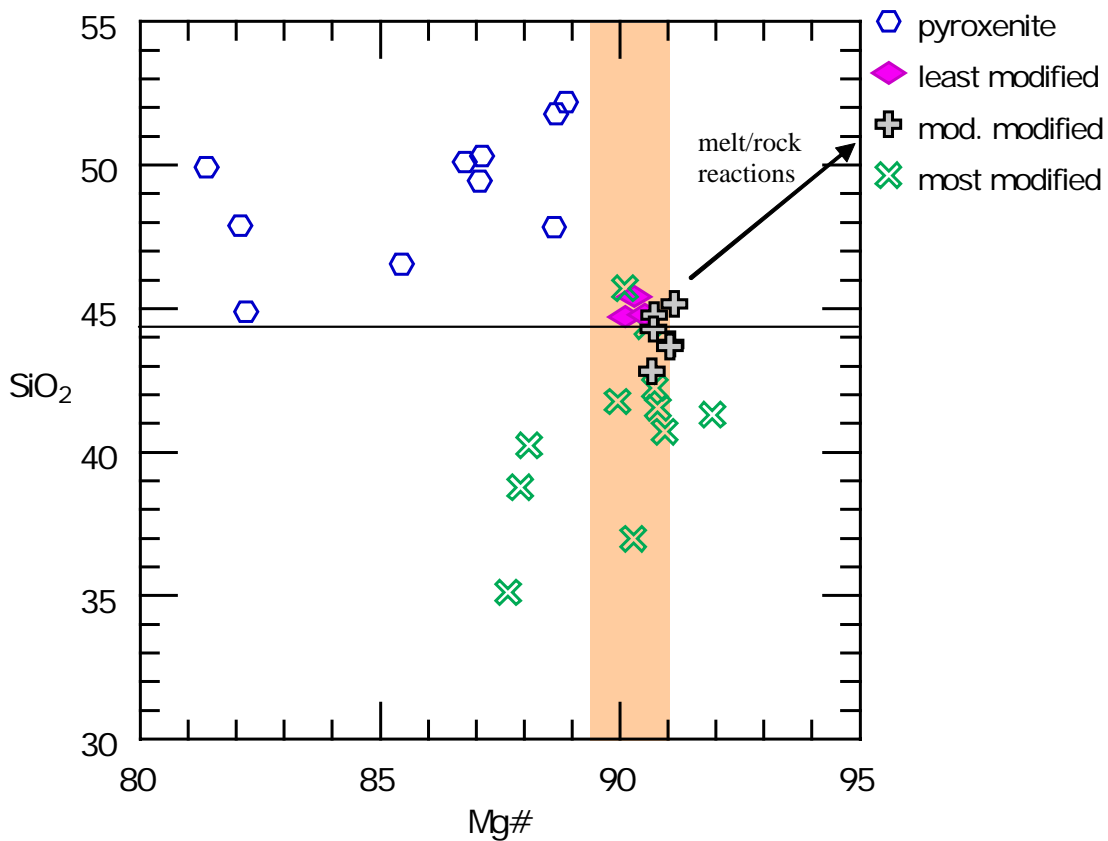


Figure 3.30. Subduction signature is shown by enrichment of  $\text{SiO}_2$  and  $\text{Mg}\# > 91.0$ . Few CM peridotites satisfy both criteria. The least modified show slight  $\text{SiO}_2$  enrichment, whereas the moderately modified peridotites have variable  $\text{SiO}_2$  content. The most modified peridotites do not show  $\text{SiO}_2$  enrichment and have a wide range of  $\text{Mg}\#$ . The pyroxenites, with lower  $\text{Mg}\#$ , show very enriched  $\text{SiO}_2$ , as expected due to the lower amount of olivine. Black line is at 44.3wt%  $\text{SiO}_2$  (Herzberg, 2004); orange field is the range of average  $\text{Mg}\#$  for depleted and fertile peridotite (Walter, 1998).

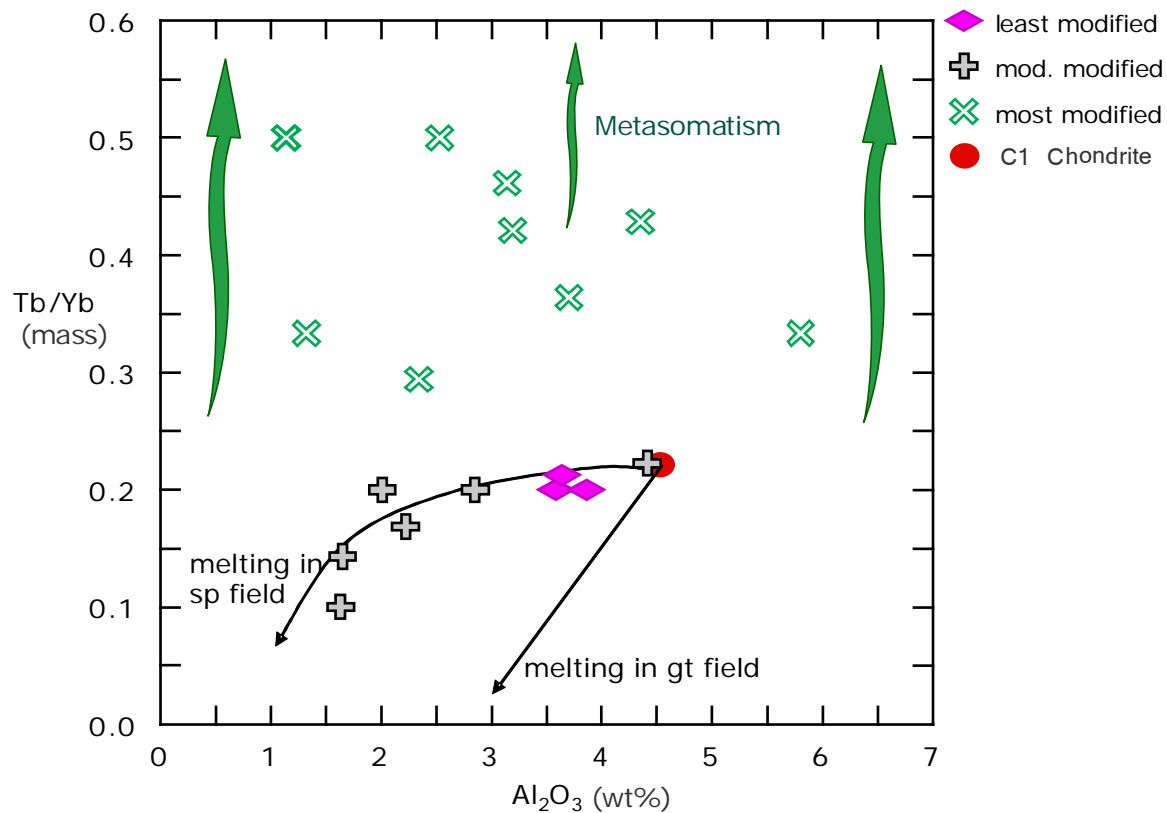


Figure 3.31.  $Tb/Yb$  vs.  $Al_2O_3$ (wt%) in Cerro Mercedes periodotites. Arrows indicate trends for melting in the spinel stability field (Bodinier et al., 1988) and for metasomatism.  $Tb/Yb$  is not normalized to chondrites, only the ratio is compared to chondritic ratio. Adapted from Peslier et al. (2002).

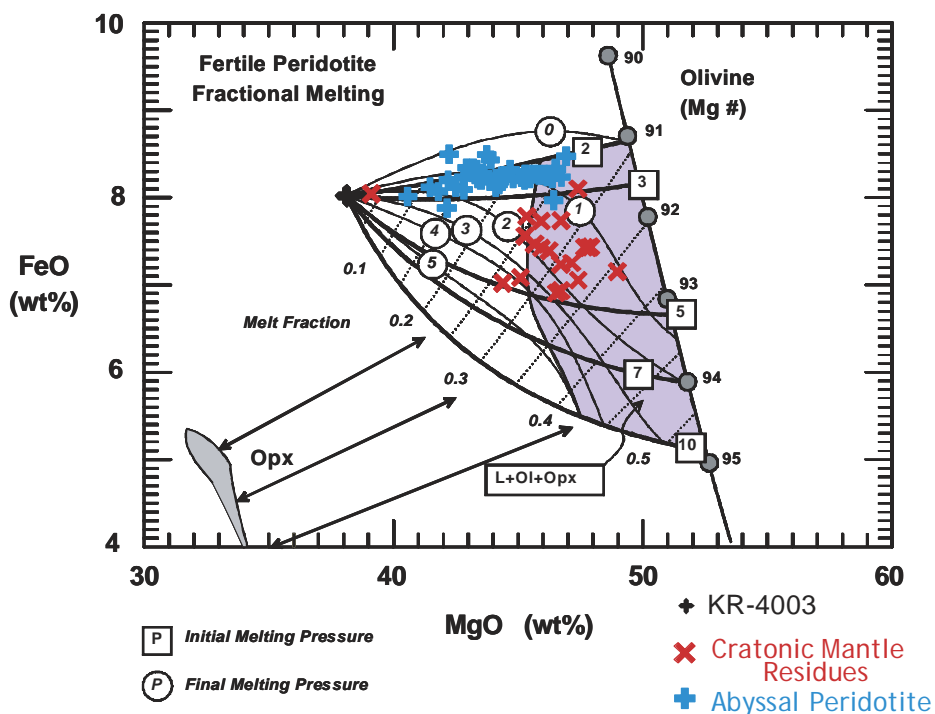


Figure 3.32. Fractional melting model from Herzberg (2004) showing different geodynamic environments for cratonic mantle residues and abyssal peridotites. Cratonic mantle residues have higher initial and final melting pressures than abyssal peridotites indicating a hotter mantle source.

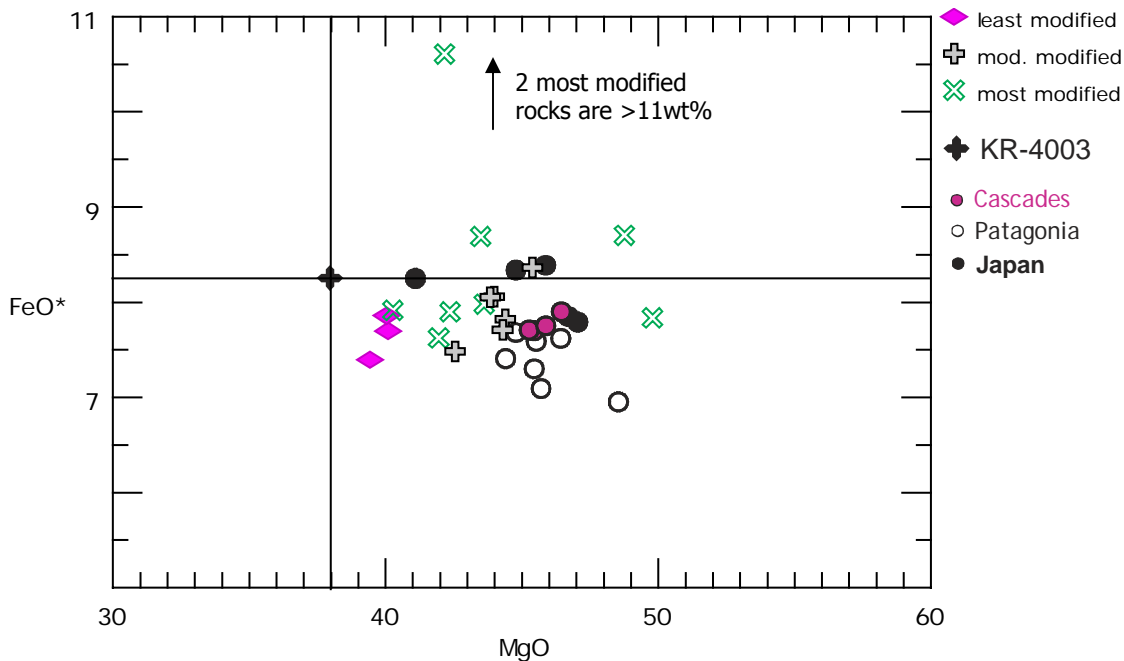


Figure 3.33.  $\text{FeO}^*$  vs.  $\text{MgO}$ . Comparison of CM peridotites with other back-arc peridotites (Brandon & Draper, 1996; Parkinson & Pearce, 1998; Laurora et al., 2001).

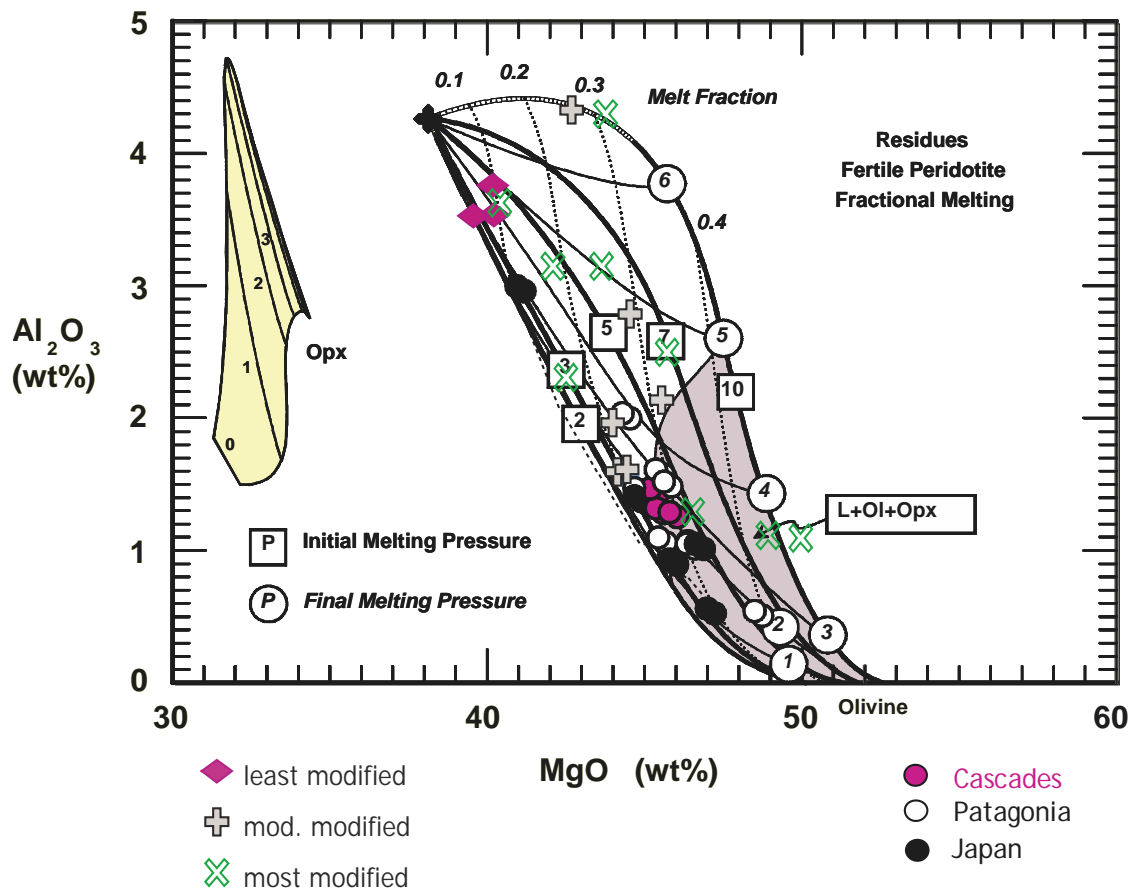


Figure 3.34.  $\text{Al}_2\text{O}_3$  vs.  $\text{MgO}$  fractional melting diagram from Herzberg (2004). Comparison of CM peridotites with other back-arc peridotites (Brandon & Draper, 1996; Parkinson & Pearce, 1998; Laurora et al., 2001) with symbols as shown.

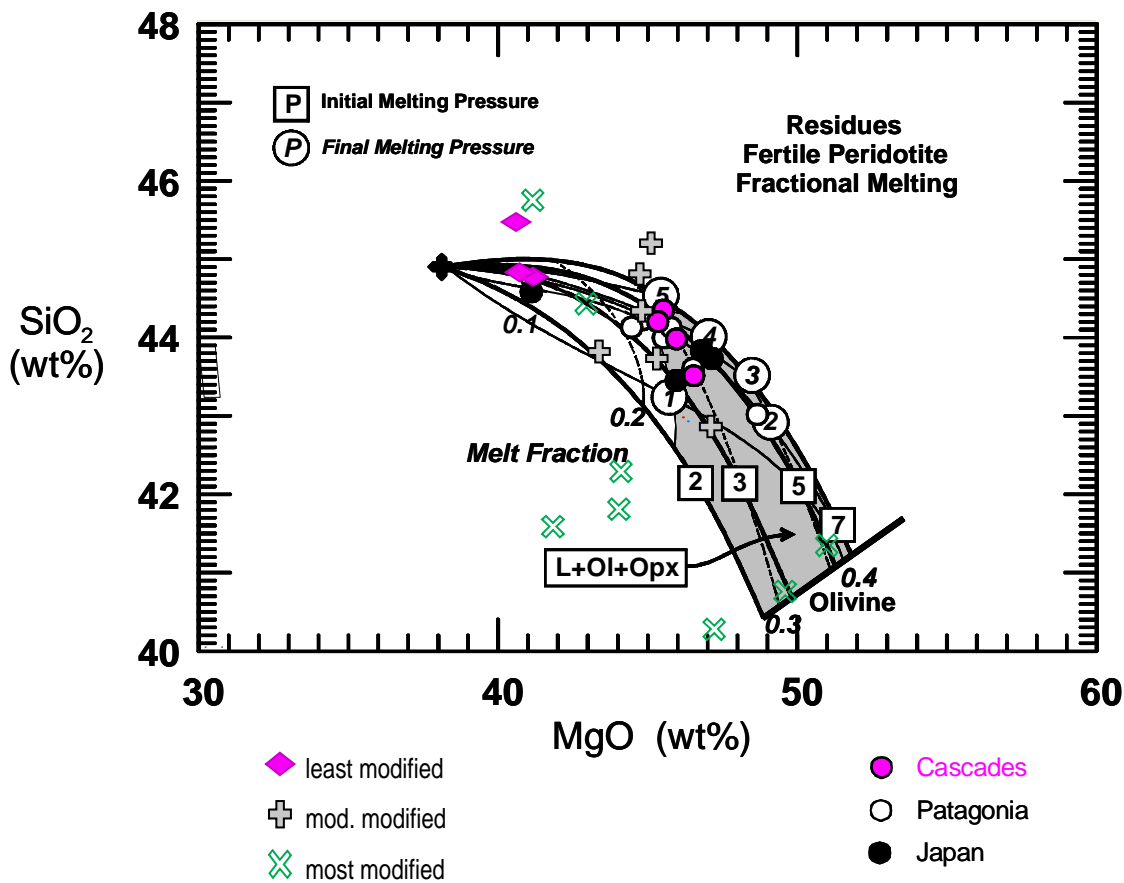


Figure 3.35. SiO<sub>2</sub> vs. MgO fractional melting diagram from Herzberg (2004). Comparison of CM peridotites with other back-arc peridotites (Brandon & Draper, 1996; Parkinson & Pearce, 1998; Laurora et al., 2001) with symbols as shown.

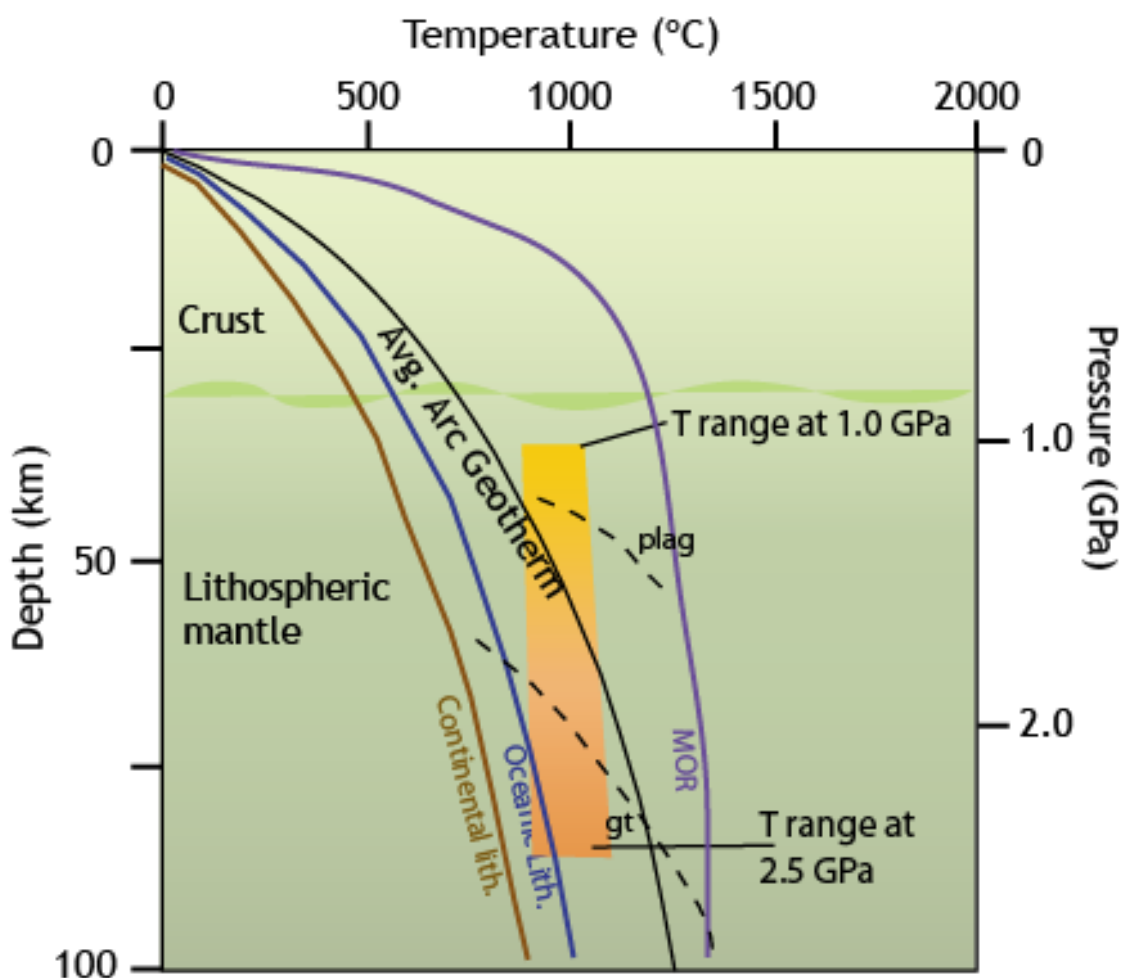


Figure 3.36. T-P-D diagram. Shows the relationship between equilibrium temperature, pressure and depth. Continental lithosphere, oceanic lithosphere and mid-ocean ridge geotherms taken from Blatt et al. (2006), plagioclase and garnet stability fields (dashed lines), which bracket the spinel stability field, taken from Green (mantle plumes.org).

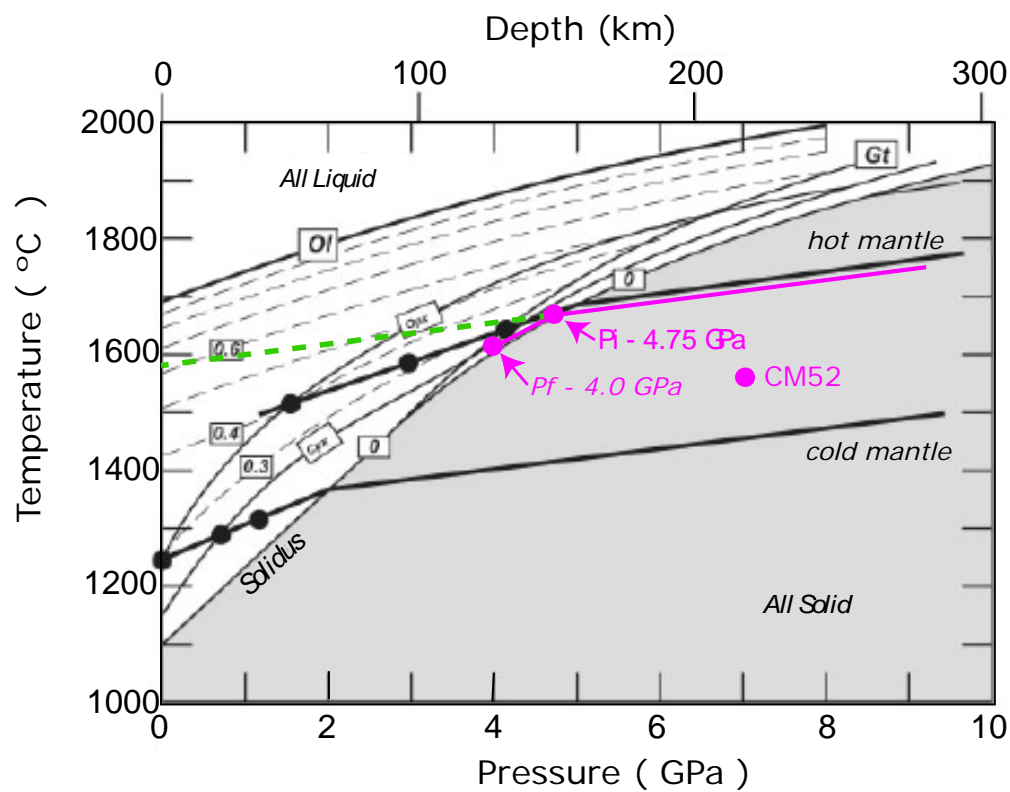


Figure 3.37. P-T diagram from Herzberg & O'Hara (2002). Green dashed line extended to read potential temperature of 1580°C. Pink dots are the path taken by CM52 at the initial pressure of melting and final pressure of melting. The placement of the dots is read from the modeling space.

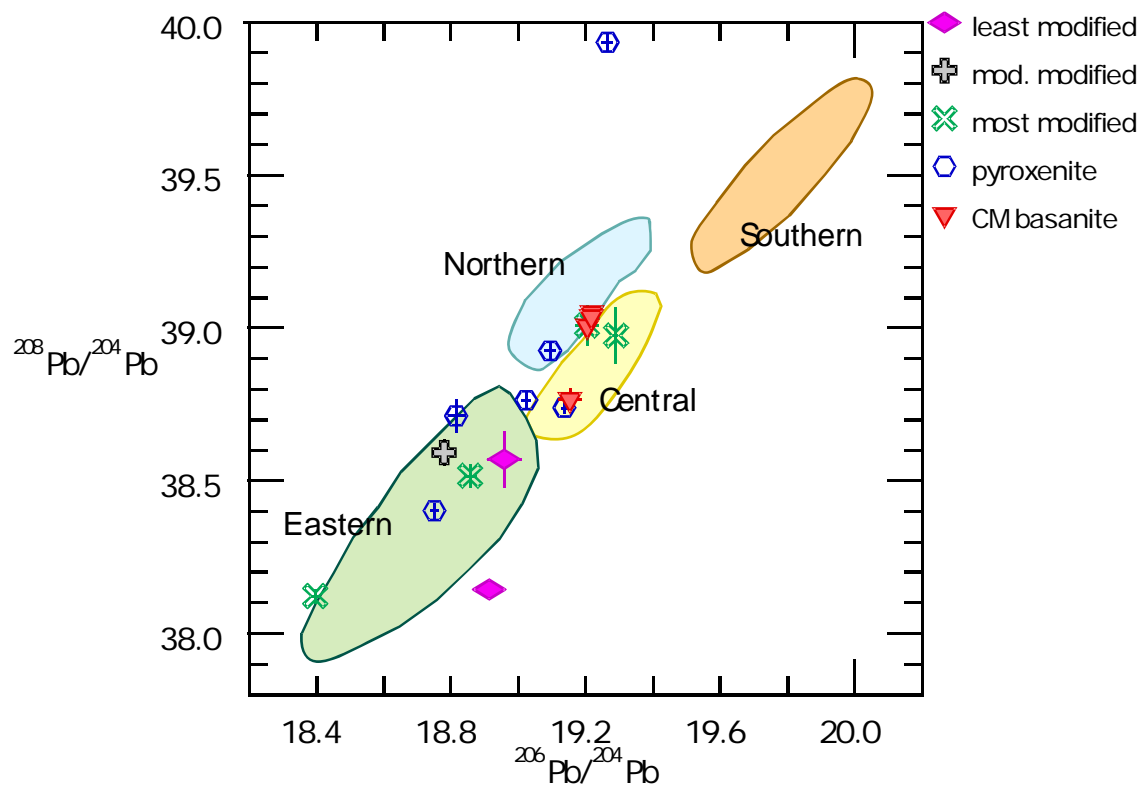


Figure 3.38. CM xenolith and host basanite Pb isotopes against the Galapagos domains as defined by Werner et al. (2003). Most samples fall in the eastern and central domains.

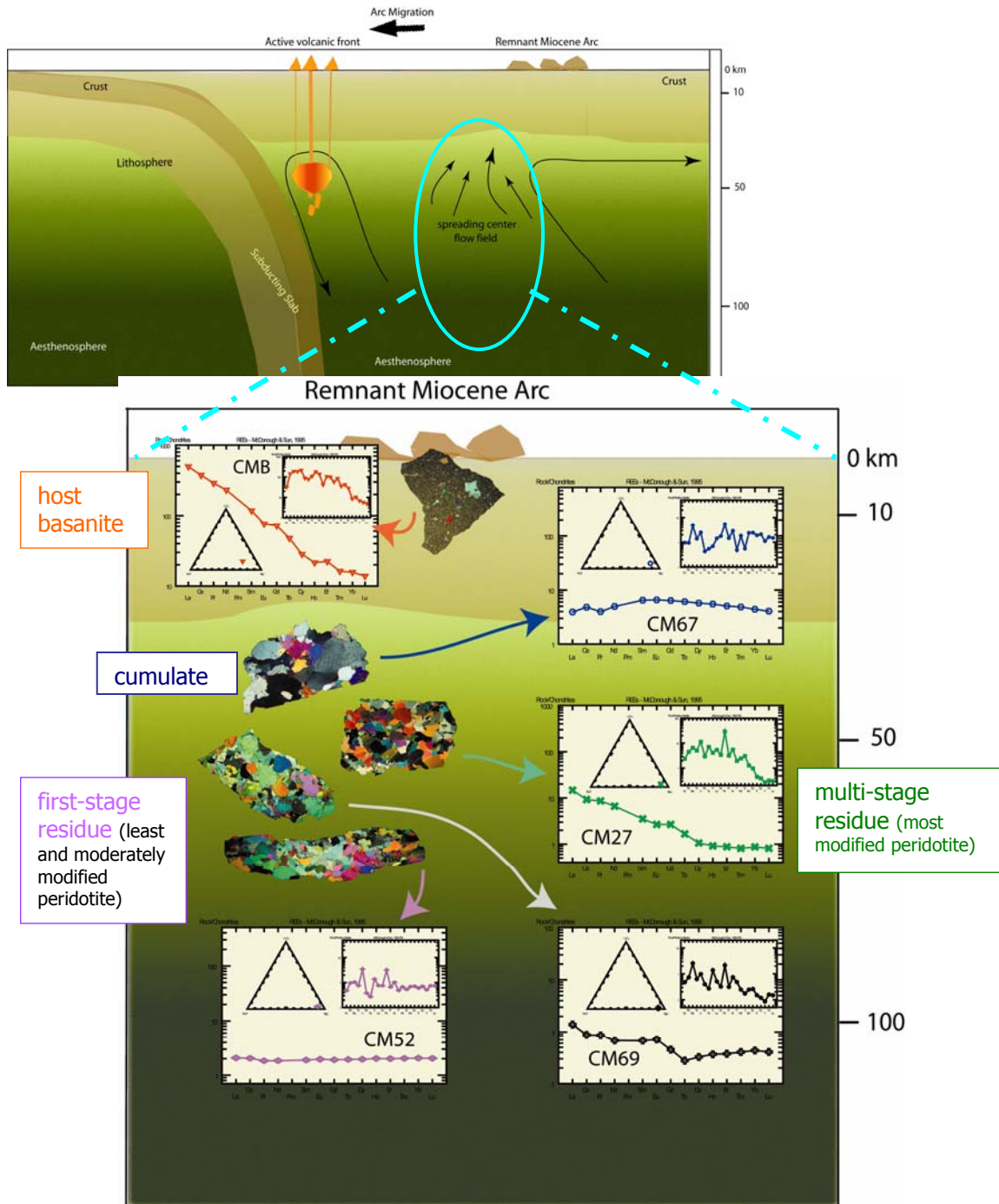


Figure 3.39. Summary. Cartoons show the location of the back-arc, where the host basanite brought up a variety of xenoliths, reflecting the heterogeneity of the mantle wedge and a blow-up of the spreading center flow field. Representatives of variably modified peridotites, pyroxenites and the host basalt are shown with significant geochemistry. Relative stratigraphy places the least modified peridotite at greatest depth.

Table 3.1. Cerro Mercedes Sample Catalog

Sample #	Bag	Lot	Bloc k	Incl .	length	width	depth	area	Incl.	Description
					h	h	h			
					cm	cm	cm			
				a	b	c	axb	diaxdi a	X#	
				dia	dia	dia				
1	AA9	5	1		3	2.5		7.5	1	Lherz Px>Ol spinel somewhat altered
2	7AA	7AA	1	a	1	1		1.0	2	Bright green PX - 2a
3	7AA	2	a		2.5	2.5		6.3	3	dark Incl w px, diop, ol, spinel
4	7AA	2	b		1.5	1.5		2.3	4	Dunite light green Ol plus a little spinel
5	7AA	3	a		0.5	0.5		0.3	5	Lherz, diop
6	7AA	3	b		0.4	0.4		0.2	6	Dunite, Ol w tiny spinel
7	7AA	3	c		1.5	1.5		2.3	7	Black Incl. Shiny black spinel
	7AA	4						0.0		4 or 5<1cm xenos, possible WR sample
8	AA	1	a		5	5		25.0	8	Dunite w black metallic spinel and some cpx
9	AA	1	b		2	2		4.0	9	Iherz.
10a	AA	1	c		1	1		1.0	10a	small dunite inclusion
10b	AA	1	d		1	1		1.0	10b	Black incl., weathering, light col.reaction rim
11	AA	2	a		1.2	1.2		1.4	11	Iherz, dunite pair
12	AA	2	b		2.8	2.8		7.8	12	Diop, spinel, plag?, react rim
13	AA	2	c		3	3		9.0	13	Drk grn Lherz
14a	AA	3a	a		3	2		6.0	14	Pale Lherz lots of ol, cpx
14b	AA	3b	a		3	2		6.0	14	"
15	AA	3b	b		1.5	1.5		2.3	15	dark green Incl; surface weathering
16	AA	3b	c		2	2		4.0	16	Black Incl
17	AA	4			1.7	1.7		2.9	17	Dark green and black incl - surface weathering
18	AA	5a	a		4	2.5		10.0	18	Dunite w balck metallic spinel and some cpx
19a	AA	5a	b		3	3		9.0	19	Lherz w yellowed core
19b	AA	5b	b		4	2	1	8.0	19	Lherz w yellowed core
19c	AA	5c	b		2.5	2	1	5.0	19	Lherz w yellowed core
20a	AA	6			1.8	1.8		3.2	20	Lherz
20b	AA	7			1.6	1.6		2.6	20b	Lherz
21a	AA	8						0.0	21	Dunite; black metallic oxide ; Cr- cpx; sp lineation
21b	AA	10			2	2		4.0	21b?	Dunite w balck metallic spinel and some cpx
22	AA	9	a		3	0.5		1.5	22	Zoned Lherz w 0.5mm olivine xtal
23	AA	9	b		3	1.4		4.2	23	Lherz
24	2-	1			2.5	2		5.0	24	Lherz pxs>ol
24	2-	2			2.5	2		5.0	24	Lherz pxs>ol
25	3-	1	a		2	1.5		3.0	25	Yellowish (altered Dunite) w bright green px
26	3-		b		2	1.5		3.0	26	Dark layered pyroxenite
27	4-	1	a		2	2		4.0	27	light colored Lherzolite
27	4-	1a	a		2.5	2	1.5	5.0	65=27	Lherz
27	4-	1b	a						65=27	Lherz
28	4-		b		1	1		1.0	28	Dark olivine pyroxenite
29	4-	2	a		1.5	1		1.5	29	Dark olivine pyroxenite; sp
30	4-		b		1.2	1.2		1.4	30	Lherzolite; sp
31	4-		c		1	1		1.0	31	Dunite; sp; Cr
32a	5-	1	a		4	3.5		14.0	32	Lherz
32b	5-	2	a		4	3.5		14.0	32b	Lherz

Table 3.1. Continued

Sample #	Bag		length	width	depth	area axb	Incl.	X#	Description
	Lot	Block	cm	cm	cm				
			a	b	c				
33	5-	b	6	1.75		10.5	33		Dunite w spinel and cr-diop
34	5-	c	1	1		1.0	34		Dunite w spinel and cr-diop
35	5-	d	1.5	1		1.5	35		Dark grained pyroxenite
36	5-	b	2	1.5		3.0	36		Lherz
37	1-	1 a	5	2.5		12.5	37		Lherz; oxides
38	1-	1 b	1.5	1.5		2.3	38		Dunite; Cr?
39	1-	2 a	3	1.5		4.5	39		Dunite (pale green); oxides; Cr
40	1-	2 b	1.5	1		1.5	40		Pyroxenite
41	1-	3a a	2.5	1.5		3.8	41		Dunite w spinel pxs
41b	1-	3b a	2.5	1.5		3.8	41b		Dunite w spinel pxs
42	1-	3a b	3	1	0.3	3.0	42		Dunite w spinel layer, apple green color
43	1-	3b b	1.5	1.5		2.3	43		dunite
43b	1-	3b d	1	1		1.0			grey glob fine grained
43c	1-	3b e	2	0.75		1.5			dunite
44	2-	1a a	2.2	2	1	4.4	44		Ol pyrnt strong cleavage drk grn and med grn
44b	2-	1b a							other half of same xeno
45	2-	2a a	2	0.9		1.8	45		Ol pyroxenite, minor spinel
46	2-	2b b	1.8	0.6		1.1	46		pyroxenite w cr diop.
47	2-	3 a	3.5	3		10.5	47		Dunite with lots of randomly placed spinel
48	2-	4 a	3	2	1	6.0	48		Dunite with spinel layers.
49	2-	5 a	2.8	1		2.8	49		Dunite with less well defined spinel layers.
50	2-	6a a	3.5	2.5		8.8	50		Lherz ol opx cr diop lght grn speckled looking
50	2-	6b a	2.5	1.5		3.8	50		Lherz
51	2-	6b b	2	1	0.5	2.0	51		Dunite w spinel
52	2-	7 a	4	2	1.5	8.0	52		Lherz similar to 6aa but may be more cr diop
53	2-	8 a	5	1.5		7.5	53		Lherz w more ol and less cr diop
54	2-	8 b	2	1		2.0	54		Lherz
55	2-	8 c	1.5	1.5		2.3	55		Lherz
55a	2-	8 other							other small xenos and 0.5 cm plag xtal
56	2-	9	2	1.2		2.4	56		Dunite fragment very glassy looking
57	3-	1a a	3.5	3	3	10.5	57		Dunite w cr diop
	3-	1b a							Dunite
	3-	1c a							Dunite
58	3-	2a a	5	3.5	3	17.5	58		Lherz, Ol opx cr diop, spinel
	3-	2b a							
59	3-	3 a	3	3		9.0	59		Dunite
60_pd	3-	3 b	3.5	3.5	0.5	12.3	60		Lherz cpx>ol> opx - faint layering
60_px	3-	3 c							pyroxenite
61	3-	4 a	4	3	0.5	12.0	61		Lherz ol> cr diop> opx>spinel
62	3-	4 b	2.2	1		2.2	62		Lherz ol>opx>spinel> cr diop
63	3-	5a a	6	3.5	2	21.0	63		Pyroxenite Opx>ol>cr diop
	3-	5bcde a	3	1.5	1	4.5			same as above but small fragments

Table 3.1. Continued

Table 3.2. Major Oxide composition of mantle peridotite from literature.

	TYPE	SiO <sub>2</sub>	TiO <sub>2</sub>	Al <sub>2</sub> O <sub>3</sub>	Cr <sub>2</sub> O <sub>3</sub>	FeO	MnO	MgO	CaO	NiO	Na <sub>2</sub> O	K <sub>2</sub> O	P <sub>2</sub> O <sub>5</sub>
Herzberg (1993)	AV	44.3	0.09	2.36	0.43	8.31	0.13	41.64	2.2	0.27	0.23	0.04	
Hutchinson, (1974)	AV	44.65	0.12	2.27	0.43	8.12	0.12	41.6	2.14		0.21	0.06	
Hischmann et al, 1998	FP	45.47	0.11	4	0.68	7.22		38.53	3.59		0.31		
Hischmann et al, 1999	DP	44.65	0.04	2.37	0.4	8.15		42.14	2.14		0.06		
Caswell, 1980*	AV	44.48	0.18	1.8	0.42	8.9	0.14	41.77	2.34		0.13	0.04	< 0.01
Hofmann (1988)	PM	45.96	0.181	4.06		7.54		37.78	3.21	0.27	0.332	0.06	
Hart and Zindler (1986)	PM	45.96	0.18	4.06	0.47	7.54	0.13	37.78	3.21	0.28	0.33	0.03	
Ringwood, 1969 McDonough & Sun, 1995	Pyrolite	45.1	0.17	3.3	0.43	8	0.14	38.1	3.1		0.13	0.57	0.06
	Pyrolite	45	0.201	4.45	0.384	8.05	0.135	37.8	3.55	0.25	0.36	0.029	0.02
AVERAGE		45.06	0.14	3.19	0.46	7.98	0.13	39.68	2.83	0.27	0.23	0.12	0.04
AVG only peridotites		44.77	0.09	2.75	0.49	7.95	0.13	40.98	2.52	0.27	0.20	0.05	

AV, average sp. Iherzolite

FP, fertile peridotite

PM, primitive mantle

DP, depleted peridotite

\* based on peridotite, kimberlite and basalt

Table 3.3. List of samples chosen for chemical analyses.

CM-3	CM-37	CM-58
CM-8	CM-39	CM-59
CM-13	CM-41	CM-60
CM-14	CM-44	CM-61
CM-18	CM-47	CM-63
CM-19	CM-48	CM-64
CM-24	CM-50	CM-67
CM-27	CM-52	CM-68B
CM-32	CM-53	CM-69
CM-33	CM-57	CM-70

Table 3.4. Major and trace element concentration and isotope ratios in CM host basanite. Major oxides are in wt%; trace elements in ppm.

Sample	SiO <sub>2</sub>	TiO <sub>2</sub>	Al <sub>2</sub> O <sub>3</sub>	Fe <sub>2</sub> O <sub>3</sub>	MnO	MgO	CaO	Na <sub>2</sub> O	K <sub>2</sub> O	P <sub>2</sub> O <sub>5</sub>	Li	Sc	V
CM8ma	44.49	1.65	11.17	9.46	0.16	14.5	10.19	2.54	2.87	1.14	5.56	16.26	157.29
CM27ma	44.37	1.76	12	9.36	0.16	12.37	10.71	2.7	3.03	1.21	5.74	18.49	175.84
CM37ma	44.42	1.71	11.96	9.25	0.15	12.73	10.37	2.74	3.16	1.17	5.81	18.61	169.34
CM53ma	44.01	1.66	11.47	9.35	0.16	14.1	10.19	2.61	3.01	1.14	5.65	16.82	169.55
Sample	Cr	Co	Ni	Cu	Zn	Rb	Sr	Y	Zr	Nb	Mo	Cs	Ba
CM8ma	546.32	41.54	383.01	56.86	103.2	105.5	1925	28.81	359.7	54.43	3.31	0.7	1232
CM27ma	411.35	36.62	274.83	64.02	99.6	66.93	2162	29.88	389	59.72	3.62	0.66	1270.4
CM37ma	484.38	39.06	316.39	67.84	99.55	86.73	2000	29.45	367.8	57.83	3.88	0.67	1254
CM53ma	529.83	41.21	378.28	60.96	102.9	65.64	1983	29.85	376.1	55.61	3.55	0.62	1219.3
Sample	La	Ce	Pr	Nd	Sm	Eu	Gd	Tb	Dy	Ho	Er	Tm	Yb
CM8ma	115.69	223.47	26.79	106.7	17.38	4.17	14.3	1.8	7	1.15	3.58	0.4	2.61
CM27ma	119.52	235.29	28.18	114.22	18.26	4.59	15.18	1.88	7.2	1.18	3.56	0.42	2.71
CM37ma	117.54	230.61	26.86	105.69	17.44	4.29	14.31	1.72	6.94	1.17	3.57	0.4	2.52
CM53ma	115.98	230.55	26.28	103.97	17.21	4.18	13.51	1.77	7.14	1.25	3.41	0.4	2.56
Sample	Lu	Hf	Ta	W	Tl	Pb	Th	U					
CM8ma	0.35	5.13	2.82	1.17	0.04	5.29	13.07	4.21					
CM27ma	0.36	5.57	3	1.26	0.03	5.55	16.06	4.62					
CM37ma	0.34	5.14	2.87	1.22	0.03	6.16	14.69	4.36					
CM53ma	0.35	5.23	2.77	1.18	0.03	5.15	14.14	4.17					
Sample	<sup>87</sup> Sr/ <sup>86</sup> Sr	<sup>143</sup> Nd/ <sup>144</sup> Nd			<sup>206</sup> Pb/ <sup>204</sup> Pb			<sup>207</sup> Pb/ <sup>204</sup> Pb		<sup>208</sup> Pb/ <sup>204</sup> Pb			
CM8ma	0.703519	0.512912			19.219			15.56		39.005			
CM27ma	0.703532	0.512896			19.233			15.562		39.05			
CM37ma	0.703526	0.512856			19.168			15.496		38.766			
CM53ma	0.703515	0.512917			19.231			15.572		39.037			

Table 3.5. Modal analysis of CM xenoliths.

Area phase %	CM8	CM14	CM19	CM27	CM32	CM41	CM50	CM52	CM53	CM57
Ol	87.7	73.2	59.9	89.7	61.0	93.6	80.2	84.3	68.5	98.0
Cpx	1.5	7.1	9.0	1.6	14.0	5.8	4.7	9.4	2.9	1.2
Opx	8.7	17.8	29.5	6.2	23.3	0.0	13.3	6.3	28.1	0.0
Sp	2.2	1.9	1.6	2.5	1.7	0.6	1.8	trace	0.6	0.8
Total	100.0	100.0	100.0	100.0	100.0	100.0	100.0	100.0	100.0	100.0
<b>density</b>										
3.8	Ol	336.0	280.4	229.4	343.6	233.6	358.5	307.2	322.9	262.4
3.4	Cpx	5.0	24.2	30.6	5.4	47.6	19.8	16.0	32.0	9.7
3.6	Opx	30.9	63.6	105.5	22.2	83.3	0.0	47.6	22.5	100.3
4.2	Sp	9.1	7.9	6.7	10.5	7.3	2.4	7.4	0.0	2.5
Total		381.0	376.1	372.2	381.7	371.7	380.7	378.3	377.4	374.9
<b>Modal Weight%</b>										
	Ol	88.2	74.6	61.6	90.0	62.8	94.2	81.2	85.6	70.0
	Cpx	1.3	6.4	8.2	1.4	12.8	5.2	4.2	8.5	2.6
	Opx	8.1	16.9	28.3	5.8	22.4	0.0	12.6	6.0	26.8
	Sp	2.4	2.1	1.8	2.8	2.0	0.6	2.0	0.0	0.7
Rock Name	hz	lz	lz	d	lz	d	hz	lz	hz	d
<hr/>										
Area phase %	CM58	CM59	CM60_pd	CM60_px	CM61	CM63	CM64	CM67	CM69	
Ol	82.8	81.8	81.6	3.9	81.9	10.9	0.8	5.6	95.3	
Cpx	2.7	4.5	2.7	84.8	10.5	84.9	76.1	82.6	3.0	
Opx	14.0	12.7	15.7	8.6	7.0	4.1	22.7	11.0	1.0	
Sp	0.6	1.0	trace	2.7	0.7	0.1	0.5	0.8	0.7	
Total	100.1	100.0	100.0	100.0	100.1	100.0	100.1	100.0	100.0	
<b>density</b>										
3.8	Ol	317.1	313.3	312.5	14.9	313.7	41.7	3.1	21.5	365.0
3.4	Cpx	9.2	15.3	9.1	288.3	35.7	288.6	258.7	280.8	10.2
3.6	Opx	50.1	45.4	56.2	30.9	25.0	14.7	81.2	39.4	3.6
4.2	Sp	2.5	4.2	0.0	11.3	2.0	0.4	2.1	3.3	3.0
Total		378.9	378.2	377.8	345.4	376.4	345.5	345.1	345.0	381.7
<b>Modal Weight%</b>										
	Ol	83.7	82.8	82.7	4.3	83.3	12.1	0.9	6.2	95.6
	Cpx	2.4	4.0	2.4	83.5	9.5	83.5	75.0	81.4	2.7
	Opx	13.2	12.0	14.9	8.9	6.6	4.3	23.5	11.4	0.9
	Sp	0.7	1.1	0.0	3.3	0.5	0.1	0.6	1.0	0.8
Rock Name	hz	hz	hz	web	lz	ol-cpx	web	ol-web	d	

Table 3.6. Major oxides (wt%), trace elements (ppm) and isotope ratios for the CM xenoliths.

Sample	SiO <sub>2</sub>	TiO <sub>2</sub>	Al <sub>2</sub> O <sub>3</sub>	Fe <sub>2</sub> O <sub>3</sub>	MnO	MgO	CaO	Na <sub>2</sub> O	K <sub>2</sub> O	P <sub>2</sub> O <sub>5</sub>	Total
CM-3	49.44	0.2	6.6	5.71	0.13	19.36	18.44	0	0.08	0.03	99.99
CM-8	40.71	0.03	1.14	9.83	0.15	49.56	0.39	0	0.01	0.01	101.83
CM-13	46.55	0.41	9.65	6.58	0.13	19.46	16.28	0.18	0.29	0.14	99.67
CM-14	45.42	0.12	3.58	8.66	0.14	40.57	2.9	0	0.16	0.04	101.59
CM-18	41.54	0.09	3.14	8.44	0.14	41.8	4.24	0	0.08	0.03	99.5
CM-19	44.72	0.1	3.86	8.97	0.13	41.13	2.76	0	0.07	0.01	101.75
CM-24	50.31	0.19	3.99	6.31	0.14	21.49	18.48	0	0.06	0.02	100.99
CM-27	42.24	0.09	4.35	8.96	0.13	44.07	1.49	0	0.12	0.04	101.49
CM-32	45.7	0.1	3.7	8.98	0.14	41.12	2.62	0	0.02	0.01	102.39
CM-33	41.76	0.11	3.19	9.77	0.15	44	2.27	0	0.13	0.04	101.42
CM-37	44.38	0.07	2.34	8.89	0.13	42.91	2.8	0	0.1	0.03	101.65
CM-39*	33.60	0.04	2.97	8.75	0.14	40.87	0.63	0.00	0.01	0.01	87.0099
CM-41	40.23	0.03	1.32	12.66	0.18	47.19	0.79	0	0.01	0.01	102.42
CM-44	52.18	0.19	4.32	4.52	0.11	18.17	20.86	0	0.06	0.03	100.44
CM-47	38.77	0.04	2.53	12.58	0.18	46.09	0.35	0	0.01	0.01	100.56
CM-48	35.11	0.06	5.8	11.78	0.17	42.13	0.57	0	0	0.01	95.63
CM-50	43.77	0.04	4.41	8.47	0.13	43.34	1.99	0	0.02	0.01	102.18
CM-52	44.78	0.12	3.64	8.48	0.13	40.69	3.51	0	0.04	0.01	101.4
CM-53	43.68	0.05	2.85	8.86	0.13	45.27	1.32	0	0.03	0.01	102.2
CM-57	41.3	0.02	1.13	8.91	0.13	50.95	0.22	0	0.01	0.01	102.68
CM-58	44.76	0.04	1.63	9.1	0.14	44.7	1.53	0	0.01	0.01	101.92
CM-59	42.81	0.03	2.22	9.64	0.14	47.08	0.96	0	0	0.01	102.89
CM-60	47.84	0.1	3.2	7.35	0.14	28.83	13.55	0	0.03	0.01	101.05
CM-61	44.29	0.04	2.01	9.14	0.14	44.77	1.95	0	0.01	0.01	102.36
CM-63	50.11	0.15	3.27	6.97	0.14	23.01	17.18	0	0.02	0.01	100.86
CM-64	49.92	0.41	7.05	8.62	0.17	18.98	15.35	0.11	0.11	0.02	100.74
CM-67	44.88	0.38	7.58	8.65	0.15	20.13	15.02	0.01	0.02	0.01	96.83
CM-68B	47.88	0.43	7.01	8.38	0.15	19.35	17.5	0.08	0.03	0.01	100.82
CM-69	45.15	0.03	1.65	8.72	0.13	45.08	1.18	0	0.04	0.01	101.99
CM-70	51.78	0.31	4.61	4.63	0.1	18.24	20.14	0.14	0.17	0.03	100.15

\* not enough sample for complete analysis

Table 3.6. Continued

Sample	Li	Sc	V	Cr	Co	Ni	Cu	Zn	Rb
CM3	7.68	63.87	197.03	2134.76	42.84	362.25	25.47	37	1.56
CM8	2.05	3.99	21.99	3798.41	124.25	1873.12	7.89	103.96	0.43
CM13	10.94	52.78	201.92	1526.17	45.22	525.78	44.95	58.03	8.5
CM14	3.83	6.76	33.28	1909.34	78.65	1414.43	36.46	136.36	1.57
CM18	6.59	13.7	67.42	3993.75	176.58	2987.04	21.33	109.3	2.57
CM19	5.3	24.9	123.09	7647.14	295.21	5646.09	53.33	217.13	3.5
CM24	7.12	14.22	65.87	5693.12	121.35	2025.9	21.94	118.94	1.79
CM27	5.6	6.41	31.69	1465.79	104.54	1892.6	55.29	88.7	2.69
CM32	9.18	15.91	68.68	2312.7	105.44	1831.95	81.3	73.1	5.39
CM33	5.09	9.62	41.06	3230.64	116.42	1893.53	39.45	73.85	5.26
CM37	6.43	11.16	50.19	1889.24	104.99	1862.27	36.28	80.9	1.95
CM41	2.59	12.23	53.31	2477.53	108.95	1862.59	9.5	75.95	0.56
CM44	5.14	73.03	195.07	2070.5	31.95	302.98	17.21	55.75	1.17
CM47	3.17	4.32	44.76	11034.11	146.28	1805.03	10.01	92.34	1.25
CM48	2.76	5.47	116.41	35589.3	148.27	1988.25	16.86	547.78	0.3
CM50	5.41	10.81	42.59	1853.66	104.14	1988.04	20.51	54.93	0.41
CM52	4.29	6.87	67.92	16159.02	132.89	1927.11	23.37	231.69	0.58
CM53	4.68	10.51	37.69	2700	116.19	2102.64	27.09	64.65	0.48
CM57	2.66	8.23	33.45	1823.34	112.73	2217.44	12.11	75.95	1.13
CM58	3.25	8.18	34.1	2185.83	113.38	2253.01	14.89	72.55	0.19
CM59	3.33	4.45	46.67	10550.53	146.37	1858.34	30.52	147.81	0.28
CM60	4.67	39.39	115.86	4549.22	72.65	839.14	15.92	54.41	0.62
CM61	3.85	7.99	30.32	2638.59	111.8	2249.29	17.13	74.95	0.26
CM63	4.25	59.53	155.11	2645.36	61.31	511.79	9.64	135.38	0.6
CM64	7.38	54.58	278.71	1866.59	87.53	1865.33	65.69	57.67	1.23
CM67	3.01	65.11	249.68	1675.94	64.31	369.02	77.04	73.72	0.57
CM68b	3.69	70.22	281.95	1160.27	57.88	337.53	45.85	78.25	0.72
CM69	2.83	10.37	39.71	2635.61	113.31	2003.13	50.88	80.81	0.44
CM70	9.69	52.97	141.47	2824.82	34.07	262.76	31.18	64.24	2.78
Sample	Sr	Y	Zr	Nb	Mo	Cs	Ba	La	Ce
CM3	155.69	3.92	15.62	1.83	0.19	0.03	50.52	2.97	5.23
CM8	13.08	0.16	2.47	0.49	0.12	0.01	11.92	0.51	0.75
CM13	229.2	5.83	34.95	4.21	0.35	0.07	139.61	9.35	16.12
CM14	11.63	1.8	4.22	0.34	0.22	0.02	12.39	0.47	1.02
CM18	16.42	1.22	12.28	2.02	0.25	0.03	48.42	2.85	4.8
CM19	24.72	2	5.45	0.53	0.23	0.03	23.22	0.79	1.39
CM24	55.62	3.01	8.8	1.31	0.14	0.03	41.91	2.28	4.24
CM27	109.31	1.15	31.96	1.95	0.63	0.05	42.97	3.49	5.65
CM32	87.48	1.8	15.21	2.68	0.31	0.04	68.36	4.08	6.61
CM33	85.25	1.95	15.9	2.21	1.82	0.04	64.03	3.4	5.61
CM37	98.4	1.3	9.72	1.4	1.13	0.03	43.64	2.41	4.1
CM41	90.38	0.2	2.6	0.47	0.2	0.01	13.82	0.55	0.86
CM44	80.66	3.06	10.71	1.45	0.22	0.02	36.82	2.7	5.48
CM47	24.46	0.16	5.14	0.52	2.93	0.02	12.69	0.65	0.93
CM48	15.23	0.15	3.85	0.29	0.3	0.01	12.34	0.69	0.82
CM50	21.84	0.52	2.61	0.38	0.19	0.01	12.07	0.49	0.82
CM52	20.51	2.21	5.55	0.25	0.17	0.01	6.93	0.49	1.25
CM53	81.71	0.56	3.41	0.42	0.22	0.01	8.21	0.62	1.04
CM57	21.88	0.16	3.36	0.46	0.3	0.02	12.69	0.64	0.9
CM58	22.5	0.45	1.37	0.16	0.09	0.01	4.12	0.13	0.26
CM59	21.4	0.31	1.43	0.18	0.14	0.01	5.67	0.17	0.3
CM60	101.19	1.44	3.41	0.53	0.12	0.02	11.95	0.8	1.56
CM61	2.21	0.48	1.93	0.24	0.11	0.01	6.45	0.31	0.56
CM63	39.81	2.07	3.23	0.57	0.09	0.02	20.07	0.65	1.71
CM64	139.28	4.19	9.48	0.82	0.24	0.02	29.86	1.79	4.16
CM67	57.46	4.73	5.82	0.28	0.14	0.02	31.44	0.93	2.95
CM68b	65.46	5.04	6.43	0.34	0.14	0.02	33.94	1.15	3.44
CM69	14.76	0.37	1.82	0.26	0.08	0.01	16.91	0.33	0.54
CM70	122.44	3.8	13.51	2.02	0.19	0.04	89.52	3.26	6.35

Table 3.6. Continued

Sample	Pr	Nd	Sm	Eu	Gd	Tb	Dy	Ho	Er
CM3	0.73	3.12	0.86	0.29	1.04	0.16	0.9	0.18	0.51
CM8	0.11	0.4	0.09	0.03	0.09	0.01	0.04	0.01	0.02
CM13	2.33	9.49	2.17	0.69	2.53	0.32	1.6	0.31	0.83
CM14	0.14	0.66	0.2	0.08	0.25	0.05	0.33	0.08	0.24
CM18	0.67	2.71	0.53	0.16	0.5	0.06	0.27	0.05	0.15
CM19	0.19	0.86	0.25	0.09	0.29	0.05	0.36	0.08	0.25
CM24	0.59	2.62	0.75	0.26	0.93	0.15	0.86	0.17	0.5
CM27	0.8	3.03	0.52	0.15	0.53	0.06	0.26	0.05	0.14
CM32	0.94	3.6	0.67	0.2	0.65	0.08	0.38	0.08	0.22
CM33	0.79	3.07	0.61	0.19	0.6	0.08	0.37	0.07	0.21
CM37	0.59	2.3	0.44	0.14	0.44	0.05	0.27	0.05	0.16
CM41	0.12	0.46	0.1	0.03	0.09	0.01	0.04	0.01	0.03
CM44	0.75	3.34	0.88	0.3	1.13	0.17	0.93	0.18	0.5
CM47	0.13	0.48	0.09	0.03	0.09	0.01	0.04	0.01	0.02
CM48	0.12	0.4	0.08	0.02	0.07	0.01	0.04	0.01	0.02
CM50	0.12	0.47	0.1	0.03	0.12	0.02	0.11	0.03	0.09
CM52	0.17	0.84	0.28	0.11	0.38	0.07	0.48	0.11	0.32
CM53	0.15	0.59	0.12	0.04	0.15	0.02	0.12	0.03	0.09
CM57	0.13	0.46	0.1	0.03	0.09	0.01	0.04	0.01	0.02
CM58	0.04	0.17	0.06	0.02	0.08	0.01	0.1	0.02	0.08
CM59	0.04	0.18	0.05	0.02	0.06	0.01	0.07	0.02	0.05
CM60	0.21	0.99	0.31	0.12	0.42	0.07	0.44	0.09	0.24
CM61	0.08	0.33	0.09	0.03	0.11	0.02	0.12	0.03	0.09
CM63	0.22	1.21	0.45	0.18	0.6	0.1	0.65	0.13	0.36
CM64	0.56	2.81	0.91	0.35	1.23	0.21	1.26	0.26	0.73
CM67	0.37	2.27	0.96	0.37	1.27	0.22	1.41	0.3	0.81
CM68b	0.45	2.55	1	0.4	1.38	0.24	1.49	0.31	0.84
CM69	0.08	0.31	0.1	0.04	0.09	0.01	0.08	0.02	0.06
CM70	0.89	4.05	1.26	0.46	1.49	0.21	1.19	0.24	0.65
Sample	Tm	Yb	Lu	Ta	W	Tl	Pb	Th	U
CM3	0.07	0.45	0.07	0.09	0.18	0.002	1.36	0.5	0.26
CM8	0.0038	0.02	0.0038	0.02	0.07	0.0006	0.43	0.11	0.05
CM13	0.12	0.72	0.11	0.21	0.27	0.0069	1.17	1.3	0.43
CM14	0.04	0.25	0.04	0.01	0.11	0.0005	0.91	0.05	0.04
CM18	0.02	0.13	0.02	0.08	0.14	0.0011	0.65	0.38	0.13
CM19	0.04	0.25	0.04	0.02	0.12	0.001	0.27	0.1	0.05
CM24	0.07	0.43	0.06	0.06	0.09	0.0016	0.35	0.35	0.2
CM27	0.02	0.14	0.02	0.26	0.57	0.0016	4.38	0.4	0.23
CM32	0.03	0.22	0.04	0.11	0.24	0.0017	0.58	0.52	0.18
CM33	0.03	0.19	0.03	0.09	0.25	0.0021	2.16	0.44	0.15
CM37	0.03	0.17	0.03	0.06	0.13	0.0009	1.33	0.31	0.19
CM41	0.0038	0.03	0.0046	0.02	0.22	0.0006	1.3	0.09	0.07
CM44	0.07	0.42	0.06	0.07	3.59	0.0019	0.81	0.39	0.14
CM47	0.0037	0.02	0.0041	0.02	0.41	0.001	0.29	0.1	0.05
CM48	0.0038	0.03	0.0038	0.01	0.15	0.0012	1.08	0.06	0.04
CM50	0.01	0.09	0.02	0.02	0.49	0.0006	1.24	0.08	0.05
CM52	0.05	0.33	0.05	0.01	0.07	0.0011	0.48	0.06	0.07
CM53	0.01	0.1	0.02	0.02	0.41	0.0009	2.15	0.1	0.1
CM57	0.0032	0.02	0.0048	0.02	0.38	0.0018	0.62	0.11	0.05
CM58	0.01	0.1	0.02	0.01	0.05	0.0007	0.2	0.03	0.02
CM59	0.01	0.06	0.01	0.03	0.08	0.0008	2.02	0.03	0.02
CM60	0.04	0.23	0.03	0.03	0.1	0.0013	0.39	0.13	0.1
CM61	0.01	0.1	0.02	0.01	0.1	0.0006	0.35	0.05	0.07
CM63	0.05	0.3	0.04	0.03	0.04	0.0029	0.34	0.16	0.06
CM64	0.11	0.67	0.1	0.04	0.11	0.0016	1.06	0.25	0.15
CM67	0.12	0.71	0.1	0.02	0.13	0.0016	0.8	0.11	0.05
CM68b	0.12	0.72	0.11	0.02	0.06	0.0009	1.06	0.14	0.05
CM69	0.01	0.07	0.01	0.01	0.05	0.001	0.32	0.05	0.02
CM70	0.09	0.59	0.09	0.1	0.09	0.0034	1.35	0.6	0.21

Table 3.6. Continued

Sample	$^{87}\text{Sr}/^{86}\text{Sr}$	$^{143}\text{Nd}/^{144}\text{Nd}$	$^{206}\text{Pb}/^{204}\text{Pb}$	$^{207}\text{Pb}/^{204}\text{Pb}$	$^{208}\text{Pb}/^{204}\text{Pb}$
CM3	0.703568		19.151	15.621	38.739
CM8	0.704188				
CM13					
CM14	0.703741		18.928	15.381	38.144
CM18	0.703532				
CM19	0.703376		18.972	15.488	38.57
CM24	0.704422		19.038	15.547	38.763
CM27	0.704588		19.218	15.647	39.008
CM32	0.703375	0.513039	18.871	15.618	38.516
CM33	0.703517	0.51295	18.079	15.554	37.955
CM37	0.703545		18.411	15.559	38.122
CM41	0.703559		19.304	15.75	38.975
CM44	0.703585		19.279	15.621	39.935
CM47	0.703603				
CM48					
CM50					
CM52	0.703462				
CM53					
CM57	0.703621				
CM58	0.703649				
CM59	0.703605				
CM60	0.703538		18.83	15.708	38.712
CM61	0.703587		18.794	15.662	38.592
CM63	0.703382				
CM64	0.703531				
CM67	0.703634		18.765	15.503	38.401
CM68b	0.703584				
CM69	0.703724	0.512914			
CM70	0.703614		19.109	15.611	38.925

Table 3.7. Equilibrium temperatures

Sample	Type	T(°C); 1GPa	T(°C); 2.5GPa
<b>CM69</b>	peridotite	949.1	975.2
<b>CM50</b>	peridotite	890.8	915.7
<b>CM27</b>	peridotite	886.6	911.9
<b>CM59</b>	peridotite	900.1	925.4
<b>CM58</b>	peridotite	907.7	933.2
<b>CM14</b>	peridotite	883.2	908.3
<b>CM52</b>	peridotite	987.8	1015.8
<b>CM19</b>	peridotite	1032.8	1062.4
<b>CM32</b>	peridotite	944.8	976.6
<b>CM60</b>	pyroxenite	870.9	897.0
<b>CM67</b>	pyroxenite	862.6	894.6

Table 3.8. Major oxide modeling results.

SiO <sub>2</sub> vs. MgO			Al <sub>2</sub> O <sub>3</sub> vs. MgO			
	Initial P	Final P		Initial P	Final P	
Sample	(GPa)	(GPa)	Melt Fraction	(GPa)	(GPa)	Melt Fraction
CM19	4	4	0.1	6	5.5	0.15
<b>CM52</b>	<b>4.75</b>	<b>4</b>	<b>0.1</b>	<b>4.75</b>	<b>4</b>	<b>0.1</b>
CM53	3	1.5	0.25	7	5	0.3
CM59	3	1	0.3	8	4.5	0.4
<b>CM61</b>	<b>4.75</b>	<b>4</b>	<b>0.275</b>	<b>4.75</b>	<b>4</b>	<b>0.275</b>

## Chapter 4 - Geochemistry of Mineral Separates from Cerro Mercedes Xenoliths

Major element chemistry of the whole rock Cerro Mercedes xenoliths elucidates compositional conditions of the mantle wedge underlying northern Costa Rica. Further information can be obtained from compositional variations of the minerals within those xenoliths. For example, spinel has been used as a petrologic indicator as it crystallizes over a wide range of conditions, exhibits a wide range of solid solution, is fairly refractory and is relatively resistant to alteration (Barnes & Roeder, 2001). This chapter describes mineral separates from the Cerro Mercedes xenoliths discussed in chapter 3 of this work with the objective of gaining insight into the physical state of the mantle and how it relates to mantle melting.

### Background

#### *Mineral characteristics*

Due to the nature of subduction zones, mantle peridotite experiences interaction with slab-derived fluid and/or melt fluxes, which will impose variable metasomatism upon the mantle wedge. If metasomatism occurs, it may be modal, wherein reactions with the mantle precipitate new phases changing both the bulk and modal chemistry, or it can be cryptic, wherein the mineralogy remains unaltered though the bulk chemistry changes. Additionally, slab-derived flux may induce melting within the mantle wedge by depressing the solidus of peridotite, thereby allowing potential melt/mantle reactions to occur that also potentially alter the chemistry of the mantle wedge. Homogeneous minerals are considered to be in equilibrium with the whole rock and so yield the most reliable information. Testing for homogeneity consists of measuring compositional variability from core to rim, or rim to rim, of a mineral grain to ascertain if zoning, which

indicates disequilibrium, is evident.

Based on textural grounds, Parkinson et al. (2003) distinguish primary spinel from spinel modified by reactions with host magma. Chemically, primary spinels (the filled circles in fig4.1) plot closer to the abyssal peridotite field and have a more restricted range of Mg# as well as lower TiO<sub>2</sub> and Fe<sub>2</sub>O<sub>3</sub> than modified spinels (open squares in fig4.1). In contrast, cumulate spinels (the Adak field in fig4.1) shows a wide range in composition because they crystallize from a wide range of melt compositions and equilibrate with a wide range of olivine compositions.

Although arc peridotites were thought to have higher spinel chromium numbers (Cr/(Cr + Al) than spinel in abyssal peridotite (Bonatti & Michael, 1989), there are now reported samples from the Cascades (Brandon & Drapper, 1996), the Mexican arc (Blatter & Carnichael, 1998) and Izu-Bonin-Mariana (Parkinson & Pearce, 1998) that overlap the abyssal peridotite field. In general, however, subduction zone peridotites are more depleted than oceanic peridotites (Bonatti & Michael, 1989; Parkinson & Pearce, 1998). At the same time, higher Cr# in spinel also indicates a lowering of pressure and temperature conditions as there is a systematic calculated decrease in these parameters within rocks having high Cr# spinel and high Mg# olivine (Frey & Prinz, 1978). Parkinson & Pearce (1998) resolve this seeming contradiction by proposing that an interaction of less depleted peridotites with subduction related magmas may produce peridotites having characteristics of high degrees of melt although low equilibration temperatures are recorded.

Partial melting systematics also affect pyroxene content (Bonatti & Michael, 1989), which decreases in Al<sub>2</sub>O<sub>3</sub> and incompatible elements with increasing percent melt. Additionally, Mg# (Mg/(Mg + Fe) of all silicate phases increase with increasing

percent melt. Clinopyroxene, significantly refractory, preserves high temperature chemical signatures, even if alteration of the rock has occurred (Johnson et al., 1990; Johnson & Dick, 1992) and is the phase least likely to have experienced subsolidus redistribution of elements (Bizimis et al., 2000). Further, the crystallography of clinopyroxene allows larger ions to incorporate into its structure than does orthopyroxene or olivine. For these reasons, clinopyroxene is useful in examining the composition of the mantle.

### ***Calculations***

#### *Oxygen Fugacity*

Oxygen fugacity ( $f_{\text{O}_2}$ ) is an important parameter of the mantle controlling phase relationships, element partitioning, diffusivity, volatility and electrical conductivity (Arculus, 1985). Since researchers have shown that both subaerial and suboceanic basalts generally have  $f_{\text{O}_2}$  values close to the Fayalite – Magnetite – Quartz (FMQ) buffer (fig4.2; Mysen et al., 1998) and that abyssal peridotite  $f_{\text{O}_2}$  values fall beneath FMQ (Bryndzia & Wood, 1990), oxygen fugacity values are now calibrated such that the FMQ buffer is used as a point of reference. Consequently, oxygen fugacity values are reported as the difference of the calculated  $f_{\text{O}_2}$  of a sample from the FMQ buffer; that is,  $\Delta \log f_{\text{O}_2}^{\text{FMQ}}$ . Xenoliths from subduction zone environments, in contrast, have  $f_{\text{O}_2}$  values above FMQ (fig4.3; Bryant et al., 2007; Frost & McCammon, 2008).

Although subduction zones are oxidized environments (Mysen et al., 1998; Bizimis et al., 2000), it remains unclear to what extent  $f_{\text{O}_2}$  correlates to mantle melting processes. Parkinson & Arculus (1999) concluded that peridotites with  $f_{\text{O}_2}$  over +2 FMQ require some degree of decompression melting within the mantle wedge as it is unlikely that the  $f_{\text{O}_2}$  of the mantle wedge is greater than 2 log units above FMQ. As

decompression melting increases  $f_{O_2}$  as much as +0.8 log units per GPa of decompression (Ballhaus & Frost, 1994) to a minimum of +0.25 log units per GPa of decompression (Parkinson & Arculus, 1999), it is possible to estimate the  $f_{O_2}$  of the source region if the initial pressure of melting is known.

Additionally, controversy over the oxidizing agent remains unresolved. Some researchers contend that oxidation is directly related to subduction processes whether it be aqueous fluids cycling through the mantle wedge (Wood et al., 1990; Arculus, 1994) or a water-rich component released during the dehydration of the subducting slab (Stolper & Newman, 1994). Brandon & Draper (1996) conclude that either hydrous fluid, water-bearing silicate melt, or some hybrid thereof, liberated from the downgoing slab is the oxidizing agent. Parkinson & Arculus (1999) argue that the oxidation must take place prior to the melting of the mantle wedge, which they conclude is oxidized relative to ancient cratonic and oceanic mantle. They propose a model in which ferric iron is added to the wedge by subduction related flux (melts or solute-rich hydrous fluid) preceding either flux or decompression melting. This allows continuity of the oxidation state of the mantle wedge environment and agrees with the proposal of constant upper mantle  $f_{O_2}$  since the Achaean (Li & Lee, 2004).

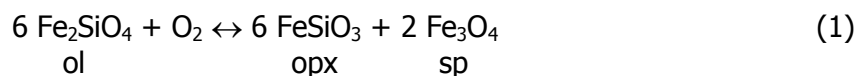
Frost & Ballhaus (1998) counter these arguments by showing that the oxidation is not likely produced by the interaction of mantle with an aqueous fluid due to the inefficiency of water dissociation in mantle conditions, making water an ineffectual oxidizing agent in the mantle wedge. Rather, they conclude that a silicate melt, with ferric iron from the mantle wedge and subduction related fluxes (Frost & McCammon, 2008) preferentially fractionating into the melt, is the oxidizing agent interacting with the mantle. In fact, hydrous minerals are neither required nor necessarily present in

highly oxidized peridotites (Frost & McCammon, 2008). This is consistent with the proposal of silicate addition during melt/rock reactions (Kelemen, 1998), which would subsequently oxidize the overlying mantle wedge.

At this time, there is no geochemical way to differentiate between the end-member candidates for the oxidation agent; elemental partitioning is either unknown (Frost & McCammon, 2008) or results are too similar for distinction. As an example, U enrichment in arc environments is often interpreted as a fluid flux signature because of its fluid mobility and incompatibility, particularly in an oxidized environment that stabilizes the  $\text{U}^{6+}$  ion (Parkinson & Arculus, 1999). Parkinson & Arculus (1999) use this argument to explain enrichment of U over Th in arc lavas and peridotites. In contrast, Brennan et al. (1995) find that, not only is U more strongly partitioned into silicate melt than aqueous fluid, but that a decrease in  $f\text{O}_2$  reduces the coefficient distribution ratio of Th/U in clinopyroxene. This means that at lower  $f\text{O}_2$ , and by extension higher pressures and greater depth, U will preferentially go into a melt over Th. Both mechanisms will result in elevated U contents over Th in mantle samples that ascend to the surface. It is likely that both mechanisms are valid under different conditions.

#### *Oxygen Thermobarometry*

Oxygen thermobarometry is based on the relative stability of  $\text{Fe}^{2+}$  and  $\text{Fe}^{3+}$  during changes of pressure and temperature and determines oxygen fugacity ( $f\text{O}_2$ ). Since observations show that both ferrous and ferric components are present in peridotite phases,  $f\text{O}_2$  can be calculated using the equilibrium:



where ol is olivine, opx is orthopyroxene and sp is spinel (Wood et al., 1990). Measurements of concentrations of total Fe in olivine and ferrous and ferric Fe in

orthopyroxene and spinel are calculated and combined with thermodynamic data to calculate  $f\text{O}_2$ . The largest source of error in this method is the uncertainty of the  $\text{Fe}^{3+}$  proportion in spinel. The calculation supports the underlying assumption that the phase maintains perfect  $\text{M}_3\text{O}_4$  stoichiometry in the  $f\text{O}_2$  range of concern. Additionally, when measurements are made with an electron microprobe, as is the case in this work, absorption of the electron beam creates error due to the relatively small grain size of spinel as opposed to larger olivine and pyroxene grains, which results in overlaps. Overlap errors, and any error in other major oxide measurements, propagate exponentially due to the relatively small amounts of  $\text{Fe}^{3+}$  in the rocks thereby limiting the absolute accuracy of the resulting concentrations.

### **Analytical Procedures**

Major oxides in mineral separates were analyzed on a JEOL 8600 electron probe microanalyzer (EPMA) at Rutgers University under the direction of Dr. J.S. Delaney and a CAMECA SX100 EPMA at the American Museum of Natural History under the direction of Dr. J. Boesenberg.

Trace elements in mineral separates were analyzed with a New Wave UP 193 Excimer laser ablation system, used as the introduction system, coupled to a ThermoFinnigan Element XR high resolution ICP-MS at the Institute of Marine Sciences of Rutgers University under the direction of Dr. L.L. Bolge.

### **Results**

#### ***Mineral Composition (major oxides)***

##### ***Olivine***

The MgO composition of olivine (table 4.1) in the CM xenoliths defines a bimodal distribution, with a lower range for the pyroxenites (fig 4.4). The most modified

peridotites show a wider range in fosterite (Fo) content (87-91) than the least and moderately modified peridotites (81-91). Olivines found in the pyroxenites have the widest range of Fo content, although it is lower (80-89). Variation in individual olivine composition is small in the least and moderately modified peridotite; most modified peridotite shows a significant variation. Rim to rim line scans across olivine grains (fig4.5) from three representative peridotites show deviations of 0.2 units in least and moderately modified peridotites fosterite content and deviation of 0.7 units in the most modified peridotite. The pyroxenite shows the least amount of compositional variability suggesting that cumulates within the system are the most equilibrated rocks. The olivine has significant NiO (up to 0.5 wt%) and is a major host phase for this oxide, along with spinel (fig4.6).

### *Spinel*

Spinel has large compositional variability (table4.2; fig4.7) in the CM xenoliths, including both hercynite-spinel series and magnesiochromite-spinel series (fig4.8). Within individual rocks (fig4.9) the Cr# and Mg# is more variable in the most modified peridotites and pyroxenites than in the least and moderately modified peridotites. At the same time, lack of compositional variability in ferric Fe vs. Mg# (fig4.10) within most individual xenoliths suggests little modification of spinel by fluid or melt components (Parkinson & Arculus, 1999). Spinel with such interactions would show significant compositional variation within individual xenoliths as well as increasing ferric Fe with decreasing Mg#. In the CM suite, only spinel from the most modified peridotites display these trends.

The least and moderately modified peridotites fall within the olivine-spinel mantle array (OSMA; Arai, 1994) whereas the majority of the most modified peridotites and

pyroxenites are displaced toward the crystal fractionation trend of Dick & Bullen (1984). Compared with other arc peridotites (figs 4.11, 4.12), the CM suite is similar to the Mexican arc (Blatter & Carmichael, 1998), Cerro del Fraile C-type (Wang et al., 2007), Simcoe (Brandon & Drapper, 1996), Ichinomegata (Takahashi, 1980; Wood & Virgo, 1989) and the less refractory samples of Grenada (Parkinson et al., 2003). Additionally, some of the most modified peridotites and pyroxenites fall within the fore-arc peridotite field as compiled by Aria & Ishimaru (2008), which includes dredged samples from Izu – Ogasawara – Mariana forearc and the South Sandwich, Mariana and Tonga Trenches. The overlap suggests that some of the most modified peridotites and some pyroxenites are modified by subduction related processes. The  $\text{Fe}^{3+}/\Sigma\text{Fe}$  of spinel in the CM xenolith suite range from 0.03 to 0.54 (fig 4.13a) and is not well correlated to the fosterite content of coexisting olivine. No significant correlation is evident between the spinel Mg# and olivine Fo (fig 4.13b) overall. However, the spinel in the least and moderately modified peridotites have both the highest Mg# and Fo with very little variability.

#### *Orthopyroxene*

In the CM peridotites, orthopyroxene is compositionally homogenous, with Mg# ranging from 90.5 to 92.5 (table 4.3; fig 4.14) and correlates well with the fosterite content of olivine. Exceptions, (e.g. outlying grain of CM19, fig 4.14), are grains in contact with the host basanite and grains with vein material. Pyroxenites have Mg# below 90.0, although there are not many analyses. The orthopyroxene is generally low in wollastonite (Wo) content (0.64 - 0.87 CaO wt%) and ferrosilite (Fs) (5.5 – 6.7 FeO wt%) content (fig 4.15; table 4.3) with the pyroxenites having higher Fs contents (8.0 – 12.0 FeO wt%). Peridotitic orthopyroxene near the boundary with the host basalt is enriched in FeO (up to 12.5 wt%). Abundances of  $\text{Al}_2\text{O}_3$  is moderate (2.5 – 5.3 wt%);

$\text{TiO}_2$  and  $\text{Na}_2\text{O}$  are low (<0.3 and <0.2 wt%, respectively). Line scans crossing orthopyroxene grains (fig4.16) show the compositional variations of En content of representative xenolith types. In most cases, the rims are slightly more enriched in Mg than the cores; that is, reversely zoned. The line of CM50 shows normal zoning with elevated En content in the core of the grain.

### *Clinopyroxene*

Clinopyroxene have high Mg# (90.0 – 92.7; table4.4) and are relatively homogenous in end member content (fig4.17), with the exception of CM67 and a few outlier grains.  $\text{Cr}_2\text{O}_3$  concentrations of individual rocks increase with increasing  $\text{Al}_2\text{O}_3$  concentrations, which are variable and range up to 8 wt% (fig4.18; table 4.4). The concentrations of  $\text{TiO}_2$  are low, though variable (0.05 – 0.5 wt%) as are  $\text{NaO}_2$  (0.25 – 2.8 wt%). Clinopyroxene is a principal host phase for  $\text{TiO}_2$  and  $\text{NaO}_2$  (fig4.19), although  $\text{TiO}_2$  is also hosted by spinel. Plotting  $\text{Na}_2\text{O}$  in clinopyroxenes against spinel Cr# (fig4.20), the CM xenoliths fall into both the continental & hotspot field and abyssal peridotite field of Arai (1991), corroborating the findings in the previous chapter of generative conditions similar to those of plumes as higher  $\text{Na}_2\text{O}$  (wt%) in clinopyroxene indicates higher pressures of equilibrium and so, higher potential temperatures. Compositional line scans across clinopyroxene grains (fig4.21) show complimentary variation in En and Wo content in larger grains. In the small grain of CM50, no variability is evident, whereas in the pyroxenite, CM67, the profiles show no symmetry in end member composition.

### *Mineral composition (trace elements)*

Crystallographic and stoichiometric constraints render clinopyroxene (cpx) the primary host for trace elements, although orthopyroxene (opx) accommodates a non

trivial amount. Chondrite normalized rare earth element (REE) patterns of clinopyroxenes (fig4.22) are depleted in light rare earth elements (LREEs), smoothly increase to the middle rare earth elements (MREEs) and level off in the heavy rare earth elements (HREEs). The LREEs range from 0.35 to 3.5 times chondritic values; the HREEs range from 2 to just over 10 times chondritic values. In extended trace element diagrams (fig4.23) normalized to primitive mantle (McDonough & Sun, 1995), cpx is 0.02 to 10 times primitive mantle (PM) with a positive U anomaly. The negative anomalies of Nb and Zr suggest influence by subduction processes, although the scatter in Ba suggests varying degrees of this influence. Most xenoliths also show a negative Pb anomaly that does not agree with the positive Pb anomaly seen in whole rock analyses (e.g., chapter 3) and this will be further discussed below.

Chondrite normalized REE patterns of orthopyroxene, in general, increase smoothly from depleted LREEs (0.01 – 0.1 times chondritic) to HREEs (0.5 – 5.0 times chondritic) (fig4.24), although there is a significant amount of scatter. Whereas a few samples show depleted Eu, other samples have elevated Eu and some show no Eu signal at all. In extended trace element diagrams (fig4.25) normalized to primitive mantle (McDonough & Sun, 1995), the orthopyroxene have positive U and Pb anomalies, in contrast to the clinopyroxene that show negative Pb anomalies. Most orthopyroxene have a significant negative Sr anomaly as well as Th and Nb, when present. In contrast, Zr is elevated in many grains as is Ti, suggesting a more complex history than straightforward subduction processes; a substantial amount of scatter in Ba and Ce suggests variations in fluid/rock reactions.

### ***Estimates of Oxygen fugacity***

Calculations for oxygen fugacity ( $f_{\text{O}_2}$ ) use coexisting olivine, orthopyroxene and

spinel and employ the methods of Ballhaus et al. (1991) and Nell & Wood (1991); averaged results for individual xenoliths range from  $0.92 - 4.16 \Delta f_{O_2}^{FMQ}$  at 1GPa to  $0.42 - 3.68 \Delta f_{O_2}^{FMQ}$  at 2.5GPa (table4.5). Results of the Ballhaus et al. (1991) method at 1GPa are given relative to the FMQ buffer (fig4.26) in order to circumvent any sensitivity to temperature and pressure (Wood et al., 1990; Parkinson et al., 2003). With the exception of two peridotites, the method of Nell & Wood (1991) yields up to 24% higher  $\Delta f_{O_2}^{FMQ}$  values than the method of Ballhaus et al. (1991). Further, the Nell & Wood method (1991) yields up to 24% lower  $\Delta f_{O_2}^{FMQ}$  values for measured pyroxenites. This is due, in part to the cancellation of orthopyroxene in the Ballhaus et al. (1990) method to simplify calculations. A limitation to the accuracy of these calculations is the uncertainty in the ferric iron content of spinel. Here, ferric iron in spinel is calculated with the method of Barnes and Roeder (2001), which assumes stoichiometry of the ideal spinel composition  $XY_2O_4$ , where X is divalent ions and Y is trivalent ions. However, errors in major oxide measurements propagate appreciably larger errors in ferric iron content (Wood & Virgo, 1989). Subsequently, there may be significant error in trivalent ion component variance, limiting accurate interpretation of relatively small variations. Nonetheless, variations in  $\Delta f_{O_2}^{FMQ}$  values of the CM xenoliths can give information about the state of the mantle, albeit only relatively. There is an inverse relationship between  $\Delta f_{O_2}^{FMQ}$  and equilibrium T (fig4.27) as  $\Delta f_{O_2}^{FMQ}$  decreases with increasing T. Of interest is the deviation from this trend of grains in CM32, which contact a veinlet near the xenolith/host basanite boundary and has some spinel enriched in  $Fe^{3+}$  relative to other spinel in CM32. It suggests the grain was imprinted with the potentially higher oxidation state of the basanite melt. This may also explain the deviation of CM19. A positive correlation between oxygen fugacity and Cr# of spinel

(fig4.28) suggests that melt/mantle interaction elevated the oxygen fugacity of the system (Ballhaus, 1993; Parkinson & Arculus, 1999).

## **Discussion**

### ***Re - categorizing CM14***

From the results, it seems likely that CM14, previously considered a least modified peridotite, is more likely a moderately modified peridotite. Its equilibration T is relatively low compared to the other least modified peridotites (fig4.27) and it shows a lower pressure of equilibration (fig4.20). The orthopyroxene within CM14 are enriched in trace elements relative to other least modified peridotites (fig4.25) and the spinel are higher in Cr#. It yields a higher  $\Delta f_{O_2}^{\text{FMQ}}$  than other least modified peridotites that, when combined with the high Cr#, indicates more melt/mantle interaction (Ballhaus, 1993; Parkinson & Arculus, 1999; fig4.28). Additionally, in the melting models of Bizimis (2000) (fig4.31, 4.32), discussed below, it lies closer to moderately modified peridotites rather than the least modified peridotites, falling on the line of the melt/mantle interaction trend defined by Kelemen et al. (1990). For this reason, I shall henceforth consider CM14 a moderately modified peridotite.

### ***Mineral zoning***

In perfect equilibration, mineral grains are homogenous with no occurrence of compositional zoning. Although the minerals in the CM xenoliths are by and large homogenous, rare compositional zoning occurs with both normally and reversed zoning in olivine and pyroxene (figs4.5, 4.16, 4.21). Location of the grains within the xenolith explains the occurrence, in part, as several of the zoned grains are in proximity to the host basanite and/or veinlet material and where it is likely that their state of equilibrium became disturbed during entrainment and ascent to the surface. This may be

particularly true of the reversely zoned grains, which occur predominantly in orthopyroxene. Spiedel & Osborn (1967) and Hewins (1974) have shown that reversed zoning may be due to increase of oxygen fugacity as temperature decreases allowing a fractional trend of decreasing Fe/Mg. The increase in fugacity will cause crystallization of magnetite, subsequently enriching the system in Mg# ( $Mg/Mg+Fe^{2+}$ ). This agrees with the spinel data that suggests melt/mantle interactions elevating the oxygen fugacity of the system (fig4.28). Larger olivine grains (fig4.5 b,c) display a saw tooth pattern with more fayalitic composition at both rims and core, indicating two episodes of equilibration and multiple melting events.

### ***Mantle melting***

The peridotite from Cerro Mercedes must have undergone low to moderate degree of melting as clinopyroxene is a significant presence in the residues (up to 12.8 modal wt%, table3.5) but cannot remain in the residue after ~30% melting in hydrous melting and 25% anhydrous melting (Bizimis et al., 2000). This is also shown by plotting  $Fe^{3+}/\Sigma Fe$  of spinel (cations based on 4 oxygen), which decreases in peridotites experiencing extensive melt (Frost & McCammon, 2008), against Cr# of spinel (fig4.29), which increases with increasing melt (Parkinson et al., 2003). Although there is some variability in the  $Fe^{3+}/\Sigma Fe$  of individual rocks, the spinel decrease in  $Fe^{3+}/\Sigma Fe$  with decreasing Cr# indicating that the xenoliths have not experienced extensive melt. This is not to say that the CM xenoliths have not experienced any melt events. Placing the  $Al_2O_3$  content of pyroxenes against Cr# of spinel, which decrease and increase as a function of percent partial melting, respectively (fig4.30), it is evident that the mantle has experienced some degree of partial melting. Interestingly, some of the most modified peridotites show relatively small amounts of partial melting. It seems likely,

then that different mechanisms of modification are at work in the mantle wedge: one possibly more aqueous in nature that modified the most modified peridotites; the other a melt that modified the least and moderately modified peridotites.

#### *Dry melting*

The compositions of spinel in fig4.11 suggest that the xenoliths have experienced varying degrees of melting. Element concentrations in clinopyroxene, such as Ti, Dy and Zr, are also useful in evaluating melting processes (Bizimis et al., 2000; Tamura & Arai, 2006). Plotting Ti against Dy and Zr in clinopyroxene, the degree of partial melting for the CM xenoliths is less than 15% (figs4.31, 4.32). The calculations for the melting trends in these figures use the parameters for the spinel stability field and anhydrous batch melting (Bizimis, 2000). Since there is no occurrence of hydrous mineral assemblages in the spinel facies CM xenoliths, the model seems an appropriate choice. In Ti vs. Dy space (fig4.32), the least modified peridotites show the least degree of melting, whereas the moderately modified peridotites show the largest degree of melt. Some CM xenoliths overlap the field of abyssal peridotite suggesting that decompression plays a part in their melting history. Others, with decreasing Dy, but constant Ti, are pulled off the trend suggesting the influence of fluid reactions. In Ti vs. Zr space, similar distribution is seen with a major difference: several xenoliths fall onto the melt mantle interaction trend (Kelemen et al., 1990; Bizimis, 2000). This trend represents melt/mantle interactions in which ascending liquids from the deeper, more fertile mantle wedge react with more depleted, shallower mantle peridotite (Kelemen et al., 1990). This process should relatively deplete the derived melts and enrich the residual peridotite in elements with high solid/melt partition coefficients. For those xenoliths that fall near the melt/mantle interaction trend line, it is thus likely that they are residues of

this process. It does not account, however, for the entire suite. Nor does it explain the depletions of HFSEs seen in many pyroxene grains (figs4.23, 4.25).

#### *Wet melting*

Enrichment of U in pyroxene grains, Sr in cpx and Pb in opx as well as depletion in HFSEs in both cpx and opx could be seen as evidence for the involvement of slab-derived fluid in mantle wedge modification (Grégoire et al., 2001; Vannucci et al., 2007). Grégoire et al. (2001) conclude that a hydrous-rich melt metasomatic agent accounts for negative Ba, Sr, Zr and Ti anomalies in orthopyroxene from Lihir as well as positive U anomalies. In their scenario, fluids coming off the downgoing slab enhance melting by lowering the solidus of peridotite and enrich the mantle wedge in fluid mobile elements without precipitating new minerals. Vannucci et al. (2007) call upon aqueous fluid interaction to explain U/Th fractionation in clinopyroxene from Grenada, which show positive U anomalies. They propose that the higher compatibility of U in aqueous fluids leads to such fractionation during dehydration reactions. In fact, high normalized U/Th ratios in pyroxene, as seen in CM clinopyroxene (fig4.23), can result from a higher pyx/melt partition coefficient for U than for Th, as predicted by Keppler (1996) as well as via aqueous fluid reactions. This agrees with the idea of initial melt/mantle interaction followed by fluid/mantle interaction (Kelemen et al., 1990). Further, in hydrous melting compared to anhydrous melting, the stability field of cpx increases (Ohtani et al., 1997) and the proportion of cpx entering the melt decreases whereas the proportion of opx entering the melt increases (Bizimis et al., 2000). Bizimis et al. (2000) use this model to extend the melting trend (fig4.32), which can then continue past the dry melting limit before cpx is exhausted, in order to account for low HFSEs in forearc peridotites from the Hellenic Peninsula. However, since the CM xenoliths are not forearc

peridotites, this does not seem applicable to this particular suite. It is more likely that if slab-derived fluids modify the CM xenoliths, they have interacted after melt/mantle processes, thereby enriching the system with fluid mobile elements (e.g., Sr, Pb) that is already depleted in HFSEs.

#### *Primary Mantle Composition – Mass Balance*

Mass balance calculations (table 4.6) performed for the least modified peridotites, CM52 and CM19 and a moderately modified peridotite, CM14, based on the observed modal weight percent of each phase and normalized major oxide weight percent, show discrepancies in major oxide weight percents between XRF chemical data and the calculated sums of each phase. Some of the discrepancies are systematic: more CaO and Al<sub>2</sub>O<sub>3</sub> in the chemical data than calculated; less FeO and MgO in the chemical data than the calculated mass balance. These differences are due, in part to error propagated by averaging mineral weight percents, sigma ( $\sigma$ ) in table 4.6, and are as high as 10 wt% for SiO<sub>2</sub>, although most error is <0.5 wt%. Thus, averaging error alone cannot explain the poor mass balance results, particularly in the case of SiO<sub>2</sub>, in which the averaging error changes the amount of SiO<sub>2</sub> significantly.

Another source of error is the method with which modal abundances are measured. The main caveat in the method described earlier is the assumption that a thin section fully represents the modality of the whole rock, which is likely not the case. Further, the analyzed thin sections retained host basalt at the perimeter of the xenoliths, possibly adding significant pixels to the backscattered images, whereas a rim of each xenolith was left contacting the host basalt during extraction to hinder contamination by the host basanite. To test the error of the observed mineral modal fractions, a mixing program (by Terra Softa), which uses least squares regression (Bryan et al., 1969), was

used to back calculate the modal fractions of each mineral phase based on whole rock and mineral chemistry (table4.7). Although the mass balance is not exact, the fit is better than when the observed modal abundances are used. A summary of the differences in major oxides are shown in table 4.8.

The results show that the observed modal weight percents done using thin sections systematically include too much olivine (10%) and too little pyroxene and spinel phases (table4.9). Using the mineral modal weight percents calculated from the mixing program enriches the system in some major oxides that make up pyroxenes ( $\text{SiO}_2$ ,  $\text{Al}_2\text{O}_3$ ,  $\text{Cr}_2\text{O}_3$ ,  $\text{CaO}$ ) and decreases the amount of  $\text{MgO}$ ,  $\text{FeO}$  and  $\text{NiO}$  in the system. The remaining excess of  $\text{Cr}_2\text{O}_3$ , without excess of  $\text{Al}_2\text{O}_3$  or  $\text{FeO}$  that would be expected in a spinel phase, may explain the occurrence of the few vermicular spinels (fig3.17). A more detailed study of the spinel in the CM xenoliths is needed to fully understand the implications of this. Although the fit is better with the calculated modal abundances, the error (sum of squares of the residuals, table4.7) is rather high and suggests that there is a missing compositional component.

Knowing that the CM peridotites have experienced modification, it is worthwhile to explore the possibility that the whole rock composition of the CM peridotites is a mixture of their minerals plus a previously extracted melt. To test this, the Miocene Sarapiquí basalt was chosen as a previous melt based on the geographical proximity to Cerro Mercedes (fig3.8) and the subduction signature evident in their trace element concentrations (fig3.29c). The same mixing program as before was executed using the averaged, normalized composition of both the Sarapiquí basalt (Gazel et al., 2005) and peridotite minerals (table4.10). The resulting negative coefficient for the Sarapiquí basalt indicates that the mixing of these components is not reasonable. Thus, although

the mass balance based on modal mineral compositions gives a good estimate of the mantle composition underlying Cerro Mercedes, the system likely experiences a complex history. Further study of possible mixing components is needed to fully quantify the primary composition of the mantle.

*Physical state of the mantle ( $f_{O_2}$ )*

The more oxidized xenoliths from Cerro Mercedes (fig4.27) are high (up to  $\Delta f_{O_2}^{\text{FMQ}} +4.1$ ) compared with other arc xenoliths (fig4.3). However, there are instances of relatively high  $\Delta f_{O_2}^{\text{FMQ}}$  from Shiveluch (Bryant et al., 2007), with a maximum  $\Delta f_{O_2}^{\text{FMQ}} +4.53$  of a clinopyroxenite, from El Peñon, central Mexico (Blatter & Carmichael, 1998) of up to 2.5 log units above FMQ (although these are hornblende andesites) and  $\Delta f_{O_2}^{\text{FMQ}} +2.7$  for carbonatite-metasomatized samples from Olmani, Tanzania (Rudnick et al., 1993). The fact that the CM peridotites lack hydrous phases corroborates the proposal that hydrous phases are not required for highly oxidized spinel (Parkinson & Arculus, 1999; Frost & McCammon, 2008). Discounting the pyroxenites, the CM peridotites have a maximum  $\Delta f_{O_2}^{\text{FMQ}} +3.25$ .

If one considers the argument of  $\Delta f_{O_2}^{\text{FMQ}}$  increasing with decompression melting and considers that the CM xenoliths surfaced within a back-arc environment, the maximum  $\Delta f_{O_2}^{\text{FMQ}}$  of +3.25 FMQ decreases by either 0.25 log units per GPa (Parkinson & Arculus, 1999) or 0.65 log unit per GPa (Ballhaus & Frost, 1994). Using a mean pressure for the spinel stability field of 1.25GPa places the source at a maximum of +2.94 FMQ or +2.44 FMQ, respectively. In fact, Ballhaus & Frost (2004) calculated a maximum increase of 0.8 log units per GPa of decompression, which would further lower the  $f_{O_2}$  to +2.25 FMQ. Of course, if the xenoliths came from greater depth, the source  $f_{O_2}$  would correspondingly decrease. Both source region values are higher than the

accepted value of +2 FMQ for the mantle wedge (Frost & McCammon, 2008) and belies the fact that spinel is not replaced by magnetite or hematite.

The difference in the two rates of  $f_{O_2}$  change is the style of melting. In the Ballhaus & Frost model,  $Fe^{3+}/\Sigma Fe$  is kept constant, whereas in the Parkinson & Arculus method, spinel Cr# and olivine Fo content increase with increasing decompression melting. For the CM peridotites, however, olivine Fo content does not increase significantly with increasing spinel Cr# (fig4.11). Thus, it is more likely that the Ballhaus & Frost model is more suitable to these rocks. The exceptions are the most modified peridotites, which are most likely influenced further by subduction fluxes, and show the most variability in spinel Cr#.

### Conclusions

The homogeneity of minerals shows that the peridotites are well equilibrated and are appropriate for estimating temperature and oxygen fugacity within the mantle underlying Cerro Mercedes. The minerals show similar modifications as the whole rocks with spinel of the least and moderately modified peridotites lying within the olive-spinel mantle array, which confirms the likelihood of these peridotites as residues. The xenoliths record some of the highest oxygen fugacity estimates found in arc peridotites, using the method of Ballhaus et al. (1991) at 1GPa, with  $\Delta f_{O_2}^{FMQ}$  of +3.25 for the peridotites and +4.06 for a websterite. The high  $f_{O_2}$  was likely gained during melt/rock reactions and subsequent decompression melting.

Thus, the CM xenoliths were seemingly formed as residues from a fertile, relatively hot mantle with maximum  $\Delta f_{O_2}^{FMQ}$  of +2.44. Subsequent melt/rock reactions modified the mantle during Miocene subduction with shallower mantle also experiencing fluid/rock reactions. The final recorded melt event occurred with the influx of low-Si

basanite and subsequent decompression melting that brought the xenoliths to the surface. During their transit, a higher oxygen fugacity became imprinted on the rocks.

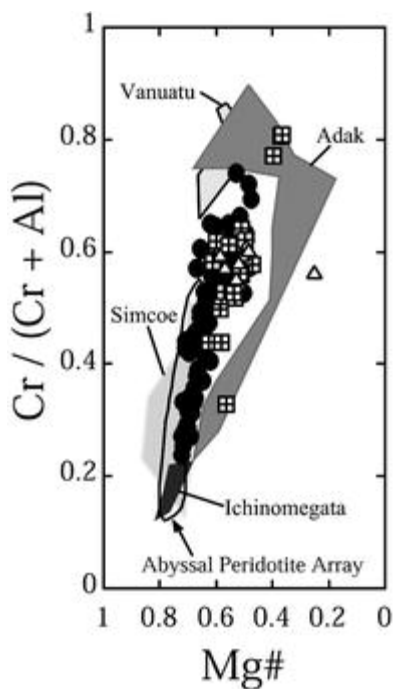


Figure 4.1. Cr# vs. Mg# of spinel from Grenada peridotites and various arcs for comparison; (from Parkinson et al., 2003). Filled circles are primary spinel, boxes are reacted spinel, open triangles are in the melt.

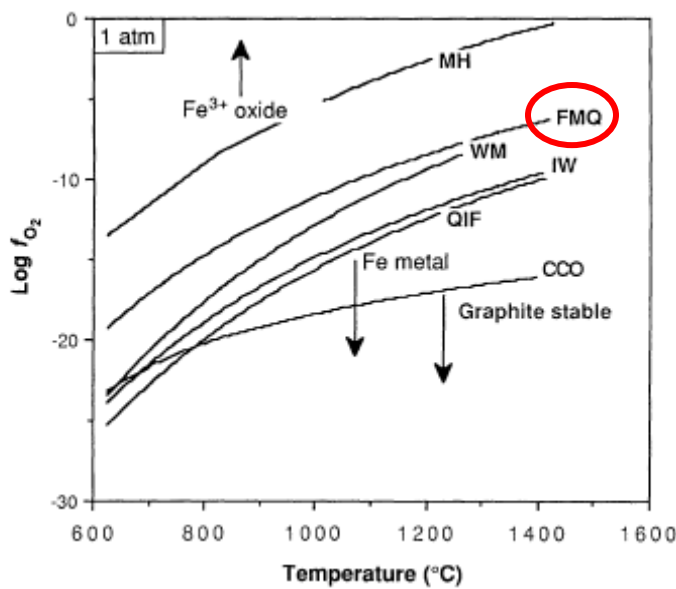


Figure 4.2.  $\log f_{\text{O}_2}$  vs. T at 1 atm showing various buffers with FMQ circled. Also shown are the stability values of  $\text{Fe}^{3+}$ ,  $\text{Fe}^0$  and C (as graphite). (Taken from Wood et al., 1990.)

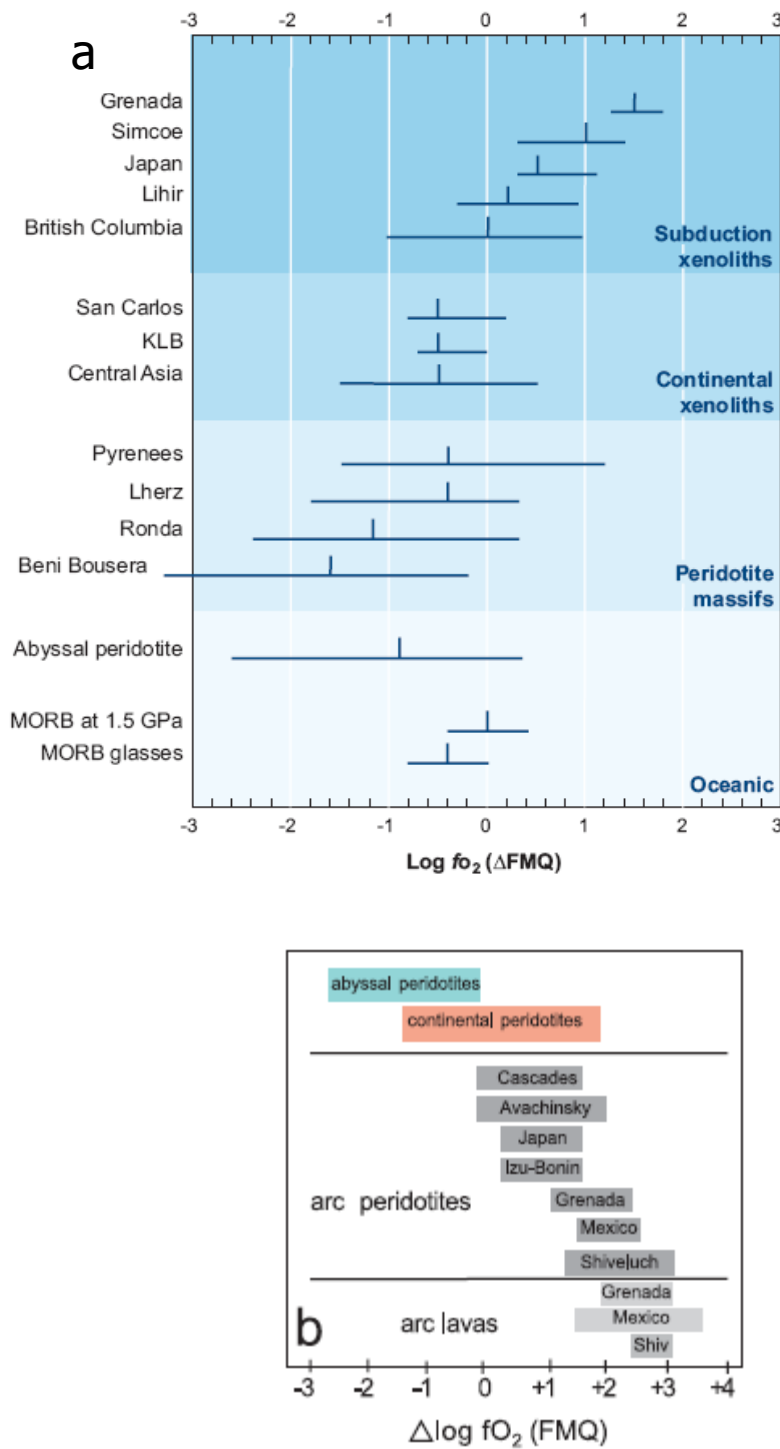


Figure 4.3. a) Oxygen fugacity (range and median value) of spinel lherzolite assemblages from a variety of tectonic settings. Taken from Frost & McCammon (2008) and references therein. b)  $\Delta\log f\text{O}_2^{\text{FMQ}}$  values for arc peridotites and lavas from Bryant et al. (2007 and references therein).

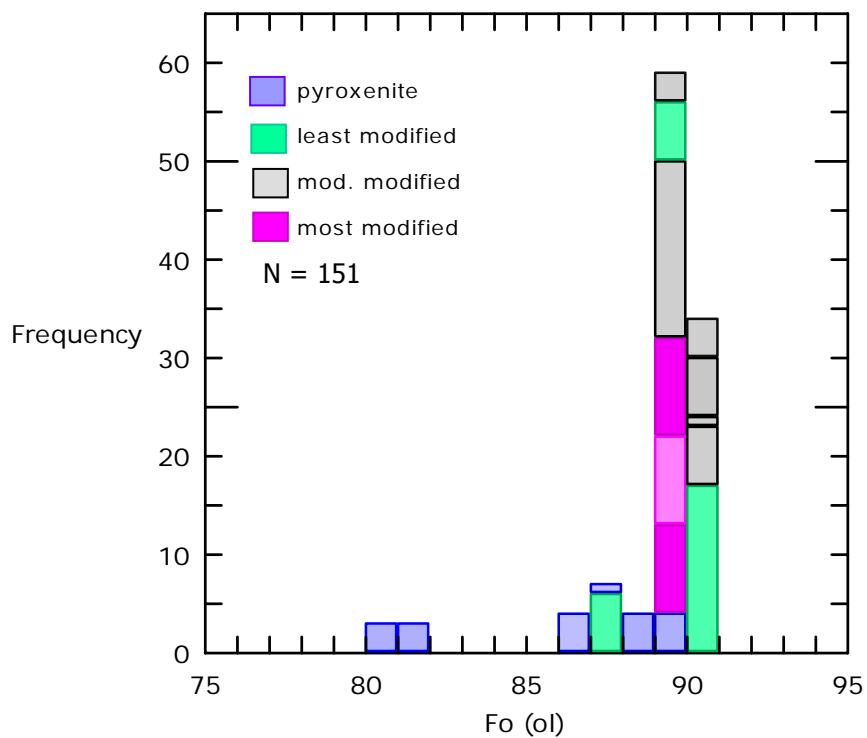


Figure 4.4. Fo content in olivines displays a bimodal pattern. The lower values are from olivines within pyroxenites. The most modified peridotites have a wider range of Fo content than the least and moderately modified peridotites, which range from  $\text{Fo}_{89}$  to  $\text{Fo}_{91}$ .

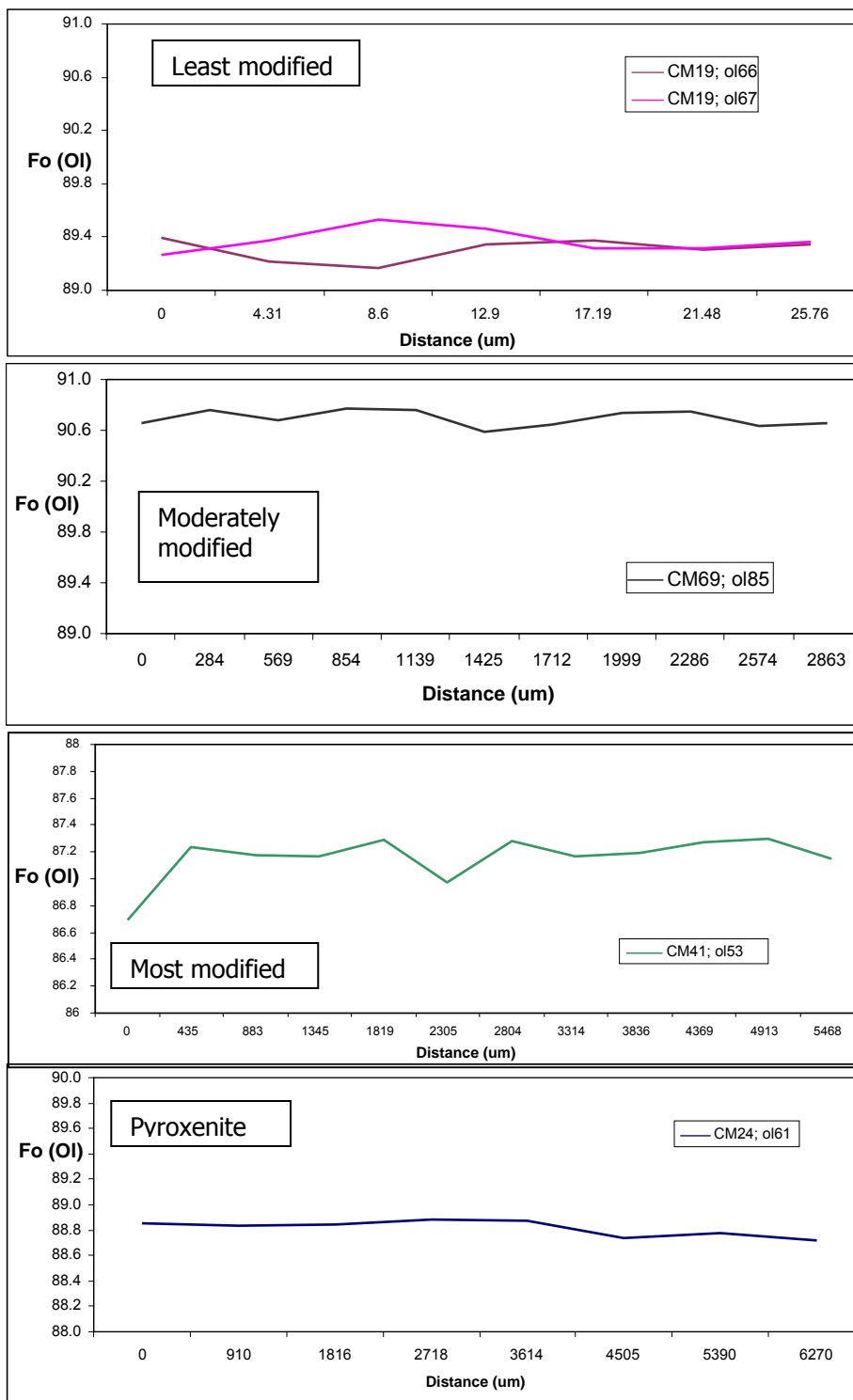


Figure 4.5. Lines across olivine in CM19, CM69, CM41 and CM24, representing least to most modified peridotites and pyroxenites, respectively. Fo content is compared to distance across the grain (note lower Fo range of CM24). The grains chosen for line scans in the olivine and other phases were chosen specifically to ascertain zoning behavior; they do not represent the majority of grains, which are homogenous.

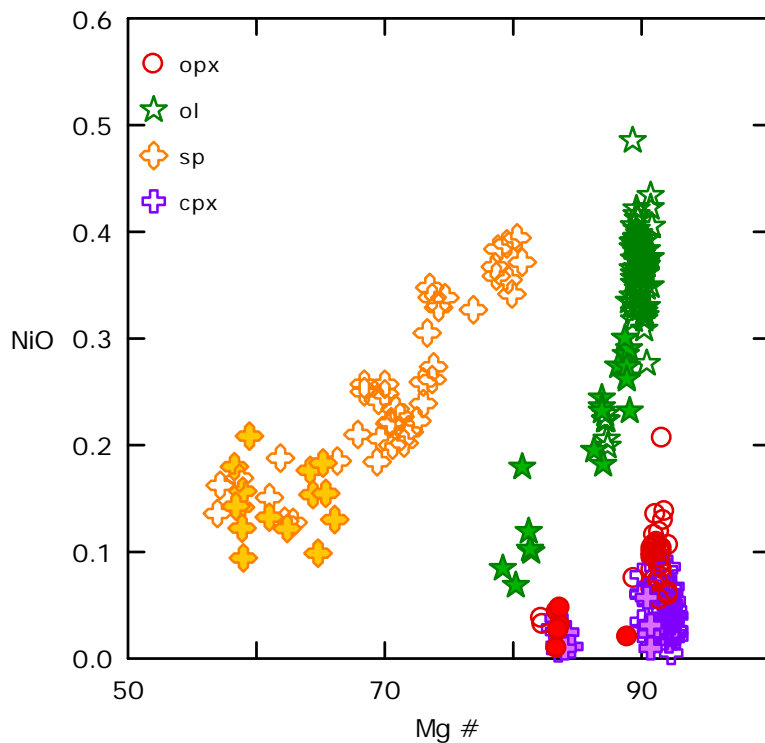


Figure 4.6. NiO (wt%) vs. Mg#. In all minerals analyzed, NiO is mainly hosted by olivine and spinel phases with a moderate amount in orthopyroxene and very little in clinopyroxene. Filled in symbols represent phases in pyroxenite; open symbols are phases in peridotite.

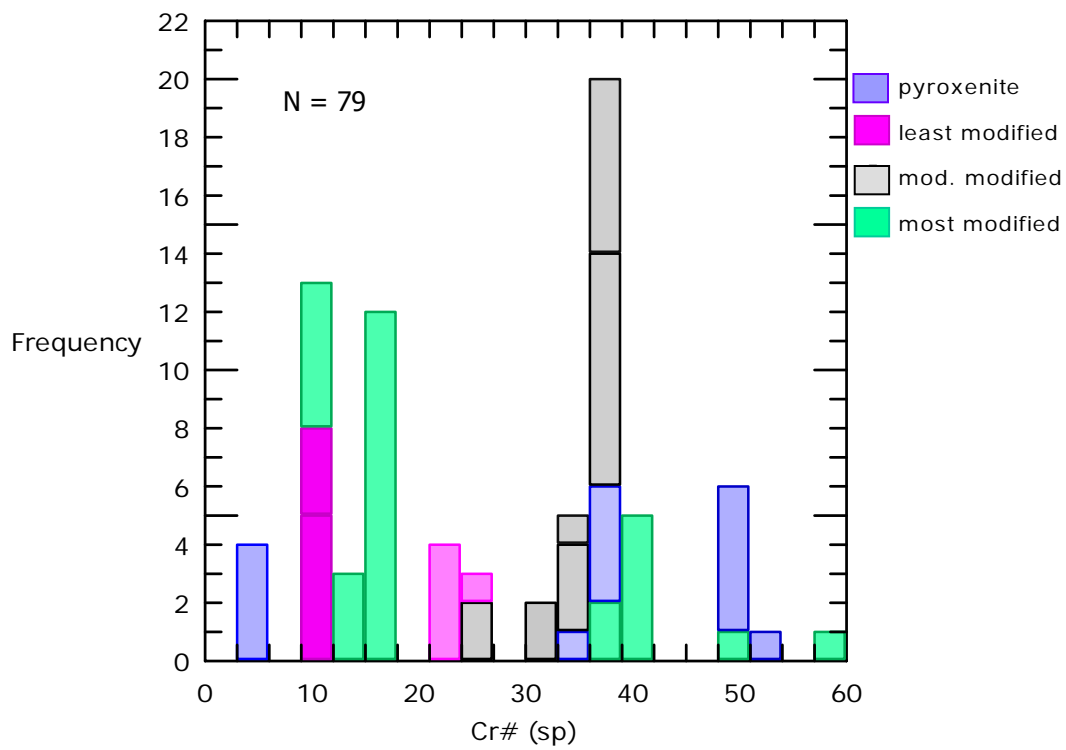


Figure 4.7. Compositional variation of spinel.

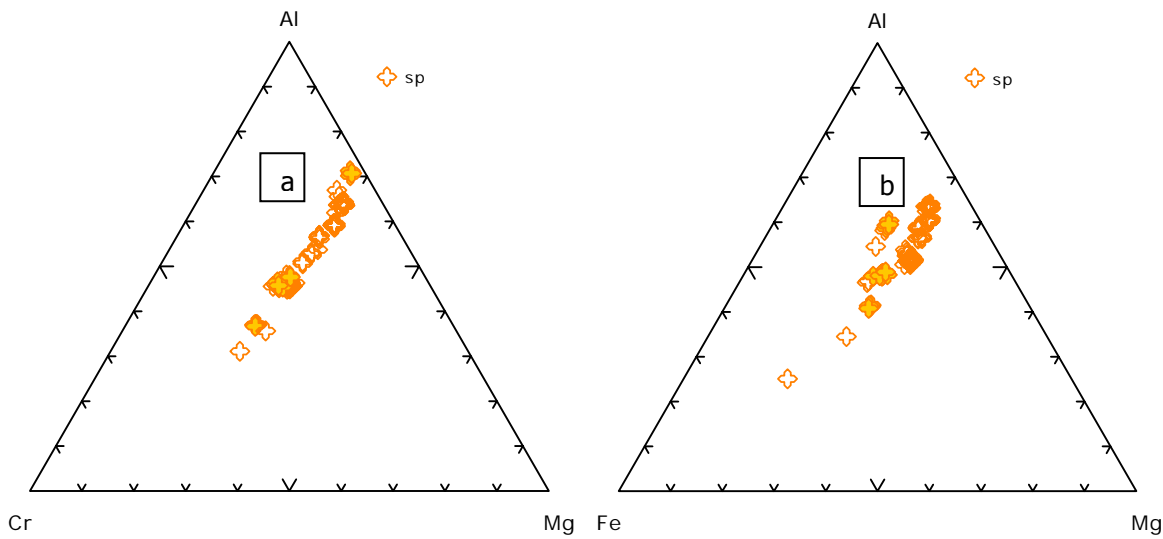


Figure 4.8. Spinel series trigrams showing both a) magnesiochromite series ( $\text{FeCr}_2\text{O}_4 - \text{MgCr}_2\text{O}_4$ ) and b) spinel - hercynite series ( $\text{FeAl}_2\text{O}_4 - \text{MgAl}_2\text{O}_4$ ). Parameters are cations based on 4 oxygen. Filled symbols represent spinels in pyroxenites; open symbols, spinels in peridotites.

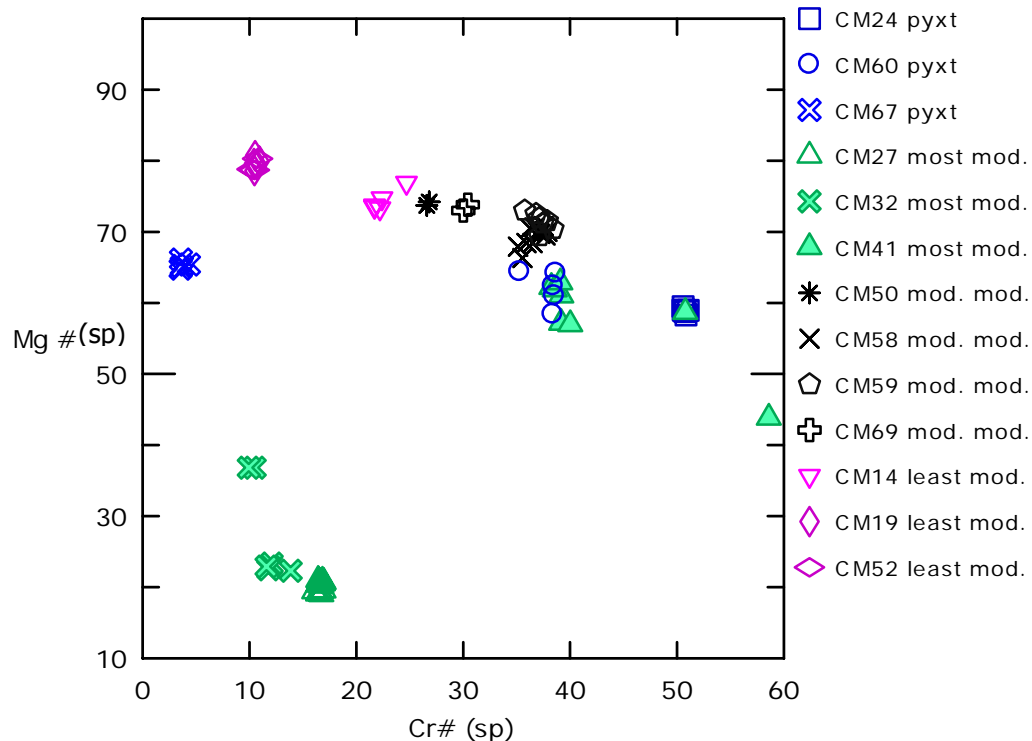


Figure 4.9.  $\text{Mg}^{\#}(\text{sp})$  vs.  $\text{Cr}^{\#}(\text{sp})$ . Pyroxenites (pyxt) and most modified peridotites show more variability in  $\text{Cr}^{\#}$  and  $\text{Mg}^{\#}$  than least and moderately modified peridotite.

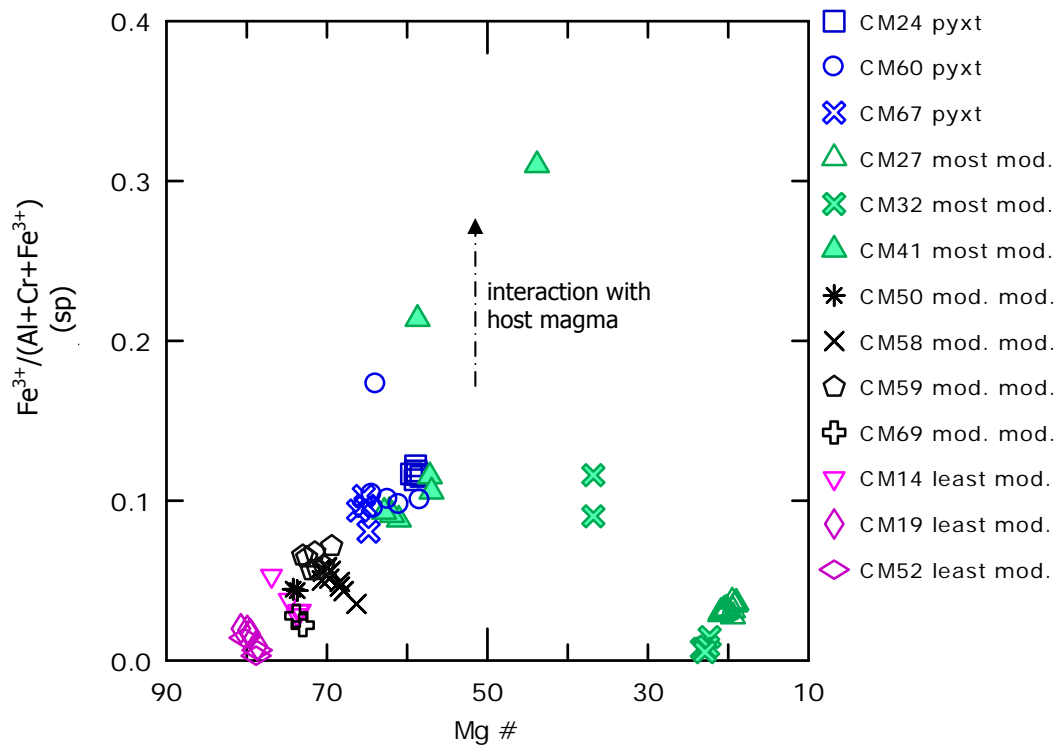


Figure 4.10.  $\text{Fe}^{3+}/(\text{Al}+\text{Cr}+\text{Fe}^{3+})$  cation amount based on 4 oxygen vs. Mg# of spinel. Lack of compositional variability within most individual xenoliths suggests little modification of spinel by the host magma. CM32 and CM27 grains with both low Fe<sup>3+</sup> and Mg# are not Cr-rich spinel phases.

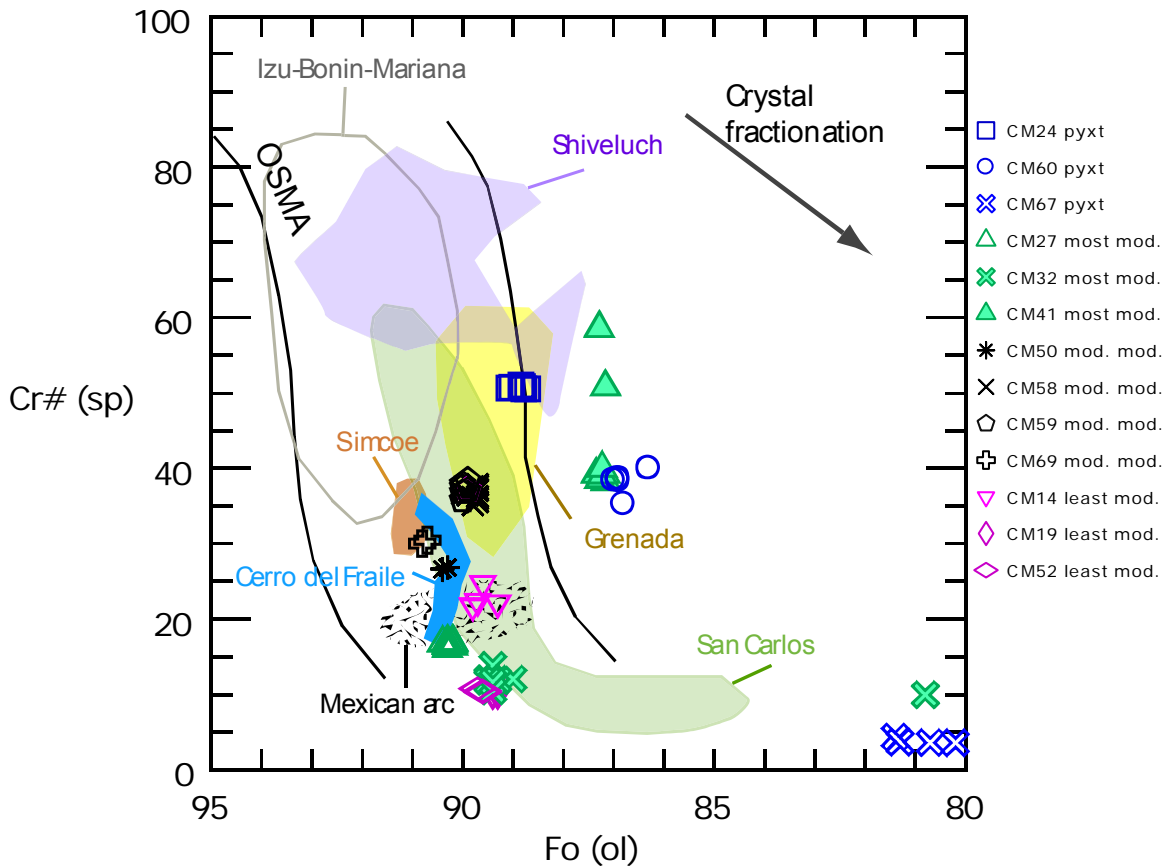


Figure 4.11. Cr# (sp) vs. Fo (ol). CM xenolith suite compared to other arc peridotites. Shaded areas shown include Izu-Bonin-Mariana arc (Parkinson & Pearce, 1998), Shiveluch (Bryant et al., 2007), Simcoe (Brandon & Draper, 1996), Grenada (Parkinson et al., 2003), Cerro del Fraile (Wang et al., 2007), the Mexican arc (Blatter & Carmichael, 1998) and San Carlos (Frey & Prinz, 1978). Olivine-spinel Mantle Array (OSMA), which delineates a residual trend in the spinel stability field, is from Arai (1994). Crystal fractionation trend is from Dick & Bullen (1984). Figure adapted from Bryant et al. (2007) and Wang et al. (2007). Cr# is  $100 \times \text{Cr}/(\text{Cr}+\text{Al}+\text{Fe}^{3+})$ ; Fo (ol) is  $100 \times \text{Mg}/(\text{Mg}+\text{Fe})$ .

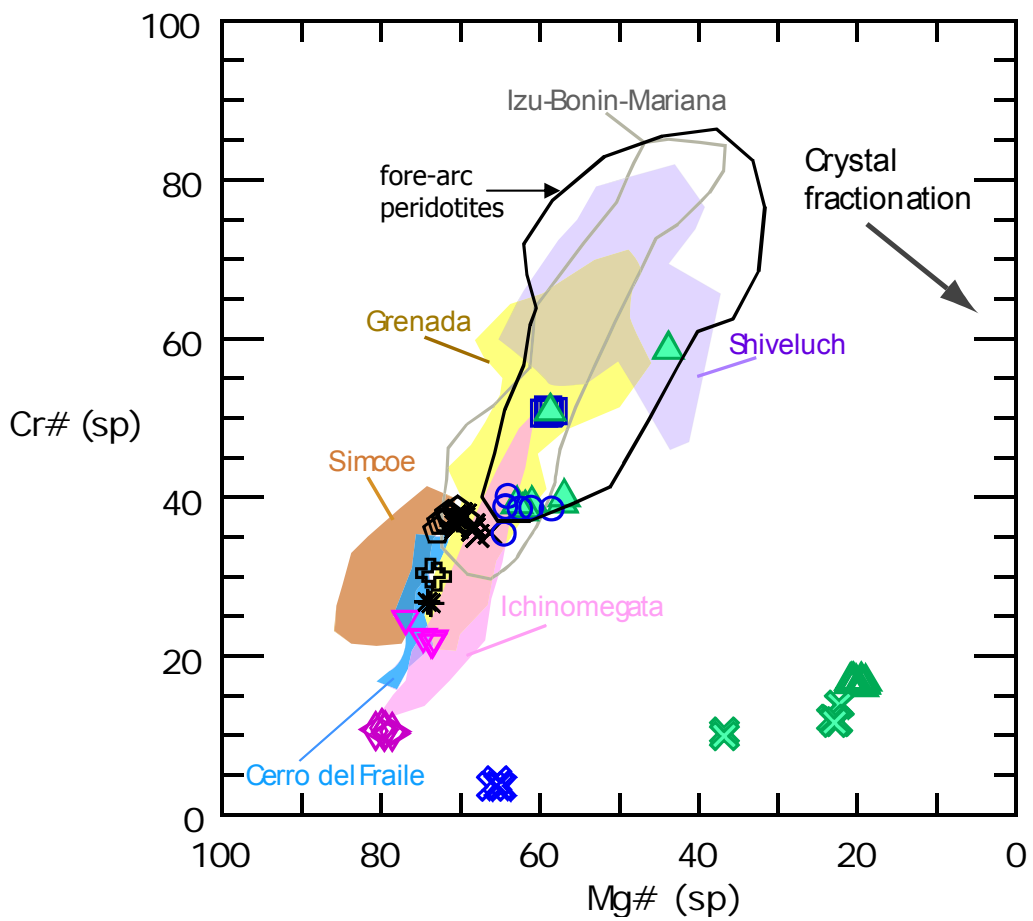


Figure 4.12. Cr# (sp) vs. Mg# (sp). Spinel from the CM xenolith suite compared to spinel in other arc peridotite. Symbols and shaded areas are as in previous figure with the addition of Ichinomegata (Takahashi, 1980; Wood & Virgo, 1989). Mg# (sp) is  $100 \times \text{Mg}/(\text{Mg}+\text{Fe}^{2+})$ . Area of fore-arc peridotites is compiled by Arai & Ishimaru (2007).

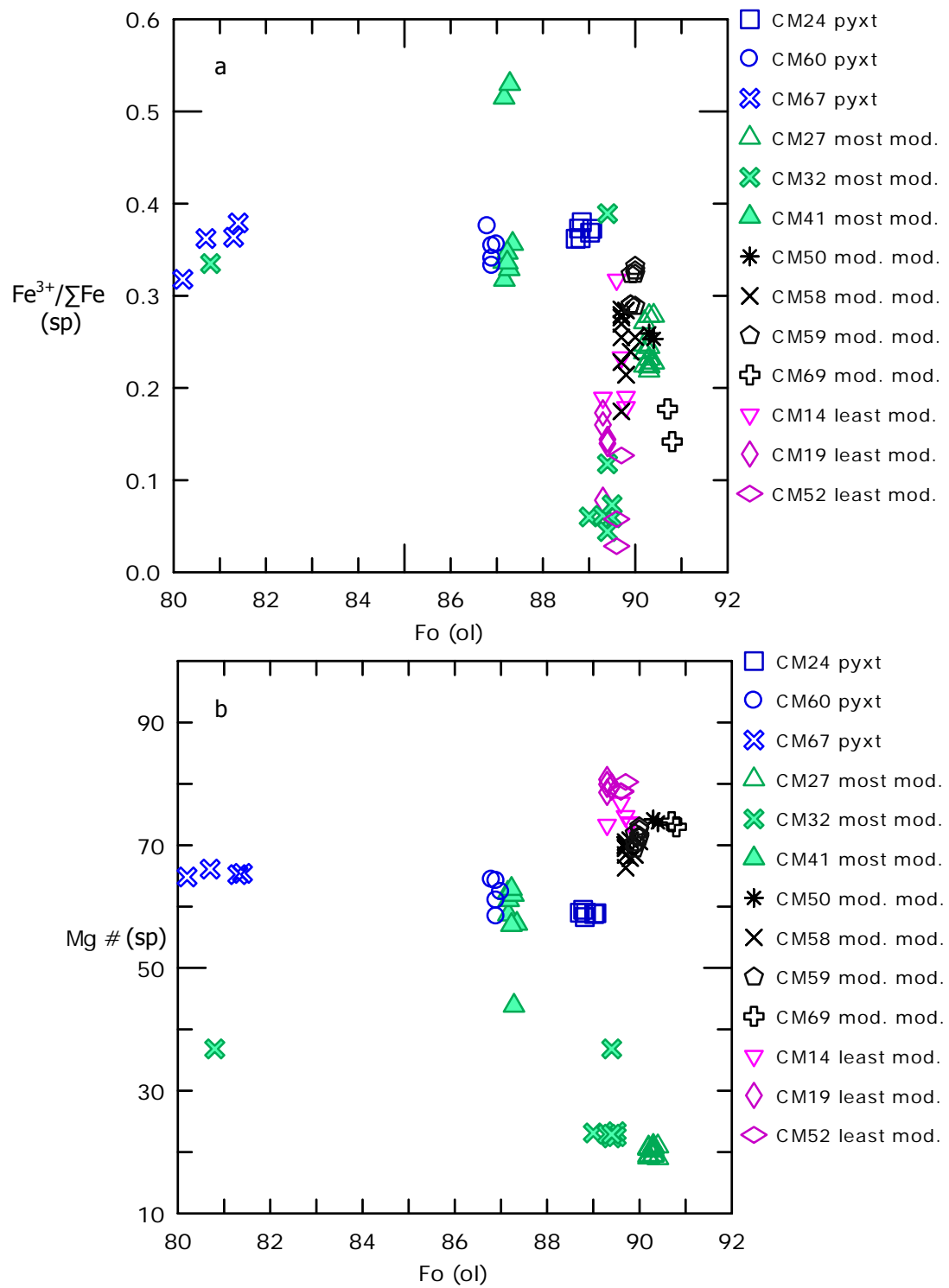


Figure 4.13. a)  $\text{Fe}^{3+}/\Sigma\text{Fe}$  (sp) vs. Fo (ol). The pyroxenes and most modified peridotites show greater concentrations of ferric iron.  $\text{Fe}^{3+}$  calculated using the method of Barnes & Roeder (2001). b) Mg# (sp) vs. Fo (ol). The least and moderately modified peridotites show little variability in both parameters and significant correlation between the two.

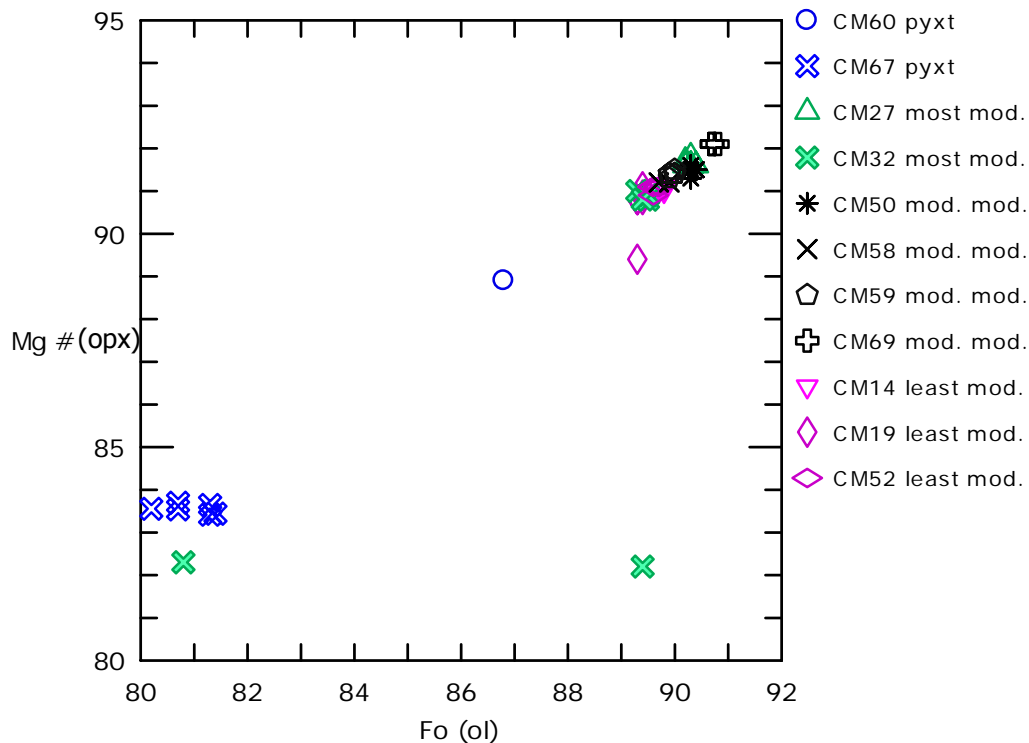


Figure 4.14. Mg# (opx) vs. Fo (ol). A very good correlation between the two parameters is shown by the orthopyroxene in both the peridotites and pyroxenites, although the Mg# in the pyroxenites is generally lower.

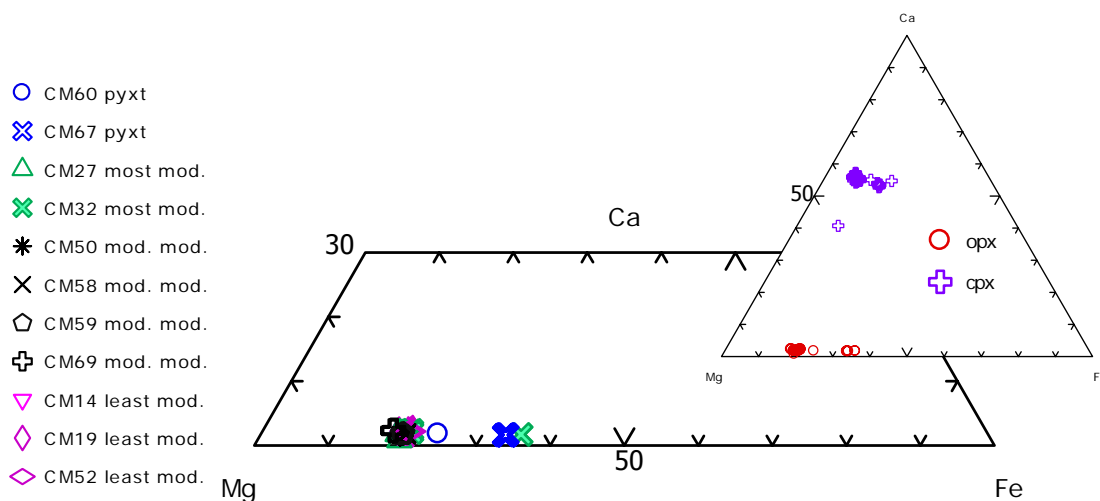


Figure 4.15. Pyroxene end member trigram with opx space enlarged. There is a larger degree of homogeneity in the orthopyroxene of the CM xenolith suite. The pyroxenites and some grains of the most modified peridotite are enriched in FeO. Parameters are concentration in ppm.

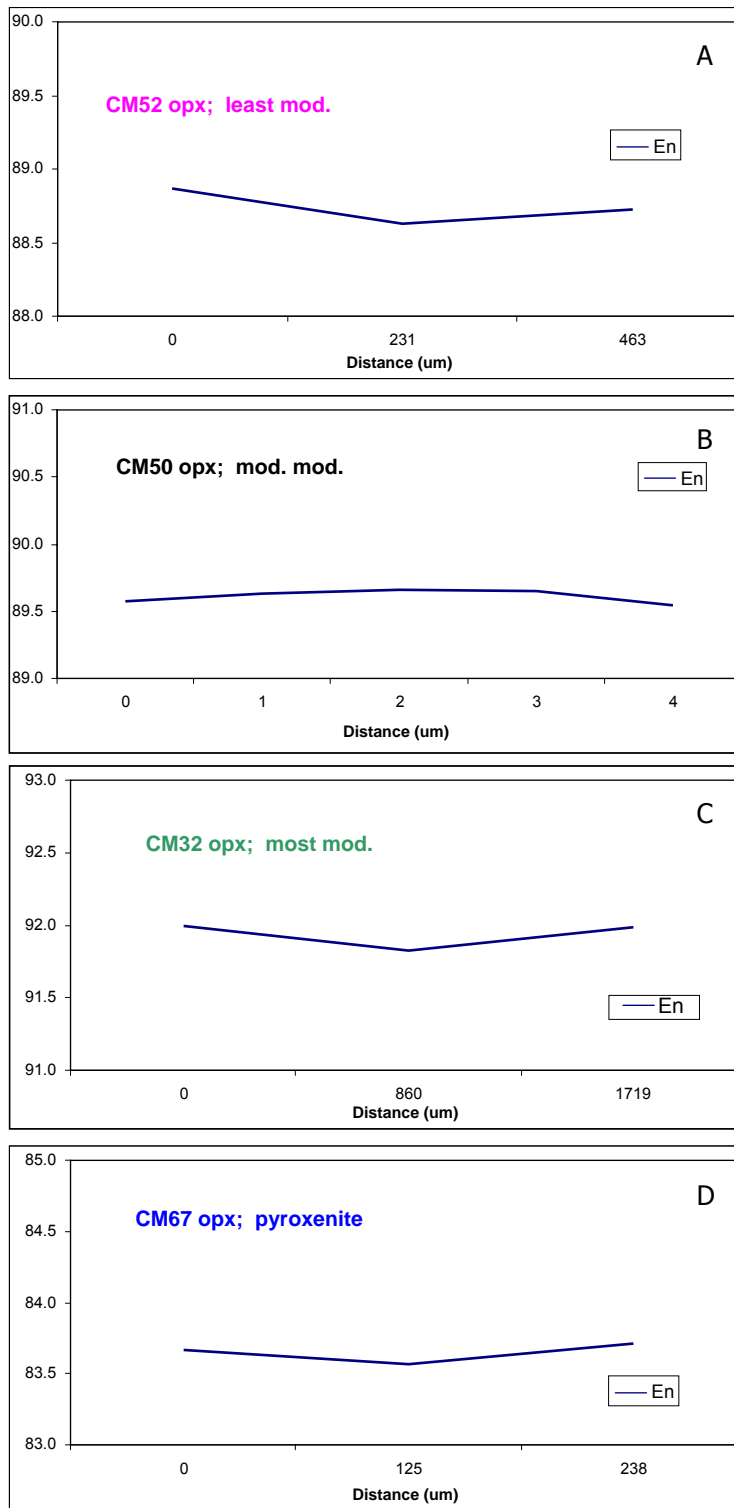


Figure 4.16. Compositional line scans across opx grains in xenoliths: A) least modified; B) moderately modified; C) most modified; D) pyroxenite.

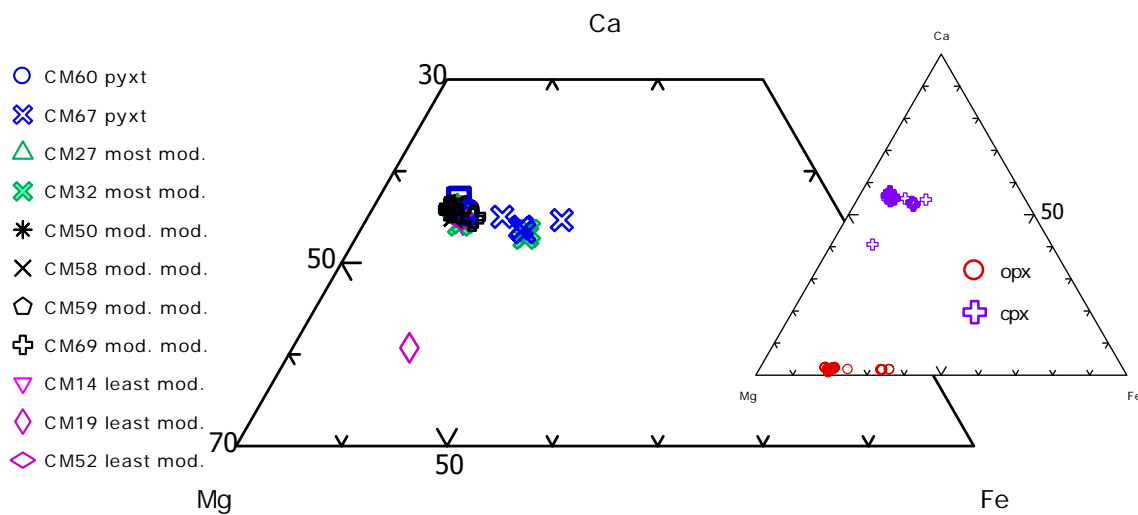


Figure 4.17. Clinopyroxene end member plot with an inset for pyroxene comparison. One pyroxenite and a grain from a most modified peridotite are relatively enriched in Fe. Values are relative to Mg; in inset, number is relative to Fe.

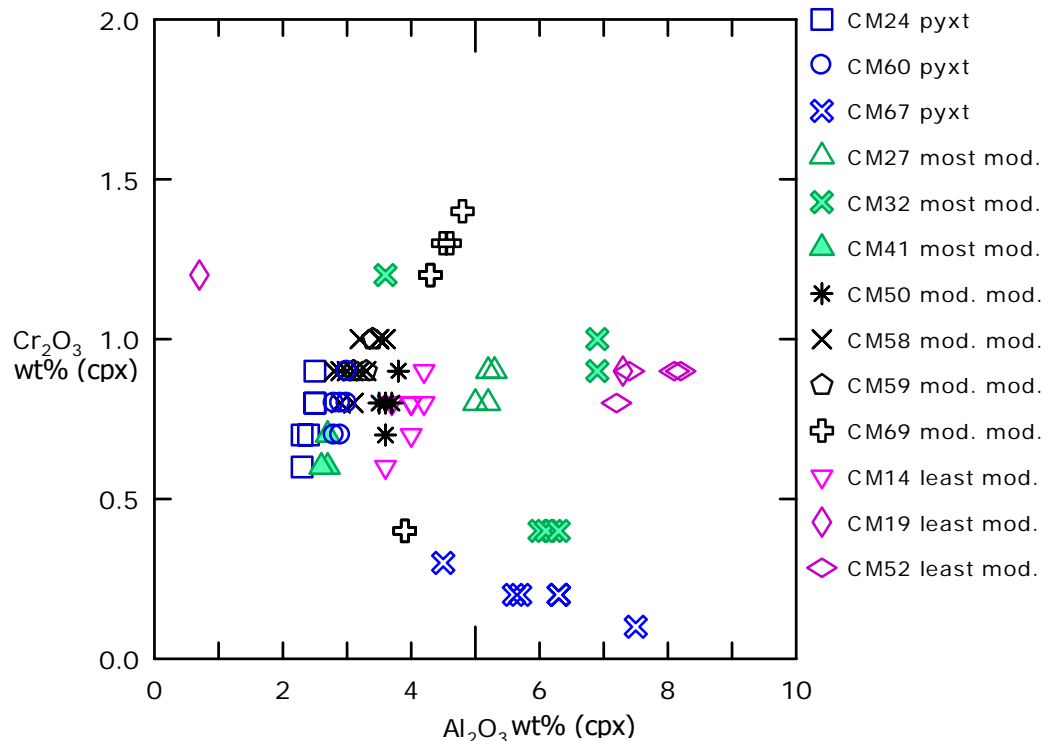


Figure 4.18.  $\text{Al}_2\text{O}_3$  wt% (cpx) vs.  $\text{Cr}_2\text{O}_3$  wt% (cpx). In individual rocks, there is a positive correlation between  $\text{Al}_2\text{O}_3$  and  $\text{Cr}_2\text{O}_3$ . Exceptions are pyroxenite CM67 and an outlier grain from CM19, which borders the host basanite.

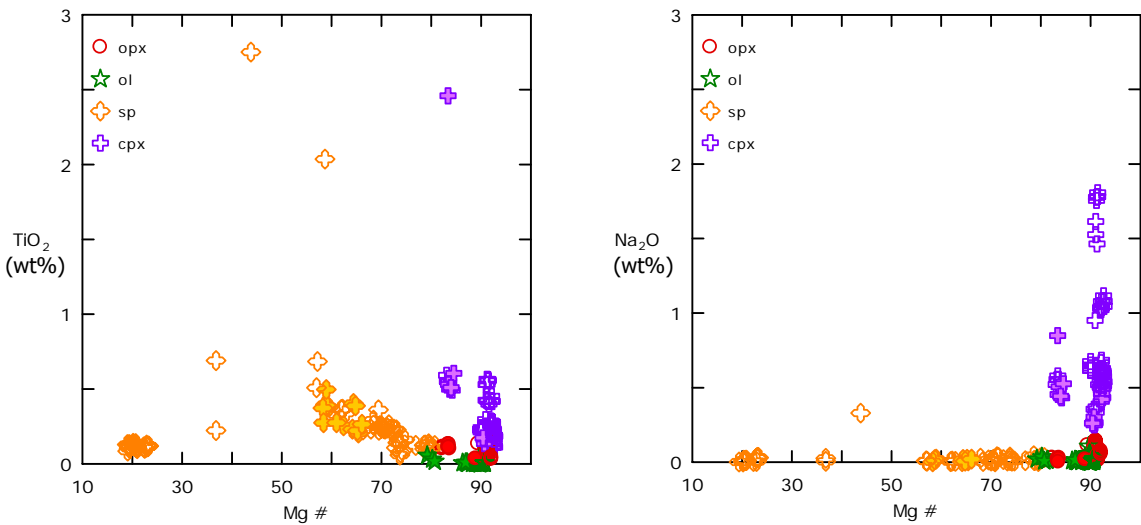


Figure 4.19.  $\text{TiO}_2$  (wt%) and  $\text{Na}_2\text{O}$  (wt%) vs. Mg# in mineral phases. Cpx is a host phase for both oxides. Filled symbols represent pyroxenite phases; open symbols are peridotite phases.

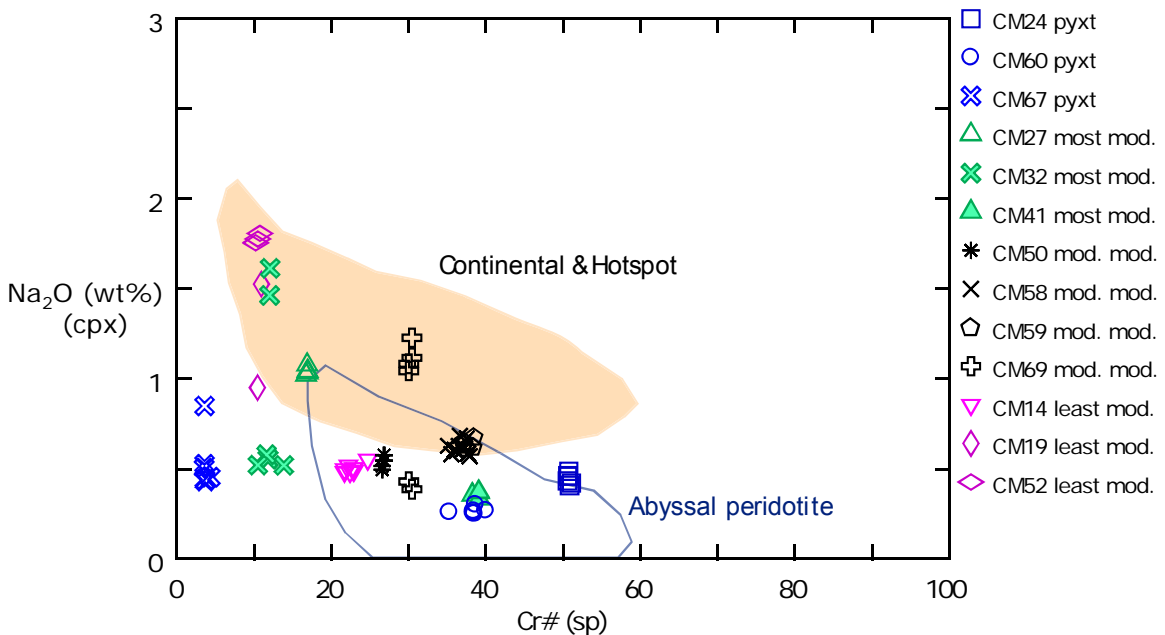


Figure 4.20.  $\text{Na}_2\text{O}$  (cpx) vs.  $\text{Cr}^\#$  (sp). Higher  $\text{Na}_2\text{O}$  in cpx grains suggests higher pressures of equilibration. Shaded peach area represents continental and hotspot peridotites and blue area of abyssal peridotite are from Japan island arcs, forearcs and the Japan Sea (Arai, 1991; Arai & Ishimaru, 2007).

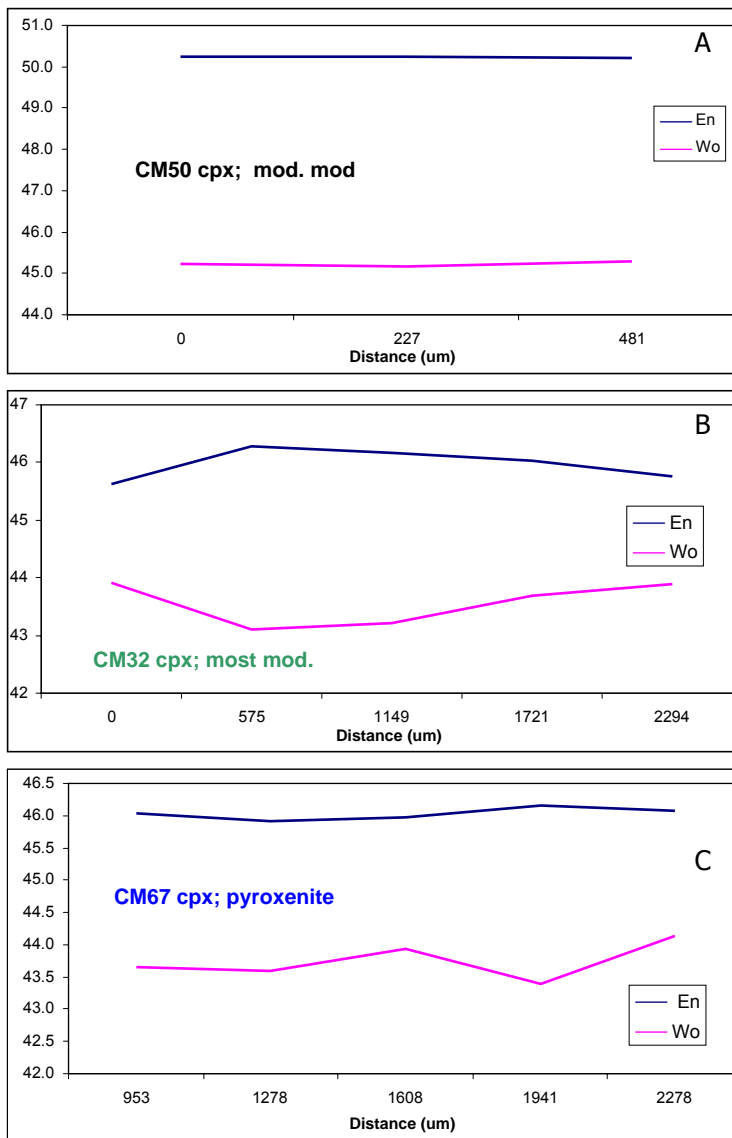


Figure 4.21. Line scans across cpx grains in representative xenoliths: A) moderately modified; B) most modified; C) pyroxenite.

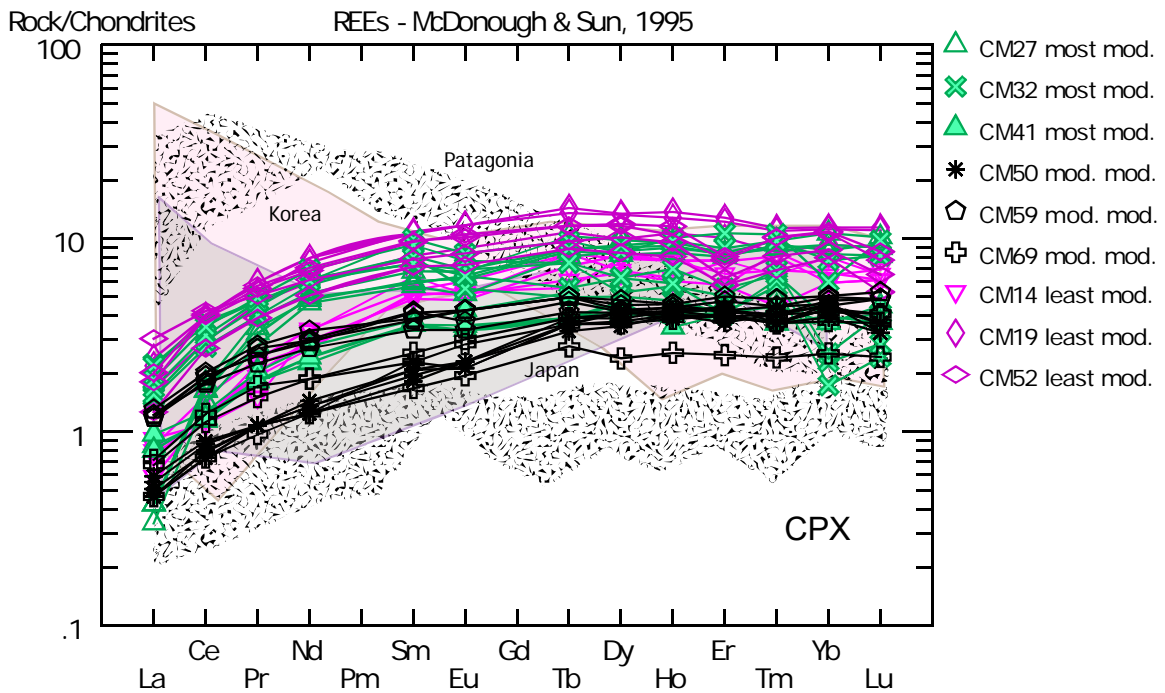


Figure 4.22. Clinopyroxene REE patterns normalized to chondrites (McDonough & Sun, 1995). Included, for comparison, is cpx data of mantle peridotites from Patagonia (Laurora et al., 2001), Korea (Choi et al., 2002) and Japan (Abe et al., 2003). The CM peridotite cpx fall within range of cpx from other suites.

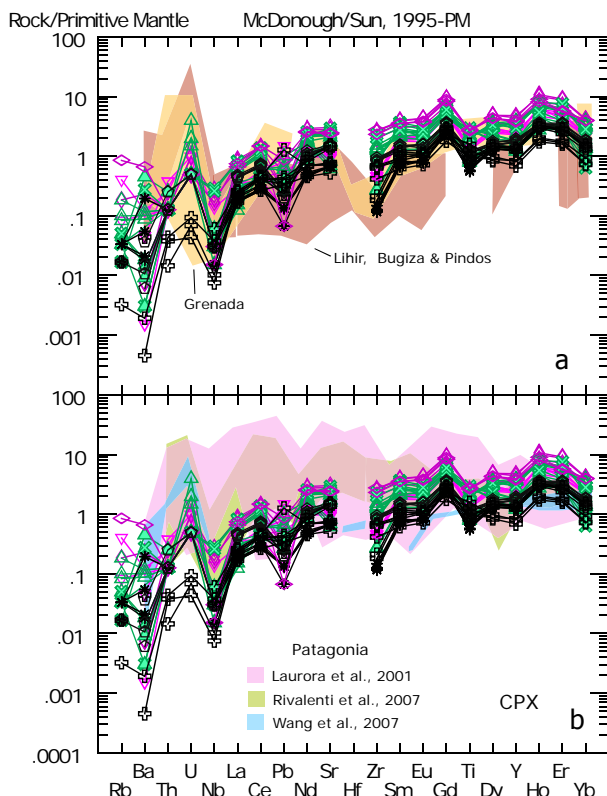


Figure 4.23. Extended trace element patterns of clinopyroxene grains normalized to primitive mantle (McDonough & Sun, 1995). Data for shaded areas in a) from Vannucci et al. (2007) and references therein; data for Patagonia as shown. The CM peridotite cpx are similar in extended trace elements to other arc peridotite cpx grains.

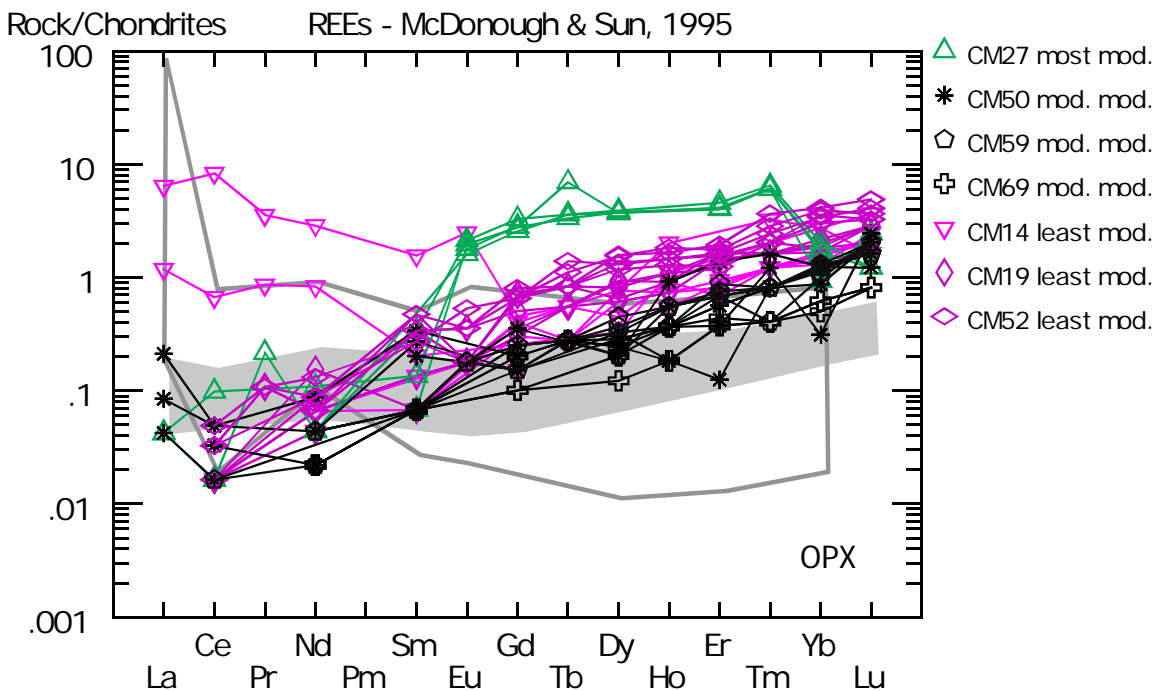


Figure 4.24. Opx REE patterns normalized to chondrites (McDonough & Sun, 1995). Outlined area from the Hellenic Peninsula (Bizimis et al., 2000); shaded area from Grenada (Parkinson et al., 2003) for comparison.

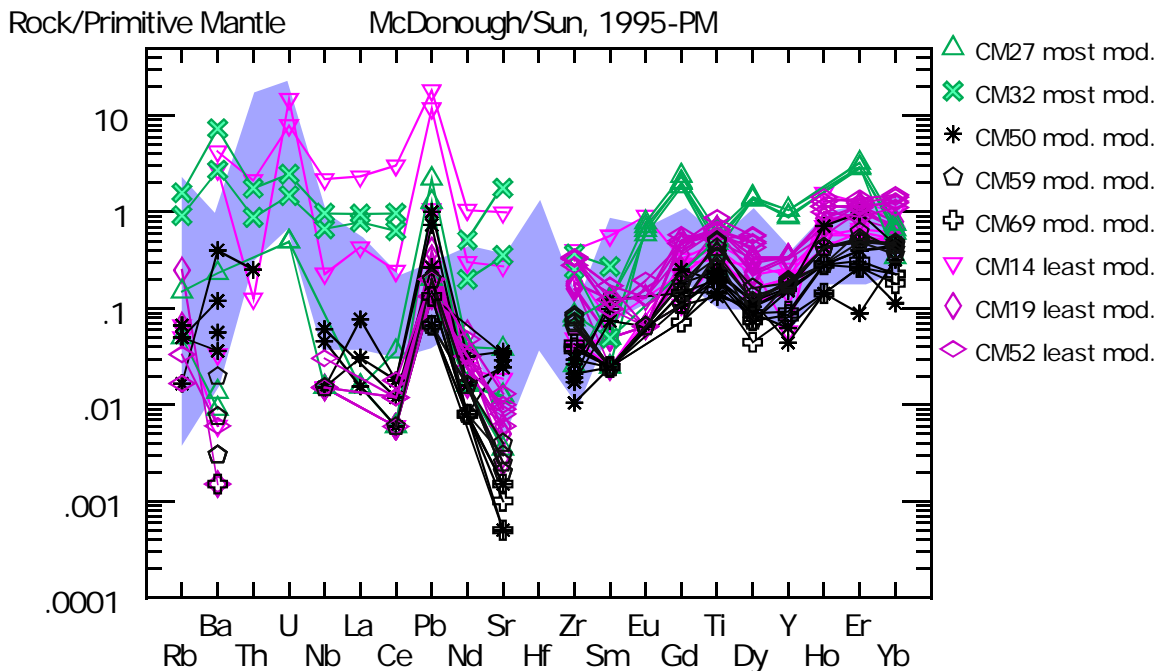


Figure 4.25. Extended trace element patterns of orthopyroxene grains normalized to primitive mantle. Shaded area includes peridotite opx grains from IBM (Parkinson et al., 1998), Lihir (Grégoire et al, 2001) and Grenada (Vannucci et al, 2007). Note CM14, a least modified peridotite that is more similar to the most modified peridotite CM32 – not the other least modified peridotites.

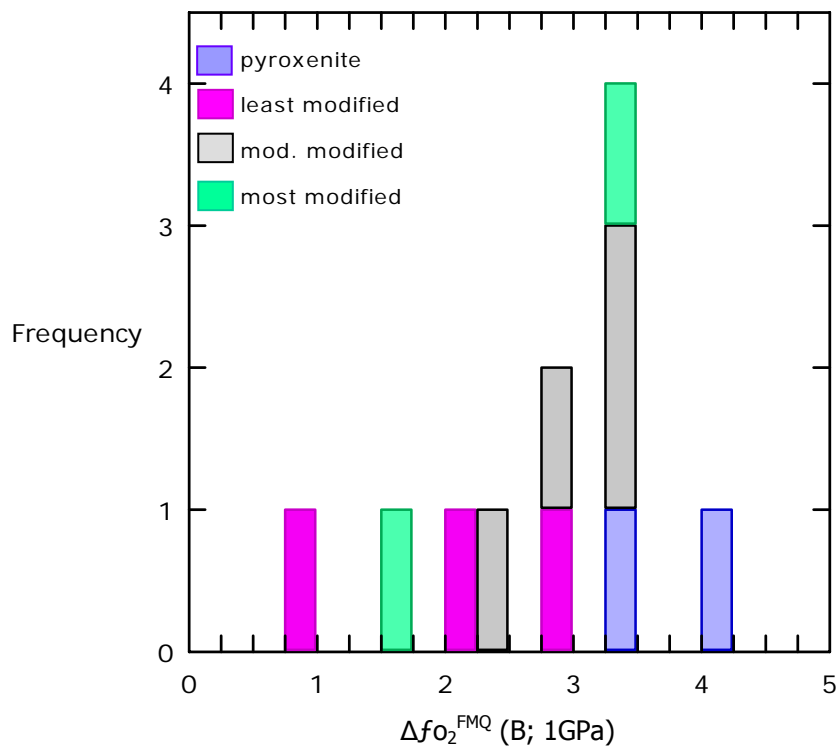


Figure 4.26. Histogram of the estimated oxygen fugacity of the CM xenoliths using the method of Ballhaus et al. (1991) at 1GPa; N = 11.

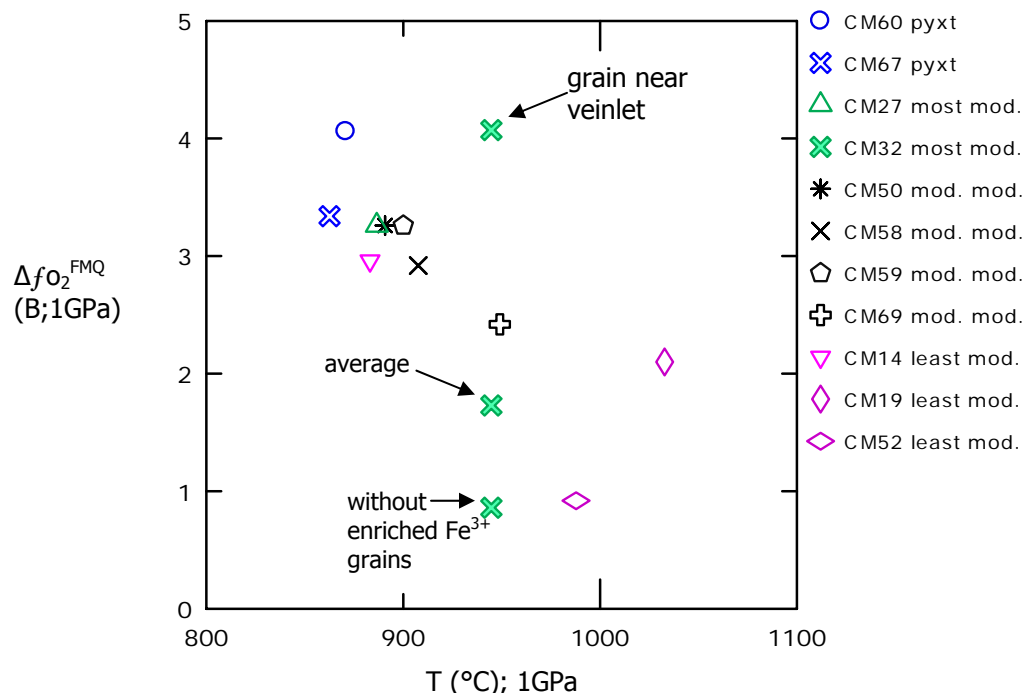


Figure 4.27. Oxygen fugacity vs. equilibrium temperature. Note the different values in grains from CM32; that with elevated  $\Delta f_{O_2}^{FMQ}$  abuts vein material near the edge of the xenolith and is enriched in  $Fe^{3+}$ . Without those grains, the  $\Delta f_{O_2}^{FMQ}$  is under +1. However, the average will be used for discussion.

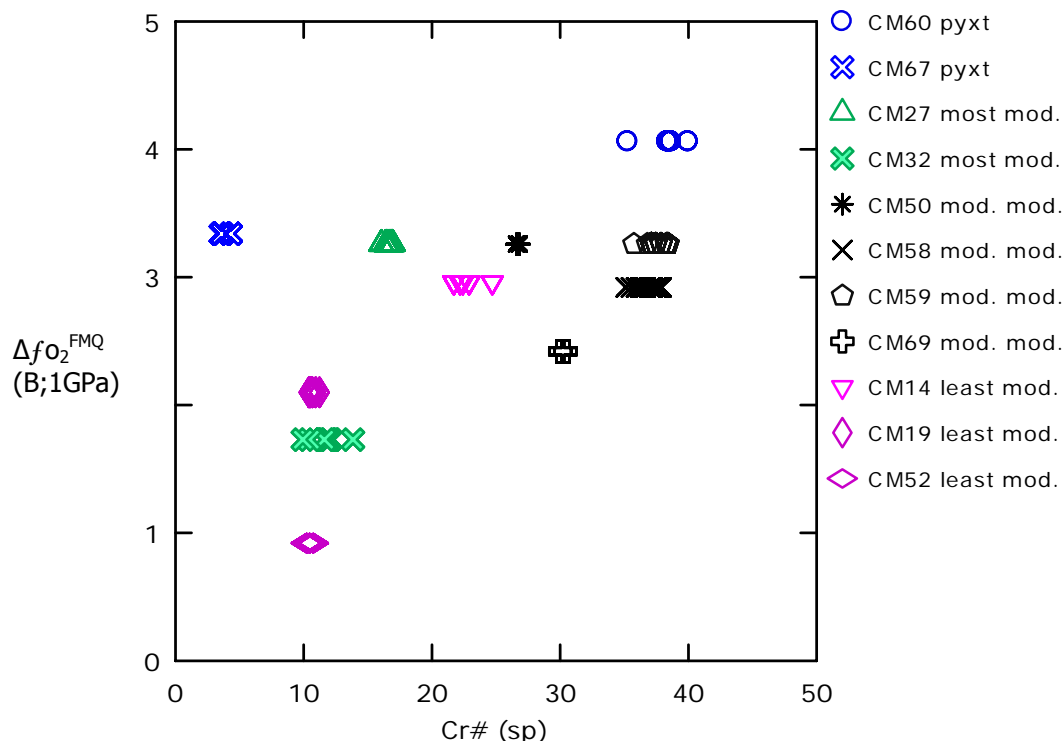


Figure 4.28. Oxygen fugacity vs. Cr# in spinel. A positive correlation between the two variables suggests a trend of melt/mantle interaction that leads to elevated oxygen fugacity (Ballhaus, 1993; Parkinson & Arculus, 1999).

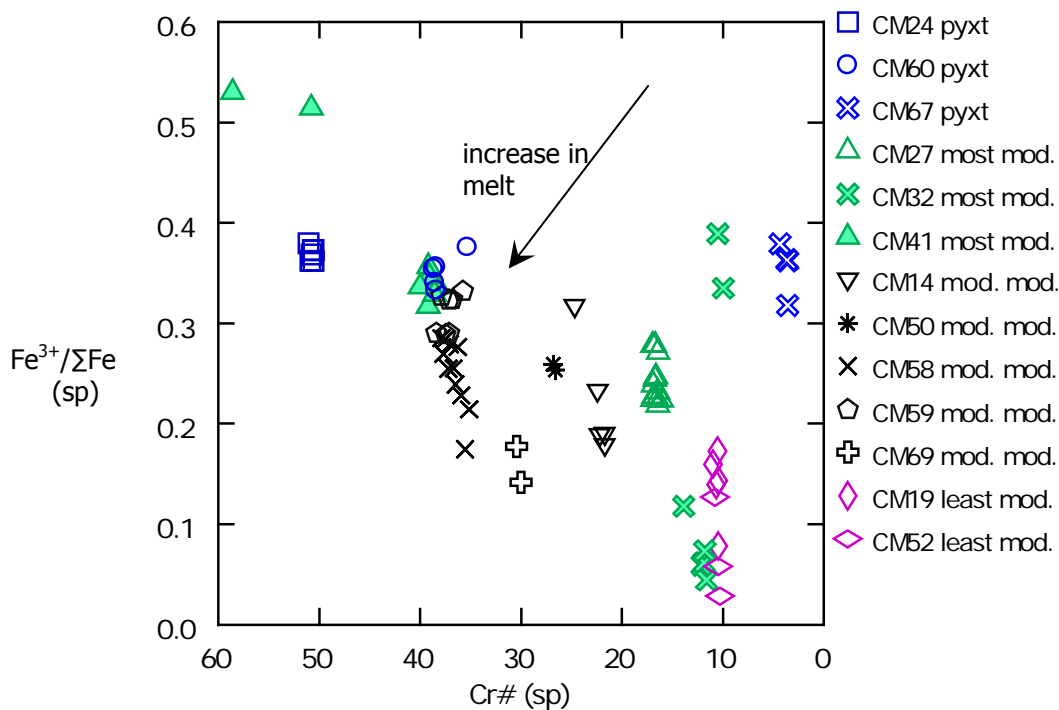


Figure 4.29.  $\text{Fe}^{3+}/\Sigma\text{Fe}$  vs. Cr# in spinel. Extensive melt decreases the  $\text{Fe}^{3+}/\Sigma\text{Fe}$  (cations based on 4 oxygen) (Frost & McCammon, 2008) and increases the Cr# (Parkinson et al., 2003). The arrow indicates the direction of increasing melt. Note the inverse range of the X-axis.

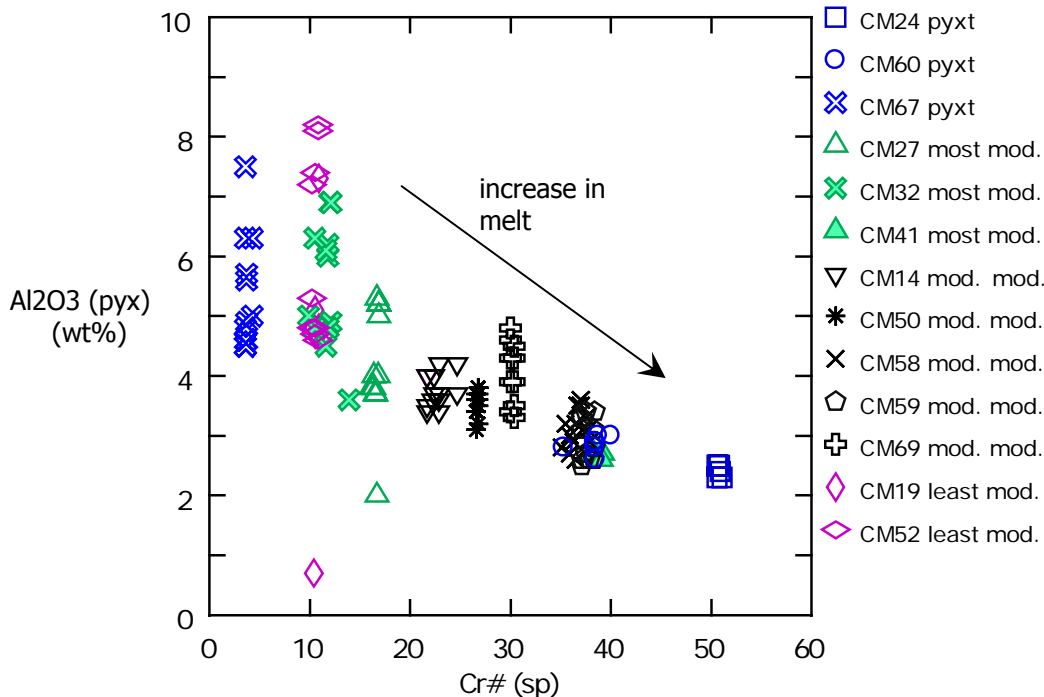


Figure 4.30.  $\text{Al}_2\text{O}_3$  wt% (pyx) vs. Cr# (sp). Decreasing  $\text{Al}_2\text{O}_3$  (wt%) in pyroxene phases with increasing Cr# indicates that the mantle has experienced some % partial melting (Bonatti & Michael, 1989).

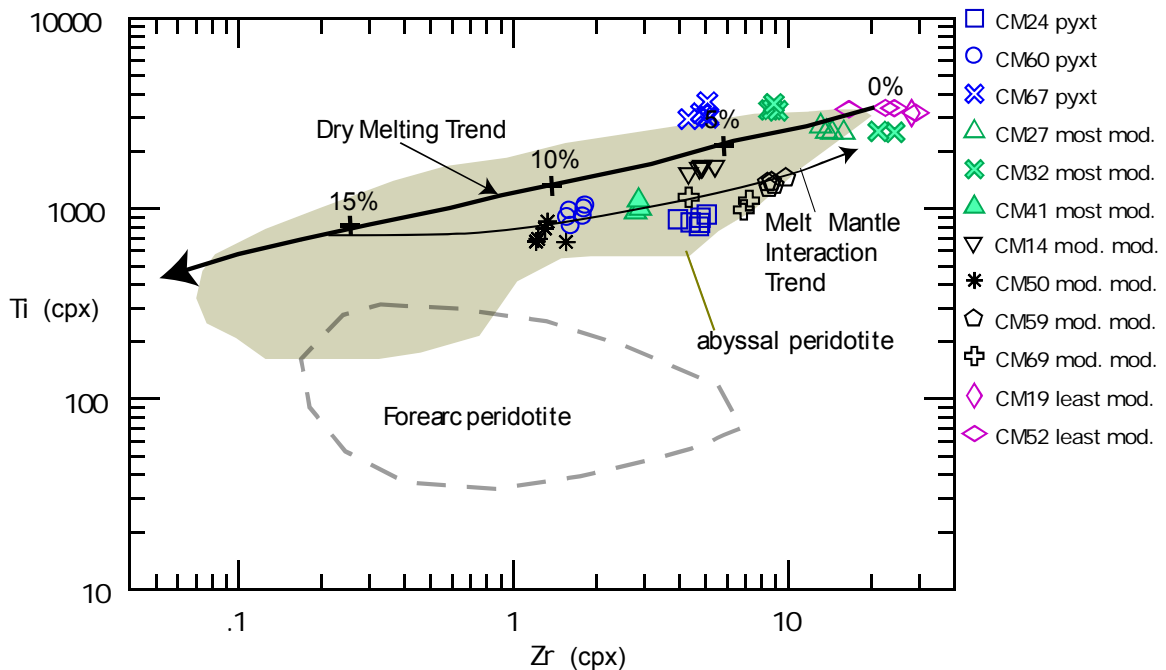


Figure 4.31. Ti (ppm) vs. Zr (ppm) of CM clinopyroxene. Partial melting trend from Bizimis et al. (2000), calculated with MORB source mantle as starting material with anhydrous incremental batch melting. Abyssal peridotite data from Johnson (1990) and Johnson & Dick (1992). Forearc peridotite field from Parkinson et al. (1992). Melt-mantle interaction trend from Kelemen et al. (1990).

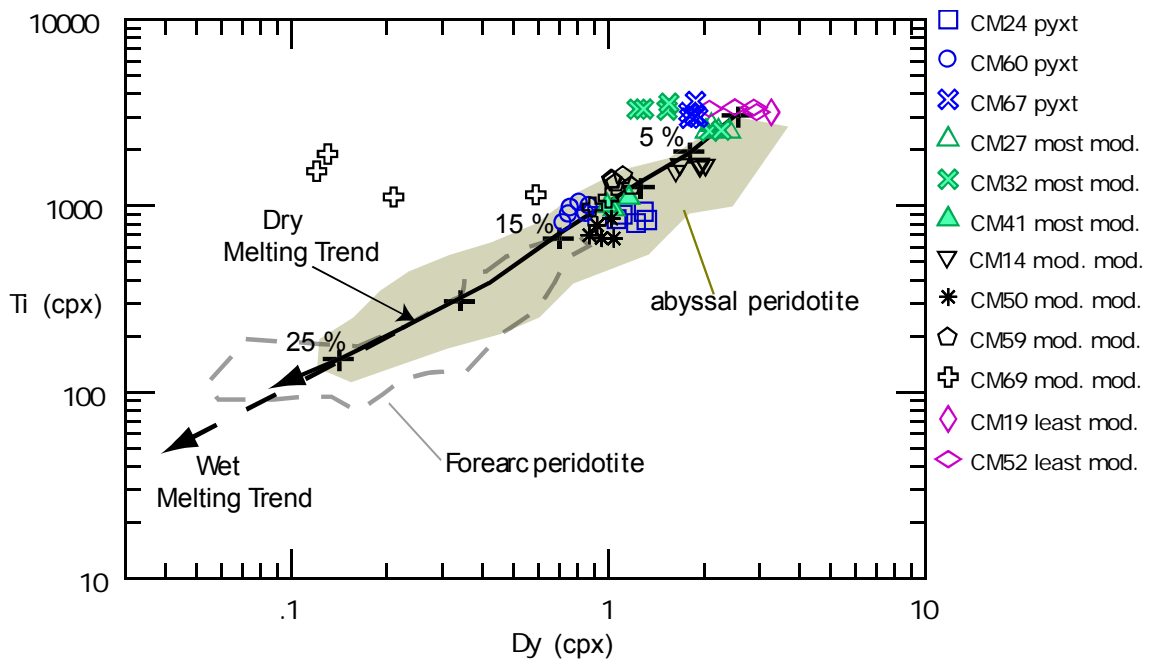


Figure 4.32. Ti (ppm) vs. Dy (ppm) of CM clinopyroxene. Wet melting trend from Bizimis (2000). Other fields as in figure 4.31.

Table 4.1. Olivine compositions in CM xenoliths; oxides in wt%; trace in ppm

Rock	Sample	SiO <sub>2</sub>	TiO <sub>2</sub>	Al <sub>2</sub> O <sub>3</sub>	Cr <sub>2</sub> O <sub>3</sub>	FeO	MnO	MgO	CaO	NiO	Na <sub>2</sub> O
CM14	ol5	40.97	0.01	0.00	0.01	10.05	0.15	49.35	0.04	0.38	0.00
CM14	ol6	41.01	0.01	0.00	0.02	10.13	0.14	49.37	0.06	0.39	0.00
CM14	ol7	41.07	0.00	0.00	0.02	10.01	0.13	49.49	0.04	0.39	0.02
CM14	ol9	41.16	0.01	0.00	0.00	10.06	0.12	49.46	0.05	0.36	0.01
CM14	ol15	40.85	0.00	0.00	0.01	10.00	0.11	49.42	0.03	0.40	0.00
CM14	ol25	40.51	0.01	0.00	0.02	10.39	0.19	48.55	0.12	0.49	0.00
CM14	ol29	40.98	0.02	0.00	0.03	10.08	0.13	49.37	0.04	0.33	0.01
CM14	ol34	41.00	0.01	0.00	0.04	10.17	0.15	49.01	0.04	0.42	0.00
CM14	ol35	40.78	0.00	0.00	0.02	9.99	0.14	49.37	0.05	0.38	0.00
CM19	ol57	41.12	0.01	0.00	0.01	10.38	0.15	49.13	0.07	0.41	0.05
CM19	ol59	40.97	0.00	0.00	0.00	10.43	0.16	49.05	0.07	0.37	0.04
CM19	ol63	41.00	0.00	0.00	0.01	10.47	0.16	49.32	0.05	0.36	0.01
CM19	ol65	41.12	0.01	0.00	0.02	10.40	0.13	49.10	0.06	0.36	0.03
CM19	ol66	41.10	0.01	0.00	0.01	10.51	0.13	49.23	0.06	0.39	0.04
CM19	ol67	40.80	0.00	0.00	0.01	10.38	0.14	48.98	0.05	0.37	0.02
CM19	ol73	40.76	0.00	0.00	0.07	10.44	0.14	48.82	0.06	0.34	0.05
CM19	ol77	40.98	0.01	0.00	0.00	10.51	0.12	49.20	0.05	0.39	0.05
CM19	ol80	40.85	0.00	0.00	0.02	10.42	0.14	49.18	0.05	0.39	0.02
CM24	ol48_1	40.81	0.00	0.00	0.00	10.85	0.16	49.08	0.06	0.29	0.01
CM24	ol48_4	40.48	0.01	0.02	0.03	10.77	0.16	49.00	0.07	0.29	0.00
CM24	ol49	40.47	0.00	0.00	0.01	10.78	0.16	49.30	0.05	0.23	0.00
CM24	ol52	40.29	0.01	0.00	0.02	11.05	0.18	48.71	0.13	0.30	0.02
CM24	ol54	37.28	0.00	0.00	0.21	11.37	0.19	47.56	0.05	0.27	0.00
CM24	ol56	39.37	0.00	0.01	0.02	10.88	0.21	48.46	0.06	0.26	0.02
CM24	ol61_3	37.88	0.00	0.02	0.01	10.84	0.19	48.43	0.06	0.27	0.02
CM24	ol62_3	38.82	0.00	0.01	0.00	10.77	0.14	48.13	0.07	0.26	0.01
CM27	ol1	40.37	0.00	0.00	0.00	9.55	0.13	50.06	0.06	0.36	0.01
CM27	ol1_2	40.22	0.00	0.00	0.02	9.57	0.14	50.10	0.07	0.37	0.00
CM27	ol1_3	40.16	0.00	0.00	0.00	9.54	0.16	50.00	0.04	0.37	0.01
CM27	ol2	39.63	0.01	0.00	0.02	9.65	0.15	49.93	0.06	0.33	0.00
CM27	ol4	40.42	0.01	0.00	0.00	9.64	0.13	50.19	0.05	0.37	0.01
CM27	ol9	40.55	0.00	0.01	0.02	9.68	0.15	50.15	0.03	0.36	0.01
CM27	ol15	40.60	0.01	0.00	0.00	9.49	0.15	50.07	0.05	0.33	0.01
CM27	ol17	40.45	0.00	0.00	0.00	9.56	0.13	50.08	0.04	0.32	0.01
CM27	ol18	40.37	0.00	0.00	0.00	9.56	0.11	50.00	0.05	0.38	0.02
CM27	ol22	40.81	0.01	0.00	0.07	9.62	0.20	50.12	0.04	0.36	0.02
CM27	ol23	40.21	0.01	0.00	0.02	9.66	0.13	50.01	0.04	0.32	0.00
CM27	ol26	40.06	0.00	0.00	0.02	9.57	0.11	49.88	0.13	0.36	0.02
CM27	ol28	40.60	0.01	0.00	0.07	9.63	0.15	49.84	0.05	0.32	0.00
CM27	ol31	40.45	0.01	0.00	0.12	9.47	0.16	49.94	0.10	0.28	0.01
CM27	ol34	40.38	0.00	0.00	0.02	9.59	0.16	46.60	0.04	0.37	0.01
CM27	ol36	40.82	0.01	0.00	0.01	9.46	0.12	49.65	0.03	0.37	0.03
CM27	ol42	40.18	0.01	0.00	0.00	9.60	0.15	49.82	0.06	0.31	0.02
CM32	ol56	40.83	0.00	0.00	0.03	10.36	0.17	49.07	0.06	0.35	0.02
CM32	ol58	40.73	0.02	0.00	0.02	10.66	0.21	48.44	0.14	0.33	0.01
CM32	ol63	40.14	0.00	0.00	0.01	10.23	0.17	48.83	0.07	0.39	0.01
CM32	ol65_2	40.29	0.02	0.04	0.02	10.37	0.15	48.66	0.06	0.33	0.01
CM32	ol65_4	39.93	0.01	0.00	0.02	10.24	0.17	48.74	0.06	0.35	0.00
CM32	ol65_9	39.57	0.00	0.00	0.01	10.22	0.17	48.42	0.06	0.32	0.01
CM32	ol67	38.09	0.00	0.00	0.02	10.22	0.13	48.15	0.05	0.32	0.02

Table 4.1. continued

Rock	Sample	SiO <sub>2</sub>	TiO <sub>2</sub>	Al <sub>2</sub> O <sub>3</sub>	Cr <sub>2</sub> O <sub>3</sub>	FeO	MnO	MgO	CaO	NiO	Na <sub>2</sub> O
CM41	ol35	39.56	0.01	0.00	0.01	12.40	0.23	47.23	0.06	0.23	0.01
CM41	ol43_12	38.82	0.00	0.00	0.01	12.25	0.19	46.93	0.04	0.22	0.01
CM41	ol43_3	38.82	0.00	0.00	0.01	12.25	0.19	46.93	0.04	0.22	0.01
CM41	ol43_7	38.82	0.00	0.00	0.01	12.25	0.19	46.93	0.04	0.22	0.01
CM41	ol48	38.44	0.00	0.00	0.02	12.21	0.18	47.29	0.05	0.20	0.00
CM41	ol53_5	39.96	0.00	0.01	0.00	12.26	0.18	47.23	0.04	0.21	0.00
CM50	ol71	41.03	0.00	0.00	0.02	9.53	0.15	50.24	0.06	0.38	0.01
CM50	ol72	40.61	0.00	0.00	0.01	9.51	0.15	49.94	0.04	0.39	0.00
CM50	ol73	41.18	0.00	0.00	0.01	9.66	0.13	50.14	0.05	0.37	0.01
CM50	ol82	40.88	0.01	0.00	0.00	9.48	0.16	50.17	0.04	0.35	0.00
CM50	ol90_1	41.22	0.00	0.00	0.01	9.51	0.14	50.00	0.03	0.37	0.01
CM50	ol90_8	40.86	0.00	0.00	0.01	9.45	0.12	49.58	0.03	0.38	0.00
CM52	ol36	40.78	0.01	0.00	0.02	10.16	0.13	49.21	0.10	0.39	0.00
CM52	ol38	41.29	0.01	0.00	0.00	10.14	0.13	49.26	0.04	0.38	0.02
CM52	ol40	40.99	0.00	0.00	0.01	10.07	0.12	49.17	0.06	0.41	0.02
CM52	ol42	41.06	0.00	0.00	0.01	10.23	0.15	49.27	0.06	0.42	0.01
CM52	ol45	41.09	0.00	0.00	0.01	10.15	0.15	49.27	0.10	0.39	0.05
CM52	ol47_8	41.12	0.00	0.00	0.03	10.23	0.13	49.37	0.06	0.40	0.02
CM52	ol51	41.15	0.01	0.00	0.02	10.13	0.11	49.10	0.07	0.39	0.02
CM52	ol52	41.05	0.01	0.00	0.01	10.11	0.13	49.41	0.06	0.39	0.02
CM52	ol54	41.01	0.00	0.00	0.01	10.20	0.08	49.49	0.06	0.39	0.03
CM52	ol56_6	40.88	0.00	0.00	0.02	10.16	0.12	49.02	0.08	0.38	0.11
CM58	ol2	41.26	0.04	0.00	0.01	9.99	0.15	48.99	0.05	0.36	0.00
CM58	ol7	40.77	0.00	0.00	0.02	9.71	0.11	48.76	0.04	0.37	0.02
CM58	ol8	41.39	0.00	0.00	0.01	10.06	0.13	49.14	0.05	0.36	0.02
CM58	ol10	41.45	0.00	0.00	0.01	10.03	0.13	49.22	0.05	0.34	0.01
CM58	ol11	41.11	0.02	0.00	0.00	9.89	0.13	49.12	0.04	0.37	0.01
CM58	ol12	40.85	0.02	0.00	0.05	9.94	0.15	49.04	0.03	0.36	0.02
CM58	ol17	41.17	0.01	0.00	0.01	9.97	0.08	48.84	0.07	0.36	0.00
CM58	ol19	40.97	0.00	0.00	0.01	9.90	0.14	48.81	0.04	0.38	0.01
CM58	ol22	40.81	0.01	0.00	0.02	9.94	0.15	48.82	0.05	0.39	0.04
CM58	ol25	40.71	0.00	0.00	0.01	9.94	0.14	48.80	0.04	0.34	0.01
CM58	ol28	40.80	0.01	0.00	0.00	10.01	0.13	48.78	0.04	0.39	0.04
CM58	ol31	41.20	0.00	0.00	0.02	9.88	0.13	48.92	0.05	0.38	0.03
CM58	ol32	41.03	0.00	0.00	0.02	9.94	0.13	48.99	0.04	0.39	0.01
CM58	ol35	41.36	0.02	0.00	0.02	10.03	0.14	49.05	0.05	0.35	0.02
CM58	ol38	41.14	0.00	0.00	0.01	10.01	0.13	48.80	0.06	0.36	0.06
CM58	ol41	41.47	0.00	0.00	0.00	9.91	0.15	49.17	0.08	0.36	0.02
CM58	ol49	40.54	0.00	0.00	0.01	9.95	0.15	48.88	0.03	0.39	0.01
CM58	ol58	40.60	0.00	0.00	0.01	9.97	0.14	49.03	0.05	0.39	0.00
CM58	ol61	40.61	0.00	0.00	0.01	10.00	0.14	48.97	0.04	0.39	0.02
CM59	ol1	40.67	0.00	0.00	0.02	9.81	0.13	49.27	0.05	0.36	0.00
CM59	ol9	40.67	0.00	0.00	0.01	9.88	0.17	49.43	0.05	0.35	0.00
CM59	ol10	40.71	0.00	0.00	0.02	9.84	0.12	49.40	0.05	0.33	0.00
CM59	ol15_6	40.97	0.01	0.00	0.01	9.89	0.17	49.65	0.05	0.38	0.00
CM59	ol19	41.24	0.01	0.00	0.02	9.90	0.12	49.54	0.04	0.35	0.01
CM59	ol28	41.48	0.01	0.00	0.00	9.87	0.14	49.70	0.05	0.35	0.01
CM59	ol33	40.83	0.00	0.00	0.01	9.81	0.15	49.62	0.04	0.35	0.03

Table 4.1. continued

Rock	Sample	SiO <sub>2</sub>	TiO <sub>2</sub>	Al <sub>2</sub> O <sub>3</sub>	Cr <sub>2</sub> O <sub>3</sub>	FeO	MnO	MgO	CaO	NiO	Na <sub>2</sub> O
CM60	ol103	40.43	0.00	0.00	0.02	12.76	0.18	47.28	0.06	0.24	0.00
CM60	ol88_4	40.41	0.00	0.00	0.00	12.55	0.22	46.99	0.10	0.18	0.00
CM60	ol89_2	40.48	0.01	0.00	0.01	13.15	0.22	46.47	0.15	0.20	0.01
CM60	ol89_4	40.33	0.00	0.01	0.04	12.58	0.20	46.93	0.07	0.24	0.01
CM60	ol98	40.55	0.01	0.00	0.02	12.67	0.22	47.01	0.06	0.23	0.00
CM67	ol68_12	38.40	0.00	0.00	0.01	17.68	0.26	43.50	0.08	0.10	0.01
CM67	ol68_13	38.32	0.00	0.00	0.00	17.83	0.27	43.52	0.05	0.10	0.01
CM67	ol68_9	37.68	0.06	0.55	0.07	18.95	0.29	40.60	0.20	0.08	0.02
CM67	ol69_10	39.06	0.00	0.00	0.00	17.82	0.28	43.21	0.05	0.12	0.00
CM67	ol72	38.99	0.03	0.01	0.06	18.61	0.30	42.35	0.20	0.07	0.03
CM67	ol83	37.93	0.02	0.01	0.01	17.90	0.45	41.96	0.24	0.18	0.01
CM69	ol81	41.18	0.00	0.00	0.01	9.15	0.15	50.12	0.04	0.43	0.00
CM69	ol84	41.45	0.00	0.00	0.02	9.15	0.14	50.52	0.04	0.41	0.01
CM69	ol85	41.34	0.00	0.00	0.01	9.14	0.11	50.36	0.05	0.38	0.00
CM69	ol87	41.24	0.00	0.00	0.03	9.24	0.13	50.29	0.05	0.42	0.02
CM69	ol90_7	41.51	0.00	0.00	0.00	9.21	0.13	50.36	0.05	0.35	0.02
CM69	ol91	41.34	0.00	0.00	0.01	9.37	0.11	49.47	0.06	0.39	0.01

Table 4.1. continued

Rock	Sample	Li	Sc	V	Cr	Co	Ni	Cu	Zn	Sr	Y	Zr	Ba	La
CM14	ol5	1.76	10.28	1.65	65.81	108.3	4460.1	1	42.39	0	0	0	0	0
CM14	ol6	5.01	9.3	4.27	157.09	273.42	11346	2.81	106.43	0	0	0	0.15	0
CM14	ol7	5.19	12.12	4.95	133.15	224.14	8974.7	2.59	86.71	0.04	0.04	0.01	0.12	0
CM14	ol9	0.9	11.52	0.9	33.59	57.38	2318.6	0.71	22.51	0.01	0.01	0.01	0.17	0
CM14	ol15	8.65	10.49	2.34	80.8	136.02	5429	4.73	52.87	0	0.01	0	0	0.01
CM14	ol25	10.78	9.87	4.65	153.06	261	10881	3.2	106.98	0.03	0	0	0.15	0
CM14	ol34	7.9	7.38	7.62	259.93	444.44	18143	5.22	178.35	0	0.02	0.03	0.02	0
CM14	ol35	3.8	11.46	4.13	167.15	272.73	11170	6.98	111.46	0	0.06	0.06	0.15	0.02
CM19	ol57	3.88	9.23	2.3	87.85	66.77	4139.8	16.63	43	0	0.03	0.03	0	0
CM19	ol59	0.36	7.8	0.41	15.74	35.23	761.7	14.62	7.61	0	0.01	0.01	0	0
CM19	ol63	1.17	8.19	1.39	51.66	50.89	2457.4	14.77	25.32	0	0.02	0.01	0.01	0
CM19	ol65	3.57	9.8	4.08	155.66	83.09	6039.1	15.52	60.7	0.01	0.05	0	0	0
CM19	ol66	1.26	8.07	1.09	42.65	46.96	2057.6	14.77	20.89	0	0.02	0	0	0
CM19	ol67	0.13	7.87	1.82	76.41	28.65	23.61	14.55	0.65	0	0.02	0.03	0	0
CM19	ol77	0.55	7.71	0.29	11.29	33.13	532.86	14.65	5.34	0	0.01	0	0	0
CM24	ol48_1	0.86	2.73	0.8	38.77	61.69	2239.9	12.8	36.01	0.01	0.01	0	0	0
CM24	ol48_4	0.87	1.24	0.79	49.3	59.48	2281.4	12.45	34.03	0	0.01	0	0.01	0
CM24	ol49	1.01	1.49	0.61	33.31	51.96	1823.1	12.97	28.54	0	0.01	0	0	0
CM24	ol61_3	0.73	1.33	0.78	39.72	58.84	2150.9	13.21	34.56	0	0.01	0.01	0.04	0
CM24	ol62_3	1.23	1.81	0.78	42.33	62.22	2056.1	13.11	35.38	0	0.01	0	0	0
CM27	ol1_2	0.96	1.59	0.97	48.47	59.97	2884.9	14.17	5.45	0	0.01	0	0.01	0
CM27	ol4	0.87	1.41	2.8	553.15	65.76	2933	14.33	10.44	0	0.01	0.01	0.01	0
CM27	ol15	1.18	1.44	0.99	45.39	57.61	2592	14.11	6.39	0	0.02	0	0	0
CM27	ol17	0.93	1.08	1.19	79.84	58.51	2525.6	14.11	4.28	0	0.01	0	0.01	0
CM27	ol23	1.07	1.21	1.09	42.47	59.38	2498.8	14.15	3.8	0	0.01	0	0	0
CM32	ol56	8.17	10.13	0	68.56	84.74	2040.2	28.17	31.48	0.17	0	0.1	0.91	0.01
CM32	ol58	15.74	13.9	0	155.64	168.49	4774.5	16.96	151.9	0.09	0	0.1	0.29	0.01
CM32	ol65_2	4.93	10.7	0	73.23	86.95	2101.3	10.82	37.99	0.13	0	0.02	0.07	0
CM32	ol65_4	2.66	11.01	0	74.27	89.73	2170.4	10.1	43.44	0	0	0.01	0.01	0
CM32	ol65_9	2.84	10.36	0	77.81	87.34	2140.6	10.1	43.59	0	0	0.02	0	0
CM41	ol35	16.43	7.1	3.82	133.34	247.67	6264.3	20.15	81.25	0	0.05	0.02	0.13	0
CM41	ol43_12	1.66	4.18	2.36	96.24	178.39	4812.3	1.7	39.14	0	0.02	0	0.03	0
CM41	ol43_3	1.37	3.74	2.01	85.49	159.47	3775.5	1.4	23.66	0	0.03	0.01	0.03	0
CM41	ol43_7	1.44	4.13	1.95	95.89	162.22	3895.6	1.3	26.34	0	0.01	0.01	0.02	0
CM41	ol48	2.68	4.5	1.93	95.14	172.29	4363.4	4.3	41.62	0	0.01	0.01	0.03	0
CM41	ol53_5	1.31	3.94	1.74	74.41	134.39	3409.7	1.28	13.72	0	0.01	0	0	0
CM50	ol71	5.71	3.78	2.66	252.69	135.58	3011.3	17.66	73.88	0	0.01	0.12	0.11	0
CM50	ol82	6.75	3.68	2.7	54.64	128.93	2732.2	18.4	68.56	0.04	0.02	0.03	0.1	0
CM50	ol90_1	8.53	4.04	1.82	48.49	136.41	2898.3	18.42	79.31	0.03	0.01	0	0.01	0
CM50	ol90_8	10.26	4.23	2.68	51.24	138.2	2950.4	24.28	75.15	0.05	0.02	0	0.02	0

Table 4.1 continued

Rock	Sample	Li	Sc	V	Cr	Co	Ni	Cu	Zn	Sr	Y	Zr	Ba	La
CM52	ol36	11.56	9.45	4.29	111.89	127.21	3093.1	21.42	105.64	7.39	0.29	2.51	5.73	0.47
CM52	ol40	3.31	9.84	4.5	124.94	130.8	3237.6	14.91	95.32	0.03	0.08	0	0	0
CM52	ol42	2.98	9.33	4.55	138.54	133.6	3268.6	17.68	93.96	0.12	0.08	0.05	0.04	0.01
CM52	ol47_8	2.99	9.62	4.27	132.01	129.07	3162.3	15.01	88.22	0.03	0.07	0.03	0	0
CM52	ol52	3.05	8.38	3.89	105.1	128.81	3053.2	14.92	80.44	0.04	0.05	0.04	0.04	0
CM52	ol56_6	2.69	8.3	3.74	102.57	126.08	2993.7	15.05	77.35	0.03	0.06	0.04	0	0
CM59	ol10	5.59	0.73	0	460.19	103.22	2575.5	16.41	55.58	0	0	0.01	0.04	0
CM59	ol15_6	5.98	1.1	0	70.78	114.37	2976.8	17.27	71.24	0.09	0	0.02	0.04	0.04
CM59	ol19	3.33	0.67	0	72.05	108.07	2761.9	15.23	66.15	0	0	0.02	0.09	0
CM59	ol28	9	0.73	0	170.22	108.57	2732.6	22.98	57.9	2.72	0	0.75	2.14	0.22
CM59	ol33	2.94	1.2	0	76.81	108.9	2724.1	14.14	61.59	0.02	0	0.02	0	0
CM60	ol103	1.65	2.03	2.02	65.26	124.34	1918.8	15.37	95.09	0	0	0	0.17	0.01
CM60	ol88_4	7.49	3.88	4.77	311.27	100.81	1429.6	20.69	79.95	0	0	0.01	0.03	0
CM60	ol89_2	10.93	4.45	2.97	220.22	109.2	1533.3	23.99	123.52	0.03	0.02	0.03	0.01	0.02
CM60	ol89_4	5.33	5.71	2.03	43.16	124.67	1854	19.37	88.77	0.03	0.02	0	0	0.01
CM60	ol98	4.8	5.13	2.31	51.81	123.74	1821.3	17.56	95.87	0	0.03	0	0	0
CM67	ol68_12	5.35	15	0	28.48	191.44	3640.9	16.83	108.72	0.05	0	0	0.63	0.01
CM67	ol68_13	3.06	11.9	0	24.72	120.45	2144.4	14.43	37.3	0.02	0	0.02	0.36	0.01
CM67	ol68_9	0.13	9.07	0	23.99	24.36	1.98	10.75	0	0.41	0	0.04	0	0
CM67	ol69_10	2.53	12.45	0	51.81	149.98	2641.7	12.04	74.36	0	0	0	0	0
CM67	ol72	0.09	9.06	0	15.76	24.37	2.13	10.78	0	0.44	0	0.05	0.01	0
CM67	ol83	14.88	3.1	0	92.99	116.89	3353.3	84.38	370.96	0.78	0	0.74	17.63	0.04
CM69	ol81	3.23	5.68	3.22	23.46	113.85	3410.2	14.29	56.05	0	0.02	0.01	0.03	0
CM69	ol84	2.69	4.75	4.88	362.27	106.92	3184.4	13.47	58.43	0	0.02	0	0	0
CM69	ol85	4.34	4.49	3.51	88.17	100.86	2953	14.24	52	0	0.04	0	0	0
CM69	ol87	3.25	5.25	3.92	119.33	111.64	3321.4	13.71	72.9	0	0.01	0	0	0
CM69	ol90_7	2.53	3.6	2.84	86.99	96.28	2745.2	13.05	53.12	0	0.01	0	0	0
CM69	ol91	3.85	4.62	5.65	291.46	105.42	3089.7	14.25	65.13	0	0.01	0.03	0.01	0

Table 4.1 continued

Table 4.1 continued

Rock	Sample	Ce	Pr	Nd	Sm	Eu	Gd	Tb	Dy	Ho	Er	Tm	Yb	Lu
CM52	ol36	1.27	0.12	0.39	0.08	0.01	0.06	0.01	0.03	0.01	0.03	0	0.04	0.01
CM52	ol40	0	0	0	0	0	0	0	0.02	0	0.01	0	0.04	0.01
CM52	ol42	0.01	0	0	0	0	0.01	0	0.01	0	0.01	0.01	0.04	0.01
CM52	ol47_8	0	0	0	0	0	0	0	0	0	0.01	0.01	0.04	0.01
CM52	ol52	0	0	0	0	0	0	0	0.01	0	0.02	0	0.02	0.01
CM52	ol56_6	0	0	0	0	0	0	0	0.01	0	0.01	0	0.04	0.01
CM59	ol10	0	0	0	0.01	0	0	0	0	0	0.01	0	0.02	0
CM59	ol15_6	0.08	0.01	0.04	0	0	0	0	0.01	0	0.01	0	0.01	0.01
CM59	ol19	0	0	0.01	0	0	0	0	0.01	0	0.01	0	0.03	0.01
CM59	ol28	0.58	0.05	0.18	0.04	0.01	0.03	0.01	0.03	0	0.03	0	0.03	0.01
CM59	ol33	0	0	0	0	0	0	0	0	0	0.01	0	0.02	0.01
CM60	ol103	0	0.01	0	0.01	0	0.03	0	0.02	0	0	0	0	0.01
CM60	ol88_4	0	0	0	0	0	0.01	0	0	0	0	0	0	0
CM60	ol89_2	0.05	0	0.01	0	0	0.01	0	0.01	0	0	0	0.01	0
CM60	ol89_4	0	0	0	0	0	0	0	0	0	0	0	0.01	0
CM60	ol98	0	0	0	0	0	0	0	0	0	0.01	0	0.01	0
CM67	ol68_12	0.01	0	0.02	0	0	0.01	0	0.01	0	0.05	0.01	0.02	0.01
CM67	ol68_13	0.01	0	0.01	0	0	0	0	0.01	0.01	0.02	0	0.02	0
CM67	ol68_9	0.01	0	0.02	0.01	0	0.01	0	0.02	0	0.01	0	0.01	0
CM67	ol69_10	0.01	0	0.02	0	0	0.01	0	0.02	0	0	0	0.01	0.01
CM67	ol72	0.01	0	0.03	0.01	0	0.02	0	0.02	0	0.01	0	0.01	0
CM67	ol83	0.05	0	0.1	0	0	0.07	0.02	0.09	0.03	0	0.05	0.29	0.02
CM69	ol81	0	0	0	0	0	0	0	0	0	0.01	0	0.01	0
CM69	ol84	0	0	0	0	0	0	0	0	0	0	0	0.01	0
CM69	ol85	0	0	0.01	0	0	0.01	0	0.01	0	0	0	0.01	0
CM69	ol87	0	0	0	0	0	0.01	0	0	0	0	0	0.01	0
CM69	ol90_7	0	0	0	0	0	0	0	0	0	0	0	0.01	0
CM69	ol91	0	0	0	0	0	0.01	0	0	0	0.01	0	0.03	0

Table 4.1 continued

Rock	Sample	Ta	Pb	Th	U	Rock	Sample	Ta	Pb	Th	U
CM14	ol5	0	0.08	0	0	CM50	ol90_8	0	0.01	0	0
CM14	ol6	0.01	0.16	0	0	CM52	ol36	0.01	0.05	0.07	0.02
CM14	ol7	0	0.1	0	0	CM52	ol40	0	0.02	0	0
CM14	ol9	0	0.06	0	0	CM52	ol42	0	0.05	0	0
CM14	ol15	0	0.1	0	0	CM52	ol47_8	0	0.01	0	0
CM14	ol25	0.02	0.1	0	0	CM52	ol52	0	0.02	0	0
CM14	ol34	0.01	0.25	0.01	0	CM52	ol56_6	0	0.01	0	0
CM14	ol35	0	0.16	0.01	0	CM59	ol10	0	0.02	0	0
CM19	ol57	0.01	0.07	0	0	CM59	ol15_6	0	0.02	0	0
CM19	ol59	0	0.01	0	0	CM59	ol19	0	0.01	0	0
CM19	ol63	0	0.02	0	0	CM59	ol28	0.01	0.05	0.02	0.01
CM19	ol65	0	0.08	0	0	CM59	ol33	0	0.06	0	0
CM19	ol66	0	0.02	0	0	CM60	ol103	0	0.04	0	0
CM19	ol67	0	0	0	0	CM60	ol88_4	0	0.01	0	0
CM19	ol77	0	0	0	0	CM60	ol89_2	0	0.02	0	0
CM24	ol48_1	0	0.03	0	0	CM60	ol89_4	0	0.02	0	0
CM24	ol48_4	0	0.01	0	0	CM60	ol98	0	0.02	0	0
CM24	ol49	0	0.01	0	0	CM67	ol68_12	0	0.08	0	0
CM24	ol61_3	0	0.01	0	0.01	CM67	ol68_13	0	0.04	0	0
CM24	ol62_3	0	0.01	0	0	CM67	ol68_9	0	0	0	0
CM27	ol1_2	0	0.02	0	0	CM67	ol69_10	0	0.02	0	0
CM27	ol4	0	0	0	0	CM67	ol72	0	0	0	0
CM27	ol15	0	0	0	0	CM67	ol83	0	0.25	0.06	0.01
CM27	ol17	0	0.01	0	0	CM69	ol81	0	0.13	0	0
CM27	ol23	0	0	0	0	CM69	ol84	0	0.01	0	0
CM32	ol56	0	0	0.01	0.01	CM69	ol85	0	0.02	0	0
CM32	ol58	0.01	0	0	0.01	CM69	ol87	0	0.03	0	0
CM32	ol65_2	0	0	0	0	CM69	ol90_7	0	0.02	0	0
CM32	ol65_4	0	0	0	0	CM69	ol91	0	0.03	0	0
CM32	ol65_9	0	0	0	0						
CM41	ol35	0	0.11	0	0						
CM41	ol43_12	0	0.01	0	0						
CM41	ol43_3	0	0.03	0	0						
CM41	ol43_7	0	0.03	0	0						
CM41	ol48	0	0.02	0	0						
CM41	ol53_5	0	0.01	0	0						
CM50	ol71	0	0.04	0.01	0						
CM50	ol82	0	0.02	0	0						
CM50	ol90_1	0	0.01	0	0						

Table 4.2. Spinel compositions in CM xenoliths; oxides in wt%; trace in ppm.

Rock	Sample	SiO <sub>2</sub>	TiO <sub>2</sub>	Al <sub>2</sub> O <sub>3</sub>	Cr <sub>2</sub> O <sub>3</sub>	FeO	MnO	MgO	CaO	NiO	Na <sub>2</sub> O	Li	V
CM14	sp1	0.03	0.17	47.79	19.76	14.56	0.11	18.25	0.01	0.35	0.00	4.89	3289.31
CM14	sp2	0.04	0.14	47.55	20.26	14.71	0.12	18.22	0.00	0.31	0.01	7.44	3351.63
CM14	sp3	0.03	0.16	46.51	20.00	14.44	0.12	18.23	0.00	0.34	0.01	4.09	2462.59
CM14	sp4	0.03	0.12	42.64	20.90	14.25	0.16	17.99	0.01	0.33	0.01	1.19	474.90
CM14	sp18	0.03	0.14	48.81	20.21	14.42	0.13	18.53	0.00	0.34	0.03	1.08	461.98
CM19	sp61	0.04	0.12	57.68	10.13	10.74	0.11	20.79	0.00	0.37	0.03	3.26	606.62
CM19	sp70	0.05	0.13	58.01	10.33	11.02	0.13	20.55	0.00	0.39	0.00	4.50	763.40
CM19	sp71	0.06	0.12	58.14	10.09	11.00	0.11	20.60	0.00	0.35	0.01	1.72	501.61
CM19	sp72	0.05	0.10	57.09	10.46	10.96	0.12	20.45	0.00	0.34	0.03	1.19	480.06
CM19	sp79	0.05	0.12	59.31	10.34	10.87	0.12	20.60	0.00	0.37	0.04	4.22	593.69
CM24	sp53_1	0.04	0.38	23.98	36.58	24.95	0.25	12.87	0.00	0.21	0.00	1.02	736.51
CM24	sp53_2	0.01	0.40	23.74	36.51	25.06	0.25	12.66	0.00	0.14	0.00	4.19	989.01
CM24	sp53_3	0.01	0.37	23.90	36.29	25.31	0.23	12.93	0.00	0.12	0.00	3.40	908.58
CM24	sp53_11	0.02	0.39	24.07	36.73	24.87	0.21	12.81	0.00	0.09	0.02	5.64	1057.37
CM24	sp53_13	0.02	0.37	23.80	36.70	25.08	0.27	12.61	0.00	0.18	0.00	5.67	1028.67
CM24	sp53_14	0.01	0.50	23.47	36.50	25.42	0.28	12.70	0.01	0.16	0.00	2.66	808.88
CM27	sp1_7	0.03	0.13	51.23	15.57	11.84	0.13	19.75	0.00	0.35	0.00	0.36	289.76
CM27	sp7	0.03	0.12	50.77	15.43	11.99	0.13	20.03	0.00	0.32	0.00	0.27	290.13
CM27	sp10	0.02	0.13	51.13	15.47	11.97	0.12	19.81	0.00	0.32	0.00	0.19	286.64
CM27	sp12	0.15	0.12	51.09	15.44	12.01	0.12	19.67	0.01	0.35	0.01		
CM27	sp14	0.03	0.14	51.44	15.40	11.79	0.08	20.00	0.00	0.30	0.00		
CM27	sp16	0.04	0.10	51.65	15.14	11.98	0.12	19.75	0.00	0.25	0.00	0.32	275.94
CM27	sp19	0.01	0.11	51.51	15.19	11.92	0.11	19.75	0.00	0.32	0.01	0.27	304.03
CM27	sp21	0.02	0.10	51.38	15.29	11.48	0.11	20.11	0.00	0.32	0.00		
CM27	sp24	0.03	0.13	52.00	14.83	11.14	0.11	20.15	0.02	0.30	0.00		
CM27	sp27	0.03	0.09	51.36	15.03	11.67	0.11	20.20	0.00	0.33	0.00		
CM27	sp29	0.03	0.13	51.17	15.32	11.74	0.11	20.24	0.01	0.36	0.00	0.33	292.07
CM27	sp35	0.04	0.13	51.41	15.08	11.74	0.12	19.81	0.00	0.35	0.01		
CM32	sp61	0.05	0.11	54.48	13.06	11.34	0.12	19.58	0.01	0.29	0.00	7.54	195.46
CM32	sp65_11	0.05	0.11	56.17	11.43	11.06	0.10	19.40	0.00	0.31	0.03	0.43	202.25
CM32	sp66	0.04	0.12	56.18	11.49	11.14	0.11	19.26	0.02	0.32	0.03		
CM32	sp68	0.03	0.13	56.34	11.29	10.97	0.11	19.49	0.00	0.31	0.03	0.41	202.19
CM32	sp69	0.04	0.10	56.50	11.23	10.97	0.14	19.63	0.00	0.31	0.00		
CM32	sp71	0.04	0.11	56.11	10.98	10.70	0.10	19.33	0.03	0.26	0.00		
CM32	sp73_15	0.03	0.69	46.66	8.15	27.77	0.36	15.10	0.02	0.19	0.03	1.96	454.57
CM32	sp74	0.03	0.22	50.90	8.37	24.14	0.18	15.45	0.00	0.22	0.00	2.43	507.53

Table 4.2. continued

Rock	Sample	SiO <sub>2</sub>	TiO <sub>2</sub>	Al <sub>2</sub> O <sub>3</sub>	Cr <sub>2</sub> O <sub>3</sub>	FeO	MnO	MgO	CaO	NiO	Na <sub>2</sub> O	Li	V
CM41	sp38	0.11	2.04	19.79	30.43	31.36	0.33	12.14	0.07	0.17	0.02		
CM41	sp41	0.03	0.36	31.95	29.52	22.85	0.21	14.01	0.00	0.13	0.01		
CM41	sp44	0.03	0.33	31.58	30.33	22.79	0.23	13.69	0.00	0.15	0.00	0.09	583.36
CM41	sp50	0.03	0.36	31.92	29.86	22.78	0.21	13.93	0.00	0.19	0.00	2.09	600.61
CM41	sp51	0.03	0.68	30.08	28.87	26.16	0.32	12.62	0.01	0.16	0.01		
CM41	sp52	0.48	2.75	13.75	29.00	42.39	0.52	8.72	0.01	0.16	0.33		
CM41	sp53_13	0.02	0.34	31.36	30.00	23.17	0.27	13.62	0.00	0.13	0.01	3.76	763.63
CM41	sp54	0.04	0.35	31.39	30.39	22.87	0.24	13.94	0.00	0.11	0.01		
CM41	sp55	0.02	0.51	30.11	29.94	25.54	0.34	12.60	0.00	0.14	0.01	1.78	645.11
CM50	sp64	0.02	0.09	42.86	23.69	15.06	0.15	17.91	0.00	0.33	0.01	1.82	1021.04
CM50	sp65	0.03	0.06	43.68	23.59	15.32	0.11	18.02	0.00	0.26	0.01	1.01	743.64
CM52	sp39	0.04	0.10	59.48	10.37	10.65	0.08	20.73	0.00	0.36	0.01	1.61	568.43
CM52	sp43	0.05	0.13	60.32	10.25	10.33	0.12	20.93	0.00	0.38	0.01	7.01	648.28
CM52	sp46	0.04	0.11	57.94	10.41	10.44	0.08	20.83	0.00	0.39	0.00	2.22	603.70
CM58	sp1	0.03	0.23	37.84	31.10	17.51	0.18	15.82	0.00	0.19	0.00		
CM58	sp4	0.03	0.23	35.83	30.94	16.65	0.13	16.49	0.01	0.20	0.01		
CM58	sp13	0.02	0.26	35.25	31.13	17.00	0.15	16.17	0.00	0.21	0.00		
CM58	sp14	0.02	0.29	37.01	30.94	17.50	0.14	16.24	0.00	0.25	0.00		
CM58	sp36	0.04	0.26	36.04	30.86	17.48	0.17	15.98	0.00	0.26	0.00		
CM58	sp42	0.02	0.23	37.35	30.17	17.36	0.14	16.03	0.00	0.21	0.03		
CM58	sp44	0.03	0.24	35.25	30.11	16.88	0.14	16.25	0.00	0.22	0.02		
CM58	sp48	0.02	0.23	34.32	30.73	17.18	0.14	16.06	0.00	0.23	0.00		
CM58	sp51	0.02	0.25	34.22	31.11	17.32	0.12	15.86	0.00	0.25	0.01		
CM58	sp55	0.02	0.22	34.23	30.89	17.32	0.14	15.93	0.00	0.24	0.02		
CM58	sp60	0.04	0.24	34.57	30.32	17.01	0.17	16.11	0.00	0.26	0.00		
CM59	sp11	0.05	0.24	34.72	31.01	16.72	0.16	16.49	0.00	0.23	0.04	2.68	948.03
CM59	sp16	0.03	0.36	33.99	29.94	18.49	0.18	15.93	0.00	0.18	0.00		
CM59	sp17	0.03	0.24	34.06	31.66	17.18	0.18	16.26	0.00	0.22	0.00		
CM59	sp23	0.04	0.23	35.14	30.90	16.46	0.16	16.74	0.00	0.21	0.00	1.62	841.01
CM59	sp26	0.03	0.26	33.90	30.81	17.37	0.18	16.47	0.01	0.20	0.03	19.66	898.06
CM59	sp27	0.03	0.23	35.61	29.53	16.80	0.15	17.03	0.00	0.24	0.00	4.48	927.85
CM59	sp30	0.03	0.23	35.05	30.44	16.88	0.16	16.91	0.00	0.22	0.02	2.94	927.76
CM60	sp87	0.03	0.28	31.34	29.11	24.77	0.36	13.02	0.00	0.14	0.00	3.10	232.93
CM60	sp89_1	0.03	0.25	31.68	29.47	23.44	0.27	14.06	0.02	0.12	0.00	2.36	1008.30
CM60	sp95	0.03	0.23	31.95	30.02	22.35	0.28	14.53	0.00	0.18	0.00	0.81	909.35
CM60	sp96	0.04	0.27	31.34	29.88	23.47	0.21	13.60	0.00	0.13	0.00	1.02	1079.71
CM60	sp101	0.03	0.40	33.44	27.18	23.09	0.25	14.66	0.00	0.15	0.02	0.76	1330.01
CM67	sp65	0.04	0.21	54.03	3.64	24.71	0.16	16.24	0.00	0.15	0.01	0	503.43
CM67	sp69_11	0.04	0.22	55.14	3.12	24.34	0.16	16.29	0.00	0.18	0.02	0	553.36
CM67	sp74	0.24	0.39	56.05	3.08	23.04	0.19	16.23	0.00	0.10	0.01	0	705.58
CM67	sp76	0.02	0.26	55.65	3.09	23.79	0.19	16.62	0.00	0.13	0.02	0	700.17
CM69	sp82a	0.04	0.08	41.70	27.19	13.80	0.14	17.82	0.00	0.27	0.03	1.01	567.63
CM69	sp82b	0.02	0.11	42.61	27.24	13.74	0.14	17.81	0.00	0.26	0.00	2.88	568.83

Table 4.2. continued

Rock	Sample	Cr	Co	Ni	Cu	Zn	Rb	Sr	Zr	Nb	Ba	Pb
CM14	sp1	135180.68	406.15	20571.51	10.80	5244.77	5.18	0.56	0.33	0.14	0	0
CM14	sp2	138585.26	413.32	20698.51	11.44	5353.81	6.08	0	0	0.28	0.41	0.0
CM14	sp3	136836.65	311.86	16011.08	8.38	3830.42	2.97	0	0	0.25	0.60	0.2
CM14	sp4	143027.84	86.52	3014.76	1.77	864.46	0.77	0	0.04	0.01	0	0.1
CM14	sp18	138306.65	82.28	2944.99	2.25	744.50	0.74	0	0	0.00	0	0.0
CM19	sp61	69308.50	363.85	8957.72	5.17	1665.40	2.60	0	0.06	0.09	0	0.2
CM19	sp70	70686.14	449.42	11369.43	3.69	1985.15	2.68	0	0	0.01	0.00	0.0
CM19	sp71	69012.45	314.99	7769.30	1.68	1421.74	0	0	0	0.03	0	0.0
CM19	sp72	71547.48	286.23	7582.81	1.28	1267.16	1.14	0	0.06	0.04	0.52	0.0
CM19	sp79	70748.54	342.83	8476.51	27.60	1423.65	0.52	0	0.00	0.04	1.96	0.2
CM24	sp53_1	250280.57	106.25	1538.99	25.44	1247.80	0.83	0	0.17	0.08	0.34	0.0
CM24	sp53_2	249771.73	380.88	6504.50	38.90	5116.60	5.38	0.72	0.40	0.41	6.35	0.3
CM24	sp53_3	248327.79	395.37	6849.43	174.6	4946.85	4.90	0.72	0.43	0.38	15.76	0.1
CM24	sp53_11	251277.03	399.86	6792.63	74.23	5365.55	4.10	0	0.70	0.47	0	0.1
CM24	sp53_13	251126.17	409.47	6406.39	28.00	5424.50	4.42	0	0.55	0.27	0.38	0.1
CM24	sp53_14	249704.61	211.39	3360.46	20.19	2532.21	1.90	0	0.39	0.17	0.18	0.1
CM27	sp1_7	106547.18	274.04	3661.12	22.03	685.21	0.10	0	0.05	0.02	0.00	0.0
CM27	sp7	105586.77	280.83	3421.19	21.85	637.13	0.00	0	0.01	0.02	0.00	0.1
CM27	sp10	105819.19	264.73	3780.26	21.94	688.22	0.13	0.83	0.08	0.03	0.09	0.0
CM27	sp16	103618.81	259.30	3420.51	21.92	657.41	0.25	0	0.03	0.03	0.10	0.0
CM27	sp19	103910.00	303.43	3772.09	21.91	705.88	0.06	0.00	0.04	0.03	0	0.0
CM27	sp29	104809.25	286.31	4010.67	25.57	762.07	0.04	128.6	0	0.02	0	0.2
CM32	sp61	89352.69	110.11	3676.09	27.30	770.24	0.10	0	0	0.02	0.24	0.0
CM32	sp65_11	78206.39	103.35	3702.73	13.82	881.25	0.15	0	0.01	0.02	0.03	0.0
CM32	sp68	77213.54	102.94	3599.84	13.84	845.51	0	0	0.05	0.03	0.00	0.0
CM32	sp73_15	55743.35	121.41	1985.57	35.76	1490.97	0.20	0.60	0.63	0.42	7.08	0.5
CM32	sp74	57238.80	128.77	2151.69	31.62	1268.22	0.17	0.05	0.34	0.06	0.96	0.0
CM41	sp44	207512.80	113.43	1619.66	14.18	760.98	0.59	0	0.08	0.06	0.13	0.0
CM41	sp50	204280.64	163.50	2457.26	16.68	1060.17	0.96	0	0.14	0.11	0	0.0
CM41	sp53_13	205280.59	187.48	2947.12	19.97	1221.45	0.93	0	0.19	0.09	0.21	0.1
CM41	sp55	207957.12	126.48	1806.15	23.19	726.81	0.62	0.04	0.14	0.08	1.12	0.1
CM50	sp64	190863.36	274.33	2584.33	18.39	1853.33	0.29	0	0.12	0.12	0.01	0.0
CM50	sp65	139661.54	213.21	2053.45	17.16	1507.45	0.23	0.01	0.11	0.11	0.04	0.0

Table 4.2. continued

Rock	Sample	Cr	Co	Ni	Cu	Zn	Rb	Sr	Zr	Nb	Ba	Pb
CM52	sp39	88613.74	244.29	4561.48	16.02	2599.16	0.05	0	0.02	0.07	0	0.1
CM52	sp43	97283.49	274.57	4882.56	16.36	3167.02	0.20	11.15	0.62	0.33	5.36	0.1
CM52	sp46	97507.56	262.59	5015.92	16.85	2912.19	0.10	0.04	0.07	0.07	0	0.0
CM59	sp11	205367	183.17	1780.47	25.31	2494.49	0.7	0.03	0.38	0.11	0	0.0
CM59	sp23	179916	168.3	1668.8	31.16	1983.93	0.68	0.62	0.18	0.21	4.82	0.1
CM59	sp26	142962.1	477.01	1586.53	232.33	8369.62	24.54	1.14	6.09	1.11	3.49	0.1
CM59	sp27	192806	183.03	1877.51	48.33	2420.59	0.73	0	0.49	0.15	0.04	0.1
CM59	sp30	185845.8	177.33	1749.43	34.35	1882.43	1.11	0	0	0.19	0.53	0.1
CM60	sp87	53200.05	166.94	1586.31	32.32	974.95	0.11	0	0.57	0.19	0.02	0.0
CM60	sp89_1	342756.6	272.69	2547.07	55.39	1369.89	0.07	0.13	0.94	0.29	0	0.0
CM60	sp95	307808.9	230.22	2178.34	30.36	1230.25	0.2	0	0.54	0.23	0	0.0
CM60	sp96	367897.6	290.28	2672.92	15.63	1323.9	0.2	0.02	0.13	0.13	0.25	0.0
CM60	sp101	415961.7	352.32	3682.22	22.7	2015.87	0.34	0	4.21	2.08	0	0.0
CM67	sp65	24918.02	95.19	1742.24	16.54	1032.97	0.09	0	0.15	0.03	0.18	0.0
CM67	sp69_11	21347.04	97.88	1767.6	17.2	1088.19	0.02	0	0.09	0.03	0	0.0
CM67	sp74	21057.9	84.16	1300.61	22.61	1082.32	0	0	0.13	0.18	0.6	0.1
CM67	sp76	21116.6	95.32	1616.03	16.91	1193.32	0	0	0.31	0.17	0	0.0
CM69	sp82a	186052.3	458.67	3216.39	20.45	5243.22	1.18	0	0.36	0.34	0	0.2
CM69	sp82b	186351.9	448.78	3071.54	25.9	5135.39	1.13	0.07	0.51	0.33	0.01	0.2

Table 4.3. Orthopyroxene compositions in CM xenoliths; major oxides in wt%; trace in ppm.

Rock	Sample	SiO <sub>2</sub>	TiO <sub>2</sub>	Al <sub>2</sub> O <sub>3</sub>	Cr <sub>2</sub> O <sub>3</sub>	FeO	MnO	MgO	CaO	NiO	Na <sub>2</sub> O	Li	Sc	V
CM14	opx13	55.78	0.08	3.51	0.47	6.62	0.16	33.68	0.65	0.06	0.00	123.9	12.01	52.54
CM14	opx19	55.49	0.06	3.74	0.60	6.56	0.11	33.20	0.65	0.12	0.02	11.73	31.63	131.7
CM14	opx21	55.22	0.09	3.68	0.62	6.60	0.13	33.34	0.64	0.07	0.04	18.53	29.37	123.7
CM14	opx22	55.94	0.09	3.45	0.42	6.61	0.13	33.68	0.66	0.06	0.04	7.52	30.55	143.7
CM14	opx24	55.69	0.06	3.61	0.52	6.64	0.14	33.31	0.79	0.10	0.03	22.16	29.33	133.6
CM14	opx30	55.75	0.10	3.39	0.48	6.53	0.14	33.56	0.64	0.11	0.04	28.89	0	23.67
CM19	opx2	50.01	0.14	4.71	0.29	6.03	0.15	33.23	0.75	0.08	0.11	10.34	23.69	53.99
CM19	opx62	55.35	0.12	4.70	0.39	6.63	0.12	33.03	0.75	0.10	0.08	9.5	23.7	52.12
CM19	opx64	54.65	0.10	4.76	0.37	6.70	0.15	34.07	0.79	0.07	0.11	12.71	23.94	54.91
CM19	opx68	55.42	0.13	4.76	0.37	6.63	0.15	32.81	0.76	0.10	0.11	8.94	23.12	48.67
CM19	opx69	55.09	0.14	4.78	0.39	6.66	0.14	32.75	0.79	0.08	0.13			
CM19	opx76	55.24	0.13	5.07	0.41	6.63	0.14	32.69	0.85	0.09	0.12	16.82	22.65	58.33
CM27	opx1_4	54.86	0.10	3.99	0.43	6.16	0.17	33.67	0.69	0.06	0.05			
CM27	opx1_5	47.69	0.05	1.99	0.22	7.80	0.15	41.82	0.36	0.21	0.02			
CM27	opx11	54.20	0.10	3.99	0.44	6.20	0.14	33.66	0.68	0.10	0.05	5.66	22.83	212
CM27	opx20	55.13	0.13	3.74	0.42	6.26	0.11	33.97	0.67	0.10	0.05	3.24	19.81	217.4
CM27	opx33	55.38	0.10	3.70	0.39	6.25	0.15	33.93	0.68	0.08	0.06			
CM27	opx38	55.20	0.08	3.77	0.40	6.19	0.11	34.44	0.66	0.14	0.06	24.22	35.96	179.8
CM27	opx47	53.08	0.11	3.82	0.41	6.15	0.15	33.88	0.64	0.13	0.05	23.54	23.54	174.1
CM32	opx64	53.68	0.13	4.86	0.43	6.57	0.14	32.34	0.75	0.06	0.12	11.51	24.05	65.44
CM32	opx65_3	54.43	0.10	4.85	0.41	6.48	0.17	32.52	0.83	0.11	0.09	10.82	25.03	83.49
CM32	opx65_6	53.98	0.13	4.84	0.45	6.56	0.15	32.51	0.87	0.10	0.10	12.21	23.31	69.87
CM32	opx65_8	53.82	0.11	4.48	0.40	6.55	0.18	32.49	0.73	0.10	0.09			
CM32	opx73_6	53.23	0.10	4.85	0.21	12.55	0.25	28.94	0.69	0.04	0.03	4.44	28.88	126
CM32	opx75	52.88	0.11	4.96	0.27	12.51	0.23	28.92	0.68	0.03	0.03	1.00	10.82	0

Table 4.3 continued

Rock	Sample	SiO <sub>2</sub>	TiO <sub>2</sub>	Al <sub>2</sub> O <sub>3</sub>	Cr <sub>2</sub> O <sub>3</sub>	FeO	MnO	MgO	CaO	NiO	Na <sub>2</sub> O	Li	Sc	V
CM50	opx74	55.73	0.04	3.81	0.42	6.23	0.13	33.20	0.63	0.07	0.01	12.9	28.67	123.4
CM50	opx75	55.58	0.03	3.42	0.46	6.22	0.14	33.49	0.63	0.10	0.10	6.42	27.66	113.7
CM50	opx77	56.37	0.05	3.20	0.43	6.32	0.12	34.28	0.60	0.10	0.06	8.94	29.49	128.8
CM50	opx78_10	55.86	0.03	3.37	0.44	6.12	0.12	33.32	0.60	0.09	0.02	55.37	55.5	25.84
CM50	opx78_18	55.28	0.05	3.74	0.41	6.10	0.17	32.91	0.61	0.08	0.03	26.66	63.06	32.66
CM50	opx80	56.33	0.04	3.13	0.44	6.34	0.12	34.29	0.61	0.06	0.02	7.26	25.02	116.7
CM52	opx44	55.39	0.12	4.74	0.39	6.55	0.14	32.76	0.80	0.11	0.10	24.98	29.75	152.7
CM52	opx53	55.29	0.17	5.27	0.43	6.43	0.13	32.87	0.79	0.10	0.13	20.91	39.59	223.1
CM52	opx55	55.70	0.10	4.60	0.39	6.42	0.12	32.95	0.79	0.10	0.11	30.44	40.61	230
CM52	opx56a	55.30	0.13	4.83	0.39	6.47	0.12	32.74	0.80	0.14	0.14	19.86	37.12	202.8
CM52	opx56b	55.28	0.13	4.76	0.36	6.45	0.15	32.89	0.78	0.08	0.14	26.82	35.22	197.9
CM58	opx5	56.91	0.07	2.71	0.45	6.55	0.12	33.82	0.63	0.11	0.05			
CM58	opx21	56.57	0.09	2.57	0.49	6.50	0.12	33.63	0.70	0.11	0.03			
CM59	opx4	56.41	0.07	2.69	0.50	6.44	0.16	34.16	0.67	0.09	0.03	4.67	26.72	82.94
CM59	opx5	56.37	0.09	2.64	0.47	6.45	0.16	34.09	0.69	0.05	0.03	6.28	26.83	86.53
CM59	opx7	55.55	0.08	2.75	0.52	6.43	0.11	33.84	0.70	0.07	0.04	3.47	27.15	85.85
CM59	opx20	56.10	0.10	2.62	0.47	6.45	0.19	34.13	0.66	0.10	0.04	5.21	25.92	78.63
CM59	opx21	56.31	0.10	2.53	0.46	6.42	0.16	34.27	0.62	0.12	0.04			
CM59	opx32	56.54	0.07	2.60	0.49	6.39	0.17	34.35	0.69	0.09	0.03	7.54	26.26	78.42
CM60	opx90	56.04	0.04	2.56	0.39	8.16	0.22	32.59	0.69	0.02	0.02	4.06	15.43	88.43
CM67	opx64	53.32	0.13	5.01	0.14	11.82	0.25	29.79	0.64	0.04	0.01	0.43	38.37	160
CM67	opx66	53.35	0.11	4.91	0.16	11.77	0.25	29.54	0.66	0.01	0.02	1.67	37.05	133.7
CM67	opx68_11	52.38	0.13	4.80	0.12	11.69	0.23	29.70	0.69	0.03	0.02	1.39	41.74	203.2
CM67	opx68_15	52.56	0.10	4.50	0.11	11.64	0.24	29.84	0.65	0.03	0.03	33.54	45.67	0
CM67	opx69_3	52.79	0.11	4.65	0.12	11.66	0.24	29.79	0.64	0.05	0.02	1.19	36.21	122.4
CM67	opx75	53.02	0.11	4.59	0.09	11.73	0.21	29.69	0.62	0.03	0.00	1.06	33.59	119.2
CM69	opx594	55.23	0.05	3.31	0.61	5.59	0.15	32.65	0.78	0.06	0.06	2.11	7.67	12.85
CM69	opx595	55.21	0.03	3.43	0.64	5.66	0.10	32.97	0.87	0.06	0.08	3.7	8.15	15.51
CM69	opx596	55.09	0.04	3.50	0.69	5.57	0.14	32.88	0.83	0.11	0.05	8.76	8.96	18.92

Table 4.3 continued

Rock	Sample	Cr	Co	Ni	Cu	Zn	Rb	Sr	Y	Zr	Nb	Ba	La	Ce	Pr	Nd
CM14	opx13	891.11	1149.63	45777.82	609	894	0	5.46	0.61	2.53	0.15	17.1	0.28	0.41	0.08	0.38
CM14	opx19	3876.05	54.63	763.57	3.75	43	0	0	0.94	0.44	0.01	0.04	0	0	0	0
CM14	opx21	3666.37	51.19	685.54	36.2	39	0	0.37	0.87	0.39	0.01	0.28	0	0.01	0	0.03
CM14	opx22	3736.64	57.77	840.06	2.15	46.9	0.03	0	1.11	0.4	0.01	0	0	0	0	0.02
CM14	opx24	4066.86	52.56	723.3	1.06	38.9	0.04	0	0.89	0.51	0	0.05	0	0.01	0	0.03
CM14	opx30	577.56	251.24	8483.93	237	216	0	19.8	0.25	4.23	1.44	27.9	1.52	5.1	0.33	1.31
CM19	opx2	2676.67	55.56	721.91	3.82	4.33	0	0.1	1.47	1.84	0.01	0	0	0.01	0	0.07
CM19	opx62	2738.13	54.38	704	3.39	3.74	0	0.1	1.48	1.8	0.01	0	0	0.01	0	0.03
CM19	opx64	2740.03	53.84	671.41	2.1	1.21	0	0.12	1.39	1.67	0.01	0	0	0.01	0	0.03
CM19	opx68	2668.2	52.95	668.32	1.6	0	0.15	0.06	1.4	1.92	0.01	0.03	0	0	0.01	0.04
CM19	opx76	3096.64	55.14	706.42	1.42	3.43	0.04	0.05	1.47	1.98	0.01	0.01	0	0.01	0	0.02
CM27	opx11	3884.73	52.54	604.87	15	38.5	0.03	0.07	4.53	0.88	0.01	0.04	0	0	0	0.02
CM27	opx20	3698.19	54.16	751.24	19	41.9	0	0.24	4.53	0.81	0.01	0.01	0	0	0	0.02
CM27	opx38	763.79	755.76	27403.79	18.5	1122	0	0.25	3.77	0.27	0	0	0.01	0.01	0.02	0.02
CM27	opx47	461.18	608.39	22046.31	19	886	0.09	0.76	3.94	0.9	0	1.17	0.01	0.06	0	0.05
CM32	opx64	2916.77	51.85	614.97	11.6	4.39	0	0.12	0	1.63	0.01	0.04	0	0.01	0	0.03
CM32	opx65_3	3286.07	56.05	706.1	11	15.6	0	0.15	0	1.78	0.02	0.01	0	0.01	0	0.03
CM32	opx65_6	3163.44	52.69	628.48	10	5.6	0	0.16	0	1.84	0.01	0.01	0	0.01	0	0.04
CM32	opx73_6	1515.53	58.93	312.23	679	20.9	0.55	7.08	0	2.69	0.44	17.9	0.51	1.07	0.07	0.25
CM32	opx75	188.99	25.29	34.26	33.3	0	0.95	35	0	3.85	0.64	47.6	0.62	1.63	0.18	0.64
CM50	opx74	3805.48	57.23	769.98	33	22.3	0.01	0.67	0.7	0.31	0.03	2.94	0.01	0.01	0	0
CM50	opx75	3483.58	53.42	687.8	14	14.3	0	0.03	0.65	0.11	0	0.01	0	0	0	0.01
CM50	opx77	3682.1	58.51	801.4	18	43.5	0	0.58	0.71	0.22	0.04	0.42	0	0.02	0	0.01
CM50	opx78_10	627.1	982.39	36862.61	55	1187	0.03	0.71	0.27	0.2	0.01	0.92	0.02	0.03	-0.01	0.04
CM50	opx78_18	704.88	1021.07	38396.7	26.5	1207	0.03	0.49	0.19	0.28	0.01	0.85	0.05	0.03	0	0.02
CM50	opx80	3497.98	55.51	749.06	16.3	18.7	0.04	0.01	0.66	0.18	0.01	0.05	0	0	0	0
CM52	opx44	4037.65	70.59	966.16	10.7	48.5	0	0.16	0	2.93	0	0	0	0.01	0	0.04
CM52	opx53	5842.52	91.84	1356.04	9.93	82.3	0.02	0.26	0	3.57	0	0.01	0	0.03	0.01	0.06
CM52	opx55	6195.62	98.71	1487.1	9.72	94.2	0	0.18	0	3.43	0.02	0	0	0.02	0	0.04
CM52	opx56a	5329.43	88.94	1311.36	10.4	77.2	0	0.2	0	3.55	0.01	0	0	0.02	0.01	0.03
CM52	opx56b	5166.64	83.98	1213.45	9.77	67.7	0.01	0.12	0	3.44	0.01	0.06	0	0.02	0.01	0.03
CM59	opx4	3537.47	59.3	644.98	13.8	24.7	0	0.06	0.78	0.76	0	0.08	0	0.01	0	0.01
CM59	opx5	3725.53	62.26	683.08	15.2	28.7	0	0.04	0.8	0.89	0	0.03	0	0	0	0.02
CM59	opx7	3790.82	61.61	666.97	12.3	29.4	0	0.05	0.84	0.84	0	0	0	0	0	0.02
CM59	opx20	3408.46	57.03	614.88	14.5	23.9	0	0.08	0.75	0.73	0.01	0.14	0	0	0	0.02
CM59	opx32	3600.62	57.77	627.07	15.1	27	0	0.04	0.79	0.67	0	0.05	0	0	0	0.02
CM60	opx90	3819.56	45.15	593.97	24.2	38.7	0.03	0.17	0.27	0.17	0.01	0.43	0	0.01	0	0
CM67	opx64	2228.34	66.95	618.87	11.5	25.5	0	0.06	0	0.51	0	0	0	0.01	0	0.02
CM67	opx66	2086.59	62.24	527.1	12.7	16.2	0	0.03	0	0.6	0	0	0	0	0	0.02
CM67	opx68_11	2197.66	72.13	685.44	11.5	30.1	0.04	0.09	0	0.6	0	0.05	0	0.01	0.01	0.02
CM67	opx68_15	155.44	1277.51	26844.55	30.4	1049	0	0.89	0	0.17	0.03	1	0.11	0.28	0	0.07
CM67	opx69_3	1673.54	59.2	487.98	11.6	10.6	0	0.02	0	0.49	0	0.02	0.01	0.01	0	0.01
CM67	opx75	1527.05	62.65	544.98	11.2	18	0	0	0	0.43	0	0.07	0	0.01	0	0
CM69	opx594	4153.09	34.43	755.46	14.7	0	0	0.02	0.37	0.41	0	0	0	0	0	0.01
CM69	opx595	4378.88	34.56	764.45	13.9	0	0	0.01	0.35	0.39	0	0	0	0	0	0.01
CM69	opx596	4734.66	35.67	820.07	13.7	0	0	0.03	0.4	0.45	0	0	0	0	0	0.01

Table 4.3 continued

Rock	Sample	Sm	Eu	Gd	Tb	Dy	Ho	Er	Tm	Yb	Lu	Ta	Pb	Th	U
CM14	opx13	0.03	0	0	0	0.08	0.06	0	0	0.44	0.09	0	1.78	0.01	0.3
CM14	opx19	0.02	0.01	0.03	0.01	0.19	0.04	0.15	0.03	0.27	0.05	0.01	0.14	0	0
CM14	opx21	0	0.01	0.08	0.01	0.11	0.05	0.11	0.03	0.25	0.05	0	0.16	0	0
CM14	opx22	0.01	0	0.06	0.01	0.15	0.04	0.13	0.03	0.21	0.06	0	0.04	0	0
CM14	opx24	0.01	0	0.08	0.02	0.11	0.03	0.14	0.03	0.23	0.04	0	0.04	0	0
CM14	opx30	0.23	0.14	0.09	0.02	0.19	0.11	0	0.08	0.44	0.04	0.04	2.75	0.17	0.16
CM19	opx2	0.01	0.01	0.06	0.02	0.23	0.05	0.27	0.04	0.27	0.07	0	0.02	0	0
CM19	opx62	0.02	0.01	0.14	0.03	0.16	0.05	0.23	0.04	0.32	0.07	0.01	0.06	0	0
CM19	opx64	0.02	0.01	0.07	0.02	0.22	0.06	0.19	0.05	0.29	0.05	0	0.05	0	0
CM19	opx68	0.05	0.02	0.1	0.02	0.15	0.04	0.23	0.04	0.3	0.07	0	0.03	0	0
CM19	opx76	0.05	0.01	0.14	0.03	0.2	0.06	0.26	0.04	0.35	0.07	0	0.05	0	0
CM27	opx11	0.01	0.11	0.55	0.12	0.93	0	0.65	0.15	0.27	0.03	0	0.02	0	0
CM27	opx20	0.05	0.12	0.65	0.13	0.96	0	0.73	0.16	0.33	0.03	0	0.03	0	0.01
CM27	opx38	0	0.09	0.51	0.13	0.91	0	0.66	0.15	0.15	0.06	0.04	0.19	0	0
CM27	opx47	0.02	0.1	0.56	0.25	0.91	0	0.64	0.15	0.29	0	0.01	0.33	0	0.01
CM32	opx64	0.02	0	0	0	0	0	0	0.05	0	0	0	0	0	0
CM32	opx65_3	0.03	0	0	0	0	0	0	0.04	0	0	0	0	0	0
CM32	opx65_6	0.03	0	0	0	0	0	0	0.05	0	0	0	0	0	0
CM32	opx73_6	0.02	0	0	0	0	0	0	0.04	0	0	0.02	0	0.07	0.03
CM32	opx75	0.11	0	0	0	0	0	0	0.02	0	0	0.04	0	0.14	0.05
CM50	opx74	0.01	0	0.03	0.01	0.07	0.02	0.09	0.02	0.19	0.04	0	0.02	0.02	0
CM50	opx75	0.01	0.01	0.03	0	0.07	0.02	0.09	0.02	0.2	0.03	0	0.01	0	0
CM50	opx77	0.01	0	0.05	0.01	0.08	0.03	0.11	0.02	0.21	0.05	0	0.04	0	0
CM50	opx78_10	0.05	0	0.04	0.01	0.06	0.01	0.02	0.02	0.14	0.05	0	0.15	0	0
CM50	opx78_18	0.04	0	0.03	0	0.08	0.01	0.06	0.03	0.05	0.06	0.01	0.11	0	0
CM50	opx80	0.03	0.01	0.07	0	0.05	0.05	0.22	0.04	0.2	0.04	0	0.01	0	0
CM52	opx44	0.04	0.01	0.13	0.03	0.29	0.07	0.2	0.05	0.49	0.08	0	0.02	0	0
CM52	opx53	0.04	0.03	0.13	0.04	0.38	0.1	0.28	0.07	0.63	0.09	0	0.03	0	0
CM52	opx55	0.07	0.02	0.16	0.03	0.39	0.09	0.31	0.09	0.66	0.12	0	0.02	0	0
CM52	opx56a	0.05	0.02	0.13	0.05	0.32	0.08	0.26	0.06	0.55	0.1	0	0.03	0	0
CM52	opx56b	0.07	0.01	0.14	0.03	0.33	0.08	0.25	0.05	0.57	0.08	0	0.02	0	0
CM59	opx4	0.01	0.01	0.03	0.01	0.05	0.03	0.11	0.02	0.2	0.04	0	0.03	0	0
CM59	opx5	0.01	0.01	0.05	0.01	0.11	0.03	0.12	0.02	0.2	0.04	0	0.01	0	0
CM59	opx7	0.01	0.01	0.03	0.01	0.08	0.02	0.11	0.02	0.21	0.04	0	0.03	0	0
CM59	opx20	0.01	0	0.04	0.01	0.09	0.03	0.11	0.01	0.16	0.05	0	0.01	0	0
CM59	opx32	0.01	0.01	0.05	0.01	0.08	0.02	0.14	0.02	0.18	0.05	0	0.03	0	0
CM60	opx90	0.01	0	0.02	0	0.02	0.01	0.03	0	0.09	0.01	0	0.01	0	0
CM67	opx64	0.01	0	0.08	0.02	0.13	0.04	0.14	0.02	0.18	0.05	0	0.03	0	0
CM67	opx66	0.02	0	0.08	0.02	0.15	0.04	0.16	0.04	0.22	0.06	0	0.03	0	0
CM67	opx68_11	0.04	0.01	0.11	0.01	0.14	0.04	0.15	0.03	0.22	0.06	0	0.05	0	0
CM67	opx68_15	0.08	0	0.12	0.01	0.12	0.01	0.07	0	0.37	0.06	0.06	0.57	0.02	0.01
CM67	opx69_3	0.02	0	0.07	0.02	0.11	0.04	0.12	0.02	0.19	0.05	0.01	0.06	0	0
CM67	opx75	0.04	0.01	0.06	0.02	0.16	0.03	0.12	0.03	0.26	0.04	0	0.02	0	0
CM69	opx594	0.01	0	0.02	0	0.05	0.02	0.06	0.01	0.1	0.02	0	0.02	0	0
CM69	opx595	0.01	0	0.02	0	0.03	0.01	0.06	0.01	0.08	0.02	0	0.01	0	0
CM69	opx596	0.01	0	0.04	0.01	0.06	0.02	0.07	0.01	0.1	0.02	0	0.02	0	0

Table 4.4. Clinopyroxene compositions in CM xenoliths; major oxides (wt%) and trace (ppm).

Rock	Sample	SiO <sub>2</sub>	TiO <sub>2</sub>	Al <sub>2</sub> O <sub>3</sub>	Cr <sub>2</sub> O <sub>3</sub>	FeO	MnO	MgO	CaO	NiO	Na <sub>2</sub> O	Li	Sc
CM14	cpx11	52.43	0.28	4.05	0.84	2.83	0.11	16.57	23.05	0.07	0.48	31.70	57.65
CM14	cpx12	52.47	0.27	3.98	0.83	2.82	0.11	16.54	22.89	0.05	0.50		
CM14	cpx14	52.58	0.27	3.55	0.65	2.81	0.08	16.91	22.93	0.05	0.52	36.70	55.93
CM14	cpx16	52.55	0.28	4.01	0.75	2.86	0.11	16.71	23.11	0.07	0.48	46.19	62.69
CM14	cpx20	52.32	0.29	4.21	0.89	2.89	0.10	16.38	22.86	0.08	0.55		
CM14	cpx26	52.09	0.26	4.20	0.85	2.91	0.12	16.49	22.58	0.04	0.50	21.11	55.90
CM14	cpx31	52.19	0.28	3.72	0.76	2.80	0.08	16.59	22.62	0.03	0.49	39.26	58.28
CM19	cpx1											17.95	53.41
CM19	cpx2											11.32	43.62
CM19	cpx3	56.87	0.30	0.67	1.18	3.60	0.10	20.14	14.86	0.10	0.95		
CM19	cpx78	51.92	0.53	7.35	0.88	3.01	0.09	15.24	20.14	0.03	1.53	18.89	51.54
CM24	cpx48_5	52.86	0.15	2.29	0.72	2.76	0.08	16.87	23.76	0.02	0.43	21.15	87.12
CM24	cpx50	52.29	0.14	2.46	0.77	2.79	0.07	16.65	23.54	0.02	0.49	21.78	81.05
CM24	cpx53_5	52.18	0.14	2.50	0.78	2.82	0.08	16.68	23.40	0.03	0.46	21.54	84.17
CM24	cpx55	51.57	0.16	2.52	0.87	2.77	0.05	16.53	23.45	0.04	0.46	20.55	92.89
CM24	cpx61_9	50.74	0.13	2.42	0.73	2.81	0.07	16.46	23.32	0.02	0.41	21.56	93.86
CM24	cpx62_6	51.64	0.15	2.25	0.63	2.82	0.06	16.73	23.46	0.05	0.42	19.09	89.31
CM27	cpx3	52.16	0.42	4.99	0.79	2.77	0.07	16.15	21.96	0.05	1.03	15.23	73.78
CM27	cpx5	51.97	0.42	5.23	0.84	2.79	0.08	16.15	21.93	0.06	1.04	10.58	77.49
CM27	cpx8	51.78	0.42	5.17	0.87	2.73	0.08	16.24	21.80	0.04	1.08	6.91	69.01
CM27	cpx43	51.60	0.45	5.26	0.86	2.75	0.06	16.12	21.71	0.04	1.02	11.58	61.35
CM32	cpx62	50.98	0.42	6.92	0.86	2.91	0.10	15.19	19.57	0.06	1.46	21.01	51.65
CM32	cpx65_1	51.17	0.42	6.90	0.97	3.03	0.10	15.21	19.94	0.06	1.61	15.55	48.85
CM32	cpx73_13	50.13	0.55	6.15	0.41	5.93	0.15	14.61	21.87	0.00	0.56	31.76	57.60
CM32	cpx73_3	50.39	0.55	5.99	0.39	5.83	0.17	14.57	22.19	0.01	0.55	20.73	59.92
CM32	cpx73_4	50.41	0.54	6.06	0.44	5.86	0.14	14.74	21.72	0.03	0.58	34.96	59.78
CM32	cpx73_7	50.12	0.59	6.32	0.37	5.91	0.17	14.45	22.17	0.03	0.52	6.87	58.15
CM41	cpx36	51.95	0.16	2.72	0.69	3.47	0.12	16.84	22.50	0.02	0.36	24.74	81.43
CM41	cpx47	52.26	0.17	2.67	0.61	3.29	0.12	16.78	22.49	0.04	0.34	36.33	95.30
CM41	cpx49	53.04	0.18	2.62	0.62	3.31	0.07	17.00	22.80	0.02	0.37	35.83	90.57
CM50	cpx67	52.76	0.11	3.53	0.82	2.76	0.07	16.91	22.86	0.07	0.55	26.39	51.05
CM50	cpx83	53.01	0.12	3.59	0.70	2.73	0.07	16.98	22.99	0.04	0.51	27.98	49.79
CM50	cpx86	52.60	0.11	3.56	0.81	2.65	0.09	16.92	22.79	0.02	0.54	36.68	50.22
CM50	cpx88	52.50	0.14	3.83	0.94	2.72	0.09	16.79	22.83	0.05	0.58	34.93	50.38
CM50	cpx89	52.53	0.13	3.65	0.82	2.73	0.10	16.91	22.72	0.05	0.49	31.01	49.46
CM52	cpx41	52.02	0.53	7.45	0.90	2.93	0.10	15.09	20.09	0.03	1.78	18.19	48.73
CM52	cpx49	52.11	0.56	7.16	0.80	2.92	0.08	15.20	20.15	0.02	1.76	11.96	42.82
CM52	cpx50a	52.28	0.55	8.14	0.88	2.93	0.07	15.16	20.06	0.05	1.78	13.57	37.40
CM52	cpx50b	52.17	0.56	8.19	0.89	2.95	0.07	15.18	19.98	0.07	1.81	9.46	47.31

Table 4.4 continued

Rock	Sample	SiO <sub>2</sub>	TiO <sub>2</sub>	Al <sub>2</sub> O <sub>3</sub>	Cr <sub>2</sub> O <sub>3</sub>	FeO	MnO	MgO	CaO	NiO	Na <sub>2</sub> O	Li	Sc
CM59	cpx8	52.10	0.22	3.40	0.99	2.76	0.11	16.73	22.41	0.03	0.62	20.73	50.93
CM59	cpx12	52.43	0.23	3.07	0.89	2.71	0.09	16.99	22.71	0.08	0.63	24.85	53.73
CM59	cpx14	52.97	0.24	3.38	1.05	2.79	0.09	16.93	22.65	0.06	0.67	26.53	54.42
CM59	cpx22	53.14	0.23	3.14	0.92	2.78	0.11	17.02	22.87	0.03	0.62	22.31	53.36
CM59	cpx24	53.18	0.21	3.28	0.93	2.84	0.08	17.07	22.58	0.06	0.65	26.44	53.49
CM60	cpx88_2	53.04	0.15	2.88	0.81	3.43	0.11	16.88	23.28	0.02	0.25	6.38	89.19
CM60	cpx89_3	53.01	0.15	2.83	0.75	3.40	0.09	16.86	23.15	0.03	0.26	35.17	79.27
CM60	cpx89_5	52.71	0.16	2.97	0.85	3.44	0.12	16.54	23.10	0.02	0.27	19.60	98.51
CM60	cpx89_7	52.73	0.14	3.05	0.90	3.56	0.11	16.78	22.78	0.01	0.30	6.13	79.96
CM60	cpx97	53.06	0.17	2.87	0.68	3.45	0.12	16.86	23.25	0.03	0.25	36.66	106.39
CM60	cpx100	51.82	0.17	2.83	0.67	3.57	0.12	16.84	23.20	0.06	0.26	20.61	101.90
CM67	cpx69_8	49.76	0.53	6.26	0.20	5.76	0.13	14.75	22.17	0.01	0.45	15.37	60.92
CM67	cpx70	50.00	0.49	5.63	0.17	5.59	0.15	14.91	22.47	0.02	0.43	13.80	59.35
CM67	cpx77_1	48.93	0.50	6.34	0.20	5.76	0.19	14.68	22.09	0.02	0.50	24.10	61.94
CM67	cpx77_3	46.15	2.46	7.50	0.13	6.79	0.13	12.62	22.53	0.04	0.85	22.38	62.16
CM67	cpx77_8	50.49	0.60	4.47	0.31	4.70	0.09	15.29	22.81	0.01	0.53	28.66	63.96
CM67	cpx77_10	49.58	0.51	5.74	0.17	5.59	0.12	14.68	22.41	0.01	0.44	31.35	62.89
CM69	cpx83	53.32	0.19	4.78	1.36	2.63	0.05	16.49	21.78	0.04	1.08	9.20	25.62
CM69	cpx89	53.18	0.16	4.46	1.31	2.62	0.05	16.32	21.73	0.03	1.12	13.36	40.39
CM69	cpx92	53.07	0.18	4.56	1.28	2.57	0.04	16.24	21.71	0.04	1.04	15.10	47.72
CM69	cpx93	53.23	0.19	4.33	1.19	2.57	0.09	16.42	21.77	0.03	1.08		
CM69	cpx538	53.00	0.19	4.34	1.23	2.50	0.10	16.02	21.45	1.20	1.23	13.19	38.21
CM69	cpx479	52.10	0.26	3.91	0.39	3.58	0.10	15.99	22.03	0.40	0.39	9.05	25.20
CM69	cpx488	51.92	0.32	3.95	0.43	3.56	0.13	16.11	21.85	0.41	0.43	12.37	29.07

Table 4.4 continued

Rock	Sample	V	Cr	Co	Ni	Cu	Zn	Rb	Sr	Y	Zr	Nb	Ba
CM14	cpx11	155.89	4563.86	32.16	284.55	23.31	0	0	19.06	10.45	4.87	0.03	0.29
CM14	cpx14	131.73	3497.24	31.60	266.22	36.02	0	0	18.55	9.78	4.74	0.09	0.14
CM14	cpx16	193.34	4864.01	33.33	324.87	63.47	0	0.24	22.76	10.94	5.40	0.03	0.70
CM14	cpx26	185.14	5509.93	33.44	323.34	14.42	0	0.05	20.02	9.72	4.33	0.02	0.09
CM14	cpx31	162.31	4485.24	32.15	291.15	27.74	0	0	20.59	10.28	4.82	0.02	0.22
CM19	cpx1	209.79	4595.06	31.33	277.30	12.33	0	0	55.68	18.85	26.53	0.11	0.10
CM19	cpx2	135.41	3379.65	28.55	219.72	37.79	0	0.11	43.65	14.48	20.56	0.13	1.59
CM19	cpx78	217.21	4802.25	31.84	287.36	11.71	0	0	60.53	20.30	28.06	0.18	0
CM24	cpx48_5	133.16	3855.73	32.60	203.78	30.04	9.34	0.06	42.14	6.28	3.96	0.02	0.24
CM24	cpx50	157.65	4302.45	32.62	208.56	33.42	10.71	0.01	43.36	6.15	4.40	0.05	2.31
CM24	cpx53_5	157.48	4362.72	33.32	204.36	8.56	9.60	0.01	47.21	7.77	4.76	0.03	0.09
CM24	cpx55	154.62	4217.18	32.60	213.45	12.69	9.22	-0.01	45.15	7.50	5.04	0.02	0.01
CM24	cpx61_9	158.05	3907.24	33.24	210.95	15.43	9.66	0.00	44.65	7.49	4.73	0.02	0.10
CM24	cpx62_6	159.00	4603.59	33.60	223.94	9.07	9.61	-0.02	46.85	7.53	4.78	0.03	0.02
CM27	cpx3	256.28	4185.86	32.67	297.23	45.49	0	0.11	16.34	15.83	13.77	0.02	0.77
CM27	cpx5	257.42	5126.03	32.84	281.93	14.35	0	0.03	13.79	16.76	15.91	0.01	0.09
CM27	cpx8	230.89	4772.05	32.34	285.46	54.17	0	0.05	41.57	15.80	14.41	0.02	0.57
CM27	cpx43	246.91	4735.48	32.25	294.22	76.67	0	0.06	12.24	15.13	13.10	0.02	1.03
CM32	cpx62	195.48	4625.19	31.02	256.35	25.77	0	0.01	57.61	15.19	24.34	0.19	1.77
CM32	cpx65_1	186.16	5013.83	30.60	228.44	11.48	0	0.03	51.62	12.91	21.23	0.17	0.11
CM32	cpx73_13	275.93	2263.20	35.28	136.07	19.62	0	0.01	44.63	7.35	8.49	0.02	0.01
CM32	cpx73_3	265.14	2280.25	34.81	136.47	14.40	0	0.02	45.78	7.88	8.74	0.03	0
CM32	cpx73_4	275.15	2265.81	34.65	135.06	17.06	0	0.03	46.63	7.54	9.15	0.03	0
CM32	cpx73_7	292.47	2505.46	35.67	146.77	11.93	0	0.02	47.98	7.88	8.86	0.03	0.00
CM41	cpx36	170.16	3691.89	33.67	176.81	26.74	8.09	0.02	31.22	5.14	2.78	0.04	2.80
CM41	cpx47	179.90	3726.62	34.96	206.19	18.25	10.53	0	34.89	5.90	2.89	0.01	0.06
CM41	cpx49	183.52	3816.87	34.97	201.30	21.32	10.26	0.00	33.59	5.51	2.85	0.02	0.08
CM50	cpx67	168.90	3934.95	31.66	240.15	20.99	0	0.02	13.74	5.90	1.21	0.01	0.16
CM50	cpx83	179.45	4325.94	31.84	243.23	16.63	0	0.02	13.18	5.55	1.23	0.01	0.07
CM50	cpx86	175.54	4185.19	31.88	246.74	42.94	0	0.02	13.54	5.83	1.55	0.02	1.28
CM50	cpx88	180.75	4715.31	32.07	252.34	21.26	0	0.01	13.22	6.26	1.33	0.01	0.01
CM50	cpx89	180.48	4431.98	31.87	248.20	27.58	0	0.02	12.92	5.97	1.30	0.02	0.42
CM52	cpx41	203.64	4340.18	29.03	227.54	13.35	0	0.51	48.94	16.86	29.02	0.02	4.31
CM52	cpx49	175.11	3568.98	29.75	543.32	314.58	0	0.51	455.17	13.55	22.54	0.10	10.57
CM52	cpx50a	159.59	3390.49	27.20	193.03	21.05	0	0.12	591.81	11.33	16.60	0.04	1.83
CM52	cpx50b	205.37	4476.18	29.32	224.50	9.03	0	0	47.00	16.01	24.23	0.01	0

Table 4.4 continued

Rock	Sample	V	Cr	Co	Ni	Cu	Zn	Rb	Sr	Y	Zr	Nb	Ba
CM59	cpx8	149.44	5535.97	21.84	229.19	14.19	0	0.01	28.02	7.41	8.87	0.02	0.02
CM59	cpx12	147.39	4817.82	22.32	228.17	24.39	0	0.00	28.06	7.28	8.67	0.02	0.11
CM59	cpx14	152.30	5306.10	22.47	237.22	24.46	0	0.00	30.77	8.25	9.77	0.02	0.06
CM59	cpx22	147.57	4498.96	22.64	233.04	20.20	0	0.00	29.00	7.51	8.39	0.02	0.23
CM59	cpx24	154.19	6763.19	24.29	239.34	19.21	0	0	29.35	7.72	8.51	0.02	0
CM60	cpx88_2	220.89	12486.45	30.90	553.54	13.72	15.75	0.00	36.02	5.41	1.79	0.03	0
CM60	cpx89_3	198.42	8977.40	29.18	510.03	47.38	15.38	0.03	34.35	4.82	1.57	0.03	1.16
CM60	cpx89_5	234.73	14035.71	33.14	575.36	14.09	16.02	-0.05	36.60	5.32	1.60	0.01	0
CM60	cpx89_7	204.82	12476.79	30.70	525.88	12.76	14.80	0.02	34.80	5.18	1.62	0.01	0.12
CM60	cpx97	258.89	13148.18	39.33	694.39	29.35	19.19	0.01	42.53	5.75	1.81	0.02	0.03
CM60	cpx100	255.31	14192.41	36.02	648.27	24.55	18.27	0	39.01	5.52	1.83	0.02	0.02
CM67	cpx69_8	291.13	2571.24	36.57	222.23	16.49	0	0.01	49.89	7.72	4.81	0.02	0.04
CM67	cpx70	292.75	2177.95	38.19	293.63	164.18	0	0.01	48.84	6.47	4.32	0.02	0.10
CM67	cpx77_1	252.61	2327.80	35.49	211.59	25.84	0	0.01	47.46	7.51	5.12	0.01	0.10
CM67	cpx77_3	281.20	2671.36	36.68	231.81	23.97	0	0	47.90	7.46	4.58	0.01	0
CM67	cpx77_8	285.21	2263.19	36.47	217.39	23.86	0	0.03	50.80	7.87	5.07	0.02	0.11
CM67	cpx77_10	258.64	2084.05	36.02	211.84	32.98	0	0.01	50.21	7.92	5.11	0.01	0.04
CM69	cpx83	73.17	9307.72	23.30	303.90	17.69	0	0.01	10.43	3.58	4.34	0.02	0.02
CM69	cpx89	108.78	8993.26	24.27	410.33	18.77	0	0.00	14.26	5.25	6.88	0.02	0
CM69	cpx92	119.05	8771.38	25.25	456.80	24.07	0	0.00	15.51	5.74	7.20	0.04	0.24
CM69	cpx538	99.33		24.50		18.66	0	0.00	14.77	5.29	6.59	0.02	0.00
CM69	cpx479	32.67		24.67		18.16	0	0.00	27.07	2.95	1.89	0.01	0.00
CM69	cpx488	41.05		25.36		15.69	0	0.00	30.50	3.45	2.23	0.00	0.00

Table 4.4 continued

Rock	Sample	La	Ce	Pr	Nd	Sm	Eu	Gd	Tb	Dy	Ho	Er	Tm	Yb	Lu
CM14	cpx11	0.22	0.67	0.14	1.51	0.94	0.29	1.56	0.30	1.68	0.34	1.22	0.20	0.95	0.15
CM14	cpx14	0.19	0.72	0.21	1.27	0.75	0.30	1.40	0.20	1.94	0.46	0.91	0.21	1.04	0.17
CM14	cpx16	0.20	0.94	0.22	1.55	0.80	0.34	1.77	0.30	1.94	0.42	1.23	0.16	1.29	0.16
CM14	cpx26	0.14	0.75	0.18	1.23	0.77	0.29	1.33	0.22	1.63	0.33	0.92	0.11	0.95	0.15
CM14	cpx31	0.18	0.73	0.19	1.35	0.72	0.27	1.34	0.26	2.02	0.42	1.05	0.17	1.07	0.15
CM19	cpx1	0.52	2.37	0.49	3.43	1.61	0.66	2.56	0.52	3.30	0.75	2.05	0.28	1.84	0.28
CM19	cpx2	0.40	1.80	0.43	2.71	1.21	0.50	1.95	0.39	2.45	0.58	1.61	0.21	1.50	0.22
CM19	cpx78	0.57	2.43	0.55	3.62	1.57	0.66	2.61	0.49	3.26	0.70	1.95	0.27	1.80	0.27
CM24	cpx48_5	0.39	1.19	0.23	1.29	0.58	0.21	0.99	0.16	0.92	0.24	0.64	0.09	0.65	0.09
CM24	cpx50	0.40	1.23	0.26	1.39	0.56	0.21	0.94	0.16	1.06	0.22	0.70	0.11	0.60	0.10
CM24	cpx53_5	0.49	1.43	0.28	1.72	0.69	0.25	1.22	0.18	1.32	0.29	0.83	0.14	0.85	0.12
CM24	cpx55	0.46	1.39	0.26	1.60	0.70	0.24	1.08	0.19	1.29	0.26	0.89	0.12	0.84	0.11
CM24	cpx61_9	0.43	1.34	0.26	1.47	0.63	0.22	1.03	0.19	1.22	0.29	0.92	0.13	0.80	0.10
CM24	cpx62_6	0.45	1.35	0.26	1.46	0.58	0.23	0.94	0.18	1.11	0.28	0.76	0.10	0.69	0.11
CM27	cpx3	0.10	1.00	0.30	2.26	0.87	0.36	1.43	0.32	2.22	0.50	1.32	0.22	1.49	0.22
CM27	cpx5	0.10	1.10	0.36	2.38	1.00	0.38	1.64	0.37	2.41	0.52	1.35	0.24	1.71	0.25
CM27	cpx8	0.10	1.01	0.32	2.20	0.89	0.35	1.45	0.31	2.03	0.46	1.29	0.23	1.40	0.23
CM27	cpx43	0.08	0.88	0.26	2.12	0.84	0.29	1.26	0.29	2.11	0.49	1.33	0.22	1.34	0.20
CM32	cpx62	0.53	2.29	0.44	2.76	1.47	0.47	1.66	0.35	2.08	0.55	1.70	0.26	0.96	0.24
CM32	cpx65_1	0.52	2.19	0.44	2.80	1.20	0.39	1.83	0.32	2.27	0.53	1.43	0.24	1.24	0.20
CM32	cpx73_13	0.36	1.69	0.37	2.62	1.19	0.31	1.34	0.18	1.23	0.26	0.66	0.14	0.28	0.06
CM32	cpx73_3	0.37	1.82	0.41	2.87	1.09	0.39	1.38	0.27	1.29	0.31	0.81	0.17	0.41	0.10
CM32	cpx73_4	0.40	1.93	0.44	2.76	1.10	0.36	1.45	0.20	1.53	0.32	0.65	0.15	0.37	0.07
CM32	cpx73_7	0.44	2.14	0.46	3.16	1.37	0.43	1.65	0.27	1.55	0.38	0.88	0.16	0.61	0.10
CM41	cpx36	0.20	0.70	0.17	1.04	0.53	0.19	0.88	0.14	1.04	0.22	0.71	0.09	0.64	0.09
CM41	cpx47	0.23	0.78	0.19	1.27	0.56	0.24	0.89	0.19	0.99	0.22	0.66	0.11	0.59	0.11
CM41	cpx49	0.19	0.72	0.17	1.11	0.53	0.20	0.85	0.14	1.16	0.19	0.65	0.09	0.59	0.09
CM50	cpx67	0.11	0.45	0.10	0.57	0.27	0.13	0.70	0.14	0.95	0.23	0.71	0.09	0.70	0.09
CM50	cpx83	0.13	0.53	0.10	0.62	0.29	0.13	0.67	0.12	0.87	0.22	0.63	0.09	0.63	0.08
CM50	cpx86	0.14	0.55	0.10	0.66	0.31	0.12	0.66	0.13	1.04	0.21	0.65	0.09	0.73	0.09
CM50	cpx88	0.11	0.49	0.10	0.57	0.34	0.12	0.75	0.13	1.02	0.23	0.68	0.11	0.74	0.08
CM50	cpx89	0.12	0.48	0.10	0.62	0.31	0.13	0.67	0.13	0.92	0.22	0.59	0.10	0.73	0.09
CM52	cpx41	0.48	2.49	0.53	3.22	1.44	0.57	2.30	0.42	2.93	0.63	1.29	0.25	1.75	0.21
CM52	cpx49	0.72	2.59	0.47	2.80	1.16	0.47	2.00	0.35	2.50	0.52	1.00	0.20	1.41	0.16
CM52	cpx50a	0.30	1.66	0.36	2.32	1.06	0.41	1.66	0.32	2.08	0.44	0.92	0.17	1.28	0.13
CM52	cpx50b	0.43	2.44	0.51	3.12	1.42	0.59	2.43	0.42	2.87	0.57	1.24	0.25	1.72	0.19

Table 4.4 continued

Rock	Sample	La	Ce	Pr	Nd	Sm	Eu	Gd	Tb	Dy	Ho	Er	Tm	Yb	Lu
CM59	cpx8	0.29	1.19	0.23	1.33	0.61	0.24	0.98	0.18	1.05	0.24	0.76	0.11	0.80	0.12
CM59	cpx12	0.29	1.09	0.21	1.24	0.50	0.19	0.82	0.15	1.02	0.22	0.63	0.09	0.70	0.10
CM59	cpx14	0.31	1.24	0.26	1.53	0.57	0.24	1.00	0.18	1.11	0.25	0.80	0.12	0.81	0.13
CM59	cpx22	0.28	1.19	0.23	1.38	0.62	0.21	0.94	0.17	1.03	0.24	0.68	0.10	0.72	0.12
CM59	cpx24	0.28	1.12	0.25	1.36	0.56	0.24	0.95	0.18	1.18	0.25	0.66	0.10	0.77	0.12
CM60	cpx88_2	0.12	0.61	0.16	1.15	0.41	0.20	0.85	0.15	0.85	0.15	0.44	0	0.62	0.05
CM60	cpx89_3	0.16	0.62	0.15	0.92	0.48	0.16	0.69	0.11	0.75	0.15	0.44	0	0.41	0.06
CM60	cpx89_5	0.13	0.66	0.16	0.99	0.48	0.19	0.66	0.12	0.76	0.17	0.38	0.00	0.44	0.07
CM60	cpx89_7	0.15	0.64	0.14	0.91	0.48	0.18	0.67	0.12	0.72	0.16	0.37	0	0.47	0.06
CM60	cpx97	0.16	0.76	0.18	1.09	0.50	0.19	0.87	0.14	0.87	0.19	0.44	0.01	0.57	0.07
CM60	cpx100	0.18	0.79	0.16	1.07	0.57	0.18	0.73	0.14	0.81	0.15	0.42	0	0.44	0.06
CM67	cpx69_8	0.27	1.40	0.36	2.57	1.13	0.51	1.65	0.32	1.79	0.39	1.02	0.14	0.88	0.15
CM67	cpx70	0.27	1.43	0.35	2.39	0.97	0.42	1.60	0.26	1.80	0.38	0.88	0.12	0.68	0.11
CM67	cpx77_1	0.26	1.35	0.36	2.46	1.07	0.44	1.72	0.29	1.91	0.39	1.01	0.14	0.94	0.12
CM67	cpx77_3	0.24	1.30	0.33	2.38	1.08	0.45	1.68	0.28	1.97	0.40	1.03	0.13	0.88	0.13
CM67	cpx77_8	0.28	1.37	0.36	2.62	1.18	0.51	1.85	0.32	1.88	0.40	1.08	0.16	0.93	0.13
CM67	cpx77_10	0.28	1.35	0.36	2.66	1.11	0.49	1.81	0.31	1.87	0.36	1.02	0.15	0.95	0.12
CM69	cpx83	0.11	0.45	0.09	0.57	0.25	0.11	0.49	0.10	0.59	0.14	0.40	0.06	0.41	0.06
CM69	cpx89	0.16	0.69	0.14	0.86	0.34	0.16	0.81	0.13	0.89	0.21	0.64	0.09	0.60	0.09
CM69	cpx92	0.17	0.76	0.16	0.86	0.38	0.17	0.77	0.14	1.00	0.23	0.63	0.10	0.67	0.10
CM69	cpx538	0.16	0.69	0.14	0.85	0.39	0.16	0.70	0.13	0.90	0.21	0.54	0.08	0.56	0.08
CM69	cpx479	0.14	0.67	0.16	1.01	0.43	0.17	0.56	0.10	0.56	0.12	0.36	0.04	0.32	0.05
CM69	cpx488	0.16	0.73	0.18	1.15	0.48	0.17	0.65	0.10	0.66	0.13	0.38	0.05	0.32	0.06

Table 4.4 continued

Rock	Sample	Ta*	Pb	Th	U	Rock	Sample	Ta*	Pb	Th	U
CM14	cpx11	0	0.02	0.01	0.00	CM59	cpx8	0	0.03	0.01	0.01
CM14	cpx14	0	0.05	0.03	0.02	CM59	cpx12	0	0.03	0.01	0.01
CM14	cpx16	0	0.12	0.02	0.03	CM59	cpx14	0	0.04	0.01	0.00
CM14	cpx26	0	0.08	0.01	0.01	CM59	cpx22	0	0.04	0.02	0.01
CM14	cpx31	0	0.22	0.01	0.02	CM59	cpx24	0	0.03	0.01	0.00
CM19	cpx1	0	0.08	0.01	0.01	CM60	cpx88_2	0	0.01	0.00	0.00
CM19	cpx2	10.0	0.04	0.01	0.02	CM60	cpx89_3	0	0.02	0.00	0.00
CM19	cpx78	10.0	0.04	0.02	0.01	CM60	cpx89_5	0	0.02	0.01	0.00
CM24	cpx48_5	10.0	0.06	0.03	0.01	CM60	cpx89_7	0	0.03	0.01	0.00
CM24	cpx50	0	0.04	0.03	0.02	CM60	cpx97	0	0.04	0.01	0.00
CM24	cpx53_5	0	0.04	0.03	0.02	CM60	cpx100	0	0.02	0.01	0.00
CM24	cpx55	0	0.03	0.03	0.01	CM67	cpx69_8	0	0.04	0.00	0.00
CM24	cpx61_9	10.0	0.03	0.03	0.01	CM67	cpx70	0	0.06	0.00	0.00
CM24	cpx62_6	10.0	0.04	0.03	0.01	CM67	cpx77_1	0	0.06	0.00	0.00
CM27	cpx3	0	0.10	0.01	0.04	CM67	cpx77_3	0	0.04	0.00	0.00
CM27	cpx5	0	0.04	0.00	0.00	CM67	cpx77_8	0	0.05	0.01	0.00
CM27	cpx8	0	0.09	0.01	0.08	CM67	cpx77_10	0	0.07	0.00	0.00
CM27	cpx43	0	0.15	0.00	0.03	CM69	cpx83	0	0.05	0.00	0.00
CM32	cpx62	0	0	0.01	0.01	CM69	cpx89	0	0.06	0.00	0.00
CM32	cpx65_1	10.0	0	0.01	0.01	CM69	cpx92	10.0	0.19	0.00	0.00
CM32	cpx73_13	0	0	0.00	0.00	CM69	cpx538	0.489	0.05	0.00	0.00
CM32	cpx73_3	0	0	0.01	0.00	CM69	cpx479	0	0.07	0.00	0.00
CM32	cpx73_4	10.0	0	0.00	0.00	CM69	cpx488	0.916	0.03	0.00	0.00
CM32	cpx73_7	10.0	0	0.01	0.00						
CM41	cpx36	0	0.06	0.02	0.01						
CM41	cpx47	0	0.05	0.01	0.01						
CM41	cpx49	10.0	0.04	0.01	0.01						
CM50	cpx67	0	0.02	0.00	0.00						
CM50	cpx83	0	0.01	0.00	0.00						
CM50	cpx86	0	0.02	0.01	0.00						
CM50	cpx88	0	0.02	0.00	0.00						
CM50	cpx89	0	0.02	0.00	0.00						
CM52	cpx41	0	0.13	0.01	0.01						
CM52	cpx49	10.0	0.17	0.03	0.06						
CM52	cpx50a	0	0.05	0.00	0.40						
CM52	cpx50b	0	0.01	0.00	0.00						

\* Ta given in ppb.

Table 4.5. Calculated Oxygen Fugacity

Sample	$\Delta fO_2^{\text{FMQ}}$ (B;1GPa)	$\Delta fO_2^{\text{FMQ}}$ (B;2.5GPa)	$\Delta fO_2^{\text{FMQ}}$ (W;1GPa)	$\Delta fO_2^{\text{FMQ}}$ (W;2.5GPa)
CM69	2.42	1.93	3.20	2.73
CM50	3.26	2.74	4.11	3.62
CM27	3.26	2.74	3.69	3.19
CM59	3.26	2.75	4.16	3.68
CM58	2.92	2.42	3.85	3.37
CM14	2.96	2.44	3.57	3.08
CM52	0.92	0.42	1.06	0.59
CM19	2.10	1.62	2.09	1.63
CM32	0.86	0.38	0.64	0.18
CM32_AVG	1.73	1.22	1.77	1.29
CM32_FeRich	4.07	3.57	4.80	4.33
CM60	4.06	3.54	3.73	3.25
CM67	3.34	2.77	2.64	2.12

B = Ballhaus et al. (1991)

W = Nell &amp; Wood (1991)

Table 4.6. Mass Balance Calculations

Values are averaged and normalized to 100.

K<sub>2</sub>O and P<sub>2</sub>O<sub>5</sub> are not included in mass balance as they were not included in mineral analyses.

---

#### LEAST MODIFIED PERIDOTITE

CM19	Wt %	Wt %	Wt %	Error in averaging minerals				
	cpx	ol	opx	sp	CM19(WR)	Mass Balance	difference	$\sigma$
Mode (wt)	0.08	0.62	0.28	0.02	sum of phases			obs - calc.
SiO <sub>2</sub>	51.55	40.50	54.10	0.05	43.54	42.37	1.17	6.81
TiO <sub>2</sub>	0.53	0.00	0.13	0.12	0.10	0.06	0.04	0.06
Al <sub>2</sub> O <sub>3</sub>	7.29	0.00	4.78	57.70	3.76	3.25	0.51	0.29
Cr <sub>2</sub> O <sub>3</sub>	0.87	0.02	0.37	10.32	1.09	0.48	0.61	0.64
FeO	2.99	10.30	6.52	10.89	7.88	9.18	-1.30	0.39
MnO	0.09	0.14	0.14	0.11	0.13	0.13	0.00	0.02
MgO	15.13	48.56	32.98	20.42	40.04	42.72	-2.68	0.73
CaO	20.00	0.06	0.78	0.00	2.69	1.37	1.32	2.37
NiO	0.03	0.37	0.09	0.37	0.70	0.30	0.40	0.05
Na <sub>2</sub> O	1.52	0.03	0.11	0.02	0.00	0.14	-0.14	0.10
K <sub>2</sub> O	0.01	0	0	0	0.07	0		
P <sub>2</sub> O <sub>5</sub>					0.01			Avg. error excluding SiO <sub>2</sub>
SUM	100	100	100	100	100.01	100.00		0.52

CM52	Wt %	Wt %	Wt %	Error in averaging minerals				
	cpx	ol	opx	sp	CM52(WR)	Mass Balance	difference	$\sigma$
Mode (wt)	0.12	0.74	0.13	0.01	sum of phases			obs - calc.
SiO <sub>2</sub>	51.45	40.60	54.73	0.04	43.40	43.51	-0.11	3.75
TiO <sub>2</sub>	0.55	0.00	0.13	0.11	0.12	0.09	0.03	0.09
Al <sub>2</sub> O <sub>3</sub>	7.63	0.00	4.78	58.36	3.53	1.95	1.58	0.33
Cr <sub>2</sub> O <sub>3</sub>	0.86	0.01	0.39	10.19	2.29	0.23	2.06	0.17
FeO	2.89	10.05	6.39	10.32	7.42	8.69	-1.27	0.18
MnO	0.08	0.12	0.13	0.09	0.13	0.12	0.01	0.05
MgO	14.95	48.72	32.45	20.52	39.43	42.25	-2.82	1.65
CaO	19.80	0.07	0.78	0.00	3.40	2.59	0.81	0.73
NiO	0.04	0.39	0.10	0.37	0.24	0.31	-0.07	0.16
Na <sub>2</sub> O	1.76	0.03	0.13	0.01	0.00	0.25	-0.25	0.35
K <sub>2</sub> O					0.04			
P <sub>2</sub> O <sub>5</sub>					0.01			Avg. error excluding SiO <sub>2</sub>
SUM	100.00	100.00	100.00	100.00	100.01	100.00		0.41

Table 4.6. Continued

## MODERATELY MODIFIED PERIDOTITE

CM14	Wt %	Wt %	Wt %	Error in averaging minerals				
	cpx	ol	opx	sp	CM14(WR)	Mass Balance	difference	$\sigma$
Mode (wt)	0.09	0.67	0.21	0.02		sum of phases	obs - calc.	
SiO <sub>2</sub>	52.21	40.55	55.22	0.03	44.87	43.88	0.99	9.24
TiO <sub>2</sub>	0.27	0.01	0.08	0.15	0.12	0.05	0.07	0.05
Al <sub>2</sub> O <sub>3</sub>	3.89	0.00	3.53	46.50	3.54	2.10	1.44	0.17
Cr <sub>2</sub> O <sub>3</sub>	0.76	0.02	0.51	20.27	0.276	0.63	-0.35	0.36
FeO	2.83	10.01	6.54	14.41	7.721	8.70	-0.98	0.19
MnO	0.10	0.14	0.13	0.13	0.14	0.13	0.01	0.04
MgO	16.60	48.82	33.19	18.17	40.08	41.86	-1.78	0.64
CaO	22.79	0.05	0.68	0.00	2.87	2.29	0.58	3.54
NiO	0.05	0.40	0.09	0.33	0.178	0.30	-0.12	0.13
Na <sub>2</sub> O	0.49	0.01	0.03	0.01	0	0.06	-0.06	0.08
K <sub>2</sub> O					0.16			
P <sub>2</sub> O <sub>5</sub>					0.04			Avg. error excluding SiO <sub>2</sub>
SUM	100.00	100.00	100.00	100.00	100.00	100.00		0.58

$\sigma$  error is calculated using the equation:

$$\sigma = (\sum(\sqrt{(\text{stdev} / \text{min wt\%})^2}) * \text{WR wt\%}$$

where  $\sqrt{\cdot}$  is square root, stdev is the standard deviation of the mineral average, WR is whole rock

Table 4.7. Mixing calculations

CM19 Least Modified

The Hybrid (Hy) magma is Whole Rock

Coef	Magma											
0.144	14.4	Avg_cpx										
0.619	62	Avg_ol										
0.196	19.6	Avg_opx										
0.04	4	Avg_sp										
	SiO <sub>2</sub>	TiO <sub>2</sub>	Al <sub>2</sub> O <sub>3</sub>	FeO	MnO	MgO	CaO	Na <sub>2</sub> O	K <sub>2</sub> O	P <sub>2</sub> O <sub>5</sub>	NiO	Cr <sub>2</sub> O <sub>3</sub>
Avg_cpx	54.53	0.41	4.02	3.31	0.1	17.74	17.55	1.24	0.01	0	0.06	1.03
Avg_ol	40.5	0	0	10.3	0.14	48.56	0.06	0.03	0	0	0.37	0.02
Avg_opx	54.1	0.13	4.78	6.52	0.14	32.98	0.78	0.11	0	0	0.09	0.37
Avg_sp	0.05	0.12	57.7	10.89	0.11	20.42	0	0.02	0	0	0.37	10.32
Hybrid	Whole	Rock										
Obs	43.54	0.1	3.76	7.88	0.13	40.04	2.69	0	0.07	0.01	0.7	1.09
Calc	43.58	0.09	3.81	8.57	0.13	39.92	2.72	0.22	0	0	0.27	0.65
Diff	-0.04	0.01	-0.05	-0.69	0	0.11	-0.03	-0.22	0.07	0.01	0.43	0.44
Sum of squares of residuals=			0.927									
	Obs	Calc	Resid	Avg_cpx	Avg_ol	Avg_opx	Avg_sp					
Cs	0	0	0	0	0	0	0					
Rb	3.5	0.1	3.4	0	0	0	1.3					
Ba	23.2	0.2	23	0.5	0.3	-0.1	-0.1					
Sr	24.7	7.9	16.8	53.3	0.3	0.1	-0.2					
Pb	0.3	0.1	0.2	0.1	0.1	0	0.1					
Nb	0.5	0	0.5	0.1	0	0	0					
U	0	0	0	0	0	0	0					
Th	0.1	0	0.1	0	0	0	0					
La	0.8	0.1	0.7	0.5	0	0	0					
Ce	1.4	0.4	1	2.2	0.1	0	0					
Nd	0.9	0.5	0.4	3.3	0	0	0					
Sm	0.2	0.2	0	1.5	0	0	0					
Eu	0.1	0.1	0	0.6	0	0	0					
Dy	0.4	0.5	-0.1	3	0	0.2	0					
Y	2	2.9	-0.9	17.9	0	1.4	0					
Yb	0.2	0.3	-0.1	1.7	0	0.3	0					

Table 4.7. Continued

CM52 Least Modified

The Hybrid (Hy) magma is Whole Rock

Coef	Magma											
0.168	16.8	Avg_cpx										
0.632	63.3	Avg_ol										
0.168	16.8	Avg_opx										
0.031	3.1	Avg_sp										
	SiO <sub>2</sub>	TiO <sub>2</sub>	Al <sub>2</sub> O <sub>3</sub>	FeO	MnO	MgO	CaO	Na <sub>2</sub> O	K <sub>2</sub> O	P <sub>2</sub> O <sub>5</sub>	NiO	Cr <sub>2</sub> O <sub>3</sub>
Avg_cpx	51.45	0.55	7.63	2.89	0.08	14.95	19.8	1.76	0	0	0.04	0.86
Avg_ol	40.6	0	0	10.05	0.12	48.72	0.07	0.03	0	0	0.39	0.01
Avg_opx	54.73	0.13	4.78	6.39	0.13	32.45	0.78	0.13	0	0	0.1	0.39
Avg_sp	0.04	0.11	58.36	10.32	0.09	20.52	0	0.01	0	0	0.37	10.19
Hybrid	Whole	Rock										
Obs	43.4	0.12	3.53	7.42	0.13	39.43	3.4	0	0.04	0.01	0.24	2.29
Calc	43.49	0.12	3.89	8.23	0.12	39.4	3.5	0.33	0	0	0.28	0.53
Diff	-0.1	0	-0.36	-0.81	0.01	0.03	-0.1	-0.33	0.04	0.01	-0.04	1.76
Sum of squares of residuals=			4.01									
	Obs	Calc	Resid	Avg_cpx	Avg_ol	Avg_opx	Avg_sp					
Cs	0	0	0	0	0	0	0					
Rb	0.6	0.1	0.5	0.3	0.1	0	0.1					
Ba	6.9	1.3	5.6	4.1	1	0	1.7					
Sr	20.5	48.9	-28.4	285.7	1.3	0.2	3.7					
Pb	0.5	0	0.4	0.1	0	0	0.1					
Nb	0.2	0	0.2	0	0	0	0.2					
U	0.1	0	0	0.1	0	0	0					
Th	0.1	0	0.1	0	0	0	0					
La	0.5	0.1	0.4	0.5	0.1	0	0.1					
Ce	1.2	0.5	0.7	2.3	0.2	0	0.2					
Nd	0.8	0.5	0.3	2.9	0.1	0	0					
Sm	0.3	0.2	0.1	1.3	0	0.1	0					
Eu	0.1	0.1	0	0.5	0	0	0					
Dy	0.5	0.5	0	2.6	0	0.3	-0.1					
Y	2.2	2.4	-0.2	14.4	0.1	-0.4	0					
Yb	0.3	0.4	-0.1	1.5	0	0.6	0					

Table 4.7. Continued

## CM14                    Moderately Modified

The Hybrid (Hy) magma is Whole Rock

Coef	Magma											
0.11	11	AVG_cpx										
0.568	56.7	AVG_ol										
0.29	29	AVG_opx										
0.032	3.2	AVG_sp										
	SiO <sub>2</sub>	TiO <sub>2</sub>	Al <sub>2</sub> O <sub>3</sub>	FeO	MnO	MgO	CaO	Na <sub>2</sub> O	K <sub>2</sub> O	P <sub>2</sub> O <sub>5</sub>	NiO	Cr <sub>2</sub> O <sub>3</sub>
AVG_cpx	52.21	0.27	3.89	2.83	0.1	16.6	22.79	0.49	0	0	0.05	0.76
AVG_ol	40.55	0.01	0	10.01	0.14	48.82	0.05	0.01	0	0	0.4	0.02
AVG_opx	55.22	0.08	3.53	6.54	0.13	33.19	0.68	0.03	0	0	0.09	0.51
AVG_sp	0.03	0.15	46.5	14.41	0.13	18.17	0	0.01	0	0	0.33	20.27
Hybrid	Whole	Rock										
Obs	44.87	0.12	3.54	7.72	0.14	40.08	2.87	0	0.16	0.04	0.18	0.28
Calc	44.82	0.06	2.96	8.36	0.13	39.78	2.74	0.07	0	0	0.27	0.9
Diff	0.05	0.06	0.58	-0.64	0.01	0.3	0.13	-0.07	0.16	0.04	-0.09	-0.62
Sum of squares of residuals=			1.29									
	Obs	Calc	Resid	AVG_cpx	AVG_ol	AVG_opx	AVG_sp					
Cs	12.4	2.3	10.1	0.3	0.1	7.6	-0.1					
Rb	11.6	3.4	8.2	20.2	0	4.3	-0.3					
Ba	0.9	0.3	0.6	0.1	0.1	0.8	0.1					
Sr	0.3	0.1	0.3	0	0	0.3	0.1					
Pb	0	0	0	0	0	0.1	0					
Nb	0.1	0	0	0	0	0	0					
U	0.5	0.1	0.4	0.2	0	0.3	0					
Th	1	0.4	0.7	0.8	0	0.9	0					
La	0.7	0.2	0.4	1.4	0	0.3	0					
Ce	0.2	0.1	0.1	0.8	0	0.1	0.1					
Nd	0.1	0	0	0.3	0	0	0					
Sm	0.3	0.2	0.1	1.8	0	0.1	0					
Eu	1.8	1.4	0.4	10.2	0	0.8	0					
Dy	0.3	0.2	0	1.1	0	0.3	0					

Table 4.8. Comparison of Mass Balance and Mixing Calculations

<b>CM19</b>		<b>Least Modified</b>			
	Obs	Mixing Calc	Mixing Diff	Obs Phase Calc	Obs. Phase Diff
SiO <sub>2</sub>	43.54	43.58	-0.04	42.37	1.17
TiO <sub>2</sub>	0.1	0.09	0.01	0.06	0.04
Al <sub>2</sub> O <sub>3</sub>	3.76	3.81	-0.05	3.25	0.51
Cr <sub>2</sub> O <sub>3</sub>	1.09	0.65	0.44	0.48	0.61
FeO	7.88	8.57	-0.69	9.18	-1.30
MnO	0.13	0.13	0	0.13	0.00
MgO	40.04	39.92	0.11	42.72	-2.68
CaO	2.69	2.72	-0.03	1.37	1.32
NiO	0.7	0.27	0.43	0.30	0.40
Na <sub>2</sub> O	0	0.22	-0.22	0.14	-0.14

<b>CM52</b>		<b>Least Modified</b>			
	Obs	Mixing Calc	Mixing Diff	Obs Phase Calc	Obs. Phase Diff
SiO <sub>2</sub>	43.4	43.49	-0.1	43.51	-0.11
TiO <sub>2</sub>	0.12	0.12	0	0.09	0.03
Al <sub>2</sub> O <sub>3</sub>	3.53	3.89	-0.36	1.95	1.58
Cr <sub>2</sub> O <sub>3</sub>	2.29	0.53	1.76	0.23	2.06
FeO	7.42	8.23	-0.81	8.69	-1.27
MnO	0.13	0.12	0.01	0.12	0.01
MgO	39.43	39.4	0.03	42.25	-2.82
CaO	3.4	3.5	-0.1	2.59	0.81
NiO	0.24	0.28	-0.04	0.31	-0.07
Na <sub>2</sub> O	0	0.33	-0.33	0.25	-0.25

<b>CM14</b>		<b>Moderately Modified</b>			
	Obs	Mixing Calc	Mixing Diff	Obs Phase Calc	Obs. Phase Diff
SiO <sub>2</sub>	44.87	44.82	0.05	43.88	0.99
TiO <sub>2</sub>	0.12	0.06	0.06	0.05	0.07
Al <sub>2</sub> O <sub>3</sub>	3.54	2.96	0.58	2.10	1.44
Cr <sub>2</sub> O <sub>3</sub>	0.28	0.9	-0.62	0.63	-0.35
FeO	7.72	8.36	-0.64	8.70	-0.98
MnO	0.14	0.13	0.01	0.13	0.01
MgO	40.08	39.78	0.3	41.86	-1.78
CaO	2.87	2.74	0.13	2.29	0.58
NiO	0.18	0.27	-0.09	0.30	-0.12
Na <sub>2</sub> O	0	0.07	-0.07	0.06	-0.06

Table 4.9. Comparison of Mineral Modal Weight Percents

Mixing results - modal comparison

**CM19**                      Least Modified

	Observed modes	Mixing modes	%difference
cpxAVG	0.06	0.14	-8.51
olAVG	0.72	0.62	10.05
opxAVG	0.19	0.20	-0.76
spAVG	0.03	0.04	-0.68

**CM52**                      Least Modified

	Observed modes	Mixing modes	%difference
cpxAVG	0.12	0.17	-4.49
olAVG	0.74	0.63	10.76
opxAVG	0.13	0.17	-3.73
spAVG	0.01	0.03	-2.44

**CM14**                      Moderately Modified

	Observed modes	Mixing modes	%difference
cpxAVG	0.09	0.11	-1.74
olAVG	0.67	0.57	10.6
opxAVG	0.21	0.29	-7.8
spAVG	0.02	0.03	-1.06

Table 4.10. Mixing Calculations with Sarapiquí basalt

CM19      Minerals & Sarapiquí  
 The Hybrid (Hy) magma is Whole Rock

Coef	Magma											
0.19	19	Avg_cpx										
0.548	54.9	Avg_ol										
0.283	28.3	Avg_opx										
0.059	5.9	Avg_sp										
-0.08	-8	AVG_Sarapiqui										
	SiO <sub>2</sub>	TiO <sub>2</sub>	Al <sub>2</sub> O <sub>3</sub>	FeO	MnO	MgO	CaO	Na <sub>2</sub> O	K <sub>2</sub> O	P <sub>2</sub> O <sub>5</sub>	NiO	Cr <sub>2</sub> O <sub>3</sub>
Avg_cpx	54.53	0.41	4.02	3.31	0.1	17.74	17.55	1.24	0.01	0	0.06	1.03
Avg_ol	40.5	0	0	10.3	0.14	48.56	0.06	0.03	0	0	0.37	0.02
Avg_opx	54.1	0.13	4.78	6.52	0.14	32.98	0.78	0.11	0	0	0.09	0.37
Avg_sp	0.05	0.12	57.7	10.89	0.11	20.42	0	0.02	0	0	0.37	10.32
AVG_Sar	50.9	0.91	17.94	10.99	0.21	5.29	10.31	2.5	0.73	0.2	0.01	0.01
Hybrid	Whole	Rock										
Obs	43.54	0.1	3.76	7.88	0.13	40.04	2.69	0	0.07	0.01	0.7	1.09
Calc	43.75	0.05	4.1	7.88	0.12	40.1	2.75	0.09	-0.06	-0.02	0.26	0.93
Diff	-0.09	0.05	-0.17	0	0.01	-0.06	-0.06	-0.09	0.13	0.03	0.44	0.16
Sum of squares of residuals=			0.29									

NOT REASONABLE TO ADD AND SUBTRACT MAGMAS

TRACE ELEMENTS NOT CALCULATED

CM52      Minerals & Sarapiquí  
 The Hybrid (Hy) magma is Whole Rock

Coef	Magma											
0.23	23.1	Avg_cpx										
0.555	55.6	Avg_ol										
0.272	27.3	Avg_opx										
0.052	5.2	Avg_sp										
-0.111	-11.2	AVG_Sarapiqui										
	SiO <sub>2</sub>	TiO <sub>2</sub>	Al <sub>2</sub> O <sub>3</sub>	FeO	MnO	MgO	CaO	Na <sub>2</sub> O	K <sub>2</sub> O	P <sub>2</sub> O <sub>5</sub>	NiO	Cr <sub>2</sub> O <sub>3</sub>
Avg_cpx	51.45	0.55	7.63	2.89	0.08	14.95	19.8	1.76	0	0	0.04	0.86
Avg_ol	40.6	0	0	10.05	0.12	48.72	0.07	0.03	0	0	0.39	0.01
Avg_opx	54.73	0.13	4.78	6.39	0.13	32.45	0.78	0.13	0	0	0.1	0.39
Avg_sp	0.04	0.11	58.36	10.32	0.09	20.52	0	0.01	0	0	0.37	10.19
AVG_Sar	50.9	0.91	17.94	10.99	0.21	5.29	10.31	2.5	0.73	0.2	0.01	0.01
Hybrid	Whole	Rock										
Obs	43.4	0.12	3.53	7.42	0.13	39.43	3.4	0	0.04	0.01	0.24	2.29
Calc	43.6	0.07	4.09	7.29	0.1	39.77	3.67	0.18	-0.08	-0.02	0.27	0.84
Diff	-0.2	0.05	-0.56	0.13	0.03	-0.34	-0.27	-0.18	0.12	0.03	-0.03	1.45
Sum of squares of residuals=			2.713									

NOT REASONABLE TO ADD AND SUBTRACT MAGMAS

TRACE ELEMENTS NOT CALCULATED

Table 4.10. Continued

## CM14 Minerals & Sarapiqui

The Hybrid (Hy) magma is Whole Rock

## Appendix A

### I. Sample Digestion and Dilution for Basalt and Basanite

1. Weigh 200mg powdered rock into acid cleaned 23ml Savillex beaker.
2. Wet rock powder with conc.  $\text{HNO}_3$
3. Add 10ml 8N  $\text{HNO}_3$ ; add 4ml conc. HF; cap beaker
4. Put capped beaker in ultrasonic bath for ½ hour minimum
5. Cook on hot plate capped (sub-boiling) for one day or until clear/white
6. Uncap and evaporate solution until almost dry (yellow color)
7. Add 6ml 8N  $\text{HNO}_3$ ; cap beaker
8. Cook on hot plate capped (sub-boiling) for one day or until clear/white
9. Uncap and evaporate solution until almost dry
10. Add 5ml 8N  $\text{HNO}_3$ ; transfer to storage bottle
11. Rinse beaker with 5ml DD  $\text{H}_2\text{O}$ , diluting sample solution to 10ml
12. Place storage bottles in ultrasonic bath until solution is clear and no cloudiness is detected.

NOTE: DO NOT OVER-DRY OR BURN SAMPLES; ALLOW A STICKY CONSISTENCY.

### II. Sample Digestion and Dilution for Ultramafic Xenoliths

Due to the prevalent oxide phases in ultramafic rocks, the digestion method must be more aggressive in order to achieve full digestion. Below is a basic recipe found to work after much trial and error. However, each sample may be slightly different, depending on the amount of oxides within the rock, and will need more or less time for full digestion. It is important to observe solutions for any undigested particles during the process and act accordingly. Further, final dilution will depend upon the desired concentration for analysis with a particular instrument.

1. Weigh 200mg powdered rock into acid cleaned PTFE liner for stainless steel body acid digestion pressure bomb.
2. Wet down with conc.  $\text{HNO}_3$
3. Add 4ml HF and 4ml  $\text{HClO}_4$
4. Place in oven at  $\sim 120$  °C for 3 – 5 days
5. Cook down; fume 2X with 1ml  $\text{HClO}_4$  and cook down
6. Add 10ml 8N  $\text{HNO}_3$ ; transfer to 23ml Savillex beaker
7. Flux on hot plate until clear (at least 1 day – time may vary)
8. Dry down.
9. Add 6ml 8N  $\text{HNO}_3$ ; flux a day, dry down
10. Add 6ml 8N  $\text{HNO}_3$ ; flux a day, dry down
11. Repeat step 10 as needed until solution is clear and light colored
12. Final dry down to “gooey” texture.
13. Transfer to storage bottle with 10ml 3%  $\text{HNO}_3$  + 0.03%HF
14. Place bottle in vortex until clear ( $\sim 20\text{min}.$ )

### **III. Accuracy, Precision and Contamination**

Frequent analysis of USGS rock standards during the analytical procedure permits estimation of sample accuracies by comparison with known concentrations. Here, BHVO-1 most closely resembles the geochemistry expected in arc basalt. The table below shows an example of five standard replications with values in ppm, the RSD in percent and standard deviation for each isotope measured.

Isotope	a	b	c	d	e	%RSD	AVERAGE	Std. Dev.
Li7(LR)	4.73	4.76	4.87	4.72	4.72	1.21	4.76	0.06
Rb85(LR)	9.22	8.79	9.00	8.88	8.92	1.60	8.96	0.14
Sr86(LR)	388.98	387.66	392.14	384.88	390.24	0.63	388.78	2.45
Sr87(LR)	324.72	326.49	335.21	333.05	329.07	1.19	329.71	3.93
Y89(LR)	24.91	23.97	24.71	24.53	24.06	1.50	24.43	0.37
Zr90(LR)	185.97	184.28	184.71	184.80	182.90	0.54	184.53	0.99
Cs133(LR)	0.10	0.10	0.10	0.10	0.10	1.55	0.10	0.00
Ba134(LR)	132.86	129.91	133.82	132.65	130.29	1.16	131.91	1.53
La139(LR)	15.64	15.44	15.98	15.50	15.51	1.25	15.62	0.20
Ce140(LR)	39.16	38.05	38.37	38.86	37.54	1.50	38.40	0.58
Pr141(LR)	5.29	5.31	5.32	5.45	5.28	1.19	5.33	0.06
Nd143(LR)	25.11	23.80	24.53	24.63	23.70	2.19	24.36	0.53
Nd145(LR)	28.71	23.77	24.69	24.24	23.94	7.37	25.07	1.85
Nd146(LR)	27.98	24.36	24.77	24.70	24.36	5.49	25.23	1.39
Sm147(LR)	5.93	6.01	6.28	6.29	5.99	2.50	6.10	0.15
Sm149(LR)	6.20	5.90	6.06	6.01	5.83	2.14	6.00	0.13
Eu151(LR)	1.78	1.93	1.97	1.98	1.90	3.84	1.91	0.07
Eu153(LR)	1.67	1.67	1.72	1.71	1.65	1.48	1.68	0.02
Gd155(LR)	5.91	6.58	6.97	7.35	7.12	7.47	6.79	0.51
Gd157(LR)	6.46	6.20	6.38	6.44	6.07	2.40	6.31	0.15
Gd158(LR)	6.67	6.83	7.21	7.34	7.02	3.48	7.01	0.24
Gd160(LR)	6.49	6.47	6.60	6.77	6.22	2.76	6.51	0.18
Tb159(LR)	0.93	0.93	0.98	0.98	0.92	2.49	0.95	0.02
Dy163(LR)	4.96	5.05	5.18	5.29	5.11	2.23	5.12	0.11
Ho165(LR)	0.93	0.90	0.95	0.94	0.92	1.93	0.93	0.02
Er166(LR)	2.53	2.44	2.59	2.54	2.45	2.26	2.51	0.06
Er167(LR)	2.35	2.31	2.43	2.45	2.31	2.46	2.37	0.06
Tm169(LR)	0.32	0.31	0.33	0.32	0.31	2.42	0.32	0.01
Yb171(LR)	2.03	1.96	2.06	2.03	1.91	2.75	2.00	0.06
Yb172(LR)	1.99	1.99	2.06	2.09	1.97	2.35	2.02	0.05
Yb173(LR)	2.22	1.92	2.07	2.03	1.93	5.46	2.03	0.11
Lu175(LR)	0.28	0.26	0.28	0.28	0.27	2.91	0.27	0.01
Pb208(LR)	2.12	2.13	2.10	2.61	2.25	8.56	2.24	0.19
Th232(LR)	1.25	1.20	1.23	1.24	1.19	2.00	1.22	0.02
U238(LR)	0.42	0.41	0.44	0.45	0.42	3.40	0.43	0.01
Sc45(MR)	30.95	29.79	29.30	29.26	30.37	2.16	29.93	0.65
V51(MR)	312.87	296.47	318.86	311.56	312.29	2.40	310.41	7.44
Co59(MR)	40.28	40.51	39.75	41.03	41.73	1.66	40.66	0.68
Ni60(MR)	108.26	135.64	108.46	109.05	112.86	9.17	114.85	10.53
Ni61(MR)	112.73	141.76	112.32	121.30	118.57	8.88	121.33	10.77
Cu63(MR)	135.85	139.55	134.16	132.74	140.16	2.14	136.49	2.92
Cu65(MR)	134.92	130.88	130.76	135.88	135.90	1.76	133.67	2.35
Zn64(MR)	94.77	80.98	92.67	81.01	84.16	6.77	86.72	5.87
Zn66(MR)	104.13	99.01	116.05	100.46	100.77	5.97	104.09	6.21
Rb85(MR)	9.34	8.98	8.98	9.36	9.60	2.60	9.25	0.24
Sr86(MR)	391.85	406.18	400.13	401.16	411.47	1.63	402.16	6.54

Analyzing sample digestion and dilution duplicates allows for the testing of precision on the part of both the instrument and the experimenter. The following tables show the percent RSD of such duplications.

Isotope	Digestion Duplication					in %RSD AVG	
	LS2	TE-2	MB4	AP6	MB5		
Li7(LR)	0.47	1.61	0.83	0.25	0.58	1.70	0.90
Rb85(LR)	1.87	0.78	0.12	1.48	1.70	0.99	1.16
Sr86(LR)	0.52	0.26	0.33	1.32	0.57	0.51	0.59
Sr87(LR)	0.20	0.40	1.06	1.58	0.47	0.42	0.69
Y89(LR)	1.97	1.84	2.53	2.45	1.45	0.34	1.76
Zr90(LR)	1.25	0.17	0.37	2.71	2.00	0.84	1.22
Cs133(LR)	1.23	0.51	1.65	1.21	1.39	0.34	1.06
Ba134(LR)	2.00	0.32	1.07	1.73	1.76	1.30	1.36
La139(LR)	0.84	0.33	0.88	1.05	2.51	0.48	1.02
Ce140(LR)	0.97	0.38	0.61	0.71	0.95	1.48	0.85
Pr141(LR)	2.01	0.88	0.77	0.44	0.49	0.75	0.89
Nd143(LR)	2.65	0.43	1.22	0.80	0.86	0.02	1.00
Nd145(LR)	1.28	0.85	0.86	1.27	1.12	1.40	1.13
Nd146(LR)	0.39	0.11	1.18	1.33	0.73	0.24	0.66
Sm147(LR)	0.07	1.37	1.29	2.16	1.74	0.44	1.18
Sm149(LR)	0.49	0.68	1.59	2.51	1.60	0.31	1.20
Eu151(LR)	1.41	0.84	0.39	1.92	1.65	2.84	1.51
Eu153(LR)	0.92	0.30	1.65	1.63	1.62	0.13	1.04
Gd155(LR)	4.39	0.70	2.65	3.19	3.43	1.26	2.60
Gd157(LR)	1.19	0.66	0.46	2.04	1.91	1.61	1.31
Gd158(LR)	2.20	0.16	0.43	1.23	0.96	1.08	1.01
Gd160(LR)	0.63	0.59	0.41	0.39	0.60	0.98	0.60
Tb159(LR)	0.35	1.00	0.04	0.99	1.53	1.85	0.96
Dy163(LR)	1.15	0.77	2.55	2.60	2.10	0.20	1.56
Ho165(LR)	2.08	1.10	0.40	1.46	1.46	0.03	1.09
Er166(LR)	2.42	1.90	1.07	3.16	1.68	1.51	1.96
Er167(LR)	2.02	0.71	2.28	3.07	2.02	0.56	1.78
Tm169(LR)	0.84	1.46	0.76	0.32	0.18	1.96	0.92
Yb171(LR)	1.89	0.77	2.93	0.66	0.87	0.93	1.34
Yb172(LR)	0.84	0.54	0.23	0.69	0.32	0.54	0.53
Yb173(LR)	0.38	0.12	0.68	0.97	2.10	0.50	0.79
W186(LR)	0.31	0.16	1.90	1.57	3.24	0.27	1.24
Pb208(LR)	1.40	6.20	2.30	1.08	1.48	2.25	2.45
Th232(LR)	1.60	2.21	1.16	0.96	2.55	0.06	1.42
U238(LR)	1.78	0.42	1.23	0.10	2.60	1.31	1.24
Sc45(MR)	1.48	0.85	0.95	0.41	0.51	0.39	0.76
V51(MR)	0.54	0.22	1.20	1.24	1.35	1.83	1.06
Cr52(MR)	38.90	16.59	12.95	5.83	13.66	1.72	14.94
Co59(MR)	0.01	0.36	0.35	1.93	1.97	58.05	10.45
Ni60(MR)	6.14	1.30	4.62	0.76	3.31	0.10	2.71
Ni61(MR)	4.06	3.09	14.66	11.19	0.06	6.77	6.64
Cu63(MR)	1.49	1.03	0.72	2.63	4.77	0.44	1.85
Cu65(MR)	0.22	0.66	0.37	0.69	3.04	1.65	1.11
Zn64(MR)	0.30	1.79	0.72	2.87	0.50	1.28	1.24
Zn66(MR)	1.77	1.34	2.98	3.32	1.22	2.89	2.25
Rb85(MR)	0.30	1.95	0.23	1.23	1.41	0.92	1.01
Sr86(MR)	1.39	0.45	1.62	1.70	0.09	1.09	1.05

Isotope	Dilution Duplication							in %RSD AVG
	MOM3	MB5	MS11	LS1L	MS17	MS20	AP6	
Li7(LR)	0.37	0.29	0.07	2.65	1.87	1.57	0.48	0.77
Rb85(LR)	0.28	0.21	0.48	0.38	2.22	0.99	0.10	0.71
Sr86(LR)	0.10	0.58	0.52	0.10	1.79	1.16	0.58	0.79
Sr87(LR)	1.26	0.84	0.40	0.63	1.63	1.74	0.26	1.02
Y89(LR)	2.80	0.03	0.34	2.34	2.00	1.25	0.07	1.08
Zr90(LR)	2.23	0.44	0.14	1.30	2.16	0.88	0.45	1.05
Cs133(LR)	0.72	1.04	0.48	0.09	1.45	1.21	0.09	0.83
Ba134(LR)	0.52	0.02	0.08	1.18	2.47	2.45	0.04	0.93
La139(LR)	1.20	0.25	1.69	0.27	2.86	2.33	1.32	1.61
Ce140(LR)	4.33	1.41	0.50	1.16	2.38	2.78	0.11	1.92
Pr141(LR)	2.73	1.63	0.42	1.95	2.41	2.31	1.57	1.85
Nd143(LR)	0.60	0.75	0.62	0.86	0.92	2.78	0.08	0.96
Nd145(LR)	0.52	0.01	0.62	0.97	1.09	2.21	0.39	0.81
Nd146(LR)	0.02	1.19	0.16	1.08	2.56	1.71	0.25	0.98
Sm147(LR)	0.76	0.76	0.40	1.83	0.90	1.41	0.30	0.76
Sm149(LR)	0.66	0.17	1.11	0.13	0.76	3.10	0.20	1.00
Eu151(LR)	0.12	1.54	0.19	1.67	2.29	1.01	0.23	0.89
Eu153(LR)	0.35	0.14	1.41	2.31	2.78	0.79	2.88	1.39
Gd155(LR)	3.63	3.77	1.21	2.58	2.21	3.27	3.36	2.91
Gd157(LR)	0.06	1.30	0.08	1.50	1.69	2.37	3.53	1.50
Gd158(LR)	1.02	0.44	0.11	0.58	2.46	2.05	1.24	1.22
Gd160(LR)	0.06	0.66	0.69	0.05	1.27	1.29	0.65	0.77
Tb159(LR)	1.73	0.69	0.75	0.65	1.07	1.36	0.91	1.09
Dy163(LR)	0.03	1.11	0.22	1.29	1.56	2.69	0.39	1.00
Ho165(LR)	0.96	1.25	0.33	0.84	0.09	2.47	0.39	0.91
Er166(LR)	0.41	1.51	0.79	0.01	1.97	1.29	0.69	1.11
Er167(LR)	1.04	0.25	0.36	0.45	0.72	2.40	0.50	0.88
Tm169(LR)	2.64	1.01	0.51	1.42	2.10	1.14	0.09	1.25
Yb171(LR)	0.22	0.57	0.14	1.17	2.34	1.25	0.79	0.89
Yb172(LR)	1.84	0.42	0.95	1.47	0.74	1.20	0.85	1.00
Yb173(LR)	1.58	1.01	1.12	0.25	1.94	1.92	0.64	1.37
W186(LR)	0.89	0.48	1.17	0.37	2.30	0.75	0.17	0.96
Pb208(LR)	1.41	0.79	1.61	1.09	1.27	2.20	0.87	1.36
Th232(LR)	1.59	0.80	0.90	2.29	2.12	2.28	1.37	1.51
U238(LR)	0.77	1.66	0.29	1.34	2.60	0.61	0.35	1.05
Sc45(MR)	0.05	0.78	1.06	0.28	1.70	3.40	0.92	1.32
V51(MR)	0.01	0.81	0.03	0.41	1.76	1.89	0.52	0.84
Cr52(MR)	31.75	4.30	13.18	15.16	9.33	1.51	19.59	13.28
Co59(MR)	0.03	1.55	0.38	0.39	1.20	0.74	0.05	0.66
Ni60(MR)	3.35	0.76	2.32	8.08	1.74	0.97	0.64	1.63
Ni61(MR)	1.84	10.21	2.38	19.47	6.76	0.76	9.62	5.26
Cu63(MR)	0.79	3.23	0.97	2.02	0.78	0.24	2.94	1.49
Cu65(MR)	0.96	2.06	0.14	1.96	0.16	2.84	2.77	1.49
Zn64(MR)	1.71	2.32	1.82	0.85	2.55	1.85	1.95	2.03
Zn66(MR)	2.99	0.87	0.30	0.69	3.38	2.15	2.08	1.96
Rb85(MR)	0.67	1.13	0.11	0.68	1.04	0.83	0.97	0.79
Sr86(MR)	0.82	0.71	0.40	1.92	1.11	0.01	1.05	0.69

Additionally, systematic introduction of blank samples during both the digestion process and the run safeguards against contamination that may occur during sample preparation or due to instrumentation. The error propagated here is so small as to be inconsequential.

Digestion blanks in ppm

Isotope	BlkB	BlkC	BlkA	BlkD	BlkE	BlkF	AVG
Li7(LR)	0.08	0.17	0.12	0.32	0.34	0.29	0.22
Rb85(LR)	0.05	0.03	0.05	0.05	0.05	0.10	0.06
Sr86(LR)	1.08	1.26	1.37	1.38	1.50	2.47	1.51
Sr87(LR)	1.04	1.11	1.38	1.55	1.52	2.50	1.52
Y89(LR)	0.10	0.12	0.12	0.13	0.15	0.17	0.13
Zr90(LR)	1.52	0.51	1.47	0.41	0.82	0.86	0.93
Cs133(LR)	0.00	0.00	0.01	0.00	0.00	0.01	0.00
Ba134(LR)	3.24	3.78	4.32	4.35	4.73	5.76	4.36
La139(LR)	0.09	0.09	0.10	0.09	0.11	0.13	0.10
Ce140(LR)	0.11	0.12	0.12	0.11	0.12	0.17	0.13
Pr141(LR)	0.01	0.00	0.01	0.00	0.00	0.01	0.01
Nd143(LR)	0.02	0.01	0.02	0.01	0.02	0.05	0.02
Nd145(LR)	0.03	0.02	0.03	0.01	0.02	0.05	0.02
Nd146(LR)	0.02	0.01	0.03	0.01	0.01	0.05	0.02
Sm147(LR)	0.00	0.00	0.01	0.00	0.00	0.01	0.01
Sm149(LR)	0.00	0.00	0.00	0.00	0.00	0.01	0.00
Eu151(LR)	0.01	0.01	0.01	0.01	0.01	0.01	0.01
Eu153(LR)	0.01	0.02	0.01	0.01	0.01	0.01	0.01
Gd155(LR)	0.02	0.02	0.02	0.02	0.02	0.03	0.02
Gd157(LR)	0.01	0.01	0.01	0.00	0.00	0.01	0.01
Gd158(LR)	0.01	0.00	0.01	0.00	0.00	0.02	0.01
Gd160(LR)	0.01	0.00	0.01	0.00	0.00	0.02	0.01
Tb159(LR)	0.00	0.00	0.00	0.00	0.00	0.00	0.00
Dy163(LR)	0.00	0.00	0.00	0.00	0.00	0.01	0.01
Ho165(LR)	0.00	0.00	0.00	0.00	0.00	0.00	0.00
Er166(LR)	0.00	0.00	0.00	0.00	0.00	0.01	0.00
Er167(LR)	0.00	0.00	0.00	0.00	0.00	0.01	0.00
Tm169(LR)	0.00	0.00	0.00	0.00	0.00	0.00	0.00
Yb171(LR)	0.00	0.00	0.00	0.00	0.00	0.01	0.00
Yb172(LR)	0.00	0.00	0.00	0.00	0.00	0.01	0.00
Yb173(LR)	0.00	0.00	0.00	0.00	0.00	0.01	0.00
Lu175(LR)	0.00	0.00	0.00	0.00	0.00	0.00	0.00
Pb208(LR)	0.23	0.12	0.17	0.10	0.23	0.19	0.17
Th232(LR)	0.01	0.00	0.01	0.00	0.01	0.01	0.01
U238(LR)	0.00	0.00	0.00	0.00	0.00	0.01	0.00
Sc45(MR)	0.01	0.03	0.03	0.01	0.02	0.07	0.03
V51(MR)	0.26	0.24	0.27	0.25	0.29	1.46	0.46
Co59(MR)	0.05	0.03	0.04	0.02	0.02	0.56	0.12
Ni60(MR)	0.58	0.42	0.40	1.18	0.32	0.33	0.54
Ni61(MR)	0.67	0.53	0.44	0.39	0.27	0.33	0.44
Cu63(MR)	0.54	0.48	0.48	0.54	0.85	1.05	0.66
Cu65(MR)	0.57	0.46	0.39	0.61	0.74	1.04	0.64
Zn64(MR)	1.50	5.19	1.60	1.99	1.33	2.95	2.43
Zn66(MR)	1.71	5.83	1.65	2.76	1.66	4.22	2.97
Rb85(MR)	0.02	0.02	0.04	0.06	0.04	0.08	0.04
Sr86(MR)	0.37	0.33	0.44	0.42	0.32	1.65	0.59

Isotope	Machine Blanks in ppm								
	Blk1	Blk2	Blk3	Blk4	Blk5	Blk6	Blk7	Blk8	Blk9
Li7	0.08	0.07	0.12	0.20	0.36	0.26	0.31	0.26	0.29
Rb85	0.02	0.03	0.04	0.06	0.06	0.04	0.05	0.05	0.04
Sr86	1.15	1.30	1.33	1.32	1.32	1.52	1.37	1.63	1.48
Sr87	1.25	1.21	1.44	1.73	1.46	1.59	1.62	1.54	1.66
Y89	0.13	0.13	0.13	0.15	0.15	0.13	0.16	0.15	0.17
Zr90	0.39	1.60	0.97	1.82	1.60	0.49	1.52	0.73	0.75
Cs133	0.00	0.00	0.00	0.00	0.00	0.00	0.01	0.00	0.00
Ba134	4.03	4.45	4.21	4.49	4.77	4.21	5.00	5.11	4.59
La139	0.08	0.09	0.10	0.11	0.11	0.11	0.11	0.12	0.12
Ce140	0.09	0.10	0.12	0.14	0.13	0.12	0.17	0.14	0.13
Pr141	0.00	0.00	0.00	0.01	0.01	0.00	0.01	0.00	0.00
Nd143	0.01	0.01	0.02	0.03	0.03	0.01	0.03	0.02	0.01
Nd145	0.01	0.01	0.02	0.03	0.02	0.01	0.03	0.02	0.01
Nd146	0.01	0.01	0.02	0.03	0.03	0.01	0.03	0.02	0.02
Sm147	0.00	0.00	0.01	0.01	0.01	0.00	0.01	0.00	0.01
Sm149	0.00	0.00	0.00	0.01	0.01	0.00	0.01	0.00	0.00
Eu151	0.00	0.01	0.01	0.01	0.01	0.01	0.01	0.01	0.00
Eu153	0.01	0.01	0.01	0.01	0.01	0.01	0.01	0.01	0.01
Gd155	0.01	0.02	0.02	0.03	0.02	0.02	0.02	0.02	0.02
Gd157	0.00	0.00	0.01	0.01	0.01	0.00	0.01	0.01	0.01
Gd158	0.00	0.00	0.01	0.01	0.01	0.00	0.01	0.01	0.01
Gd160	0.00	0.00	0.01	0.01	0.01	0.00	0.01	0.01	0.01
Tb159	0.00	0.00	0.00	0.00	0.00	0.00	0.00	0.00	0.00
Dy163	0.00	0.00	0.00	0.01	0.01	0.00	0.01	0.00	0.00
Ho165	0.00	0.00	0.00	0.00	0.00	0.00	0.00	0.00	0.00
Er166	0.00	0.00	0.00	0.00	0.00	0.00	0.00	0.00	0.00
Er167	0.00	0.00	0.00	0.00	0.00	0.00	0.00	0.00	0.00
Tm169	0.00	0.00	0.00	0.00	0.00	0.00	0.00	0.00	0.00
Yb171	0.00	0.00	0.00	0.00	0.00	0.00	0.00	0.00	0.00
Yb172	0.00	0.00	0.00	0.00	0.00	0.00	0.00	0.00	0.00
Yb173	0.00	0.00	0.00	0.00	0.00	0.00	0.00	0.00	0.00
Lu175	0.00	0.00	0.00	0.00	0.00	0.00	0.00	0.00	0.00
Pb208	0.03	0.03	0.06	0.11	0.10	0.06	0.10	0.07	0.06
Th232	0.00	0.00	0.01	0.01	0.01	0.00	0.01	0.00	0.00
U238	0.00	0.00	0.00	0.00	0.00	0.00	0.00	0.00	0.00
Sc45	0.06	0.11	0.08	0.04	0.05	0.06	0.04	0.05	0.05
V51	0.18	0.32	0.42	0.32	0.27	0.51	0.34	0.58	0.43
Co59	0.05	0.09	0.08	0.08	0.06	0.11	0.08	0.08	0.10
Ni60	0.31	0.35	0.35	0.40	0.32	0.67	0.43	0.31	0.40
Ni61	0.58	0.47	0.46	0.30	0.20	0.85	0.50	0.42	0.48
Cu63	0.62	0.64	0.70	0.65	0.71	0.81	0.60	0.76	0.81
Cu65	0.68	0.61	0.82	0.64	0.58	0.89	0.67	0.85	0.84
Zn64	1.00	1.12	1.02	1.13	0.98	1.13	1.00	1.07	1.21
Zn66	1.42	1.24	1.51	1.50	1.26	1.74	1.26	1.25	1.52
Rb85	0.03	0.02	0.04	0.02	0.03	0.05	0.04	0.03	0.03
Sr86	0.33	0.38	0.69	0.51	0.49	0.66	0.40	0.37	0.57

Isotope	Machine Blanks in ppm						
	Blk1a	Blk2a	Blk3a	Blk4a	Blk5a	Blk6a	AVG
Li7	0.05	0.06	0.09	0.12	0.19	0.15	0.17
Rb85	0.08	0.07	0.05	0.04	0.05	0.05	0.05
Sr86	0.89	0.93	1.09	1.22	1.31	1.41	1.29
Sr87	0.96	0.96	1.12	1.21	1.33	1.42	1.37
Y89	0.10	0.11	0.11	0.11	0.13	0.13	0.13
Zr90	0.47	1.70	0.80	0.57	0.77	0.72	0.99
Cs133	0.00	0.00	0.00	0.00	0.00	0.00	0.00
Ba134	3.29	2.98	3.43	3.51	3.89	4.22	4.15
La139	0.07	0.08	0.09	0.10	0.09	0.11	0.10
Ce140	0.08	0.09	0.11	0.11	0.12	0.11	0.12
Pr141	0.00	0.00	0.00	0.00	0.01	0.01	0.00
Nd143	0.01	0.02	0.03	0.02	0.02	0.02	0.02
Nd145	0.01	0.02	0.02	0.02	0.03	0.03	0.02
Nd146	0.01	0.02	0.02	0.02	0.03	0.03	0.02
Sm147	0.00	0.01	0.01	0.01	0.01	0.01	0.01
Sm149	0.00	0.01	0.01	0.00	0.01	0.01	0.00
Eu151	0.00	0.00	0.01	0.01	0.01	0.01	0.01
Eu153	0.00	0.00	0.01	0.01	0.01	0.01	0.01
Gd155	0.01	0.01	0.02	0.02	0.02	0.02	0.02
Gd157	0.00	0.01	0.01	0.01	0.01	0.01	0.01
Gd158	0.00	0.01	0.01	0.01	0.01	0.01	0.01
Gd160	0.00	0.01	0.01	0.01	0.01	0.01	0.01
Tb159	0.00	0.00	0.00	0.00	0.00	0.00	0.00
Dy163	0.00	0.01	0.01	0.01	0.01	0.01	0.00
Ho165	0.00	0.00	0.00	0.00	0.00	0.00	0.00
Er166	0.00	0.00	0.00	0.00	0.00	0.00	0.00
Er167	0.00	0.00	0.00	0.00	0.00	0.00	0.00
Tm169	0.00	0.00	0.00	0.00	0.00	0.00	0.00
Yb171	0.00	0.00	0.00	0.00	0.00	0.00	0.00
Yb172	0.00	0.00	0.00	0.00	0.00	0.00	0.00
Yb173	0.00	0.00	0.00	0.00	0.00	0.01	0.00
Lu175	0.00	0.00	0.00	0.00	0.00	0.00	0.00
Pb208	0.06	0.05	0.07	0.06	0.08	0.08	0.07
Th232	0.01	0.00	0.01	0.00	0.01	0.01	0.01
U238	0.00	0.00	0.00	0.00	0.00	0.00	0.00
Sc45	0.10	0.18	0.09	0.09	0.08	0.07	0.08
V51	0.18	0.45	0.54	0.55	0.47	0.54	0.41
Co59	0.04	0.15	0.12	0.12	0.10	0.10	0.09
Ni60	0.39	0.26	0.35	0.35	0.42	0.31	0.37
Ni61	0.37	0.13	0.50	0.25	0.39	0.92	0.46
Cu63	1.58	0.94	0.97	0.96	0.94	0.85	0.83
Cu65	1.50	0.86	0.91	0.93	0.82	1.04	0.84
Zn64	1.31	1.28	1.32	1.47	1.51	1.34	1.19
Zn66	1.48	1.51	1.76	1.45	1.50	1.36	1.45
Rb85	0.05	0.05	0.03	0.04	0.04	0.05	0.04
Sr86	0.42	0.38	0.59	0.69	0.53	0.58	0.51

Finally, other error taken in to account is that of pipetting and the weighing scale.

<u>Pipette</u>		
5.1019		
5.0983		
5.0990		
5.0979		
5.0981		
5.0854		
5.1017		
5.0968		
5.0971		
5.0990		
<u>Scale</u>		
5.09752	Avg	200
0.002652	AvgDeviation	
0.0043556	Std. Dev.	0.1
0.0026996	95% confidence	
0.08545	%RSD	0.05

Taken all together,  $1\sigma$  in %RSD is inclusive of error propagated by pipette, scale, digestion duplication and dilution duplication. All are less than 3.2% except cobalt. The reason for this discrepancy is unknown. Nickel, at 3.2% is apparently high due to using a nickel cone within the ICP-MS.

Isotope	dig.Dup.	dil.Dup	TOTAL	Isotope	dig.Dup.	dil.Dup	TOTAL
			$1\sigma$				$1\sigma$
Li7(LR)	0.9043	0.7745	1.195	Dy163(LR)	1.5590	1.0008	1.855
Rb85(LR)	1.1571	0.7135	1.363	Ho165(LR)	1.0882	0.9138	1.424
Sr86(LR)	0.5877	0.7890	0.989	Er166(LR)	1.9579	1.1098	2.253
Sr87(LR)	0.6875	1.0204	1.234	Er167(LR)	1.7752	0.8785	1.983
Y89(LR)	1.7639	1.0829	2.072	Tm169(LR)	0.9208	1.2472	1.553
Zr90(LR)	1.2249	1.0519	1.618	Yb171(LR)	1.3414	0.8855	1.610
Cs133(LR)	1.0555	0.8341	1.349	Yb172(LR)	0.5259	0.9993	1.134
Ba134(LR)	1.3613	0.9298	1.651	Yb173(LR)	0.7918	1.3708	1.586
La139(LR)	1.0154	1.6092	1.905	W186(LR)	1.2423	0.9588	1.572
Ce140(LR)	0.8500	1.9201	2.102	Pb208(LR)	2.4508	1.3591	2.804
Pr141(LR)	0.8896	1.8469	2.052	Th232(LR)	1.4228	1.5096	2.077
Nd143(LR)	0.9960	0.9589	1.386	U238(LR)	1.2405	1.0456	1.625
Nd145(LR)	1.1277	0.8059	1.390	Sc45(MR)	0.7642	1.3196	1.528
Nd146(LR)	0.6647	0.9787	1.187	V51(MR)	1.0622	0.8359	1.355
Sm147(LR)	1.1771	0.7567	1.403	Co59(MR)	10.4453	0.6592	10.467
Sm149(LR)	1.1982	0.9991	1.563	Ni60(MR)	2.7058	1.6313	3.161
Eu151(LR)	1.5091	0.8948	1.757	Ni61(MR)	6.6393	5.2612	8.472
Eu153(LR)	1.0407	1.3919	1.741	Cu63(MR)	1.8461	1.4915	2.375
Gd155(LR)	2.6032	2.9068	3.903	Cu65(MR)	1.1054	1.4888	1.857
Gd157(LR)	1.3114	1.5048	1.998	Zn64(MR)	1.2445	2.0323	2.385
Gd158(LR)	1.0100	1.2201	1.587	Zn66(MR)	2.2515	1.9615	2.988
Gd160(LR)	0.6001	0.7692	0.981	Rb85(MR)	1.0071	0.7930	1.286
Tb159(LR)	0.9617	1.0860	1.454	Sr86(MR)	1.0549	0.6852	1.262

## References

- Abe N., Takami M., and Arai S. (2003) Petrological feature of spinel lherzolite xenolith form Oki-Dogo Island: An implication for variety of the upper mantle peridotite beneath southwestern Japan. *The Island Arc* **12**, 219-232.
- Abratis M. and Wörner G. (2001) Ridge collosion, slab-window formation, and the flux of Pacific asthenosphere into the Caribbean realm. *Geology* **29** (2), 127-130.
- Alt J., Laverne C., Vanko D., Tartarotti P., Teagle D., Bach W., Zuleger E., Erzinger J., Honnorez J., Pezard P., Becker K., Salisbury M., and Wilkens R. (1996) Hydrothermal alteration of section of upper oceanic crust in the eastern equatorial Pacific: a synthesis of results from site 504 (DSDP legs 69, 70 and 83, and odd legs 111, 137, 140 and 148). *Proceedings of the ODP, Scientific Results*. 417-433.
- Alva-Valdivia L. M., Goguitchaichvili A., Arredondo-Guerrero P., Urrutia-Fucugauchi J., and Royo-Ochoa M. (2003) A pilot rock magnetic and ore microscopy study of xenolith-bearing young basaltic rocks from the Camargo cinder cone field, Chihuahua, northern Mexico. *Journal of South American Earth Sciences* **15** (7), 823-833.
- Aoki K. (1987) Japanese island arc: xenolith in alkali basalts, high-alumina basalts and calc-alkaline andesites and dacites. In *Mantle xenoliths* (Ed. by P. Nixon), pp. 319-333. Wiley, Chichester.
- Aoki K.-I. and Shiba I. (1973) Chemical composition and origin of inclusions in alkali basalt. *Lithos* **6** (1), 41-51.
- Arai S. (1991) Petrological Characteristics of the Upper Mantle Peridotites beneath the Japan Island Arcs - Petrogenesis of Spinel Peridotites -. *Soviet Geology and Geophysics* **32** (1), 8-25.
- Arai S. (1994) Characterization of spinel peridotites by olivine-spinel compositional relationships: Review and interpretation. *Chemical Geology* **113**, 191-204.
- Arai S. and Ishimaru S. (2008) Insights into petrological characteristics of the lithosphere of mantle wedge beneath arcs through peridotite xenoliths; a review. *Contributions to Mineralogy and Petrology* **49** (4), 665-695.
- Arai S. and Kida Megumi (2000) Origin of fine-grained peridotite xenoliths form Iraya volcano of Batan Island, Philippines: deserpentization or metasomatism at the mantle wedge beneath an incipient arc? *The Island Arc* **9**, 458-471.
- Arculus R. (1994) Aspects of magma genesis in arcs. *Lithos* **33** (1-3), 189-208.
- Arculus R. J. (1985) Oxidation state of the mantle: past and present. *Annual Review of Earth and Planetary Sciences* **13**, 75-95.
- Ayers J. (1998) Trace element modeling of aqueous fluid - peridotite interaction in the mantle wedge of subduction zones. *Contributions to Mineralogy and Petrology* **132**, 390-404.
- Ballhaus C. (1993) Oxidation states of the lithospheric and asthenospheric upper mantle. *Contributions to Mineralogy and Petrology* **114**, 331-348.
- Ballhaus C., Berry R., and Green D. (1991) High pressure experimental calibration of the olivine-orthopyroxene-spinel oxygen geobarometer: implications for the oxidation state of the upper mantle. *Contributions to Mineralogy and Petrology* **107**, 27-40.
- Ballhaus C. and Frost B. (1994) The generation of oxidised CO<sub>2</sub>-bearing basaltic melts from reduced CH<sub>4</sub>-bearing upper mantle sources. *Geochimica et Cosmochimica Acta* **58**, 4931-4940.
- Barnes S. J. and Roeder P., L. (2001) The Range of Spinel Compositions in Terrestrial Mafic and Ultramafic Rocks. *Journal of Petrology* **42** (12), 2279-2302.
- Barsdell M. and Smith I. (1989) Petrology of recrystallized ultramafic xenoliths from Merelava volcano, Vanuatu. *Contributions to Mineralogy and Petrology* **102** (230-241).
- Batumike J., O'Reilly S., and Griffin W. (2008) Peridotitic garnet geochemistry: key to the understanding of lithospheric structures and kimberlites diamond potential in Southern Congo. *9th International Kimberlite Conference Extended Abstract No. 9IKC-A-00122*.

- Bebout G. E., Ryan J., Leeman W. P., and Bebout A. E. (1999) Fractionation of trace elements by subduction-zone metamorphism; effect of convergent-margin thermal evolution. *Earth and Planetary Science Letters* **171** (1), 63-81.
- Berly T. J., Hermann J., Arculus R. J., and Lapierre H. (2006) Supra-subduction Zone Pyroxenites from San Jorge and Santa Isabel (Solomon Islands). *Journal of Petrology* **47** (8), 1531-1555.
- Best M. G. (1982) *Igneous and metamorphic petrology*. W.H. Freeman and Company, San Francisco, CA, USA.
- Bizimis M., Salters V. J., and Bonatti E. (2000) Trace and REE content of clinopyroxenes from supra-subduction zone peridotites. Implications for melting and enrichment processes in island arcs. *Chemical Geology* **165**, 67-85.
- Blatt H., Tracy R. J., and Owens B. E. (2006) *Petrology: igneous, sedimentary, and metamorphic*. Macmillan, New York.
- Blatter D. L. and Carmichael I. S. (1998) Hornblende peridotite xenoliths from central Mexico reveal the highly oxidized nature of subarc upper mantle. *Geology* **26**, 1035-1038.
- Bodinier J., Dupuy C., and Dostal J. (1988) Geochemistry and petrogenesis of eastern Pyrenean peridotites. *Geochimica et Cosmochimica Acta* **52**, 2893-2907.
- Bolge L. L. (2000) Geochemistry of tephras form Arenal Volcano, Costa Rica: Repeated cycles of explosive volcanism, pp. 211. Rutgers University, Geological Sciences.
- Bolge L. L. (2005) Constraining the magmatic sources of Hawaiian and Central American volcanics. diss. Rutgers University, New Brunswick, NJ, USA, Geological Sciences.
- Bolge L. L., Carr M. J., Milidakis K. I., Lindsay F. N., and Feigenson M. D. (in review) Correlating Tectonics, Geochemistry, and Volcanic Volume along the Central American Volcanic Front. *Geochemistry Geophysics Geosystems*.
- Bonatti E. and Michael P. (1989) Mantle peridotites from continental rifts to oceanic basins to subduction zones. *Earth and Planetary Science Letters* **91** (297-311).
- Borgia A. and van Wyk de Vries B. (2003) The volcano-tectonic evolution of Concepcion, Nicaragua. *Bulletin of Volcanology* **65**, 248-266.
- Brandon A. and Draper D. (1996) Constraints on the origin of the oxidation state of mantle overlying subduction zones: an example from Simcoe, Washington, USA. *Geochimica et Cosmochimica Acta* **60**, 1739-1749.
- Brenan J., Shaw H., Ryerson F., and Phinney D. (1995) Mineral-aqueous fluid partitioning of trace elements at 900°C and 2.0 GPa: Constraints on the trace element chemistry of mantle and deep crustal fluids. *Geochimica et Cosmochimica Acta* **59** (16), 3331-3350.
- Brey G. and Köhler T. (1990) Geothermobarometry in four-phase Iherzolites; II, New thermobarometers, and practical assessment of existing thermobarometers. *Journal of Petrology* **31** (6), 1353-1378.
- Bryan W. B. (1969) Some applications of linear least squares calculations to petrographic problems. *EOS Transactions* **50** (4), 354 American Geophysical Union.
- Bryant J., Yogradzinski G., and Churikova T. (2007) Melt-mantle interactions beneath Kamchatka arc: Evidence from ultramafic xenoliths from Shiveluch volcano. *Geochemistry Geophysics Geosystems* **8** (4), 24pp.
- Bryndzia L. and Wood B. (1990) Oxygen thermobarometry of abyssal spinel peridotites: the redox state and the C-O-H volatile composition of the earth's sub-oceanic mantle. *American Journal of Science* **290**, 1093-1116.
- Cameron B., Walker J., Carr M., Patino L., Matías O., and Feigenson M. (2002) Flux versus decompression melting at stratovolcanoes in southeastern Guatemala. *Journal of Volcanology and Geothermal Research* **119**, 21-50.
- Carr M., Feigenson M., and Bennett E. (1990) Incompatible element and isotopic evidence for tectonic control of source mixing and melt extraction along the Central American arc. *Contributions to Mineralogy and Petrology* **105**, 369-380.
- Carr M. J. (1976) Underthrusting and Quaternary faulting in northern Central America. *Geological Society of America Bulletin* **87** (5), 825-829.

- Carr M. J. (1984) Symmetrical and segmented variation of physical and geochemical characteristics of the Central American volcanic front. *Journal of Volcanology and Geothermal Research* **20**, 231-252.
- Carr M. J., Feigenson M. D., Patino L. C., and Walker J. A. (2003) Volcanism and Geochemistry in Central America: Progress and Problems. In *Inside the Subduction Factory* (Ed. by J. Eiler), pp. 153-174. American Geophysical Union, Washington, DC.
- Carr M. J. and Rose Jr. W. I. (1987) CENTAM - a data base of Central American volcanic rocks. *Journal of Volcanology and Geothermal Research* **33**, 239-240.
- Carr M. J. and Stoiber R. (1977) Geological setting of some destructive earthquakes in Central America. *Geological Society of America Bulletin* **88** (1), 151-156.
- Carr M. J., Saginor I., Alvarado G. E., Bolge L. L., Lindsay F. N., Milidakis K., Turrin B. D., Feigenson M. D., and Swisher III C. C. (2007) Element fluxes from the volcanic front of Nicaragua and Costa Rica. *Geochemistry Geophysics Geosystems* **8** (6), 22.
- Cervantes P. and Wallace P. J. (2003) Role of H<sub>2</sub>O in subduction-zone magmatism; new insights from melt inclusions in high-Mg basalts from central Mexico. *Geology* **31** (3), 235-238.
- Chan L., Leeman W. P., and You C.-F. (2002) Lithium isotopic composition of Central American volcanic arc lavas; implications for modification of subarc mantle by slab-derived fluids; correction. *Chemical Geology* **182** (2-4), 293-300.
- Conceição R., Mallmann G., Koester E., Schilling M., Bertotto G., and Rodriguez-Vargas A. (2005) Andean subduction-related mantle xenoliths: Isotopic evidence of Sr-Nd decoupling during metasomatism. *Lithos* **82**, 273-287.
- Cox K., Bell (1979) *The Interpretation of Igneous Rocks*. George Allen & Unwin, London, Boston, Sydney.
- Dasgupta R., Hirschmann and Smith N. D. (2007) Partial Melting Experiments of Peridotite + CO<sub>2</sub> at 3 GPa and Genesis of Alkalic Ocean Island Basalts. *Journal of Petrology* **48** (11), 2093-2124.
- DeBari S., Kay S., and Kay R. (1986) Xenolithic evidence for the nature of the crust - mantle boundary and primitive magmas in the Aleutian Arc. *Journal of Geology* **94** (3), 329-341.
- Dengo G. (1968) *Estructura geológica, historia tectónica y morfológia de América Central*. American Geological Institute.
- Dick H. and Bullen T. (1984) Chromian spinel as a petrogenetic indicator in abyssal and alpine-type peridotites and spatially associated lavas. *Contributions to Mineralogy and Petrology* **86**, 54-76.
- Dollfus A. and Montserrat E. d. (1867) Nevado de Toluca; volcan de Colima. *La Naturaleza* **6**, 29-35.
- Edwards C., Morris J. D., and Thirwall M. (1993) Separating mantle from slab signatures in arc lavas using B/Be and radiogenic isotope systematics. *Nature* **362**, 530-533.
- Eiler J. M., Crawford A. J., Elliot T. R., Farley K. A., Valley J. W., and Stolper E. M. (2000) Oxygen isotope geochemistry of oceanic-arc lavas. *Journal of Petrology* **41** (2), 229-256.
- Elliot T., Plank T., Zindler A., White W., and Bourdon B. (1997) Element transport from slab to volcanic front at the Mariana arc. *Journal of Geophysical Research* **102** (B7), 14,991-15,019.
- Ertan I. E., and Leeman W. P. (1999) Fluid inclusions in mantle and lower crustal xenoliths from Simcoe volcanic field, Washington. *Chemical Geology* **154**, 83-95.
- Faure G. (1986) *Principles of Isotope geology*. John Wiley & Sons, New Youk, NY, USA.
- Feigenson Mark D. and Carr M. J. (1986) Positively correlated Nd and Sr isotope ratios of lavas from the Central American volcanic front. *Geology* **14**, 79-82.
- Feigenson M. D. and Carr M. J. (1993) The source of Central American lavas: inferences from geochemical inverse modeling. *Contributions to Mineralogy and Petrology* **113**, 226-235.
- Feigenson M. D., Carr M. J., Maharaj S. V., Juliano S., and Bolge L. L. (2004) Lead isotope composition of Central American volcanoes: Influence of the Galapagos plume. *Geochemistry Geophysics Geosystems* **5** (6), 14.

- Foley S. F., Barth M. G., and Jenner G. A. (2000) Rutile/melt partition coefficients for trace elements and an assessment of the influence of rutile on the trace element characteristics of subduction zone magmas. *Geochimica et Cosmochimica Acta* **64** (5), 933-938.
- Franz L., Becker K.-P., Kramer W., and Herzig P. M. (2002) Metasomatic mantle xenoliths from the Bismarck Microplate (Papua New Guinea); thermal evolution, geochemistry and extent of slab-induced metasomatism. *Journal of Petrology* **43** (2), 315-343.
- Frey F. A. and Prinz M. (1978) Ultramafic inclusions form San Carlos, Arizona: Petrologic and geochemical data bearing on their petrogenesis. *Earth and Planetary Science Letters* **38**, 129-176.
- Frost B. and Ballhaus C. (1998) Comment on "Constraints on the origin of the oxidation state of mantle overlying subduction zones: an example from Simcoe, Washington, USA" by A.D. Brandon and D.S. Draper. *Geochimica et Cosmochimica Acta* **62**, 329-331.
- Frost D. J. and McCammon C. A. (2008) The Redox State of Earth's Mantle. *Annual Review of Earth and Planetary Sciences* **36**, 389-420.
- Gazel E., Alvarado G. E., Obando J., and Alfaro. Arístides (2005) Geología y Evolución magmática del arco de Sarapiquí, Costa Rica. *Revista Geológica de América Central* **32**, 13-31.
- Gazel E., Carr M. J., Hoernle K., Feigenson M. D., Szymanski D., Hauff F., and van den Bogaard P. (2009) Galapagos-OIB signature in southern Central America: Mantle refertilization by arc-hot spot interaction. *Geochemistry Geophysics Geosystems* **10** (2), 32pp.
- Geist D. J., Fornari D. J., Kurz M. D., Harpp K. S., Soule S. A., Perfit M. R., and Koleszar A. M. (2006) Submarine Fernandina; magmatism at the leading edge of the Galapagos hot spot. *Geochemistry Geophysics Geosystems* **7** (12), 27pp.
- Gorring M. L. and Kay S. M. (2000) Carbonatite metasomatized peridotite xenoliths from southern Patagonia: implications for lithospheric processes and Neogene plateau magmatism. *Contributions to Mineralogy and Petrology* **140**, 55-72.
- Gorring M. L. and Kay S. M. (2001) Mantle Processes and Source of Neogene Slab Window Magmas from Southern Patagonia, Argentina. *Journal of Petrology* **42** (6), 1067-1094.
- Green D. H. Primary magmas at mid-ocean ridges, 'hot-spots' and other intraplate settings: constraints on mantle potential temperatures. [www.mantleplumes.org/MantleTemp.html](http://www.mantleplumes.org/MantleTemp.html). Mantle plumes.org.
- Gregoire M., McInnes B., and O'Reilly S. (2001) Hydrous metasomatism of oceanic sub-arc mantle, Lihir, Papua New Guinea Part 2. Trace element characteristics of slab-derived fluids. *Lithos* **59**, 91-108.
- Gribble R. F., Stern R. J., Bloomer S. H., Stuben D., O'Hearn T., and Newman S. (1996) MORB mantle and subduction components interact to generate basalts in the southern Mariana Trough back-arc basin. *Geochimica et Cosmochimica Acta* **60** (1-2), 2153-2166.
- Gurnis M. (1986) Stirring and mixing in the mantle by plate-scale flow: Large persistent blobs and long tendrils coexist. *Geophysical Research Letters* **13** (13), 1474-1477.
- Gurnis M. and Davies G. F. (1986) The effect of depth-dependent viscosity on convective mixing in the mantle and the possible survival of primitive mantle. *Geophysical Research Letters* **13** (6), 541-544.
- Haggerty S. E. (1995) Upper Mantle Mineralogy. *Journal of Geodynamics* **20** (4), 331-364.
- Harry D. L. and Green Nathan L. (1999) Slab dehydration and basalt petrogenesis in subduction systems involving very young oceanic lithosphere. *Chemical Geology* **160**, 309-333.
- Hart S. and Zindler A. (1986) In search of a bulk-earth composition. *Chemical Geology* **57**, 247-267.
- Hart S. R. and Staudigel H. (1989) Isotopic characterization and identification of recycled components. In *Crust/Mantle Recycling at Convergent Zones* (Ed. by S. R. Hart and L. Gülen), pp. 15-28. NATO ASI Series C: Mathematical and Physical Sciences, vol. 258. Kluwer Academic Publishers, Dordrecht, Netherlands.

- Harte B. (1983) Mantle peridotites and processes - the kimberlite sample. In *Continental basalts and mantle xenoliths* (Ed. by C. Hawkesworth and M. Norry), pp. 46-91. Shiva Publishing, Nantwich, Cheshire.
- Hawkesworth C., Gallagher K., Hergt J., and McDermott F. (1994) Destructive plate margin magmatism: Geochemistry and melt generation. *Lithos* **33**, 169-188.
- Hawkesworth C., Gallagher K., Hergt J., and McDermott F. (1993) Mantle and slab contributions in arc magmas. *Annual Review of Earth and Planetary Sciences* **21**, 175-204.
- Herrstrom E., Reagan M., and Morris J. (1995) Variations in lava compositions associated with flow of asthenosphere beneath southern Central America. *Geology* **23**, 617-620.
- Herzberg C. T. (1993) Lithosphere peridotites of the Kaapvaal craton. *Earth and Planetary Science Letters* **120**, 13-29.
- Herzberg C. T. (2004) Geodynamic Information in Peridotite Petrology. *Journal of Petrology* **45** (12), 2507-2530.
- Herzberg C. T. and O'Hara M. (2002) Plume-associated ultramafic magmas of Phanerozoic age. *Journal of Petrology* **43**, 1857-1883.
- Hewins R. H. (1974) Pyroxene Crystallization Trends and Contrasting Augite Zoning in the Sudbury Nickel I eruptive. *American Mineralogist* **59**, 120-126.
- Hirschmann M., Ghiorso M., Wasylenski L., Asimow P., and Stolper E. (1998) Calculation of Peridotite Partial Melting from Thermodynamic Models of Minerals and Melts I. Review of Methods and Comparison with Experiments. *Journal of Petrology* **39** (6), 1091-1115.
- Hochstaedter A. G., Kepezhinskas P., Defant M., Drummond M., and Koloskov A. (1996) Insights into the volcanic arc mantle wedge from magnesian lavas from the Kamchatka arc. *Journal of Geophysical Research* **101** (B1), 697-712.
- Hoernle K., Abt D. L., Fischer K. M., Nichols H., Hauff F., Abers G. A., van den Bogaard P., Alvarado G., Protti M., and Strauch W. (2008) Arc-parallel flow in the mantle wedge beneath Costa Rica and Nicaragua. *Nature* **451**, 1094-1097.
- Hofmann A. (1988) Chemical differentiation of the Earth: the relationship between mantle, continental crust, and oceanic crust. *Earth and Planetary Science Letters* **90**, 297-314.
- Hofmann A. (1997) Mantle geochemistry: the message from oceanic volcanism. *Nature* **385**, 220-229.
- Hradecky P. (1987) *Geología del Volcán Mombacho y sus Alrededores*. Instituto Nicaraguense de Estudios Territoriales. Instituto Nicaraguense de Estudios Territoriales, Managua. 47pp.
- Hutchison R. (1974) The formation of the Earth. *Nature* **250** (5467), 556-558.
- Irvine T. a. B., W.R.A. (1971) A guide to the chemical classification of the common volcanic rocks. *Canadian Journal of Earth Sciences* **8**, 523-548.
- Ishimaru S., Arai S., Ishida Y., Shirasaka M., and Okrugin V. M. (2007) Melting and Multi-stage Metasomatism in the Mantle Wedge beneath a Frontal Arc Inferred from Highly Depleted Peridotite Xenoliths from Avacha Volcano, Southern Kamchatka. *Journal of Petrology* **48** (2), 180-199.
- Jaques A. and Green D. (1980) Anhydrous melting of peridotite at 0 - 15 Kb pressure and genesis of tholeiitic basalts. *Contributions to Mineralogy and Petrology* **73**, 287-310.
- Johnson K. and Dick H. (1992) Open system melting and temporal and spatial variation of peridotite and basalt at the Atlantis II fracture zone. *Journal of Geophysical Research* **97**, 9219-9241.
- Johnson K., Dick H., and Shimizu N. (1990) Melting in the oceanic upper mantle: An ion microprobe study of diopsides in abyssal peridotites. *Journal of Geophysical Research* **95**, 2661-2678.
- Johnston S. and Thorkelson D. (1997) Cocos-Nazca slab window beneath Central America. *Earth and Planetary Science Letters* **146**, 465-474.
- Kelemen P., Hart S. R., and Bernstein S. (1998) Silica enrichment in the continental upper mantle via melt/rock reaction. *Earth and Planetary Science Letters* **164**, 387-406.

- Kelemen P., Shumizu N., and Dunn J. (1993) Relative depletion of niobium in some arc magmas and the continental crust: Partitioning of K, Nb, La and Ce during melt/rock reaction in the upper mantle. *Earth and Planetary Science Letters* **120**, 111-133.
- Kelemen P. B., Johnson K., Kinzler R., and Irving A. (1990) High-field-strength element depletions in arc basalts due to mantle-magma interaction. *Nature* **345**, 521-524.
- Kepezhinskas P. and Defant M. J. (2001) Nonchondritic Pt/Pd ratios in arc mantle xenoliths: Evidence for platinum enrichment in depleted island-arc mantle sources. *Geology* **29** (9), 851-854.
- Keppler H. (1996) Constraints from partitioning experiments on the composition of subduction-zone fluids. *Nature* **380**, 237-240.
- Kinzler R. (1997) Melting of mantle peridotite at pressures approaching the spinel to garnet transition: Application to mid-ocean ridge petrogenesis. *Journal of Geophysical Research* **102** (B1), 853-874.
- Kinzler R. and Grove T. (1992) Primary magmas of mid-ocean ridge basalts 2. Applications. *Journal of Geophysical Research* **97**, 6907-6926.
- Kogiso T., Tatsumi Y., and Nakano S. (1997) Trace element transport during dehydration processes in the subducted oceanic crust; 1, Experiments and implications for the origin of ocean island basalts. *Earth and Planetary Science Letters* **148** (1-2), 193-205.
- Kohut E. J., Kent A. J., and Bloomer S., H. (2006) Evidence for adiabatic decompression melting in the Southern Mariana Arc from high-Mg lavas and melt inclusions. *Contributions to Mineralogy and Petrology* **152**, 201-221.
- Laurora A., Mazzucchelli M., Rivalenti G., Vannucci R., Zanetti A., Barbieri M. A., and Cingolani C. A. (2001) Metasomatism and Melting in Carbonated Peridotite Xenoliths form the Mantle Wedge: The Gobernador Gregores Case (Southern Patagonia). *Journal of Petrology* **42** (1), 69-87.
- Leeman W. P., Carr M. J., and Morris J. D. (1994) Boron geochemistry of the Central American Volcanic Arc: Constraints on the genesis of subducted-related magmas. *Geochimica et Cosmochimica Acta* **58**, 149-168.
- Li Z.-X. and Lee C.-T. (2004) The constancy of upper mantle  $fO_2$  through time inferred from V/Sc ratios in basalt. *Earth and Planetary Science Letters* **228**, 483-493.
- Lindsay F. N., Bolge L. L., Carr M. J., and Feigenson M. D. (2004) Geochemistry of Concepcion and Maderas volcanoes, Nicaragua, Central America. In *Eos, Transactions*, pp. V13B-1483. AGU fall meeting, vol. 85. American Geophysical Union.
- McBirney A. R. (1969) Compositional variations in Cenozoic calc-alkaline suites of Central America. *Bulletin - Oregon Department of Geology and Mineral Industries Report* **16**, 186-189.
- McBirney A. R. and Williams H. (1965) *Volcanic History of Nicaragua*. University of California Press, Berkeley, CA, USA.
- McCulloch M. T. and Gamble A. (1991) Geochemical and geodynamical constraints on subduction zone magmatism. *Earth and Planetary Science Letters* **102** (3-4), 358-374.
- McDonough W. and Frey F. A. (1990) Rare earth elements in upper mantle rocks. In *Geochemistry and Mineralogy of Rare Earth Elements* (Ed. by B. Lipin and G. McKay), pp. 99-145. Reviews in Mineralogy, vol. 21. Mineralogical Society of America.
- McDonough W. and Sun S. (1995) The composition of the Earth. *Chemical Geology* **120** (3-4), 223-253.
- McInnes B., I.A., Gregoire M., Binns R. A., Herzig P., M., and Hannington M. D. (2001) Hydrous metasomatism of oceanic sub-arc mantle. Lihir, Papua New Guinea: petrology and geochemistry of fluid-metasomatised mantle wedge xenoliths. *Earth and Planetary Science Letters* **188**, 169-183.
- Miller M., Gorbatov A., Kennett B., Stern R., and Gvirtzman Z. (2004) Tear in the subducting slab beneath the Southern Mariana Arc: evidence from P-wave Tomography. *Eos Transactions* **85**.

- Morris J. D., Leeman W. P., and Tera F. (1990) The subducted component in island arc lavas: constraints from Be isotope and B-Be systematics. *Nature* **344**, 31-36.
- Mullen E. D. (1983) MnO/TiO<sub>2</sub>/P<sub>2</sub>O<sub>5</sub>; a minor element discriminant for basaltic rocks of oceanic environments and its implications for petrogenesis. *Earth and Planetary Science Letters* **62** (1), 53-62.
- Müntener O., Kelemen P. B., and Grove T. L. (2001) The role of H<sub>2</sub>O during crystallization of primitive arc magmas under uppermost mantle conditions and genesis of igneous pyroxenites: an experimental study. *Contributions to Mineralogy and Petrology* **141**, 643-658.
- Mysen B. O., Ulmer P., Konzett J., and Schmidt M. W. (1998) The Upper Mantle Near Convergent Plate Boundaries. In *Ultrahigh-Pressure Mineralogy*, pp. 98-138. Reviews in Mineralogy, vol. 37. Mineralogical Society of America.
- Nell J. and Wood B. J. (1991) High-temperature electrical measurements and thermodynamic properties of Fe<sub>3</sub>O<sub>4</sub>-FeCr<sub>2</sub>O<sub>4</sub>-MgCr<sub>2</sub>O<sub>4</sub>-FeAl<sub>2</sub>O<sub>4</sub> spin. *American Mineralogist* **76**, 405-426.
- Niu Y., O'Hara M., and Pearce J. (2003) Initiation of subduction zones as a consequence of lateral compositional buoyancy contrast within the lithosphere: a petrological perspective. *Journal of Petrology* **44**, 851-866.
- Noll P., Newsom H., Leeman W. P., and Ryan J. (1996) The role of hydrothermal fluids in the production of subduction zone magmas: Evidence from siderophile and chalcophile trace elements and boron. *Geochimica et Cosmochimica Acta* **60**, 587-612.
- Obando J. (1995) Estudio geológica del Arco de Sarapiquí: Contribución a las nuevas exploraciones mineras de la región. *Placer Dome de Costa Rica (Informe interno)* 74pp.
- Ohtani E., Asahara Y., Suzuki A., and Moro N. (1997) A link between cratonic peridotite and komatiite: experimental evidence for melting of wet archean mantle. *Eos Transactions* **78**, 46American Geophysical Union.
- O'Neill H. S. C. and Wood B. (1979) An experimental study of Fe-Mg partitioning between garnet and olivine and its calibration as a geothermometer. *Contributions to Mineralogy and Petrology* **70**, 59-70.
- Parkinson I. J., Arculus R. J., and Eggins S. M. (2003) Peridotite xenoliths from Grenada, Lesser Antilles Island Arc. *Contributions to Mineralogy and Petrology* **146**, 241-262.
- Parkinson I. J. and Pearce J. (1998) Peridotites from Izu-Bonin-Mariana Forearc (ODP Leg 125): Evidence for Mantle Melting and Melt-Mantle Interaction in a Supra-Subduction Zone Setting. *Journal of Petrology* **39** (9), 1577-1618.
- Parkinson I. J. and Arculus R. J. (1999) The redox state of subduction zones: insights from arc-peridotites. *Chemical Geology* **160**, 409-423.
- Parlak O., Höck V., and Delaloye M. (2002) The supra-subduction zone Pozanti-Karsanti ophiolite, southern Turkey: evidence for high-pressure crystal fractionation of ultramafic cumulates. *Lithos* **65**, 205-224.
- Patino L. C., Carr M. J., and Feigenson M. D. (2000) Local and regional variations in Central American arc lavas controlled by variations in subducted sediment input. *Contributions to Mineralogy and Petrology* **138**, 265-283.
- Patino L. C., Velbel M. A., Price J. R., and Wade J. A. (2003) Trace element mobility during spheroidal weathering of basalts and andesites in Hawaii and Guatemala. *Chemical Geology* **202** (3-4), 343-364.
- Peacock S., Rushmer T., and Thompson A. B. (1994) Partial melting of subducting oceanic crust. *Earth and Planetary Science Letters* **121**, 227-244.
- Peacock S., M., van Keken P. E., Holloway S. D., Hacker B. R., Abers G. A., and Fergason R. L. (2005) Thermal structure of the Costa Rica - Nicaragua subduction zone. *Physics of the Earth and Planetary Interiors* **149**, 187-200.
- Pearce J. and Peate D. (1995) Tectonic implications of the composition of volcanic arc magmas. *Annual Review of Earth and Planetary Sciences* **23**, 251-285.

- Peccerillo A. and Taylor S. (1976) Geochemistry of Eocene calc-alkaline volcanic rocks from Kastamonu area, northern Turkey. *Contributions to Mineralogy and Petrology* **58** (1), 63-81.
- Peslier A. H., Francis D., and Ludden J. (2002) The Lithospheric Mantle beneath Continental Margins: Melting and Melt-Rock Reaction in Canadian Cordillera Xenoliths. *Journal of Petrology* **43** (11), 2013-2047.
- Plank T. and Langmuir C. H. (1988) An evaluation of the global variations in the major element chemistry of arc basalts. *Earth and Planetary Science Letters* **90** (4), 349-370.
- Plank T. and Langmuir C. H. (1998) The chemical composition of subducting sediment and its consequences for the crust and mantle. *Chemical Geology* **145** (3-4), 325-394.
- Portnyagin M., Hoernle K., Avdeiko G., Hauff F., Werner R., Bindeman I., Uspensky V., and Garbe-Schönberg D. (2005) Transition from arc to oceanic magmatism at the Kamchatka-Aleutian junction. *Geology* **33** (1), 25-28.
- Protti M., Guendel F., and McNally K. (1995) Correlation between the age of the subducting Cocos Plate and the geometry of the Wadati-Benioff zone under Nicaragua and Costa Rica. In *Geologic and tectonic development of the Caribbean Plate boundary in southern Central America* (Ed. by P. Mann), pp. 309-326. Geological Society of America, USA.
- Reagan M. K., Morris J. D., Herrstrom E. A., and Murrell M. T. (1994) Uranium series and beryllium isotope evidence for an extended history of subduction modification of the mantle below Nicaragua. *Geochimica et Cosmochimica Acta* **58** (19), 4199-4212.
- Richardson S., Erlank A., and Hart S. (1985) Kimberlite-borne garnet peridotite xenoliths from old enriched subcontinental lithosphere. *Earth and Planetary Science Letters* **75**, 116-128.
- Ringwood A. (1969) Composition and evolution of the upper mantle. In *The Earth's Crust and Upper Mantle* (Ed. by P. Hart), pp. 1-17. Geophysical Monograph, vol. 13. American Geophysical Union.
- Rudnick R. L., McDonough W. F., and Chappell B. W. (1993) Carbonatite metasomatism in the northern Tanzanian mantle: Petrographic and geochemical characteristics. *Earth and Planetary Science Letters* **114** (4), 463-475.
- Rüpke L., Morgan J. P., Hort M., and Connolly J. A. (2002) Are the regional variations in Central American arc lavas due to differing basaltic versus peridotitic slab sources of fluids? *Geology* **30** (11), 1035-1038.
- Ryan C., Griffin W., and Pearson N. (1996) Garnet geotherms: Pressure-temperature data from Cr-pyrope garnet xenocrysts in volcanic rocks. *Journal of Geophysical Research* **101**, 5611-5626.
- Rymer H., van Wyk de Vries B., Stix J., and Williams-Jones G. (1998) Pit crater structure and processes governing persistent activity at Masaya Volcano, Nicaragua. *Bulletin of Volcanology* **59** (5), 345-355.
- Sapper K. (1916) Alte und neue Bilder des Masaya und Momotombo [volcanoes, Nicaragua]. *Zeitschrift für Vulkanologie* **2** (4), 226-231.
- Sarbas B. (2008) The GEOROC database as part of a growing geoinformatics network. In *Geoinformatics 2008 - Data to Knowledge* (Ed. by S. Brady, A. Sinha, and L. Gunderson), pp. 42-43. Proceedings: U.S. Geological Survey Scientific Investigations Report, no. 2008-5172.
- Sisson T. and Bronto S. (1998) Evidence for pressure-release melting beneath magmatic arcs from basalt at Galunggung, Indonesia. *Nature* **391**, 883-886.
- Sisson T. and Layne G. (1993) H<sub>2</sub>O in basalt and basaltic andesite glass inclusions from four subduction related volcanoes. *Earth and Planetary Science Letters* **117**, 619-635.
- Spiedel D. and Osborn E. (1967) Element distribution among coexisting phases in the system MgO-FeO-Fe<sub>2</sub>O<sub>3</sub>-SiO<sub>2</sub> as a function of temperatures and oxygen fugacity. *American Mineralogist* **52**, 1139-1152.
- Stalder R., Foley S., Brey G., and Horn I. (1998) Mineral-aqueous fluid partitioning of trace elements at 900-1200 degrees C and 3.0-5.7 GPa; new experimental data for garnet,

- clinopyroxene, and rutile, and implications for mantle metasomatism. *Geochimica et Cosmochimica Acta* **62** (10), 1781-1801.
- Stoiber R. and Carr M. (1973) Quaternary volcanic and tectonic segmentation of Central America. *Bulletin of Volcanology* **37**, 304-325.
- Stolper E. and Newman S. (1994) The role of water in the petrogenesis of Mariana trough magmas. *Earth and Planetary Science Letters* **121**, 293-325.
- Sun S. and McDonough W. (1989) Chemical and isotopic systematics of oceanic basalts: implications for mantle composition and processes. In *Magmatism in the Ocean Basins* (Ed. by A. Saunders and M. Norry), pp. 313-345. Geology Society Special Publication, vol. 42.
- Sussman D. (1985) Apoyo caldera, Nicaragua: A major quaternary silicic eruptive center. *Journal of Volcanology and Geothermal Research* **24** (3-4), 249-282.
- Syracuse E. M. and Abers G. A. (2006) Global compilation of variations in slab depth beneath arc volcanoes and implications. *Geochemistry Geophysics Geosystems* **7** (5), 18.
- Takahashi E. (1980) Thermal history of Iherzolite xenoliths: I. Petrology of Iherzolite xenoliths from Ichinomegata crater, Oga peninsula, northeast Japan. *Geochimica et Cosmochimica Acta* **44**, 1643-1658.
- Takazawa E., Frey F. A., Shumizu N., and Obata M. (2000) Whole rock compositional variations in an upper mantle peridotite (Horoman, Hokkaido, Japan): Are they consistent with a partial melting process? *Geochimica et Cosmochimica Acta* **64** (4), 695-716.
- Tamura A. and Arai S. (2006) Geochemistry of clinopyroxene in peridotites from the Nukabira complex, Kamuikotan zone, Hokkaido, Japan: a LA-ICP-MS study. *Science Reports of Kanazawa University* **50**, 1-27.
- Tatsumi Y., Hamilton D. L., and Nesbitt R. W. (1986) Chemical characteristics of fluid phase released from a subducted lithosphere and origin of arc magmas; evidence from high-pressure experiments and natural rocks. *Journal of Volcanology and Geothermal Research* **29** (1-4), 293-309.
- Tatsumi Y. and Kogiso T. (1997) Trace element transport during dehydration processes in the subducted oceanic crust: 2. Origin of chemical and physical characteristics in arc magmatism. *Earth and Planetary Science Letters* **148**, 207-221.
- Thirwall M., Smith T., Graham A., Theodorou N., Hollings P., and Arculus R. (1994) High field strength element anomalies in arc lavas; source or process? *Journal of Petrology* **35** (3), 819-838.
- Tournon J. and Alvarado G. (1997) *Mapa Geológico de Costa Rica. Scale 1:500,000*. Editorial Tecnológica de Costa Rica, Cartago-Costa Rica.
- Tournon J., Seyder M., and Astorga A. (1995) Les peridotites du río San Juan (Nicaragua et Costa Rica): jalons d'une suture ultrabasique E-W en Amérique Centrale Meridionale. *Les Comptes Rendus de l'Académie des sciences* **320** (I), 757-764.
- Ui T. (1972) Recent Volcanism in Masaya-Granada Area, Nicaragua. *Bulletin volcanologique: organe de la Section de volcanologie de l'Union GeoDesique et Geophysique internationale* **36**, 174-190.
- van Wyk de Vries B. (1993) Tectonics and Magma Evolution of Nicaraguan Volcanic Systems. diss, pp. 328pp. The Open University, Department of Earth Sciences.
- van Wyk de Vries B., Kerle N., and Petley D. (2000) Sector collapse forming at Casita Volcano, Nicaragua. *Geology* **28** (2), 167-170.
- Vannucci R., Tiepolo M., Defant M., and Kepezhinskis P. (2007) The metasomatic record in the shallow peridotite mantle beneath Grenada (Lesser Antilles arc). *Lithos* **99**, 25-44.
- Vargas F. and Alfaro A. (1992) Presencia de serpentinitas, basaltos alcalinos y rocas volcánicas en la zona norte-atlántica de Costa Rica. *Revista Geológica de América Central* **14**, 105-107.
- Vaselli O., Downes H., Thirwall M., Dobosi G., Coradossi N., Seghedi I., and Szakacs A. V., R. (1995) Ultramafic Xenoliths in Plio-Pleistocene Alkali Basalts from the Eastern Transylvanian Basin: Depleted Mantle Enriched by Vein Metasomatism. *Journal of Petrology* **36** (1), 23-53.

- Walker J. A. (1984) Volcanic rocks from the Nejapa and Granada cinder cone alignments, Nicaragua, Central America. *Journal of Petrology* **25** (2), 299-342.
- Walker J. A., Carr M. J., Feigenson Mark D., and Kalamides R. (1990) The petrogenetic significance of inter-stratified high- and low-Ti basalts of Central Nicaragua. *Journal of Petrology* **31**, 1141-1164.
- Walker J. A., Patino L. C., Carr M. J., and Feigenson M. D. (2001) Slab control over HFSE depletions in central Nicaragua. *Earth and Planetary Science Letters* **192**, 533-543.
- Walker J. A., Williams S., N., Kalamides R. I., and Feigenson M. D. (1993) Shallow open-system evolution of basaltic magma beneath a subduction zone volcano: the Masaya Caldera Complex, Nicaragua. *Journal of Volcanology and Geothermal Research* **56**, 379-400.
- Walter M. (1998) Melting of garnet peridotite and the origin of komatiite and depleted lithosphere. *Journal of Petrology* **39**, 29-60.
- Wang J., Hattori K. H., Kilian R., and Stern C. R. (2007) Metasomatism of sub-arc mantle peridotites below southernmost South America: reduction of  $fO_2$  by slab-melt. *Contributions to Mineralogy and Petrology* **153**, 607-624.
- Werner R., Hoernle K., Barckhausen U., and Hauff F. (2003) Geodynamic evolution of the Galápagos hot spot system (Central East Pacific) over the past 20 m.y.: Constraints from morphology, geochemistry and magnetic anomalies. *Geochemistry Geophysics Geosystems* **4** (12), 28pp.
- Weyl R. (1980) *Geology of Central America*. Gebruder Borntraeger, Berlin - Stuttgart.
- White W. M. (1998) *Geochemistry*. <http://www.geo.cornell.edu/geology/classes/geo455/Chapters.HTML>, 2007. Cornell University.
- White W. M. and Dupré B. (1986) Sediment subduction and magma genesis in the Lesser Antilles; isotopic and trace element constraints. *Journal of Geophysical Research* **91** (B6), 5927-5941.
- Wilson M. (1989) *Igneous Petrogenesis*. Chapman & Hall, London.
- Witt-Eickschen G. and Seck H. (1991) Solubility of Ca and Al in orthopyroxene from spinel peridotite: an improved version of an empirical geothermometer. *Contributions to Mineralogy and Petrology* **106**, 431-439.
- Wood B., Bryndzia L., and Johnson K. (1990) Mantle oxidation state and its relationship to tectonic environment and fluid speciation. *Science* **248**, 337-345.
- Wood B. and Virgo D. (1989) Upper mantle oxidation state: ferric iron contents of Iherzolite spinels by  $^{57}\text{Mössbauer}$  spectroscopy and resultant oxygen fugacities. *Geochimica et Cosmochimica Acta* **53** (1277-1291).
- Woodhead J., Eggins S., and Gamble J. (1993) High field strength and transition element systematics in island arc and back-arc basin basalts; evidence for multi-phase melt extraction and a depleted mantle wedge. *Earth and Planetary Science Letters* **114** (4), 491-504.
- Yogodzinski G., Bailey D., Volynets O., Braitseva O., Sulerzhitsky L., Melekestev I., Churikova T., and Kay R. (1993) Ultramafic xenoliths and melt-peridotite interaction in a calc-alkaline igneous system; examples form Avachinsky volcano, eastern Kamchatka. *EOS* **74**, 679.
- Yogodzinski G., Lees J., Churikova T., Dorendorf F., Wörner G., and Volynets O. (2000) Geochemical evidence for the melting of subducting oceanic lithosphere at plate edges. *Nature* **409**, 500-504.
- You C.-F. and Gieskes J. M. (2001) Hydrothermal alteration of hemi-pelagic sediments; experimental evaluation of geochemical processes in shallow subduction zones. *Applied Geochemistry* **16** (9-10), 1055-1066.
- Zindler A. and Hart S. R. (1986) Chemical geodynamics. *Annual Review of Earth and Planetary Sciences* **14**, 493-571.

## Curriculum Vitae

Fara N. Lindsay

**Education:**

Presently - Doctoral candidate in Geochemistry, Geological Sciences, Rutgers University;

\* Graduate Advisor: Michael J. Carr

9/1995 -1/2000: B.S./B.A. with high honors in Geology/Chemistry, Rutgers University

1/1992-5/1992: Graduate Courses in Technical Writing, Fairleigh Dickinson University, NJ

9/1982-12/1983: B.A. with honors in General Studies-conc. Movement Analysis, SUNY, NY

6/1980-5/1982: Undergraduate Courses in Chemical Engineering, Union County College, NJ

9/1978-5/1980: Undergraduate Courses in Theatre Arts, Webster University, MO

**Occupation:**

09/2008: Research assistant – Cosmochemistry, Rutgers University, Piscataway, NJ  
Meteorite petrography; noble gas analyses

01/2008: Assistant technician – Rutgers University Microanalysis Lab, Piscataway, NJ  
Oversee installation, training, running JXA8200 Superprobe

09/2007: Adjunct Faculty – School of Earth and Environmental Sciences, Queens College, NYC

06/2007: Lecturer of Earthquakes & Volcanoes – Rutgers University, Piscataway, NJ

06/2004: Petrological Consultant – Steven's Institute of Technology, Hoboken, NJ

2004-2007: Geochemical clean-lab coordinator; duties include purchasing, reagent make-up,  
equipment maintenance, training, waste handling

1999 – 2001; 2004 – 2008: Research Assistant – Geological Sciences, Rutgers University,  
organization and upkeep of mineral, rock and thin section collections

Substitute Lecturer – Mineralogy, Rutgers University, NJ

Teaching Assistant – Geological Sciences, Rutgers University, NJ

Instructor: Introductory Geology Laboratory, Mineralogy/Petrology  
Laboratory, Petrology Laboratory

1998: Research internship – Institute of Marine and Coastal Sciences, Rutgers University, NJ  
\* PI – Dr. R. Sherrell

Filter digestion and analysis of oceanic sediments via HR-ICP-MS

1997: Research internship – Lamont-Doherty Earth Observatory, NY

\* PI – Dr. G. Henderson

Sediment digestion and subsequent silver-plating for  $\alpha$ -counting

**Publications:**

*Peer Reviewed*

Lindsay, F.N. & Carr, M.J., Occurrence of slab signature minimum in front-arc lavas of  
Isla de Ometepe, Nicaragua: evidence from Concepción and Maderas volcanoes, *In  
Preparation*

Bolge, L.L., Carr, M.J., Milidakis, K.I., Lindsay, F.N. and Feigenson, M.D., Correlating Tectonics, Geochemistry, and Volcanic Volume along the Central America Volcanic Front, *Geochemistry, Geophysics, Geosystems, Submitted*

Carr, M.J., Saginor, I., Alvarado, G.E., Bolge, L.L., Lindsay, F.N., Turrin, B., Feigenson, M.D. and Swisher III, C.C., Element fluxes from the Volcanic Front of Nicaragua and Costa Rica, *Geochemistry, Geophysics, Geosystems*, **8**, doi:10.1029/2006GC001396, 2007

Henderson, G.M., Lindsay, F.N. & Slowey, N.C., Variation in bioturbation with water depth on marine slopes: a study on the Little Bahamas Bank, *Marine Geology*, **160:105-118**, 1999.

#### *Talks*

Lindsay, F.N., Gazel, E., Herzberg, C.T., Carr, M.J. and Feigenson, M.D., Xenoliths of Cerro las Mercedes, Costa Rica: a Record of Arc History?, *AGU Fall Meeting*, 2006.

#### *Abstracts and Invited Posters*

Lindsay, F.N., Carr, M.J. and Feigenson, M.D., Decompression melting behind a major offset of the volcanic front of Nicaragua: Concepción and Maderas volcanoes, *GSA NC Spring Meeting*, 2009

Lindsay, F.N., Gazel, E., Herzberg, C.T., Carr, M.J. and Feigenson, M.D., Insights into the mantle underlying northern Costa Rica: evidence from xenoliths of Cerro las Mercedes, *Workshop to Integrate Subduction Factory and Seismogenic Zone Studies in Central America*; Costa Rica, 2007

Bolge, L.L., Carr, M.J., Feigenson, M.D., Lindsay, F.N. and Milidakis, K., High Field Strength Elements Reflect Segmentation of the Central American Volcanic Front, *AGU Fall Meeting*, 2006.

Lindsay, F.N., Bolge, L.L., Carr, M.J. & Feigenson, M.D., Geochemistry of Concepción and Maderas Volcanoes, Nicaragua, Central America, *AGU Fall Meeting*, 2004.

Lindsay, F.N., Carr, M.J. & Feigenson, M.D., Mantle Xenoliths of Cerro Mercedes, Costa Rica, Central America, *AGU Fall Meeting*, 2003.

Lindsay, F.N., Carr, M.J. & Feigenson, M.D., Contrasts in Subduction Signal between Southeastern and Northwestern Nicaragua, *AGU Fall Meeting*, 2001.

Lindsay, F.N., Carr, M.J. & Feigenson, M.D., Preliminary Data of Geochemical Signatures in Southeastern Nicaragua, *Subduction Factory Workshop*, Costa Rica, 2001.

Field, M.P., Sherrell, R.M., Rosenthal, Y. & Lindsay, F., Novel Applications of High Resolution Sector Field Inductively Coupled Plasma Mass Spectrometry to Problems in Chemical Oceanography, *AGU Fall Meeting*, 1998.